Homo- and Heterometallic Polyyne Complexes: Synthesis and Characterisation

Robinson, Thomas

Award date:
2013

Awarding institution:
University of Bath

Homo- and Heterometallic Polyyne Complexes: Synthesis and Characterisation

Thomas Peter Robinson

A thesis submitted for the degree of Doctor of Philosophy

University of Bath

Department of Chemistry

October 2013

University of Bath, October 2013

Abstract

The focus of this thesis is the development of conjugated homo- and heterometallic polyyne complexes for which the opto-electronic properties may be tuned to provide potential applications in molecular electronic devices.

Chapter 1 outlines the requirement of molecular systems for the development of the electronics industry, and describes the underlying chemistry of Pt-acetylide and $\{Mo_2\}$-carboxylate systems that makes them promising materials in this respect.

Chapter 2 describes the development of ester-functionalised Pt-acetylide complexes, representing potential building blocks for complicated heterometallic frameworks. The relationship between the opto-electronic properties of these materials and the identity of their ligand systems is explored both spectroscopically and theoretically.

Chapter 3 outlines the development of a series of conjugated heterometallic frameworks *via* the systematic assembly of appropriate Pt-acetylide and $\{Mo_2\}$-carboxylate building blocks. The combinative effects of the two metal fragments on the properties of the materials are investigated spectroscopically and electrochemically and theoretical studies provide a greater understanding of the electronic structures of the novel species.

Chapter 4 describes the design and syntheses of novel ethynyl-functionalised *bis*-amidine systems and their application as bridging ligands in a series of Ru-*bis*-amidinate complexes. The highly tuneable opto-electronic properties of these complexes are probed both spectroscopically and electrochemically and interesting solid-state packing interactions are explored.

Chapter 5 illustrates the diverse coordination chemistry of N-heterocyclic carbenes towards $\{Mo_2\}$ carboxylate dimers. Structural analyses provide an important insight into the different coordination modes that are available by tuning the steric demands of the carbene and reveal rare Mo-Aryl π-interactions. Spectroscopic analyses are implemented to illustrate the ability to tune the energy of the $Mo_2\delta \rightarrow Mo_2\delta^*$ electronic transition.

Chapter 6 presents preliminary results from the TR-IR spectroscopic analyses of several Pt-ethynyl-ester complexes and a mixed Pt-$\{Mo_2\}$ system. Attempts are made to identify ultra-fast charge transfer and charge redistribution processes following photo-excitation from the ground state.

Acknowledgements

Firstly I would like to thank my supervisors Paul Raithby and Andy Johnson for their help and support throughout my PhD and for giving me the freedom to develop my own chemistry, which has helped me to become a better chemist. I'd also like to thank the numerous members of the Johnson/Raithby group, past and present, who have provided a fantastic working environment and have all contributed to my work and my time in Bath. Special thanks to Simon Brayshaw and Sara Fuertes who were both instrumental in the progress of my research. My time at Bath would also have been no where near as enjoyable had it not been for the multitude of friends that have come and gone over the years and for each of them I am truly grateful.

A number of people have been invaluable in providing guidance on a number of techniques during my PhD. These include: John Lowe for his help and patience with NMR, Mary Mahon and Gabi Kociok-Köhn for their help with XRD, Frank Marken for introducing me to electrochemistry and Mike Towrie and the rest of the ULTRA team at the RCaH for their expertise in TR-IR spectroscopy.

Whilst I have been interested in science since an early age, I think significant thanks should go to my A-Level chemistry teacher Mrs Gottesman, for it was her enthusiasm and approach to teaching that made me want to continue the subject to a higher level. In the same light I want to thank Neil Burford and Mike Hill, for if it wasn't for the research projects under their supervision I would almost certainly not be where I am today.

I would like to extend special thanks to both of my parents, who have always supported/put up with me regardless of what I have wanted to do in life and have always been there for me during difficult times. I'd also like to thank Nick and Philippa, for providing welcome distractions whenever I visit.

Finally, I would like to thank my amazing fiancée Anna, whose love and support has always meant a lot to me. Thanks also to her parents and brother who have become like family to me.

Abbreviations

Å: Angstrom

^{t}Bu: *tertiary*-Butyl

cm^{-1}: Wavenumber

Cy: Cyclohexyl

°: Degree

^{o}C: Degrees Celsius

δ: Chemical Shift

ΔE_p: Separation between oxidation and reduction peaks

CIF: Crystallographic information file

d: Doublet

DCM: Dichloromethane

DFT: Density functional theory

Dipp: 2,6-diisopropylphenyl

DPTF: di-*p*-tolyl-formamidinate

ε: Extinction/absorption coefficient

$E_{1/2}$: Half-wave potential

e.s.d.s: Estimated standard deviations

eV: Electron Volts

Et: Ethyl

HOMO: Highest occupied molecular orbital

Hz: Hertz

$^{n}J_{a-b}$: Magnetic coupling though 'n' bonds between nuclei 'a' and 'b'

K: Degrees Kelvin

λ_{max}: Maxima of lowest energy absorption band

LED: Light Emitting Diode

LUMO: Lowest unoccupied molecular orbital

μ: Bridging coordination mode

μs: Microseconds

m: Multiplet

Me: Methyl, CH_3

Mes: Mesityl (2,4,6-trimethyphenyl)

MHz: Megahertz

Mp: Melting point

mV: Millivolts

NMR: Nuclear Magnetic Resonance

nm: Nanometres

ns: Nanoseconds

^{i}Pr: *iso*-Propyl

Ph: Phenyl

ppm: Parts Per Million

ps: Picoseconds

q: Quartet

R: Alkyl or aryl substituent

s: Singlet

sept: Septet

τ: Lifetime

t: Triplet

TD-DFT: Time-dependant density functional theory

THF: Tetrahydrofuran

TiPB: 2,4,6-triisopropylbenzoate

TMS: Trimethylsilyl

TR-IR: Time-resolved infrared

VT-NMR: Variable-temperature NMR

Declaration

The work described in this thesis was conducted by the author at the University of Bath between September 2009 and October 2013. It represents the author's original and independent work, except where specific reference is made to the contrary. Neither the whole nor any part of this thesis has been submitted previously in support of a degree at this or any other university. It does not exceed the prescribed limit, including tables, references and appendices.

Contents

Figures, Schemes and Tables

Chapter 1

Chapter 2

Chapter 3

Chapter 4

Chapter 5

Chapter 6

Chapter 1

Introduction

Chapter 1– Introduction

1.1.1 – Molecules for Electronic Devices

In the 1960s Gordon Moore projected that the electronics industry would develop following a trend that would see the number of transistors on an integrated circuit double very two years.[1] Now commonly known as 'Moore's Law', this projection has been largely accurate to the current day and has provided a driving force for the continued development in this field. However, the continued miniaturisation of silicon-based electronics is creating a number of problems suggesting that these systems are fast approaching their limit. These include spiralling manufacturing costs and increased heat generation from the small conducting components.

In light of these problems a lot of interest has been placed into the development of molecular systems that can be applied as components within electronic circuits or perform as devices in their own right. In contrast to silicon-based electronics, downsizing to a molecular level reduces resistivity. This is because these assemblies involve the movement of discreet numbers of electrons per molecule rather than mass electron flow. In addition to this, manufacture by synthesis provides a lot of scope for the tuning of molecules to perform a wide range of functions. Examples of potential applications include: molecule wires, [2-3] sensors,[4] switches,[5] LEDs[6] and optical limiting devices.[7]

In 1977 MacDiarmid reported that *n*- and *p*-type doping of polyacetylene resulted in conducting organic polymers though either electron or hole migration.[2-3] Since these pioneering studies a wide range of conjugated organic polymers have been developed, showing that their electronic structures are highly tuneable. In addition to conductive properties many examples, including the polythienyl[8-9] and substituted polyfluorenyl[10-11] examples in **Figure 1.1**, show semiconductor properties providing potential applications in devices such as transistors,[12-13] photodiodes,[14] photovoltaics[15] and LEDs.[6,16]

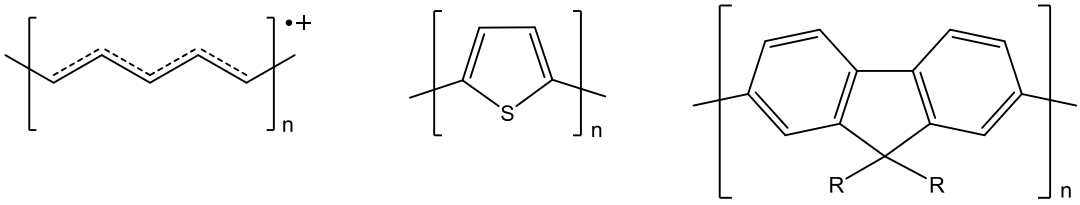

i **ii)** **iii)**

Figure 1.1: Examples of conjugated organic polymers including iodine-doped polyacetylene,[2] polythienylene[8-9] and polyfluorene[10-11] systems.

Whilst clearly providing a lot of promise towards the development of molecular electronic devices there are a number of drawbacks to purely organic systems. One point to consider is the low solubility of long chain organic material which makes processing them difficult. In addition to this, the nature of organic systems means that emissive processes are largely restricted to the singlet manifold due to the spin selection rule. Statistically this means that emissive devices can only be a maximum of 25 % efficient. A simplified Jablonski diagram is shown in **Figure 1.2** to aid this discussion.

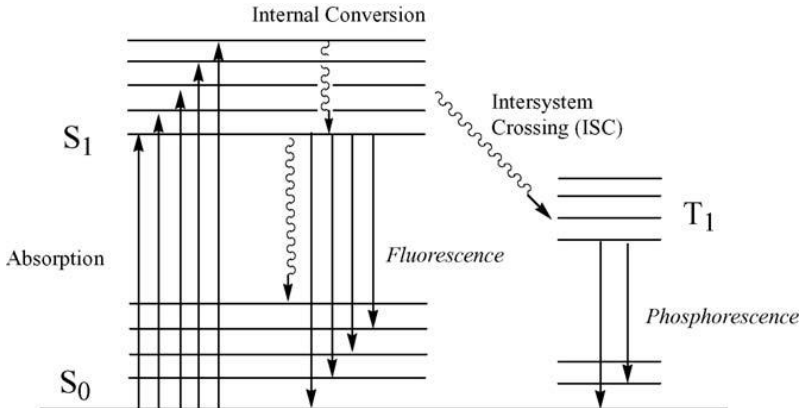

Figure 1.2: A simplified depiction of the excited state electronic dynamics of organic and organometallic polymers. [17]

The incorporation of metallic units into organic polymers and oligomers provides a broader scope with regards to tuning the optical and electronic properties of the materials and the identity of both the metals used and their associated ligand systems can be used to modify these properties. Spin-orbit coupling stemming from the use of heavy metal centres also relaxes the spin selection rule, thus facilitating efficient

population of the triplet states which is not possible in purely organic systems. This can potentially afford 100% emission efficiency.

A substantial range of organometallic polymers and oligomers have been reported in the literature using a variety of methods to include the metal fragments. Main-chain systems incorporate the metals directly into the extended network so that they effectively separate the organic components. The earliest examples were simple polyferrocene systems in which the iron atoms were sandwiched between organic chains (**Figure 1.3-i**).[18] More intricate example of these have since been reported.[19] The development of metal acetylide chemistry has expanded the field greatly and there are now many examples of redox-active (e.g. Fe, Ru, Os)[20-26] and electron-rich late transition metal (Pd, Pt, Hg, Au)[17,20,27-29] polymers and oligomers in which the metal bound directly within the σ- and π-bonded network (**Figures 1.3-ii** and **1.3-iii**). Other examples of main chain systems include the porphyrin complexes of Ziessel and Harriman.[30-31]

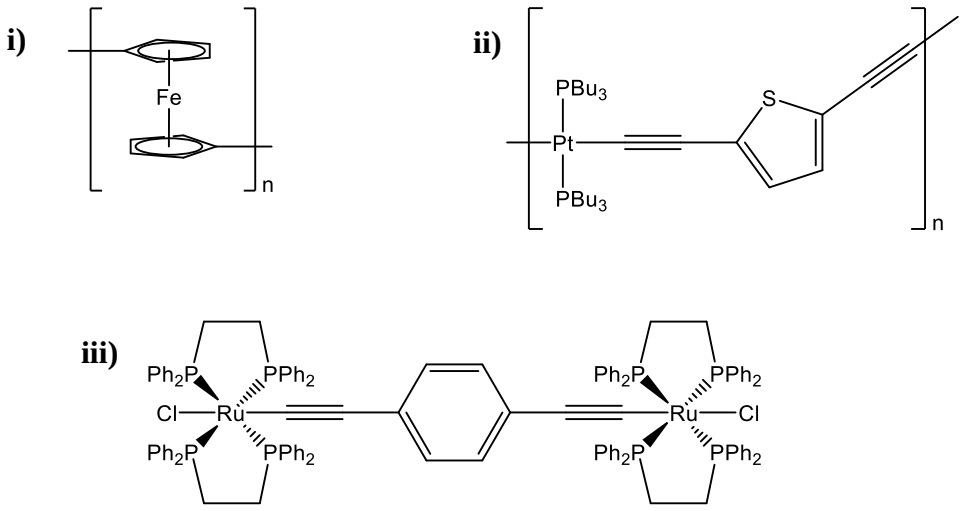

Figure 1.3: Ferrocene (**i**),[18] electron-rich Pt (**ii**)[27] and redox-active Ru (**iii**)[32] main-chain organometallic polymers and oligomers.

Metal centres can also be incorporated in the periphery of an unbroken organic chain. These so called 'side-chain' systems, often utilise Lewis-basic groups, which are part of the polymer/oligomer main chain, to coordinate the metals, such as the recent

pyridyl example shown in **Figure 1.4-i**.[33] Pendant metal-polyyne containing systems have also been reported in which the metal is bound to cyclobutadiene (**Figure 1.4-ii**), cyclopentadiene or arylene moieties within the organic chain.[34-35]

While this synopsis has focussed on examples in which metal containing moieties are part of a linear chain, it is important to recognise that many systems have also been developed into more complicated hyperbranched or dendritic frameworks.[36-39]

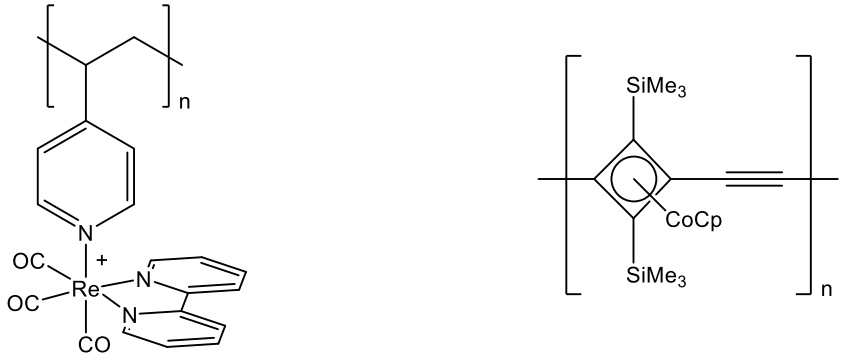

Figure 1.4: Examples of side-chain (**i**)[33] and polyene containing (**ii**)[35] organometallic polymers.

This discussion is by no means comprehensive and an in depth review is beyond the discussion of this thesis but is well documented within the literature.[17,19,40-47] The remainder of this introduction will focus on two classes of extended systems which contain Pt-acetylide and quadruply bonded $\{Mo_2\}/\{W_2\}$ units that allow us to put our own work into context.

1.1.2 – Platinum Acetylide Complexes

Our group has a long-standing interest in electron-rich late transition metal acetylide systems, specifically those incorporating Pt units in the form shown in **Figure 1.5**. This encompasses both polymeric material and shorter chain oligomeric systems. These phosphine stabilised species have potential applications in a range of molecular electronic devices including: LEDs, switches and molecular wires.[17,48] Non-linear optical properties in certain systems have also led to studies into their use as optical power limiting devices.[49-50]

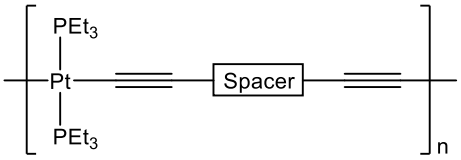

Figure 1.5: A generic phosphine-stabilised Pt-acetylide polymer

The relaxation of the spin selection rule in polymetallyne systems has allowed analysis of the photophysics of both singlet and triplet excited states, which has led to a greater understanding of conjugated polymers roles within emitting devices. The facile access of the triplet state also means that emission from metallated polymers is far more efficient and long-lived than organic analogues.

The first example of a platinum acetylide polymers was reported by Hagihara and was synthesised via the Cu-catalysed coupling of a Pt(II) di-bis-acetylene complex with a Pt(II) chloride reagent (**Scheme 1.1**). Later studies have shown that the same result could be achieved using only a diethynyl precursor and $(PR_3)PtCl_2$ but the Cu-catalysed coupling is still in regular use to this date. Alternative synthetic methods involving stannyl acetylides have also been proposed for systems that are sensitive to the amine solvent.[51]

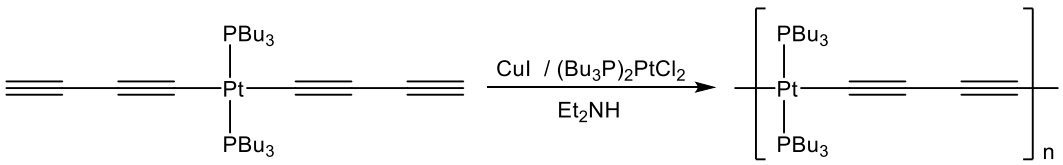

Scheme 1.1: The first reported synthesis of a Pt-acetylide polymer.[52-53]

In order to understand the properties of polymeric material and also to gain an insight into how their solid-state structure influence these properties it became clear that study of model oligomer complexes was required. These were synthesised by reacting the *bis*-acetylene ligands with a modified Pt precursor in which one chloride is replaced by an unreactive moiety, typically a phenyl ligand (**Scheme 1.2**). The nature of the spacer incorporated into these systems is extremely versatile and many examples have been reported and reviewed in the literature.[17,54-57] It should also be

mentioned that work has also be performed in the area of non-linear platinum acetylide oligomers and polymers utilising poly-ethynyl bridging groups.[39,58]

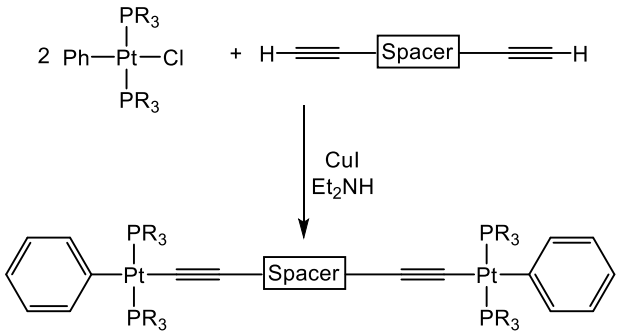

Scheme 1.2: Synthesis of Pt-acetylide oligomers. [27,59]

An attractive aspect of Pt-acetylide complexes is the relative ease by which their physical and electronic properties may be manipulated by varying the ligand systems. Altering the substituents on the phosphine ligands has been shown to have little electronic effect on the polymetallynes but can influence both their solubility and the solid-state structure. In contrast the electronic structure of these systems is very sensitive to the properties of the diethynyl bridging ligand. A simplified energy level diagram is shown in **Figure 1.6** to aid our discussion of these electronic effects.

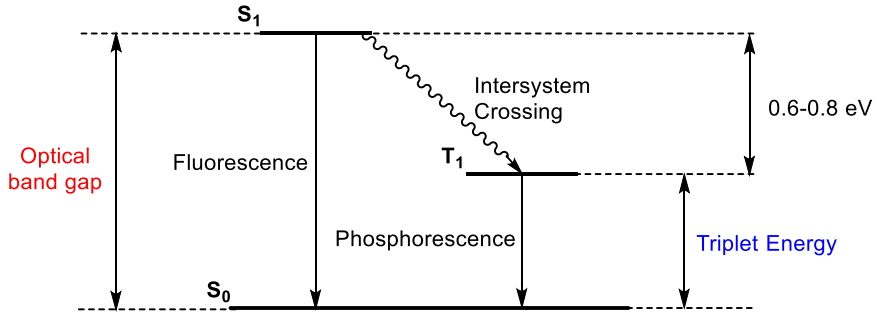

Figure 1.6: A simplified diagram showing the important energy level separations in a Pt-acetylide polymer

Studies into the electronic dynamics of a wide range of platinum acetylide systems have shown that the energy separation between the excited singlet (S_1) and triplet (T_1) states remain essentially constant (*ca*. 0.6-0.8 eV) regardless of the type of acetylide

spacer that is used.[60] Variation of the ligand system therefore perturbs the energies of both the singlet (S_1) and triplet (T_1) excited states relative to the singlet ground state (S_o). This affects both the efficiency and the wavelength of emission from both excited spin states and also influences the electronic communication throughout the extended system. A combination of theoretical and experimental studies have provided evidence that, whilst the singlet states are delocalised along the length of the extended system, the triplet state is largely localised within a single unit of the polymer. In the literature the term "optical band gap" is used as a parameter to describe the electronic perturbation within a polymetallyne. This specifically refers to the energy separation between the ground and excited singlet states in polymeric material in which valence and conducting bands can be envisaged. In a molecular system consisting of low numbers of repeating units this relates to the HOMO-LUMO energy gap.

Over the last two decades a large amount of research has taken place in this field. Pt-acetylide polymers and oligomers have been reported with a seemingly limitless variety of diethynyl bridging ligands providing a range of optical and electronic properties. A thorough discussion of many of these systems can be found in reviews in the literature[17,40,48] but for the purposes of this work we have selected specific examples to explain the relationship between the nature of the bridging ligand and the properties of the respective Pt-containing complex.

A significant factor in determining the energy of the band gap in Pt-acetylide systems is the degree of conjugation within diethynyl spacer ligands. Raithby *et al*. reported a series of Pt complexes containing phenylene, naphthalene and anthracene spacers.[57] The study showed that increasing the conjugation of the spacer resulted in a decrease in the optical bandgap and increased donor-acceptor interactions between metal and ligand. A separate study has shown that incorporation of a third acetylene unit in place of the polycyclic spacer results in a smaller optical band gap than was reported for the phenylene and naphthalene containing analogues.[61] This shows that the aryl spacers disrupt electronic conjugation, which has been attributed to the difference in energy between the acetylenic and aryl π-orbitals. These examples are shown in **Figure 1.7**.

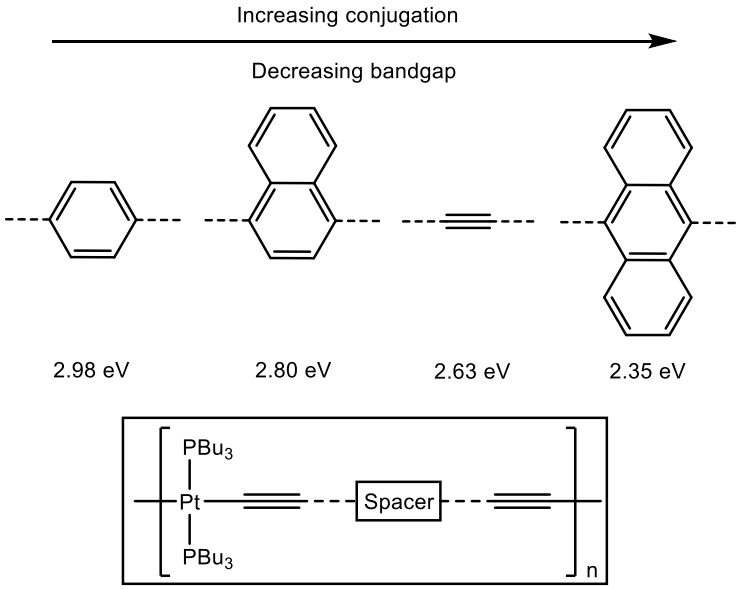

Figure 1.7: Some simple organic spacers and the bandgaps of their respective Pt polymers.[57,61-62]

The incorporation of heterocyclic spacers also provide a means by which the band gap energy may be tuned. Studies have shown that polymers containing thienyl spacer groups exhibit relatively low energy band gaps (2.80 eV) which has been attributed to the diffuse nature of the sulphur orbitals, providing greater π-orbital overlap.[62] By studying a range of Pt ethynyl-chalcogenophene oligomers, Wilson *et al*. showed that the HOMO-LUMO gap and the donor-acceptor interactions could be tuned by changing the identity of the chalcogen incorporated.[63] Upon descending the group from O to Te the onset of absorption was significantly red shifted and unusual long range heteronuclear coupling was observed in the NMR spectra of the heavier chalcogenide systems (**Figure 1.8**).[63]

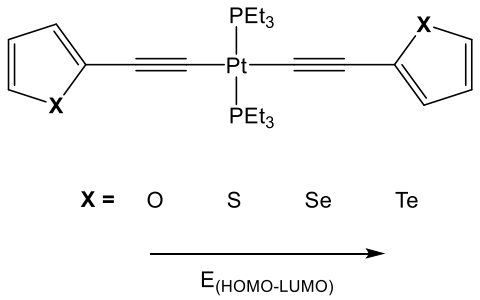

Figure 1.8: Diagram illustrating the decrease in the HOMO-LUMO energy gap in Pt-chalcogenophene species.[63]

A polymer with small optical band gap will promote efficient delocalisation of electron density between the Pt centres and the ligand systems. This is desirable for certain functions, such as molecular wires, but can be detrimental towards emission because low-lying triplet states can result in non-radiative decay. In terms of emission it is the systems in which the larger band gaps were observed that offer the strongest and most efficient phosphorescence. A study performed by Wong *et al*. showed that by introducing the conjugation disrupting units such as -CH_2-, -O-, -S-, -S(O)- and -$S(O)_2$-, the increase in optical bandgap was associated with efficient triplet state population and emission (**Figure 1.9**).[64-65] Separate studies have shown that silane spacers provide a stronger conjugation disrupting effect allowing access to even higher energy excited states (3.70 eV for a $SiPh_2$ spacer).[66]

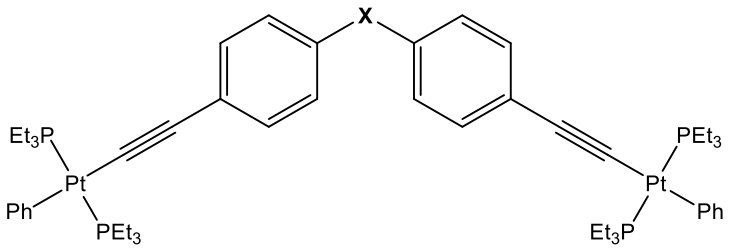

X =	none	CH_2	O	S	S(O)	$S(O)_2$
T_1-S_0 (eV)	2.29	2.79	2.77	2.57	2.64	2.66

Figure 1.9: Correlation between chalcogen containing Pt-acetylide dimers and their experimentally measured T_1 triplet state energies.[64-65]

Conjugation can also be extended by incorporating a longer chain of aromatic rings into the spacer group. For instance, a study focussed on thiophene-bridged species showed that increasing the chain size from one to three thiophene rings changed the band gap from 2.80 eV to 2.40 eV significantly lowering the energy of the triplet state.[66] However, the relationship was not linear as the difference between the band gap for the mono- and di-thiophene species was considerably larger than that between the di- and the tri-thiophene-bridged species and no significant change was observed when extending this chain further. A related study showed that polymers featuring fused thiophene ring spacers exhibited higher energy S_1 and T_1 states than related systems in which the thiophene rings are not fused (**Figure 1.10**).[56] Despite the planarity of the fused ring systems it was suggested that the important factor was

the number of conjugated C=C bonds along the backbone of the thiophene ligand systems. The unfused ligands contained more double bonds and thus present greater conjugation and lower optical band gaps.

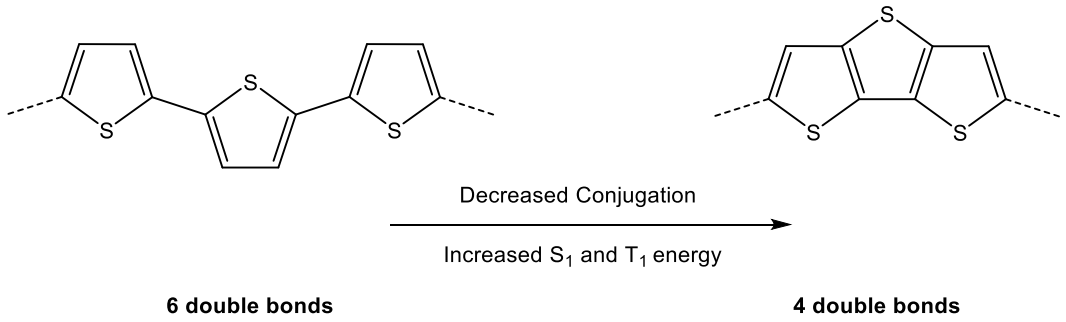

Figure 1.10: Comparing non-fused and fused polythiophene spacers.[56]

Although an increase in ligand conjugation has been shown to relate to a decrease in the optical band gap, Rogers *et al.* has shown that as the conjugation length of an acetylide ligand increases the spin-orbit coupling from the Pt is reduced as the $S_0 \rightarrow S_1$ electronic transitions become more ligand based.[67] This has the effect of lowering the phosphorescence quantum yields of the longer chain systems but extending the triplet lifetimes.

In addition to conjugation effects, a study by Friend *et al.* showed that the optical band gap was also highly sensitive to the electron withdrawing properties of the spacer.[60] Platinum acetylide polymers containing the spacers shown in **Figure 1.11** were prepared and spectroscopic studies of these species showed that the optical band gap decreased with increasing electronegativity. This allowed tuning of the band gap between 1.7 and 3.0 eV.[60]

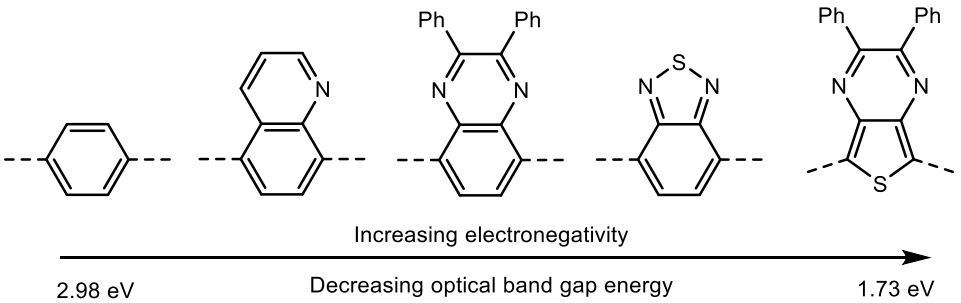

Figure 1.11: Trend between bandgap and the electronegativity of the spacer.[60]

With potential applications within electronic devices there has been significant interest in how the solid-state structure of Pt-acetylide species can be related to their optical and electronic properties. In line with this Raithby *et al.* investigated a series of model oligomeric systems incorporating several of the spacers shown in **Figure 1.7**.[59] The spectroscopic properties were recorded and analysed in combination with structural data obtained from single crystal X-ray diffraction studies. It was shown that there was no correlation between the electronic properties exhibited by the complexes and the torsion angle between the conjugated spacer and the platinum square planes. The spectroscopic analysis suggested that conjugation throughout the complex was retained despite the observed twists in the ligand systems. The observation was attributed to the cylindrical nature of the acetylinic π-orbitals that is illustrated in **Figure 1.12**. Rotation of the phenylene moiety in the diagram would result in less conjugation with one set of acetylinic *p*-orbitals (shown in green) but increase the π conjugation with the orthogonal set of *p*-orbitals (shown in red). Minimum conjugation can therefore be expected at 45° ligand torsions. It is therefore considered that the orientation of the acetylide ligand is strongly influenced by solid-state packing effects.

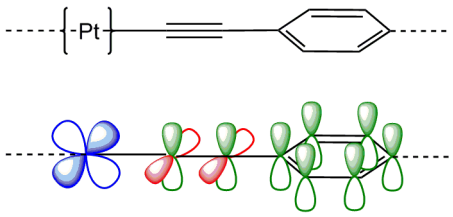

Figure 1.12: The π-conjugated orbital network in a Pt-acetylide system.

To access hybrid electronic properties, unobtainable when using purely organic ligand systems, a number of groups have reported platinum acetylide complexes in which metal centres are incorporated into the bridging ligand systems. The versatility in the design of ethynyl substituted ligand systems has even allowed the synthesis of a heterometallic species featuring seven different metal centres.[68] The groups of Harvey and Shiotsuka showed that ethynyl-bipyridine ligands could be used to combine highly emissive Ru and Ir units with the Pt-acetylide functionality (**Figure 1.13**).[69-70] The systems exhibited significant charge transfer from Pt to the Ru/Ir

centres which leads to a modulation in the absorption and emissive properties. The hybrid electronic properties persist in polymeric material for Ir complexes without significant decrease in the quantum efficiency or lifetimes.

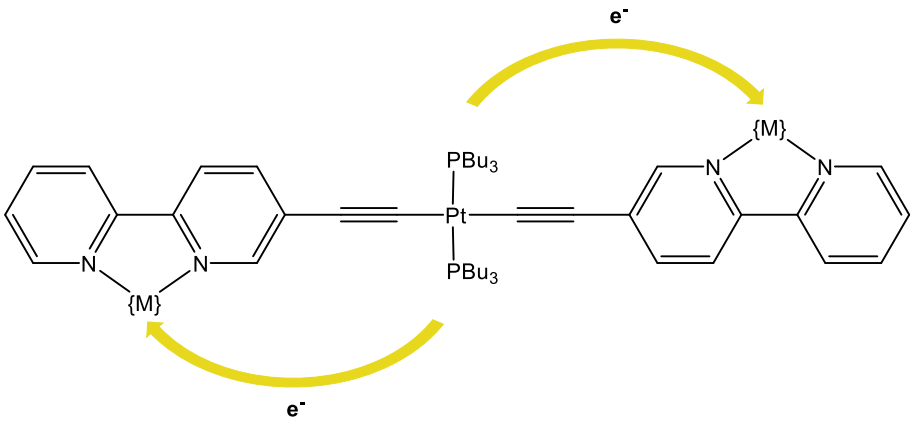

Figure 1.13: Ru and Ir substituted Pt-acetylide complexes exhibiting Pt→M charge transfer.

A series of studies has also been performed on ferrocene-containing Pt-acetylide polymers and oligomers of which examples are shown in **Figure 1.14**. Raithby has shown that, by employing ferrocenyl-fluorene bridging ligands, charge transfer can be observed from the ferrocene moiety to the platinum.[71] The polymers containing this ligand exhibited a significantly lower optical band gap than was observed in an analogous species in the absence of the ferrocene. However, a separate study by Long *et al*. showed that when ethynyl ferrocene units were used to bridge platinum centres there was no electronic communication observed between metallocenes.[72] This was attributed to the poor mixing between the platinum acetylide and ferrocene-based orbitals.

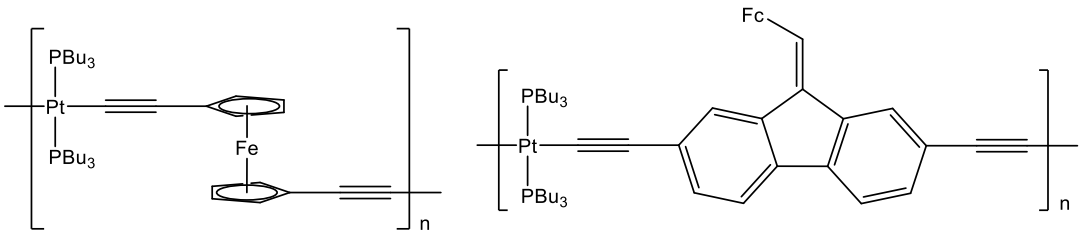

Figure 1.14: Examples of ferrocene-containing Pt-acetylide polymers.[71-72]

A series of heterometallic complexes reported by Younus *et al*. showed that it was possible to substitute each end of a diacetylide ligand with a different transition metal fragment.[20] The systems that were reported included two mixed Pt-Ru acetylide systems in which both metals are directly connected within the σ- and π-bonded framework. Charge transfer from the Pt fragment to the Ru was observed in the cyclopentadienyl-stabilised system, shown in **Figure 1.15,** through a significant decrease in the Ru oxidation potential relative to a platinum free model. The interaction between metal fragments could also be observed in the electronic absorption spectrum in which there was a clear contrast between the absorption bands for the mixed metal complexes and for those of the model Pt and Ru systems.

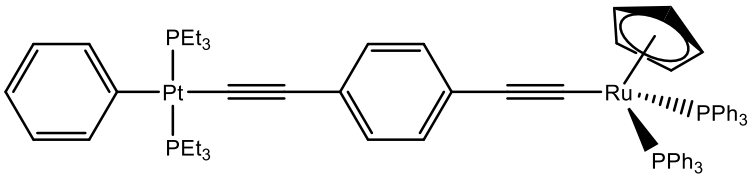

Figure 1.15: A mixed Pt-Ru-acetylide complex.[20]

1.1.3 – Electronic Communication in Mixed-Valence Molecules

Before discussing the chemistry of quadruply bonded $\{Mo_2\}$ oligomers it is necessary to address the nature of the electronic communication in networks containing redox active metal centres. This section therefore provides a brief introduction to the mechanisms of charge transfer in mixed valence complexes and the means by which it can be measured and classified.

Following the report of the Creutz-Taube ion $[(NH_3)_5Ru\text{-pyrazine-}Ru(NH_3)_5]^{5+}$ in the late 1960s it became clear that metal centres were able to communicate electronically through conjugated bridges.[73] Since then many studies have shown that electronic communication between mixed-valence metal centres in oligomeric or polymeric systems can have a large influence on the resulting properties of the material.

Charge transfer in mixed valence complexes has largely been described using two mechanisms, although other tunnelling mechanisms have also been discussed in the

literature.[74] The first is a charge-hopping model (**Figure 1.16**).[75] The transfer process involves charge injection from a donor (D) at one terminus of the system followed by a number of random charge hopping steps between weakly coupled bridging units until the charge meets the acceptor (A) at the opposite terminus. For the purposes of this discussion, D and A represent metal centres. Increasing the number of hopping processes (N) decreases the rate of electron transfer by a factor of $N^{-\eta}$ (η = 1-2).

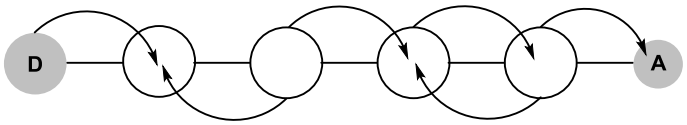

$$k_{ET} = N^{-\eta}$$

(N = no. of hops, η = 1-2)

Figure 1.16: A simplified representation of the charge-hopping charge transfer mechanism accompanied by an equation relating the rate of transfer to the number of hopping processes.[75]

An important requisite of the charge-hopping theory is that the metal and bridge orbitals must be fairly close in energy. When the energy gap becomes too large for charge hopping to occur, charge transfer can persist though the two site super exchange mechanism as shown in **Figure 1.17**.[74-76] This is a tunnelling mechanism involving significant mixing of the metal and bridge electronic states. Electron transfer is mediated by the conjugated bridge either by electron transfer into π^*-orbitals or by hole transfer involving the filled ligand π-orbitals. In reality this is a simplified picture and other orbitals may be involved and the two processes may both contribute to the electron transfer process. The rate of electron transfer by super exchange is inversely proportional to the exponential of the intermetallic separation and as such communication falls of sharply with distance, more so than the charge hopping mechanism.

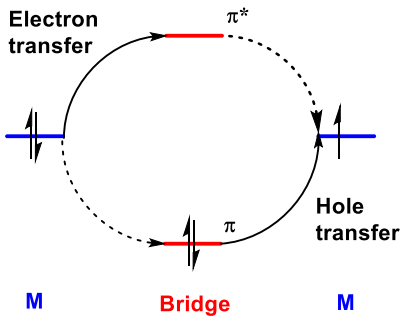

$$k_{ET} \propto \exp^{(-\beta r)}$$

(r = M-M separation, β = damping coefficient)

Figure 1.17: A simplified representation of the superexchange charge transfer mechanism accompanied by an equation relating the rate of transfer to the intermetallic separation.[76]

The mechanisms described above both involve 'through-molecule' charge transfer. It is however important to add that a degree of electronic communication is attributed to electrostatic interactions between metal centres.[77]

The electronic coupling between mixed-valence metal centres originates from the orbital interactions between the metal *dπ* -orbitals and the π-conjugated network of the bridging ligand system. The Creutz-Taube ion is used as an example in **Figure 1.18** to illustrate how the in-phase and out-of-phase combinations of the Ru *d*-orbital (blue) interact with different π-type orbitals on the pyrazine linker (red).

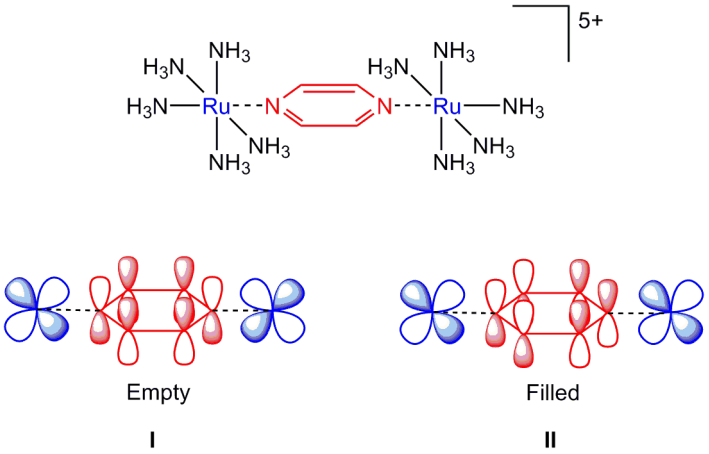

Figure 1.18: Key orbital interactions for the discussion of electronic communication in a pyrazine-bridged Ru-dimer.

The in-phase Ru d orbitals are of the correct symmetry to mix with the unoccupied π*-orbital of the pyrazine linker (**I**). This is essentially a backbonding interaction and stabilises this metal orbital combination. The out-of-phase *d*-orbital set is able to mix with the symmetry appropriate pyrazine π-orbital, which destabilises the metal orbital set due to the filled-filled nature of this interaction The overall effect is to cause a splitting of the Ru *d*-orbitals. A simplified molecular orbital diagram is shown in **Figure 1.19** to illustrate these effects in a strongly electronically coupled system.

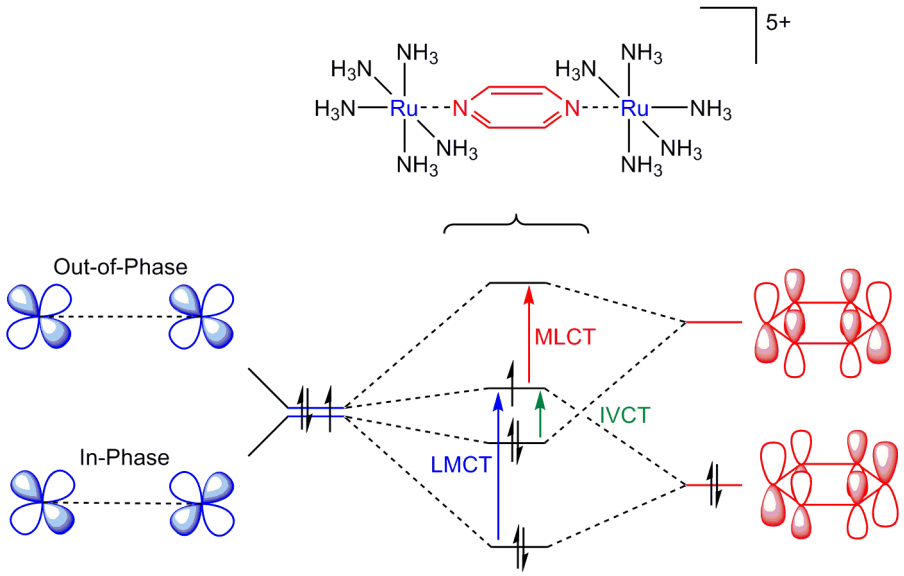

Figure 1.19: Molecular orbital diagram for the strongly coupled Creutz Taube ion.[76]

In the ground and oxidised state, complexes in which metal centres are coupled in this manner display a fully allowed $M_2\delta$ to ligand π^* electronic transition, the energy of which usually describes the magnitude of the HOMO-LUMO separation. Upon oxidation of one of the metal centres an additional electronic transitions become apparent due to the singly occupied HOMO. These include LMCT and charge resonance between the energetically separated metal orbitals. The latter is known as the inter-valence charge transfer band (IVCT) and its observation is indicative of electronic communication within the system.

The molecular orbital diagram in **Figure 1.19** represents a strongly coupled mixed valence system, however, varying the degree of electronic coupling can result in a significant difference in both the optical and electronic properties of a complex. Using a simple model, **Figure 1.20** shows three possible outcomes upon applying an oxidative potential to a conjugated dimetallic system. In the absence of significant electronic communication between metal centres, the difference between the oxidation potentials of the two metals will be negligible as each metal centre is essentially independent from the other. In the presence of electronic communication throughout the system, the oxidation of the first metal is felt by the second. This causes a perturbation to the oxidation potential of the second metal centre (ΔE_2). This results in greater stability of the mixed valence system. A range of hybrid properties can then be observed depending on whether the charge is localised on a single metal centre or delocalised throughout the system.

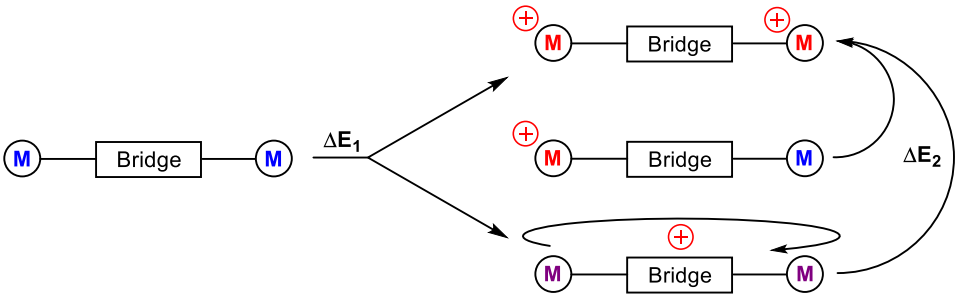

Figure 1.20: Oxidation of a dimetallic complex to give dicationic and delocalised monocationic products.

With these examples in mind, mixed valence systems can be categorised into three groups known as Robin-Day classes that can be expressed by the potential energy curve diagrams shown in **Figure 1.21**.[78] Class I complexes are essentially valence trapped species, reflected by the lack of mixing between the potential energy curves for each metal centre in **Figure 1.21-i**. The properties observed in such systems are equal to the sum of the two metal components. At the other end of the spectrum Class III systems exhibit no energetic barrier to electron transfer and are thus fully charge delocalised (**Figure 1.21-iii**), presenting novel optical and electronic properties. Class II systems lie between these extremes, exhibiting a surmountable energy barrier towards electron transfer as shown in **Figure 1.21-ii**. The properties of Class II complexes are slightly more complex in that they represent both discreet metal centres but can also exhibit properties that stem from thermal or photo initiated electron transfer processes for which the energy barrier to electron transfer is overcome.[79]

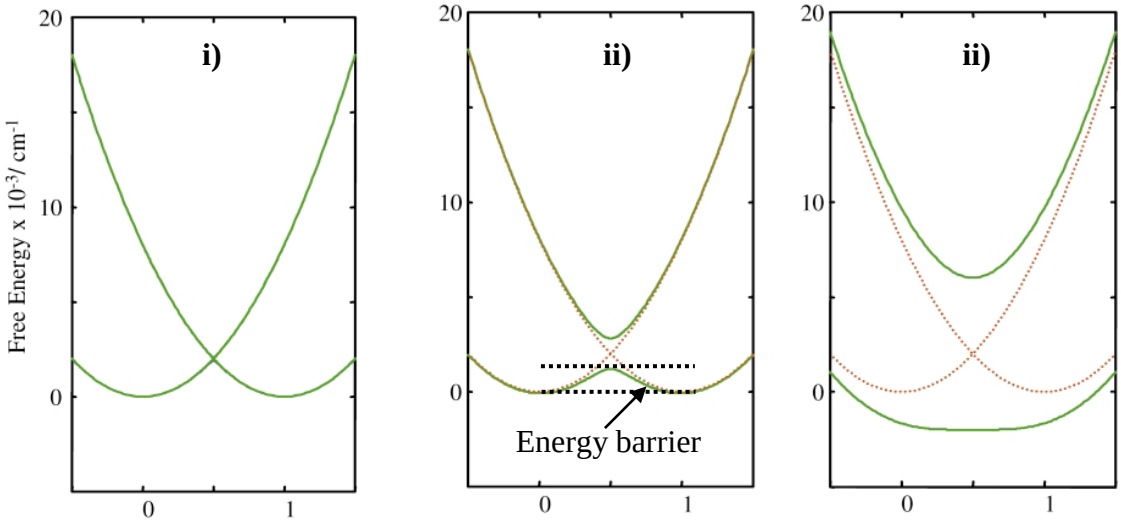

Figure 1.21: Potential energy curve diagrams representing Robin-Day Class I(**i**), II(**ii**), and III (**iii**) mixed-valence systems.[79]

In terms of mixed valence systems that would potentially have application in molecular electronics, it is those that lie on the Class II / Class III boundary that inspire the most interest. This is on account of the relatively small energy barrier for

electron transfer that would allow facile switching between the tuneable properties of the valence trapped and valence delocalised species.

Generally speaking there are two methods that can be utilised to assess the electronic communication within mixed valence systems. The first of which is the calculation of the comproportionation constant, K_{com}, which can be derived from electrochemical analysis. The K_{com} parameter refers to the stability of the mixed valence system in solution towards disporportionation as is depicted in **Equation 1.1** and **1.2**.[32,80]

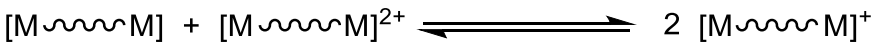

$$K_{com} = \left(\frac{2\left[\text{M}\sim\text{M}\right]^{+}}{\left[\text{M}\sim\text{M}\right]\left[\text{M}\sim\text{M}\right]^{2+}} \right) = \exp\left(\Delta E_{1/2} / 25.69\right)$$

Equation 1.1: Equilibrium equation between a neutral, singly oxidised and doubly oxidised dimetal complex and related equation to calculate the stability of the singly oxidised mixed-valence system.[32,80]

The equation shows that the stability of a mixed valence system is related to $\Delta E_{1/2}$, representing the difference between half-wave potentials of the first and second redox couples in a cyclic voltammetry (CV) experiment. These correspond to the formation of the mixed-valent and fully oxidised species respectively. **Figure 1.22** shows an example of a CV plot in which the waves are labelled to show the assignment of $\Delta E_{1/2}$.[81] This assignment relies on the system exhibiting reversible oxidation and reduction waves. In a fully reversible system $\Delta E_p n$ will be constant at 59/n mV, where n is the number of electrons involved in the process. The ratio between the currents measured for the coupled oxidation and reduction wave relative to their baselines should also be unity for a reversible system.[81]

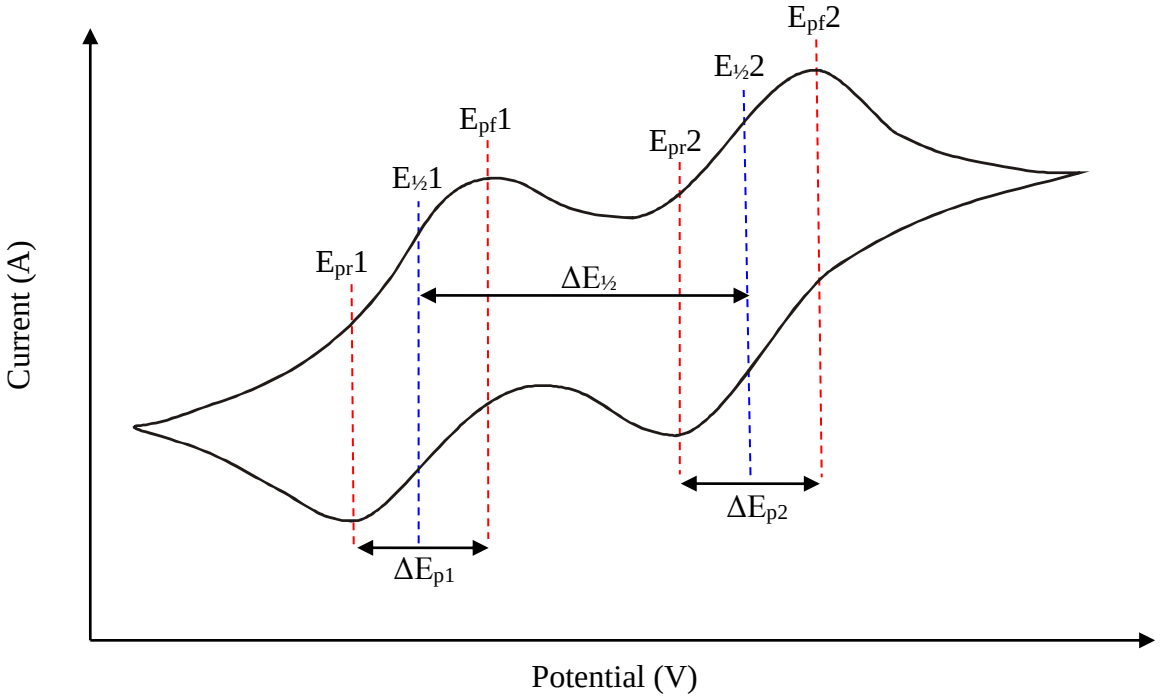

Figure 1.22: A generic CV plot for a mixed-valence metal complex showing two reversible oxidation and reduction couples. E_{pf} = potential of forward peak, E_{pr} = potential of reverse peak.

Systems that exhibit little electronic communication will exhibit near identical oxidisation potentials for both metal centres which, using **Equation 1.1**, correlate to low K_{com} values. Conversely, a strongly coupled system will present a more pronounced $\Delta E_{1/2}$ indicating greater stability of the mixed valence species and thus a higher K_{com} value. **Table 1.1** illustrates how the K_{com} may be used to classify a complex using the Robin-Day notation.[82]

Table 1.1: Assignment of the Robin-Day class based on the magnitude of the comproportionation stability constant

$K_{com} < 10^2$	Robin-Day Class I
$10^2 < K_{com} < 10^6$	Robin-Day Class II
$K_{com} > 10^6$	Robin-Day Class III

Although the separation between oxidation potential is often used to discuss the electronic communication between metal centres it should not be used as definitive

characterisation. Solvation and ion pair effects can act to stabilise mixed valence species to different degrees which can lead to wide variation of the value of K_{com} that is obtained.[83]

A second method of analysing the electronic properties of mixed valence systems requires consideration of the splitting of the conjugated metal *d*-orbitals, depicted in **Figure 1.19**. The splitting creates two non-degenerate and unequally occupied metal based orbitals, making charge resonance between the two states possible. These low energy transitions can be observed in the near infra-red region of the spectrum and data obtained from these measurements can be used to obtain a delocalisation parameter (α^2). Works by Hush *et al*. showed that, for a weakly communicating valence system the width at half height of the IVCT band was related to the electron transition energy (**Equation 1.2**). [28] This in turn can be used to calculate a delocalisation parameter (**Equation 1.3**) based on the separation of the two redox centres.[84-85]

$$\upsilon_{max} - \upsilon_0 = \frac{(\Delta\upsilon_{1/2})^2}{2310\ cm^{-1}} \text{ (Hush equation)}$$

$$\alpha^2 = \frac{(4.2 \times 10^{-4})(\varepsilon_{max} \cdot \Delta\upsilon_{1/2})}{\upsilon_{max} \cdot r^2}$$

υ_{max} = Transition energy (cm^{-1})
$\Delta\upsilon_{1/2}$ = Band width at half height (cm^{-1})
υ_0 = Change of free energy (cm^{-1})
r = Distance between redox sites (Å)
ε_{max} = Extinction coefficient ($dm\ mol^{-1}cm^{-1}$)

Equation 1.2 and 1.3: The Hush equation (top) and derived equation for the delocalisation parameter of a mixed-valence system (bottom).[84-85]

A relationship that has been proposed between the delocalisation parameter and the Robin-Day class of a system is shown in **Table 1.2**.[86] IVCT bands are not observed for type one compounds but the nature of the absorption bands observed in Class II and III species differ on account of the degree of delocalisation within the system. The energy of the IVCT in a Class II system, in which charge is localised on one metal, has been shown to be solvent dependant as a result of solvent reorganisation upon charge transfer.[87-88] Conversely, the charge is delocalised in a Class III species and as such there is no associated solvent reorganisation and there are therefore no

solvent effects. Intermediate behaviour is also observed on the boundary of the two Robin-Day classes.

Table 1.2: Assignment of the Robin-Day class based on the magnitude of the delocalisation parameter.[86]

$\alpha \approx 0$	Robin-Day Class I
$0 < \alpha < 0.202$	Robin-Day Class II
$\alpha = 0.707$	Robin-Day Class III

In addition to experimental analysis, theoretical calculations can also be used to probe the electronic delocalisation in both the ground and mixed valence states. A study by Wiest *et al.* showed that the SOMOs of Class II and Class III species exhibit electron density localised on a single metal centre and electron density on both metal centres respectively, consistent with the Robin-Day model.[89] The LUMO in both systems is situated on the conjugated bridge which is required for the charge transfer mechanism. In the Class I system the SOMO is ligand based and the SOMO-1 is located on a single metal centre. The unoccupied orbital corresponding to the bridge was pushed to much higher energy (LUMO+12) reflecting the lack of communication in these systems.

While the Robin-Day classifications suggest three discreet classes of mixed valence systems the properties, hybrid properties observed on the Class II/III boundary have led to the suggestion of sub classes. The Creutz-Taube ion for example is essentially charge delocalised but exhibits some properties that suggest a degree of localisation.[90] In addition to this Chisholm showed that quadruply bonded group VI metal dimers, in their mixed valence state, provide optical and electronic properties slightly removed from those of a Robin-Day Class III system.[91] This is attributed to strong mixing between the metal and ligand electronic states, in a three state model, and provoked the suggestion of a novel Class IV mixed valence species.

1.1.4 – Quadruply-Bonded {Mo_2} and {W_2} Oligomers

Since the characterisation of the first {M_2} quadruple bond by Cotton in 1964,[92] there has been a great deal of research performed in the area on account of the interesting bonding properties and the resultant range of accessible optical and electronic properties that arise from these.[93] In particular the interactions between M-M quadruple bonds and the π-conjugated networks of μ-ligands have provided a rich area of research. M-M quadruple bonds are composed of one σ, two π and one δ interaction between the *d*-orbitals of the two metal centres. These are illustrated in **Figure 1.23** and generate a new set of dimetallic molecular orbitals.[94] For a quadruple bond, the electron-count of the metals must be such that the M-M bonding orbitals are all fully occupied and the corresponding anti-bonding orbitals are vacant.

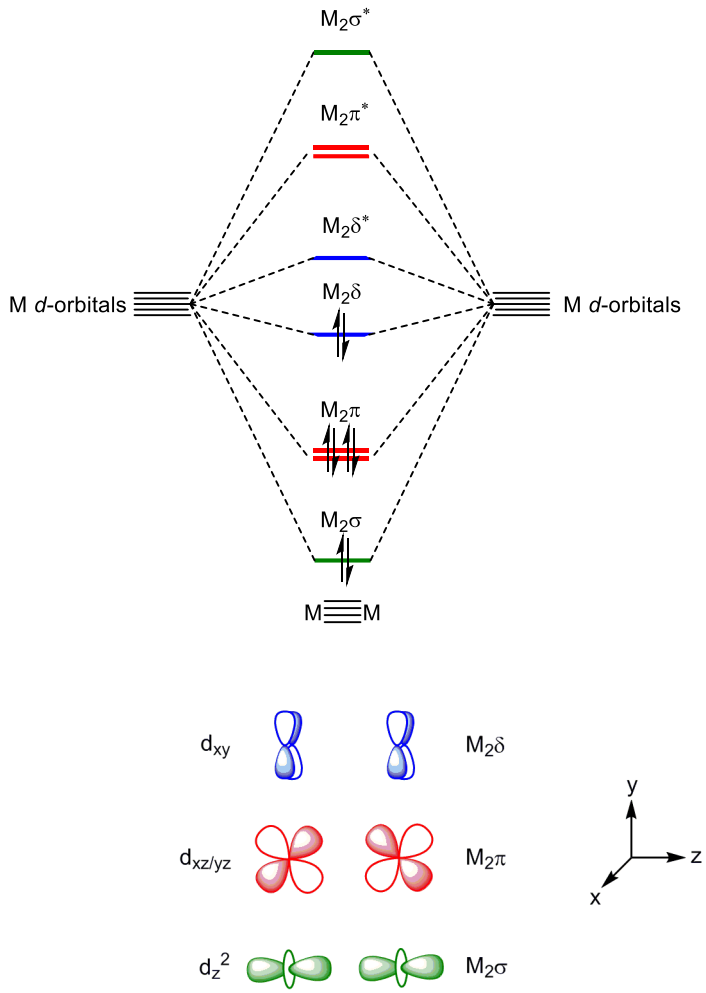

Figure 1.23: A molecular orbital diagram showing the *d*-orbital components {M_2} quadruple bond.[94]

Explorations within the last 25 years have sought to couple redox-active quadruply bonded systems together to harness their unique optical and electronic properties into oligomeric and polymeric materials.[95] In addition to this it was postulated that a new range of properties could be unlocked as a result of switchable electronic communication between metal centres. Extensive work by the groups of Chisholm and Cotton have shown that dicarboxylates are very effective bridging ligands for coupling quadruply bonded $\{M_2\}$ fragments (M = Mo or W). In many cases the ligands facilitate good electronic communication.[76-77,96] It is noteworthy that a variety of related ligand types, based on hetero-functionalised aromatic systems,[76,97-99] have been used to bridge quadruply bonded $\{M_2\}$ units and a range of $\{\mu\text{-X}\}$ bridging systems (X = H,[100] O,[101-102] OH,[101] S,[103] Se[104] or Cl[105]) have also shown to provide interesting optical and electronic properties. More recently, electronic communication has also been reported to occur across hydrogen bonding interactions in solution.[106]

In general two synthetic approaches that have been used to access $\{M_2\}$-carboxylate complexes. The first of these is ligand metathesis, starting from a tetra-carboxylate precursor (**Scheme 1.3**). In addition to the dicarboxylate bridged system shown below the method is also applicable to the synthesis of both *trans*-di-substituted[107-111] and tetra-substituted $\{M_2\}$ species.[112-113]

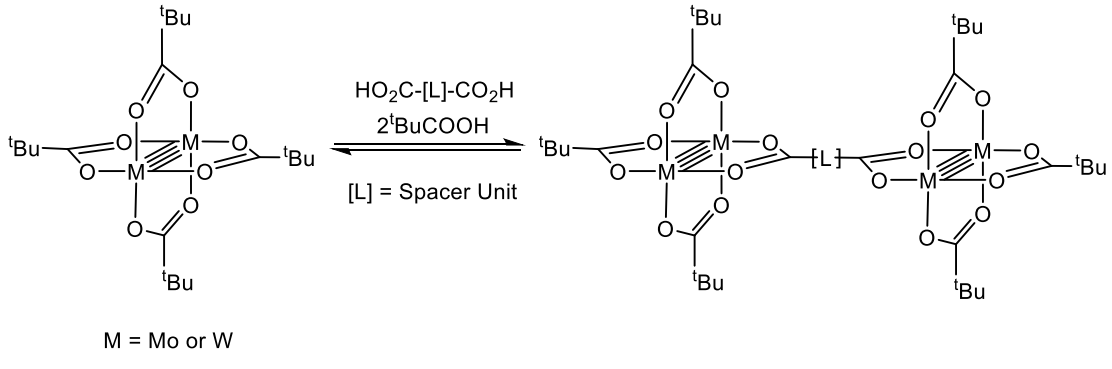

Scheme 1.3: Synthesis of substituted $\{Mo_2\}$ and $\{W_2\}$ carboxylate complexes *via* ligand metathesis.

The second method, which has been predominantly utilised with formamidinate stabilised precursors, is salt metathesis reactivity.[77,96] The example shown in **Scheme 1.4** illustrates this using a dichloride salt precursor that has been widely used by Cotton *et al*.. This also requires reduction prior to reaction with the ligand salt. Salt metathesis holds advantages both in the fact that substitution is directed kinetically by the bulky spectator ligands but also because the reaction is not in equilibrium. This means that solubility of the product is much less of an issue allowing compatibility with a much wider range of bridging ligands. However, this reactivity has only been applied for Mo-containing systems. This is likely due to the lower stability of complexes of tungsten and the consequential difficulties involved in the synthesis of analogous precursors.

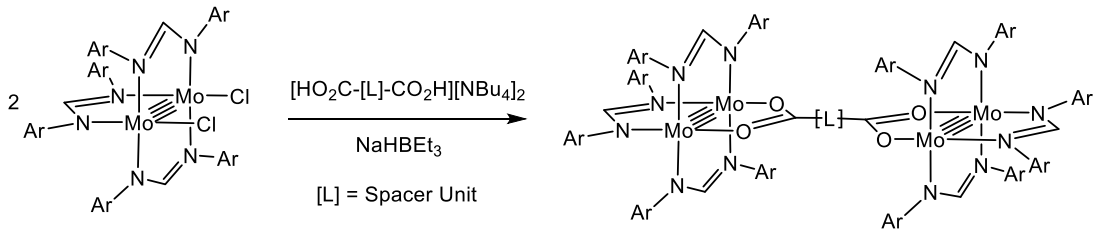

Scheme 1.4: Synthesis of a formamidinate stabilised Mo_2 dimer *via* salt metathesis reactivity.[77,96]

In addition to the synthesis of linear oligomers, the above methods have also been applied to access more complex frameworks ranging from molecular triangles[114] to large spherical arrays (**Figure 1.24**).[115] Alterative precursors were required for formamidinate containing complexes, increasing the number of activated substitution sites.[114,116-120]

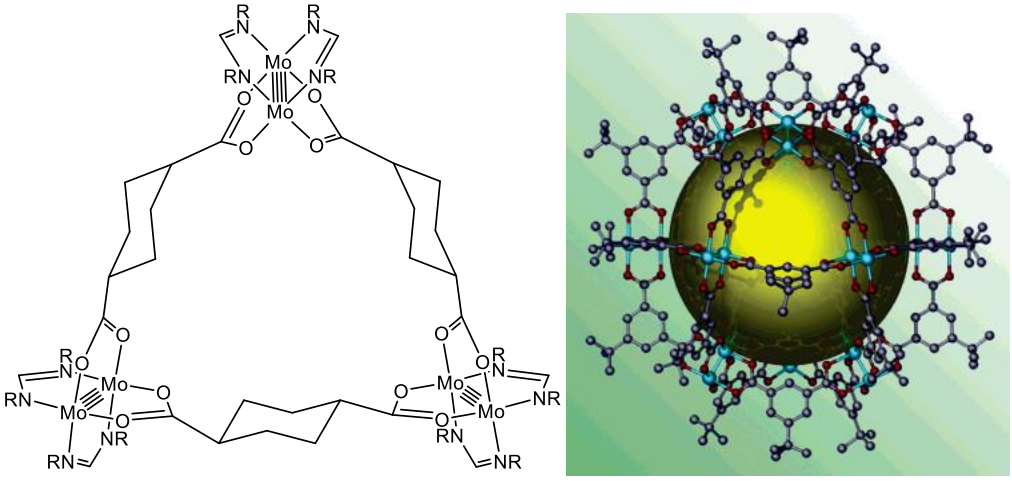

Figure 1.24: Examples of non-linear oligomers containing Mo-Mo quadruple bonds.[114-115]

An understanding of how the metal and ligand orbitals interact is key to the understanding the occurrence of electronic communication through such systems. The interactions of the greatest importance in a simple oxalate bridged dimer are shown in **Figure 1.25**. Though this example reflects the simplest case, involving the shortest possible dicarboxylate linker, the incorporation of conjugated spacers into the bridge only changes the situation by introducing π-interactions between the spacer and the carboxylate moieties of the ligand.[76]

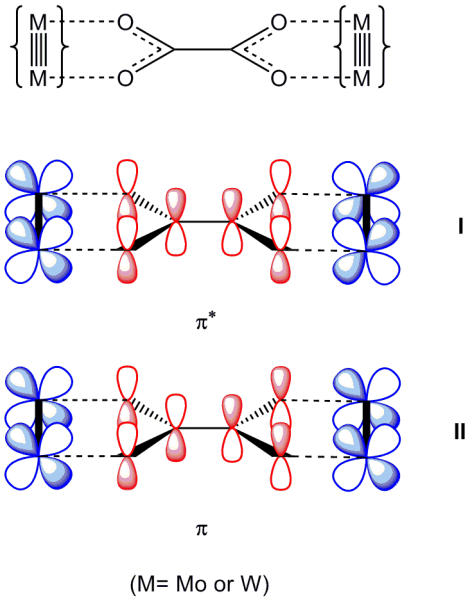

Figure 1.25: Frontier π-orbital interactions in an oxalate bridged $\{M_2\}$ dimer.[76]

The in-phase $M_2\delta$ orbitals are shown to interact with the empty π^* orbitals of the bridge, stabilising the $[M_2\delta]_2$ combination through backbonding (**I**). This interaction is also responsible for the stabilisation of the planarity of the conjugated ligand. The second interaction shown (**II**) involves the out-of-phase $M_2\delta$ combination, which interacts with the π orbitals of the carboxylate moiety. This filled-filled interaction is a destabilising one which increases the energy of the $[M_2\delta]_2$ set. The overall effect is to cause a splitting of the $[M_2\delta]_2$ orbitals.

This situation is equally well represented by the molecular orbital diagram discussed previously (**Figure 1.19**) showing electronic transitions between metal and ligand systems, as well as charge resonance between the energy separated $M_2\delta$ orbitals. Manipulation of the energy of these orbitals allows the optical and electronic properties of these systems to be tuned and to do this there are two key areas of these systems to consider as shown in **Figure 1.26**. The first of these is the orbital mixing between the metal centres and the carboxylate (or other isoelectronic fragment) of the bridge (**A**) and the second (**B**) is the continuation of orbital mixing into the spacer (L).

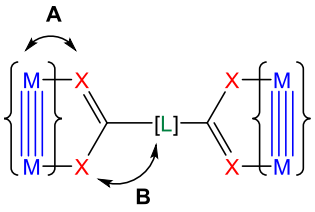

Figure 1.26: A diagram highlighting the key orbital interactions that can be manipulated to affect the optical and electronic properties of such systems.

The radial extension of the orbitals involved in both **A** and **B** has a large impact on the amount of mixing between the moieties and it is therefore not surprising that W-containing complexes offer significantly more electronic delocalisation than molybdenum systems.[76,80] This is highlighted by the data shown in **Table 1.3** for a series of molybdenum and tungsten analogues. [98,121-122] The difference arises both from the greater radial expansion of the tungsten orbitals and the fact that they are higher in energy than those of molybdenum (*ca.* 0.5 eV) bringing them nearer to the

energy of the unoccupied ligand orbitals. The metal bound ancillary ligands also affect the electronic communication. For instance, a comparison between the oxalate bridged complexes with carboxylate and formamidinate stabilised $\{M_2\}$ units show greater degrees of communication in the former under the same conditions. However, Cotton *et al*. have shown that there is a lot of scope to tune the properties of the formamidinate complexes by altering the aryl substituents.[123]

Table 1.3: A comparison of the electronic communication observed in analogous molybdenum and tungsten complexes.

Bridge	$\Delta E_{1/2}$ (mV) Mo / W	K_{com} Mo / W
Oxalate[98]	280 / 717	5.4×10^4 / 1.3×10^{12}
Perfluoroterephthalate[98]	65 / 285	1.3×10^1 / 6.6×10^4
2,6-Azulenedicarboxylate[121]	112 / 468	7.8×10^1 / 8.2×10^7
2,5-Thiophenedicarboxylate[122]	110 / 310	7.2×10^1 / 1.7×10^5

It is intuitive that the nature of the bridging ligand must also affect the properties of the system as a whole and these must be considered in two parts; the Mo_2 binding $\{CX_2\}$ termini and the spacer that separates them. Although the majority of studies have been performed with dicarboxylate ligands, there are a range of isoelectronic alternatives that have also been investigated.[96,100,101] **Figure 1.27** illustrates how substituting the O atoms for S in the $\{CX_2\}$ moiety significantly decreases the energy of the HOMO-LUMO gap and increases electronic communication in terephthalate bridged complexes of molybdenum and tungsten. This has been attributed to the more diffuse sulphur orbitals, which provide greater orbital overlap with both the metal and the conjugated spacer.

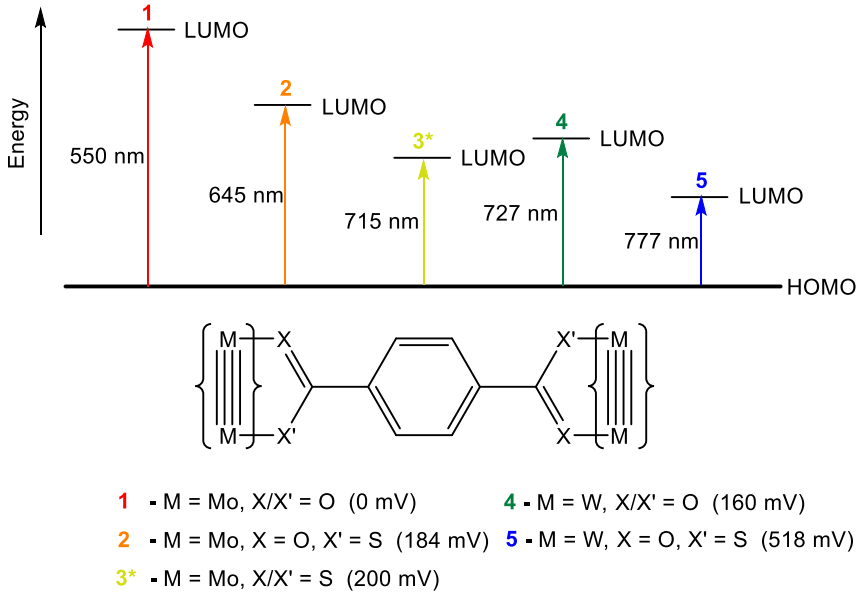

Figure 1.27: A diagram comparing the experimentally measured wavelengths of the MLCT bands in molybdenum and tungsten terephthalate and sulphur-substituted terephthalate complexes. All complexes apart from **3*** contain pivalate attendant ligands whereas **3*** has formamidinate attendant ligands. [98,124-125]

Studies into the use of other ligand types based on the carboxylate motif have also been made. Cotton *et al* have investigated the application of diaryloxamidate ligands {CX_2 = Ar-NCO} but showed that intra-ligand steric interactions resulted in an anti-planar ligand conformation, preventing π-conjugation throughout the bridge.[126] Interestingly a second isomer was also isolated in which the ligand coordinates to the Mo_2 units side on which constrains the geometry of the complex to a planar geometry (**Figure 1.28**). The conformational difference was accompanied by a large increase in electronic communication in the side-on coordinated system. Diarylterephthaloyldiamidate bridged species have also been investigated in which the amidate moieties of the ligand are separated by a phenylene spacer.[127] This reduces the intra-ligand steric interactions and facilitates significantly greater electronic communication than the terepthalate containing analogue.

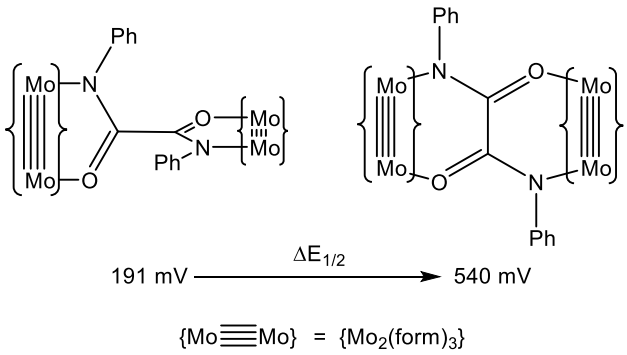

Figure 1.28: Diagram showing the two isomers that were isolated for a diamidate-bridged molybdenum complex.[126]

To investigate the importance of planarity with respect to electronic communication, a series of calculations have also been performed on oxalate-bridged complexes in both planar (D_{2h}) and antiplanar (D_{2d}) conformations. These showed that, in the perpendicular conformation, the $M_2\delta$ orbitals become degenerate which effectively "turns off" electronic communication between the metal centres.[128] Deviation from planarity also results in an increase in the HOMO-LUMO gap as a function of the torsion angle. Although the orbital mixing between the $M_2\delta$ and carboxylate π^*-orbitals stabilise the planar arrangement of the bridge, the energy gap between the D_{2h} and D_{2d} conformations of the oxalate bridge complexes are shown to be very small (ΔE = 5.9 kJmol^{-1} for molybdenum and 7.9 kJmol^{-1} for tungsten). It is this small barrier that is likely to be responsible for the thermochromism that is observed in a range of these systems.[129-131] Experimentally, the effect of ligand planarity is well illustrated by the dihydroxyterephthalate bridged system shown in **Figure 1.29**.[130]

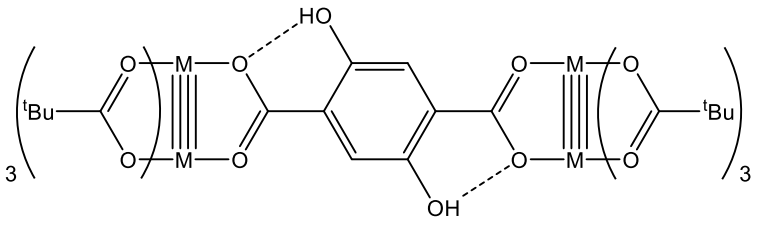

Figure 1.29: A dihydroxyterephthalate bridged dimer where M = Mo or W.[130]

In neutral medium the hydroxyl moieties partake in hydrogen bonding interactions with the carboxylate units which stabilise the planar form. Electrochemical and

spectral analysis does indeed show a greater level of electronic communication for this system relative to related complexes, such as the tetrafluoroterephthalate (M = Mo and W) and terephthalate bridged systems (M = W). In basic conditions the hydroxyl groups are deprotonated and the hydrogen bonding interaction is lost. This is reflected by a large blue-shift in the MLCT band as shown in the electronic absorption data reported from this study which is displayed in **Figure 1.30** for the Mo-containing complex. The process is shown to be partially reversible upon addition of acid to the deprotonated form and highlights utilisation of chemical switching to modulate the electronic communication in these "dimer of dimer" complexes.

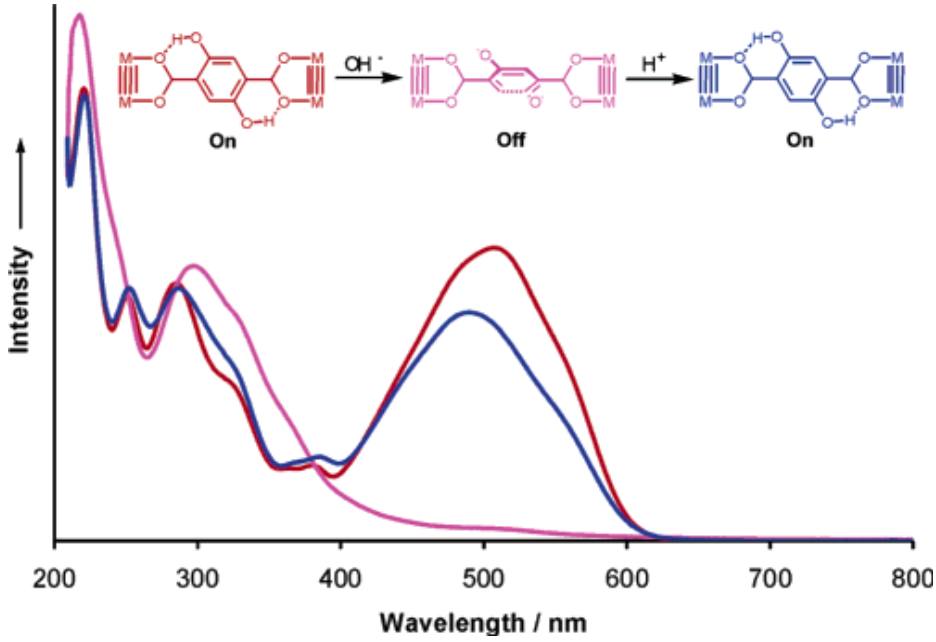

Figure 1.30: Electronic absorption data showing the chemical switching properties of a dihydroxyterephthalate bridged {Mo_2} dimer.[130]

An area which has presented great scope for tuning the properties of these complexes is the changing of the identity of the spacer within the bridging ligands. Through the combined works of the groups of Cotton and Chisholm, a large catalogue of these dimer systems now exist and a selection of the different ligands that have been used is shown in **Figure 1.31**. This is by no means exhaustive and a greater variety is available in the literature.[77,80,95-96,98]

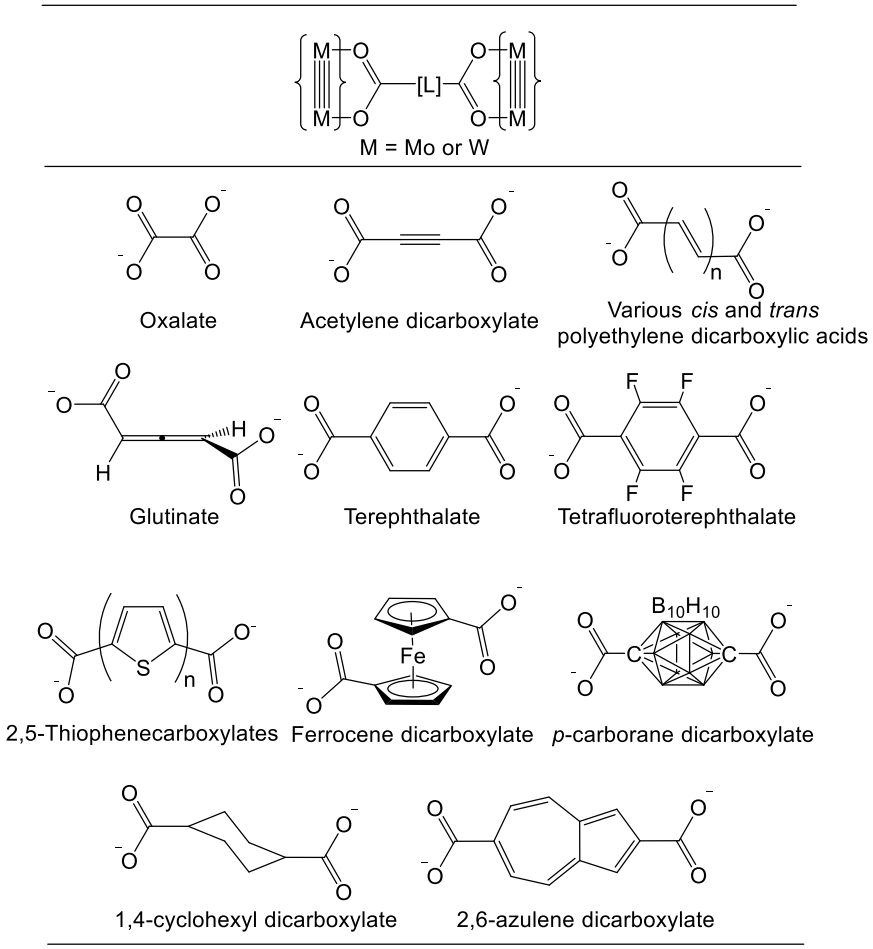

Figure 1.31: A selection of dicarboxylate ligands that have been used to bridge quadruply bonded $\{M_2\}$ units.[77,80,95-96,98]

Through spectroscopic and electrochemical analysis of complexes bearing a variety of these ligands, several characteristics have been shown to have an influence on the electronic communication that is observed. Intuitively, conjugated spacers facilitate communication to a much greater extent than complexes containing the cyclohexyl or carborane ligands for example.[96] However, complexes containing non conjugated ligands such as these may also show a small degree of communication *via* electrostatic interactions which fall off with increasing $\{Mo_2\}\cdots\{Mo_2\}$ separation. Distance is also an issue with conjugated dicarboxylate ligands, which was illustrated neatly in a study by Cotton *et al*. in which a range of polyethene dicarboxylates, of the form $[^{-}O_2C\text{-}(C{=}C)_n\text{-}CO_2^{-}]$, were investigated.[77] The results are shown in **Table 1.4** and clearly show that electronic communication falls off with increasing number of ethene units. In addition to this, the data shows that the

{Mo_2}⋯{Mo_2} separation is also important with *cis*-conformations facilitating greater communication than *trans*-isomers.

Table 1.4: Table and accompanying diagram showing how electronic communication changes by alterning the length of an unsaturated spacer.[77]

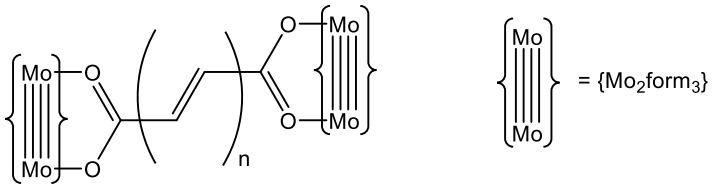

form = Di-*p*-anisylformamidinate

n	$\Delta E_{½}$ (mV)	K_{com}	[Mo_2]-[Mo_2] (Å)
0	212	3.8 x 10^3	6.95
1 (*cis*)	172	7.2 x 10^2	7.69
1 (*trans*)	145	2.0 x 10^2	9.19
2 (*cis*, *cis*)	125	1.3 x 10^2	10.35
2 (*trans*, *trans*)	105	60	11.58
3 (all *trans*)	75	19	13.92
4 (all *trans)*	65	13	16.16

The extent of conjugation within the spacer also has the potential to alter the amount of communication that is observed. For instance, azulene bridged complexes show a smaller HOMO-LUMO gap and greater separation of the two M(II)/M(II)→ M(II)/M(III) electrochemical processes compared to the terephthalate containing analogues.[121] Conversely, the 9,10-anthracene dicarboxylate exhibits much lower communication than is expected considering the conjugation.[132] This highlights another important factor when considering electronic delocalisation which is the coplanarity of the conjugated spacer and the {Mo_2O_2C} moieties. Without torsion this offers optimum π-orbital overlap throughout the complex. In the case of the anthracene complex, the *peri*-hydrogens are repelled by the carboxylate oxygen atoms, which prevent the planarity of the complex. Although crystallographic analysis has not been conducted, theoretical studies show a minimum energy with ligand torsion of 54°.

The electronic coupling between a Mo_2 quadruple bond and a π-conjugated ligand presents a means to tune the electronic communication in oligomeric species. However, by incorporating other metal centres into these ligand systems there are potentially a much wider range of hybrid properties that may be accessed. There have been relatively few heterometallic complexes reported in the literature but the examples that exist highlight both the diversity of the possible molecular motifs and also the range of properties that can be observed.

One approach to synthesising these heterometallic complexes has been to design carboxylate ligands that contain a metallic moiety. These can then be coordinated to a Mo_2 centre via ligand metathesis. **Figure 1.32** shows two systems made in this way. The incorporation of the $\{Co_3(CO)_9\}$ moiety in **Figure 1.32-i** not only adds an electrochemical probe into the ligand system but also causes significant perturbation of the optical properties on account of low energy charge transfer from the Mo_2 to the Co_3 fragments.[133] This effect is lessened when one Co atom in the tetrahedral cluster is replaced by carbon.[112] Electrochemical probes have also been incorporated into bridged dimers by using ferrocene dicarboxylate, however, because the π-orbitals are not aligned along the length of the complex, electronic communication through the ligand is poor.[96] **Figure 1.32-ii** shows that secondary metal fragments can also be used as spectroscopic probes.[134] A combination of time resolved infrared spectroscopy (TRIR), looking at the metal carbonyl vibrations, and theoretical studies were used to show that electron density resides on both metal centres in the frontier orbitals and excitation of the groundstate results in MLCT processes for both $\{Mo_2\}$ and Cr.

i)

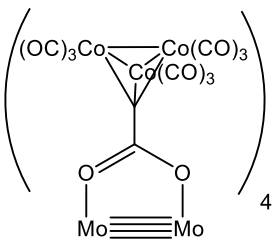

ii)

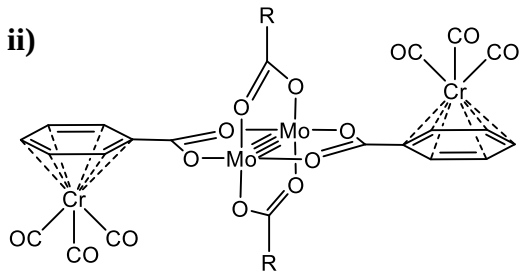

Figures 1.32: Examples of heterometallic $\{Mo_2\}$-carboxylate complexes.[133-134]

Nakamura *et al*. have shown that late transition metals, when incorporated into a {Mo_2} ligand system, can provide novel reactivity. They reported a {Mo_2} tetra-diphenylphosphinopyridonate (pyphos) system to which either Pd(II) or Pt(II) halides could be coordinated (**Figure 1.33**).[135-137] The reaction places the coordinated metals over the axial positions of the Mo-Mo bond. For clarity, the diagram shows only one set of *trans*-pyphos ligands and their associated {MX_2} moiety. Upon reduction, both Pt/Pd centres in the complex lose a halide ligand and form bonding interactions with the adjacent Mo atom. This provides an M-Mo-Mo-M motif and reduces the Mo-Mo bond order to three, which can be observed in the molecular structures of these species. The reaction significantly changes the electronic environment of the two metal centres and a significant red shift in the electronic absorption of each species was observed.

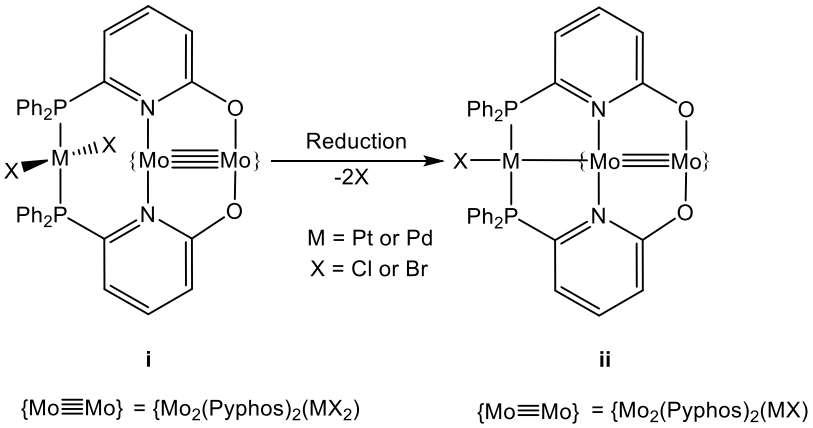

Scheme 1.5: Formation of M-Mo bonds *via* reduction of a heterometallic species.[135]

Ligand systems that contain Lewis basic moieties can also be used to incorporate transition metal fragments into the bridging ligands of {Mo_2} dimeric systems. This was first shown by the group of Cotton when they reported that {Mo_2} isonicotinate precursors could be bridged *via* the coordination of a range of metal complexes including [Ni(acetoacetate)$_2$] and [Rh(acetate)$_4$] (**Figure 1.34**).[117] The latter contains the longest {Mo_2}···{Mo_2} separation that has currently been reported for such a {Mo_2} dimer and this is reflected in the very weak electronic coupling between the two termini. Chisholm has also utilised the same ligand to synthesise a {Mo_2} *trans*-diisonicotinate precursor which, when combined with [Rh(acetate)$_4$], provide 1D coordination polymers or polymer networks in the solid state.[111] Using the same system there was also evidence that a Pt cyclooctadiene fragment could be

coordinated, which provided a significant red shift in the absorption of the complex. Using theoretical studies, evidence was provided that the isonicotinate ligands do facilitate electronic coupling between the Mo_2 and secondary metal fragments.

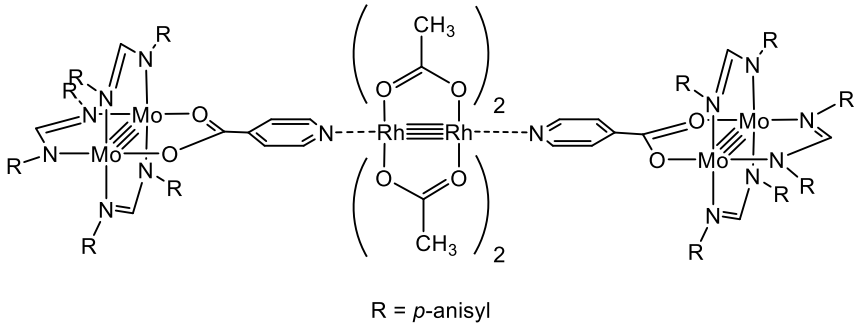

Figure 1.34: A rhodium acetate bridged {Mo_2} dimer.[117]

Using a closely related ligand system, Chisholm has reported a Ru-bridged {Mo_2} dimer in which the Ru atom is bound by two terpyridylcarboxylate ligands (**Figure 1.35**).[138-139] Unlike the simpler isonicotinate systems, the meridonal coordination mode of the terpyridine results in a 90 ^{o} torsion between the {Mo_2} termini. The magnitude of electronic coupling was not quantified but this torsion is likely to have a detrimental effect on the coupling of the {Mo_2} moieties. However, transient absorption studies have shown significant coupling between electronic structures of the electronic manifolds of the {Mo_2} and Ru although the dynamic processes observed were complicated and not fully understood.

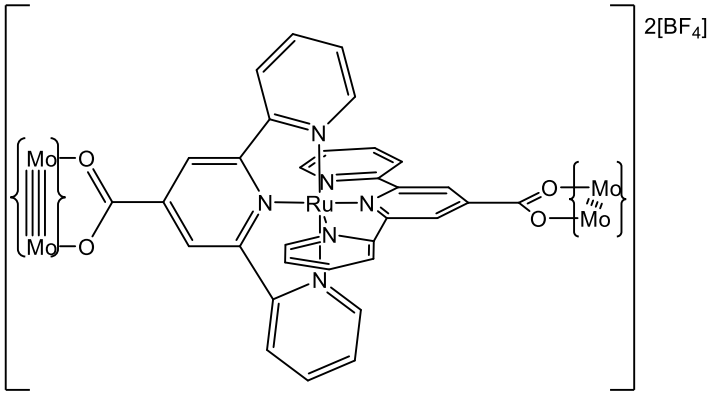

Figure 1.35: A Ru-*bis*-terpyridine-bridged {Mo_2} dimer.[138]

1.1.5 – Aims of the Project

Within our group, we have particular interest in the development of organometallic oligomers and polymers, and methods by which their optical and electronic properties may be tuned. Following previous work within the group in the area of Platinum acetylide chemistry,[20-21,27-28,54-57,59-60,62,71,85,140-141] our primary goal is to extend this field through the design and synthesise of platinum acetylide complexes that incorporate $\{Mo_2\}$, and potentially $\{W_2\}$, quadruple bonds into the rigid-rod-like motif **Figure 1.36**. Both Pt-acetylide and $\{Mo_2\}$-carboxylate systems have interesting optical and electronic properties in their own right and we hope that combining the two types of system will result in novel hybrid properties which could potentially be tuned by changing the identity of the spacer between the metal fragments. Using these combinations of metal-containing units we will also introduce polarity into dimeric and oligomeric systems, with electron transfer from the electron rich $\{Mo_2\}$ units into the platinum-containing-ligand systems.

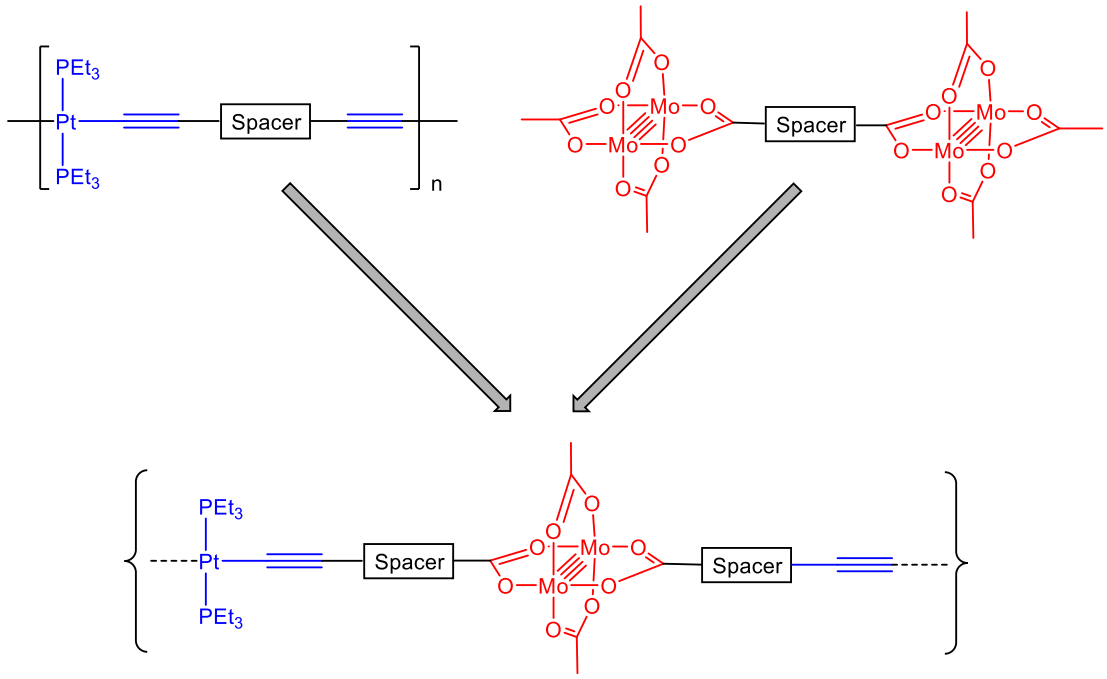

Figure 1.36: Combining of Pt-acetylide and $\{Mo_2\}$-carboxylate subunits into an extended heterometallic system.

In addition to our primary goal we are interested in alternative methods of manipulating the properties of {Mo_2}-carboxylate complexes through the design of novel ligand systems and through intermolecular Lewis basic interactions.

Chapter 2

Ester-Functionalised Pt-Acetylide Complexes

Chapter 2 – Ester-Functionalised Pt-Acetylide Complexes

2.1 – Introduction

Within **Chapter 1.2** the incorporation of heterometallic subunits into Pt-acetylide chains has been discussed with respect to the interesting optical and electronic properties that may be accessed and tuned within these complexes. These hybrid properties arise through the charge transfer processes that occur between the different metal fragments.[20,69-70,72,142-143] The aim of this study is to extend the scope of heterometallic Pt-acetylide complexes by incorporating quadruply bonded {Mo_2} units into the conjugated frameworks, which exhibit unusual optical and electronic properties in their own right as was discussed in **Chapter 1.4**.

With the ultimate goal of combining Pt-acetylide and quadruply bonded {Mo_2} units into a polymeric network, we envisaged that the chemistry of such systems would be better understood through the design and synthesis of smaller oligomeric systems. To this end we have targeted three different heterometallic motifs, as shown in **Figure 2.1**.

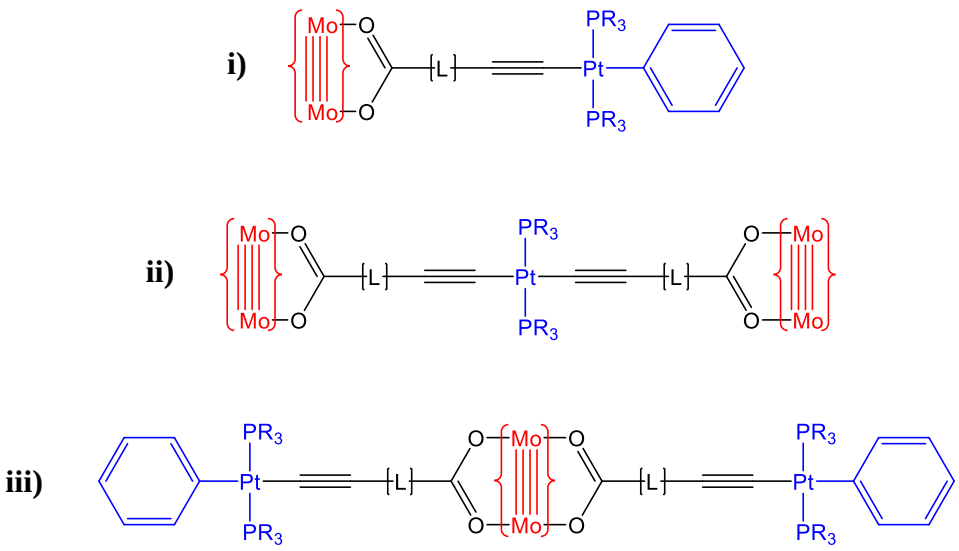

Figure 2.1: Three oligomeric motifs that model units from a 1D heterometallic polymeric framework.

The three motifs include a discrete {Mo_2}-{Pt} system (**i**), a {Mo_2}-{Pt}-{Mo_2} system (**ii**) and finally a {Pt}-{Mo_2}-{Pt} system (**iii**). These model complexes can be deconstructed into three components; the {Pt} unit, the {Mo_2} unit and the conjugated bridging ligand. Whilst the bridging ligand remains the same throughout the series, both bridging and terminating {Pt} and {Mo_2} units are required to assemble the three differing motifs. The optical and electronic properties of the resultant heterometallic frameworks could potentially be tuned by incorporating a range of different conjugated spacers (L) within the organic ligand.

Within this section, the focus is on the design and synthesis of Pt-acetylide complexes, of the form shown in **Figure 2.2**, which could potentially be applied as terminal or bridging precursors within the targeted heterometallic systems.

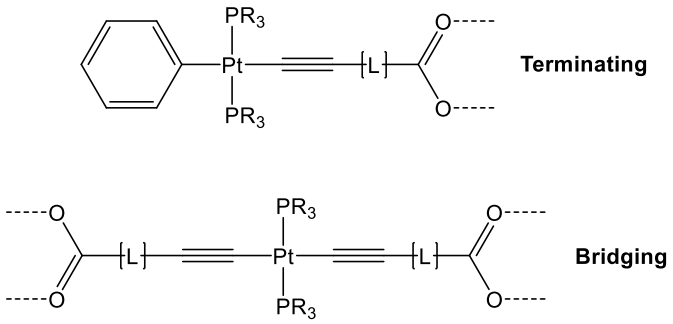

Figure 2.2: Terminating and bridging Pt-acetylide fragments.

2.2 – Results and Discussion

2.2.1 – Design and Syntheses of Ethynyl-Ester Ligand Systems

A structural feature common to both Pt-acetylide frameworks shown in **Figure 2.1** is the conjugated bridging ligand system. In order to facilitate coordination to both Pt and {Mo_2} centres, ethynyl and carboxylate functionality are required at opposite ends of the ligand system. The ability to incorporate a range of different conjugated units between these functional groups is also very important with regards to tuning the optical and electronic properties of the projected organometallic systems. With these criteria in mind, a series of ethynyl-ester systems were identified as potential precursors for Pt-acetylide complexes. The carboxylate functionality is protected to

allow compatibility with the Pt-acetylide coupling reactions but the ester could potentially be hydrolysed post-synthetically. The ethynyl-esters utilised within this study are shown in **Figure 2.3**.

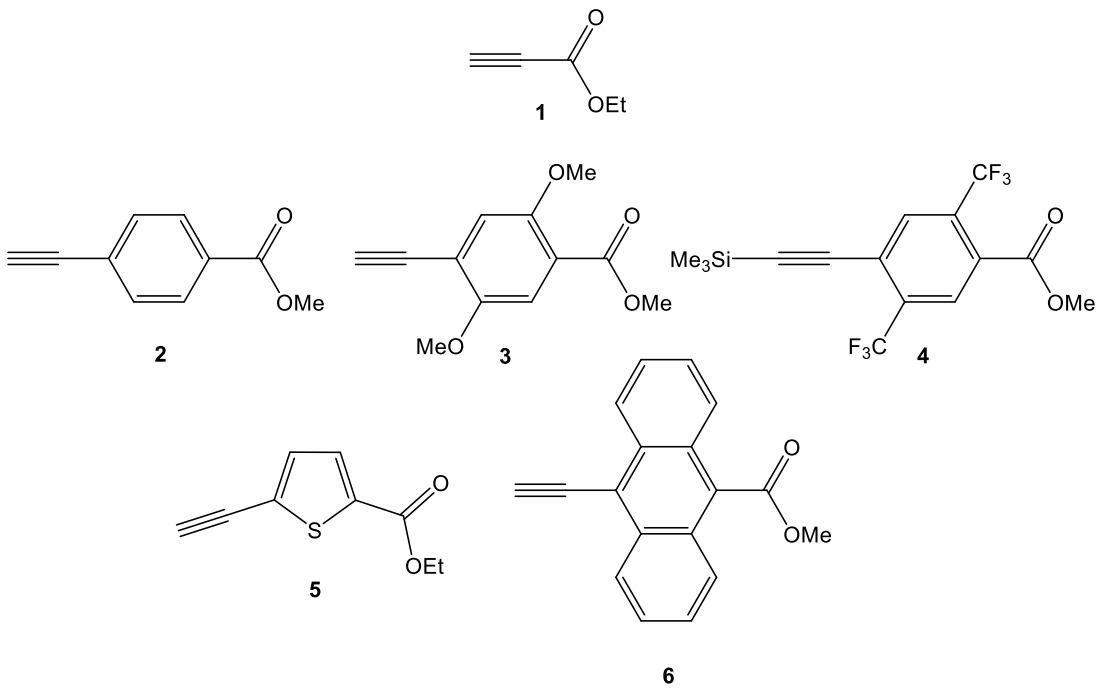

Figure 2.3: A range of ethynyl-ester ligands containing different conjugated spacer groups.

Of the species identified in **Figure 2.3**, those containing the phenylene (**2**),[144] thienyl (**5**)[145] and anthracene (**6**)[146] spacers have previously been reported within the literature whereas ethylpropiolate (**1**) is commercially available. To the best of our knowledge the methoxy- (**3**) and trifluoromethyl-substituted (**4**) species have not previously been reported. With this series of precursors it is possible to investigate how conjugation, heteroatom inclusion and electron-donating/-withdrawing effects can be used to tune the optical and electronic properties of the organometallic systems in which they are coordinated. Within the literature there are examples in which both the phenylene and propiolate ethynyl-esters have been coordinated to a number of metal centres such as; Ru[147-148] Pt,[149] Au[150] and Ag,[149,151] providing evidence that these species are suitable precursors for the synthesis of functionalised metal acetylide complexes.

Ethylpropiolate (**1**) is commercially available so was used as received whilst all other ethynyl-esters required synthetic preparation. The first step of each preparation involved the synthesis of a range of bromo-carboxylic acid precursors followed by esterification. For **2**, methyl-4-iodobenzoate is commercially available and as such this initial step was not required. The syntheses for the bromo-ester precursors for **3-6** are outlined in **Scheme 2.1**.

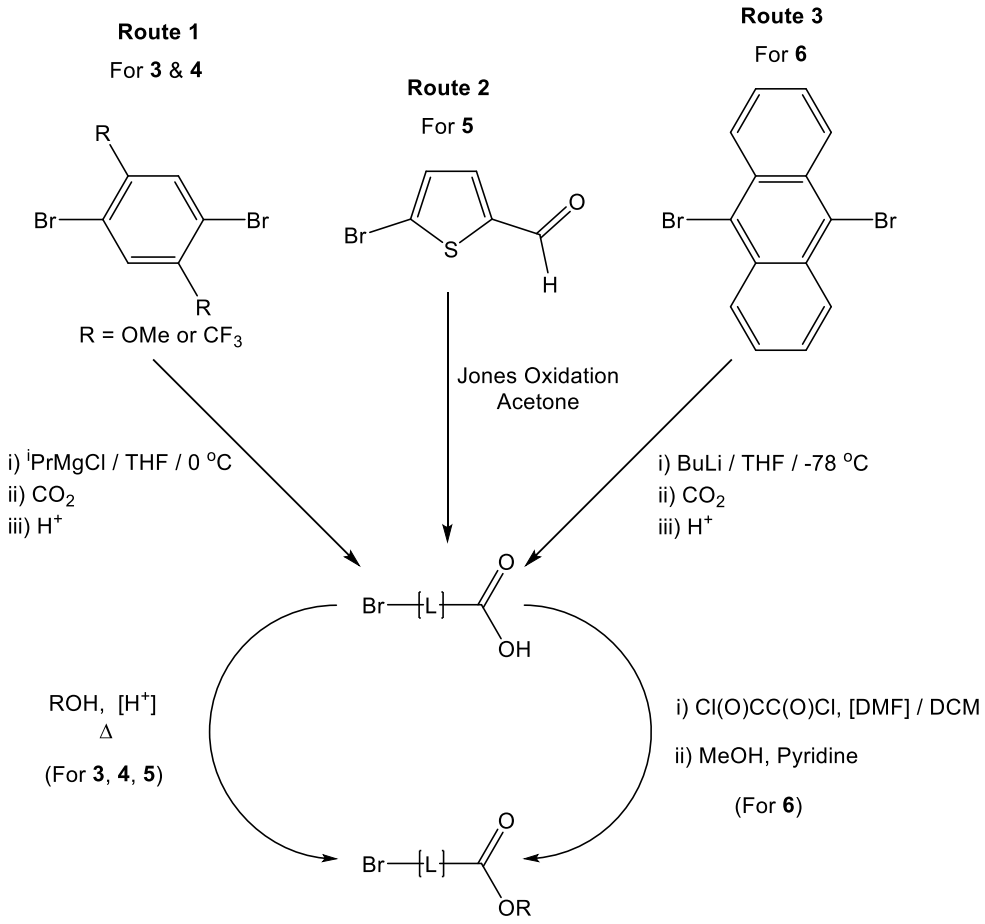

Scheme 2.1: Syntheses of bromo-ester precursors for pre-ligands **3-6**.

For **3** and **4** the syntheses began with the appropriately substituted 1,4-dibromobenzenes which, in turn, were synthesised *via* bromination of the 1,4-disubstituted benzenes.[152] Subsequent reaction of both dibromobenzenes with ^{i}PrMgCl and CO_2 followed by an acid work up provided the {-OMe} or {-CF_3} substituted 1,4-bromobenzoic acid.[153-154] The acids were converted to esters by heating in MeOH, under reflux, with H_2SO_4. The synthesis of **5** started with 5-bromo-2-thiophenecarboxaldehyde which was converted to the carboxylic acid *via* a

Jones oxidation.[155] Esterification was performed using the same method as **3** and **4** but EtOH was used in place of MeOH. Finally, **6** was synthesised from 9-10-dibromoanthracene, which was converted to 9-anthracene-10-carboxylic acid *via* selective lithiation, insertion of CO_2 followed by an acid work up. Following a modified literature preparation the carboxylic acid was converted to the acyl-chloride, through reaction with oxalyl chloride, which was converted to the ester using MeOH and pyridine.[156]

The halo-esters precursors of **2-6** were converted to their respective ethynyl-ester species using Sonogashira coupling[157] reactions involving trimethylsilyl-acetylene followed by selective hydrolysis of the silyl-protected ethynyl group using K_2CO_3 (**Scheme 2.2**). The deprotected form of **4** proved to be unstable under ambient conditions and as such was isolated as the silyl-protected species.

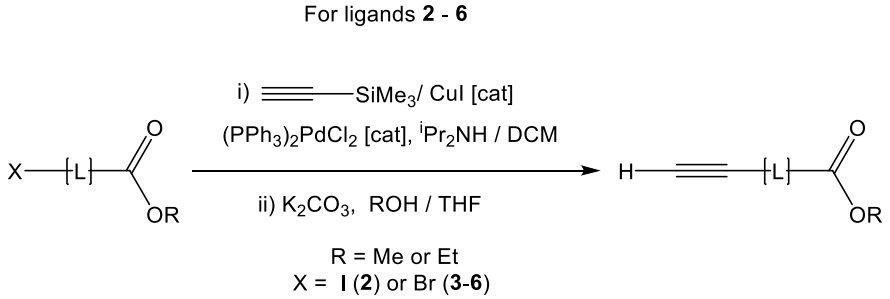

Scheme 2.2: Syntheses of ethynyl-esters using Sonogashira coupling.

The spacer groups present in **1**,[149] **2**,[57] **5**[27] and **6**[57,158] have previously been incorporated into Pt-acetylide polymers and oligomers providing a great deal of scope with which to tune the optical band gaps of these systems. Alkoxy-substituted phenylene spacers ({-$C_6H_2(OR_2)$-} R= -Me,[54] -C_8H_{17}[54,159] and -$C_{16}H_{33}$[160]) have also been studied and have been shown to aid conjugation throughout the complexes in addition to increasing the solubility of the products. To the best of our knowledge, there are no examples of Pt complexes featuring the trifluoromethyl substituted phenylene unit. Although fluorinated phenylene spacers, {-C_6F_4-} and {-$C_6H_2F_2$-}, have been used before in Pt-acetylide dimers,[54] these spacers were not stable under the conditions required for the ethynyl-ester synthesis.

Ethynyl,[96] phenylene,[96,98] thienyl[109,122] and anthracene spacers[132] have also previously been incorporated into the bridging dicarboxylate ligands of {Mo_2} dimers resulting in a range of optical and electronic properties. This literature precident provides evidence that a {Mo_2} centre is able to support our own ligand systems.

2.2.2 – Synthesis of Pt-Ethynyl-Ester Complexes

Ligands **1**-**6** were coordinated to Pt using standard Cu-catalysed coupling techniques as reported by Hagihara *et al*.[52-53] The methods followed to synthesise both mono- and disubstituted Pt-acetylide complexes are outlined in **Scheme 2.3**. To synthesise 'terminating' Pt complexes a phenyl-capped precursor was utilised ($Ph(PEt_3)_2PtCl$) to prevent multiple ligand substitution whilst 'bridging' systems were synthesised from *trans*-$(PEt_3)_2PtCl_2$, allowing *trans*-disubstitution. The reactions were performed by dissolving the appropriate Pt precursor and a slight excess of the ethynyl-ester (**1**-**6**) in a dichloromethane/amine mixture. The solutions were then degassed prior to the addition of the CuI after which the mixtures were stirred for 12 h with the progress monitored by TLC (2:1 hexane/dichloromethane). Each of the products was purified by silica column chromatography for which the details are available in the experimental section. The synthesis of the {CF_3}-substituted complexes, **Pt4a** and **Pt4b** differed slightly, requiring *in situ* deprotection of the TMS-protected ethynyl group using an equivalent of NaOMe.

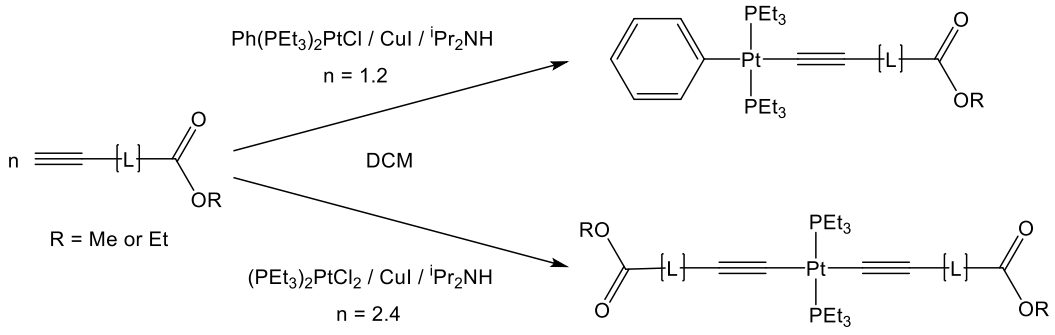

Scheme 2.3: Syntheses of Pt-ethynyl-ester complexes.

The series of both mono- (**Pt1a**-**Pt6a**) and disubstituted (**Pt1b**-**Pt6b**) Pt-ethynyl-ester complexes synthesised in this study are summarised in **Figure 2.4**. Crystals suitable for single crystal X-ray diffraction studies were grown for each of the products from cooled solutions of either pentane or hexane with the exception of **Pt6b**, which was crystallised by dichloromethane/hexane layering. The crystals of **Pt1a/b** were colourless, those of **Pt2a** were very pale green and the thienyl derivatives (**Pt5a/b**) were bright orange. All other complexes yielded yellow crystals.

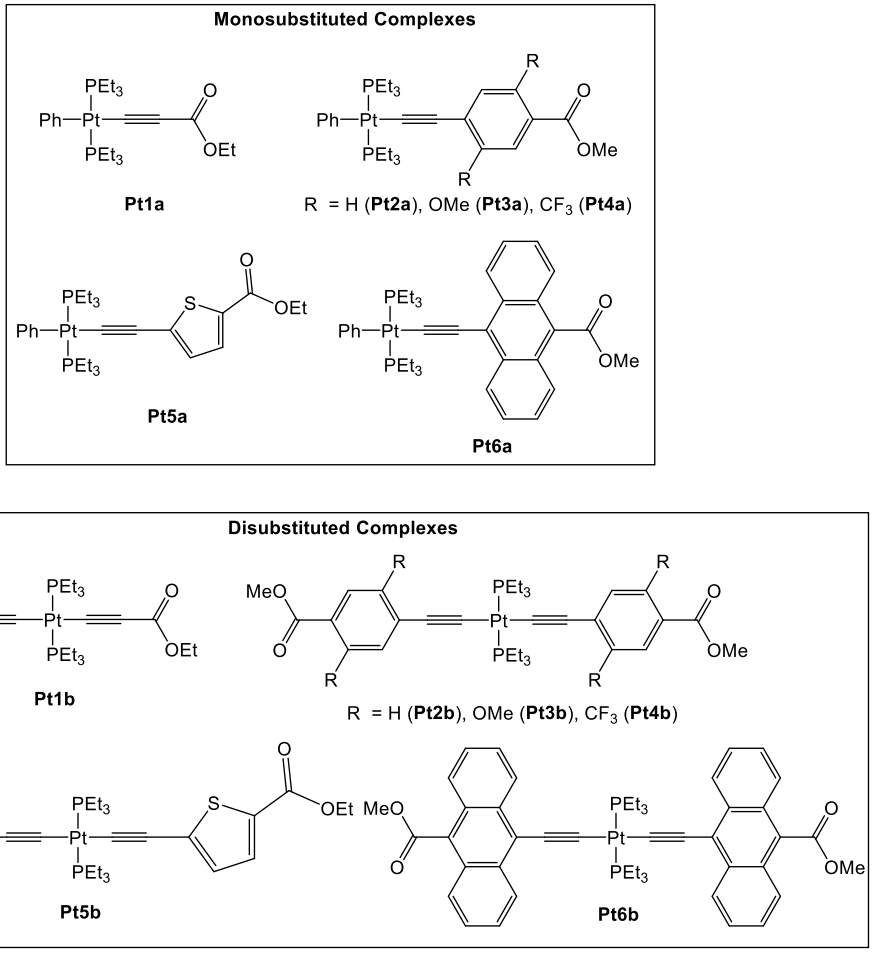

Figure 2.4: Pt-ethynyl-ester complexes synthesised in this study.

To the best of our knowledge only **Pt1b** is currently known within the literature, synthesised by Osakada *et al*. in a study to investigate ligand metathesis reactions between Pt- and Pd-acetylide complexes.[149] The method used within this study was analogous to that reported in the literature, however, a significant amount of a secondary product was also formed in this reaction which was not noted within the literature report. The same side-product was also observed following preparation of

Pt1a. The impurity was isolated using silica column chromatography and, following ^{1}H and ^{13}C NMR spectroscopic analysis, was shown to be a known propenoate species formed through the hydro-chlorination of the ethylpropiolate {C≡C} bond (**Scheme 2.4**).

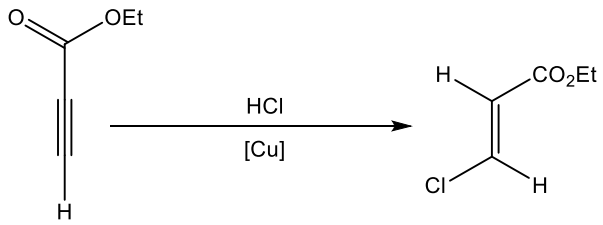

Scheme 2.4: Formation of a propenoate side-product during the syntheses of **Pt1a** and **Pt1b**.

Interestingly it was only the *E*-conformation of this species that was observed although literature precedent suggests that the *Z*-isomer is the more usual product.[161-163] The HCl involved in the transformation is produced during the catalytic reaction between the ethylpropiolate and the CuCl catalyst, and the reactivity at the {C≡C} bond is likely to stem from polarisation induced due to the adjacent electron-withdrawing ester functionality. In future syntheses of Pt complexes bearing the ethylpropiolate ligand, it would be worth considering an alternative synthetic strategy to avoid the formation of this side product, for instance the use of stannyl coupling could be attempted.[51]

2.2.3 – Structural Analyses of the Monosubstituted Pt Complexes

Complex **Pt1a** crystallised in the orthorhombic space group *Pcmn* with half a molecule in the asymmetric unit. A mirror plane runs along the length of the molecule, bisecting the plane of the phenyl ligand and continuing through the Pt-acetylide fragment. Slight rotation of the ester, relative to the mirror plane, provides symmetry-imposed disorder of this moiety. **Pt2a**, **Pt3a** and **Pt5a** crystallise in the monoclinic space group $P2_1/c$, **Pt4a** in the monoclinc space group $P2_1/n$ and **Pt6a** in the triclinic spacegroup *P-1*, each with a single molecule in the asymmetric unit. The molecular structures of complexes **Pt1a-6a** are all extremely similar and as such, only the molecular structures of **Pt2a** and **Pt5a** are shown as representative examples

in **Figure 2.5**. Selected bond lengths and angles observed within the series of molecular structures are presented in **Table 2.1** and **Table 2.2**. The molecular structures of the remainder of the series are available in the appendices.

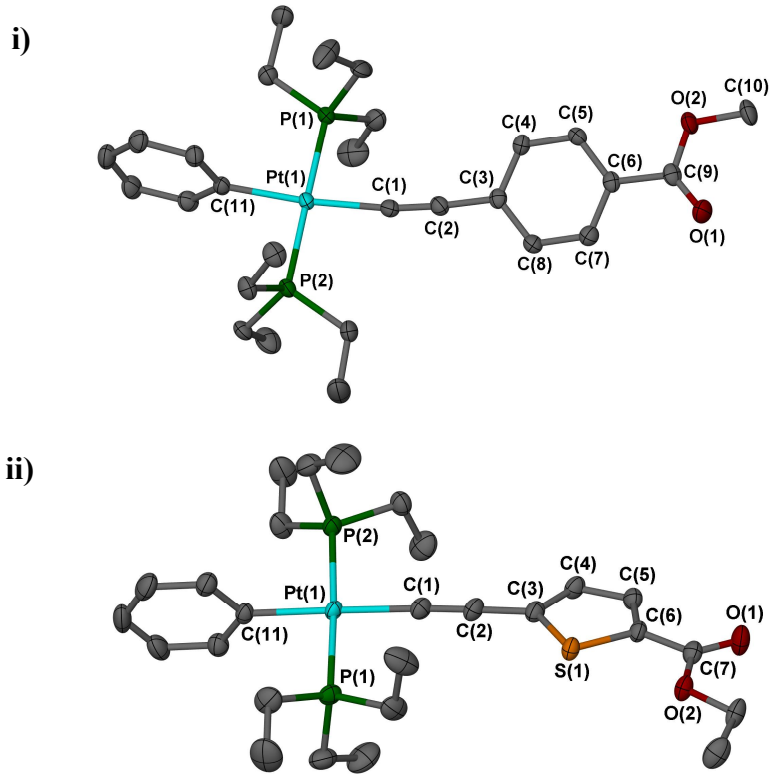

Figure 2.5: Molecular structures of **Pt2a** (**i**) and **Pt5a** (**ii**) shown with ellipsoids at 50% probability and hydrogen atoms removed for clarity.

Analogous to the catalogue of 'rigid-rod' Pt(II) acetylide complexes reported in the literature, the structures of **Pt1a**-**Pt6a** exhibit square-planar geometries around the Pt centre and a *trans*-orientation of the phosphine ligands. In each structure the Pt-coordinated phenyl ligand lies approximately perpendicular to the Pt square plane, relieving the sterics incurred from the phosphine ligands. An analysis of the bond lengths observed for complexes **Pt1a**-**Pt6a**, shown in **Table 2.1**, shows that the analogous bond lengths in each species show negligible difference within the error of the measurements. The parameters reported are also very similar to Pt-acetylide complexes that have been reported in the literature which feature a wide range of spacer molecules.[39,54,57,59,65-66,71] The spacer therefore has no observable effect on the geometry around the Pt-centre. The bond angles displayed in **Table 2.1** are in keeping with the square-planar geometry, with all P-Pt-C angles within a few

degrees of 90, although slightly more distortion was noticed in the P-Pt-C(C≡C) angles for **Pt2a**. This is likely to be a result of crystal packing interactions (*vide infra*). The lateral bond angles of P-Pt-P and C-Pt-C are close to linear but again a degree of distortion can be observed, most significantly in **Pt2a**, **Pt4a** and **Pt6a**.

Table 2.1: Selected bond lengths (Å) from the molecular structures of **Pt1a**-**Pt6a**

	Pt-C (C≡C)	**Pt-C (Ph)**	**Pt-P**	**C≡C**
Pt1a	2.022(8)	2.060(8)	2.294(2)	1.18(1)
Pt2a	2.022(3)	2.070(3)	2.2915(7), 2.2871(7)	1.211(4)
Pt3a	2.024(6)	2.073(6)	2.287(2), 2.289(2)	1.208(8)
Pt4a	2.009(3)	2.062(3)	2.2940(8), 2.2922(8)	1.206(4)
Pt5a	2.011(4)	2.060(3)	2.2939(9), 2.2895(9)	1.216(5)
Pt6a	2.012(3)	2.072(3)	2.2955(7), 2.2931(7)	1.219(4)

Table 2.2: Selected bond angles (°) from the molecular structures of **Pt1a**-**Pt6a**

	P-Pt-C(Ph)	**P-Pt-C(C≡C)**	**P-Pt-P**	**C-Pt-C**
Pt1a[a]	89.10(3)	90.90(3)	177.27(7)	179.8(3)
Pt2a	89.19(8), 91.20(8)	94.33(8), 85.50(8)	177.66(3)	173.4(1)
Pt3a	88.7(2), 91.0(2)	91.5(2), 88.7(3)	176.94(7)	177.1(3)
Pt4a	88.76(8), 90.21(8)	92.54(9), 88.69(9)	173.62(3)	177.8(1)
Pt5a	88.26(9), 88.92(9)	91.9(1), 91.0(1)	177.07(3)	178.4(2)
Pt6a	88.54(8), 90.14(8)	91.84(8), 89.00(8)	174.57(2)	174.7(1)

[a] Other angles are symmetry related to those provided.

The predominant differences between **Pt1a**-**Pt6a** lie in the orientation of the different ethynyl-ester ligand systems. The torsion of the conjugated spacer, relative

to the Pt-square plane, varies from complex to complex and the magnitude of this measurement is of interest when considering the degree of π-orbital overlap throughout the different systems. The extent of conjugation can also be increased *via* coplanarity of the spacer and ester moieties and these planar torsions also vary between complexes. Data relating to these parameters are shown in **Table 2.3**. In addition to planar torsions within each complex it was also observed that several of the systems exhibited a noticeable 'bowing' of the Pt-acetylide fragment, distorting the linear geometry that would be expected. The distortion can be seen in the molecular structure of **Pt2a** shown in **Figure 2.5-i**. This effect has been quantified in **Table 2.3** using the Pt-C≡C and C≡C-C(spacer) angles. Similar observations have been noted in a number of previously reported Pt-acetylide complexes.[57,59]

Table 2.3: Selected angles (°) to describe the ligand geometries within the molecular structure of **Pt1a**-**Pt6a**.

	[Pt][a] ∠ [Spacer][b]	[Spacer] ∠ [CO_2][c]	-Pt-C≡C-	-C≡C-C-
Pt1a	n/a	n/a	179.6(7)	174.4(9)
Pt2a	ca. 17.8	ca. 8.6	171.9(2)	175.6(3)
Pt3a	ca. 64.2	ca. 15.5	177.3(3)	179.0(4)
Pt4a	ca. 73.0	ca. 23.0	178.6(3)	176.7(4)
Pt5a	ca. 21.1	ca. 4.6	175.9(6)	176.4(7)
Pt6a	ca. 60.4	ca. 78.5	173.5(2)	174.2(3)

[a] [Pt] represents the platinum square plane and is defined though the Pt and four directly bonded atoms. [b] Plane defined through the conjugated ring (not including pendant substituents). [c] Plane defined though the CO_2 fragment of the ester.

The variation in the torsion angles of the conjugated spacer units, relative to the Pt square plane, suggests that any energetic bias towards the coplanarity of these units is not strong. This is consistent with suggestions in the literature that the acetylide orbitals are "cylindrical in nature" and retain conjugation regardless of the ligand torsions observed.[56,59] However, the complexes featuring larger spacer groups, **Pt3a**,

Pt4a and **Pt6a** show significantly greater torsions than the smaller phenylene and thienyl-containing species. An inspection of similar complexes reported in the literature containing ethynylbenzene,[44] ethynylthiophene[63,158,164] and ethynylanthracene[23] ligands show that much greater spacer torsions are observed in the absence of the ester (45.0°, 74.0° and 77.9° respectively). The differences observed are likely to be due to a difference in crystal packing facilitated by the more polar ester moiety, which are able to aid π-π stacking and hydrogen bonding interactions (*vide infra*).

The torsion angles of the esters, relative to the plane of the spacers, are more closely related in all but **Pt6a**. The angles show small deviation from planarity which again seems to be influenced by the steric properties of the spacer, with **Pt4a** exhibiting the greatest spacer torsion angle. However, the torsion of the polar group is also likely to be affected by intermolecular interactions within the crystal lattice. The trend towards planarity can be attributed to a conjugation effect because, unlike the cylindrical nature of the acteylide orbitals, the π-orbital conjugation between the spacer and the ester will decrease significantly upon rotation of the ester. The bias towards planarity can also be observed in the Ru complexes of **2** reported by Low *et al*. in which only small {phenylene}···{ester} torsion angles were observed.[147-148] The position of the *peri*-anthracene hydrogen atoms in **Pt6a** prevents close contact with the ester O atoms and as such the ester rotates to an almost perpendicular geometry to minimise the steric interactions. This is a common observation within molecular structures containing anthracene carboxylate moieties.[132,165-166]

The data in **Table 2.3** shows that the 'bowing' of the ethynyl-ester ligands originates from distortion of both the Pt-C≡C and C≡C-C angles. The effect is also amplified by bending of the C-Pt-C angles shown in **Table 2.2**. Analysis of these angles shows that the overall distortion is greatest in **Pt2a** and **Pt6a** for which the greatest deviation from linearity is seen in the {Pt-C≡C} moiety. A smaller distortion is also observed in the remaining complexes. These observations highlight the flexibility of the acetylide ligands, an observation that has also been made in many systems reported in the literature.[27,57,64,71]

Predicting that the distortions were a result of intermolecular interactions within the crystal lattice, the nature of the crystal packing was analysed for each of the complexes. For complexes **Pt2a-Pt5a**, pairs of molecules form dimers within the crystal lattice through packing interactions. These dimers were formed through stacking of the ethynyl-ester ligands of two molecules, providing a degree of intermolecular π-orbital overlap and the effect is maximised by coplanarity of the conjugated spacers of the two adjacent molecules. No such interactions were observed in the crystal lattices of **Pt1a** and **Pt6a**. An inspection of the crystal packing of ethynyl-benzene,[164] ethynyl-thiophene[63] and ethynyl-anthracene[158] complexes of Pt showed that no such stacking was observed. This provides evidence that the polar ester group is important in the formation of the stacked dimers. The dimeric interactions for each of the phenylene containing species (**Pt2a**, **Pt3a** and **Pt4a**) are very similar and pictures of these interactions are displayed in **Figure 2.6**.

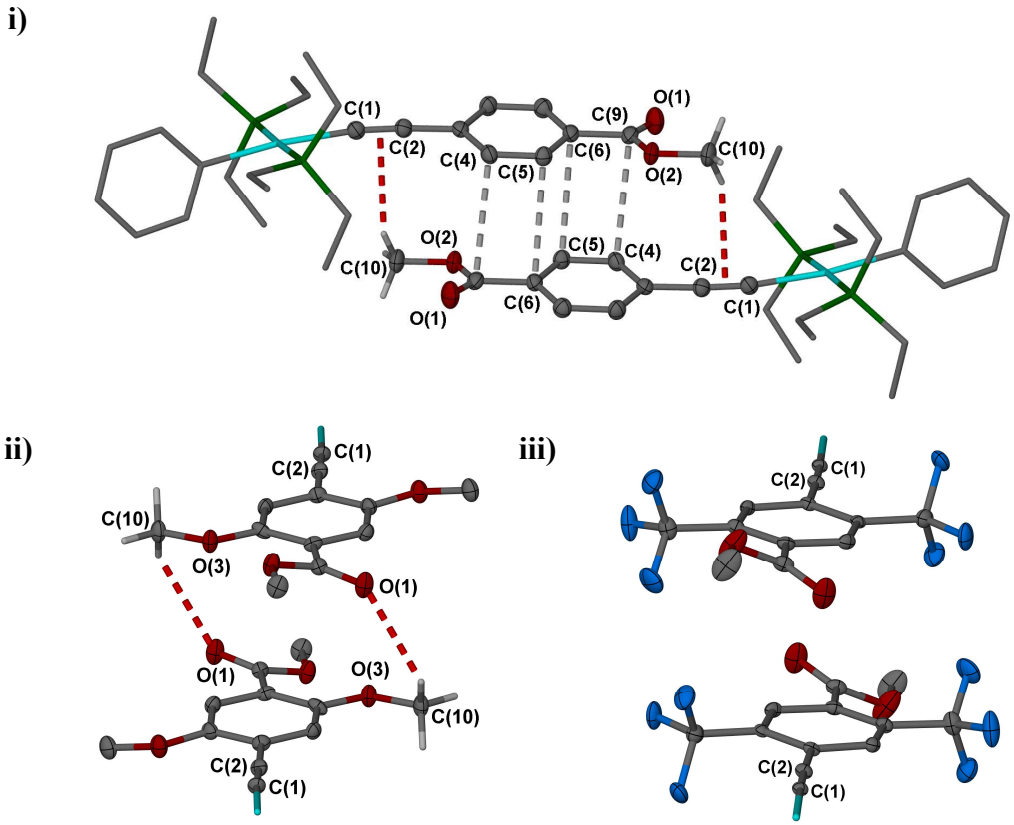

Figure 2.6: A dimer unit from the crystal lattice of **Pt2a** (**i**), with proposed H-bonds shown in red and inter-planar close contacts shown in grey, and simplified structures of the analogous interactions for **Pt3a** (**ii**) and **Pt4a** (**iii**). The ethynyl-ester moieties are shown with ellipsoids at 30% probability and selected hydrogen atoms are removed for clarity.

To aid the discussion of these interactions the distance between the two interacting molecules within the dimers of **Pt2a**-**Pt5a** have been measured, based on the separation between the planes of the phenylene or thienyl rings, and are shown in **Table 2.4**.

Table 2.4: Data quantifying the separation between molecules within the stacking dimers of **Pt2a**-**5a**.

Compound	Interplanar distance (Å)[a]
Pt2a	ca. 3.33
Pt3a	ca. 3.33
Pt4a	ca. 3.62
Pt5a	ca. 3.29

[a] Calculated as the separation between the average coplanes defined though the spacer.

The stacking interaction observed for **Pt2a** appears to be stabilised by both π-π stacking interactions in addition to {C≡C}···MeO hydrogen bonding interactions (D···A = *ca.* 3.62 Å) (shown in red in **Figure 2.6-i**). Similar hydrogen bonds have previously been observed within both Pt-acetylide[57] and organic acetylide[54] systems and the interatomic separations observed in the former are comparable to those of **Pt2a**. **Figure 2.6-i** also shows that the two ethynyl-ester ligand systems bend towards each other, providing evidence for the proposed intermolecular interactions and helping to explain the distortions outlined in **Table 2.3**. The dimers of **Pt3a** and **Pt4a** exhibit a lesser degree of intermolecular overlap in which the ester moieties are positioned over the phenylene ring of the second molecule. This packing precludes similar hydrogen bonding interactions, however, the dimer of **Pt3a** does exhibit alternative intermolecular hydrogen bonding interactions between the {Ph-OCH_3} and {C=O} moieties (D···A = 3.39 Å). The separation between molecules within **Pt2a** and **Pt3a** is approximately the same whilst the analogous distance in **Pt4a** is significantly greater. This is likely to be a result of the absence of intermolecular hydrogen bonding interactions coupled with repulsive intermolecular F···F

interactions (*ca.* 2.89 and 3.27 Å). It is interesting to note that the methoxy substituents of **Pt3a** both lie in approximately the same plane as the phenylene ring, aiding the close contact between molecules. Each of the inter-ligand separations are well within the range expected for graphitic packing.[167-169]

The dimers formed in the lattice of **Pt5a** are similar to those of **Pt3a** and **Pt4a** in which the ester moiety is positioned over the thienyl ring of the second molecule. However, unlike the phenylene-containing species, the stacked dimers are connected *via* {C=O}···H-thienyl hydrogen bonding interactions (C(5)-O(1) = 3.370(4) Å) as shown in **Figure 2.7**. The entirety of the thienyl-ester moiety is approximately coplanar, which aids the close proximity of the stacking ligands, a distance that is slightly smaller for **Pt5a** than was observed for **Pt2a** and **Pt3a**.

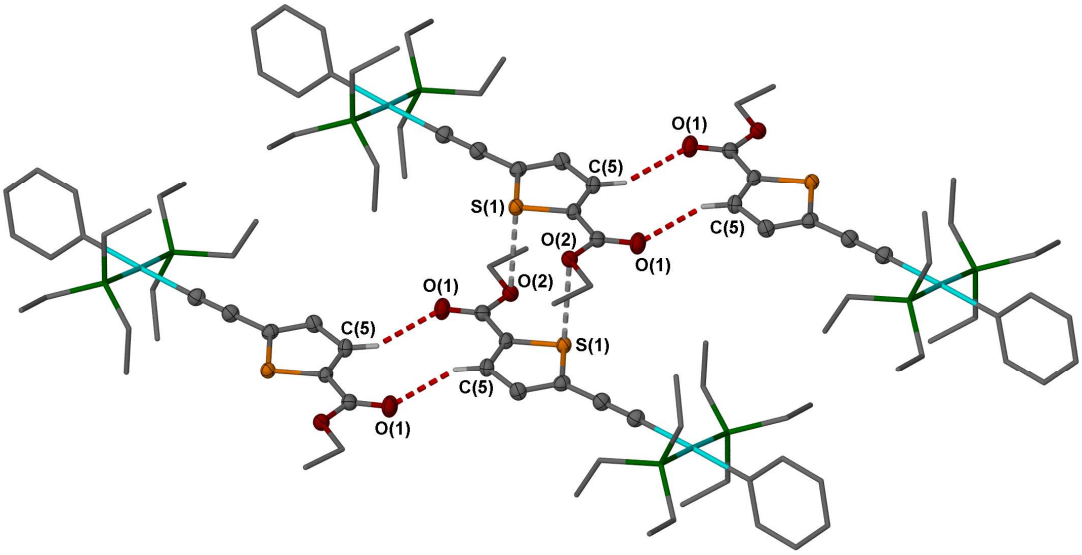

Figure 2.7: Dimer network formed in the crystal lattice of **Pt5a** with proposed H-bonds shown in red and inter-planar close contacts shown in grey. The ethynyl-carboxylate moiety is shown with 50% thermal ellipsoids and the non-interacting thienyl hydrogen atoms are removed for clarity.

2.2.4 – Structural Analyses of the Disubstituted Pt Complexes

Each of the disubstituted Pt-acetylide complexes, **Pt1b-6b**, crystallise in the triclinic spacegroup *P-1* with the exception of **Pt2b**, which crystallised in the monoclinic spacegroup *C2/c*. In complexes **Pt1b-5b** the asymmetric unit contains half a molecule with the platinum lying on a special position, with the second half a molecule generated by inversion through this coordinate. The asymmetric unit of **Pt6b** contains an entire molecule in which the two ethynyl-ester ligands exhibit significantly different torsions relative to the Pt square plane, breaking the symmetry across the Pt centre. The molecular structure of **Pt2b** is shown in **Figure 2.8-i**, as an example of the fully symmetrical complexes and the structure of **Pt6b** is also presented to highlight the unsymmetrical ligand geometries (**Figure 2.8-ii**).

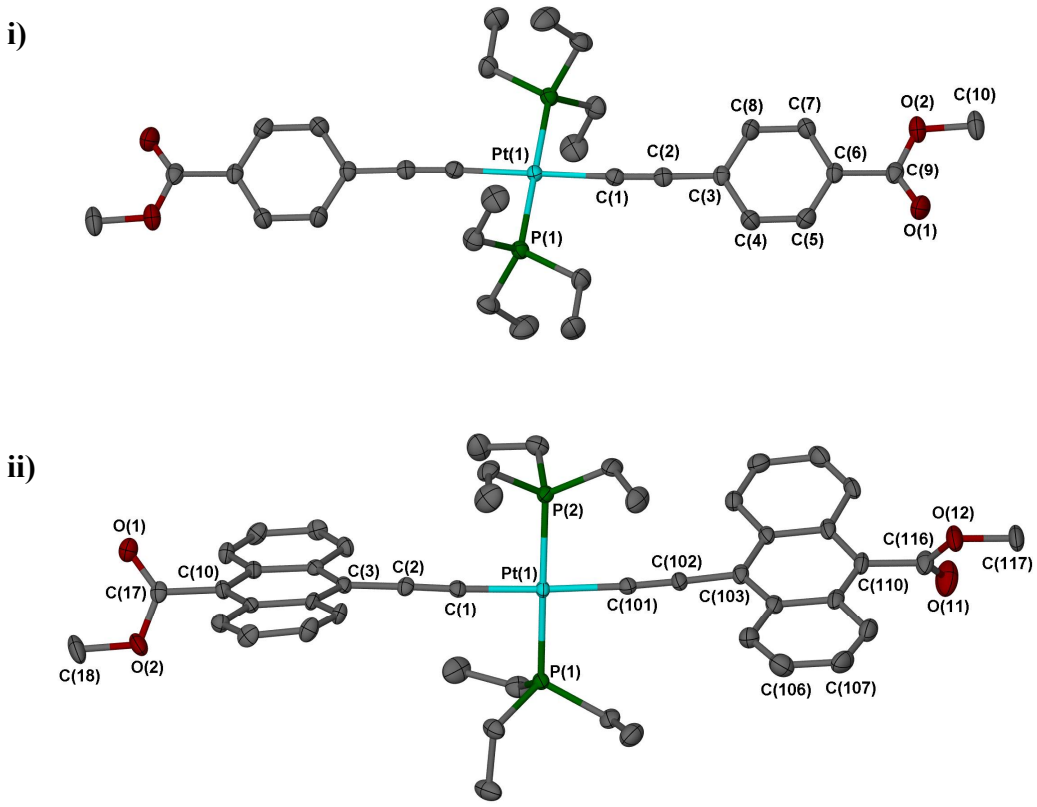

Figure 2.8: Molecular structures of **Pt2b** (**i**) and **Pt6b** (**ii**) shown with ellipsoids at 50% probability and hydrogen atoms removed for clarity.

The geometry of surrounding the Pt centres in each of the disubstituted complexes is square-planar, exhibiting *trans*-conformations of the phosphine and ethynyl-ester ligands. The symmetry present in the crystal structures of **Pt1b-Pt5b** dictates a

coplanar arrangement of the ethynyl-ester ligands in these complexes, maximising π-orbital overlap across the length of the molecules. In contrast, there is no inversion centre at the centre of **Pt6b** and as such the two anthracene-containing ligands are symmetry-independent and exhibit significant torsion angles relative to each other. This may reflect that conjugation does not extend across the Pt centre within **Pt6b**. Selected bond lengths and bond angles for each complex are shown in **Table 2.5** and **Table 2.6** respectively.

Table 2.5: Selected bond lengths (Å) from the molecular structures of **Pt1b**-**Pt6b**

	Pt-C (C≡C)	**Pt-P**	**C≡C**
Pt1b	1.986(3)	2.2964(7)	1.215(4)
Pt2b	1.994(2)	2.2993(5)	1.199(2)
Pt3b	2.004(3)	2.3080(7)	1.210(4)
Pt4b	1.994(3)	2.2989(6)	1.201(4)
Pt5b	1.998(3)	2.3022(6)	1.209(4)
Pt6b	1.992(4), 1.995(4)	2.315(1), 2.316(1)	1.218(5), 1.214(5)

Table 2.6: Selected bond angles (°) from the molecular structures of **Pt1b**-**Pt6b**

	Pt-P- C(C≡C)	**P-Pt-P[a]**	**C-Pt-C[a]**
Pt1a	92.74(7), 87.26(7)	180	180
Pt2a	93.28(5), 86.72(5)	180	180
Pt3a	95.37(8), 84.63(8)	180	180
Pt4a	92.23(7), 87.77(7)	180	180
Pt5a	92.74(7),87.26(7)	180	180
Pt6a	91.3(1), 91.0(1), 87.9(1), 89.7(1)	176.71(4)	177.6(2)

[a] Inversion symmetry dictates the linearity of these parameters for all but **Pt6b**.

Negligible differences are observed between the bond lengths observed for complexes **Pt1b**-**Pt6b** which are the same within error to those observed for the monosubstituted complexes **Pt1a**-**Pt6a**. The bond angles around the Pt centre exhibit a small amount of distortion, in particular **Pt3b** exhibits a deviation of almost 5^{o} from the 90^{o} expected for square-planar geometry. Analysis of the molecular geometry of **Pt3b** suggests that this distortion is not caused by steric repulsion between the phosphine and the methoxy substituents on the phenylene ring. Solid-state intermolecular interactions are therefore more likely to be the cause (*vide infra*). Similar to the observations made for **Pt1a**-**Pt6a** the predominant differences between the molecular structures of **Pt1b**-**Pt6b** lie in the geometries of the ethynyl-ester ligands which are expressed by the angles presented in **Table 2.7**.

Table 2.7: Selected angles (^{o}) to describe the ligand geometries within the molecular structure of **Pt1b**-**Pt6b**.

	[Pt]^{a}∠[Spacer]^{b}	**[Spacer]∠ [CO_2]^{c}**	**-Pt-C≡C-**	**-C≡C-C-**
Pt1b	n/a	n/a	177.1(2)	179.3(3)
Pt2b	13.1(1)	8.5(3)	177.4(2)	178.3(2)
Pt3b	22.1(1)	26.3(1)	175.0(3)	178.0(3)
Pt4b	74.35(6)	32.0(4)	176.8(2)	173.9(3)
Pt5b	12.3(1)	6.4(2)	177.3(2)	175.6(3)
Pt6b	89.5(1), 67.8(1)	66.7(2), 66.0(3)	177.2(3), 175.1(3)	175.9(4), 177.6(4)

[a] [Pt] represents the platinum square plane and is defined though the Pt and four directly bonded atoms. [b] Plane defined through the conjugated ring (not including pendant substituents). [c] Plane defined though the CO_2 fragment of the ester.

The torsion angles of the conjugated spacer of **Pt2b**, **Pt3b** and **Pt5b**, relative to the Pt square planes, are all relatively small and are significantly smaller than observed for the monosubstituted analogues and much smaller than the ligand torsions observed in Pt-ethynylbenzene and Pt-ethynylthiophene complexes reported in the

literature (45.0° and 74.0° respectively).[63,164] As with the monosubstituted complexes, this observation is likely to be related to intermolecular packing interactions. **Pt4b** and **Pt6b** exhibit much larger spacer torsion angles, consistent with the observations for **Pt4a** and **Pt6a**, an observation that can be correlated to the greater steric demands of the ligands in these systems, resulting in greater repulsion from the phosphine ligands. Indeed, it has been shown that in $(PBu_3)_2Pt$(*bis*-ethynylanthracene), containing a bulkier phosphine, the torsion angles of both spacers relative to the Pt square-plane are 90°.[158] The differing torsion angles for the two anthracene containing ligands of **Pt6b** provide evidence that the packing environment within the crystal lattice can play a major role in determining this parameter.

The ester moieties of the less sterically hindered complexes **Pt2b** and **Pt5b** are very close to coplanar with their respective spacers. The systems with bulkier spacers exhibit larger torsion angles, but these are significantly greater for **Pt6b** due to steric interactions involving the anthracene *peri*-protons. Similar to the observations made for the monosubstituted complexes, a slight bending within the Pt-acetylide moiety is observed within the disubstituted Pt-acetylide structures. The symmetry imposed linearity of the square-planar core of **Pt1b**-**5b** means that the bending of the ligands is purely a factor of the Pt-C≡C and C≡C-C bond angles in these systems whereas **Pt6b** also exhibits a slight distortion in the C-Pt-C angle. The greatest distortion is observed within the structure of **Pt4b**, although this lies within the range of angles that have previously been reported for Pt-acetylide complexes.[17,27,59,65-66,71]

To allow comparisons to be drawn between the mono- and disubstituted Pt-ethynyl-ester complexes, the molecular packing within crystal lattices of **Pt1b**-**Pt6b** were explored. Similar to our previous observations, intermolecular stacking interactions between ethynyl-ester ligands were observed for **Pt2b**-**Pt5b** resulting in the formation of continuous chains within the crystal lattice. **Figure 2.9** displays three interacting molecules of **Pt4b**, showing that the interactions also appear to result in the bending of the ligand system.

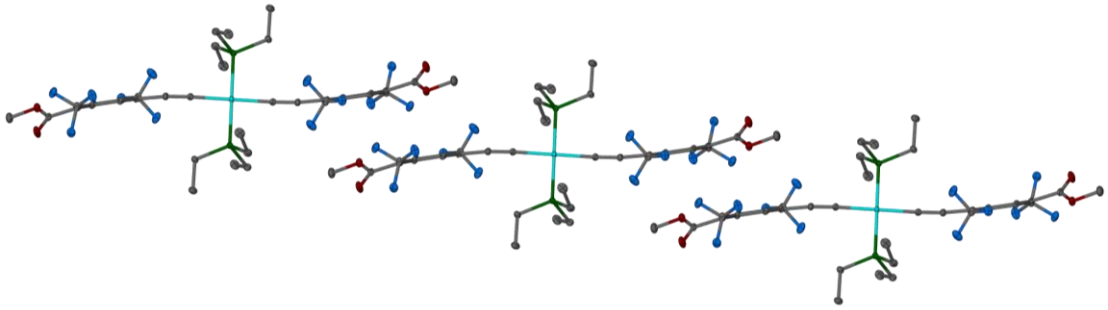

Figure 2.9: A chain formed within the crystal lattice of **Pt4b**, shown with ellipsoids at 30% probability and hydrogen atoms removed for clarity.

The intermolecular interactions observed for the **Pt2b**, **Pt3b** and **Pt5b** are similar to those of **Pt4b** although, consistent with the observations made for **Pt2a**, there is significantly greater ethynyl-ester overlap within the lattice of **Pt2b** and similar {C≡C}···MeO hydrogen bonding interactions were observed (D···A = *ca*. 3.58 Å). Similar to **Pt3a**, **Pt3b** also exhibits weak intermolecular hydrogen bonds between the {Ph-OCH_3} and {C=O} moieties (D···A = 3.563 Å). Unlike **Pt5a**, **Pt5b** exhibits no inter-chain hydrogen bonding interactions.

Table 2.8: Data quantifying the separation between molecules within the stacking dimers of **Pt2b-5b** compared to the data recorded for **Pt2a-5a**.

Compound	Interplanar distance (Å) x = a[a]	Interplanar distance (Å) x = b[a]
Pt2x	3.33	3.37
Pt3x	3.33	3.42
Pt4x	3.62	3.46
Pt5x	3.29	3.50

[a] Calculated as the separation between the average coplanes defined though the spacer

The data in **Table 2.8** shows that the distance between the planes of the stacking molecules for **Pt2b-Pt5b** vary slightly from the observations made for **Pt2a-Pt5a** The separation of the phenylene rings in **Pt4b** is significantly smaller than in **Pt4a**

which is accompanied by slightly closer F···F contacts (*ca*. 2.79 Å) and the thienyl rings of **Pt5b** are significantly further apart than in **Pt5a**. Both **Pt2b** and **Pt3b** exhibit only a slight increase in interplanar separation compared to the monosubstituted analogues. Once again these distances are well within the range expected for graphitic packing.[167-169]

Linear arrays are also formed within the crystal lattices of both **Pt1b** and **Pt6b**, facilitated by intermolecular hydrogen bonding interactions between adjacent ester groups (D···A = *ca*. 3.48 Å an 3.37 Å respectively). The interactions within the crystal lattice of **Pt1b** are shown in **Figure 2.10**. It is likely that, for **Pt6b**, the significant torsion of the ester group relative to the anthracene ring precludes significant overlap between ethynyl-ester ligands thus preventing the π-π stacking interactions observed for the phenylene- and thienyl-containing systems.

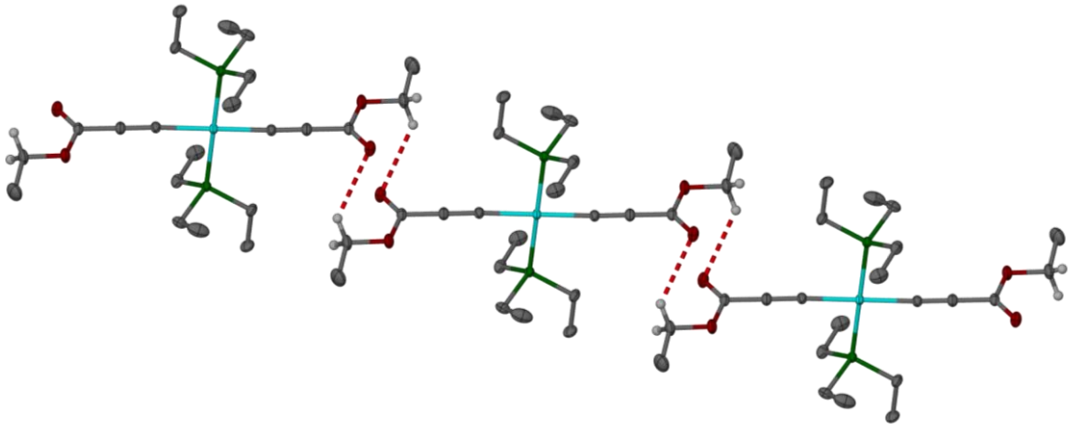

Figure 2.10: Diagram showing three molecules of **Pt1b** interacting via hydrogen bonding interactions. Ellipsoids shown at 50% probability with only selected hydrogens shown for clarity.

The crystal lattice of each of the disubstituted complexes with the exception of **Pt2b** exhibit solely linear arrays of molecules, as is shown for **Pt4b** in **Figure 2.11-i**. This is logical considering the long rod shape of the molecules which preferentially pack length ways. However, the *C2/c* space group of **Pt2b** dictates that, whilst linear chains of molecules are formed in the crystal lattice, these are multidirectional (**Figure 2.11-ii**).

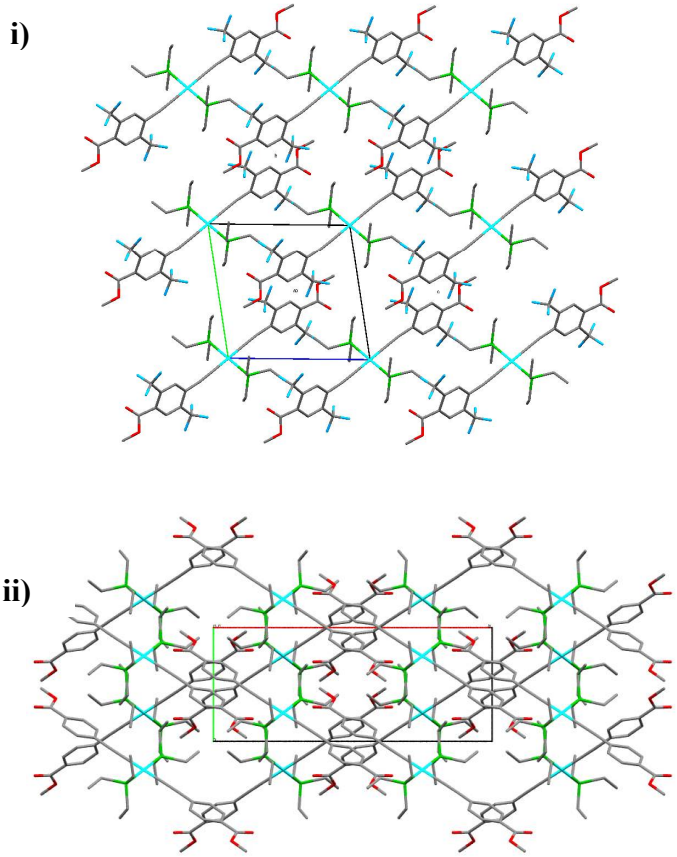

Figure 2.11: A picture of a section of the crystal lattice of **Pt4b** viewed down the a-axis (**i**) and a section of the crystal lattice of **Pt2a** viewed down the c-axis (**ii**).

2.2.5 – NMR Spectroscopic Analyses

The ^{1}H and $^{13}C\{^{1}H\}$ NMR spectra recorded for complexes **Pt1a-Pt6a** and **Pt1b-Pt6b** are each consistent with the molecular structures determined from the single crystal X-ray diffraction studies. The absence of an ethynyl proton resonance differentiates each complex from the respective free ethynyl-ester systems and coordination of the ethynyl-esters to the Pt centres is shown to result in an up-field shift in the resonances corresponding to the close proximity protons on the conjugated spacers. Within the $^{13}C\{^{1}H\}$ NMR spectra, the resonances corresponding to the {Pt-C≡C} carbon atoms are significantly shifted down-field relative to the free ligands corresponding to electronic deshielding of the nuclei within the Pt complexes. **Pt4a** and **Pt4b** and their respective pre-ligands were also analysed using ^{19}F NMR

spectroscopy, but no perturbation of the resonances corresponding to the $\{CF_3\}$ groups was observed between any of these species.

The $^{31}P\{^1H\}$ NMR spectra recorded for each of the Pt complexes exhibited a single resonance, providing evidence that only the *trans*-isomers, observed within the molecular structures of each complex, are present in solution. The chemical shift of the phosphorus resonances exhibited negligible difference throughout the entire range of complexes and are thus insensitive to the identity of the conjugated spacer. This is common for *trans*-substituted Pt-acetylide systems containing phosphine ligands. [17,27,59,65-66,71] The ^{31}P resonances of each complex also exhibited a pair of ^{195}Pt satellites, corresponding to $^1J_{P\text{-}Pt}$ coupling, which differ significantly between mono- and disubstituted complexes but more subtly within similarly substituted species (*vide infra*).

To investigate how the identity of the conjugated spacer affects the electronic environment at the metal centre each of the Pt-acetylide complexes were also studied using ^{195}Pt NMR spectroscopy. The chemical shifts and $^1J_{Pt\text{-}P}$ coupling constants recorded for each species are shown in **Table 2.9**.

Table 2.9: ^{195}Pt NMR data recorded for **Pt1a**-**Pt6a** and **Pt1b**-**Pt6b**. Chemical shifts reported in ppm and $^1J_{Pt\text{-}P}$ reported in Hz.

Terminal Sytems		**Bridging Systems**	
Complex	**^{195}Pt δ and ($^1J_{Pt\text{-}P}$)**	**Complex**	**^{195}Pt δ and ($^1J_{Pt\text{-}P}$)**
Pt1a	-4571.5 (2607 Hz)	**Pt1b**	-4757.2 (2292)
Pt2a	-4551.2 (2638 Hz)	**Pt2b**	-4724.0 (2358)
Pt3a	-4539.9 (2634 Hz)	**Pt3b**	-4704.3 (2343)
Pt4a	-4543.4 (2630 Hz)	**Pt4b**	-4709.3 (2302)
Pt5a	-4547.8 (2623 Hz)	**Pt5b**	-4716.1 (2329)
Pt6a	-4546.7 (2638 Hz)	**Pt6b**	-4706.3 (2367)

The ^{195}Pt NMR data shows that the 'phenyl-capped' Pt-acetylide complexes exhibit more downfield chemical shifts than those of the disubsituted species, showing that upon the addition of a second ethynyl-ester ligand the Pt nuclei become more shielded. The acetylide ligands are therefore stronger donors of electron density than the phenyl ligand present in complexes **Pt1a**-**Pt6a**. The Pt-P coupling is also reduced in the presence of the second acetylide ligand. Within the monosubstituted complexes the chemical shifts observed span *ca*. 30 ppm. **Pt1a**, containing no conjugated spacer, exhibits the most shielded Pt nucleus of the series whereas that of **Pt3a** is the most deshielded despite the electron donating methoxy substituents. The chemical shift of the remaining complexes follow the trend **Pt4a**>**Pt6a**>**Pt5a**>**Pt2a** although the differences between the values are small and it is only the chemical shift of **Pt1a** that differs significantly. The magnitude of $^{1}J_{Pt\text{-}P}$ does not directly correlate with the order of the chemical shifts but once again the values are similar across the series of complexes. The weakest coupling was observed for **Pt1a** and the strongest for **Pt2a** and **Pt6a**.

The ^{195}Pt chemical shifts observed for the disubstituted complexes exhibit a greater range than was observed for the monosubstituted systems. Once again it is the system without a spacer that exhibits the most shielded Pt nuclei by a significant margin followed by **Pt2a**. The remaining systems exhibit similar chemical shifts in the order **Pt3b**>**Pt6b**>**Pt4b**>**Pt5b**. The $^{1}J_{Pt\text{-}P}$ coupling is again weakest within the ethyl propiolate complex **Pt1b**. The strongest coupling was observed for **Pt6b**. With the exception of **Pt1a** and **Pt1b** there appears to be no correlation between the chemical shifts or the magnitude of $^{1}J_{Pt\text{-}P}$ between the mono- and disubstituted complexes.

2.2.6 – Electronic Absorption and Emission Spectroscopy

To investigate the solution-state optical properties of the Pt-ethynyl-ester complexes, each system was analysed using electronic absorption and emission spectroscopy. All samples were analysed at room temperature using dichloromethane as solvent. The absorption and emission spectra for **Pt1a**-**6a** are shown in **Figure 2.12** and the data is summarised in **Table 2.10**.

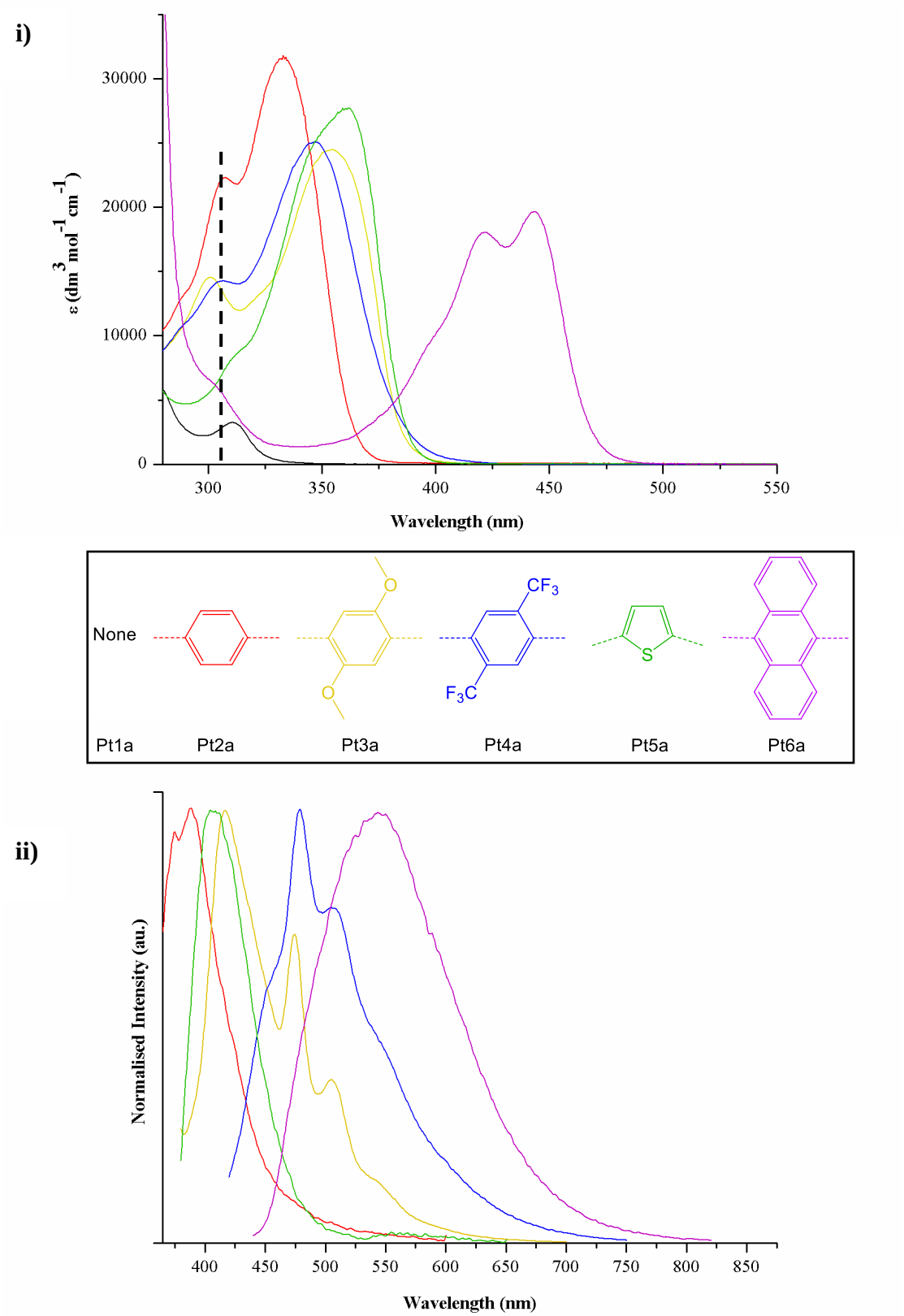

Figure 2.12: Electronic absorption spectra (**i**) and emission spectra (**ii**) of **Pt1a-6a** recorded at room temperature in DCM. Absorption data are reported using the respective absorption coefficients and the emission data are normalised (recorded in a 0.01 mmol solution)

The electronic absorption spectra for the monosubstituted complexes exhibit principal absorption bands which vary in energy depending on the identity of the conjugated spacer, with λ_{max} increasing in the order **Pt1a**<**Pt2a**<**Pt4a**<**Pt3a**<**Pt5a**<**Pt6a**. Previous studies into the optical properties of Pt-acetylide polymers and oligomers have shown that the absorption bands exhibited by such species are largely ligand $\pi \rightarrow \pi*$ in character but involve a degree of mixing with the appropriate symmetry Pt *d*-orbitals. It is therefore unsurprising that the highest energy absorption band is observed for **Pt1a**, which contains extremely limited conjugation, whilst the lowest energy absorption band is that of **Pt6a**, containing the highly conjugated anthracene spacer. A comparison of the relative absorption energies of **Pt2a**-**Pt4a** show that addition of either electron-donating {OMe} or electron-withdrawing {CF_3} moieties to the phenylene spacer result in a red-shift in the observed absorption band. **Pt5a** also exhibits a significantly lower energy absorption band than the phenylene containing system, which can be attributed to the diffuse nature of the sulphur *p*-orbital, providing greater π-orbital overlap within the ligand system, and thus increasing the effective conjugation.

In all cases, the shape of the absorption bands for complexes **Pt2a**-**Pt5a** are very similar, exhibiting a lower intensity band on the higher energy side of λ_{max}. These bands appear at similar energies for each of the complexes, as depicted by the broken line in **Figure 2.12-i**, and exhibit no apparent dependence on the identity of the conjugated spacer. Due to the similar energy of λ_{max} in **Pt1a** it is possible that the electronic transitions responsible for this relatively high energy band are localised on the {Pt-C≡C} fragment of each complex. The structure of the absorption band of **Pt6a** differs from the other complexes, exhibiting two well defined bands with a slight shoulder to higher energy. The structure of the absorption band is likely to be indicative of vibrational coupling within the rigid ethynyl-anthracene unit and is consistent with the calculated peak separation of 1230 cm^{-1}, comparable to an aromatic {C=C} stretch. The absorption spectrum of **Pt6a** also exhibits a shoulder at roughly the same energy as the low energy absorption bands observed for each of the other Pt-ethynyl-esters.

Table 2.10: Summarised electronic absorption and emission data for complexes **Pt1a**-**Pt6a**.

	Electronic absorption bands (nm)[a]	Emission bands (nm)	Stokes shift[b] (cm^{-1})
Pt1a	311 (3247)	n/a	n/a
Pt2a	308 (22334), 334 (31712)	390 (350)	2971
Pt3a	301 (14558), 355 (24467)	415*, 474, 505 (360)	1611
Pt4a	307 (14273), 347 (25982)	479*, 504 (390)	4123
Pt5a	*ca.*312 (8779), 362 (27714)	405 (360)	2631
Pt6a	*ca*. 300 (6574), *ca*. 400 (10163), 421 (18035), 444 (19652),	550 (420)	4341

[a] Extinction coefficients shown in brackets, [b] calculated as the difference between the excitation and emission energies. *signifies the highest intensity band where appropriate.

The normalised emission spectra (**Figure 2.12-ii**) show that dichloromethane solutions of **Pt2a**-**Pt6a** emit over a range of wavelengths. The relative energies of the observed emission bands follow the order **Pt2a**<**Pt5a**<**Pt3a**<**Pt4a**<**P6a**. Although solutions of **Pt1a** were also analysed, a combination of the weak emission and the observation of a number of overlapping artefact signals has precluded the recording of accurate data for this species. Consistent with the observations made in the electronic absorption analysis, the presence of either electron-donating or electron-withdrawing substituents on the phenylene spacer result in a red-shift of the emission bands relative to **Pt2a**, although the shift is a lot more pronounced for the {CF_3}-substituted complex **Pt4a**. The thienyl-containing complex (**Pt5a**) emits at a similar wavelength to **Pt3a** whilst the anthracene complex, **Pt6a**, exhibits the lowest energy emissive state. Whilst both **Pt2a** and **Pt5a** exhibit fairly sharp emission profiles, those of the remaining complexes are significantly broader and, in the case of **Pt3a** and **Pt4a**, exhibit a significant degree of vibrational coupling with peak separations comparable to aromatic {C=C} vibrations.

The Stoke's shift observed between the excitation and emission maximum for each of the complexes is within the magnitude expected for fluorescent emission from a singlet excited state.[17,48,143,170-171] The shift is largest for **Pt4b** and **Pt6b** suggesting a greater structural rearrangement in the excited states of these species. The smallest Stokes shift was observed for **Pt3a** indicating a much smaller Frank-Condon shift.

The same investigations were performed on the disubstituted Pt-acetylide complexes **Pt1b**-**Pt6b** and the absorption and emission spectra observed for these species are shown in **Figure 2.13** and the data is summarised in **Table 2.11**.

The absorption spectra recorded for **Pt1b**-**Pt6b** are similar in profile to those of the related monosubstituted complexes, providing evidence that analogous $\pi\rightarrow\pi^*$ electronic transitions are occurring within each class of complexes, although the absorption coefficients are significantly higher in the presence of the second ethynyl-ester ligand system. The magnitude of λ_{max} increases in the order **Pt1b**<**Pt2b**≡**Pt4b**<**Pt5b**≈**Pt3b**<**Pt6b**. Consistent with the observations made for the monosubstituted species, the ethylpropiolate-containing system exhibits the highest energy absorption band whilst the lowest energy was observed for the anthracene containing complex. This can once again be attributed to the degree of conjugation within the ligand system. The principal absorption bands of **Pt2b**, **Pt3b** and **Pt5b** are each significantly red-shifted relative to those observed for the related monosubstituted species suggesting a greater degree of π-conjugation within the disubstituted complexes, which extends across the metal centre. Conversely, the absorption bands of **Pt1b**, **Pt4b** and **Pt6b** are each very similar in energy to the analogous absorption bands of **Pt1a**, **Pt4a** and **Pt6a**, suggesting that the $\pi\rightarrow\pi^*$ electronic transitions within these species may be more localised than the previously described disubstituted species. The absorption spectra of **Pt2a**-**Pt5a** also exhibit similar secondary absorption bands, each lying within a narrow energy range. These are consistent in energy with the similar bands exhibited by each of the monosubstituted complexes, providing further evidence that these absorption bands originate from {Pt-C≡C} localised electronic transitions. The spectrum recorded for **Pt6b** also exhibits weak shoulders at approximately the same energy.

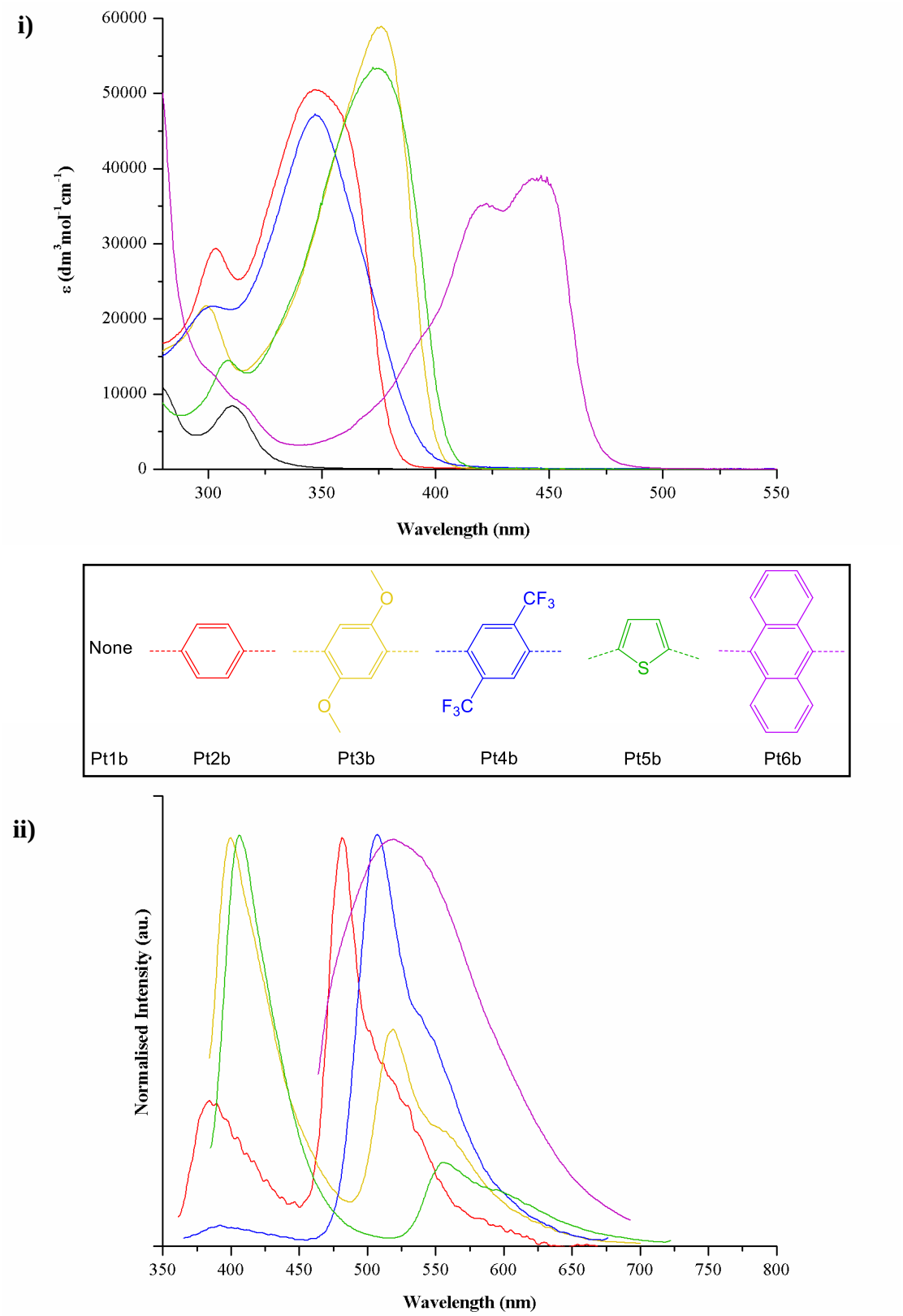

Figure 2.13: Electronic absorption spectra (**i**) and emission spectra (**ii**) of **Pt1b-6b** recorded at room temperature in DCM. Absorption data are reported using the respective absorption coefficients and the emission data are normalised (recorded in a 0.01 mmol solution).

Table 2.11: Summarised electronic absorption and emission data for complexes **Pt1b**-**Pt6b**.

	Electronic absorption bands (nm)[a]	Emission bands (nm)[b]	Stokes shift (cm^{-1})[c]
Pt1b	312 (8295)	n/a	n/a
Pt2b	303 (29348), 347 (50489)	385, 482* (345)	1959, 7186
Pt3b	300 (21728), 376 (58945)	400*, 519 (375)	1882, 7236
Pt4b	302 (21676), 347 (47229)	400, 507* (347)	3249,8525
Pt5b	309 (14492), 375 (53371)	405*, 561 (375)	950, 7816
Pt6b	*ca.* 300 (13082), *ca*. 310 (9637), *ca*. 395 (18087), 420 (35105), 445 (38742).	520 (444)	3141

[a] Extinction coefficients shown in brackets, [b] excitation wavelength shown in brackets, [c] calculated as the difference between the excitation and emission energies *signifies the highest intensity band where appropriate.

Unlike the emission spectra of the related monosubstituted complexes, **Pt2b**-**Pt5b** each exhibit two emission bands separated by a relatively large energy gap, for which the relative intensities vary depending on the identity of the spacer. Reports within the literature suggest that the high and low energy bands originate form singlet and triplet emission respectively, and this is supported by the characteristic shape of the lower energy emission bands exhibited by each of the complexes.[170,172] For both **Pt2b** and **Pt4b** it is the emission from the triplet state that dominates, suggesting efficient population of the triplet manifold within these systems. **Pt4b** exhibits only a very weak emission band corresponding to the singlet state emission. Conversely, it is the emission from the excited singlet state that is most intense for **Pt3b** and **Pt5b**, suggesting that intersystem crossing occurs more slowly for these systems. The singlet state emission bands of **Pt2b**, **Pt3b** and **Pt5b** are all very similar in energy to those observed for the monosubstituted systems but that of **Pt4b** is significantly blue shifted relative to the sole emission band observed for **Pt4a**. A

single broad emission band was observed for **Pt6b** and it is very similar in profile to that observed for **Pt6a**. However, the energy of the band is significantly blue-shifted relative to that of **Pt6a**, reflecting a higher energy emissive state within the disubstituted species. This provides further evidence that the excited state of **Pt6b** is not delocalised throughout the molecule but the reasoning behind the blue-shift observed is unknown. It is possible that the emissive state of **Pt6a** involves conjugation into the Pt-coordinated phenyl ligand which could result in lower energy emission but this postulation is not supported by theoretical analysis of the system (*vide infra*).

The Stokes shifts calculated for **Pt2b-6b**, relating to the high energy emission band, are all significantly smaller than those observed for the monosubstituted analogues, indicating a lesser extent of structural reordering within the excited states. The values are however still within the range indicative of singlet state emission. Consistent with the data recorded for the monosubstituted systems, the largest Stokes shift is observed for **Pt4b** and **Pt6b**. Within the literature it has been suggested that large Stokes shifts can be indicative of restricted ligand rotation about the Pt-acetylide bond,[171] a characteristic that is reflected by the larger spacer torsion angles observed within the molecular structures of **Pt4b** and **Pt6b** (**Table 2.7**). The Stokes shifts of the remaining complexes are significantly smaller consistent with the much smaller ligand torsion angles observed. The large Stokes's shifts that are observed for the lower energy emission bands of **Pt2a**-**Pt4a** are consistent with the assignment of triplet state emission.

The optical properties of a number of related Pt *bis*-acetylide complexes have been reported within the literature and relevant data from these studies is presented in **Table 2.12**. These systems do not contain the ester functionality present in the complexes within this study and thus allow the effects of these substituents to be assessed. Although the majority of the species described in the literature contain PBu_3 rather than PEt_3 ligands, it is generally accepted that the identity of the phosphine in such systems has negligible bearing on the electronic structure of the complex.[17]

Table 2.12: Absorption and emission data reported for *trans*-substituted Pt *bis*-ethynyl-aryl complexes.

Complex	λ_{max} (nm)	$\lambda_{emission}$ (nm)
$(PEt_3)_2Pt(-C\equiv CH)_2$[173]	305	n/a
$(PBu_3)_2Pt(-C\equiv C-Ph)_2$[67]	324	364[a], 435[b]
$(PBu_3)_2Pt(-C\equiv C-Thio)_2$[63]	349	n/a
$(PBu_3)_2Pt(-C\equiv C-Anth)_2$[158]	435	449

[a] S_1-S_0 emission recorded at room temperature, [b] T_1-S_0 emission recorded at 77 K.

The absorption bands reported for each of the literature species appear at significantly higher energy than those exhibited by the related ethynyl-ester complexes (**Pt1b**, **Pt2b**, **Pt5b** and **Pt6b**), showing that the addition of the ester functionality results in a reduction in the energy of the HOMO-LUMO gaps of these species. This suggests that π-conjugation within these systems extends into the ester moieties and is consistent with reports by Raithby *et al.* showing that increasing the electron-withdrawing ability of the conjugated spacer results in smaller optical band gaps.[60] The room temperature emission data reported for $(PBu_3)_2Pt(-C\equiv C-Ph)_2$ showed emission occurred predominantly from the singlet state, differing from the observations made for **Pt2b**. The less electron-withdrawing ligand system also renders this emission slightly higher in energy than the related ethynyl-ester species. Although $(PBu_3)_2Pt(-C\equiv C-Ph)_2$ exhibited negligible phosphorescence at room temperature, analyses conducted at 77 K did result in stronger triplet state emission. Once again this emission band is higher in energy than observed in the room temperature emission spectrum of **Pt2b**. Consistent with our own observations for **Pt6b**, only a single emission band was reported for $(PBu_3)_2Pt(-C\equiv C-Anth)_2$ and this occurs at significantly higher energy than the emission band of **Pt6b**. This difference may be a result of the bulkier phosphine within the literature complex, restricting the rotation of the relatively bulky ethynylanthracene ligands, although the electron-withdrawing ester groups of **Pt6b** are also likely to contribute to the energy shift.

2.2.7 – Theoretical Studies

To aid the interpretation of the spectroscopic data, and to assess the degree of electronic delocalisation in the ethynyl-ester complexes, theoretical studies have been employed. Through these studies the electronic structures of each complex have been calculated, based on geometry optimised molecules and all calculations were performed using the B3LYP functional[174-175] with the 6-31G* basis set[176] for all non-metal atoms and the SDD energy consistent pseudopotential basis set for Pt.[20] For most complexes the geometry optimisation was performed using atomic coordinates from the experimentally determined molecular structure as a starting point, however, symmetry related issues meant that modified structures were required for **Pt4b** and **Pt5b**. For each of the complexes, the PEt_3 ligands were modified to PMe_3 and any ethyl esters were changed to methyl esters to simplify the calculation. To avoid confusion with the experimentally synthesised complexes, these simplified systems will be discussed using ***** as a suffix (e.g. **Pt1a***).

Following the geometry optimisation of complexes **Pt1b*-5b*** the coplanarity of the two ethynyl-ester ligands that was observed in the molecular structures was retained. There was no apparent energetic bias towards coplanarity between the conjugated spacer and the Pt square-plane for either the mono- or disubstituted systems. These results are consistent with studies in the literature that have shown little difference in the groundstate energy upon rotation of Pt bound acetylide ligands.[177] The geometry optimisation of **Pt6b*** resulted in coplanarity of the anthracenyl-ester ligands, despite starting from an out of plane geometry. However, this may be a result of steric interactions as oppose to electronic stabilisation because the anthracene rings are orthogonal to the Pt square plane in the optimised structure, moving the anthracene *peri*-hydrogen atoms as far from the phosphine ligands as possible. In all but the bis(trifluoromethyl)phenylene and anthracene containing systems the geometry optimisations moved the ester moieties entirely into the plane of the conjugated spacer units due to the stabilising π-orbital overlap. Presumably, steric effects prevent coplanarity of these units within **Pt4a/b*** and **Pt6a/b***, which will restrict the electronic delocalisation into the termini of these systems.

The frontier orbitals calculated for **Pt2a*-Pt6a*** are all very similar in structure and those of **Pt2a*** are presented in **Figure 2.14** as an example.

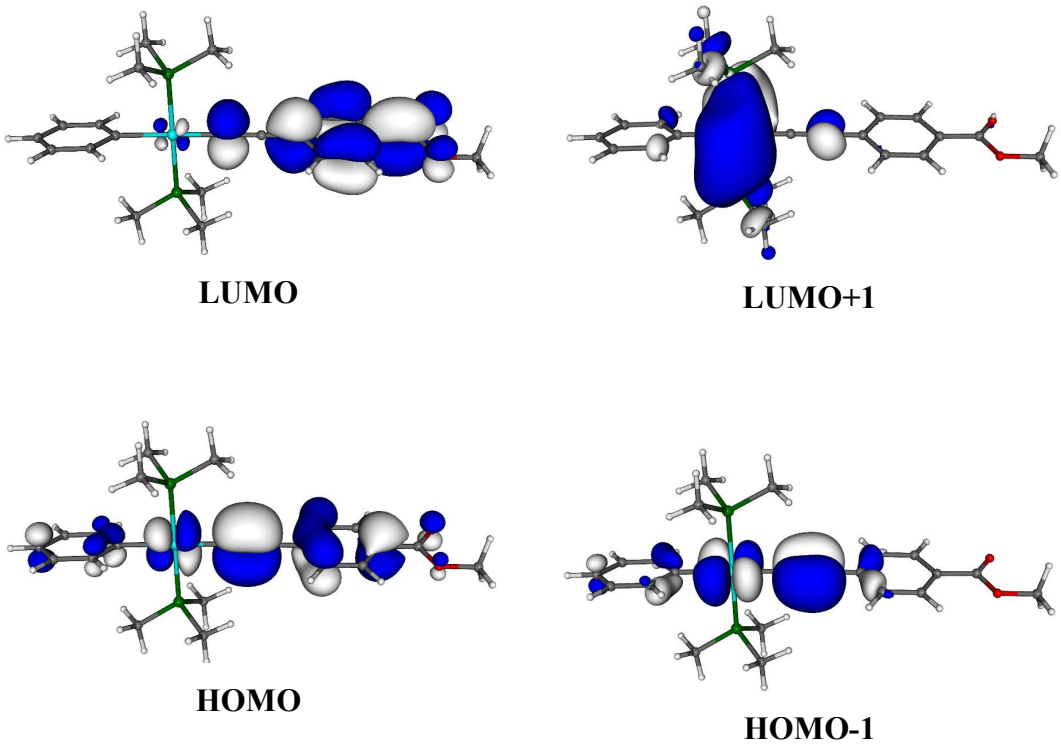

Figure 2.14: Calculated frontier orbitals for **Pt2a***.

The frontier orbitals of **Pt2a*** show that electron density within the HOMO is delocalised along the length of the molecule, facilitated by the extended π-conjugated network. This delocalisation is also shown to extend into ester moiety, which may prove to be important in regards to the electronic communication within the targeted heterometallic complexes. The HOMO-1 is largely isolated within the {Pt-C≡C} fragment of each complex, involving the short π-network orthogonal to those of the phenylene spacer. The LUMO is predominantly the π*-orbitals of the ethynyl-ester ligand with only a small amount of metal contribution and the LUMO-1 is a diffuse orbital surrounding the Pt centre. The frontier orbitals calculated for **Pt3a*-Pt6a*** are very similar in composition to those shown for **Pt2a***. The only notable difference is that the HOMO of **Pt6a*** only exhibits a very small degree of mixing with the Pt(dπ)-orbital, renders it almost entirely ligand based.

Time-dependant DFT calculations (TD-DFT) were also performed on each of the monosubstituted complexes and showed that the lowest energy electronic transitions were between the HOMO and LUMO and therefore largely $\pi \rightarrow \pi^*$ in nature. This is consistent with the assignments made within the analysis of the experimental electronic absorption data of these species and explains the sensitivity of λ_{max} to the identity of the spacer. The calculations also suggest that the lower intensity absorption bands that were observed between 300 nm and 312 nm originate from HOMO-1$\rightarrow$LUMO+1 electronic transitions. These orbitals contain little contribution from the spacer units, explaining why the energies of the absorption bands for each complex are very similar.

The absence of a conjugated spacer in **Pt1a*** results in a slightly different set of frontier orbitals to those observed in **Pt2a*-Pt6a*** and these are shown in **Figure 2.15**. The HOMO and HOMO-1 contain contributions from the two sets of acetylide π-orbitals which mix with the appropriate symmetry Pt *d*-orbitals. The HOMO also exhibits a significant amount of electron density within the phenylene π-orbitals whilst the HOMO-1 is the correct symmetry to mix with the ester π-orbitals. The LUMO orbital is similar in character to the LUMO+1 calculated for **Pt2a*** in terms of the diffuse orbital surrounding the Pt centre, but also shows a significant contribution from the ester π*-orbitals which is not observed in **Pt2a*-6a***. TD-DFT studies suggest that the absorption band observed for **Pt1a** (311 nm) is similar in character to the high energy absorption bands exhibited by **Pt2a**-**Pt6a**, predominantly involving electron transfer from the {Pt-C≡C}-localised orbitals (HOMO and HOMO-1) to the diffuse LUMO orbital. Consistent with the electronic absorption data collected for **Pt1a**, the calculation reveals a relatively low oscillator strength for this electronic transition, helping to explain the low absorption coefficient observed within the electronic absorption spectrum of **Pt1a**.

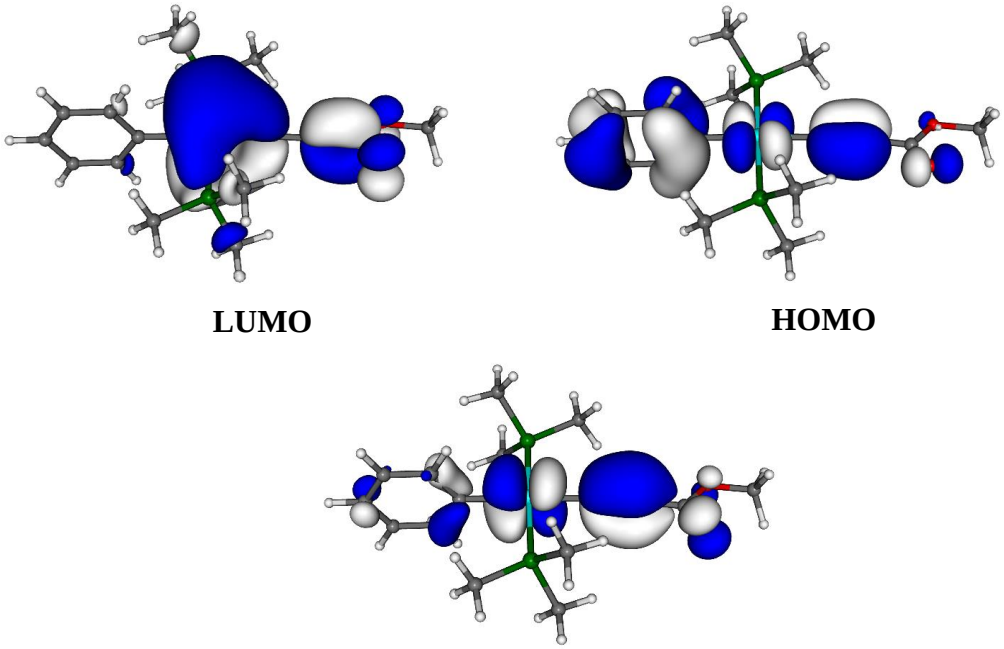

LUMO **HOMO**

HOMO-1

Figure 2.15: Calculated frontier orbitals for **Pt1a***.

The calculated frontier orbitals of the disubstituted complexes (**Pt1b*-Pt6b***) are similar in composition to those of the monosubstituted analogues with the exception that contributions from both ethynyl-ester ligands are observed. Selected frontier orbitals calculated for **Pt2b*** are presented in **Figure 2.16** as an example for this series of complexes.

The HOMO and HOMO-2 of **Pt2b*** are composed of the out-of-phase and in-phase π-orbitals of the two ethynyl-ester ligands respectively. These orbitals are separated in energy due to significant mixing with the Pt *d*-orbital in the former. Similarly, the HOMO-1 and HOMO-4, composed of the acetylenic π-orbitals orthogonal to those of the phenylene ring, are also split in energy due to metal orbital mixing. The HOMO-3 is the Ptd_z^2 orbital with electron density localised solely on the metal centre. The LUMO and LUMO+1 of **Pt2b*** are composed of the in-phase and out-of-phase combinations of the ethynyl-ester π*-orbitals respectively, again separated in energy due to mixing with the Pt *d*-orbital, destabilising the out-of-phase combination. Both the HOMO and LUMO orbitals exhibit conjugation that extends the length of the molecule including the ester termini.

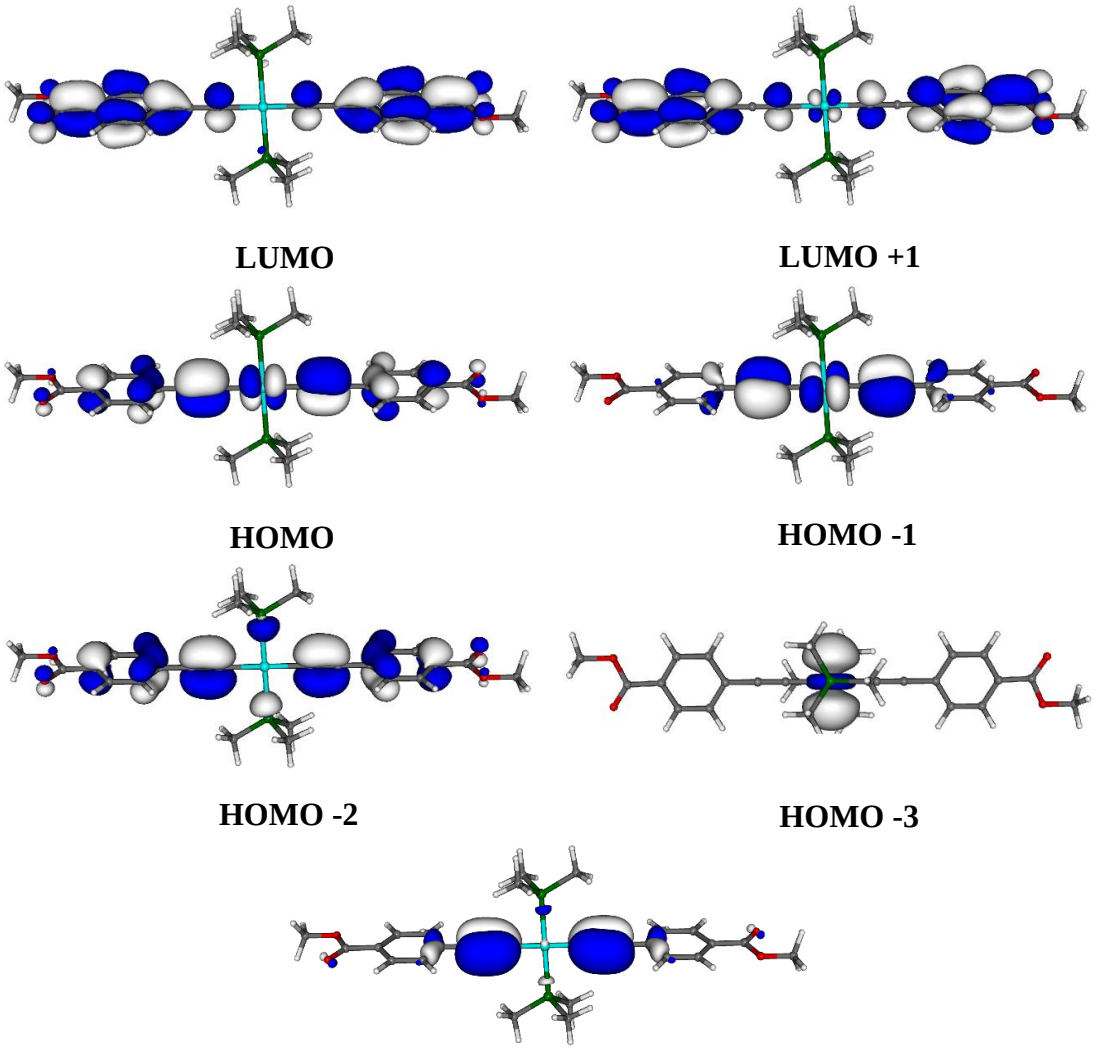

Figure 2.16: Calculated frontier orbitals for **Pt2b***.

The frontier orbitals calculated for **Pt3b***-**Pt5*** are each very similar to those shown for **Pt2b***. However, the in-phase ligand π-orbital (HOMO-2 for **Pt2b***) appear higher in energy than the {Pt-C≡C} localised π-orbitals (HOMO-1 for **Pt2b***). Additionally, **Pt3b*** also exhibits a second set of occupied ethynyl-ester π-orbitals (HOMO-2 and HOMO-4) with the relative energies of the remaining orbitals analogous to those of **Pt4b*** and **Pt5b***. The frontier orbitals of **Pt1b*** are also very similar to those of **Pt2b*** although an additional orbital localised on the {P-Pt-P} fragment (LUMO+1) separates the in- and out-of-phase π*-orbitals of the ethylpropiolate ligands (LUMO and LUMO+2). An important point to note is that the HOMO of each complex is composed of the out-of-phase π-orbitals of the two

ethynyl-ester ligands and the LUMOs are the in-phase π*-orbitals. TD-DFT calculations have shown that the lowest energy electronic transitions occur between these orbitals, which is consistent with the assignments within the electronic absorption spectra of these species.

The frontier orbitals of **Pt6b*** exhibit some significant differences to those observed for **Pt1b*-Pt5b***. The HOMO/HOMO-1 and LUMO/LUMO+1 (**Figure 2.17**) are predominantly localised on individual anthracene units, severely limiting the extent of electronic delocalisation throughout the system. There is also negligible mixing of the ligand orbitals with the *d*-orbitals of the Pt. Electronic transitions within **Pt6b*** are therefore shown to be between the π- and π*-orbitals of the isolated anthracene ligands, which helps to explains why the experimentally observed absorption band of **Pt6b** was not red-shifted relative to that of **Pt6a**.

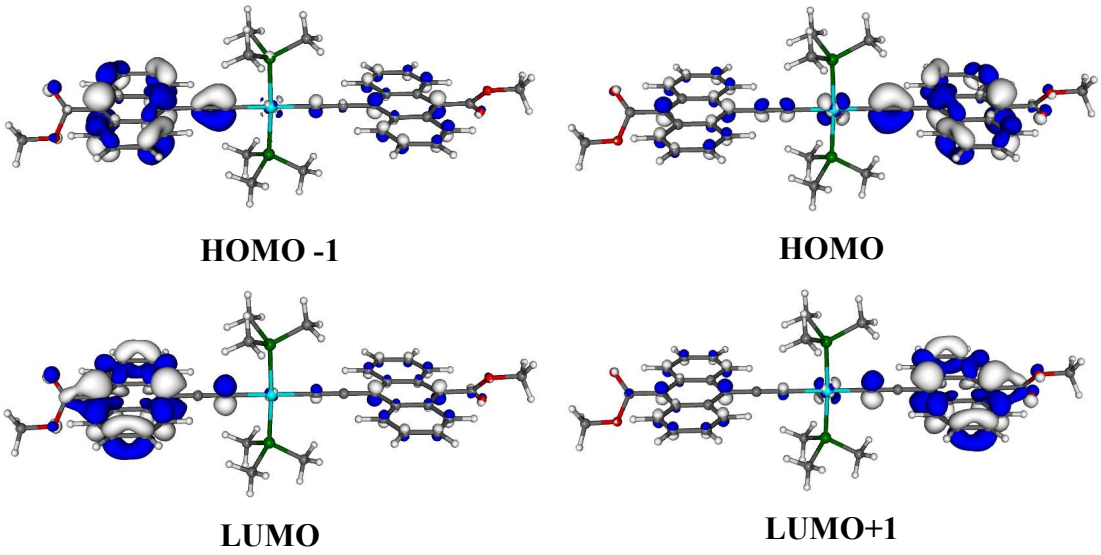

Figure 2.17: Calculated frontier orbitals for **Pt6b***.

The HOMO-LUMO energy separations within the Pt-ethynyl-ester complexes are very sensitive to the identity on the conjugated spacer, which is consistent with previous studies on Pt-acetylide complexes. Simplified molecular orbital diagrams for both the mono- and disubstituted Pt-ethynyl-ester complexes are displayed in **Figure 2.18**, highlighting the magnitudes of the HOMO-LUMO gaps for each species.

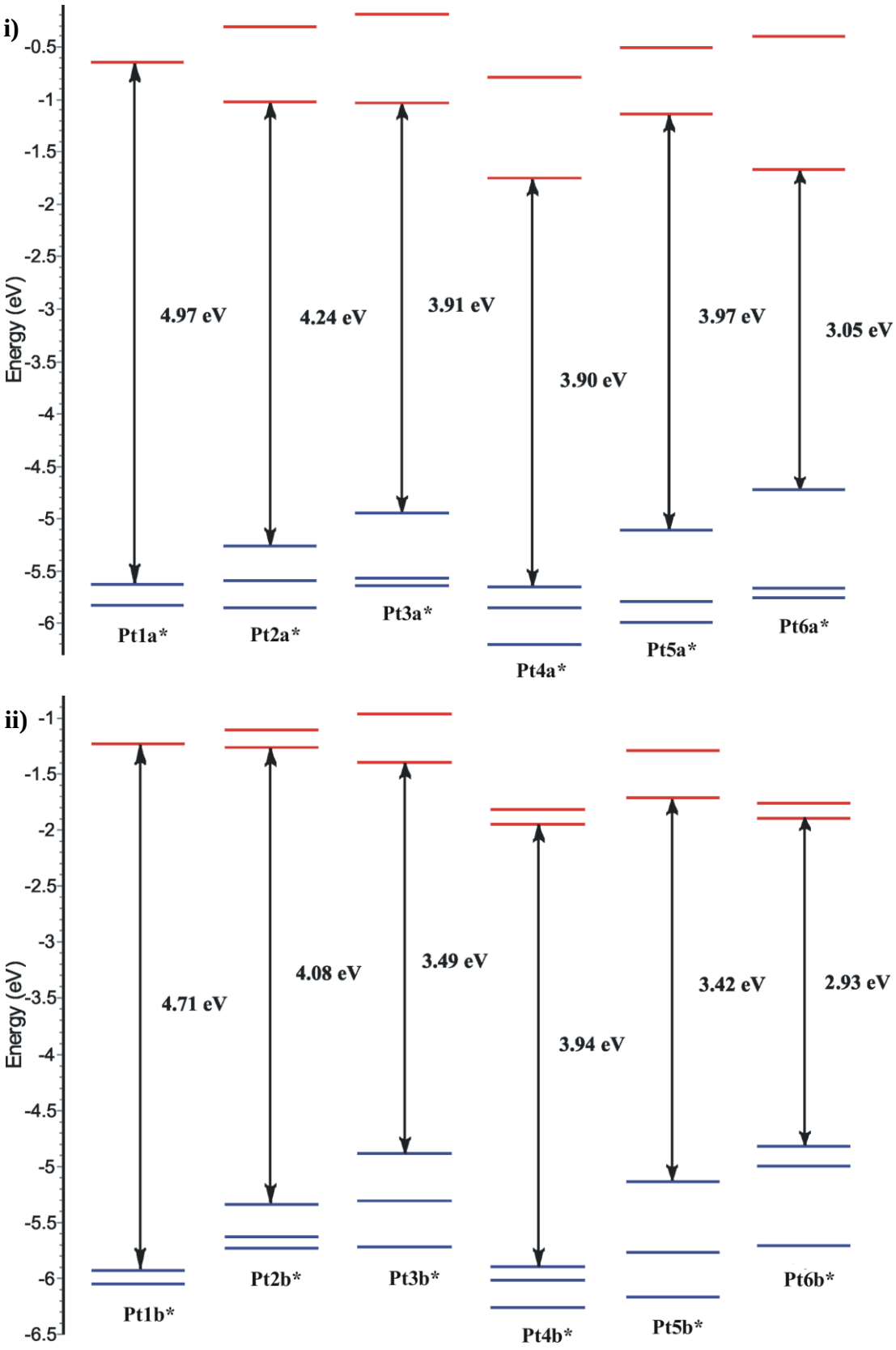

Figure 2.18: Molecular orbital diagrams of complexes **Pt1a*-Pt6a*** (**i**) and **Pt1b*-Pt6b*** (**ii**) highlighting the calculated HOMO-LUMO gaps within each system.

The data in **Figure 2.18** shows that the largest HOMO-LUMO gaps within each series of modelled complexe are exhibited by the ethylpropiolate complexes, **Pt1a*** and **Pt1b***, whilst the smallest were exhibited by the anthracene-containing species **Pt6a*** and **Pt6b***. These values correlate with the degree of conjugation present within the respective ethyny-ester ligand systems and are in agreement with the experimentally measured electronic absorption spectra for these species. The monosubstituted system **Pt2a*** exhibits the second highest HOMO-LUMO separation although it is significantly lower than that of **Pt1a*** on account of the additional conjugation from phenylene spacer. This is again consistent with the experimental electronic absorption data for which the principal band of **Pt2a** is significantly red shifted. The electron donating {OMe} and electron withdrawing {CF_3} groups of **Pt3a*** and **Pt4a*** result in a reduction in the HOMO-LUMO separation relative to the unsubstituted analogue **Pt2a***. For **Pt3a*** this is due to destabilisation of the HOMO relative to **Pt2a*** whereas **Pt4a*** exhibits a significantly stabilised LUMO and a slightly destabilised HOMO. The thienyl ligand of **Pt5a*** also provides a smaller HOMO-LUMO separation than **Pt2b***. The higher energy sulphur orbitals destabilise the HOMO and the LUMO is stabilised through the greater conjugation provided by the diffuse sulphur *p*-orbital. The HOMO-LUMO gaps of **Pt3a*-Pt5a*** are all very similar but do not follow the same trend as the energies absorption bands observed for these species, although these too are close in energy. The slight differences are likely to relate to the simplifications to the systems made for the purposes of the calculations, which are performed for gas-state molecules, negating intermolecular interactions and dynamic rotation of the acetylide ligands that is likely to occur in solution. Indeed, studies within the literature have shown that different rotameric forms of the same complex can result in different energies of the calculated electronic transition.[178]

Of the disubstituted complexes, **Pt2b*** exhibits the second largest HOMO-LUMO separation, but is significantly smaller than that observed for **Pt2a*** on account of the more extended conjugation. The {OMe} substituents within **Pt3b*** effect a significant destabilisation of the HOMO relative to **Pt2b***, resulting in a much smaller HOMO-LUMO gap, which is also significantly smaller than the related monosubstituted system (**Pt3a***). Conversely, the {CF_3} substituents of **Pt4b*** stabilise both the HOMO and LUMO providing a comparable energy gap to **Pt2b***,

which is oberseved experimentally by the similar values of λ_{max} of **Pt2b** and **Pt4b** within their respective electronic absorption spectra. The calculations are also in agreement with the near iso-energetic absorption bands exhibited by of **Pt4a** and **Pt4b**. The HOMO-LUMO gap of **Pt5b*** is shown to be very similar to that of **Pt3b*** and significantly smaller than that of **Pt5a***, again consistent with the electronic absorption data recorded for these species. Finally, whilst the HOMO-LUMO separation of **Pt6b*** is the smallest observed for the series, it does not differ greatly from that calculated for the monosubstituted system **Pt6a**. This supports the similar energy of the absorption bands exhibited by each species and is likely to be a result of the restricted electronic delocalisation observed within the calculated frontier orbitals of **Pt6b*** (**Figure 2.17**).

2.2.8 – Ethynyl-ester Complexes Containing Other Metal Centres

Within this chapter the Pt complexes have been shown to be highly tuneable by changing the identity of the ethynyl-ester ligand. An alternative approach to manipulating these properties is to change the identity of the metal centre. A wide range of metals have been shown to support acetylide ligands and these offer a range of characteristic properties. Low *et* al. have previously shown that the phenylene containing ligand (**2**) can be coordinated to a range of Ru centres.[147-148] In terms of precursors for heterometallic complexes these are interesting on account of their redox activity as well as potential acetylide/vinylidine switching, which have previously been utilised in Ru-acetylide dimers.[179]

Preliminary work within the group has seen the synthesis a range of Au-ethynyl-ester complexes, showing that the ligands provide scope beyond the syntheses of Pt and Ru systems. Complexes of Au are of particular interest because of their emissive properties and the additional properties that can arise from aurophilic interactions.[180] PPh_3-supported complexes containing **2**(**Au2**), **5** (**Au5**) and **6** (**Au6**) were synthesised using the method shown in **Scheme 2.5** and the molecular structure of **Au2** is shown in **Figure 2.19**.

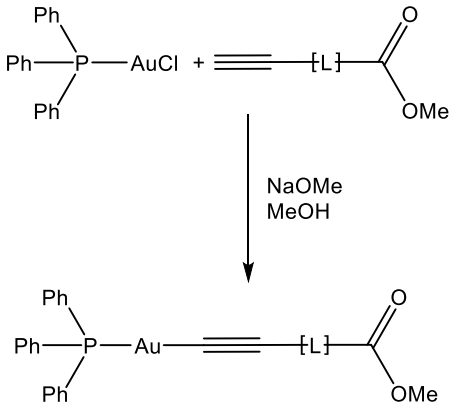

Scheme 2.5: Synthesis of Au-ethynyl-ester complexes.

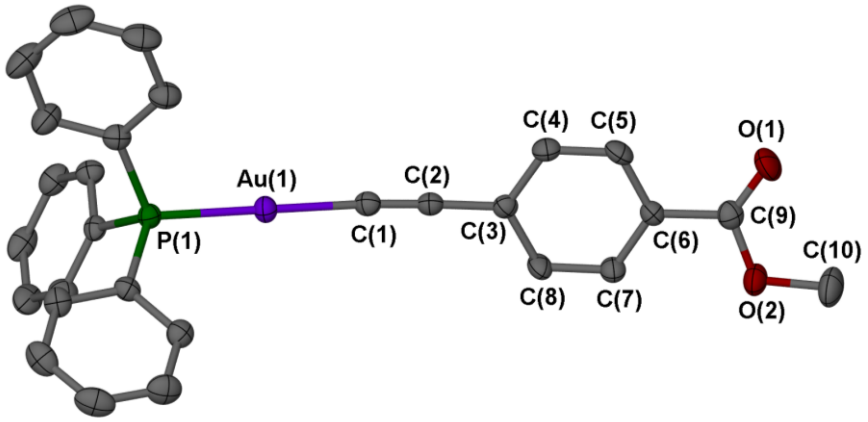

Figure 2.19: Molecular structure of **Au2** shown with 30% thermal ellipsoids. Hydrogen atoms have been omitted for clarity.

Each of the Au complexes exhibit very similar rigid-rod structures in which the bond lengths and angles are within the range expected for Au acetylide complexes.[181-183] Although a full discussion of these complexes will not be presented here it is interesting to note that the intermolecular dimers observed in the crystal lattices of the Pt-acetylide analogues are not observed for any of the Au complexes, suggesting that the $\{Pt(PEt_3)_2\}$ fragment is important in this respect. Unfortunately intermolecular Au···Au interactions were not observed in any of the structurally characterised species. Consistent with the related Pt complexes, the ester groups of **Au2** and **Au5** were almost coplanar with the conjugated spacer whereas that of **Au6** was near perpendicular.

Studies into the optical and electronic properties of these complexes are ongoing but their syntheses demonstrate the versatility of the ethynyl-ester ligand systems. This

allows the consideration of range of metal acetylide precursors for {Mo_2} containing oligomers and polymers that extends beyond Pt.

2.3 – Conclusions

In summary, we have designed and synthesised a series of ester-functionalised Pt-acetylide complexes, incorporating a variety of different conjugated spacer units to allow the optical and electronic properties of these materials to be tuned. These species represent potential precursors for the 'terminating' and 'bridging' Pt subunits within the targeted heterometallic frameworks outlined at the beginning of this chapter.

Single crystal X-ray diffraction studies have allowed us to determine the solid-state molecular structures of each of the Pt-containing complexes, showing that, where sterically possible, the ester groups are close to coplanar with the conjugated spacer units, providing efficient π-orbital overlap throughout the ligands systems. The majority of the disubstituted Pt-complexes (**Pt1b-Pt5b**) are composed of two symmetry equivalent half-molecules, dictating crystallographic coplanarity of the *trans*-ethynyl-ester ligands, which allows conjugation to extend through the metal centre and between ligands in these species. However, the structure of **Pt6b** exhibited two symmetry independent ethynyl-ester ligands, with a significant torsion angle between the two anthracene units. This suggests that electron density is localised within the individual ligand systems, which is supported by the computationally calculated frontier orbitals for this complex. Interestingly, the polarisation of the ethynyl-ester ligand systems facilitate intermolecular stacking interactions within the crystal lattices of most of the Pt-complexes, facilitated by hydrogen bonding and π-π interactions. These have not been observed for closely related systems within the literature.

Electronic absorption spectroscopy showed that the HOMO-LUMO energy gaps are highly sensitive to the identity of the conjugated spacer, allowing λ_{max} to be tuned over *ca*. 150 nm. This was also demonstrated by theoretical electronic structure calculations. The highest energy absorption bands were observed in the absence of a chromophore (**Pt1a/1b**) whereas the anthracene-containing complexes (**Pt6a/6b**) provided the lowest energy absorption bands, highlighting the importance of

conjugation towards manipulating the properties of these systems. Interestingly the absorption bands observed for **Pt4b** and **Pt6b** are almost identical in energy to those of the related mono-substituted complexes, suggesting that the π*-conjugation in these systems does not efficiently extend through the Pt centre. For **Pt6b** this is consistent with the observations made from both the structural and theoretical analyses.

Emission spectroscopic analyses of the monosubstitted Pt-complexes have shown that the energy of the fluorescence of these species can be tuned over a range of wavelengths, spanning the UV to red regions of the spectrum. The lowest energy emission was exhibited by the highly conjugated anthracene-containing complex **Pt6a**. The disubstituted complexes **Pt2b-Pt5b** exhibit both fluorescent and phosphorescent emission at room temperature, with the lower energy emission tuneable over *ca*. 80 nm. For both **Pt2b** and **Pt4b** the phosphorescent emission is significantly more intense than the fluorescence, suggesting that ISC is efficient within these complexes. Only a single emission band is observed for **Pt6b** and strangely, it is blue-shifted relative to that of the mono-substituted analogue, reflecting a higher energy emissive state.

The Pt-acetylide systems developed within this study are interesting as materials in their own right, on account of their highly tuneable opto-electronic properties; however, the ester functionalities also make them promising precursors for the construction of heterometallic frameworks. With this in mind, **Chapter 3** continues the study by addressing the application of these Pt-containing building blocks towards the systematic assembly of our targeted mixed Pt-{Mo_2} complexes.

Chapter 3

Heterometallic Pt-{Mo_2} Polyyne Oligomers

Chapter 3 – Heterometallic Pt-{Mo2} Polyyne Oligomers

3.1 – Introduction

In **Chapter 2**, three model heterometallic frameworks were identified, composed of {Pt acetylide} and quadruply-bonded {Mo2 carboxylate} fragments (**Figure 3.1**). Each of these molecular species represent subunits within a proposed mixed-metal extended polymer network. Using these models as a guide, a series of 'bridging' and 'terminating' Pt ethynyl-ester complexes were designed and synthesised as potential precursors for the targeted heterometallic systems.

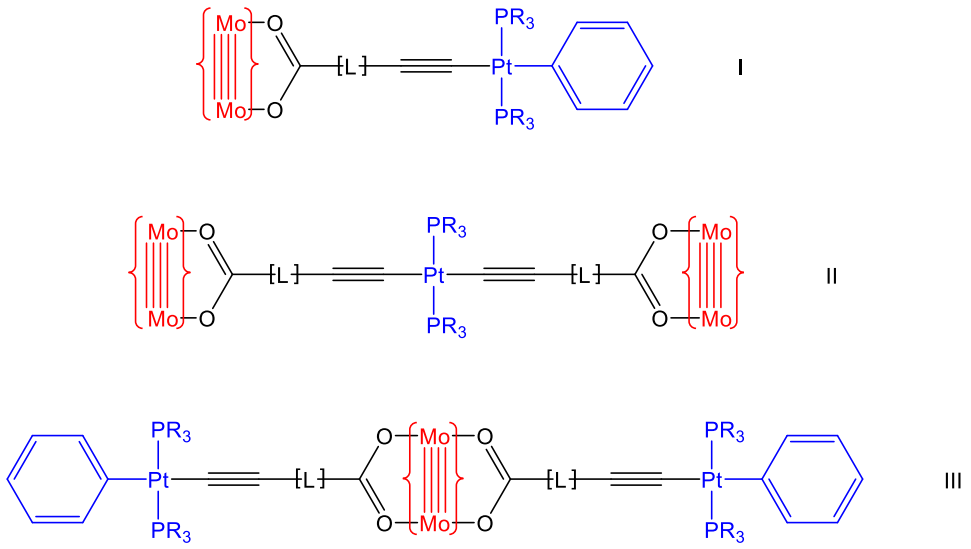

Figure 3.1: Three targeted heterometallic frameworks containing Pt acetylide and {Mo2}-carboxylate units.

Within this chapter, suitable 'bridging' and 'terminating' {Mo2} precursors are identified and the chemistry by which they can be combined with the previously discussed Pt complexes is developed.

3.1.1 – Controlling Ligand Substitution About {Mo2} Centres

In order to achieve the molecular architectures shown in **Figure 3.1** we must first consider some fundamental aspects of the chemistry surrounding {Mo2} carboxylate systems.

{Mo_2} carboxylate dimers, such as $Mo_2(O_2CCH_3)_4$, are common precursors towards the templating and synthesis of more complicated heteroleptic species. This is largely due to the substitutional lability of the alkyl carboxylate ligands, which can readily be exchanged for more electron-withdrawing ligand systems.[98,121,139,184] However, a significant challenge encountered when designing a heteroleptic {Mo_2} complex is gaining control over the degree of ligand substitution around the {Mo_2} core. For instance, the reaction between an {Mo_2} carboxylate dimer ($Mo_2(O_2CR)_4$) and a carboxylic acid (HO_2CR' where R ≠ R') can result in the formation of a mixture of substitution products regardless of the stoichiometry used. This results from both uncontrolled ligand substitution and ligand scrambling processes.[98,185] The possible products from a 1:1 stoichiometric reaction are depicted in **Scheme 3.1**. To target the mono- and *trans*-disubstituted motifs, required for the synthesis of the previously outlined heterometallic complexes (**Figure 3.1**), the chemistry must be refined to favour a single substitution product.

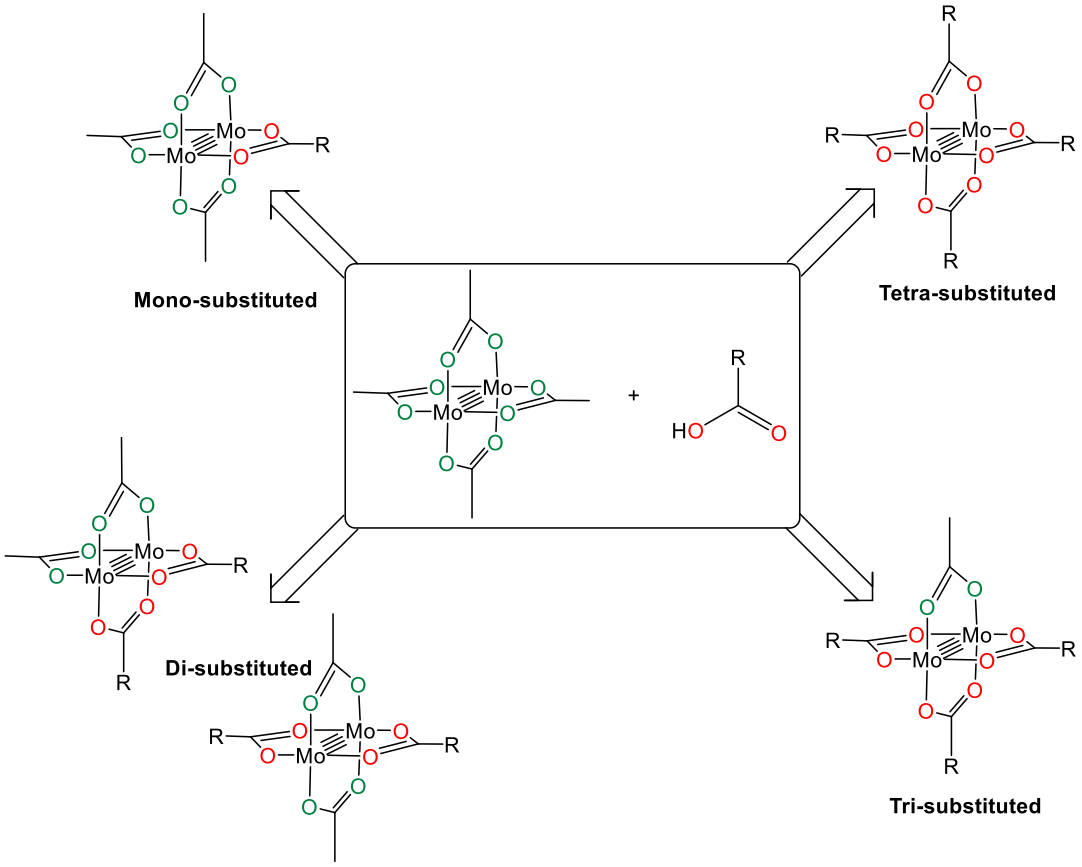

Scheme 3.1: Multiple substitution products possible upon a 1:1 reaction between $Mo_2(O_2CCH_3)_4$ and a carboxylic acid.

Monosubstituted complexes offer a particular synthetic challenge because the coordination of a single relatively electron-withdrawing ligand can result in the activation of the *trans*-ligand towards substitution, on account of the *trans*-influence applied. Despite these difficulties Chisholm *et al*. have shown that {Mo_2} carboxylate dimers can be used to access a number of dicarboxylate bridged oligomers by carefully selecting appropriate ligand systems.[76,95,98,121,124,130-131,186] Carboxylic acid metathesis reactions are reversible processes and to drive the reaction towards the product side, products that would precipitate upon formation were targeted. An example of the synthesis of an oxalate bridged system is shown in **Scheme 3.2**.[98]

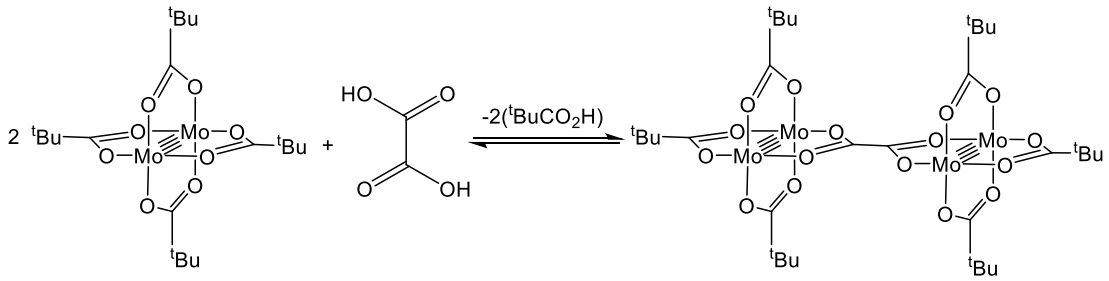

Scheme 3.2: Synthesis of an oxalate bridged {Mo_2} dimer *via* carboxylic acid metathesis.[98]

Although the technique was effective for certain ligand systems it was not universally applicable to all carboxylic acid ligands, especially those that offer more soluble products. The chemistry is also largely limited to dicarboxyates or closely related ligand systems, which would not support the syntheses of the full range of complexes targeted within this study. A more recent example in which mono-substitution has been observed at a {Mo_2} tetracarboxylate centre was reported by Patmore *et al*., resulting from the stoichiometric reactions between $Mo_2(O_2CAr)_4$ (Ar = 2,4,6-triisopropyl benzene) and 2,7-dihydroxy- naphthyridine or 3,6-dihydroxypyridazine.[106] Although the reason behind the unusual substitution chemistry was not approached it is possible that intermolecular hydrogen bonding in solution may hinder further ligand substitutions.

The most efficient method by which to access monosubstituted {Mo$_2$} products is to use a precursor that contains only a single reactive coordination site. To provide this control Cotton *et al*. developed a range of {Mo$_2$} *tris*-formamidinate complexes in which three coordination sites are blocked by the bulky ligand systems and reactivity is directed to the remaining coordination site (**Figure 3.2**).[77,100,126,187]

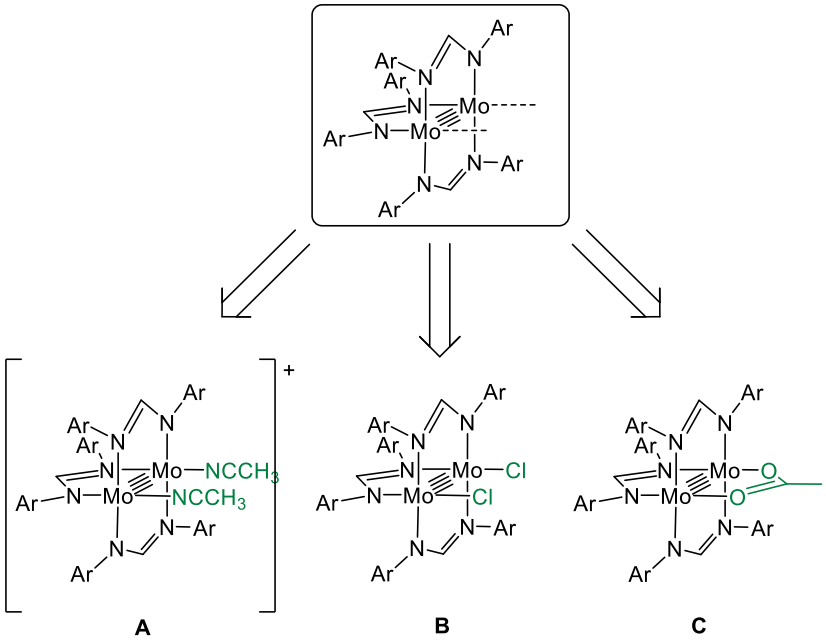

Figure 3.2: Examples of {Mo$_2$}-*tris*-formamidinate complexes as synthons for 'terminating' {Mo$_2$} units.[77,100,126,187]

The *tris*-formamidinate complexes have proven to be extremely versatile synthons for {Mo$_2$} 'terminating' units. In addition to the compatibility with a wide range of dicarboxylate ligands,[77,96,125] the systems also facilitate reactions with *mono*-carboxylic acids.[77,117] It is noteworthy that Chisholm *et al*. have also reported the preparation of $[(^t BuCO_2)_3Mo_2(NCCH_3)_2]^+$, an analogue of **Figure 3.2-A**, in which pivalate ligands replace the formamidinates (**Figure 3.3**).[98] This system was used to synthesise systems that could not be isolated using the corresponding tetracarboxylate as a precursor, however, the preparation of this species is difficult, involving a reversible comproportionation reaction, and is therefore not a practical choice as a precursor.

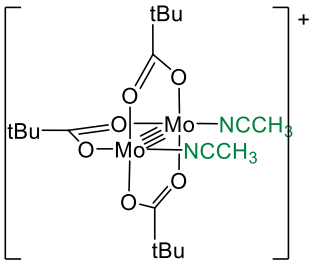

Figure 3.3: A carboxylate stabilised complex for directing mono-ligand substitution.[98]

Although *trans*-substituted {Mo_2} *bis*-amidinate[184] and *bis*-formamidinate[118] have also been synthesised in the past, there is only limited evidence that they support *trans*-ligand substitution[188] and studies have shown that the amidinate complexes are subtitutionally labile towards ligand scrambling, especially when heated above room temperature.[184] Instead, it has been reported that *trans*-substitution can be efficiently facilitated using a precursor that contains bulky carboxylate ligands. More specifically the complex $Mo_2(T^iPB)_4$,[189-190] where T^iPB = 2,4,6-triisopropylbenzoate (**Figure 3.4**), has been widely used as a synthon for {Mo_2} 'bridging' units and presents a promising precursor towards the synthesis of the targeted {Pt}-{Mo_2}-{Pt} framework (**Figure 3.1-III**).[107-109,191]

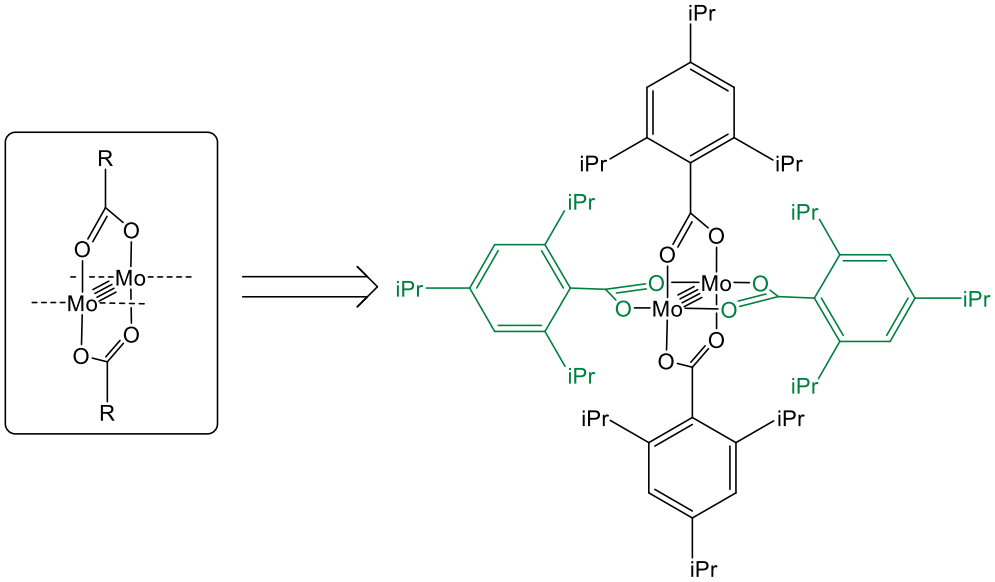

Figure 3.4: $Mo_2(T^iPB)_4$ as a synthon for a {Mo_2} bridging unit.[189]

The ^{i}Pr substituents on the arene rings prevent planarity of the carboxylate ligands, and as such there is no conjugation extending from the {Mo_2} core to the arene rings. The ligands therefore behave as bulky alkyl carboxylates in which the ligands can be readily substituted for those that are more electron withdrawing. *Trans*-disubstitution is both electronically favoured by increasing the length of the π-conjugated network, which passes through the {Mo_2} core, and sterically, by relieving the steric interactions between the bulky *cis*-T^{i}PB ligands. Products formed from these ligand substitution reactions are often poorly soluble in solvents such as EtOH and toluene. Reactions performed in these solvents therefore result in precipitation of the desired product, protecting the integrity of the disubstituted system and potentially facilitating straightforward isolation.

3.2 – Results and Discussion

3.2.1 – Synthesis of a {Mo_2} *Tris*-Formamidinate Complex

The discussion in section **3.1** showed that the most versatile method of ensuring single ligand substitution about a {Mo_2} core is to use a precursor with a single activated site and preferably three kinetically inert ligands, to negate post-synthetic ligand scrambling. The formamidinate-stabilised complexes shown in **Figure 3.2** are ideal in this respect and, for the purposes of this study, the complex containing a kinetically labile acetate ligand (**C**) was selected as a potential precursor for our targeted heterometallic frameworks (**Figure 3.1-I** and **-II**). The decision was made both on the relative ease of synthesis for this species and on account of the versatile reactivity that is reported for the species within the literature.[101,117,126,192-194]

The preparation reported for the heteroleptic species involves the 3:1 reaction between the desired formamidinate ligand and $Mo_2(O_2CCH_3)_4$ using three equivalents of NaOMe. Upon repeating this method for our own study it was found that significant amounts of the *trans*-disubstituted and *tetra*-substituted compounds were formed in addition to the desired product and, due to the similar solubility of the three substitution products, purification of the product was not possible. To overcome this problem a modified synthetic approach was employed in which three equivalents of a lithiated formamidine system were reacted with $Mo_2(O_2CCH_3)_4$

at -78 °C (**Scheme 3.3**). The same preparation has previously been reported in the literature for related complexes containing alkyl-substituted amidinate ligands.[195]

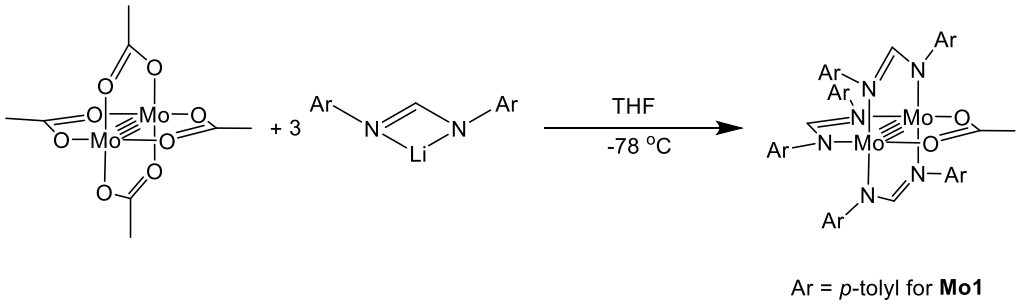

Scheme 3.3: Synthesis of a {Mo_2} chain-terminating unit.

Preliminary studies showed that when Ar = *p*-anisyl the product was highly air-sensitive and difficult to work with. However, by replacing these groups with less polar *p*-tolyl substituents the product (**Mo1**) was markedly more stable, providing a more attractive precursor for our chemistry. This observation is consistent with studies in the literature, which have shown that, $Mo_2(DPTF)_4$,[196] is air-stable in dichloromethane solution whereas the p-anisyl analogue is highly air-sensitive.[123] To synthesise **Mo1**, a slight excess of the lithiated ligand was used to ensure that no disubstituted product remained in solution. Although a small amount of the *tetra*-formamidinate complex is formed in the reaction, this species exhibits very low solubility in non-polar solvents and, as such, **Mo1** can be purified *via* extraction into toluene followed by filtration. Bright yellow needle-like crystals of **Mo1**, suitable for single crystal X-ray diffraction studies, were obtained by layering a concentrated dichloromethane solution of **Mo1** with pentane.

The identity of **Mo1** was confirmed through elemental analysis and both ^1H and $^{13}C\{^1H\}$ NMR spectroscopy, for which the data was consistent with the structure shown in **Scheme 3.3**. Within the ^1H NMR spectrum, the methyl protons of the *p*-tolyl substituents and the protons on the backbone of the DPTF ligands each exhibit two well resolved resonances in a 2:1 ratio. These correspond to the DPTF ligands *cis* and *trans* to the acetate ligand and in both cases the resonances corresponding to the two *cis* ligands appear downfield from those of the single *trans* ligand. The ^1H NMR spectrum also exhibits a single resonance corresponding to the acetate methyl

protons (δ = 2.51 ppm) and relative resonance integrals confirm the desired 3:1 ligand ratio within **Mo1**.

3.2.2 – Synthesis of a {Pt}-{Mo_2} Complex

Having identified suitable {Mo_2} 'terminating' (**Mo1**) and 'bridging' ($Mo_2(T^iPB)_4$) precursors, the chemistry was then developed by which they could be combined with the previously described Pt ethynyl-ester precursors (presented in **Chapter 2**).

Within the literature it has been reported that the acetate ligand within precursors such as **Mo1** can be replaced with a number of different ligand systems using salt metathesis reactions.[97,117,125,192-194] With this in mind we sought a means by which the ester groups within the Pt precursors could be converted to carboxylate metal salts, which could potentially facilitate ligand substitution reactions with **Mo1**.

Through these studies it was found that **Pt2a** could be cleanly converted to the corresponding K-carboxylate *via* reaction with a slight excess of KO^{t}Bu (in THF at 50 ^{o}C). The progress of the reaction was followed using TLC analysis (DCM eluent) and ^{1}H NMR analysis of the reaction mixture after 12 h confirmed quantitative conversion of the starting material. KO^{t}Bu is an ideal base for the reaction due its solubility in common organic solvents, removing the requirement for an aqueous medium, and it's relatively large molecular mass makes it applicable within small scale reactions. When synthesised under an inert atmosphere, the K-carboxylate of **Pt2a** can be used *in situ* for a further reaction with **Mo1**, which is outlined in **Scheme 3.4**. Upon combining a yellow solution of **Mo1** with the colourless solution of the K-carboxylate, the mixture immediately turned bright orange, reflecting the formation of the heterometallic species **PtMo1**. The solution was stirred for 2 h after which solvent was removed *in vacuo* and the orange residue was extracted into toluene and filtered to remove the potassium acetate. After removing all volatiles *in vacuo* the residue was suspended in hexane and the solvent was heated to reflux. With continued heating, toluene was added drop-wise until all solid material had dissolved. Slow cooling of the solution to room temperature followed by further cooling to -28 ^{o}C yielded a crop of orange block-like crystals of **PtMo1** suitable for single crystal X-ray diffraction studies (*vide infra*).

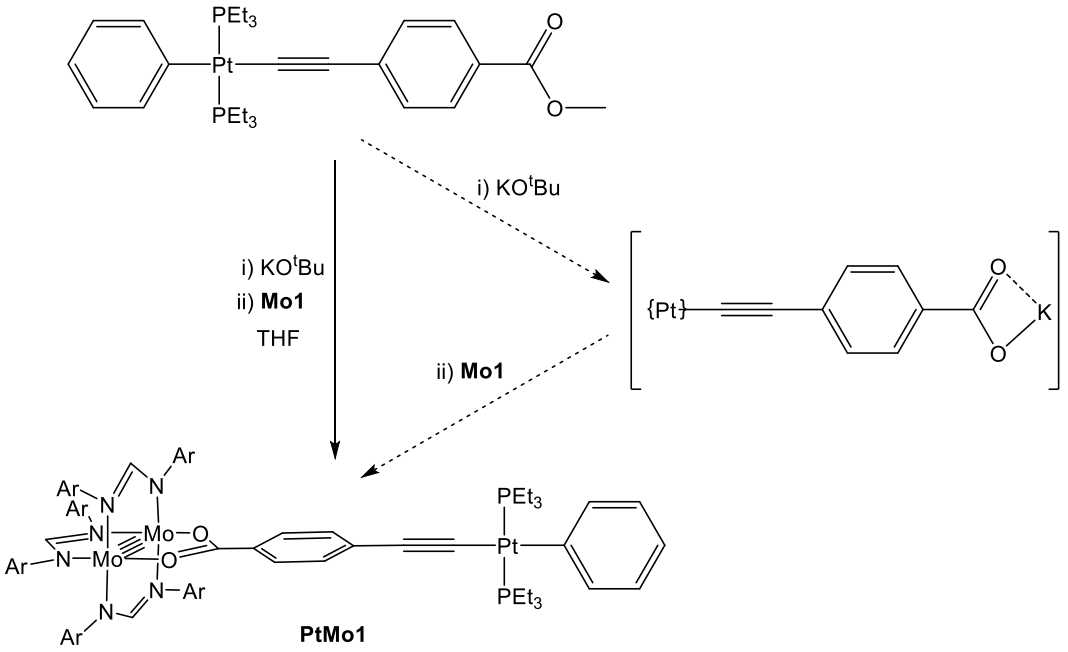

Scheme 3.4: Synthesis of **PtMo1** involving *in situ* de-esterification of **Pt2a**.

PtMo1 was characterised using multinuclear NMR spectroscopy. The ^{1}H NMR spectrum of **PtMo1** is presented in **Figure 3.5** with those of the two parent compounds **Pt2a** and **Mo1**. The spectrum of the heterometallic complex exhibits resonances closely resembling those of the two precursors, but the absence of the ester-C*H*$_3$ resonance of **Pt2a** (δ = 3.48 ppm) and the acetate-C*H*$_3$ resonance of **Mo1** (δ = 2.51 ppm) are evidence of the successful ligand substitution reaction. Within the ^{1}H NMR spectrum of **PtMo1**, the resonances corresponding to the formamidinate {NC(*H*)N} protons are reversed relative to the analogous resonances observed for **Mo1**, with those corresponding to the two *trans* DPTF ligands appearing at lower field strength. This can be attributed to the greater degree of $Mo_2\delta\rightarrow$carboxylate-π^* backbonding in **PtMo1**, an effect that has been observed for previously reported complexes containing formamidinate ancillary ligands.[77,96,117,125] The coordination of **Pt2a** to the {Mo_2} centre also results in a significant down-field shift of the doublet resonance corresponding to the phenylene protons of **PtMo1** (*ortho* to the carboxylate) reflecting a significant deshielding effect on this proton environment in the heterometallic species. The chemical shift corresponding to the second phenylene proton environment is not affected by the reaction.

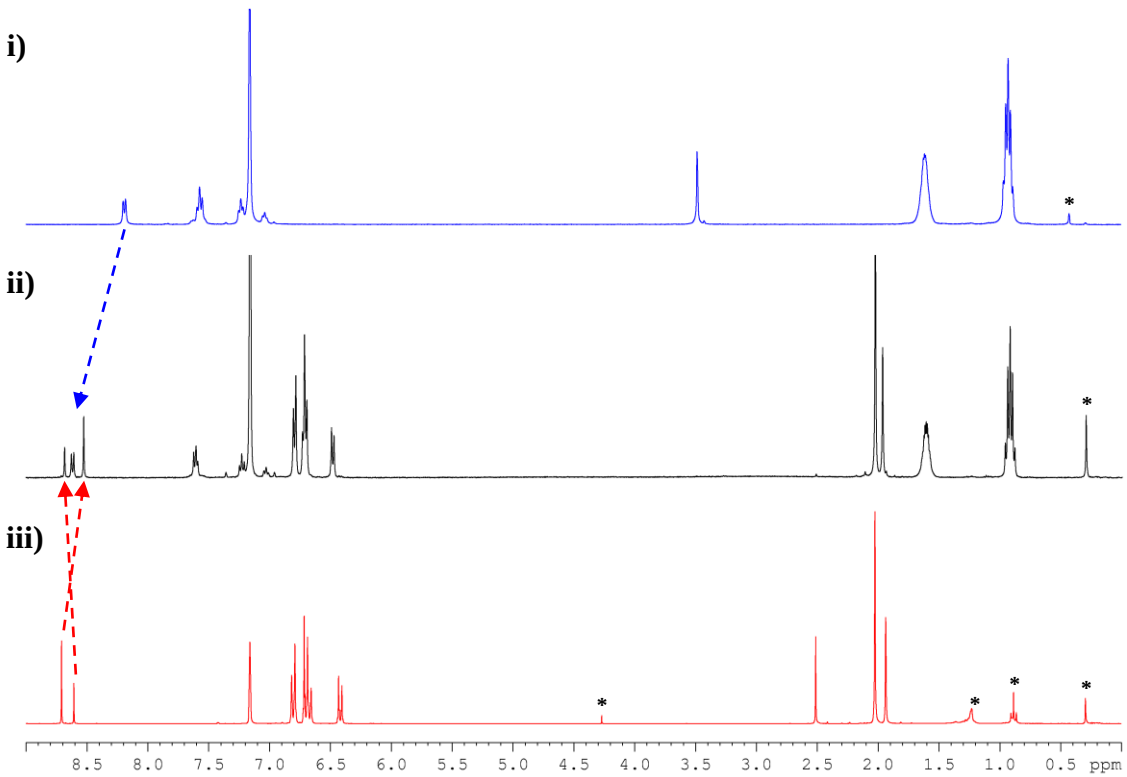

Figure 3.5: A comparison of the ^{1}H NMR spectra of **Pt2a** (**i**), **PtMo1** (**ii**) and **Mo1** (**iii**), each recorded in C_6D_6. The signals marked with an asterisk represent solvent of crystallisation, H_2O or silicon grease.

The $^{31}P\{^{1}H\}$ NMR spectrum of **PtMo1** exhibits a single resonance with associated Pt-satellites, consistent with the single isomeric form expected for the product. The magnitude of the chemical shift and $^{1}J_{P\text{-}Pt}$ are negligibly different from those observed for **Pt2a**. **PtMo1** was also analysed by ^{195}Pt NMR spectroscopy, however, the chemical shift observed (δ = -4559 ppm) only differs slightly to that observed for **Pt2a** (δ = -4551 ppm), exhibiting only a slight up-field shift. The presence of the {Mo_2} moiety within the complex therefore has negligible effect on the magnetic environment of the Pt centre.

Although the reaction outlined in **Scheme 3.4** proceeds efficiently using **Pt2a**, it was not applicable to the full range of Pt ethynyl-ester precursors. When analogous reactions were attempted using **Pt1a** and **Pt3a**, it was found that hydrolysis of the ester groups was inefficient. Although the ^{1}H NMR spectra of the reaction mixtures, recorded following the addition of **Mo1**, showed that some heterometallic product

was formed in each case, we were unable to isolate these products on account of their similar solubility to the unreacted starting material. The same problem was experienced when using **Pt5a**, however, a small number of crystals were isolated from the reaction by cooling a toluene / hexane solution of the crude product to -28 ^{o}C. This allowed structural characterisation of the thienyl-bridged heterometallic complex **PtMo2** (*vide infra*). Interestingly the reaction between **Pt4b** and KO^{t}Bu resulted in complete deprotection of the carboxylate functionality, however, the subsequent reaction with **Mo1** was largely unsuccessful. We have attributed this to the bulky {CF_3} subsitutents of **Pt4a** which are too sterically demanding to facilitate reaction with **Mo1**.

The ester group of **Pt6a** proved to be entirely inert towards KO^{t}Bu and all other common bases that were trialled in its place. It is likely that the stability of the ester relates to the steric demands of the anthracene spacer, preventing conjugation between the ester and the ring system, which would offer little stabilisation towards an anionic carboxylate species. This is supported by the molecular structure determined for **Pt6a** (Available in the **Appendix**) in which the ester is orientated almost 90^{o} to the plane of the anthracene. Difficulties regarding the ester hydrolysis of several anthracene-containing complexes have been described within the literature. The difficulties were overcome using relatively harsh methods, such as high temperature pyrolysis on silica and acid catalysed hydrolysis using F_3CCOOH, which are not applicable to the Pt-containing complex.[197-198]

3.2.3 – Synthesis of a {Mo_2}-{Pt}-{Mo_2} Complex

The second targeted heterometallic framework (**Figure 3.1-II**) differs from **PtMo1** in that it requires the use of a bridging Pt precursor, but **Mo1** remains applicable as a Mo_2 'terminating' unit. Following the successful application of the phenylene containing precursor **Pt2a** for the synthesis of **PtMo1**, the disubstituted analogue **Pt2b** was employed in an attempt to synthesise the more extended framework. Unfortunately, when **Pt2b** was reacted with KO^{t}Bu, under the same conditions described for the synthesis of **PtMo1**, the potassium salt of the dicarboxylate species precipitates from solution and the subsequent addition of **Mo1** resulted in no reaction. The solubility of the potassium salt is therefore too poor to facilitate reaction with

Mo1, which is likely to be due to the formation of a coordination polymer in the solid-state.

In search of an alternative route to access the Pt-bridged heterometallic system it was found that treatment of **Pt2b** with KO^{t}Bu followed by and acid work up led to formation of a *trans*-substituted Pt *bis*-carboxylic acid species (**Pt2d**) as shown in **Scheme 3.5**. The product was purified by washing with DCM and characterisation by both multinuclear NMR spectroscopy and elemental analysis confirmed the identity of the product.

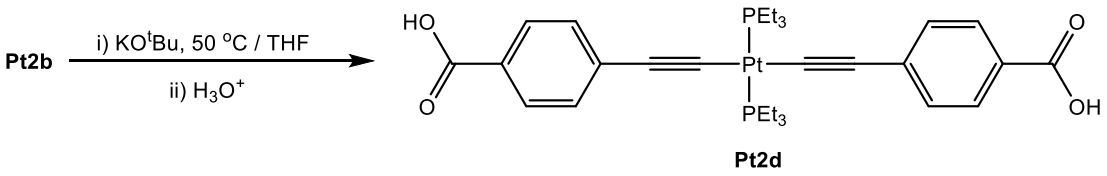

Scheme 3.5: Hydrolysis of the esters within **Pt2b** using KO^{t}Bu to prepare **Pt2d**.

The dicarboxylic acid is soluble in THF, making it a more attractive precursor for the desired heterometallic complex than the potassium salt that was described above. Cotton *et al*. have previously reported that, to react carboxylic acids with {Mo_2} precursors such as **Mo1**, the {Mo_2} precursor must first be 'activated' by removing the acetate ligand,[117] which can be achieved through reaction with NaOMe. It is thought that the reaction forms a basic {Mo_2}-methoxide intermediate, which can deprotonate the carboxylic acid to facilitate coordination of the new ligand system.

Following the method outlined in **Scheme 3.6**, **Mo1** was reacted with one equivalent of NaOMe in THF, providing a bright orange solution. After 3 h the solution was filtered directly onto half an equivalent of **Pt2d**, which darkened the solution significantly. After stirring for a further 3 h, the volatiles were removed *in vacuo* and the resulting residue was washed with EtOH and hexanes. The crude product was then extracted into toluene, filtered through celite. After removing the solvent *in vacuo* the residue was dissolved in a small amount of THF and cooled to -28 ^{o}C to yield a bright orange precipitate of **MoPtMo**. Single crystals of **MoPtMo** were

obtained from a toluene / hexanes mixture using the same method outlined for **PtMo1** (*Vide supra*).

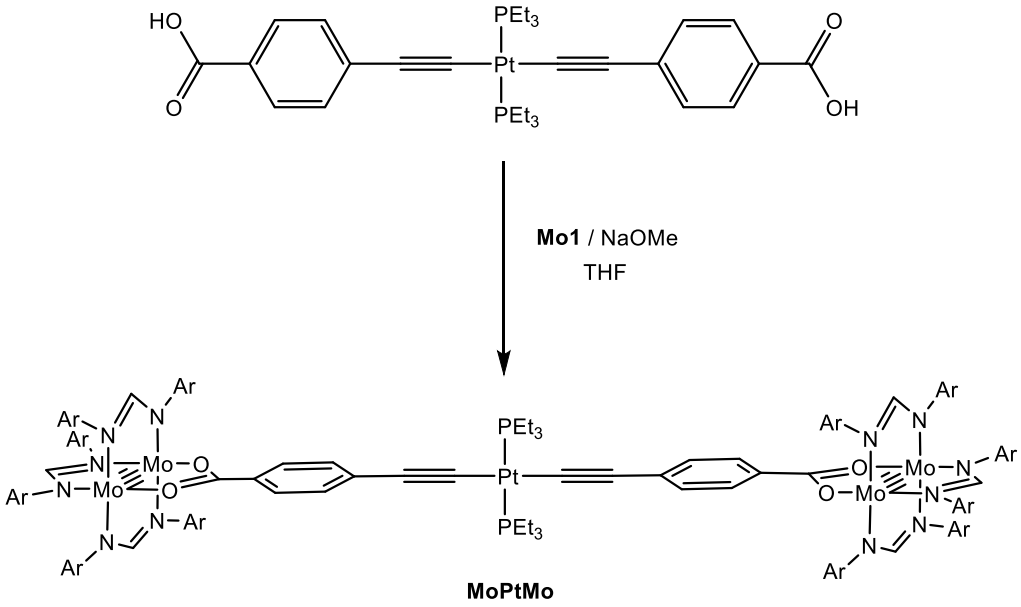

Scheme 3.6: The synthesis of **MoPtMo**.

The ^{1}H NMR spectrum of **MoPtMo** is consistent with the coordination of a {Mo_2DPTF$_3$} unit to the carboxylate groups at either end of the Pt precursor and the spectrum closely resembles that of **PtMo1**, but for the absence of the phenyl hydrogen resonances. Once again the two resonances corresponding to the formamidinate backbone protons are reversed relative to those observed for **Mo1** and a similar down-field shift is observed for the doublet resonance corresponding to the phenylene protons (*ortho* to the carboxylate) relative to the analogous resonance of **Pt2b**. Similar to the observations made for **PtMo1**, the ^{31}P{^{1}H} resonance of **MoPtMo** exhibits negligible difference to that of **Pt2b** and $^{1}J_{P\text{-}Pt}$ is only slightly larger for the heterometallic species. The ^{195}Pt resonance for **MoPtMo** is observed at δ = -4735 ppm which is again very similar to that of **Pt2b** (δ = -4724 ppm), however, it is notable that the ^{195}Pt chemical shifts of both **PtMo1** and **MoPtMo** appear slightly up-field relative to the parent Pt complexes. This suggests that the presence of the {Mo_2} unit has a slight shielding effect on the nuclei of the Pt centres.

3.2.4 – Synthesis of a {Pt}-{Mo_2}-{Pt} Complex

For the synthesis of the third of the targeted model complexes (**Figure 3.1-III**) {$Mo_2T^iPB_2$} was employed as a synthon for the required {Mo_2} bridging fragment. The initial approach used to synthesise the heterometallic system utilised the carboxylic acid form of **Pt2a** (**Pt2c**), which was synthesised using the same approach outlined for **Pt2d** in **Scheme 3.5**. Two equivalents of **Pt2c** were combined with $Mo_2T^iPB_4$ in EtOH and stirred for 24 hours, yielding a bright orange precipitate of **PtMoPt**, which was isolated on a glass frit and washed with both EtOH and hexane. The reaction is outlined in **Scheme 3.7**.

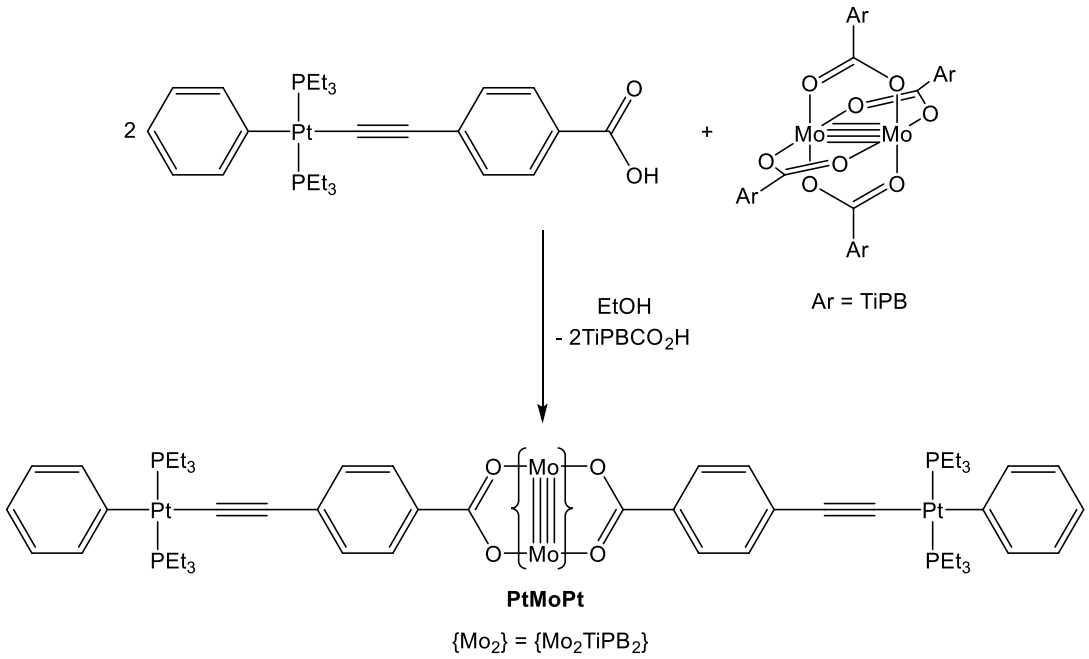

Scheme 3.7: Synthesis of **PtMoPt** *via* a carboxylic acid metathesis reaction.

Although the reaction described above resulted in the isolation of pure **PtMoPt**, the yield was poor (35 %). In order to isolate a greater amount of the product, for the purposes of characterisation and further spectral and electrochemical analysis, a second approach was developed.

Following a literature preparation, 1,4-trimethylsilyl-methyl-ethynyl-benzoate was hydrolysed in the presence of NaOH to remove both the silyl and ester protecting groups, yielding an ethynyl-carboxylic acid species (**Scheme 3.8-i**).[199] The

carboxylic acid was then reacted with $Mo_2T^iPB_4$ in a 2:1 stoichiometry, using an identical method to that described for the synthesis of **PtMoPt**, yielding the *trans*-substituted complex (**Mo2**) (**Scheme 3.8-ii**). This species contains ethynyl groups at the extremities of the two ligands, which provide sites at which Pt can potentially be coordinated. The reaction was also used to synthesise the thienyl containing analogue (**Mo3**) by starting with 2,5-trimethylsilyl-ethynyl-thiophenecarboxylate.[200]

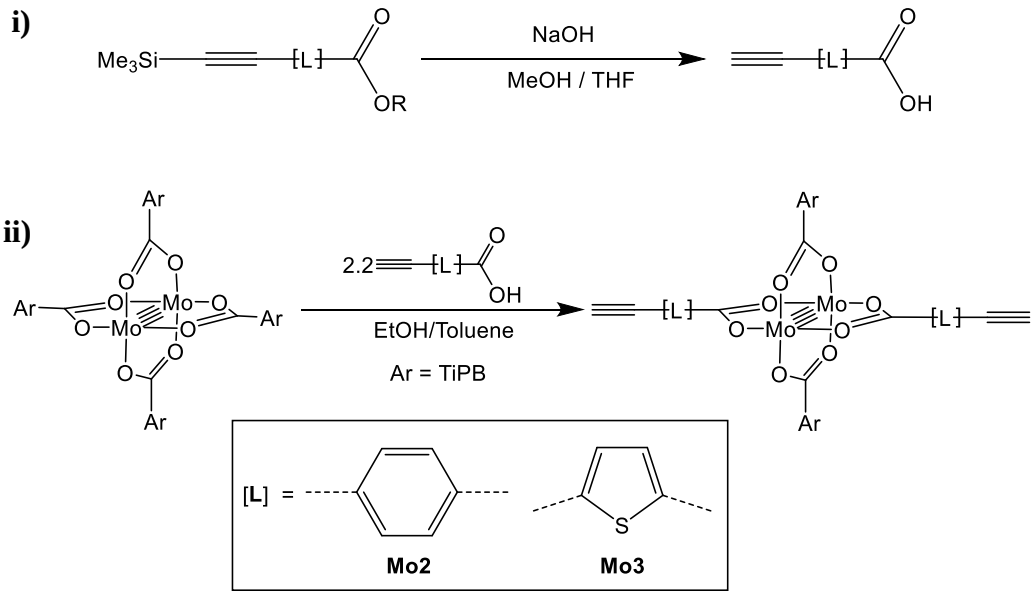

Scheme 3.8: Synthesis of ethynyl-carboxylic acid systems (**i**) and their coordination to {Mo_2} centres (**ii**).

The ^{1}H NMR spectra of **Mo2** and **Mo3** were consistent with the structure depicted in **Scheme 3.8**, exhibiting singlet resonances at 3.8 and 4.1 ppm respectively, corresponding to the two acetylinic protons of each product. The terminal ethynyl functionalities were also confirmed through solid-state IR spectroscopy, in which the ethynyl C-H stretch was observed at 3330 cm^{-1} for both systems. A signal corresponding to the {C≡C} stretch was not observed for **Mo2**, but a weak signal was observed for **Mo3** at 2106 cm^{-1}. Both products have also been characterised structurally using single crystal X-ray diffraction studies (*vide infra*).

During the writing of this work **Mo3** was reported independently by Chisholm *et al.* using an identical synthetic approached to that outlined above.[108] The work also outlined the synthesis of the {W_2} analogue of **Mo3**, attainable using the precursor

$W_2T^iPB_4$. Through our own work we also obtained small amounts of the {W_2} analogues of **Mo2** and **Mo3**, which were characterised by multinuclear NMR spectroscopy. However, the products form as very fine precipitates that could not be isolated by filtration. For this reason sufficient amounts of each product could not be isolated to facilitate full characterisation and analysis. Chisholm *et al.* report that centrifugation is required to isolate greater quantities of these products, a technique that we are currently unable to perform air-sensitively.

The terminal ethynyl functionality of **Mo2** and **Mo3** make these systems attractive synthons for a number of organic and organometallic transformations. This has been illustrated in the work of Chisholm *et al*. in which **Mo3** was utilised as a precursor for a Sonogashira reaction and the synthesis of a Au-acetylide complex (**Scheme 3.9**).[108] Work within the group has shown that an analogue of Chisholm's mixed Mo_2-Au complex can be accessed using a similar method using **Mo2** and NaOMe in place of NEt_3.

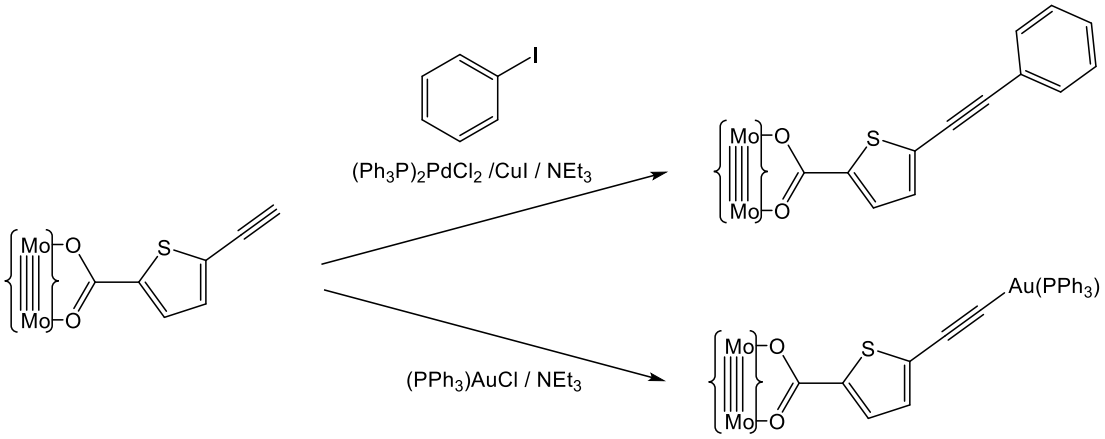

Scheme 3.9: Sonogashira coupling (**i**) and Au-acetylide coupling (ii) using **Mo3**.[108]

Of particular relevance to this study is the application of these ethynyl functionalised {Mo_2} systems in the synthesis of {Pt}-{Mo_2}-{Pt} frameworks and as such **Mo2** was tested as an alternative precursor for the synthesis of **PtMoPt**. Using standard Cu-catalysed Pt acetylide coupling methodology,[52-53] **Mo2** and *trans*-Ph$(PEt_3)_2$PtCl were dissolved in a THF / NEt_3 solvent mixture followed by the addition of a small amount of CuI. The reaction is outlined in **Scheme 3.10**. The solution was stirred for 24 h after which all volatiles were removed *in vacuo*, providing an orange residue. The product was purified by washing with EtOH and hexane followed by extraction

into toluene and filtration through celite. The solvent was removed *in vacuo*, yielding **PtMoPt** as an orange powder. The isolated yield from the reaction was 60%, proving the method to be more efficient than the previously utilised carboxylic acid metathesis approach. Orange block-like crystals of **PtMoPt** were grown by layering a concentrated THF solution of **PtMoPt** with hexane.

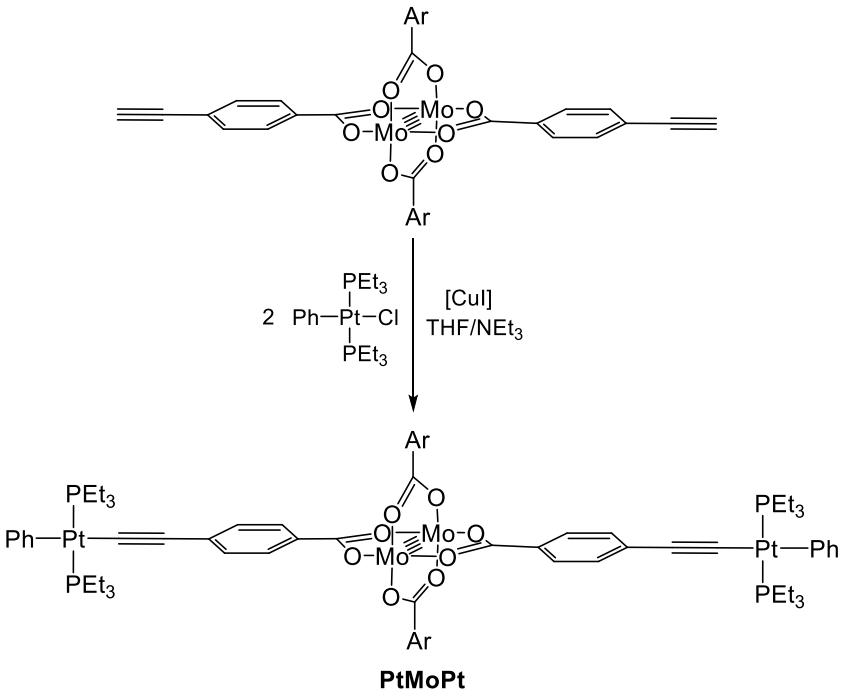

Scheme 3.10: Synthesis of **PtMoPt** *via* a Cu-catalysed Pt acetylide coupling reaction.

The ^{1}H NMR spectrum of **PtMoPt** (black) is shown in **Figure 3.6** and compared to those of **Pt2a** (blue) and **Mo2** (red).

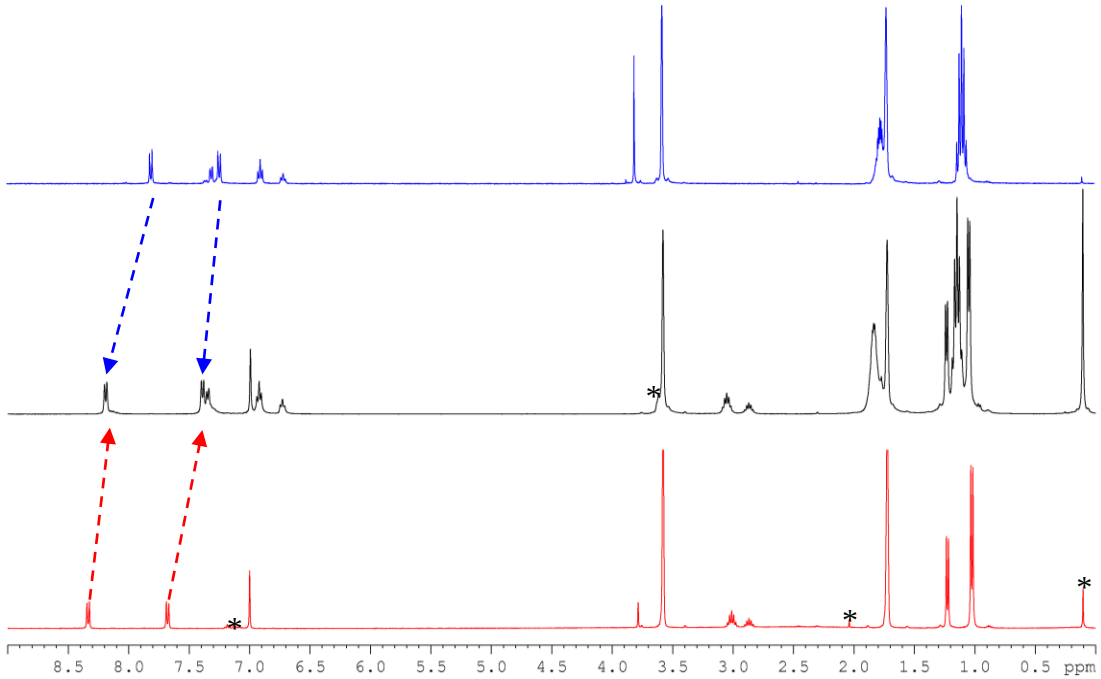

Figure 3.6: A comparison of the ^{1}H NMR spectra of **Pt2a** (**i**), **PtMoPt** (**ii**), **Mo2** (**iii**) recorded in d_8-THF. The signals marked with an asterisk represent solvent of crystallisation and silicon grease.

The ^{1}H NMR spectrum of **PtMoPt** closely resembles those of the related complexes **Pt2a** and **Mo2**. The acetylinic proton resonance of **Mo2** (δ = 3.79 ppm) is absent from the spectrum of **PtMoPt**, consistent with the Pt coupling reaction and all resonances corresponding to the T^{i}PB ligands are negligibly affected by the reaction. The only significant perturbations that are observed are for the two doublet resonances that correspond to the phenylene protons. Within **PtMoPt** these resonances are both shifted up-field relative to those of **Mo2** and down-field relative to those of **Pt2a**. The latter is consistent with the observations made for **PtMo1** and **MoPtMo**. The presence of the {Pt} unit therefore has a shielding effect on these proton environments.

Analogous to the observations made for **PtMo1** and **MoPtMo,** neither the ^{31}P NMR resonance (10.4 ppm) nor the $^{1}J_{P\text{-}Pt}$ (2635 Hz) of **PtMoPt** is significantly different from those observed for **Pt2a**. The ^{195}Pt resonance, appearing at -4564 ppm, is, however, shifted slightly up-field from that of **Pt2a** showing a slightly more shielded metal centre in the heterometallic complex. This is again consistent with the observations made in the previously discussed mixed metal complexes.

3.2.5 – Structural Analyses

Mo1 crystallises in the triclinic space group *P-1* with one molecule in the asymmetric unit. The asymmetric unit also contains a mixture of both DCM and pentane solvent molecules disordered over the same site in a relative occupancy of 30%:70% respectively. One of the *p*-tolyl moieties exhibits rotational disorder which was modelled over two positions, with the greater component present at 55% occupancy. The molecular structure of **Mo1** is presented in **Figure 3.7** and selected bond lengths and angles are shown in **Table 3.1**.

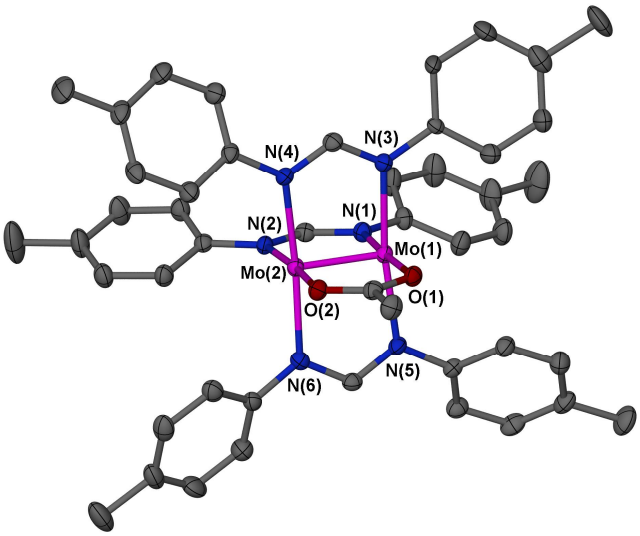

Figure 3.7: Molecular structure of **Mo1** with ellipsoids shown at 50% probability and hydrogen atoms removed for clarity.

The structure of **Mo1** contains three formamidinate ligands and a single acetate ligand coordinated to the {Mo_2} core. The Mo-Mo bond length observed in **Mo1** is within the range of parameters that have been reported for related heteroleptic species within the literature (2.0702(3) – 2.1057(6) Å),[126,195,201] which include the *p*-anisyl analogue of **Mo1**. An analysis of the Mo-N bond lengths of **Mo1** shows that there is negligible difference between those *trans* or *cis* to the acetate ligand. These bond lengths also lie within the range of Mo-N bonds lengths reported for the tetra-formamidinate complex $Mo_2(DPTF)_4$),[196] showing that the acetate ligand has no influence over these parameters. The Mo-O bond lengths of **Mo1** are also within the range of values observed for both the *p*-anisyl analogue and $Mo_2(O_2CCH_3)_4$.[202] The

cis-N-Mo-O angles of **Mo1** are each *sub*-90^o and are significantly smaller the *cis*-N-Mo-N angles, reflecting the steric repulsion between the relatively bulky formamidinate ligands. The fact that the *trans*-N-Mo-N angles are smaller than the *cis*-N-Mo-O can be justified by the same steric effects. Similar steric effects have been reported within a large number of {Mo_2} complexes that contain three formamidinate and one carboxylate ligand.

Table 3.1: Selected bond lengths (Å) and bond angles (^{o}) observed within the molecular structure of **Mo1**.

Bond lengths (Å)		**Bond angles (^{o})**	
Mo-Mo	2.0823(3)	***trans*-N-Mo-N**	171.18(8), 173.02(9)
Mo-N[a]	2.145(2), 2.112(2)	***cis*-N-Mo-N**	92.25(9), 94.09(9), 90.87(9), 93.30(9)
Mo-N[b]	2.113(2), 2.145(2), 2.156(2), 2.153(2)	***trans*-N-Mo-O**	175.82(8), 174.42(8)
Mo-O	2.146(2), 2.145(2)	***cis*-N-Mo-O**	86.50(8), 86.74(8), 88.30(8), 87.01(8)

[a] *trans* to acetate, [b] *cis* to acetate.

Mo2 crystallises in the orthorhombic space group *Pbca* with half a molecule in the asymmetric unit. The second half of the molecule is generated through an inversion centre located at the centre of the Mo-Mo bond. The asymmetric unit also contains three molecules of THF. One solvent molecule is loosely coordinated to the axial site of the Mo-Mo bond (Mo-O(THF) = 2.614(3) Å) and is present at 100% occupancy. The other two solvent molecules occupy void space and exhibit lower occupancies of 15% and 30%, respectively. The latter is disordered and was modelled over two positions with the greatest component present at 20% occupancy. The molecular structure of **Mo2** is shown in **Figure 3.8-i** accompanied by diagrams showing sections of the crystal lattice viewed down the *b*- and *a*-axes respectively. Selected bond lengths and angles are presented in **Table 3.2**.

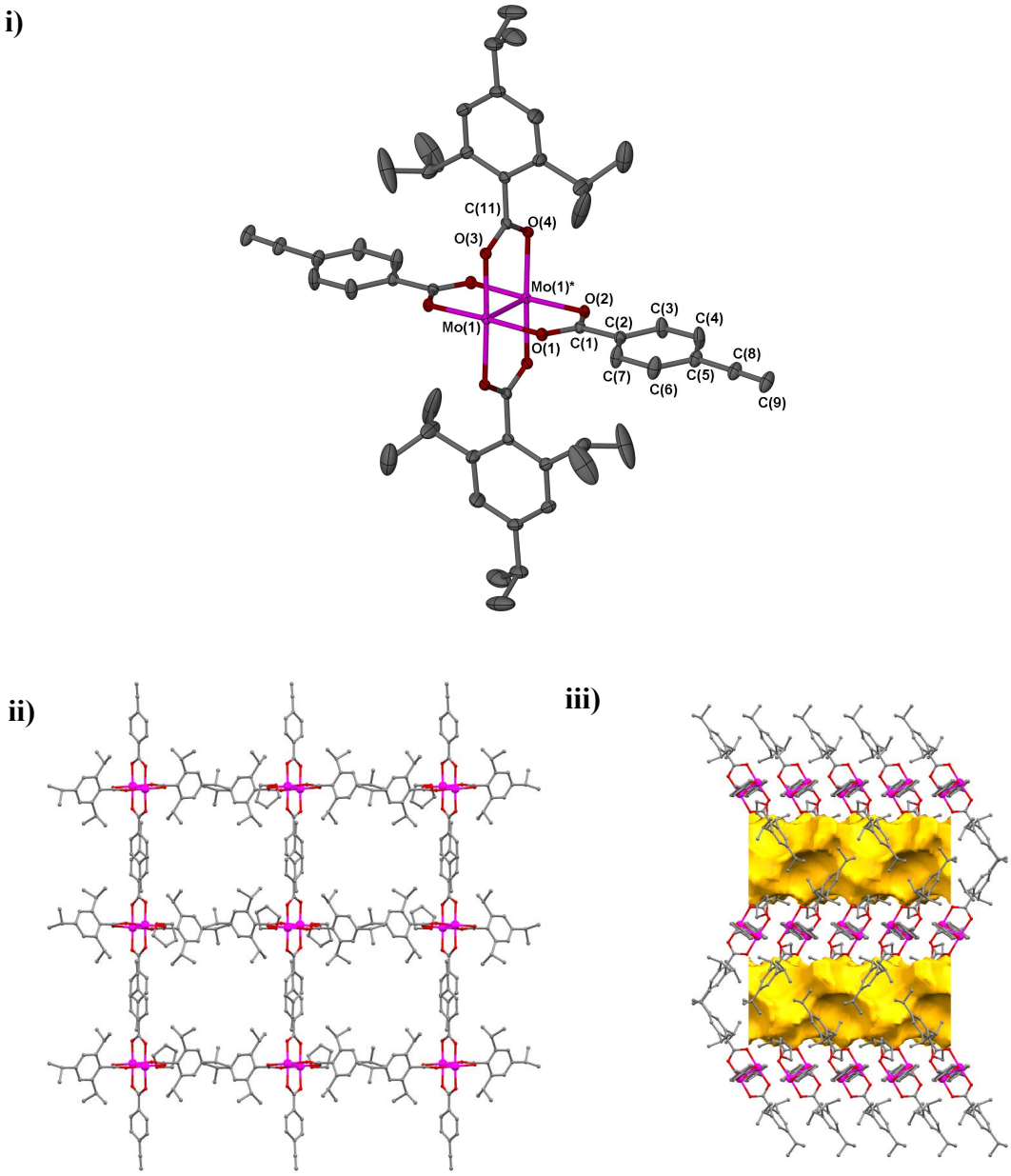

Figure 3.8: i) Molecular structure of **Mo2** shown with ellipsoids at 30% probability and hydrogen atoms and solvent of crystallisation removed for clarity. **ii)** Section of the crystal lattice of **Mo2** viewed along the *b*-axis with solvent molecules removed. **iii)** Section of the crystal lattice of **Mo2** viewed down the *a*-axis, showing calculated void space in the absence of solvent, using a contact surface calculation with a 1.2 Å probe radius and 0.1 Å grid spacing.

Although the molecular structure of **Mo3** was also determined within this study, the data has since been reported by Chisholm *et al.*[108] and, as such, the structure is not presented here. The data recorded within this study (shown in **Table 3.2**) is in full

agreement with that presented by Chisholm; however, the asymmetric unit of **Mo3** contains one molecule of uncoordinated THF in addition to the axially coordinated solvent, which was not mentioned within the literature.

Both **Mo2** and **Mo3** exhibit the desired *trans*-geometry of the ethynyl-carboxylate ligands and in both complexes the aromatic spacers of these ligands are vey close to co-planar with their attendant carboxylate groups, providing near optimum π-orbital alignment along the length of the entire complexes. The aryl groups of the T^iPB ligands are essentially perpendicular to their attendant carboxylate moieties, with the *o*-^{i}Pr groups projecting above and below the plane of the ethynyl-carboxylate ligands. The core structures of the two systems are almost identical to each other within the error of the measurements, and there is negligible difference between the Mo-O bond lengths exhibited by the different carboxylate ligand systems. The Mo-Mo and Mo-O bond lengths are typical for molybdenum tetracarboxylate species.[107,111,189,191]

Table 3.2: Selected bond lengths (Å) bond angles (°) and planar torsion angles (°) observed in the molecular structures of **Mo2** and **Mo3**.

	Mo2	**Mo3**
Mo-Mo	2.100(1)	2.1080(7)
Mo-O[a]	2.093(3), 2.105(3)	2.105(5) – 2.118(5)
Mo-O[b]	2.099(3), 2.106(3)	2.112(5) – 2.123(5)
Mo-O(THF)	2.614(3)	2.568(6), 2.581(6)
C≡C	1.177(7)	1.17(1), 1.18(1)
***cis*-O-Mo-O**	89.5(1) - 90.4(1)	88.4(2) - 91.3(2)
***trans*-O-Mo-O (T^iPB)**	176.6(1)	176.8(2), 176.6(2)
***trans*-O-Mo-O (Ethynyl-carboxylate)**	176.4(1)	176.1(2), 176.8(2)
[L]∠{CO_2}[c]	4.5	4.1, 5.4

[a] ethynyl-carboxylate, [b] T^iPB, [c] [L] = -C_6H_4- or -C_4H_2S- (torsion defined between the plane defined through [L] and one defined through the adjacent CO_2 fragment).

An analysis of the crystal lattice of **Mo2** revealed that that the uncoordinated molecules of THF reside in large channels that extend along the length of the *b*-axis. These channels are shown in the absence of solvent in **Figures 3.8-ii** and **3.8-iii**. The channels facilitate desolvation of the crystals at room temperature resulting in rapid loss of crystallinity. No such channels are observed within the lattice of **Mo3** and, as a result, the crystals are significantly less susceptible to loss of structure. In addition to this, the axial Mo-O(THF) contacts observed within **Mo2** are significantly longer than those of **Mo3**, which may also aid desolvation in the former.

PtMo1 crystallises in the triclinic space group *P-1* with one molecule in the asymmetric unit. One of the PEt_3 ligands is disordered over two positions by rotation about the Pt-P bond, with the larger component present at 58% occupancy. The second phosphine ligand is disordered over two positions by both rotation and a slight translation out of the Pt square plane with the larger component present at 71% occupancy. The asymmetric unit also contains three molecules of toluene and a molecule of hexane. One molecule of toluene and the hexane molecule are present in 100% occupancy but are both disordered over inversion centres. The remaining toluene molecules are present with 52% and 48% occupancies and are both disordered by rotation. This disorder has precluded the location of the methyl carbons for these solvent molecules. **PtMo2** crystallises in the monoclinic space group *C2/c* with one molecule of **PtMo2** and two molecules of toluene in the asymmetric unit. One toluene molecule is disordered over two postions by rotation with each component exhibiting an occupancy of 40%. The second toluene molecule is present at 80% occupancy.

The molecular structures of both **PtMo1** and **PtMo2** are shown in **Figure 3.9-i** & **3.9-ii** and selected bond lengths and angles are presented in **Table 3.3**.

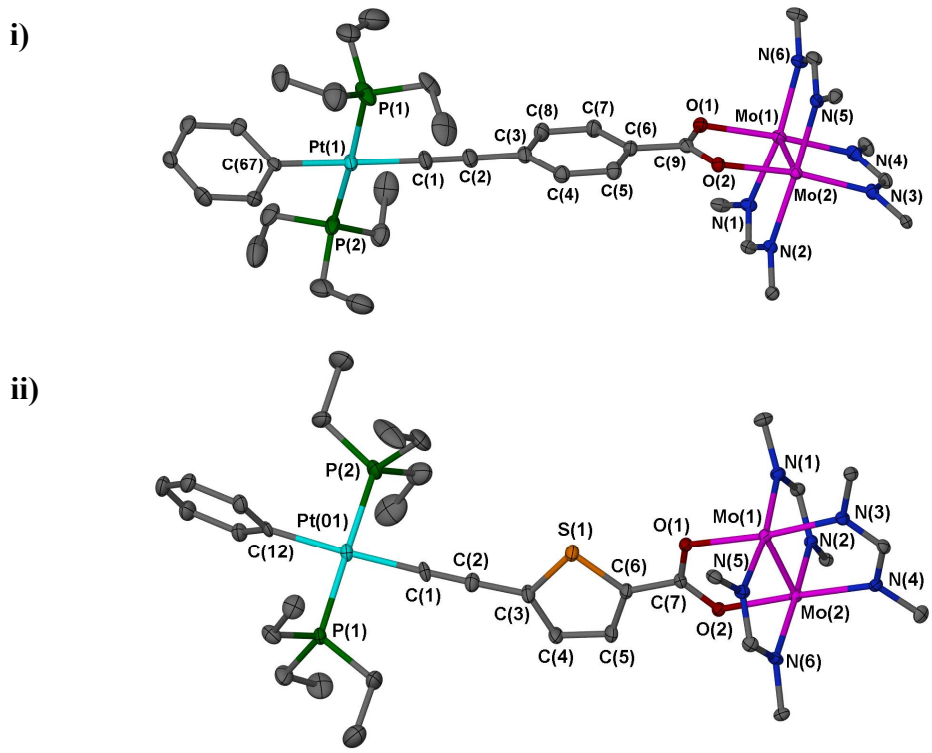

Figure 3.9: The molecular structures of **PtMo1** (**i**) and **PtMo2** (**ii**) shown with ellipsoids at 30% probability. In both structures the hydrogen atoms and solvent of crystallisation have been removed for clarity. All but the *i*-carbons of the *p*-tolyl substituents have also been omitted.

The data presented in **Table 3.3** shows that the geometries of the two heterometallic complexes are very similar. The bond lengths surrounding both the {Mo_2} and Pt centres of each complex are the same within error for both species. The same is true for the C≡C and Mo-Mo bond lengths, which do not differ from the analogous measurements recorded for the parent complexes. The geometry around the Pt centre of both complexes is square planar with only slight deviations from the idealised 90° and 180° bond angles. The geometry around the {Mo_2} core of each complex is also very similar in which steric repulsion between the formamidinate ligands results in a slight distortion of the cis-N-Mo-N and *cis*-N-Mo-O bond angles, consistent with our observations for **Mo1**. However, within the structure of **PtMo1** only one set of *cis*-N-Mo-O bond angles is affected by the steric interactions, unlike both **Mo1** and **PtMo2**, in which each of the *cis*-N-Mo-O angles are contracted. The Mo_2···Pt distances observed in both structures, are longer than has been reported for any intramolecular {Mo_2}···heterometal distance within the literature. The longest

previous to this is the {Mo_2}···Rh distance reported by Cotton *et al.* in a $Rh_2(O_2CCH_3)_4$-bridged {Mo_2}-isonicotinate dimer (*ca.* 9.23 Å).[117].

Table 3.3: Selected bond lengths (Å), bond angles (°) and planar torsion angles (°) within the molecular structures of **PtMo1** and **PtMo2**.

	PtMo1	**PtMo2**
Pt-C(Ph)	2.061(5)	2.060(6)
Pt-C(C≡C)	2.017(5)	1.998(7)
Pt-P	2.278(2), (2.222(1) and 2.300(4))[f]	2.273(2), 2.284(2)
C≡C	1.199(7)	1.22(1)
C-Pt-C	179.1(2)	177.2(3)
P-Pt-P	(169.1(4) and 173.8(2))[f]	179.27(8)
P-Pt-C(Ph)	90.1(1), (89.4(2) and 90.9(3))[f]	90.1(2), 90.6(2)
P-Pt-C(C≡C)	88.9(2), (90.1(4) and 91.5(2))[f]	86.6(2), 92.7(2)
Mo-Mo	2.0861(6)	2.0842(7)
Mo-O	2.131(3), 2.135(3)	2.131(4), 2.136(4)
Mo-N[a]	2.119(4), 2.132(4)	2.121(5), 2.130(5)
Mo-N[b]	2.137(4), 2.142(4), 2.150(4), 2.164(3)	2.138(5), 2.140(5), 2.145(5), 2.147(5)
***trans*-N-Mo-N**	171.1(2), 174.1(1)	171.1(2), 172.6(2)
***cis*-N-Mo-N**	88.9(1), 91.0(2), 94.7(1), 94.8(2)	89.6(2), 91.4(2), 94.9(2), 95.4(2)
***trans*-N-Mo-O**	172.8(1), 173.3(1)	174.3(2), 175.4(2)
***cis*-N-Mo-O**	83.1(1), 85.2(1), 90.7(1), 90.7(1)	86.3(2), 86.9(2), 87.1(2), 87.5(2)
{O_2C}∠{spacer}[c]	*ca.* 2.3	*ca.* 8.0
{Pt}∠{spacer}[d]	*ca.* 53.3	*ca.* 77.0
Pt···Mo_2[e]	*ca.* 11.7	*ca.* 11.0

[a] *trans* to carboxylate, [b] *cis to* carboxylate, [c] torsion angle between the planes of the {CO_2} and {spacer} moieties, [d] torsion angle between Pt square plane and the plane of the spacer, [e] through space separatiom between Pt and {Mo_2} centroid, [f] bond lengths and angles for both positions of the disordered PEt_3 provided.

Within both **PtMo1** and **PtMo2** the phenylene and thienyl spacer units are close to coplanar with their attendant carboxylate groups, maximising the π orbital overlap within these species. In contrast, the Pt square plane of both of the heterometallic complexes exhibit large torsion angles relative to the respective phenylene and thienyl spacer units, suggesting that there is no energetic bias towards coplanarity of these fragments. The torsion angles are also significantly larger than observed for the parent Pt complexes (*ca.* 17.8^{o} (**Pt2a**) and *ca.* 21.1^{o} (**Pt5a**)). However, electronic delocalisation throughout these systems can still be considered on account of the proposed 'cylindrical nature' of the acetylinic π-orbitals.[56,59,203]

MoPtMo crystallises in the triclinic space group *P-1* with half a molecule in the asymmetric unit. The Pt lies on a special position and the second half of the molecule is generated by inversion through this point. The asymmetric unit of **MoPtMo** also contains three molecules of toluene, each present at 100% occupancy. Two of these solvent molecules are disordered by rotation with the major components present at 50% and 56% respectively. Two of the *p*-tolyl rings are also disordered by rotation and were modelled over two positions with the larger component of each present at 76% occupancy. It is also noteworthy that a significant amount of thermal motion is observed in the ethyl substitutents of the phosphine ligands that could not rationally be modelled as disorder. The molecular structure of **MoPtMo** is shown in **Figure 3.10-i** and selected distances and angles are displayed in **Table 3.4**.

The structure of **MoPtMo** exhibits a linear conformation in which {Mo_2} termini are bridged by the Pt-containing ligand system. Consistent with observations made for most of the crystal structures of the Pt *bis*-ethynyl-ester complexes (discussed in **Chapter 2**), the 'rigid-rod' type structure promotes a 1D packing motif in which all molecules are oriented along a single vector (**Figure 3.10-ii**).

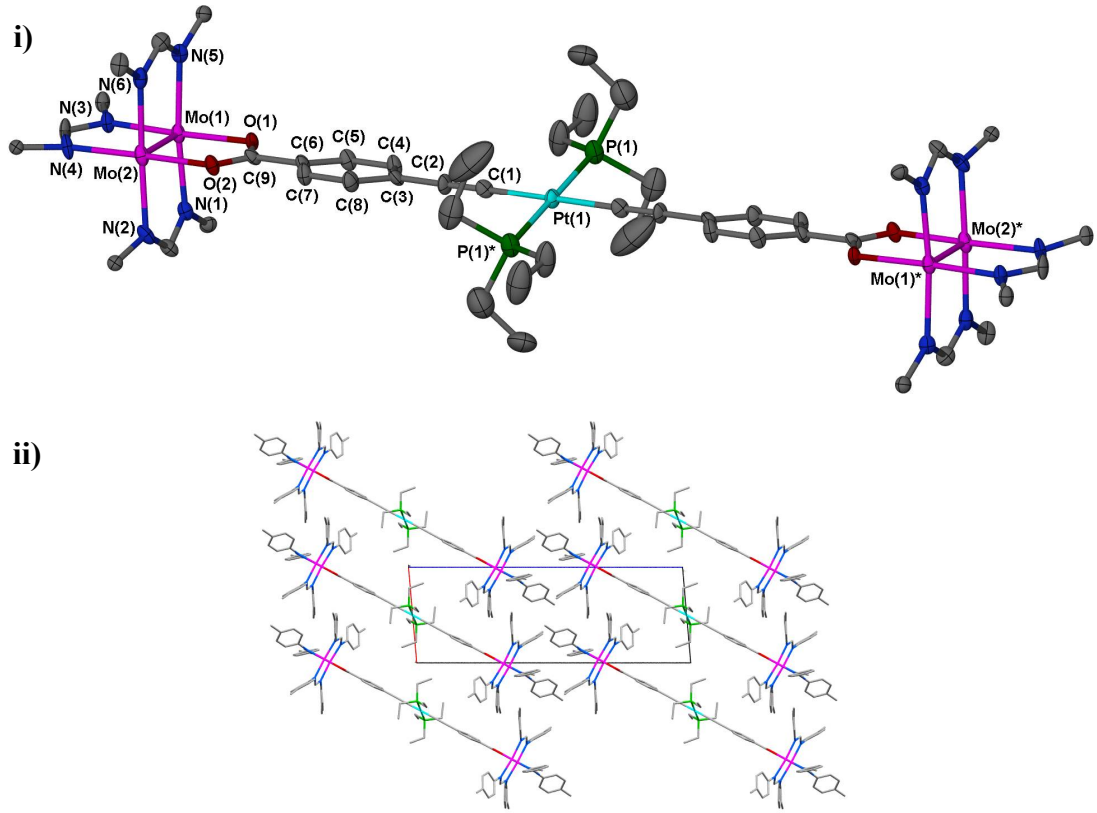

Figure 3.10: Molecular structure of **MoPtMo** (**i**) shown with 30% thermal ellipsoids and crystal packing diagram viewed down the *b*-axis. Hydrogen atoms, *p*-tolyl groups and solvent of crystallisation have been omitted from diagram **i** and hydrogen atoms and solvent of crystallisation are omitted from diagram **ii**.

The geometry around the Pt centre is square-planar with only slight deviations from 90° in the P-Pt-C angles whilst the 180° C-Pt-C and P-Pt-P angles are defined by symmetry. All bond lengths and angles surrounding the Pt, in addition to the C≡C bond length, are the same within error to those of **Pt2b**. The geometry about the Mo_2 core is very similar to that of the parent complex, **Mo1**, in which the *cis*-N-Mo-O angles are each lower than 90° due to steric interactions between the formamidinate ligands. The Mo-Mo bond length is the same as that observed in **PtMo1** within error, and negligibly larger than that of the parent complex **Mo1**. The distance between the $\{Mo_2\}$ termini, measured using centroids at the centre of the Mo-Mo bonds, is 23.3 Å, representing the largest separation that has been reported within conjugated $\{Mo_2\}$ oligomers. Previous to this the largest $\{Mo_2\}\cdots\{Mo_2\}$ distances had been observed for $\{Rh(O_2CCH_3)_4\}$-bridged $\{Mo_2\}$ isonicotinate complexes, for which the distances

were 20.8 and 20.9 Å respectively.[111,117] These systems are distinctly different from our own complex, however, as they are assembled through Lewis basic interactions.

Table 3.4: Selected bond lengths (Å), angles (°) and planar torsion angles (°) observed in the molecular structure of **MoPtMo**.

Distances (Å)		**Angles (°)**	
Pt-C	2.015(7)	**C-Pt-C**	180
Pt-P	2.286(2)	**P-Pt-P**	180
C≡C	1.182(9)	**P-Pt-C**	88.3(2), 91.7(2)
Mo-Mo	2.0872(8)	***cis*-N-Mo-N[c]**	90.5(2), 91.6(2), 93.4(2), 93.5(2)
Mo-O	2.141(4), 2.120(4)	***trans*-N-Mo-N[d]**	173.4(2), 172.2(2)
Mo-N[a]	2.135(7)-2.419(6)	***cis*-N-Mo-O[c]**	86.8(2), 87.4(2), 87.6(2), 88.3(2)
Mo-N[b]	2.133(5), 2.134(6)	***trans*-N-Mo-O[d]**	175.6(2), 174.5(2)
{Mo_2}···{Mo_2}	*ca.* 23.3	**{O_2C}∠{C_6H_4}[c]**	*ca.* 6.7
		{Pt}∠{C_6H_4}[c]	*ca.* 23.5

[a] *cis* to carboxylate, [b] *trans* to carboxylate, [c] torsion angle between planes defined though both fragments, [d] torsion angle between Pt square plane and the plane of the phenylene ring.

Consistent with the observations made for **PtMo1**, the phenylene ring is close to coplanar with the attendant carboxylate fragment. The angle between the planes defined through the Pt square plane and the phenylene ring is significantly smaller than was observed for **PtMo1** but is slightly larger than that observed for **Pt2b** (*ca.* 13.1°). The π-orbital alignment within the solid state structure of **MoPtMo** is therefore greater than was observed within the smaller oligomeric system **PtMo1**.

PtMoPt crystallises in the monoclinic space group $P2_1/c$ with half a molecule in the asymmetric unit. The second half molecule is generated by an inversion centre though the centre point of the Mo-Mo bond. The asymmetric unit also contains a single molecule of THF, which is coordinated to the axial position of the Mo-Mo bond (Mo-O_{THF} = 2.593(5) Å). The molecular structure of **PtMoPt** is shown in **Figure 3.11-i**.

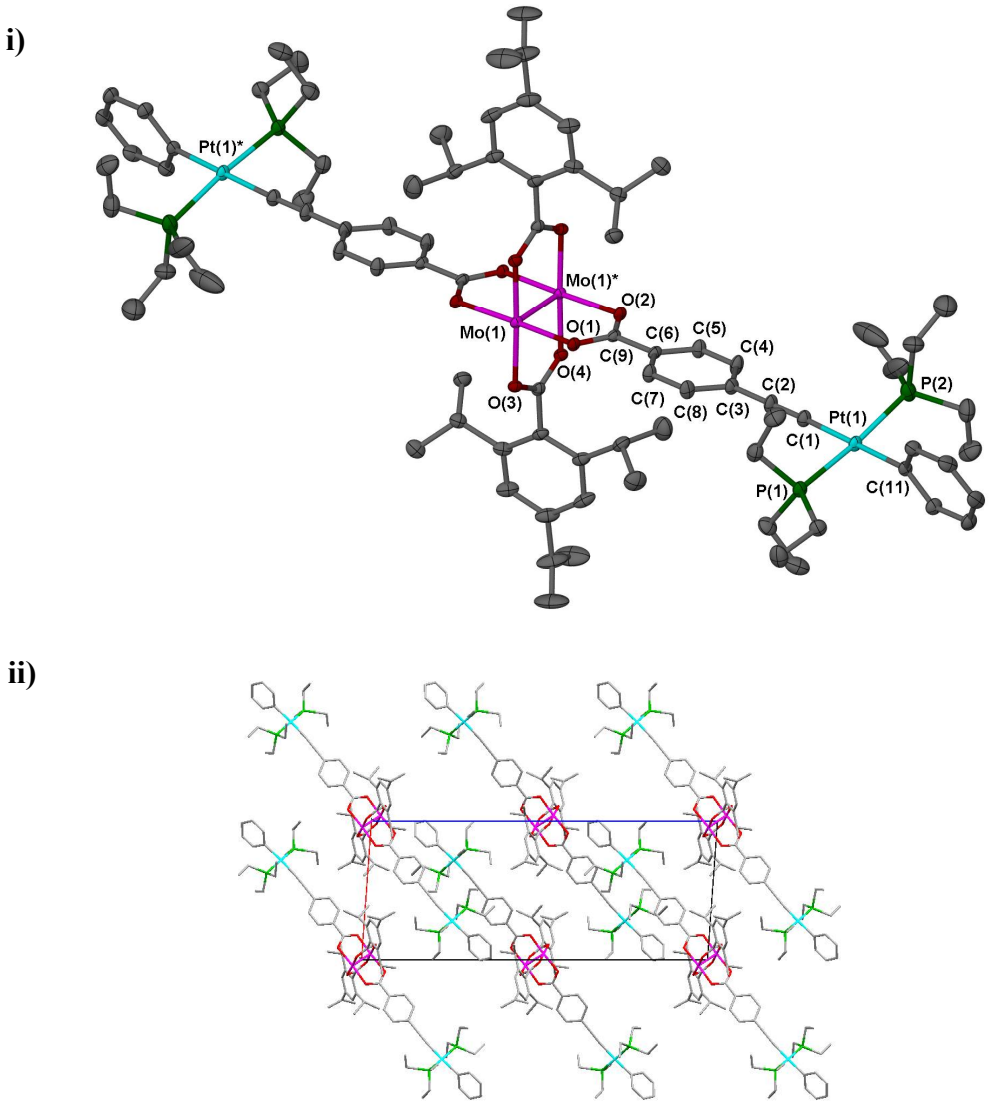

Figure 3.11: i) Molecular structure of **PtMoPt** shown with 30% thermal ellipsoids and a packing diagram viewed down the b-axis. Hydrogen atoms and THF molecules have been removed for clarity. **ii)** a section of the crystal lattice of **PtMoPt** viewed along the *b*-axis.

The molecular structure of **MoPtMo** exhibits a *trans*-geometry of the Pt-containing carboxylate ligands about the Mo-Mo bond, in which the through-space separation of the two Pt cores is *ca*. 23.3 Å, the same as the separation between {Mo_2} units within **MoPtMo**. Consistent with the observations made within the structure of the parent complex, **Mo1**, the aryl groups of the T^iPB ligands are close to perpendicular to their attendant carboxylate units. Similar to the molecular packing of **MoPtMo**, the molecules of **PtMoPt** are arranged in linear arrays within the crystal lattice, which is likely to be promoted by the long rod-like shape of the molecules. This packing is illustrated by the packing diagram presented in **Figure 3.11-ii**, viewed along the *b*-axis. Selected bond lengths and angles are shown in **Table 3.5** with other relevant distances and angles.

Table 3.5: Selected bond lengths (Å), bond angles (°) and planar torsion angles (°) within the molecular structure of **PtMoPt**.

Distances (Å)		**Angles (°)**	
Mo-Mo	2.103(9)	***cis*-O-Mo-O**	90.0(1), 89.3(1), 89.8(1), 90.7(1)
Mo-O[a]	2.096(3), 2.105(3)	***trans*-O-Mo-O[a]**	176.3(1)
Mo-O[b]	2.107(4), 2.110(4)	***trans*-O-Mo-O [b]**	176.3(1)
Pt-C(C≡C)	2.001(6)	**P-Pt-C(C≡C)**	93.7(2), 86.3(2)
Pt-C(Ph)	2.058(5)	**P-Pt-C(Ph)**	91.4(2), 88.2(2)
Pt-P	2.284(2), 2.281(2)	**P-Pt-P**	172.83(7)
C≡C	1.223(8)	**C-Pt-C**	176.2(2)
{Mo_2}···Pt[c]	*ca.* 11.7	**{O_2C}∠{C_6H_4}[d]**	*ca.* 6.8
{Pt}···{Pt}	*ca.* 23.3	**{Pt}∠{C_6H_4}[e]**	*ca.* 26.9

[a] ethynyl carboxylate, [b] T^iPB, [c] using Mo_2 centroid, [d] torsion angle between planes defined through the two fragments, [g] angle between planes defined though phenylene ring and Pt square plane.

The bond lengths and angles of **PtMoPt**, about the {Mo_2} core, are comparable, within error, to those observed for the parent complex **Mo2**, showing that there is no influence from the introduced {Pt} units. There is also no difference in the length of the Mo-Mo bond. The geometries exhibited at the Pt centres are both square planar and the associated bond lengths and angles do not differ greatly to those observed for **Pt2a**, with the exception of a greater P-Pt-P angle within **Pt2a** (177.66(3)^o). There is also negligible difference between the lengths of the C≡C bonds of **PtMoPt** to those observed within **Mo2**, reflecting no influence from the coordinated Pt centre. Similar to both **PtMo1** and **MoPtMo**, the phenylene rings within the bridging ligands are close to coplanar with their attendant carboxylate groups, facilitating efficient π-orbital alignment with the Mo_2δ orbitals. The torsion angles between the phenylene rings and the Pt square plane are also relatively small and similar in magnitude to the analogous parameter within **MoPtMo**.

3.2.6 – Electronic Absorption Spectroscopy

To investigate the solution-state optical properties of the novel heterometallic complexes, each product was analysed using electronic absorption spectroscopy and the data were compared to that recorded for the related {Pt} and {Mo_2} species. All experiments were performed at room temperature under an inert atmosphere using THF as the solvent. The data for all complexes are summarised in **Table 3.6**, at the end of this section.

The normalised absorption spectrum of **PtMo1** and those recorded for the related species, **Pt2a** and **Mo1** are presented in **Figure 3.12**.

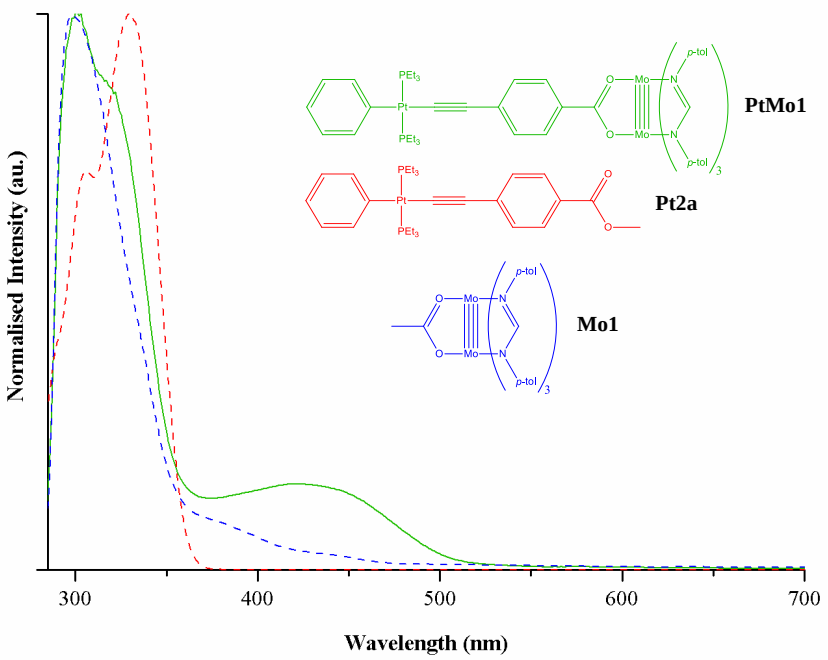

Figure 3.12: Normalised electronic absorption spectra of **PtMo1**, **Pt2a** and **Mo1**, recorded at room temperature in THF.

The absorption spectrum of **PtMo1** exhibits a broad absorption band at 421 nm, which can be attributed to the $Mo_2\delta \rightarrow$bridge-π^* electronic transition. A similar absorption band is not observed for **Mo1** on account of the poor electron withdrawing nature of the acetate ligand. **PtMo1** also exhibits a second, higher energy, absorption band at 301 nm with a shoulder at *ca.* 317 nm. This absorption band is close in energy to the principal absorption bands of both **Mo1** and **PtMo1** but the intensity is more similar to that of the former (see **Table 3.6**). Theoretical studies performed by Cotton *et al.* on the complex $Mo_2(DPTF)_4$ suggest that the intense absorption bands within {Mo_2} formamidinate complexes arise from $N \rightarrow Mo_2\pi^*$ electronic transitions.[196] This provides a possible assignment for the intense absorption band exhibited by **PtMo1**. However, there is also likely to be a contribution form the bridging ligand $\pi \rightarrow \pi^*$ electronic transition, which is exhibited by **Pt2a**.The corresponding absorption band would be significantly lower in intensity than that of the $N \rightarrow Mo_2\pi^*$ process and would therefore obscured by the more intense absorption band. For this reason we are unable to assess the perturbation in energy of the $\pi \rightarrow \pi^*$ transition process upon coordination to the {Mo_2} centre.

The spectrum of **Mo1** is very similar to that reported for $Mo_2(DPTF)_4$.[196] In addition to the intense absorption band, described above, **Mo1** also exhibits two low intensity shoulders at *ca*. 436 nm and 375 nm. The former can be attributed to the $Mo_2\delta \rightarrow Mo_2\delta^*$ electronic transition, and appears at almost the same energy as the analogous transition within the *p*-anisyl analogue of **Mo1**. The calculations performed by Cotton *et al*. suggest that the second shoulder originates from $N \rightarrow Mo_2\delta^*$ electronic transitions,[196] which could also potentially be the case for **Mo1**. However, the $Mo_2\delta \rightarrow$DPTF π^* orbital has also been shown to occur at a similar energy so cannot be ruled out. The energy of the shoulder is too low to be considered for a $Mo_2\delta \rightarrow$acetate π^* transition which Gray *et al*. calculated would appear at *ca*. 300 nm,[204] which would be obscured by the $N \rightarrow Mo_2\pi^*$ absorption band.

The electronic absorption spectrum of **MoPtMo** is presented in **Figure 3.13** alongside the spectra recorded for **Pt2b** and **Mo1**.

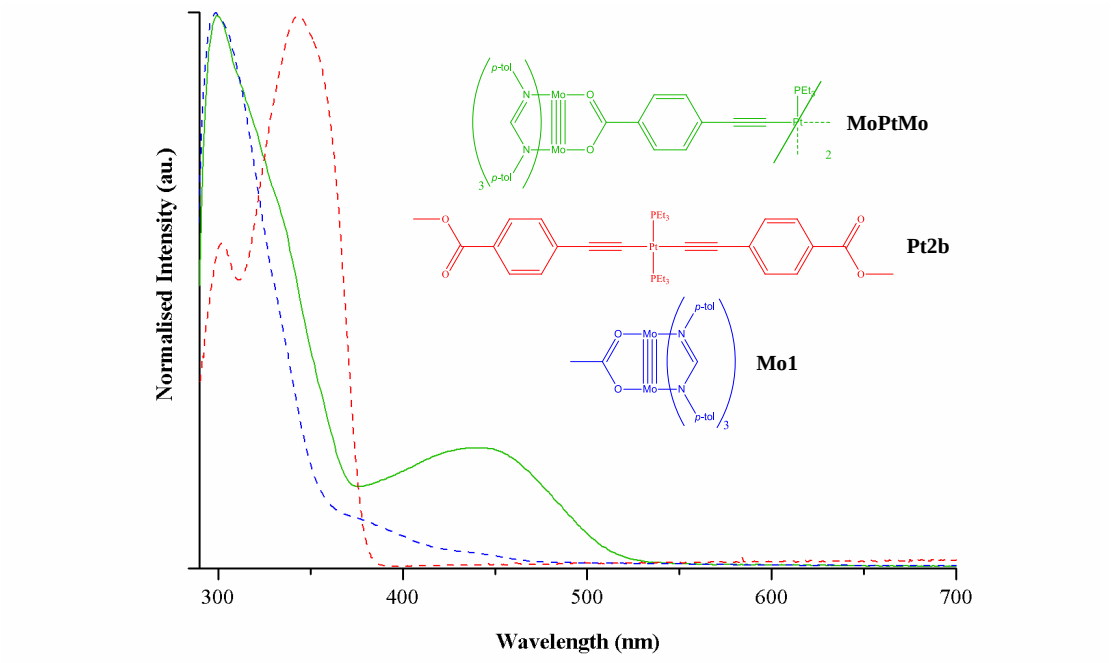

Figure 3.13: Normalised electronic absorption spectra of **MoPtMo**, **Pt2b** and **Mo1** recorded at room temperature in THF.

The electronic absorption spectrum of **MoPtMo** is very similar in appearance to that of **PtMo1**, exhibiting a broad absorption band at 438 nm and a more intense band at 300 nm. The latter exhibits a slight shoulder at *ca.* 325 nm, which is poorly resolved.

The low energy absorption band, attributed to the $Mo_2\delta \rightarrow$bridge-π^* electronic transition, is observed at slightly lower energy to that of **PtMo1**, which is likely to reflect slightly lower energy bridge-π^* orbitals within **MoPtMo**. This is consistent with the lower energy of the $\pi \rightarrow \pi^*$ electronic transition of **Pt2b**, relative to that of **Pt2a**. The absorption band observed at 300 nm can again be attributed to $N \rightarrow Mo_2\pi^*$ electronic transitions. The absorption coefficient observed for this process in **MoPtMo** is approximately double that of **PtMo1** (see **Table 3.6**) which correlates with the presence of double the amount of {Mo_2DPTF_3} units within the former. The absorption coefficient for the MLCT band of **MoPtMo** is also significantly larger than that of **PtMo1**.

The electronic absorption spectrum of **PtMoPt** is shown in **Figure 3.14** with the corresponding spectra of **Pt2a** and **Mo2** to aide comparison between the species.

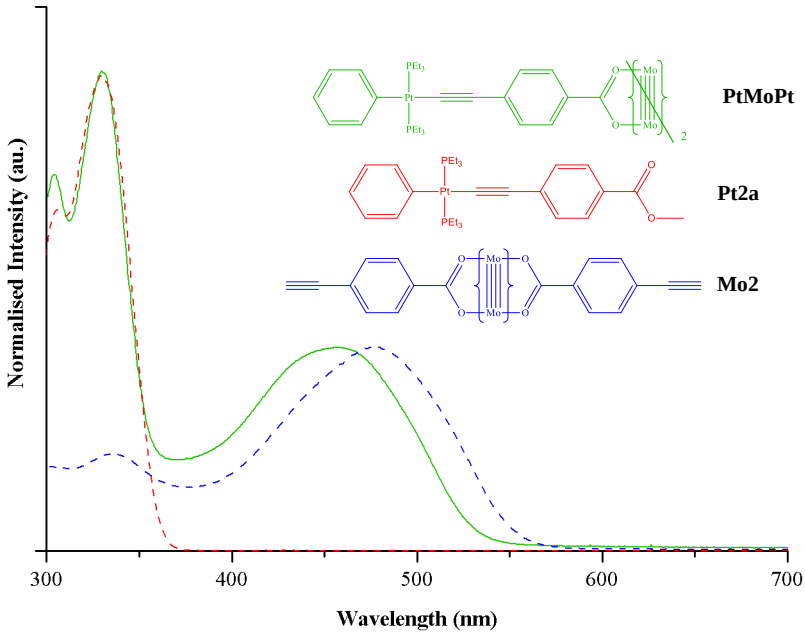

Figure 3.14: Normalised electronic absorption spectra of **PtMoPt** and the parent complexes **Pt2a** and **Mo2** all recorded at room temperature in THF.

The electronic absorption spectrum of **PtMoPt** exhibits a broad absorption band at 457 nm ($Mo_2\delta \rightarrow$bridge-π^*) and a second, more intense, absorption band at 329 nm with a shoulder at 304 nm. The MLCT band is the lowest energy that has been observed throughout the series of mixed-metal complexes. The high energy

absorption bands are almost identical to those observed for **Pt2a**, suggesting that they originate from bridge $\pi \rightarrow \pi^*$ electronic transitions. The absorption coefficient of this process is significantly greater for **PtMoPt**, which is likely to be due to the presence of two bridging ligands and the mixing between $Mo_2\delta$ and bridge-π-orbitals. Interestingly the energy of this $\pi \rightarrow \pi^*$ transition does not appear to be affected by the presence of the {Mo_2} unit.

A comparison between the spectra recorded for **PtMoPt** and **Mo2** reveals a blue-shift of the absorption band corresponding to the $Mo_2\delta \rightarrow$bridge-π^* electronic transition upon coordination of the two {Pt} units. Correlated with electrochemical data recorded for these species (*vide infra*), this can be related to an increase in the energy of the bridge-π^* in the heterometallic species. Chisholm *et al*. also noted a red-shift in the analogous absorption band of **Mo3** following the coordination of {$AuPPh_3$} at the termini.[108] It is likely that these observations related to destabilising orbital mixing between the metal *d*-orbitals and the π^*-orbitals of the bridging ligands. The absorption spectrum of **Mo2** does not exhibit the intense band observed for **PtMoPt** at 329 nm, suggesting that the ethynyl-carboxylate $\pi \rightarrow \pi^*$ transition occurs at higher energy within **Mo2**, which is consistent with the observations made by Chisholm *et al*. for **Mo3**.[108]

In addition to the broad MLCT band observed in the absorption spectrum of **Mo2**, a weaker band is also observed at 336 nm. Similar absorption bands have been observed at approximately the same energy for a range of {$Mo_2T^iPB_2$}-bridged complexes within the literature,[108-110,191] and are attributed to $Mo_2\delta \rightarrow T^iPB$-$\pi^*$ electronic transitions. This absorption band appears at lower energy than the previously described MLCT band due to the lesser degree of conjugation within the T^iPB ligands relative to the ethynyl-carboxylate ligands.

In order to illustrate our ability to tune the optical properties of these systems, the electronic absorption spectra of **Mo2** and **Mo3** are presented in **Figure 3.15** and are compared to the absorption spectrum of $Mo_2(T^iPB)_4$. It should be noted that the data presented for **Mo3** is in direct agreement with that published by Chisholm *et al*..[108]

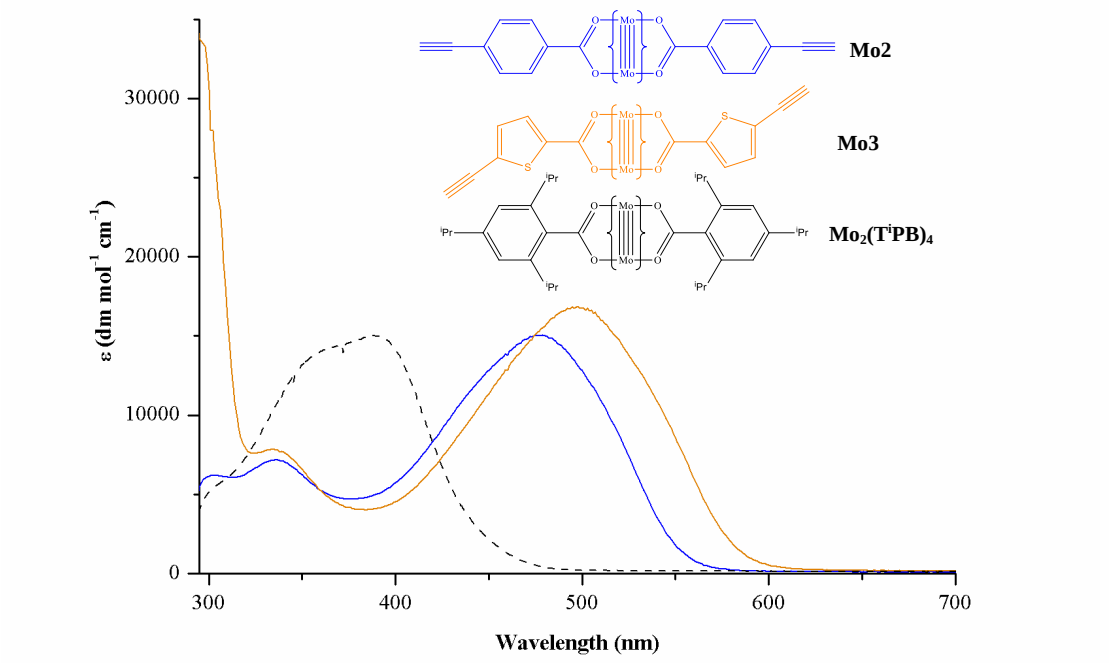

Figure 3.15: Electronic absorption spectra of **Mo2**, **Mo3** and $Mo_2(T^iPB)_4$ recorded at room temperature in THF. {Mo_2} represents $Mo_2(T^iPB)_2$.

Consistent with the discussion above, both **Mo2** and **Mo3** exhibit low intensity absorption bands at almost identical energies (ca. 330 nm), corresponding to the $Mo_2\delta \rightarrow T^iPB\text{-}\pi^*$ electronic transition. However, the absorption band corresponding to the $Mo_2\delta \rightarrow$bridge-π^* electronic transition is red-shifted upon changing form a phenylene to a thienyl spacer unit due to the difference in electron withdrawing ability of the two ligand systems. In a study by Chisholm *et al*. it was suggested that the relatively low energy MLCT processes observed within thienyl bridged {Mo_2} dimers could be ascribed to efficient conjugation in the low lying ligand-π^* orbital due to the resonance form shown in **Figure 3.16**.[122] A similar explanation can be used to support our experimental observations, although the diffuse nature of the conjugated sulphur *p*-orbital is also likely to aid conjugation within the ligand system.

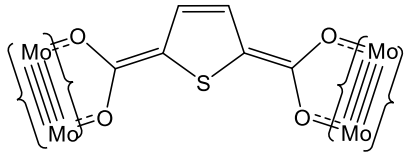

Figure 3.16: Resonance form of the 2,5-thiophene-dicarboxylate ligand-π* orbital responsible for the relatively low energy MLCT band observed for the {Mo_2} dimer.[122]

Although it was not mentioned within the literature, the energy of the MLCT of **Mo3** is significantly red shifted relative to the analogous band that was reported for the related *bis*-thienyl-carboxylate analogue (443 nm). This shows that the ethynyl moieties significantly lower the energy of the ligand π*-orbitals within **Mo3**.

Finally, the MLCT bands exhibited by **Mo2** and **Mo3** are both significantly red-shifted relative to the absorption band observed for the parent complex, $Mo_2(T^iPB)_4$, which correlates to the lesser degree of conjugation within the latter. This is largely due to the steric demands of the T^iPB ligands which hinders the conjugation between the aryl and carboxylate moieties.[189]

All of the electronic absorption data discussed within this section is summarised within **Table 3.6**.

Table 3.6: A summary of the electronic absorption data for the mixed metal species and their parent complexes. All data was collected in THF solution. Extinction coefficients are given in brackets ($dm.mol^{-1}.cm^{-1}$).

Complex	λ (nm)
PtMo1	421 (9069), *ca*. 317 (51174), 301 (58863)
MoPtMo	438 (26276), *ca*. 325(89514), 300 (120590)
PtMoPt	457(24649), 329 (58185), 304 (45581)
Mo1	ca. 436 (3075), ca. 375 (7342), 300 (59323)
Mo2	479 (15065), 336 (7173)
Mo3	495 (16825), 334 (7828)
$Mo_2T^iPB_4$	387 (15033)
Pt2a	330 (17894), 298 (6603)
Pt2b	343 (48936), 302 (28272)

3.2.7 – Electrochemical Analyses

To investigate the effect that the Pt centres have on the electronic environment of the {Mo_2} centres within the novel heterometallic complexes, each system was analysed electrochemically using cyclic voltammetry and compared to the analogous data of the appropriate {Mo_2} precursor. Specifically, this is to investigate the relative energy of the $\{Mo_2\}^{4+/5+}$ redox couple, reflecting the energies of the $Mo_2\delta$ orbitals.

The analysis of each complex was carried out under Ar, using a 1 mM THF solution of the analyte and 0.1M concentration of $[NBu_4][PF_6]$ as the electrolyte. The working, counter and reference electrodes were glassy carbon, gold and platinum respectively for each of the analyses. Initially a silver wire reference electrode was used but there were signs that it was reacting with the heterometallic complexes during the analyses and, as such, a Pt reference was found to be a more reliable option. Each data set was referenced using the ferrocene (Fc), $Fc^{0/1+}$, redox couple *via* the addition of a small

amount of $FeCp_2$ to the analysed solutions. The redox couple for **PtMoPt** was not resolvable from that of $FeCp_2$ and as such a secondary cobaltocenium reference was used to provide a more accurate value for the half-wave potential ($E_{1/2}$).

The cyclic voltammograms recorded for **PtMo1** (yellow), **MoPtMo** (cyan) and **Mo1** (black), which all contain the {Mo_2DPTF_3} fragment, are presented in **Figure 3.17-i**.

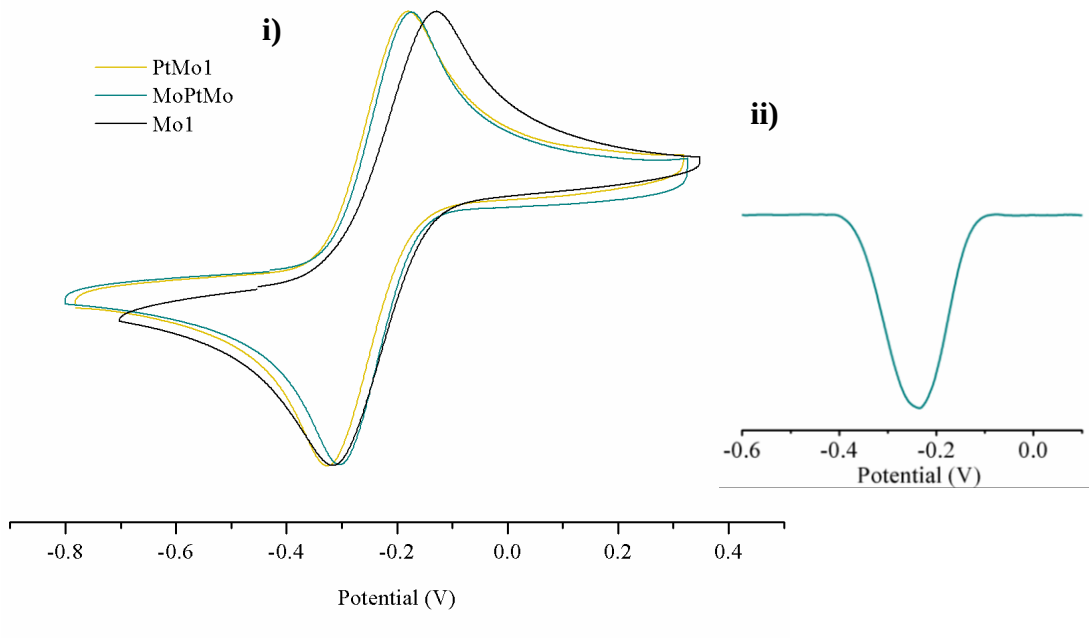

	PtMo1	MoPtMo	Mo1
$E_{1/2}$	-253 mV	-239 mV	-223 mV
ΔE_p	147 mV	131 mV	188 mV

Figure 3.17: i) Normalised cyclic voltammogram plots for **PtMo1** (yellow), **MoPtMo** (cyan) and **Mo1** (black) collected in 0.1 M THF solutions of [NBu_4][PF_6] and referenced to the $Fc^{0/+}$ couple, **ii)** Differential pulse plot for **MoPtMo** recorded under the same conditions at a scan rate of 100 mV s^{-1}. (ΔE_pFc = 142 mV)

The data presented in **Figure 3.17-i** shows that each of the complexes exhibits a single reversible redox process, corresponding to the {Mo_2}$^{4+/5+}$ redox couple, and exhibit negative $E_{1/2}$ values relative to the Fc reference. This is common for formamidinate-stabilised {Mo_2} systems.[123] The magnitude of the $E_{1/2}$ for the three complexes increases in the order **Mo1**>**MoPtMo**>**PtMo1**, although there is little

difference between the three values. **PtMo1** is therefore the easiest to oxidise, relating to the highest energy $Mo_2\delta$ orbital, whilst the precursor **Mo1** is the hardest to oxidise, with the lowest energy $Mo_2\delta$ orbital. It is likely that $E_{1/2}$ of **MoPtMo** is not as high as that of **PtMo1** because the destabilising effect of the Pt is shared between two {Mo_2} units within the former.

The cyclic voltammogram of **MoPtMo** exhibited no signs of broadening relative to that of **PtMo1**, which suggested that the former exhibits a single two electron redox process with both termini oxidising at the same potential. This observation was supported by a differential pulse analysis **Figure 3.17-ii**, showing a single peak. There is therefore no evidence of electronic coupling between the two {Mo_2} termini within **MoPtMo**, which is likely to be due to the large {Mo_2}···{Mo_2} separation (23.3 Å in the solid-state).

The comparisons made from the data in **Figure 3.17** show how $E_{1/2}$ is affected upon coordination of the Pt ethynyl-carboxylate complexes to **Mo1**. However, performing the same analysis on **PtMoPt** and **Mo2** allows the discrete effect of the {Pt} fragment to be investigated, because **Mo2** already contains the conjugated bridging ligand. The cyclic voltammograms of **PtMoPt** (green), **Mo2** (blue) are shown in **Figure 3.18** to facilitate this investigation. The electrochemical data for **Mo3**, which was not discussed within the literature, is also presented in the diagram.

Once again, each of the complexes exhibits a single reversible redox wave, corresponding to the $\{Mo_2\}^{4+/5+}$ redox couple, each of which appear at positive potential relative to the Fc reference. The carboxylate complexes therefore exhibit lower energy $Mo_2\delta$ orbitals than the previously studied formamidate species, which is consistent with data reported in the literature.[98] Interestingly, the data shows that $E_{1/2}$ of **PtMoPt** is significantly anodically shifted from that of the precursor, **Mo2**. The {Pt} unit, therefore, has a significant destabilising effect on the $Mo_2\delta$ orbital. This shows that, within the heterometallic complex, the ligand system is significantly less electron withdrawing than the ethynyl-carboxylate ligands of **Mo2** and therefore less able to stabilise the electron density in the $Mo_2\delta$ orbital. It is likely that this is due to mixing between the filled Pt *d*-orbital and the ligand π-orbitals, resulting in a

more electron rich ligand system. This theory also helps to explain why the MLCT band of **PtMoPt** is blue-shifted relative to that of **Mo2**.

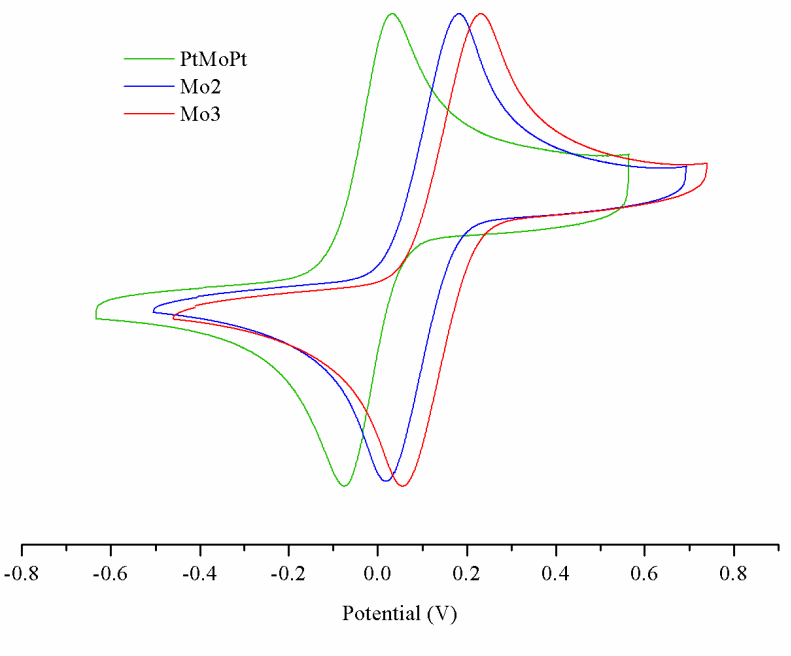

	PtMoPt	Mo2	Mo3
$E_{1/2}$	-48 mV	110 mV	154 mV
ΔE_p	109 mV	164 mV	176 mV

Figure 3.18: Normalised cyclic voltammogram plots for **PtMoPt** (green), **Mo2** (blue) and **Mo3** (red), recorded in 0.1 M THF solutions of $[NBu_4][PF_6]$ and referenced to the $Fc^{0/1+}$ couple. Each recorded at a scan rate of 100 mV s^{-1}. (ΔE_pFc = 150 mV)

The data in **Figure 3.18** also show that the thienyl-containing complex, **Mo3**, exhibits a more positive $E_{1/2}$ than the phenylene analogue, relating to a more stabilised $Mo_2\delta$ orbital. This can be correlated with the more electron-withdrawing nature of the thienyl spacer unit and illustrates how the electronic properties of these systems can be tuned.

In addition to the reversible oxidation waves, presented in **Figures 3.17** and **3.18**, the heterometallic complexes each exhibit a second irreversible process at more positive oxidation potential. An example of this process is shown in **Figure 3.19** for **PtMoPt**,

for which three consecutive scans are shown. The data shows that, following the initial scan of the high potential region, the intensity of the reversible oxidation wave drops considerably, and subsequent scans show that the intensity of the irreversible process also drops. The intensity of the signals does not recover unless the surface of the working electrode is polished using alumina. Solely rinsing the surface of the electrode has no effect. This shows that a layer of material is being coated onto the electrode during the analysis, although the identity of the substance is currently unknown. Irreversible processes were also observed for the Pt-free complexes **Mo1**, **Mo2** and **Mo3**, however, high potential scans for these complexes did not result in a change in the intensity of the $Mo_2^{4+/5+}$ oxidation waves, suggesting the {Pt} units are responsible for the unusual behaviour that was observed.

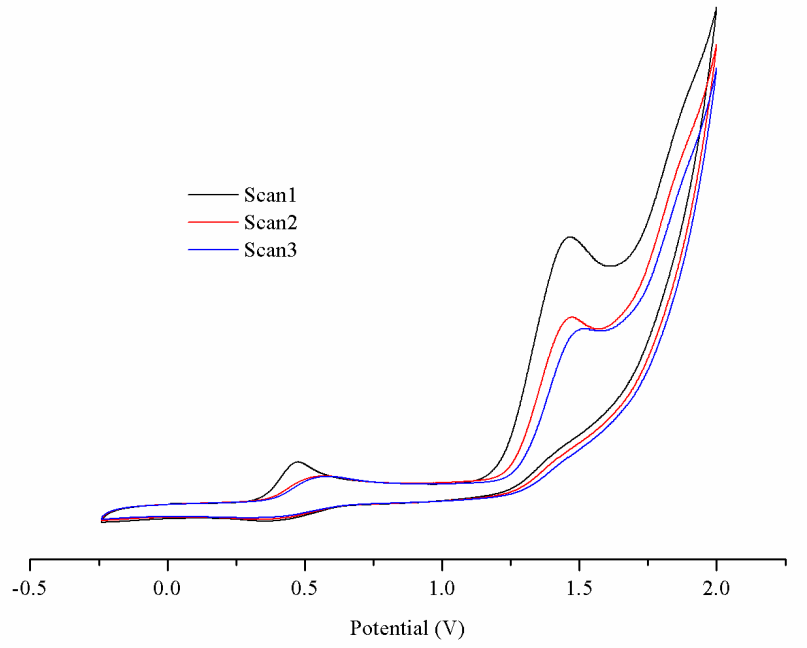

Figure 3.19: Cyclic voltammogram plot showing an irreversible process occurring at high potential for **PtMoPt**.

3.2.8 – Theoretical Studies

In order to gain a greater understanding of the electronic structures of the novel heterometallic complexes, **PtMo1** and **PtMoPt** were investigated using theoretical studies. Analogous studies have also been extended to the {Mo_2} complexes, **Mo2**

and **Mo3**, to investigate how the identity of the conjugated spacer affects the electronic structures of these species. Calculations performed on **Mo2** also allow comparisons to be drawn with the related heterometallic system (**PtMoPt**), to assess how the presence of the {Pt} units affects the properties of the frontier molecular orbitals.

All electronic structure studies were preceded by geometry optimisation calculations, using the experimentally determined atomic coordinates (from single crystal diffraction experiments) as a starting point. All calculations reported within this section utilised the B3LYP functional[174-175] with the 6-31G* basis set[176] for all non metal atoms and the SDD energy-consistent pseudopotential basis set for Mo and Pt.[20] Where relevant the calculations were simplified by replacing PEt_3 ligands with PH_3 and replacing both T^iPB and DPTF ligands with formates ({O_2CH}). The simplified molecules will be referred to using '*' as a suffix. Although identical conditions were used in an attempt to model **MoPtMo**, attempts to optimise the geometry did not converge and as such a reliable electronic structure is yet to be calculated.

The geometry optimisation of the structures of **Mo2***and **Mo3*** resulted in retention of the coplanar conformation of the ethynyl-carboxylate ligand systems that was observed in the experimentally determined structures. This provides optimum π-orbital overlap along the length of the two complexes. Using these optimised geometries, the frontier orbitals of both molecules were calculated and those of **Mo2*** are presented in **Figure 3.20**. The orbitals calculated for **Mo3*** are identical in structure to those shown for **Mo2*** and have previously been reported by Chisholm *et al*. Our results are entirely consistent with those presented within the literature.[108] **Figure 3.20** also displays calculated molecular orbital diagrams for **Mo2*** and **Mo3***, allowing the energies of the frontier orbitals to be compared.

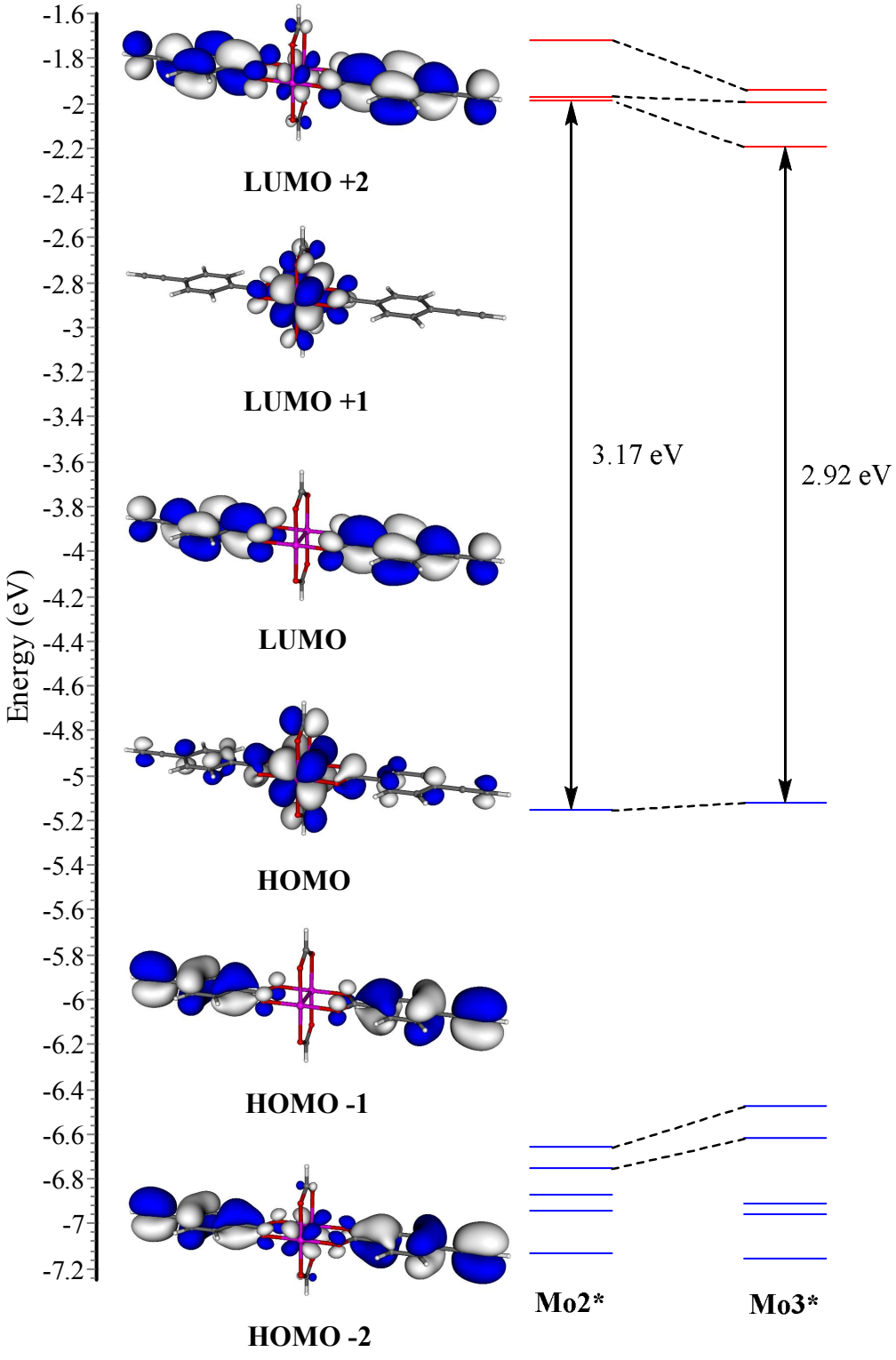

Figure 3.20: Calculated frontier molecular orbitals of **Mo2*** and molecular orbital diagram showing the relative energies of the frontier molecular orbitals of **Mo2*** and **Mo3***.

The HOMO for both **Mo2*** and **Mo3*** is the $Mo_2\delta$ orbital, which exhibits significant mixing with the filled ligand π-orbitals. The HOMO-1 and HOMO-2 are the in-phase and out-of-phase ethynyl-carboxylate π*-orbitals respectively, which are separated in energy on account of significant mixing with the $Mo_2\delta$ orbital in the latter. Below these in energy lie the $Mo_2\pi$- and $Mo_2\sigma$-orbitals. The LUMO for both complexes is the in-phase combination of the ethynyl-carboxylate π*-orbitals which lie just lower in energy than the $Mo_2\delta$* orbital (LUMO-1). The out-of-phase ethynyl-carboxylate π*-orbitals, LUMO-2, are raised in energy due to mixing with the filled $Mo_2\delta$ orbitals.

The molecular orbital-diagrams presented in **Figure 3.20** show that the ethynyl-carboxylate π-orbitals of **Mo3*** are higher in energy than those of **Mo2***. Conversely the π*-orbitals of **Mo3*** are energetically stabilised. This results in a smaller $Mo_2\delta \rightarrow$ligand-π* (HOMO-LUMO) energy gap for **Mo3*** and is consistent with the significant red-shift that was observed for the MLCT absorption band of **Mo3** relative to that of **Mo2**. Whilst the theoretical calculations support the experimental electronic absorption data that was recorded for **Mo2** and **Mo3**, the calculated energies of the $Mo_2\delta$ orbitals do not agree with the electrochemical analyses, in which the $Mo_2\delta$ of **Mo3** was shown to be the most stable. It is possible that this irregularity arises due to the simplifications required to run the calculation, which was performed on static molecules within the gas-state. These simplifications do not take into account the dynamic nature of molecules in solution and both intermolecular and solvent interactions are not taken in consideration.

The geometry optimisation calculations for both **PtMo1*** and **PtMoPt*** resulted in retention of the coplanar geometries of the ethynyl-carboxylate ligand systems. However, the significant torsion angles between the Pt square planes and the phenylene rings remained following the optimisation. This provides further evidence that there is no significant energetic bias towards coplanarity of the two moieties. The frontier molecular orbitals calculated for **PtMo1** are displayed in **Figure 3.21**.

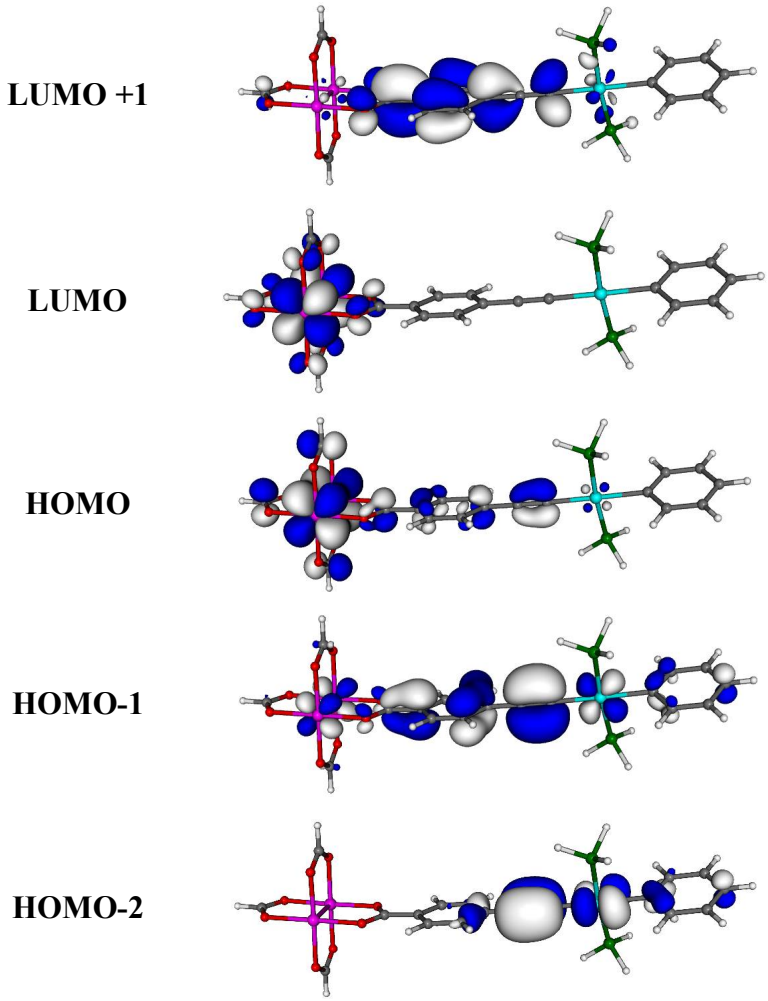

Figure 3.21: Calculated frontier molecular orbitals for **PtMo1***.

The HOMO of **PtMo1*** is dominated by the $Mo_2\delta$ orbital with a smaller contribution from the ethynyl-carboxylate π-orbitals and those of the formate supporting ligands. The HOMO-1 is the filled π-orbital orbital of the bridging ligand and exhibits electronic delocalisation along the length of the molecule with significant contributions from the Pt (15%) and {Mo_2} (12%) orbitals. This suggests a degree of electronic communication between the two metal termini. The HOMO-2 is largely localised around the {Pt-CC} fragment, involving the acetylenic π-orbitals perpendicular to those of the phenylene spacer. The orbital is similar in structure to the HOMO-1 that was calculated for **Pt2a** (discussed in **Chapter 2**). The lowest lying unoccupied orbital of **PtMo1** is the $Mo_2\delta^*$ orbital and the LUMO+1 is almost entirely localised on the bridge π*-orbitals with negligible mixing with the orbitals

of the Pt or {Mo_2}. The LUMO+2 and LUMO+3 (not shown) are both {Pt}-localised orbitals. The compositions of the above frontier orbitals, regarding the contributions from the Pt, {Mo_2} and bridging ligand orbitals, are summarised in **Table 3.7**.

Table 3.7: Calculated {Pt}, {Mo_2} and {bridging ligand} contributions to the frontier molecular orbitals of **PtMo1***. (%)

	2{Pt}	**{Mo_2}**	**2{4-ethynylbenzoate}**
LUMO+1	5	3	75
LUMO	0	86	4
HOMO	1	70	15
HOMO-1	15	12	63
HOMO-2	36	1	55

TD-DFT calculations performed on **PtMo1*** support the assignment of the low energy MLCT, observed within the electronic absorption spectrum of **PtMo1**, arising from HOMO→LUMO electronic transitions. The calculations also suggest that the higher energy absorption band of **PtMo1**, observed at *ca.* 300 nm, is contributed to by the ethynyl-carboxylate $\pi\rightarrow\pi^*$ transition (HOMO-1→LUMO+1). This could not be assigned experimentally due to overlap with the intense N→$Mo_2\delta$ absorption band.

The calculated frontier orbitals for **PtMoPt*** are shown in **Figure 3.22**.

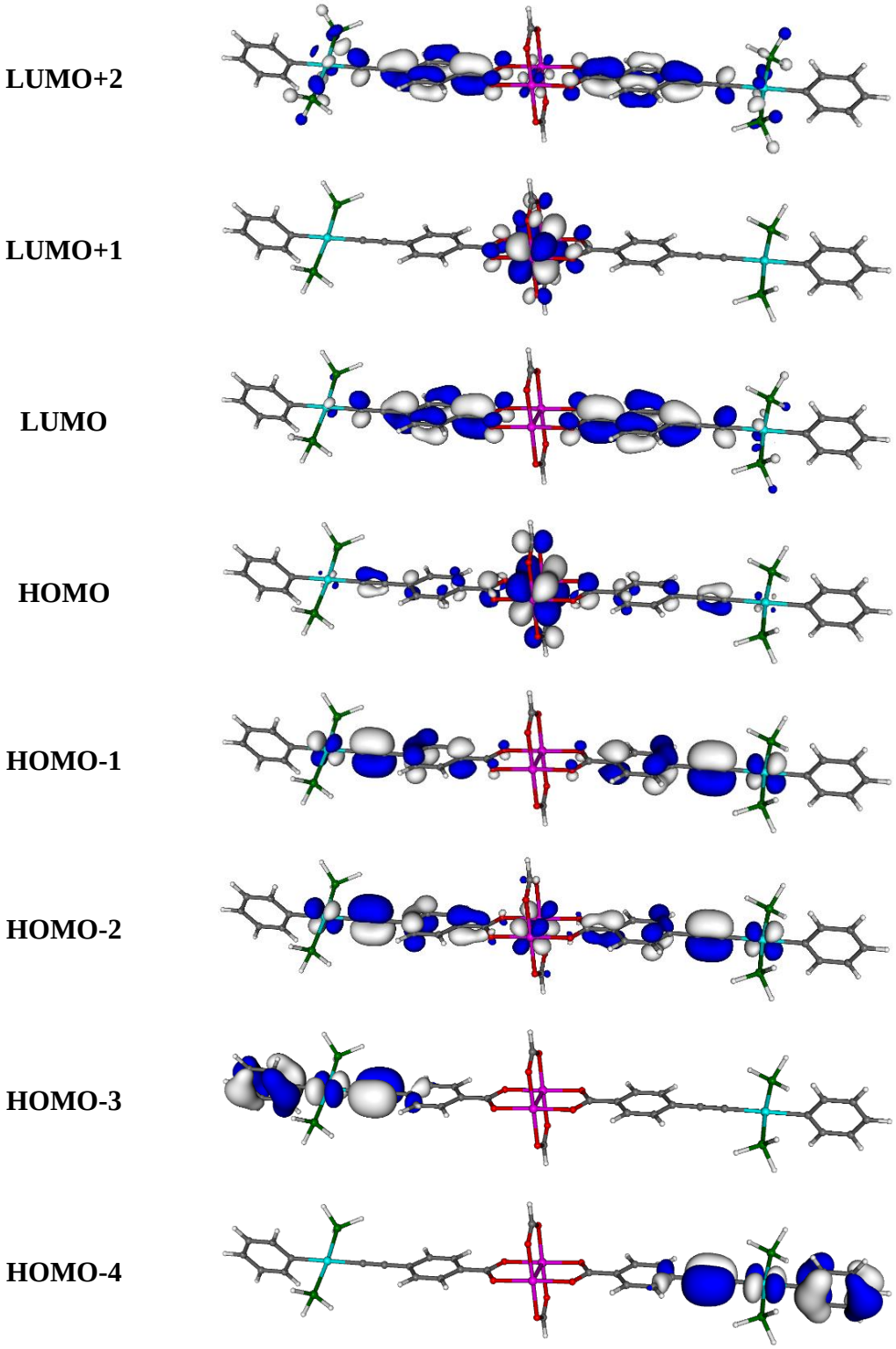

Figure 3.22: Frontier molecular orbitals calculated for **PtMoPt***.

Consistent with the previously described complexes, the HOMO of **PtMoPt*** is the $Mo_2\delta$ orbital, which mixes with the ethynyl-ester π-orbitals, and below this in energy lie the in-phase (HOMO-1) and out-of-phase (HOMO-2) combinations of the filled

Pt ethynyl-carboxylate π-orbitals. The latter exhibits mixing with both the Mo_2δ (13%) and Pt (20%) orbitals, facilitating electronic delocalisation throughout the molecule within the groundstate. The HOMO-3 and HOMO-4 are both predominantly localised on the {Ph-Pt-C≡C} fragments, involving π-orbitals perpendicular to those of the phenylene rings, analogous to the HOMO-2 of **PtMo1***. The LUMO of **PtMoPt*** is composed of the in-phase combination of the ethynyl-carboxylate π*-orbital with the Mo_2δ* orbital (LUMO+1) observed at slightly higher energy. The out-of-phase combination of the ligand-π* orbitals (LUMO+2) is raised in energy due to a small amount of mixing with the filled Mo_2δ and Pt *d*-orbitals.

The data presented in **Table 3.8** summarises the compositions of the frontier orbitals of **PtMoPt*** with respect to the Pt, {Mo_2} and ethynyl-carboxylate subunits, illustrating the degree of metal contributions to these orbitals.

Table 3.8: Calculated {Pt}, {Mo_2} and {bridging ligand} contributions to the frontier molecular orbitals of **PtMoPt***.(%)

	2{Pt}	**{Mo_2}**	**2{4-ethynylbenzoate}**
LUMO+2	11	3	46
LUMO+1	0	86	8
LUMO	8	0	65
HOMO	2	68	22
HOMO-1	21	0	75
HOMO-2	20	13	63

Analogous to the studies for **PtMo1***, TD-DFT calculations performed on **PtMoPt*** support the assignment of the low energy electronic absorption band of **PtMoPt** as a Mo_2δ→ethynyl-ester π* MLCT process whilst the higher energy absorption band is predicted to be predominantly ethynyl-carboxylate π-π* in character.

In order to assess how the {Pt} units within **PtMoPt** perturb the electronic structure of the molecule, relative to the parent complex **Mo2***, the relative energies of the of the frontier orbitals of both systems are compared within **Figure 3.23**.

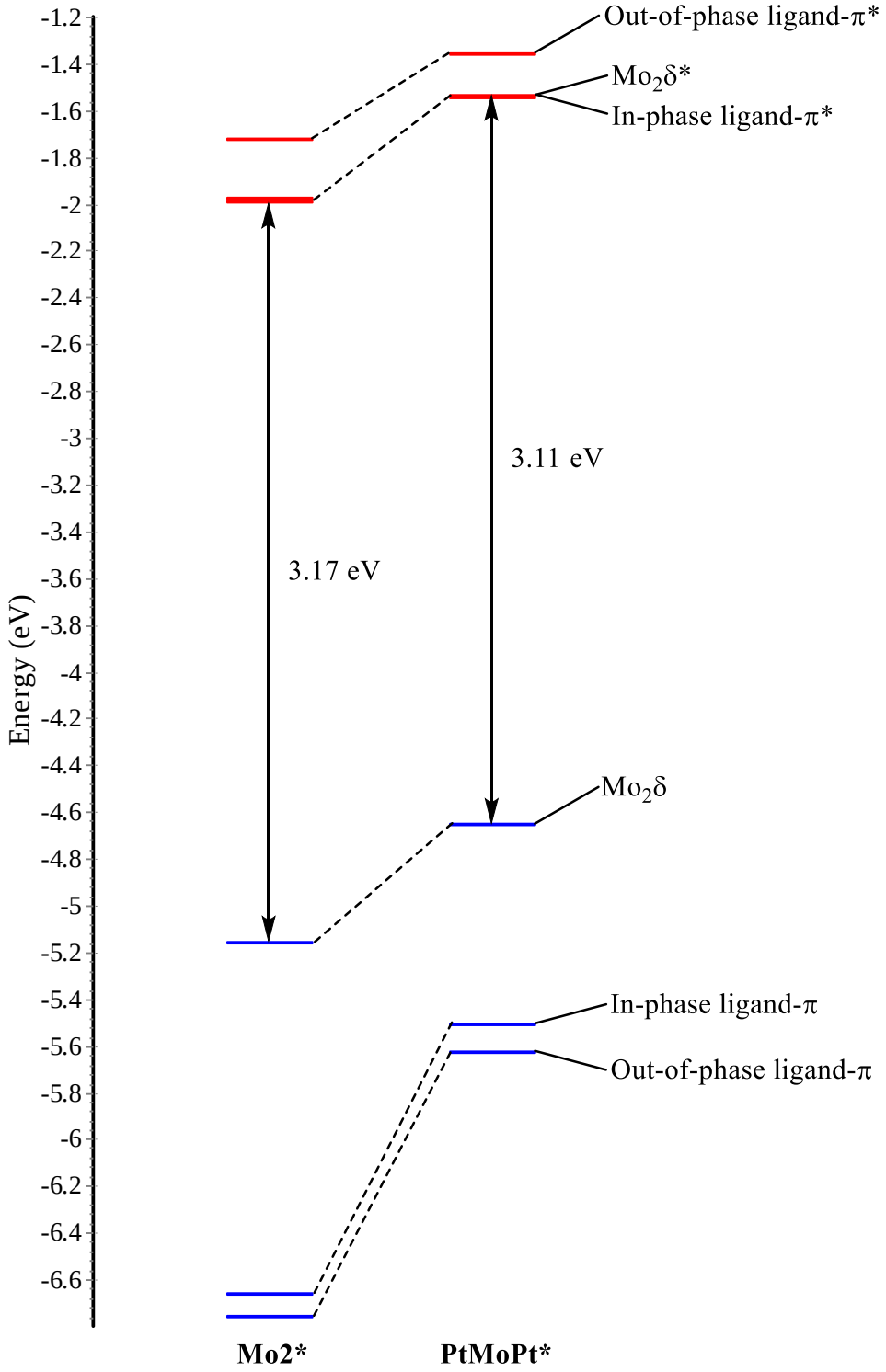

Figure 3.23: Molecular orbital diagram comparing the frontier orbital energies of **Mo2*** (left) and **PtMoPt*** (right).

The molecular orbital diagrams show that upon replacing the acetylinic protons of **Mo2*** with {Pt} units, the energy of the ethynyl-carboxylate π- and π*-orbitals are significantly increased. This is likely to be due to the mixing with the filled Pt *d*-orbitals, which is observed in the frontier orbital plots within **Figure 3.22**. Both the Mo_2δ and Mo_2δ* orbitals of **PtMoPt*** are also higher in energy than the analogous orbitals of **Mo2***. This is consistent with the experimental electrochemical measurements for **Mo2** and **PtMoPt**, in which $E_{1/2}$ was significantly more negative for the heterometallic complex. The HOMO-LUMO energy gaps of the two complexes are calculated to be very similar, however, the electronic absorption data for **Mo2** and **PtMoPt** exhibited a red-shift in the MLCT of the latter, suggesting a smaller HOMO-LUMO separation in this complex. This small inconsistency is likely a result of the simplifications effected by the gas-phase calculations which do not take into account potentially important intermolecular and solvent interactions.

3.3 – Conclusions

In summary, we have demonstrated the syntheses of a series of novel mixed-metal complexes through the assembly of purpose designed Pt and {Mo_2} building blocks. Utilising different combinations of these precursors has allowed us to systematically synthesise three different heterometallic motifs, which represent model subunits within a hypothetical polymeric system.

The molecular structures of the heterometallic complexes have been unambiguously determined using single crystal X-ray diffraction studies and each systems exhibits the expected planar arrangement of the ethynyl-ester bridging ligand, providing efficient π-orbital alignment between the Mo_2δ orbitals and the π-network of the ligands. However, there appears to be no energetic bias that influences the orientation of the Pt square plane in each complex. What is observed is the result of a combination of a range of solid state intermolecular interactions, however, the cylindrical nature of the acetylide ligands means that conjugation is possible along the principle axis of the molecule, This is supported by DFT studies, performed on **PtMo1** and **PtMoPt**, which have shown that electron density is delocalised throughout the entire molecules within the HOMO-1 and HOMO-2 respectively, including significant orbital contributions from both Pt and {Mo_2} metal centres.

The electronic absorption spectra recorded for each of the mixed-metal systems exhibit low energy absorption bands attributed to $Mo_2\delta \rightarrow$bridge-π^* electronic transitions. These were observed at similar energy for both **PtMo1** and **MoPtMo** but appeared at significantly lower energy for **PtMoPt** on account of the *trans*-disubstituted {Mo_2} core. A comparison between the spectra of **Mo2** and **PtMoPt** show that the MLCT band is blue-shifted in the presence of the {Pt} fragments, relating to a greater separation of the HOMO-LUMO energy gap. DFT studies reveal that this is largely due to significant destabilising interactions within the LUMOs of the heterometallic complexes, involving mixing between the filled Pt($d\pi$) orbitals and the π^*-orbitals of the bridging ligands. Therefore, by careful choice of metal and ligand fragments it is possible to tune the energy gap and thereby manipulate the optical properties of the materials.

Electrochemical analyses provide no evidence of electronic coupling between the {Mo_2} termini within **MoPtMo**, which is likely to be in part due to the large distance between these fragments in the molecular structure (23.3 Å). However, the analyses do show that the Pt units can be used to tune the energy of the $Mo_2\delta$ orbitals and, therefore, the energy of the overall molecular system, consistent with the spectroscopic observations. Most notably, comparison between the $E_{1/2}$ values recorded for **Mo2** and **PtMoPt** show that $Mo_2\delta$ orbitals are significantly higher in energy in the presence of the {Pt} fragments, due to a reduction in the electron-withdrawing nature of the carboxylate ligand system.

The work reported here demonstrates the scope for the tuning of the optical/electronic properties of mixed-metal acetylide complexes by altering both the nature of the linker group and of the metal fragment involved. There is great potential for extending these studies to a wide range of organometallic oligomers and polymers with potential applications in new opto-electronic materials.

Chapter 4

Ru-Amidinate and Bis-Amidinate Complexes

Chapter 4 – Ru-Amidinate and -*Bis*-amidinate Complexes

4.1 – Introduction

4.1.1 – Conjugated Bridging Ligands

To date, a wide range of ligand systems have been used to bridge, and in many cases electronically couple, pairs of quadruply bonded $\{M_2\}$ centres (M = Mo or W), but the field has been largely dominated by the study of π-conjugated dicarboxylate ligands and their derivatives of the type shown in **Figure 4.1**.

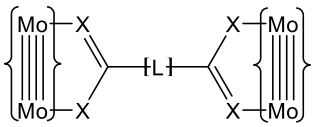

L = Spacer unit
X = O, S or N

Figure 4.1: Generic form of a bridged $\{Mo_2\}$ dimer

Through these studies it was discovered that the degree of electronic coupling between $\{M_2\}$ units could be tuned by either changing the identity of the conjugated spacer (L) or by changing the coupling $\{CX_2\}$ moiety. A series of related ligand systems containing different $\{CX_2\}$ termini are presented in **Figure 4.2**.

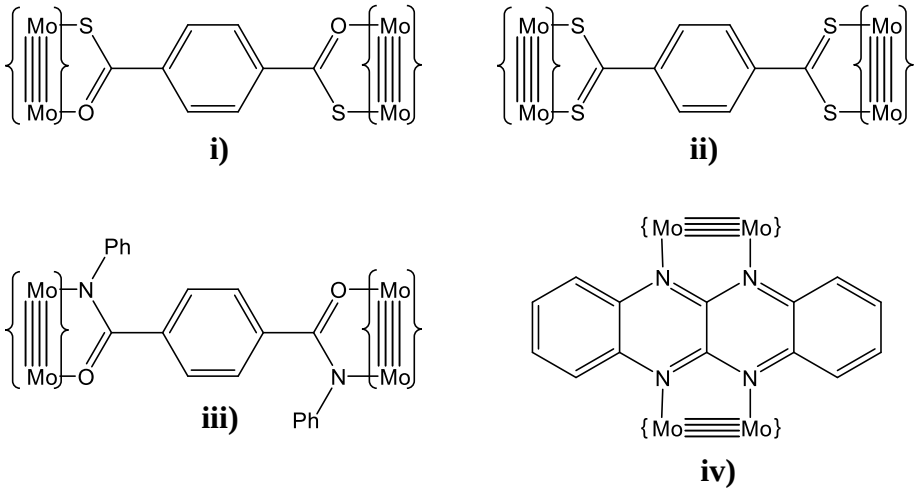

Figure 4.2: $\{Mo_2\}_2$ complexes featuring O, S and N substituted ligand systems.

The groups of Chisholm and Liu have shown that replacement of the carboxylate units within a terephthalate bridging ligand with isoelectronic {CSO} (**Figure 4.2-i**)[124] or {CS_2} (**Figure 4.2-ii**) [125] units results in greater electronic coupling between the {Mo_2} termini, which improves with increasing sulphur content. In a similar study Cotton *et al.* showed that a N,N'-diphenylterephthaloyldiamide bridged complex, containing {CN(Ph)O} termini (**Figure 4.2-iii**), facilitated greater electronic communication than the analogous terephthalate {CO_2} bridged system.[116,127]

At present there is only one example of a complex in which {Mo_2} units are bridged by a {CN_2} type ligand and this is the fluoflavinate system shown in **Figure 4.2-iv**.[205] The complex facilitates excellent electronic communication, aided by the locked planarity and extended conjugation of the ligand. However, derivatisation of this ligand system is not easy and, as such, unfused *bis*-amidine ligands potentially have more scope for investigation (**Figure 4.3**).

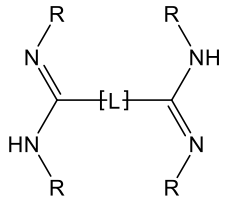

[L] = Conjugated Spacer
R = Alkyl or Aryl group

Figure 4.3: Structural framework for a linear *bis*-amidine ligand.

Aryl-substituted formamidinate ligands have long been used as supporting ligands for {Mo_2} quadruply bonded complexes and it has been shown that the electronic properties of the {Mo_2} core can be tuned by altering the substituents on the aryl rings.[123] More recently, Chisholm *et al*. have extended the field by synthesising a range of {Mo_2} and {W_2} ethynyl-amidinate complexes, such as the example shown in **Figure 4.4-i**,[184,206] which exhibit tuneable absorption within the visible region of the spectrum. The inclusion of the ethynyl units minimise the steric repulsion between the amidinate backbone and the N-bound substituents. This is an important consideration because, as the steric interactions between these moieties increase, the directionality of the nitrogen lone pairs is distorted making the ligand less conducive

towards a bridging coordination mode (**Figure 4.4-ii**).[184] The ethynyl units therefore provide greater flexibility of the amidinate backbone, which may facilitate multiple coordination modes. A second advantage of the ethynyl linker is to maintain conjugation between the amidinate backbone and the aryl terminus; an aspect that has been supported by theoretical studies.[184,206]

i)

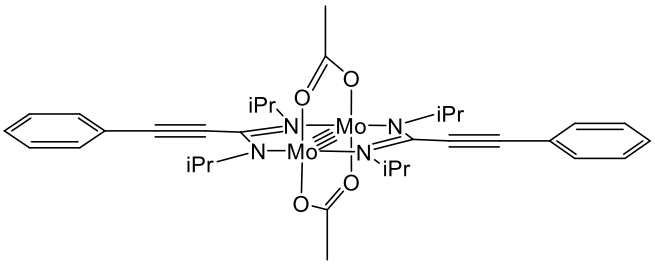

ii)

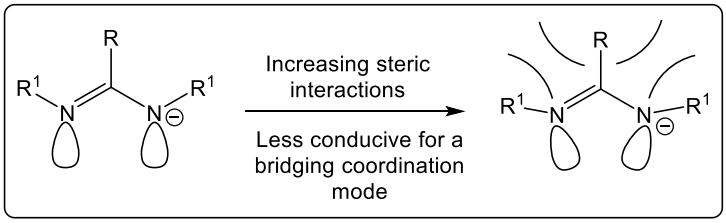

Figure 4.4: i) An example of a $\{Mo_2\}$ complex bearing ethynyl-amidinate ligands reported by Chisholm *et al*. **ii)** Illustration of the impact of bulky substituents on the directionality of the nitrogen lone pairs.[184]

Several *bis*-amidine ligand systems have previously been reported in the literature and some examples of these are presented in **Figure 4.5**.[207-212]

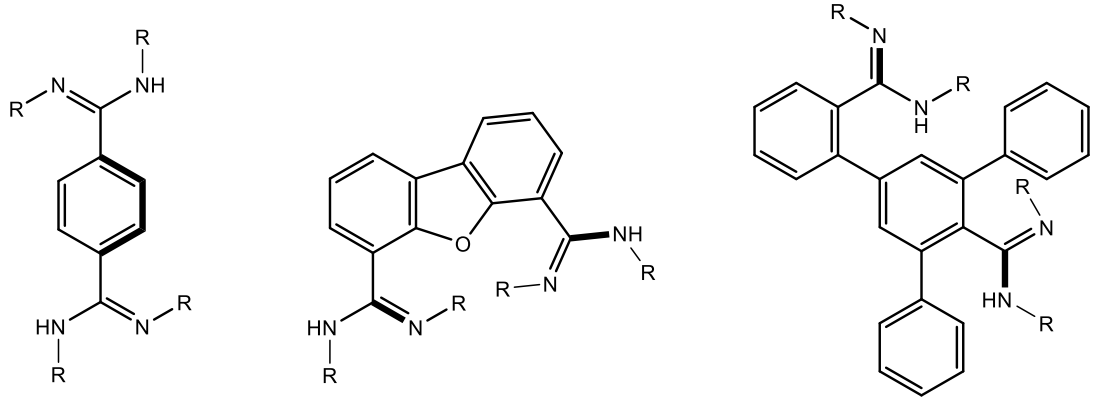

Figure 4.5: A series of *bis*-amidine ligands present in the literature.[207,209-210]

Analyses of the molecular structures of these *bis*-amidines, and those of their respective metal-amidinate complexes, reveal large torsion angles of the $\{CN_2\}$ units relative to the conjugated backbone of the ligand, due to steric repulsion between these parts of the molecules. This prevents effective π-orbital overlap throughout the systems, making them inappropriate ligand systems to facilitate electronic communication between metal centres.

Within this work we propose the development of novel ethynyl-functionalised *bis*-amidine ligand systems (of the form shown in **Figure 4.6**). The ethynyl units will help to minimise the undesirable intraligand steric interactions, which will potentially provide more effective π-conjugation than has been possible in previously reported *bis*-amidine systems. The tuning of the resultant optical and electronic properties can then be envisaged by varying both the conjugated spacer (L) and the N-bound substituents (R).

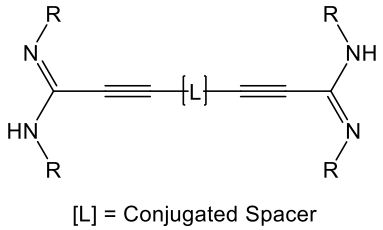

Figure 4.6: A generic ethynyl functionalised *bis*-amidine ligand.

4.2 – Results and Discussion

4.2.1 – Syntheses of Conjugated Amidine and *Bis*-Amidine Systems

Studies reported within the literature describe the syntheses of a series of lithium-ethynyl-amidinate complexes *via* the insertion of lithium acetylides into carbodiimides.[184,213] Using an analogous method, followed by an acid work up, we have shown that neutral ethynyl-amidine systems can be isolated (**Scheme 4.1**), which represent simple models for the targeted *bis*-amidine systems. The scope of the reaction has been demonstrated by incorporating both phenyl and anthracenyl groups into the backbone as well as utilising both ^{i}Pr and Cy substituted

carbodiimides. Prior to this study both **A1a** and **A1b** have been reported by Wang *et al*. and were prepared using an alternative lanthanide-catalysed method.[214]

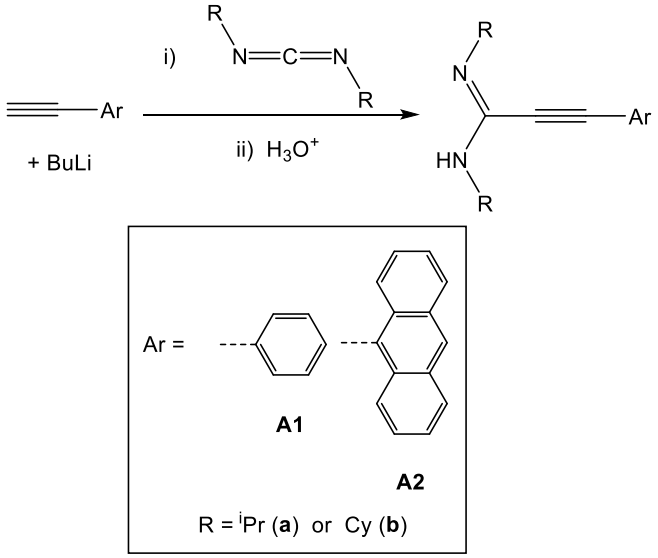

Scheme 4.1: Synthesis of ethynyl-amidines systems.

To access the desired *bis*-amidine systems an analogous procedure was followed using a series of diethynyl-arene precursors and two equivalents of both BuLi and the appropriate carbodiimide (**Scheme 4.2**).

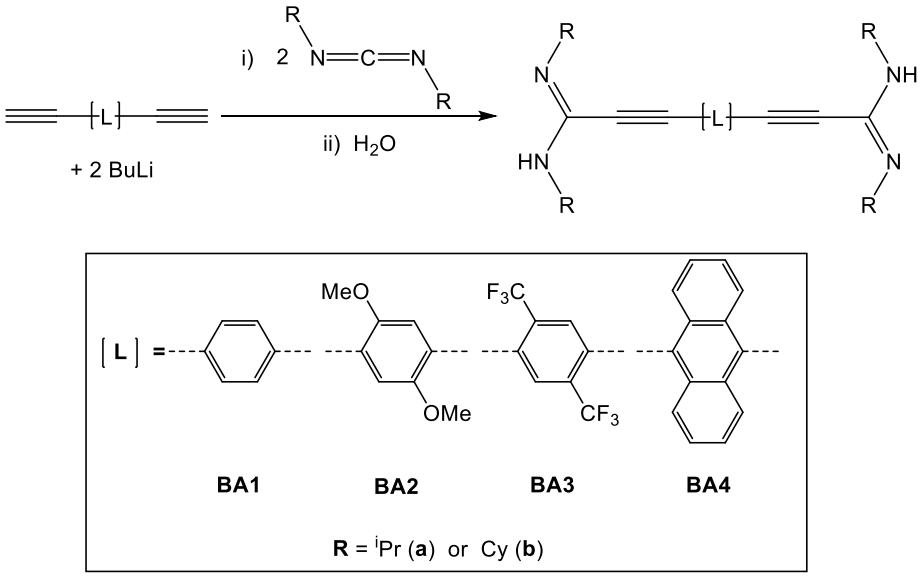

Scheme 4.2: Synthesis of ethynyl-*bis*-amidine systems.

Using this method, four different conjugated spacers have been incorporated into the ligand systems, providing variation in the electron-donating/-withdrawing character of the ligands as well as the degree of conjugation present. Unfortunately the Cy-derivatives of **Ba2a** and **Ba3a** could not be obtained due to solubility issues.

The ^{1}H NMR spectra of the amidines and *bis*-amidines are consistent with the structures depicted in **Schemes 4.1** and **4.2**. Each system exhibits resonances corresponding to a single ^{i}Pr or Cy environment suggesting that interconversion between isomers, which has been observed in related systems in the literature,[207,210,215-217] occurs faster than the NMR time-scale. However, evidence for a degree of solution-state fluxionality can be observed in the corresponding ^{13}C{^{1}H} NMR spectra in which the resonances corresponding to the N-bound ^{i}Pr or Cy carbon atoms are significantly broadened.

4.2.2 – Syntheses of Ru-Amidinate and -*bis*-Amidinate Complexes

Prior to investigating the compatibility of the novel amidine ligand systems towards the synthesis of complicated {Mo_2} containing complexes, a series of Ru-containing complexes were initially targeted as simpler model systems, on account of their relative ease of synthesis and the air-stability of the products.

Significantly, a number of Ru-amidinate and -guanidinate complexes have been reported within the literature, showing that Ru is able to support chelating ligand systems similar to our own amidine-functionalised systems.[218-232] The literature complexes include a series of phenyl-substituted amidinate species, such as the example shown in **Figure 4.7-i**. Analyses of the respective molecular structures reveal {phenyl}-{NCN} torsion angles close to 90^{o}, highlighting the steric interaction between these two sections of the ligand and the requirement to relieve these interactions to promote more extended electronic delocalisation. During the course of this work, Seidel *et al* have also reported two ethynyl functionalised Ru-amidinate complexes (**Figure 4.7-ii**),[213] containing ligands very similar to our own amidine species.

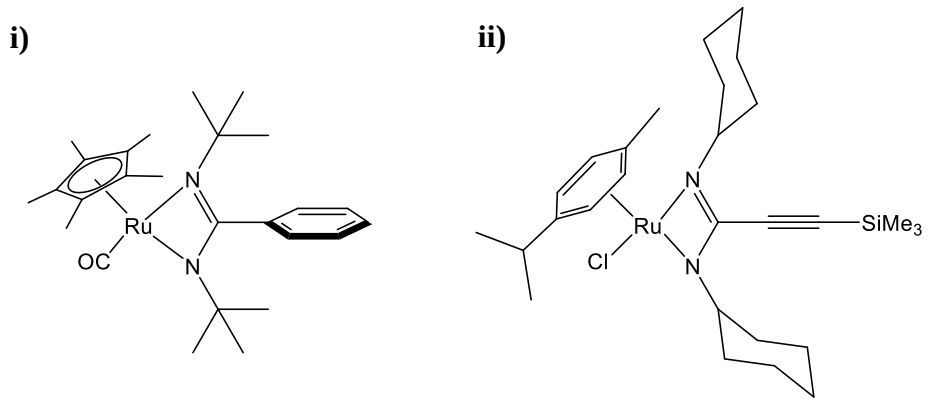

Figure 4.7: i) An example of a phenyl-substituted amidinate coordinated to a Ru centre. **ii)** A Ru-arene complex supported by an ethynyl-amidinate ligand.[213]

The syntheses for the majority of the Ru-amidinate complexes reported within the literature involve salt metathesis reactions between the lithium salts of the appropriate ligand and a {Ru-Cl}-containing precursor.[218,224-226] For our own studies [(*p*-cymene)$RuCl_2$]$_2$ was utilised as the Ru precursor, however, reactions performed with the lithiated amidines resulted in the production of a significant amount of black material and no products could be isolated from the reactions. Instead, it was found that treatment of the amidine ligands with a stoichiometric amount of NaOMe prior to the addition of [(*p*-cymene)$RuCl_2$]$_2$ was a much more successful approach. The syntheses of the Ru-*bis*-amidinate complexes are outlined in **Scheme 4.3** and an identical approach was used to access the ethynyl-benzene (**Ru1a**/**Ru1b**) and ethynyl-anthracene (**Ru2a**/**Ru2b**) Ru-monoamidinate complexes, using a single equivalent of the Ru precursor.

Upon combining the Na-amidinates with the [(*p*-cymene)$RuCl_2$]$_2$ in THF, dark red solutions were formed, which were stirred for 12 h to ensure that the reaction had gone to completion. After this time the solvent was removed *in vacuo* and the product was extracted into toluene and filtered to remove any salt. Each product was then purified by crystallisation, for which individual details are reported within the experimental section of this work. All complexes yielded red/orange crystals although those of the anthracene-containing systems were significantly darker in colour and the needle crystals obtained for **Ru6b** were almost black.

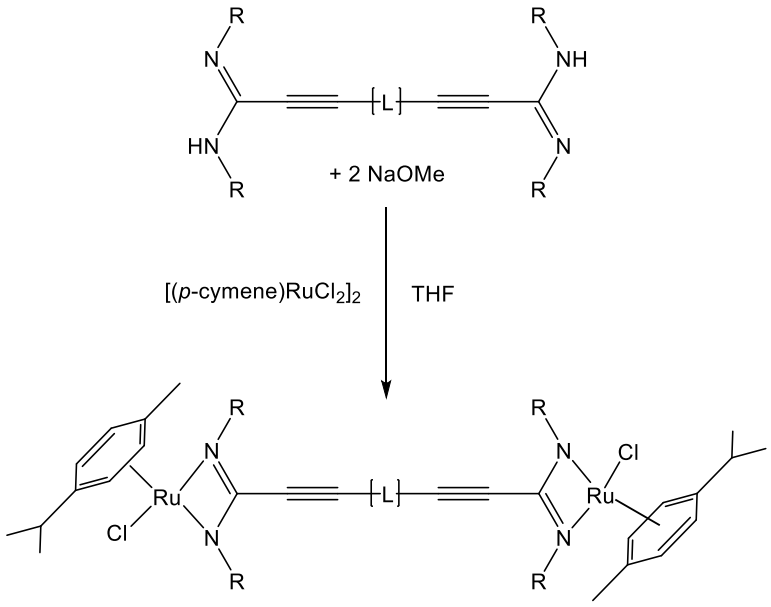

	[L]			
	-C_6H_4-	-$C_6H_2(OMe)_2$-	-$C_6H_2(CF_3)_2$-	-$C_{14}H_8$-
R = ^{i}Pr	**Ru3a**	**Ru4a**	**Ru5a**	**Ru6a**
R = Cy	**Ru3b**	**n/a**	**n/a**	**Ru6b**

Scheme 4.3: Synthesis of Ru-*bis*-amidinate complexes *via* a salt metathesis reaction.

The ^{1}H NMR spectra of each of the complexes were very similar exhibiting characteristic resonances corresponding to the *p*-cymene and amidinate ligand ligand systems. The ^{i}Pr-C*H*$_3$ protons of the amidinate ligands exhibit two doublet resonances for each of the relevant complexes. This presumably reflects differing magnetic environments above and below the plane of the amidinate ligand. The ^{19}F NMR resonance of **Ru5a** is observed at δ = -63 ppm, which is unshifted from that of the free ligand (**BA3a**). ^{13}C NMR spectra were also recorded for each complex and were consistent with the proposed structures.

4.2.3 – Attempted Syntheses of {Mo$_2$}-*bis*-Amidinate Complexes

Following the successful coordination of the novel *bis*-amidine ligands to monometallic Ru centres, attention was then turned to their potential application as bridging ligands within {Mo$_2$} complexes. Due to the lower acidity of amidine

ligands *vs*. carboxylic acids, direct ligand exchange reactions using $Mo_2(O_2CCH_3)_4$ and $Mo_2(O_2C^tBu)_4$ are not possible. In order to promote reactivity between *bis*-amidines and the {Mo_2} precursors, the ligands were first lithiated using BuLi. This results in a more reactive species and provides a driving force for the reaction through the formation of Li-acetate or Li-pivalate. The proposed coordination reaction is shown in **Scheme 4.4**.

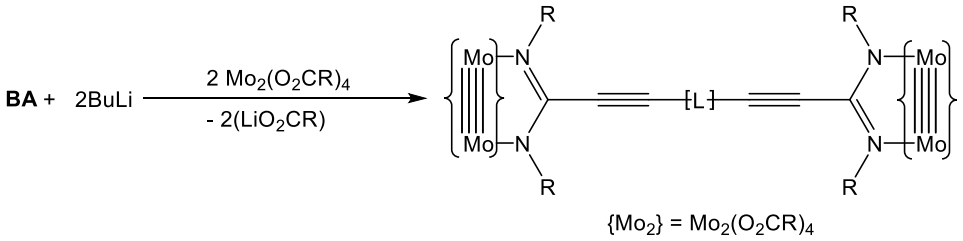

Scheme 4.4: Proposed synthesis of an amidinate-bridged {Mo_2} dimer using salt metathesis methodology.

To test the proposed reaction the phenylene-containing ligand (**BA1a**) was utilised on account of its relative ease of synthesis and isolation. Following double lithiation of the *bis*-amidine in THF, a white precipitate formed and, after stirring for 30 mins to ensure that the reaction was complete, the slurry was combined with a solution of the {Mo_2} carboxylate dimer. In the reactions involving both $Mo_2(O_2CCH_3)_4$ and $Mo_2(O_2C^tBu)_4$, dark purple solutions were formed immediately upon addition of the Li-ligand. The dramatic colour changes suggest the formation of products that exhibit strong and relatively low energy MLCT processes. After stirring the solutions for 2 h the solvent was removed *in vacuo* and the residues extracted into toluene and filtered to remove any salts. Upon removing the toluene dark purple powders were obtained, however, analysis of the respective ^{1}H NMR spectra revealed a large number of unidentifiable resonances which suggests that the reaction yields a number of different substitution products.

In order to try and impose some control over the substitution around the {Mo_2} core, the *tris*-formamidinate precursor, **Mo1** (introduced in **Chapter 3**), was utilised on account of its single labile acetate ligand.

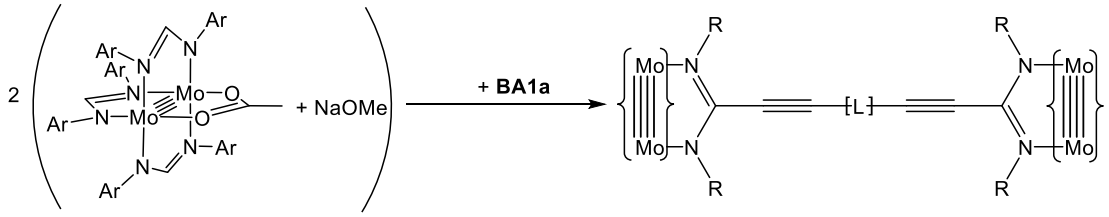

Scheme 4.5: The attempted reaction between **BA1a** and **Mo1** following activation of the precursor with NaOMe. $\{Mo_2\} = \{Mo_2DPTF_3\}$.

The proposed coordination reaction is shown in **Scheme 4.5**, using NaOMe to first remove the acetate ligand of **Mo1** to form a reactive $\{Mo_2\}$ methoxide species *in situ*.[194] However, the addition of the *bis*-amidine to a solution of the activated $\{Mo_2\}$ precursor resulted in no colour change and an analysis of the ^{1}H NMR spectrum of the reaction mixture showed that no reaction had occurred. Although this synthetic approach is established for the coordination of carboxylate and amidate ligand systems,[97,127] the observations made in this study suggest that the additional steric demands of **BA1a**, due to the two N-bound substituents, precludes reaction with the $\{Mo_2\}$ reagent. Work is continuing to develop a more refined method by which the *bis*-amidine species may be utilised as bridging ligands for $\{Mo_2\}$ dimers.

4.2.4 – Structural Analyses

During the course of this study, crystals suitable for single crystal X-ray diffraction analyses were grown for the novel *bis*-amidine systems **BA1a** and **BA1b**, which allow the structural characteristics of the free-ligands to be compared to those within the organometallic complexes.

Both **BA1a** and **BA1b** crystallise independently in the orthorhombic space group *Pbca* with half a molecule in the asymmetric unit. The second half-molecule is generated by an inversion centre located at the centre of the phenylene ring. The structures of the two compounds are very similar and that of **Ba1a** is presented in **Figure 4.8-i** as an example. The packing motifs exhibited by the two systems are also extremely similar, in which hydrogen bond arrays form 'zig-zag' layers that run along the *a*- and *b*-axes of each crystal lattice. Packing diagrams for **Ba1a**, which illustrating these interactions, are presented in **Figure 4.8-ii** and **-iii**. To aid the

analyses of the hydrogen bonding interactions, the amidine N-*H* protons were located with the structural solutions and allowed to refine without constraint. Data regarding these interactions for both *bis*-amidines, in addition to selected bond lengths and angles, are presented in **Table 4.1**.

i)

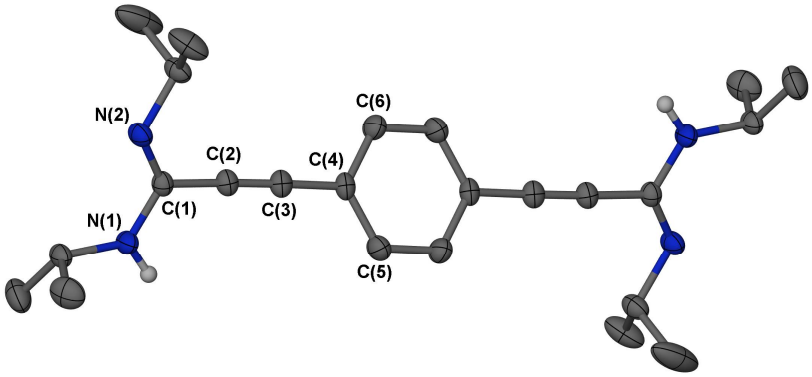

ii)

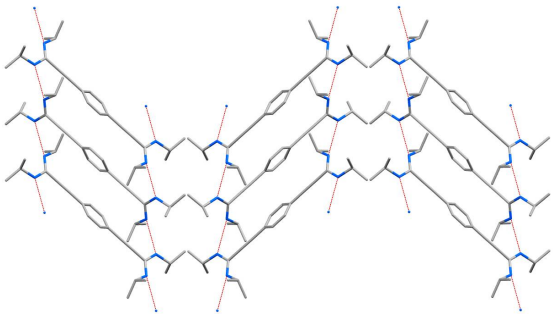

iii)

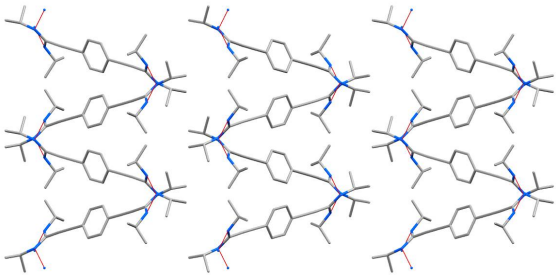

Figure 4.8: i) Molecular structure of **BA1a** shown with 50 % thermal ellipsoids with all but the amidinate hydrogen atoms removed for clarity. **ii)** A section of the crystal lattice of **BA1a** viewed down the *a*-axis showing the H-bonding interactions. **iii)** A section of the crystal lattice of **BA1a** viewed down the *b*-axis.

BA1a and **BA1b** each crystallise with E-syn conformations of both amidine termini, which is consistent with the geometry observed for the similar 1,4-phenylene-*bis*-amidines reported by Coles *et al.*.[208] The bond lengths and angles observed within the two systems are highly comparable. Both exhibit one long and one short C-N bond length, reflecting localised single and double bonds and the C≡C bond length is

typical for an alkyne moiety. The N-C-N bond angles reflect the sp^2-hybridisation within the amidine functionality and the similarity of these angles for the two complexes reveals negligible influence from the size of the N-bound substituents. The H-bonds observed within the crystal lattice of **BA1b** are significantly longer and weaker than those observed for **BA1a**, suggesting that the proximity of the H-bond donor and acceptor are limited by the greater steric demands of the Cy substituent.

Table 4.1: Selected bond lengths (Å) and angles (°) in the molecular structures of **BA1a** and **BA1b**.

	BA1a	**BA1b**
C(1)-N(1)	1.362 (1)	1.370(2)
C(1)-N(2)	1.289(1)	1.280(2)
C≡C	1.199(2)	1.192(2)
N-C-N	123.35(9)	122.2(1)
{CN_2}∠{C_6H_4}[a]	*ca.* 32.5	*ca.* 14.8
H-Bond D···A[b]	3.292(1)	3.642(2)
H-Bond H···A[b]	2.43(2)	2.81(0.02)
H-Bond D-H···A[b]	173(1)	176(2)

[a] The angle between the planes defined through the {CN_2} and phenylene moieties, [b] symmetry operation relating H-bonding components for **BA1a** and **BA1b** are 3/2-x, y +1/2, z and –x-1/2, y-1/2, z respectively.

The torsion angle of the phenylene ring within **BA1a**, relative to {CN_2} moieties, is approximately twice that observed within the structure of **Ba1b**, however, these angles are significantly smaller than those reported for the 1,4-phenylene-*bis*-amidinates by Coles *et al*. (62.4-80.3°).[208] This shows that the ethynyl units effectively reduce the steric interactions between {CN_2} and {C_6H_4}, which will potentially result in greater π-conjugation throughout the molecules than in the previously reported ligand systems. A similar observation was made by Wang *et al*., who have previously reported the molecular structure of **A1a**, showing that the phenylene and {NCN} moieties are near coplanar in the solid-state (*ca.* 6.5°).[214] The

mono-amidine was also shown to share the same E-*syn* conformation to those observed within our own *bis*-amidine species.

With the exception of **Ru4a**, for which high quality crystals could not be obtained, each of the Ru-amidinate and -*bis*-amidiante complexes were also structurally characterised using single crystal X-ray diffraction studies. However, on account of the similarity between the structures determined for the related ^{i}Pr- and Cy-substituted species, where relevant, only the former will be discussed within this section. The molecular structures and structural data corresponding to **Ru1b**, **Ru2b**, **Ru3b** and **Ru6b** are available within the appendices of this work.

For the Ru monoamidinate complexes, **Ru1a** crystallises in the monoclinic space group $P2_1/c$ with two molecules in the asymmetric unit. The anthracene analogue, **Ru2a**, crystallises in the triclinic space group *P-1* and also contains two molecules in the asymmetric unit in addition to a molecule of toluene. The solvent molecule is disordered over two positions with the greater component modelled at 65 % occupancy. The molecular structures of both complexes are presented in **Figure 4.9** and selected bond lengths and angles are displayed in **Table 4.2**. Data is also included for the related complex, reported by Seidel *et al*. (**RuSiMe$_3$**),[213] which contains TMS functionality at the terminus of the ethynyl group (**Figure 4.7-ii)**.

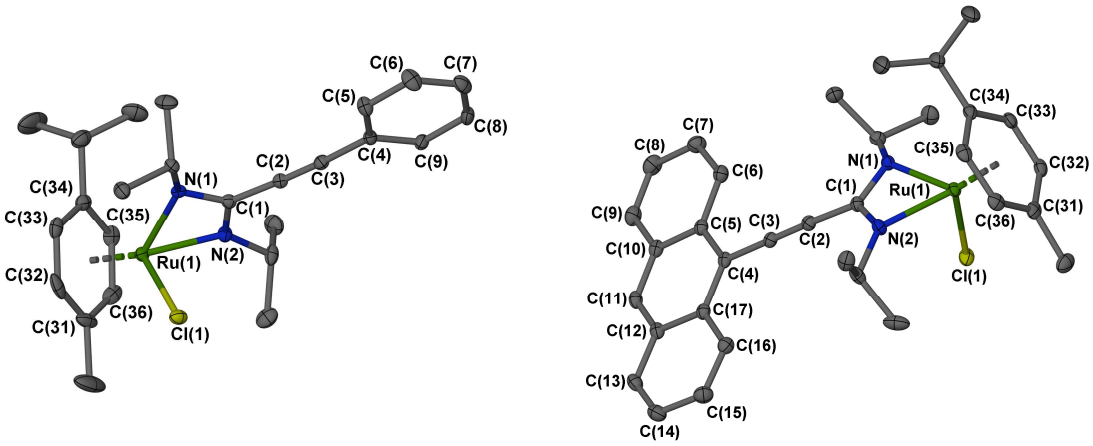

Figure 4.9: Molecular structures of **Ru1a** and **Ru2a** shown with ellipsoids at 30% probability and hydrogen atoms omitted for clarity.

Table 4.2: Selected bond lengths (Å) and angles (°) observed for **Ru1a** and **Ru2a** compared with a literature complex **RuSiMe$_3$** (**Figure 4.7**).

	Ru1a	**Ru2a**	**RuSiMe$_3$**[213]
Ru-N	a) 2.098(3), 2.117(3) b) 2.090(3), 2.102(3)	a) 2.091(2), 2.106(2) b) 2.091(2), 2.114(2)	2.088(2), 2.106(2)
Ru-Cl	a) 2.407(1) b) 2.411(1)	a) 2.424(6), b) 2.4049(6)	2.4083(7)
Ru-C(arene)[a]	a) 2.139(4)-2.219(4) b) 2.160(4)-2.211(4)	a) 2.179(2)-2.205(3) b) 2.150(3)-2.219(3)	2.14-2.19
N-C(amidinate)	a) 1.324(4), 1.321(5) b) 1.333(4), 1.322(4)	a) 1.321(3), 1.331(3) b) 1.329(3), 1.331(3)	1.327(3), 1.320(3)
N-Ru-N	a) 62.1(1) b) 62.5(1)	a) 62.41(2) b) 62.58(8)	*ca*. 62.2
N-Ru-Cl	a) 86.79(9), 85.64(8) b) 85.92(9), 85.16(8)	a) 86.41(6), 84.72(6) b) 85.16(6), 84.85(5)	*ca*. 86.9, 87.1
N-C-N	a) 110.5(3) b) 110.1(3)	a) 110.1(2) b) 110.3(2)	110.3(2)
C(1)-C≡C	a) 176.3(4) b) 176.7(4)	a) 176.2(3) b) 174.7(2)	176.6(3)
C≡C-(C4/Si)	a) 178.4(4) b) 177.3(4)	a) 179.5(3) b) 177.7(2)	177.0(3)
{NCN}∠{spacer}[b] **(°)**	a) *ca.* 7.19 b) *ca.* 50.0	a) *ca.* 13.1 b) *ca.* 14.7	n/a

[a] Provided as a range of the Ru-C(arene) separations, [b] angle between planes defined through each fragment.

The molecular structures of **Ru1a** and **Ru2a** exhibit *pseudo*-octahedral geometries about the Ru centres, in which the η^6-*p*-cymene ligands cap one of the octahedral faces and the amidinate ligands are coordinated through bidentate interactions. The orientation of the *p-cymene* ligand is approximately the same in both of symmetry independent molecules of each system, with the ^{i}Pr moieties projecting away from

the chloride ligand, occupying the void between the two ^{i}Pr substituents of the amidinate ligand.

The data in **Table 4.2** shows that the bond lengths and bond angles that surround the Ru centres are extremely similar in all three complexes, providing evidence that the steric demands of the amidinate backbone substituents have negligible influence over these parameters. The range of Ru-C bond lengths observed in each complex reflects a slight slant of the *p*-cymene ligands, resulting from steric interactions between the methyl substituent and the close proximity chloride ligand. The bond lengths and angles observed within the amidinate ligands are also very similar for all three complexes. The two N-C bond lengths observed are the identical, within e.s.d.s, reflecting the delocalisation of electron density throughout the amidinate backbones. The N-C-N bond angles are each significantly lower than were observed by Chisholm *et al*. within their {Mo_2} ethynyl-amidinate complexes (118.5^{o} and 118.7^{o}),[184] illustrating the flexibility of this class of ligand towards both bridging and chelating coordination modes. Analysis of the angles surrounding the {C≡C} moieties of each complex reveals only slight deviation from the idealised linear geometries.

The torsion angles observed between the {NCN} and phenyl moieties of **Ru1a** differ significantly between the two symmetry independent molecules. This shows that, whilst small torsion angles can be tolerated by these ligand systems, there appears to be no significant energetic bias for planarity of the ligand. Conversely, the analogous angles observed in the two symmetry independent molecules of **Ru2a** are very similar and there is only slight deviation from ligand planarity in each case. However, this ligand geometry is likely to be influenced by intermolecular crystal packing interactions (*vide infra*)

An analysis of the molecular packing within the crystal lattice of **Ru2a** revealed that each of the independent molecules within the asymmetric unit interact with a second through {anthracene}$\cdots${anthracene} π-stacking interactions to form discrete dimeric units (**Figure 4.10-i**). The distances between planes defined through the anthracene rings for the two symmetry independent dimers are *ca.* 3.47 Å and 3.52 Å, respectively. **Figure 4.10-ii** shows that the two sets of stacking anthracene rings are

offset from one another resembling graphite AB-type stacking.[167-169] Although it is not shown here, analogous π-stacked dimers are also observed within the crystal lattice of the Cy-substituted analogue **Ru2b** (see appendices) for which the inter-anthracene planar separation is comparable to that of **Ru2a** (*ca.* 3.49 Å).

i)

ii)

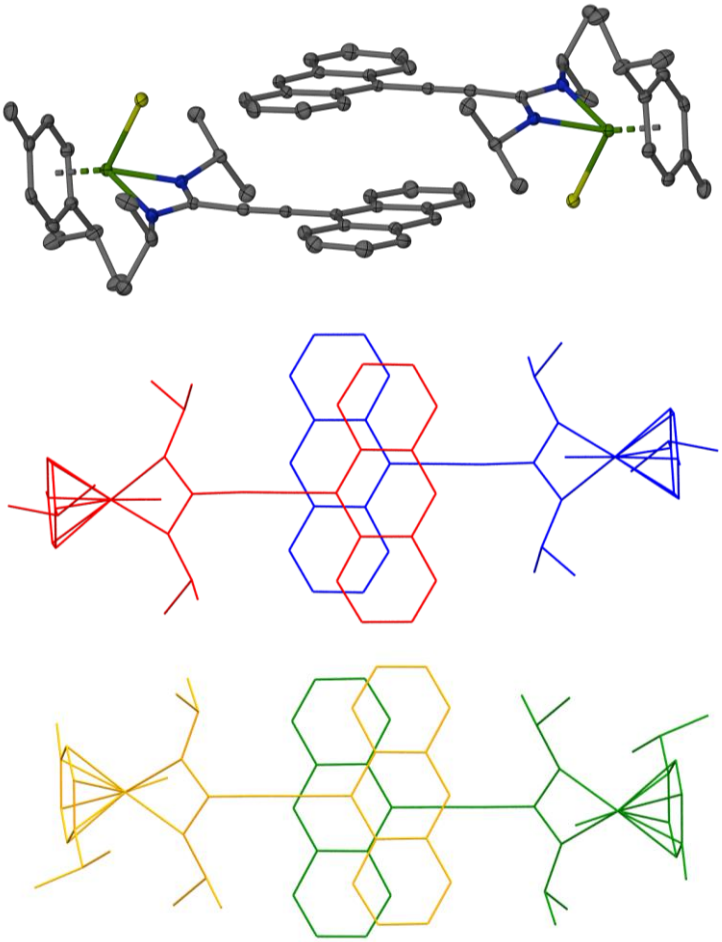

Figure 4.10: i) Intermolecular stacking interaction exhibited in the crystal lattice of **Ru2a**. **ii)** Diagrams exhibiting the offset of anthracene rings (normally observed for graphitic packing)[167-169].

For the Ru-*bis*-amidinate complexes; **Ru3a** and **Ru6a** crystallised in the tetragonal space groups $P4_2/n$ and $I4_1/a$ respectively. Both contain half a molecule in the asymmetric unit with the full molecule generated through an inversion centre at the centre of the phenylene or anthracene spacer units. **Ru5a** crystallises in the triclinic space group *P-1*, containing two independent half molecules in the asymmetric unit. Inversion centres at the centre of the substituted phenylene rings again generate the

complete molecules. The asymmetric unit of **Ru5a** also contains one molecule of toluene which is disordered over two positions in a 1:1 ratio. An isopropyl group located on the amidinate ligand of a single half molecule is also disordered by rotation about the N-^{i}Pr bond and was modelled over two positions with the larger component at 57% occupancy. The molecular structures of **Ru3a**, **Ru5a**, and **Ru6a** are displayed in **Figure 4.11** and selected bond lengths and angles observed within each system are presented in **Table 4.3**.

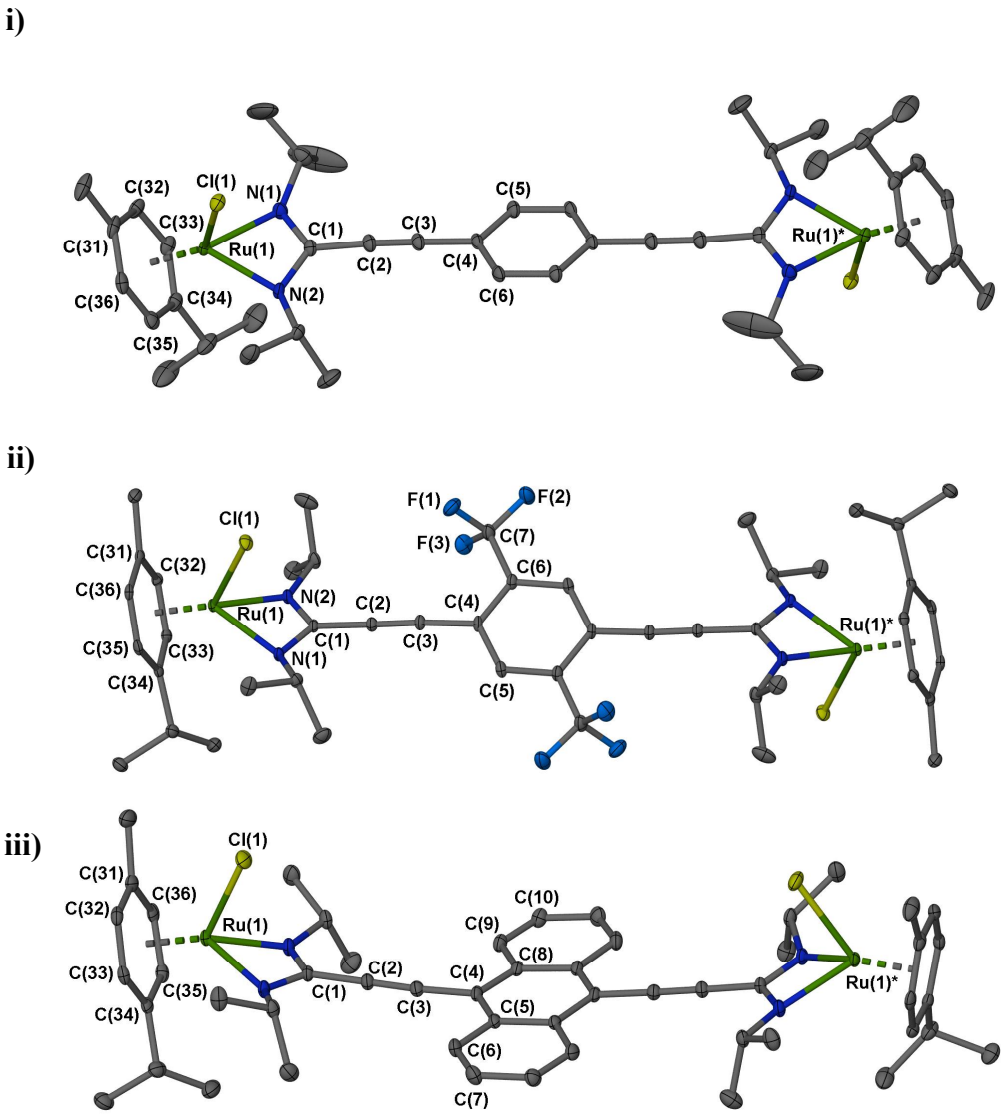

Figure 4.11: Molecular structures of **Ru3a** (**i**), **Ru5a** (**ii**) and **Ru6a** (**iii**) shown with ellipsoids at 30% probability with hydrogen atoms and solvent of crystallisation removed for clarity.

Table 4.3: Selected bond lengths (Å) and angles (°) within Ru-*bis*-amidinate complexes **Ru3a**, **Ru5a** and **Ru6a**.

	Ru3a	**Ru5a**[d]	**Ru6a**
Ru-N	2.096(2), 2.099(1)	a) 2.087(2), 2.131(2) b) 2.087(2), 2.137(2)	2.095(2), 2.121(2)
Ru-Cl	2.4110(4)	a) 2.4082(6), b) 2.4180(6)	2.4131(7)
Ru-C(arene)[a]	2.151(2) – 2.230(2)	a) 2.173(2)-2.205(2) b) 2.170(1)-2.204(2)	2.155(3) – 2.229(3)
N-C (amidinate)	1.324(2), 1.326(2)	a) 1.321(3), 1.335(3) b) 1.324(3), 1.332(3)	1.332(3), 1.332(3)
C≡C	1.189(2)	a) 1.196(3) b) 1.195(3)	1.195(4)
N-Ru-N	62.58(6)	a) 62.32(7) b) 62.29(7)	62.51(8)
C(1)-C≡C	177.0(2)	a) 179.2(3) b) 178.7(3)	179.4(3)
C≡C-C(Ar)	178.9(2)	a) 176.4(3) b) 178.4(30	176.5(3)
N-Ru-Cl	86.18(4), 85.08(4)	a) 86.79(6), 83.67(5) b) 86.67(6), 83.58(5)	86.51(7), 85.15(6)
N-C-N	110.6(1)	a) 110.8(2) b) 110.5(2)	110.4(2)
{NCN}∠{spacer}[b]	*ca.* 22.26	a) *ca.*10.91 b) *ca.* 23.69	*ca.* 9.61
Ru···Ru[c]	*ca.* 15.93	a) *ca.* 15.92 b) *ca.* 15.89	ca. 15.73

[a] Provided as a range of the Ru-C(arene) separations, [b] angle between planes defined through each fragment, [c] intramolecular separation of Ru atoms, [d] different symmetry independent molecules reported as ‘a)’ and ‘b)’.

The molecular structures of the Ru-*bis*-amidinate complexes exhibit the desired 'rigid-rod'-type motifs, in which a ruthenium atom is chelated at either end of the bridging ligand. The intramolecular separation between the metal centres is *ca*. 16 Å in each of the complexes. Similar to the structures previously described for **Ru1a** and **Ru2a**, the geometries about the Ru centres are pseudo-octahedral, with the *p*-cymene ligands orientated such that the ^{i}Pr groups project away from the Chloride ligand.

The bond lengths angles observed within the three *bis*-amidinate complexes are almost identical to the analogous parameters observed within the structures of **Ru1a** and **Ru2a**. One slight difference is that within **Ru5a** and **Ru6a**, one of the Ru-N bond lengths is slightly longer than the second. For **Ru5a** this can be related to steric interactions between the {CF_3} and {^{i}Pr} moieties of the bridging ligand, however, the anthracene spacer of **Ru6a** is symmetrical and, as such, a similar explanation cannot be used. It is therefore possible that intermolecular packing interactions also play a role. The torsion angles observed between the conjugated spacer units and the amidinate backbones of each complex are all relatively small, facilitating efficient π-orbital alignment along the length of each molecule within the solid-state. This shows that the introduction of the ethynyl units have successfully alleviated the intra-ligand steric interactions that have prevented planarity within previously reported *bis*-amidinate metal complexes.[207-208,210-211] It is, however, difficult to assess whether the small torsion angles observed here are due to favourable π-conjugation or subtleties within the crystal packing environment.

A significant difference between the structures of the three complexes reported here is that **Ru4** exhibits an alternative structural isomer to those observed for **Ru1a** and **Ru3a**. In both of the latter the chloride ligands project in different directions, one above the plane of the *bis*-amidinate and one below, providing a '*trans*' geometry. Conversely, the chloride ligands of **Ru4** are both oriented over the same face of the *bis*-amidinate ligand, providing a '*cis*' geometry. Side-on views of each of the molecules are shown in **Figure 4.12**. Although there is no evidence of fluxionality within the room temperature ^{1}H NMR spectra of these complexes, it is probable that the conversion between isomers occurs faster than the NMR time-scale.

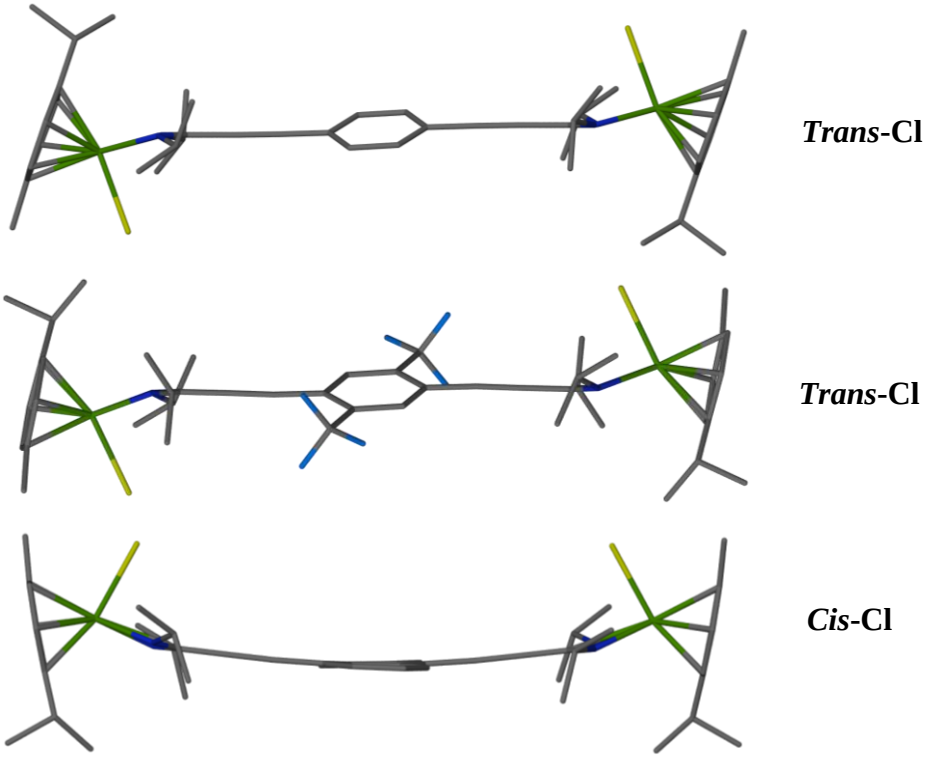

Figure 4.12: Side-on views of **Ru3a**, **Ru5a** and **Ru6a** to illustrate the two different isomeric forms.

The molecular profiles presented in **Figure 4.12** also reveal that there is a significant deviation from linearity along the length of the molecules, in which the Ru atoms lie out of the plane of the bridging ligand system. This is particularly apparent by the bowed shape of **Ru6a**, with the ruthenium atoms lying *ca*. 1.26 Å above the plane of the anthracene ring. These distortions arise from a non-linear coordination mode of the amidinate ligands within each complex, which can be quantified by the angles presented in **Table 4.4**.

Table 4.4: Data showing the bend in the amidinate coordination mode defined by the angle between the Ru atom, a centroid calculated between the two N atoms and the closest ethynyl-C. This is depicted in the accompanying diagram.

Complex	θ (°)
Ru3a	*ca*. 165.3
Ru5a	*ca*. 159.5 and 159.4
Ru6a	*ca*. 163.6

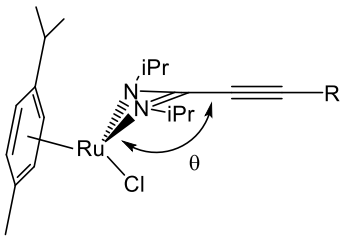

The data in **Table 4.4** shoes that the deviation from linearity increases with the steric demand of the aromatic spacer, with the CF_3-substituted structures exhibiting the smallest angles. Similar observations have been made within the structures of Ru-amidinate and -guanidinate complexes within the literature, where it was also suggested that the effect is influenced by the steric environment.[213,218,221-224] However, Nagashima *et al.* reported a large distortion (*ca.* 150^o) in the significantly less congested complex [(Arene)Ru(Amidinate)][PF_6], suggesting that electronic factors may also play an important role.[225]

An analysis of the crystal lattice of **Ru6a** reveals that π-π stacking interactions result in the formation of discrete dimers in the solid-state in which the anthracene rings are separated by *ca*. 3.57 Å. However, unlike the intermolecular interactions previously described for **Ru2a** (*vide supra*), the interacting molecules of **Ru6a** are orientated perpendicular to each other, involving overlap of both the anthracene and ethynyl moieties of the bridging ligand. This interaction is illustrated in **Figure 4.13-i**.

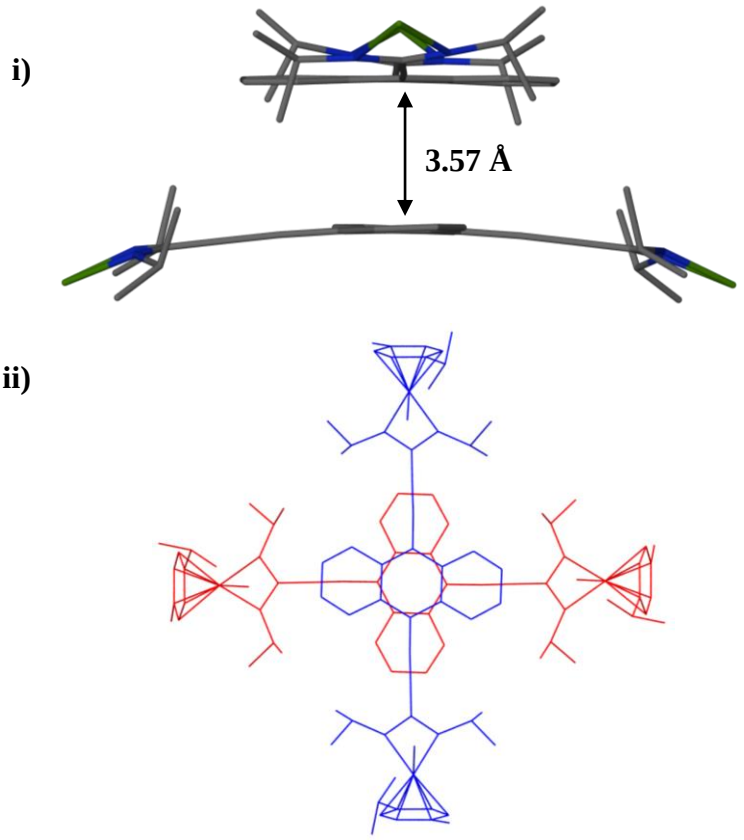

Figure 4.13: A stacking dimer of **Ru6a** viewed down the *c*-axis (**i**) and down the plane of the stacking anthracene rings (**ii**).

The two stacking amidinate ligands bend towards each other, which is facilitated by the '*cis*' arrangement of the {Ru} termini, unique to this complex. **Figure 4.13-ii** shows that the central six-membered rings of the anthracene fragments are perfectly overlapped but rotated by 90° relative to each other. This potentially provides π-orbital interactions between the ethynyl moiety of one molecule and the anthracene ring system of the other. Although various stacking modes of diethynyl-anthracene units have been observed in the literature, to the best of our knowledge this is the first example of this precise stacking motif.[233-237] Unlike graphitic type stacking, the 90° rotation of the anthracene rings does not impose a significant offset of the two ring systems.[167-169] For this reason there is likely to be greater electron repulsion between the two molecules, which may be in part responsible for the greater {anthracene}···{anthracene} separation than was observed for **Ru1a** and **Ru1b**. It must also be considered that the overall steric requirements of the crystal packing may 'lock' the two molecules in this orientation within the crystal lattice.

The crystal lattice of the related complex, **Ru6b**, reveals that no intermolecular π-stacking interactions were present, which may reflect the greater steric demands of the Cy-substituents. Interestingly, the molecular structure of **Ru6b** exhibits the *trans*-arrangement of the {Ru} termini (**Figure 4.14**), not the *cis*-arrangement that is observed for **Ru6a**. This may suggest that *cis*-form is only favoured in the presence of the {anthracene} stacking interactions.

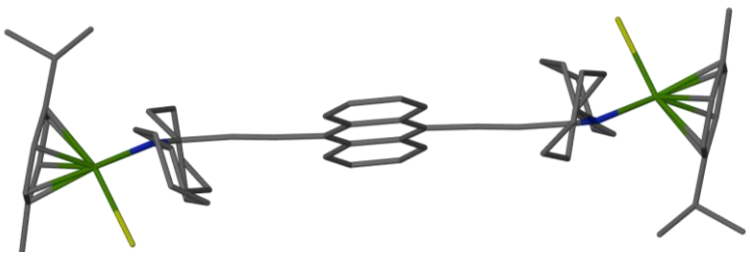

***Trans*-Cl**

Figure 4.14: Side-on view of a molecule of **Ru6b** showing the *trans*-orientation of the {Ru} termini.

4.2.5 – Electronic Absorption Spectroscopy

With a particular interest in how the identity of the ligand systems could be used to tune the optical and electronic properties of the novel Ru-amidinate and -*bis*-

amidinate complexes, each of the ^{i}Pr-substituted products has been analysed by electronic absorption spectroscopy. To aid the interpretation of the spectroscopic data the corresponding amidine and *bis*-amidine preligands were also analysed under the same conditions.

The electronic absorption spectra of the amidines, **A1a** and **A2a**, and their corresponding Ru-amidinate complexes, **Ru1a** and **Ru2a**, are presented in **Figure 4.15-i** and **-ii** respectively. The electronic absorption spectrum of [(*p*-cymene)$RuCl_2$]$_2$ has been included in the latter to allow comparison. All data was recorded at room temperature using DCM as solvent.

The Electronic absorption spectrum of **A1a** exhibits a single absorption band within the spectral window shown (λ_{max} = 255 nm), which is attributed to a $\pi\rightarrow\pi^*$ electronic transition. **Ru1a** exhibits an absorption band at almost identical energy and the similar shape of this band to that of **A1a** again suggests a $\pi\rightarrow\pi^*$ transition. However, **Ru1a** also exhibits a second, broader, absorption band at lower energy (λ_{max} = 300 nm), which has been attributed to a Ru($d\pi$)$\rightarrow\pi^*$ electronic transition.

The electronic absorption spectra of **A2a** and **Ru2a** are very similar, exhibiting an intense absorption band in the high energy region of the spectrum and a second lower intensity band, which extends into the visible region of the spectrum. **Ru2a** also exhibits a shoulder at *ca*. 295 nm which is not observed for the free ligand. For **A2a** the lower energy absorption band (λ_{max} = 410 nm) exhibits well defined vibrational structure, which is common for anthracene based $\pi\rightarrow\pi^*$ electronic transitions.[57] The low energy absorption band of **Ru2a** (λ_{max} = 424 nm) is slightly red-shifted relative to that of **A2a** and the vibrational structure is much less resolved, which may indicate a degree of MLCT character. However, the comparable shape and energy of this absorption band to that of **A2a** suggests that responsible electronic transition remains predominantly $\pi\rightarrow\pi^*$ in character. Once again, the absorption coefficient of the lower energy absorption band is significantly greater for the metal complex. There are no correlations between the absorption bands observed for **Ru1a** or **Ru2a** and those exhibited by [(*p*-cymene)$RuCl_2$]$_2$, showing that the amidinate ligand is responsible for the observed absorption processes.

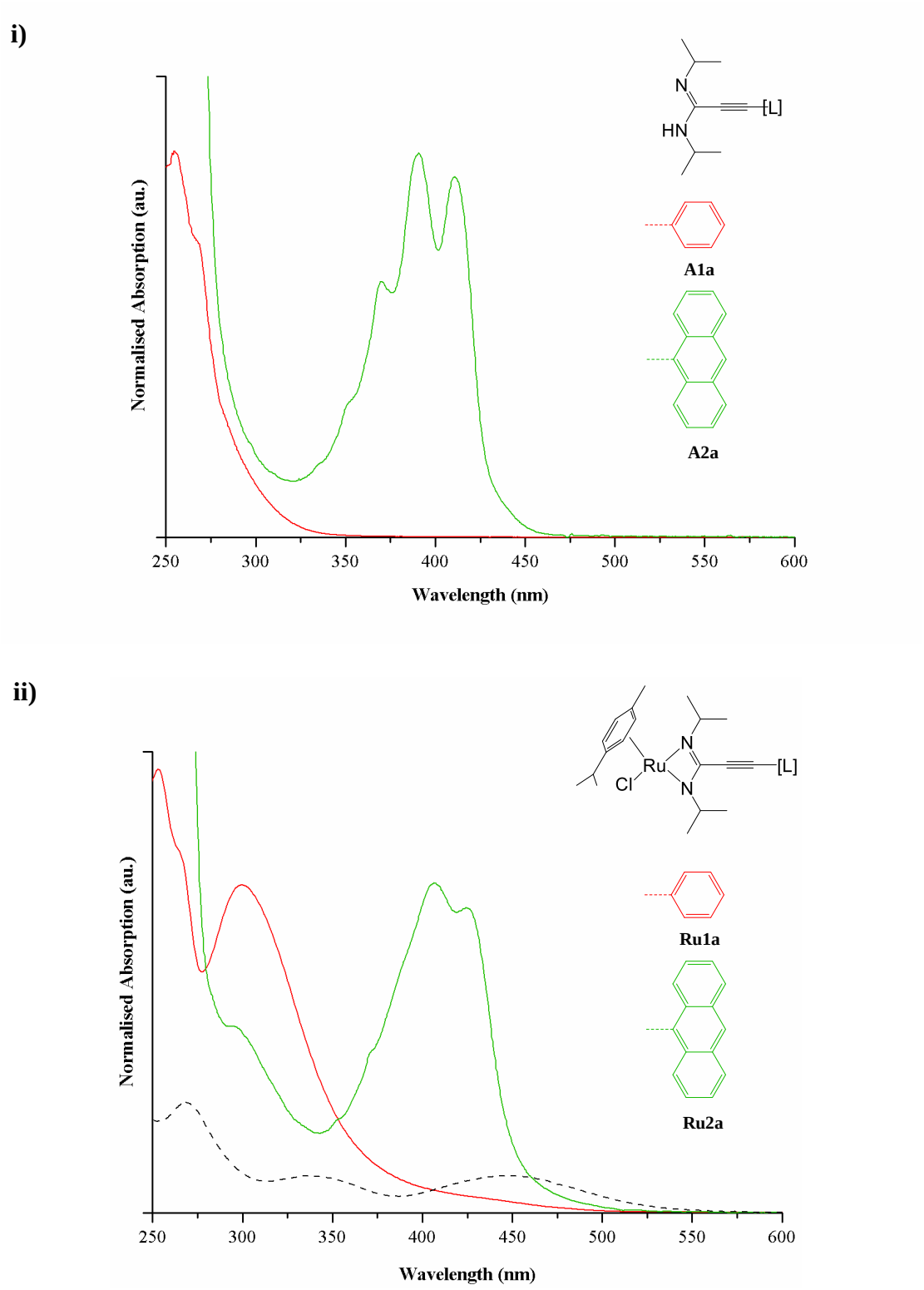

Figure 4.15: Normalised electronic absorption spectra of **i) A1a** and **A2a** and **ii) Ru1a**, **Ru2a** and [(*p*-cymene)$RuCl_2$]$_2$ (black). All data was recorded at room temperature from DCM solutions.

The electronic absorption data recorded for the monoamidines and the Ru-monoamidinate complexes are summarised in **Table 4.5**.

Table 4.5: Electronic absorption data for **A1a**, **A2a, Ru1a**, **Ru2a** and [(*p*-cymene)$RuCl_2]_2$.

Complex	λ (nm)[a]
A1a	*ca*. 266 (15130), 255 (19558)
A2a	410 (10117), 390 (10785), 370 (7188), *ca.* 351 (3733)
Ru1a	300 (13765), 253 (18626)
Ru2a	424 (16180), 406 (17469), 294 (10206)
[(*p*-cymene)$RuCl_2]_2$	447 (1123), 338 (1116), 269 (3347)

[a] Absorption coefficients shown in brackets ($dm.mol^{-1}.cm^{-1}$)

The electronic absorption spectra of the *bis*-amidines **BA1a**-**BA4a** and Ru-*bis*-amidinate complexes **Ru3a**-**Ru6a** are shown in **Figure 4.16-i** and **-ii**. All data was recorded at room temperature from DCM solutions of the analytes.

BA1a-**BA3a** and their respective Ru complexes each exhibit high energy absorption bands, observed between 286 and 295 nm, showing negligible dependence on either the {Ru} fragment or the identity of the conjugated spacer unit. For this reason these absorption bands do not reflect electronic transitions from charge-delocalised states but are more likely to represent π-π* electronic transitions from orbitals localised within the {NC(C≡C)N} fragment of each ligand. Similar absorption bands were observed by Chisholm *et al*. for a series of related $\{Mo_2\}$-ethynyl-amidinate complexes (example shown in **Figure 4.4-i**), but the band was absent from the absorption spectrum of a related complex containing no ethynyl functionality,[184] which supports our assignment. Although analogous absorption bands are not observed for the **Ru6a** and **BA4a**, they may be masked by the intense absorption bands that extend further into the UV-region of each spectra.

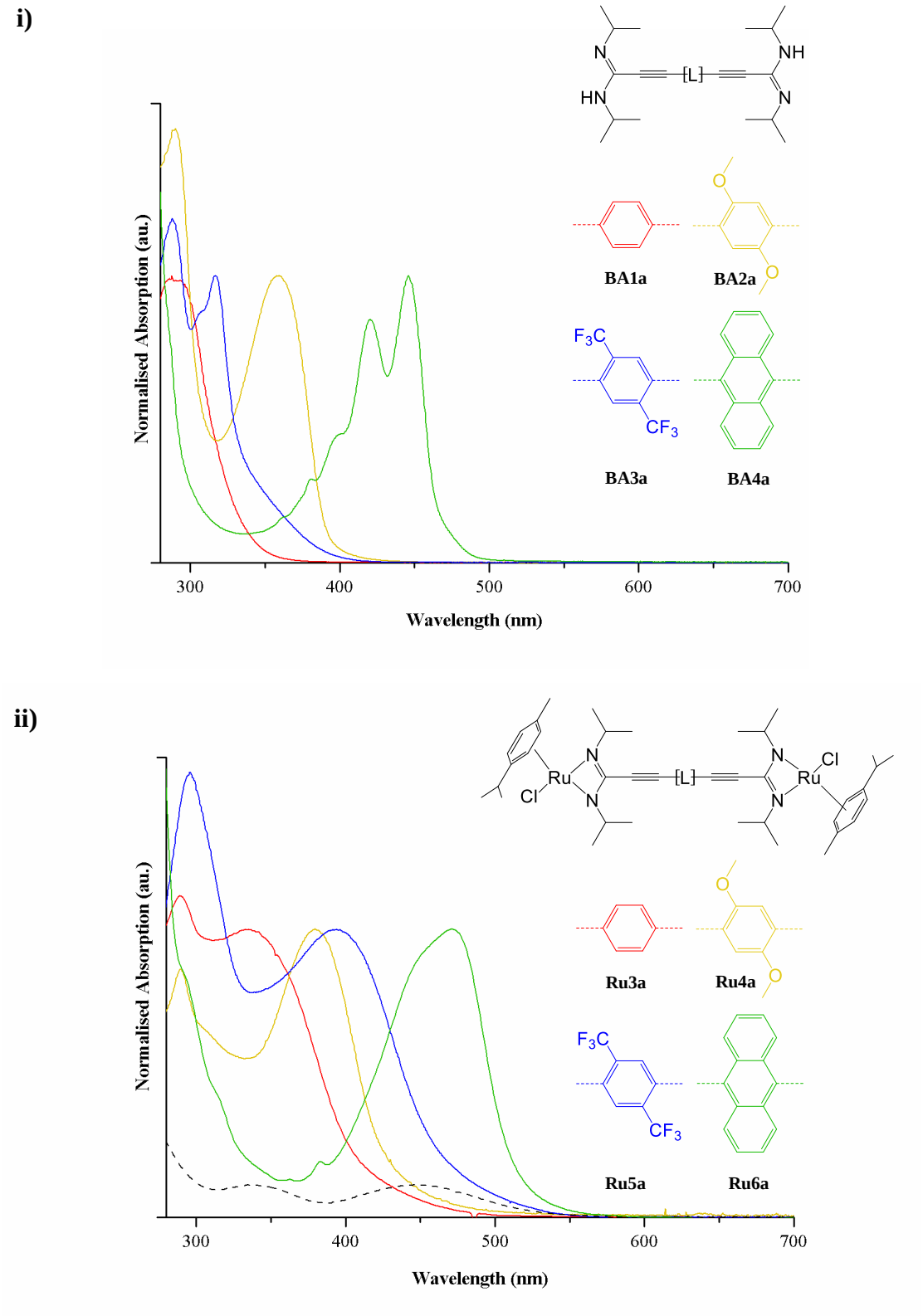

Figure 4.16: Normalised electronic absorption spectra of **i) BA1a-BA4a** and **ii) Ru3a-Ru6a** and [(*p*-cymene)$RuCl_2$]$_2$ (black). All data was recorded at room temperature from DCM solutions.

The electronic absorption spectra of the *bis*-amidines each exhibit second lower energy absorption bands which are attributed to π-π* electronic transitions. λ_{max} increases in the order **Ba1**<**BA3**<**BA2**<**BA4**. The lowest energy absorption band is therefore observed for the highly conjugated anthracene containing system, which also exhibits a significant degree of vibrational structure. The highest energy absorption band is that of the phenylene containing system **BA1a**, although, this is red-shifted from the analogous absorption band of **A1a**, reflecting the greater degree of conjugation within the *bis-amidine*. Both electron-donating and electron-withdrawing substituents on the phenylene spacer units result in a red-shift of λ_{max} relative to **BA1a**, but this is much more pronounced for the methoxy-substituted system, **BA2a**.

The Ru complexes also exhibit second, lower energy absorption bands, which are red-shifted relative to those of the related free ligands and are relatively broad in each case. The energies of these bands again vary greatly depending on the identity of the conjugated spacer unit, with λ_{max} increasing in the order **Ru3a**<**Ru4a**<**Ru5a**<**Ru6a**. Interestingly the relative energies observed for **Ru4a** and **Ru5a** are reversed relative the trend observed for the free ligands (**BA2a** and **BA3a**), with the electron-withdrawing spacer unit providing a slightly lower energy absorption band. This provides evidence that responsible electronic transitions differ from the π-π* processes assigned for the free ligands. On account of the similarity between the spectra of **Ru3a-Ru5a** the low energy absorption bands for these species are attributed to MLCT processes, similar to that discussed previously for **Ru1a**. The low energy absorption band of **Ru6a** exhibits very little vibrational structure, which is also consistent with a degree of MLCT character. However, due to the similar appearance of the absorption spectra of **Ru6a** and **BA4a** it is likely that the electronic transition remains predominantly π-π* in character, similar to the assignment of the analogous absorption band in **Ru2a**.

The electronic absorption data for the ruthenium *bis*-amidinate complexes and the parent *bis*-amidine ligands are summarised in **Table 4.6**.

Table 4.6: Electronic absorption data for *bis*-amidinate ligands (**BA1a**-**BA4a**) and their respective Ru complexes (**Ru3a-Ru6a**).

Complex	λ (nm)[a]
BA1a	292 (32452), 286 (32726)
BA2a	360 (22712), 290 (34400)
BA3a	317 (24086), 287 (28800)
BA4a	446 (25640), 420 (21709), 398 (11388), 380 (7463)
Ru3a	333 (33118), 289 (36955)
Ru4a	382 (34601), 289 (29891)
Ru5a	396 (25678), 295 (39749)
Ru6a	471 (34430), *ca*. 313 (14981), *ca* 291 (29424)
[(*p*-cymene)RuCl$_2$]$_2$	447 (1123), 338 (1116), 269 (3347)

[a] Absorption coefficients shown in brackets (dm.mol^{-1}.cm^{-1}).

4.2.6 – Electrochemical Analyses

To investigate the electronic properties of the Ru-amidinate and -*bis*-amidinate complexes and to aid the interpretation of the electronic absorption data, each of the ^{i}Pr-substituted complexes were analysed electrochemically using cyclic voltammetry. This facilitates the measurement and analysis of the $Ru^{2+/3+}$ redox couple which corresponds to removing an electron from the highest lying Ru *d*-orbitals.

Each of the experiments was carried out using a 1 mM solution of the analyte and a 0.1 M [NBu_4][PF_6] electrolyte solution in DCM. A glassy carbon working electrode, gold counter electrode and platinum reference electrode were also utilised in each study and the data was referenced relative to the ferrocene (Fc) $Fe^{2+/3+}$ redox couple.

The normalised cyclic voltammograms of the Ru-*mono*-amidinate complexes, **Ru1a** and **Ru2a**, are shown in **Figure 4.17**. Both complexes exhibit a single reversible redox process, corresponding to the $Ru^{2+/3+}$ couple, which appear at positive potential relative to the ferrocene reference. The half-wave potential ($E_{1/2}$) of the anthracene derivative is slightly higher than that of **Ru1a**, suggesting that the additional

conjugation presented by the anthracene group stabilises the Ru($d\pi$) orbital to a small degree.

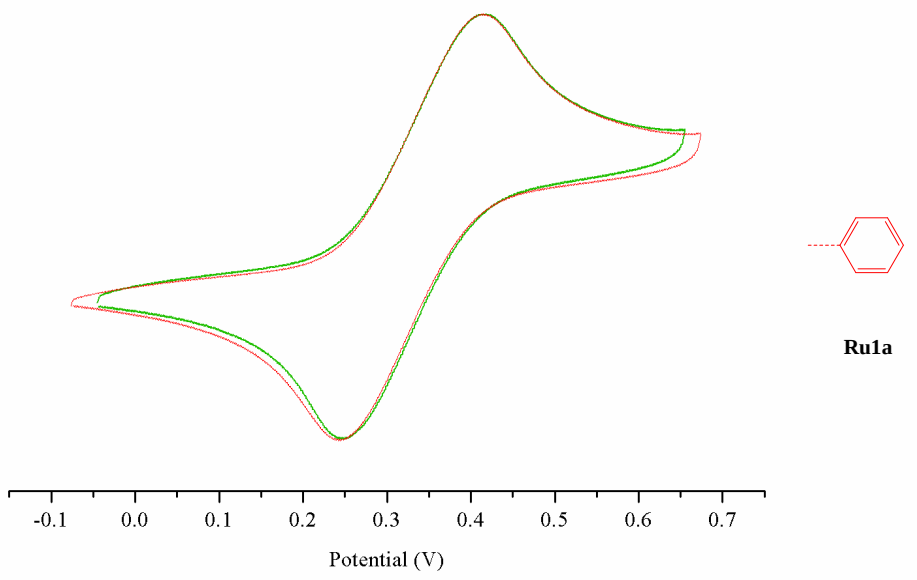

	Ru1a	Ru2a
$E_{1/2}$	325 mV	333 mV
ΔE_p	173 mV	169 mV

Figure 4.17: Cyclic voltammograms of **Ru5a** (red) and **Ru6**a (green) recorded in a 0.1 M [NBu_4][PF_6] DCM solution using a glassy carbon w/e, Au c/e and Pt r/e. Data is referenced to the $Fc^{0/+}$ couple. ($\Delta E_p Fc$ = 150 mV)

The normalised cyclic voltammograms of the Ru-*bis*-amidinate complexes are displayed in **Figure 4.18**, showing that each of the dimetallic species also exhibits only a single reversible oxidation process. No splitting of the oxidation or reduction waves was observed for any of the complexes studied, providing no evidence for the formation of mixed-valence species. Analogous observations were also made using differential pulse analysis in which single peaks were observed. The absence of electronic coupling between the bridged ruthenium centres may be, in part, a result of the relatively large interatomic separations present in these complexes. However, electronic communication has previously been observed between ruthenium centres over greater distances.[238]

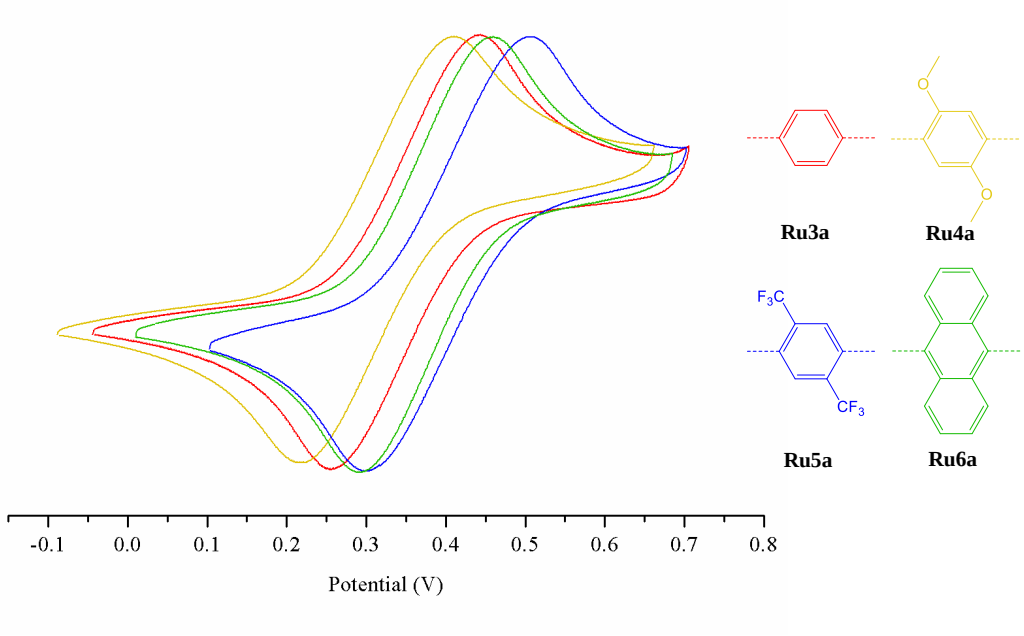

	Ru3a	Ru4a	Ru5a	Ru6a
$E_{1/2}$	348 mV	314 mV	403 mV	375 mV
ΔE_p	188 mV	192 mV	205 mV	170 mV

Figure 4.18: Cyclic voltammograms of **Ru3a** (red), **Ru4a** (yellow), **Ru5a** (blue) and **Ru6a** (green), recorded in a 0.1 M [NBu_4][PF_6] THF solution using a glassy carbon w/e, Au c/e and Pt r/e. Data is referenced to the $Fc^{0/+}$ couple. (ΔE_pFc = 148 mV)

The magnitude of the $E_{1/2}$ of **Ru3a-Ru6a** increases in the order **Ru4a**<**Ru3a**<**Ru6a**<**Ru5a**. **Ru5a** is therefore the most stable complex towards oxidation which is likely to be a result of the electron-withdrawing ligand system which promotes Ru→Ligand backbonding. Conversely the complex most susceptible to oxidation is that which contains the electron-donating {OMe} substituents, which reduce the amount of back-bonding. The $E_{1/2}$ of **Ru3a**, containing the un-substituted phenylene-*bis*-amidinate ligand, is approximately halfway between those of the {OMe}- and {CF_3}-substituted analogues. Increasing the conjugation within the ligand system, by changing from a phenylene to an anthracene spacer (**Ru6a**), results in a slightly higher oxidation potential, which is again likely to reflect a greater degree of metal→ligand back-bonding. Both **Ru3a** and **Ru6a** exhibit significantly higher $E_{1/2}$ values than the related monometallic species (**Ru1a** and **Ru2a**), which can be correlated with the greater degree of π-

conjugation within the *bis*-amidinate ligand systems, resulting in more electron-withdrawing character.

The electrochemical data provides further evidence to support the assignment of the MLCT bands in the electronic absorption spectrum. Both **Ru4a** and **Ru5a** exhibit comparable λ_{max} energies (382 and 396 nm) despite the electron-donating and electron-withdrawing nature of the substituents respectively. The {OMe} groups destabilise the ligand π*-orbitals relative to the unsubstitiuted phenylene spacer, whereas the {CF_3} groups have the opposite effect. The electrochemical data shows that the difference in the energy of the π*-orbitals are offset by the relatively high energy of the appropriate Ru *d*-orbital in **Ru4a** and low energy of the analogous orbital of **Ru5a**.

4.3 – Conclusion

In summary, a series of ethynyl-functionalised amidine and *bis*-amidines have been developed as potential ligand systems for redox-active metal centres. These have been designed to remove undesirable intraligand steric interactions that have precluded π-conjugation within related ligand systems reported in the literature.[207-212] In line with the goals of this thesis, a number of different conjugated subunits have been incorporated into these species, providing scope to tune the optical and electronic properties of the organometallic complexes in which they are coordinated.

In order to test the properties accessible though these ligand systems, a series of Ru-complexes were synthesised. The Ru-centre offers ready redox conversion that does not alter the coordination geometry around the metal centre during this process. Both monometallic and dimetallic complexes were prepared and their spectroscopic and electrochemical properties investigated.

The molecular structures of the Ru-*bis*-amidinate complexes showed that the bridging ligand systems were close to planar in each case, facilitating efficient π-orbital alignment along the length of the molecules in the solid-state. This reflects the utility of the ethynyl subunits within the ligand systems, which effectively

prevent steric interactions between the conjugated spacer unit and the amidinate backbone. With the exception of **Ru6b**, each of the anthracene-containing complexes form dimers in the solid-state through π-π stacking interactions and, for **Ru6a**, these interactions are aided by the alternative isomeric geometry exhibited by this complex.

Electronic absorption analyses of the Ru-*bis*-complexes reveal that λ_{max} is tuneable over *ca.* 140 nm by changing the identity of the conjugated spacer unit. λ_{max} of both **Ru3a** and **Ru6a** are also red-shifted relative to the absorption bands of the related monoamidinate complexes on account of their more extended π-conjugated networks. The lowest energy absorption bands were observed for the anthracene-containing complexes, reflecting their highly conjugated ligand systems. However, the data suggests that the low-energy electronic transitions within these species are predominantly π→π* in character, contrasting with the MLCT bands exhibited by each of the phenylene-containing complexes.

Electrochemical analyses of **Ru3a**-**Ru6a** provide no evidence of electronic coupling between the bridged metal centres, although, the energy of the $Ru^{2+/3+}$ redox couple varies significantly, depending on the electronic properties of the bridging ligand. The electron-withdrawing substituents of **Ru5a** promote efficient Ru→Ligand back-bonding, stabilising the appropriate Ru *d*-orbital, whereas the electron-rich bridging ligand of **Ru4a** imparts the opposite effect. The $E_{1/2}$ of the anthracene containing complex, **Ru6a**, is closer in energy to that of **Ru2a** than would be expected, based upon the degree of conjugation within each complex. This provides evidence of limited mixing between the Ru and ligand orbitals in **Ru6a**, which is likely to stem from the small energy separation between the π- and π*-orbitals of this ligand system.

Although the *bis*-amidinate ligand systems were originally designed as bridging ligands for {Mo_2} dimers, attempts to synthesise such species have been largely unsuccessful and, as such, the preparative chemistry requires further refinement in order to access these complexes.

Chapter 5

N-Heterocyclic Carbene Adducts of {Mo_2} Carboxylate Dimers

Chapter 5: N-Heterocyclic Carbene Adducts of {Mo_2} Carboxylate Dimers

5.1 – Introduction

Throughout this thesis so far, the work and background have largely focussed on the ability to tune the optical and electronic properties of quadruply bonded {Mo_2} complexes *via* ligand substitution reactions. In this way there is much scope for tuning the energy of the $\delta \rightarrow \pi^*$ electronic transitions in such complexes, and by extension the degree of electronic communication within the system, resulting in a wide range of accessible properties. Within this chapter, we investigate the application of Lewis bases, specifically N-heterocyclic carbenes, to provide an alternative method by which the electronic and physical structure of simple {Mo_2} carboxylate dimers can be manipulated.

5.1.1 – Lewis Base Adducts of {M_2} Carboxylate Dimers

To put this work into context, we are interested in methods by which the optical, electronic and structural properties of quadruply bonded {Mo_2} complexes can be tuned. In addition to ligand substitution reactions, reports in the literature show that the coordination of Lewis basic ligands can also have significant effects on both the electronics and structure of these systems.[95,111,239-240] We hold a particular interest in how these reactions affect the properties of simple {Mo_2} carboxylate dimers as these represent model subunits of the di-carboxylate bridged oligomers discussed in **Chapter 1** as well as the more complicated heterometallic species developed in **Chapter 3**. It is conceivable therefore that interaction between these species and Lewis bases may facilitate post synthetic tuning/switching of the observed optical and electronic properties or templating of their solid-state structures.

To aid the discussion within this chapter **Figure 5.1** displays a series of isomeric mono- and di-substituted adducts that may be obtained through the reaction of Lewis bases with {Mo_2} or {W_2} carboxylate dimers. For relevance to this study we have limited this to complexes containing up to two Lewis base ligands.

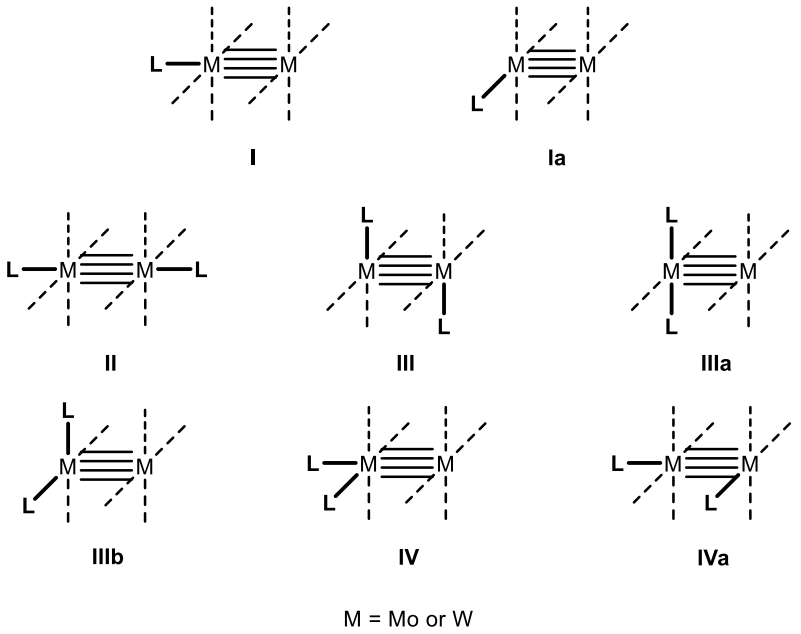

Figure 5.1: Potential geometric isomers of *mono*- and *bis*-Lewis base adducts of quadruply bonded {M_2} carboxylate dimers.

{Mo_2} carboxylate dimers possess only two unsaturated coordination sites, which are situated at the termini of the M-M bonds. Coordination to these 'axial' sites has been shown to be weak, relative to carboxylate dimers containing metals from other periodic groups such as {Rh_2} and {Ru_2} systems.[95] This has been attributed to the strong *trans*-effect imparted by the σ-component of the Mo-Mo bond.[95] Despite the relative weakness of these interactions coordination to the axial sites is possible and **Figure 5.1** shows that this can potentially lead to the formation of mono- (type-**I**) or diaxial (type-**II**) coordination complexes. Examples of both types of substitution product are reported in the literature but mono-substituted complexes are extremely rare and only limited structurally characterised species have been reported.[98,115,241-245] Examples of these are shown in **Figure 5.2** and whilst most exhibit some form of steric protection at the uncoordinated axial site (**Figure 5.2-i** and **Figure 5.2-ii**),[98,242,245] the absence of steric hindrance in examples such as **Figure 5.2-iii** and **Figure 5.2-iv** suggest that electronic factors are also important in determining the coordination mode that is observed.

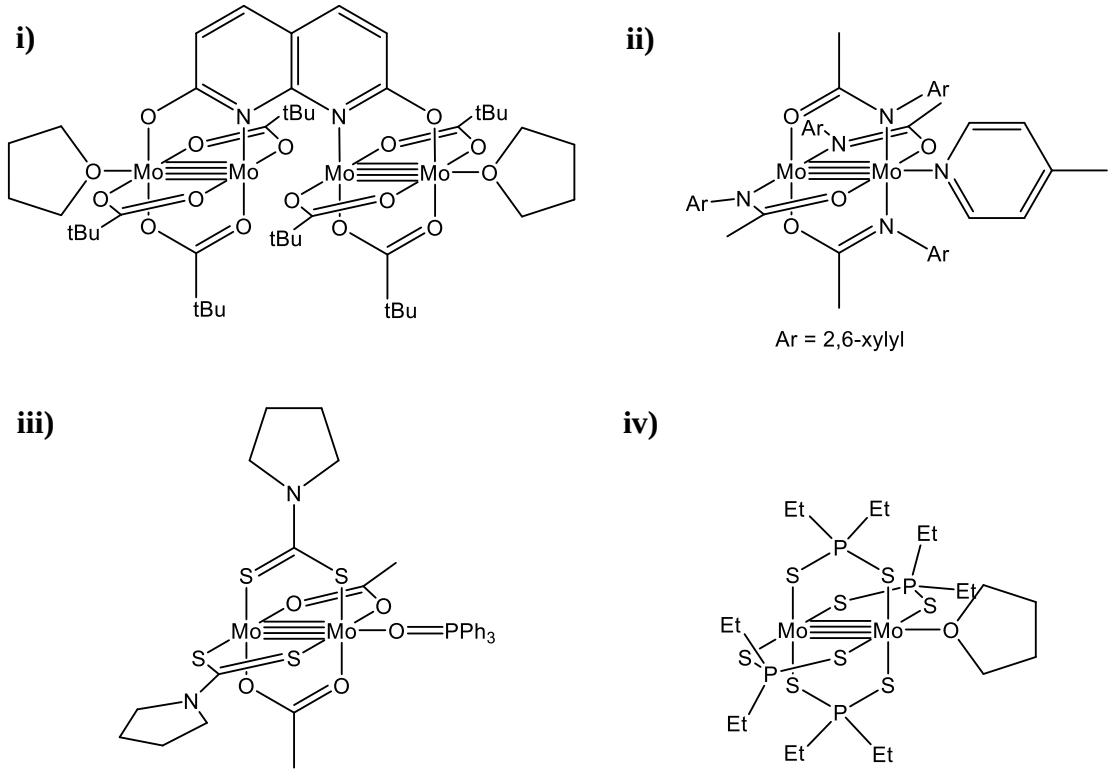

Figure 5.2: Examples of type **I** adducts of quadruply bonded Mo complexes.[98,242,245]

Symmetrically coordinated type **II** adducts are significantly more common within the literature and two representative examples are displayed in **Figure 5.3**.

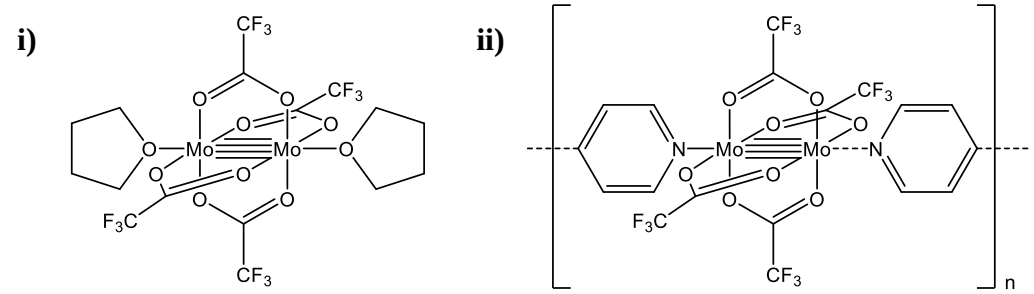

Figure 5.3: THF[246] and 4,4'-bipyridine[239] adducts of $Mo_2(O_2CF_3)_4$.

Bis-solvent adducts, such as the complex depicted in **Figure 5.3-i**, are often obtained from syntheses conducted in coordinating solvents. The use of trifluoroacetate substituted systems increases the Lewis acidity of the metal centres and for this reason it has been utilised in coordination studies that span a greater range of ligands that provide type **II** motifs. An interesting extension of these studies has seen the

synthesis of a variety of polymeric systems made though the 1:1 reaction with bidentate Lewis bases such as 4,4-bipyridine (**II-ii**),[239] *bis*-phosphines[247] and polynitriles.[248] There are also examples of {Mo_2} complexes that contain Lewis base substituted carboxylate ligands, such as pyridyl[111] and phosphine oxide functionalities,[249] which facilitate the formation of intermolecular coordination networks.

The remaining adduct types shown in **Figure 5.1** involve equatorial interactions around the M-M core. Although this does not seem intuitive, because these sites are saturated by μ-carboxylate ligands, it has been shown that certain phosphines are able to displace one arm of the carboxylate to assume the equatorial coordination site.[250-251] All {Mo_2} equatorial phosphine adducts have been shown to adopt the type **III** conformation in the solid state, however there is an isolated example of a type **IV** complex with a {W_2} core.[252] Studies using phosphines have also been shown to provide complexes of type **II** but none of the other motifs in **Figure 5.1** have been observed in the solid-state.[250,253] Examples of the two phosphine adduct types that have been structurally characterised for {Mo_2} systems are shown in **Figure 5.4**.

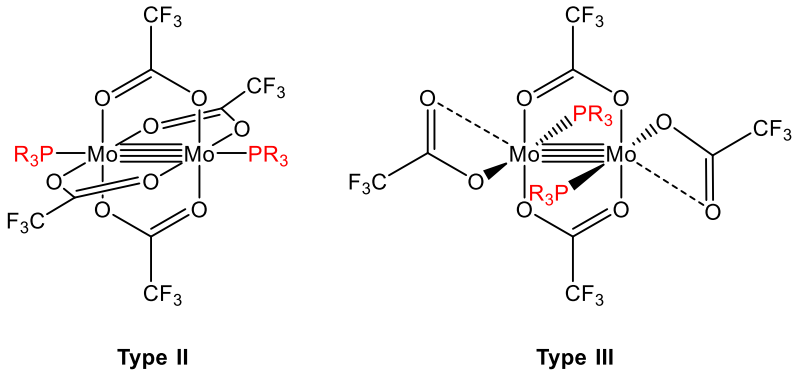

Figure 5.4: Type **II** and type **III** phosphine adducts of $Mo_2(O_2CCF_3)_4$.[250-251,254]

The molecular structures that have been obtained for type **III** adducts show that the monodentate carboxylate ligands rotate about their Mo-O bonds, which seemingly allows an axial interaction between the uncoordinated oxygen atom and the metal centre. The equatorial Mo-P bonds are significantly shorter than those observed at

axial sites, reflecting the stronger nature of the interaction. Although crystallographic analysis has shown that all equatorial adducts of molybdenum carboxylate dimers are type **III** in the solid state, NMR analysis has shown that the systems are fluxional in solution and are likely to exist in a number of different forms.[250-251,254] These are likely to include the remaining adduct types suggested in **Figure 5.1**.

Although our primary interest concerns {Mo_2} complexes, it is worth mentioning that both type **II** and **III** phosphine adducts have also been reported for {W_2} carboxylate systems in addition to isolated reports of a type **IV** complex and a tris-phosphine adduct (**Figure 5.5**).[240,252,255] All of these systems exhibit stronger M-P bonds at both equatorial and axial sites than the respective bonds observed in Mo complexes. The complexes also hold their structural integrity in solution with no obvious fluxionality. This has been justified on account of the greater radial extension of the W *d*-orbitals, which providing better orbital overlap with the phosphine, and thus a stronger bonding interaction.

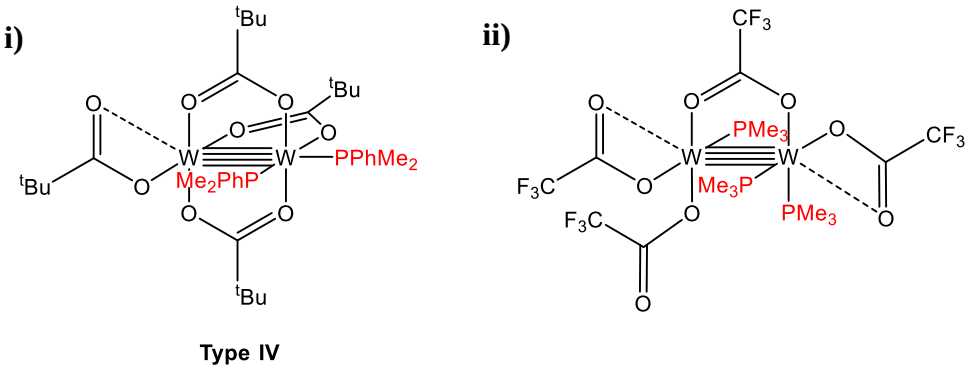

Type IV

Figure 5.5: A type **IV** adduct and tris-phosphine adduct of W carboxylate dimers.[240,252]

Following studies with a wide variety of phosphines, it was determined that the factors determining whether a phosphine forms type **I** or **II** adducts involve a delicate balance between the electronic and steric properties of the phosphine. Bulky phosphines such as PPh_3 have been shown to provide axial coordination products whereas a smaller more basic phosphine such as PEt_3 assume equatorial sites (**Figure 5.6**).[251] PPh_2Me has been shown to lie on the borderline between type **I** and **II** and

both forms have been isolated and structurally characterised, made possible through the use of different reaction solvents.[250,253]

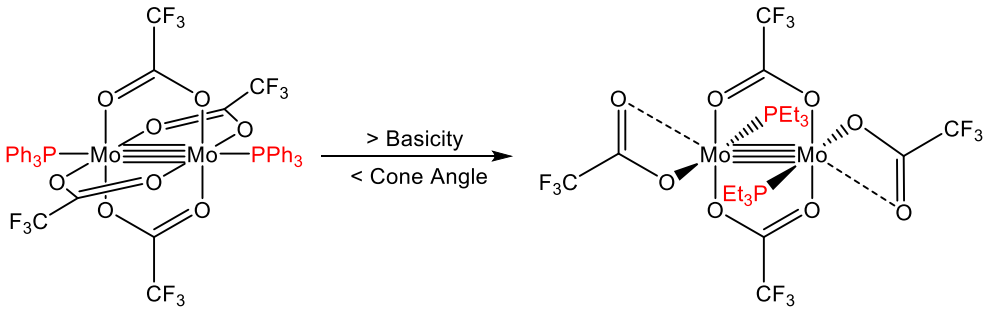

Figure 5.6: A demonstration of how the nature of the phosphine ligand affects the coordination mode.[250]

5.1.2 – Electronic Effects of Equatorial Lewis Base Coordination

Consistent with our interest in manipulating the optical and electronic properties of quadruply bonded carboxylate dimers, it has been shown that the displacement of carboxylate bridging ligands into monodentate coordination modes, as in type **III** systems, results in a significant red shift of λ_{max}, observed by electronic absorption spectroscopy. Specifically, this relates to a decrease in the energetic separation of the $Mo_2\delta$ and $Mo_2\delta^*$ orbitals. This observation can be rationalised by considering the π-orbital interactions between the carboxylates and the $M_2\delta$ orbitals, which are shown in **Figure 5.7**.

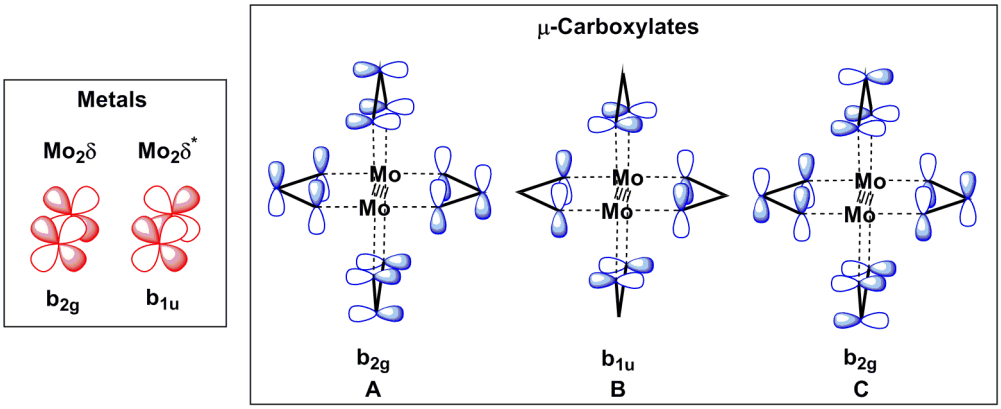

Figure 5.7: Symmetry-labelled $Mo_2\delta$ and $Mo_2\delta$ orbitals (red) and π-orbital combinations for the four μ-carboxylate ligands (blue).

The orbital pictures **A-C**, Shown in **Figure 5.7**, are composed of the bonding, non bonding and antibonding combinations of the {$^{-}O_2CR$} π-orbitals (blue). When combined into the 'paddlewheel' motif shown, the combined ligand orbitals span b_{2g} (**A** and **C**) and b_{1u} (**B**) symmetry which allow interaction with the $M_2\delta$ (b_{2g}) and $M_2\delta^*$ (b_{1u}) orbitals (red). Both **A** and **B** are filled orbitals whereas **C** is empty. A simplified molecular orbital diagram, constructed by Sattelberger *et al*. shows how the interaction between the π/π* and $M_2\delta/\delta^*$ orbitals affect the electronic structure of the complex (**Figure 5.8**). The red orbital levels on the left represent the $M_2\delta/\delta^*$ orbitals in a system with purely σ-type donors, e.g $[Mo_2Cl_8]^{4-}$, and the blue orbital levels represent the three ligand orbital combinations, **A-C** (shown in **Figure 5.7**). The molecular orbitals levels shown at the centre (ψ_1 - ψ_5) represent a metal carboxylate dimer in which all carboxylate ligands are bridging.

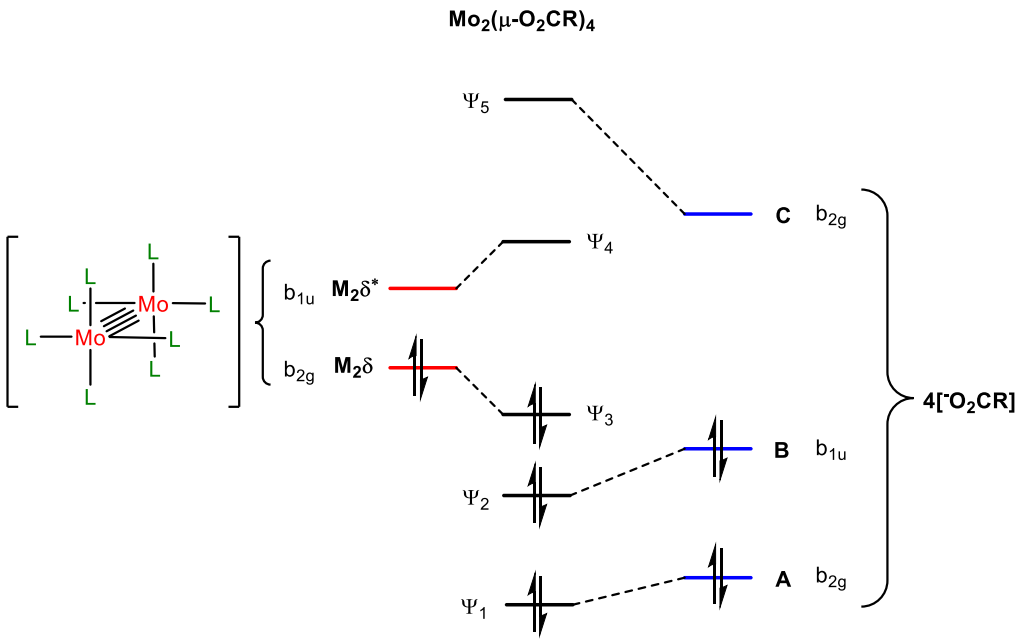

Figure 5.8: π-Molecular orbital combinations between a {Mo_2} quadruple bond and a set of carboxylate ligands.[254]

In a complex of form $Mo_2(O_2CR)_4$ the interactions between the $M_2\delta$ orbitals and the π-manifold of the carboxylate ligands significantly perturb the energy of the metal orbitals. Calculations by Gray *et al*.[204] have shown that, of the two b_2g orbital combinations of the ligands (**A** and **C**), it is the higher energy set, **C**, that predominantly interacts with the $Mo_2\delta$ orbital combinations. This has a stabilising

effect on this metal orbital (ψ_3) whilst destabilising the orbital combination of the ligands (ψ_5). The $M_2\delta^*$ orbital is destabilised *via* interaction with the filled ligand orbital combination **B**, pushing it to higher energy (ψ_4) whilst stabilising the ligand orbital combination (ψ_2). The overall effect of this orbital mixing is to increase the energy gap between the Mo_2 δ and δ* orbitals.

The type **III** phosphine adducts lie in between the two extremes of $[MoL_8]$ and $Mo_2(O_2CR)_4$ (**Scheme 5.9**). The replacement of two μ-carboxylate ligands by σ-interactions, results in a decrease in the δ→δ* energy gap relative to the system with four μ-carboxylate ligands. This is observed by a significant red shift in the absorption spectrum for this electronic transition.

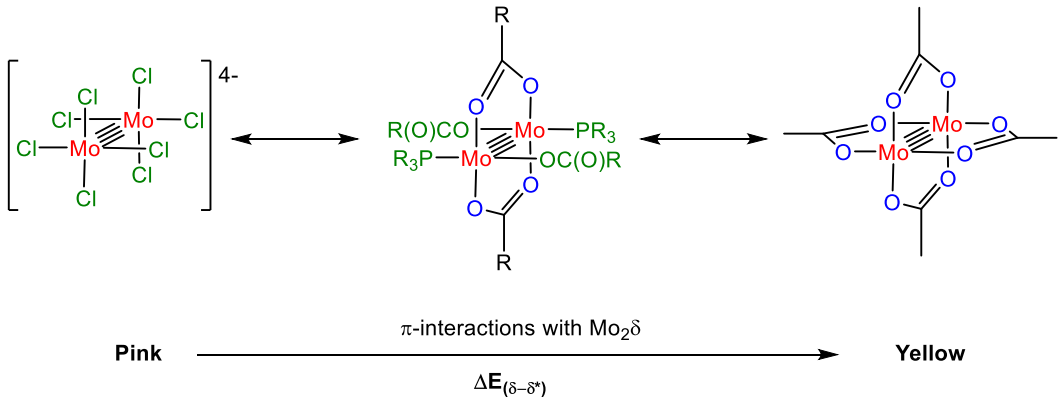

Figure 5.9: Diagram showing how the $M_2\delta \rightarrow M_2\delta^*$ energy gap is affected by the number of μ-O_2CR ligands using $[Mo_2Cl_8]$ and $Mo_2(O_2CCH_3)$ as examples of the two extremes and a "Type **II**" phosphine adduct as an intermediary case.

5.1.3 – N-Heterocyclic Carbenes

Since Arduengo reported the first example of a stable N-heterocyclic carbene in the early 1990s,[256] they have been shown to be extremely popular as ligands and applied in a wide range of organometallic and maingroup complexes. Electronically they are singlet species in which the high energy lone pair of electrons occupies a sp^2 hybridised orbital making the carbenes strong σ-donors. The empty *p*-orbital on the carbenic carbon is stabilised by donation of electron density from the two adjacent nitrogen lone pairs, which renders N-heterocyclic carbenes very poor π-acceptors. These orbitals are shown in **Figure 5.10**. Unlike Fisher and Schrock type carbenes,

which are related only by the presence of a divalent carbon atom, N-heterocyclic carbenes can be isolated in the absence of a stabilising metal atom making them significantly more versatile. It is also very easy to introduce a wide range of substituents on both the nitrogen atoms and upon the backbone of the ligand.

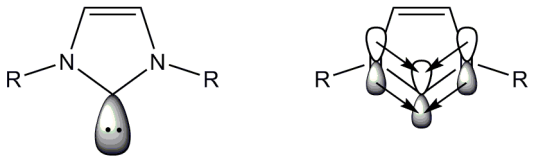

Figure 5.10: Diagram showing the lone pair and π-electron delocalisation in a simple N-heterocyclic carbene.

Comparisons are frequently drawn between N-heterocyclic carbenes and phosphines as they are both good σ-donors and can be modified in order to tune their σ-donor ability.[257-259] As such these ligands can be used to tune the steric and electronic properties of the species to which they are attached. Typically carbenes are stronger σ-donors than phosphines on account of the stabilisation provided by the adjacent heteroatoms. The steric demands of N-heterocyclic carbenes differ from phosphines and can be hard to quantify.[260-261] The geometry of a phosphine bound to a metal is roughly conical and for this reason, the relative sizes of phosphines are discussed in terms of a cone angle.[262] The shape of a carbenes is very different as their projection parallel and perpendicular to the imidazolylidene can differ greatly. For this reason Nolan proposed that two "wedge" angles (A_L and A_H) could be used to express the two dimensions (**Figure 5.11**).[261] These however do not fully describe the steric properties and, although other parameters have also been suggested,[260] it is difficult to predict reactivity of these ligands based on their expected steric demands.

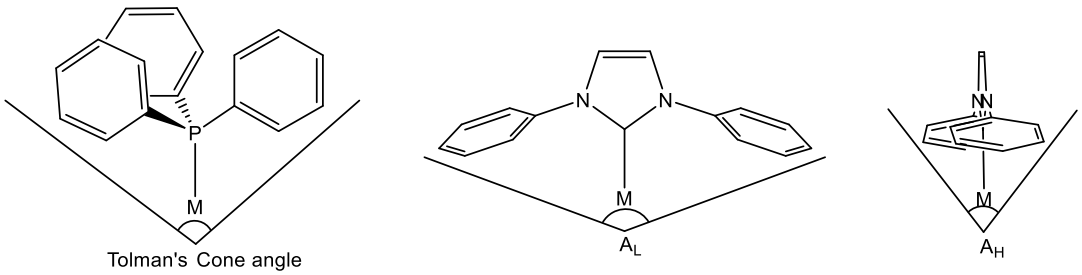

Figure 5.11: Tolman's cone angle and similar angles measurable within N-heterocyclic carbenes to describe the ligands steric demands.[260,262]

To the best of our knowledge, there are no examples of carbene adducts of quadruply bonded dimolybdenum complexes within the literature. We therefore set out to investigate such reactivity to allow comparison with the existing phosphine coordination products. To this end, we have used a range of N-heterocyclic carbene ligands with varying steric properties (**Figure 5.12**).

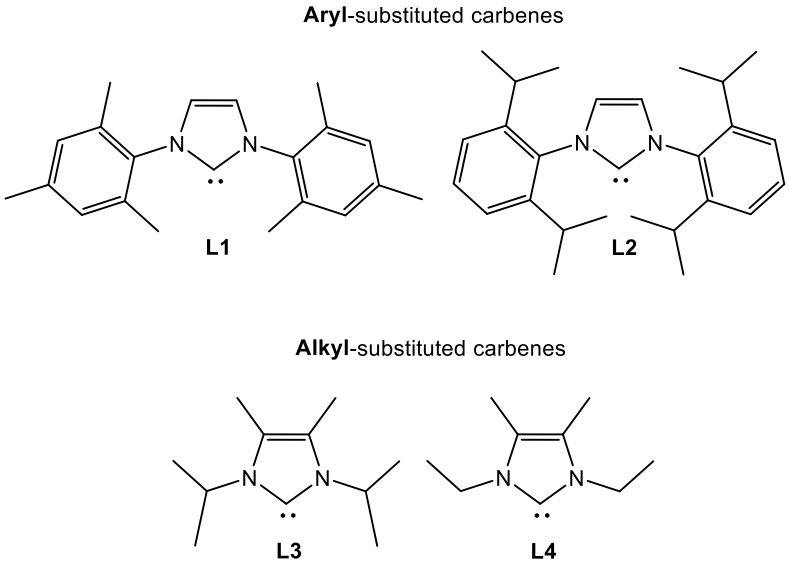

Figure 5.12: N-heterocyclic carbenes studied within this work.

Two of these are aryl-substituted carbenes and contain either mesityl (**L1**) or 2,6-diisopropylphenyl (dipp) (**L2**) groups attached to the nitrogen atoms and have an unsubstituted and unsaturated carbon backbone. The second class of carbenes studied within this work are alkyl-substituted systems with ^{i}Pr (**L3**) or Et (**L4**) groups attached to the nitrogen atoms and methyl substituted, unsaturated carbon backbones. The alkyl substituted carbenes are significantly less sterically demanding

than the aryl containing species, which will potentially effect different reactivity with {Mo_2} carboxylate systems. The presence of the unsaturated backbone in each of the carbene investigated in this study mean that, by Huckel's rule,[263] they are pseudo-aromatic through the five-membered ring.

5.2 – Results and Discussion

5.2.1 –Aryl-Substituted Carbene Adducts of {Mo_2} Carboxylate Dimers

Following the known reactivity between {Mo_2} carboxylate dimers and phosphine ligands, we proposed an analogous approach to the synthesis of N-heterocyclic carbene adducts (**Scheme 5.1**), involving a 2:1 reaction stoichiometry. We began our study by investigating the reactivity of the mesityl-substituted carbene (**L1**) and, to extend the study, a variety of {Mo_2} carboxylates were used to investigate how their steric and electronic properties affect their reactivity.

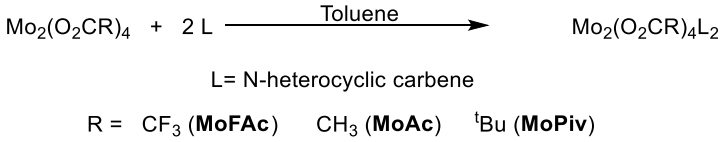

Scheme 5.1: The proposed reaction of $Mo_2(O_2CR)_4$ with N-heterocyclic carbenes.

The 2:1 reaction between **L1** and **MoFAc** in toluene resulted in the immediate formation of a fine yellow precipitate which, on account of the appreciable solubility of both reagents in toluene, suggested that a reaction had occurred. A very similar observation was made for the reaction between **L1** and **MoAc** and, although **MoAc** exhibits negligible solubility in toluene, the morphology of the precipitate differed from the needle-like appearance of the precursor. The precipitates obtained from each reaction could be dissolved by heating the supernatant solvent to reflux. Slow cooling of the resultant solutions yielded highly air sensitive yellow block-like crystals of **MoFAc·L1** and **MoAc·L1**. Interestingly, upon crystallisation both products became essentially insoluble in toluene. The analogous reaction between **L1** and **MoPiv** in toluene produced an orange solution and no precipitate. However, yellow needle-like crystals of **MoPiv·L1** were obtained by cooling a concentrated solution of the reaction mixture to -28 ^{o}C. These too were highly sensitive, rapidly

turning black upon exposure to air. The crystals obtained from the above reactions were all suitable for single crystal X-ray diffraction studies and the molecular structures determined for each product are presented in **Figure 5.13**

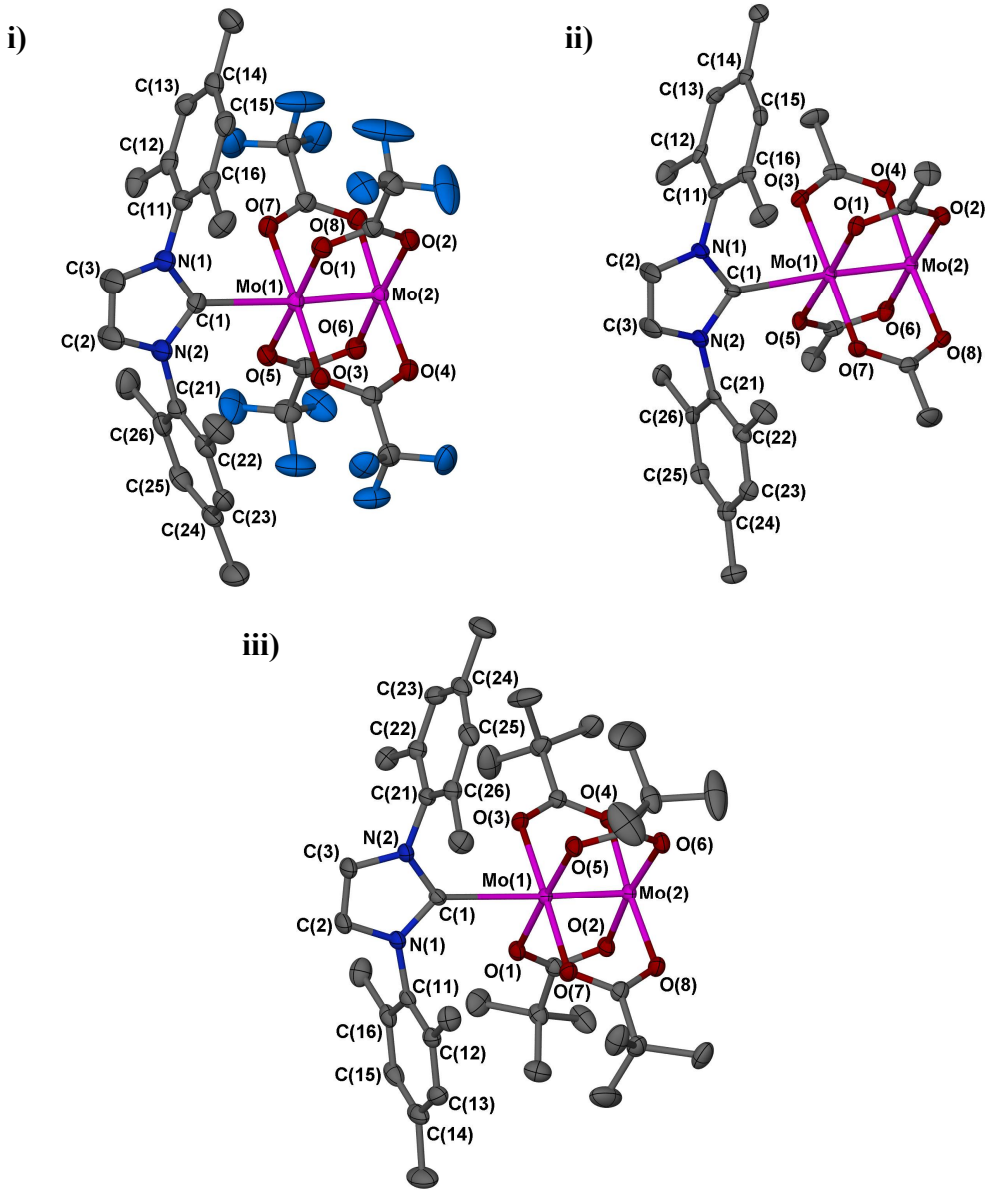

Figure 5.13: Molecular structures of **MoFAc·L1** (**i**), **MoAc·L1** (**ii**) and **MoPiv·L1** (**iii**) with ellipsoids shown at 50 % probability and hydrogen atoms removed for clarity.

MoFAc·L1 and **MoPiv·L1** both crystallise in the monoclinic spacegroup $P2_1/n$ with one molecule in the asymmetric units. The latter also contains a single molecule of toluene within the asymmetric unit which is disordered over an inversion centre in full occupancy. **MoAc·L1** crystallises in the triclinic spacegroup *P-1* with two

symmetry independent molecules within the asymmetric units. Selected bond lengths within the three structures are displayed in **Table 5.1**.

Unlike the common type **II** diaxial adducts obtained from the analogous reactions with a number of bulky phosphine ligands,[247,250,253] the solid state structures containing **L1** are each examples of the much rarer type **I** monoaxial adducts, despite the 2:1 reaction stoichiometry applied in these reactions. Following these observations each of the experiments was repeated using only a single equivalent of the carbene, resulting in the formation of the same species. To the best of our knowledge there are currently no examples of type **I** mono-phosphine adducts of a {Mo_2} dimer.

Table 5.1: Selected bond lengths (Å) within the structures of **MoFAc·L1**, **MoAc·L1** and **MoPiv·L1**

	MoFAc·L1	**MoAc·L1**	**MoPiv·L1**
Mo-Mo	2.1393(3)	2.1119(4), 2.1117(4)	2.1087(2)
Mo-C	2.550(3)	2.562(4), 2.576(4)	2.6965(19)
Mo-O[a]	2.122(2)–2.130(2)	2.115(2)– 2.126(2), 2.115(2)–2.132(2)	2.125(1)–2.136(1)
Mo-O[b]	2.106(2)–2.112(2)	2.108(2)–2.119(2), 2.104(2)–2.116(2)	2.090(1)–2.102(1)

[a] On carbene bound {MoO_4} face, [b] On vacant MoO_4 face

The Mo-Mo bond lengths in all three adducts are longer than their parent {Mo_2} carboxylate dimers (**MoFAc** = 2.1036(4)[246], **MoAc** = 2.0931(2)[264] and **MoPiv** = 2.096(1)[264]) which is consistent with donation of electron density into the respective $Mo_2\sigma^*$ orbitals by the carbene ligands. The most significant elongation is observed for **MoFAc·L1** which exhibits the longest Mo-Mo bond of the series. The Mo-Carbene bond lengths of **MoFAc·L1** and **MoAc·L1** are very similar whilst that of **MoPiv·L1** is significantly longer, signifying a weaker interaction. We surmise that this is likely to be due to a combination of the increased steric demands of the

pivalate ligands and the lower Lewis acidity of the Mo centres due to the electron rich carboxylate ligands. Each of the Mo-carbene bond lengths are however each significantly longer than have been observed in previously reported Mo-Carbene coordination complexes, which a search of the 'Cambridge structural database'[265] revealed lie in the range *ca*. 2.16[266]-2.35 Å[267]. Finally, a comparison of the Mo-O bond lengths shows that those on the carbene-bound {MoO_4} face tend to be slightly longer than those on the carbene-free face. This is intuitive when considering that the donation of electron density from the carbene would reduce the effective positive charge on the coordinated Mo centre thus weakening the interactions with the anionic carboxylate ligands.

An analysis of the crystal lattices of each of the type **I** carbene adducts revealed that each of the 'free' axial coordination sites on the Mo-Mo bonds were involved in long range π-interactions with a mesityl ring from a second molecule. This interaction repeats throughout each of the lattices resulting in the formation of coordination polymer-type arrays. One such chain observed in the crystal lattice of **MoAc·L1** is displayed in **Figure 5.14**.

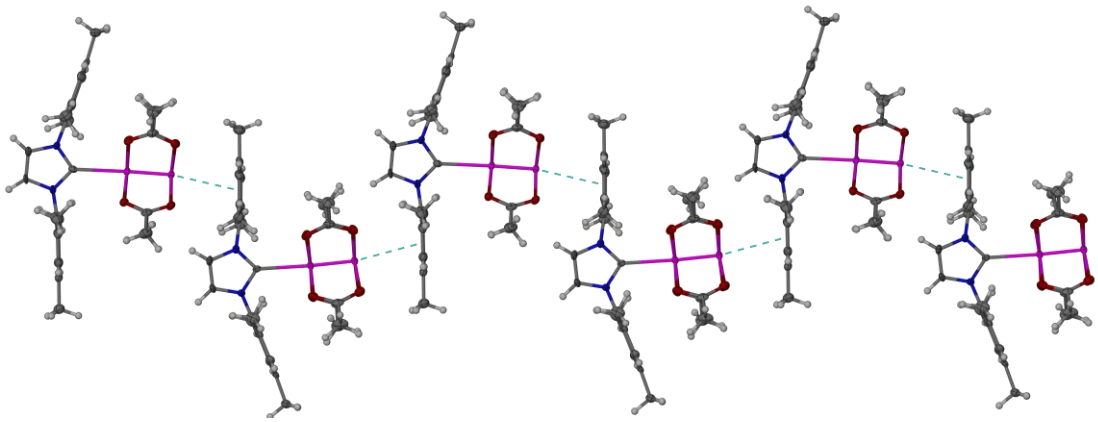

Figure 5.14: A section of the polymeric chain formed within the crystal lattice of **MoAc·L1**

It is likely to be the formation of these supramolecular arrays that results in the observed low solubility of **MoFAc·L1** and **MoFAc·L1**. It is noteworthy that the second mesityl ring of the carbene is not involved in similar interactions.

Side-on aryl interactions such as these are extremely rare for {Mo_2} carboxylate complexes and to the best of our knowledge only four examples have been characterised in the solid state. Unlike our own observations, these examples are limited to interactions with solvent molecules. Both Chishholm and Campana have reported discrete {Mo_2}·Ar_2 units (where Ar = C_6H_6[268] and *m*-xylene[248]) and more recently Calvo-Pérez has provided an example in which *p*-xylene, or toluene, solvent molecules stack between adjacent molybdenum dimers forming continuous "pillar" type conformations within the crystal lattice.[112] The latter used DFT studies to show that the interaction involves electron donation from the filled π-orbitals of the arene to the Mo_2π* orbitals. Selected parameters concerning the Mo-aryl interactions of the three carbene adducts are presented in **Table 5.2** and compared to the analogous data from the related systems from the literature. Any required data that was not reported within the publications was obtained from the respective CIFs.[112,248,268]

Table 5.2: An analysis of known axial-interactions between arene rings and Mo-Mo quadruple bonds.

Complex	Mo-Mo (Å)	Mo···Ar[a] (Å)	{MoO_4}-Ar[b] angle (°)
MoFAc·L1	2.1393(3)	3.179(1)	8.29(4)
MoAc·L1	2.1119(4), 2.1117(4)	3.264(2), 3.271(2)	4.98(5), 4.49(6)
MoPiv·L1	2.1087(2)	3.376(9)	10.70(8)
$Mo_2(O_2CC_2Co_2(CO)_6)_4$ – toluene[112]	2.102	3.12	0.6
$Mo_2(O_2CC_2Co_2(CO)_6)_4$ – 1,4-xylene[112]	2.102(3)	3.09	2.0
$Mo_2(O_2CP^tBu_2)_4$ - benzene[268]	2.092(3)	3.01	22.3
$Mo_2(O_2CCF_3)_4$ – 1,3-xylene[248]	2.113(1)	2.99(1)	8.9

[a] Defined as the closed point of contact between Mo and an average plane defined through the arene. [b] The torsion angle between planes defined through the appropriate {MoO_4} face and through the arene.

The lengths of the Mo···Arene interactions increase in the order **MoFAc·L1** < **MoAc·L1** < **MoPiv·L1**. This trend can be attributed to the decreasing Lewis acidity of the Mo centres along this series in addition to the increased steric demands of the pivalate containing complex. These interactions are all significantly longer than those observed in the related systems within the literature for which the interacting arenes are significantly smaller and less sterically demanding than the carbene within our own studies. The torsion angles observed between the {MoO_4} and aryl planes exhibit only slight deviation from coplanarity and appear to increase with the increasing steric demands of the carboxylate ligands (Me < CF_3 < ^{t}Bu). Very small torsion angles were also observed in the majority of the literature reported species providing evidence of side-on π-interactions with the metal centre in this class of complex. Interestingly, the Mo-Mo bond length within the 1,3-xylene adduct is only slightly elongated relative to the parent carboxylate dimer (2.1036(4)[246] Å). The variation in the analogous bond lengths observed within our own complexes are therefore likely to be dominated by the σ-carbene interaction at the other end of the molecule. This is also supported by the relatively small Mo-Mo bond lengths in the remaining literature species, for which molecular structures in the absence of the solvent moleules have not been obtained.

It is noteworthy that analogous *mono*-**L1** adducts have previously been reported for singly-bonded Rh(II) acetate dimers in addition to an example bearing the bulkier 2,6-diisopropylphenyl substituted carbene (**L2**).[269-271] Although it was not reported, the mesityl containing system also exhibits the same axial interactions between the Rh-Rh bond and the mesityl ring. However, the origin of this interaction must involve different orbitals to those in the molybdenum complexes because the $Rh_2\pi^*$ orbitals are occupied, so cannot accept electron density. The 2,6-diisopropylphenyl substituted carbene did not display the same stacking which is likely due to the isopropyl moieties preventing close enough approach of the aromatic ring to the M-M bond. In addition to the reports of aryl-substituted carbene monoadducts of dirhodium adducts, there is also an example of a tetramethyl N-heterocyclic carbene monoadduct.[272]

The π-interactions proposed for these systems are very weak and involve only a small amount of orbital overlap. The position of the arene ring relative to the Mo

atom will therefore be important in determining how much electron density can be donated in the interaction. **Figure 5.15** shows each of the carbene *mono*-adducts viewed along the length of the Mo-Mo bond.

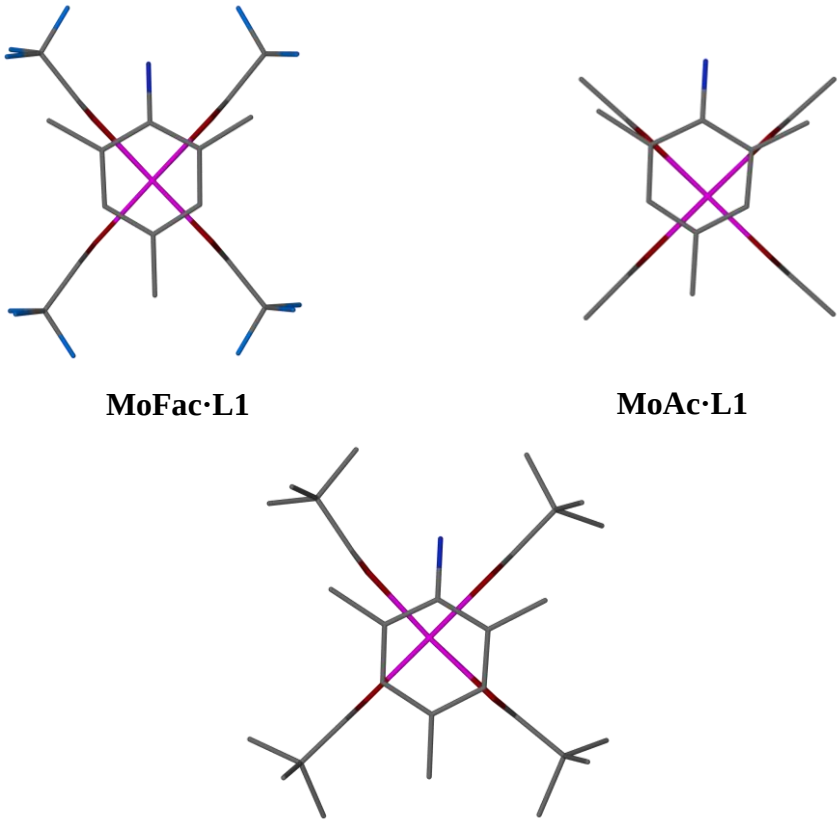

Figure 5.15: Diagrams showing the position of the mesityl ring relative to the axial position on the three $Mo_2(O_2CR)_4$ units.

The images show that, in both **MoAc·L1** and **MoPiv·L1**, the ring is significantly offset from the axial position of the Mo-Mo bonds. In contrast, the mesityl ring in the **MoFAc·L1** is almost completely centred over the molybdenum atom. This is likely to increase the π-orbital overlap in this complex and result in a stronger interaction than in the alkyl carboxylate systems. This observation correlates with the relatively short Mo-Arene separation in this species and may once again be a factor of the increased Lewis acidity of the Mo atoms in this system.

In consideration that the each of the type **I** *mono*-carbene adducts were initially obtained in the presence of two equivalents of carbene, it is intuitive that, in the solid-state, the mesityl π-interaction is favoured over the coordination of a second carbene ligand. This therefore precludes the formation of type **II** diaxial adducts when using **L1**. In order to investigate whether it is possible to access type **II** carbene adducts, the bulkier dipp-substituted carbene (**L2**) was investigated to try and prevent the Mo-aryl interactions. Reactions were carried out in a 2:1 carbene to {Mo_2} ratio as depicted in **Scheme 5.2**.

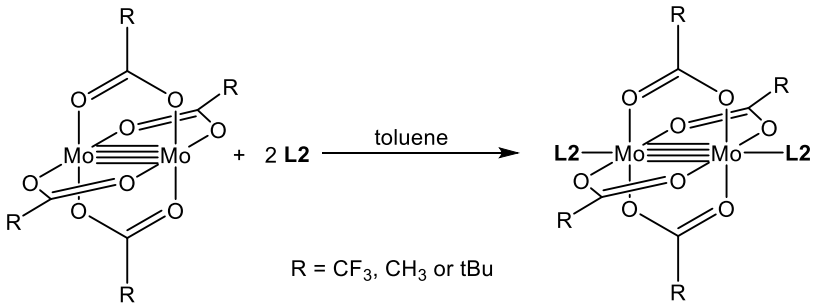

Scheme 5.2: Proposed synthesis of type **II** carbene adducts of {Mo_2} carboxylate dimers.

The reaction between **MoFAc** and **L2** in toluene resulted in the formation of a pale orange solution, which immediately contrasted with the analogous reaction using **L1** in which the product precipitated immediately upon addition of the solvent. A large crop of highly air sensitive yellow block-like crystals of **MoFAc·L2** were isolated by cooling the concentrated reaction mixture to - 28 ^{o}C. Unfortunately, no products could be isolated from the reactions involving either **MoAc** or **MoPiv**. It is possible that this relates to the lower Lewis acidity of the Mo centres in these systems, which are unable to facilitate strong enough bonding interactions with the relatively bulky carbene.

Despite the large size of the crystals isolated for **MoFAc·L2** they diffracted X-rays very poorly and as such we were unable to obtain a structure from those grown from toluene. However, crystals grown from xylene allowed the collection of a low quality dataset through which the molecular structure could be determined (**Figure 5.16**), solved in the monoclinic spacegroup *$P2_1/c$* with one molecule in the asymmetric unit and one molecule of **MoFAc·L2** and one molecule of xylene within

the asymmetric unit. Although the poor quality of the data precludes a discussion of the magnitude of the geometric parameters, the structure definitively shows the formation of the targeted type **II** diaxial adduct in the solid-state. The two carbene molecules are arranged perpendicularly with respect to each other and the ^{i}Pr substituents on the aryl rings project into the voids between the carboxylate ligands. On account of the poor quality of the crystallographic data, the purity of the solid sample of **MoFAc·L2** was confirmed through elemental analysis.

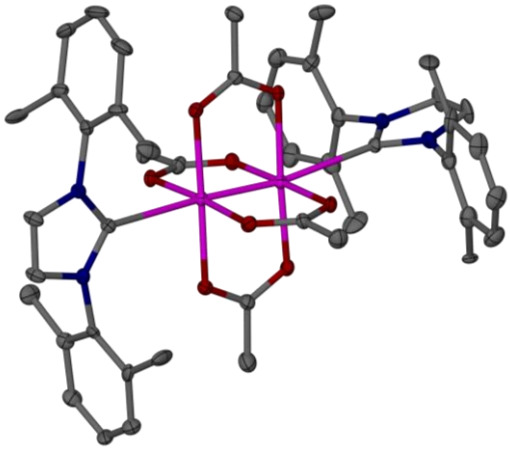

Figure 5.16: The core structure of **MoFAc·L2** shown at 20% probability with hydrogens, fluorines and ^{i}Pr-CH_3 groups removed for clarity.

To further analyse how the carbene interactions affect the nature of the Mo-Mo bond in the solid-state we have used Raman spectroscopy to measure the Mo-Mo stretching frequencies in each system. This also provides a means by which to characterise the Mo-Mo bond of **MoFAc·L2**, which was not possible though single crystal X-ray diffraction studies. The data recorded is displayed in **Table 5.3** and, where possible, the data is compared to the experimentally measured Mo-Mo bond lengths. To allow comparison the analogous data for the parent {Mo_2} carboxylate dimers is also presented.

Table 5.3: A comparison between the Mo-Mo bond length (Å) and Raman stretching frequency (cm^{-1}) of the {Mo_2} axial carbene adducts.

Complex	Mo-Mo bond length (Å)	υ(Mo-Mo) (cm^{-1})
MoFAc	2.1036(4)[246]	397[247]
MoAc	2.931(2)[264]	403
MoPiv	2.096(1)[264]	403
MoFAc·L1	2.1393(3)	363
MoAc·L1	2.1119(4)	386
MoPiv·L1	2.1087(2)	378
MoFAc·L2	n/a	382

The data measured shows that axial coordination of the carbenes results in a decrease in the υ(Mo-Mo) relative to the parent complexes. This correlates with the concomitant elongation of the Mo-Mo bonds within the adduct species and reflects the destabilising donation of electron density into the Mo_2σ* orbitals. The lowest energy υ(Mo-Mo) was observed for **MoFAc·L1** which has been shown to contain the longest Mo-Mo bond length of the series. However, the highest energy bond vibration was measured for **MoAc·L1**, which exhibits a slightly longer Mo-Mo bond length than **MoPiv·L1**. This suggests that other subtle electronic effects within the complexes also play a role in determining the magnitude of υ(Mo-Mo). The data measured for **MoFAc·L2** suggests an intermediate bond strength lying between those of **MoAc·L1** and **MoPiv·L1**. This is slightly surprising considering that there are two carbene molecules donating into the Mo_2σ* orbitals in **MoFAc·L2**, however, the greater steric demands of **L2** versus **L1** may result in a weaker bonding interaction within this species. The υ(Mo-Mo) of **MoFAc·L2** is also significantly higher in energy than was reported by Cotton *et al*. for the related *bis*-pyrdine adduct of **MoFAc** (367 cm^{-1}),[273] again providing evidence for the relatively weak Mo-carbene interaction.

5.2.2 – Theoretical Studies on Type I {Mo_2} Carbene Adducts

On account of the unusual coordination modes observed within the solid-state structures of the type **I** {Mo_2} carbene adducts, we used DFT studies to gain a greater understanding of the electronic structure of these species and to try and ascertain why a π-aryl interaction appears to be favoured over the coordination of a second σ-bound carbene. Within this study we have focussed on **MoFAc·L1**, as this species exhibited the strongest Mo-carbene interactions. The gas-phase geometry of **MoFAc·L1** was optimised prior to the calculation of electronic surfaces. All calculations were performed using the B3LYP exchange correlation functional and the 6-31G(d) basis sets for all atoms except molybdenum for which SDD energy consistent pseudopotential and the SDD energy consistent basis set was used.

A section of the molecular orbital diagram calculated for **MoFAc·L1** is presented in **Figure 5.17**, accompanied by electron density plots of selected calculated frontier orbitals. The HOMO of the system is the $Mo_2\delta$ orbital, which is standard for quadruply bonded {Mo_2} carboxylate species.[76,108,126,186,204,274-275] The HOMO -1 is the $Mo_2\sigma$ orbital which is higher in energy than the two $Mo_2\pi$ combinations due to mixing with the carbene σ-orbitals. The HOMO-2 to HOMO-4 are largely composed of mesityl-localised π-orbitals, exhibiting negligible mixing with the orbitals of the metal centres. The HOMO-5 and HOMO-6 both contain significant contribution from one set of $Mo_2\pi$ orbitals and exhibit significant mixing with the π-orbitals of the imidazolylidene ring. The second $Mo_2\pi$ orbital (HOMO-7) is not of appropriate symmetry to mix with the carbene based orbitals and is thus lower in energy.

The LUMO of **MoFAc·L1** is the $Mo_2\delta^*$ orbital and the LUMO +1 and LUMO +2 are the $Mo_2\pi^*$ orbitals. These are split in energy due to mixing from the carbene π-system in the former, stabilising the orbital. The $Mo_2\sigma^*$ orbital (LUMO+9) is higher in energy than a series of carboxylate based π*-orbitals (LUMO +3 to LUMO + 6) and two mesityl based π*-orbitals (LUMO +7 and LUMO+8).

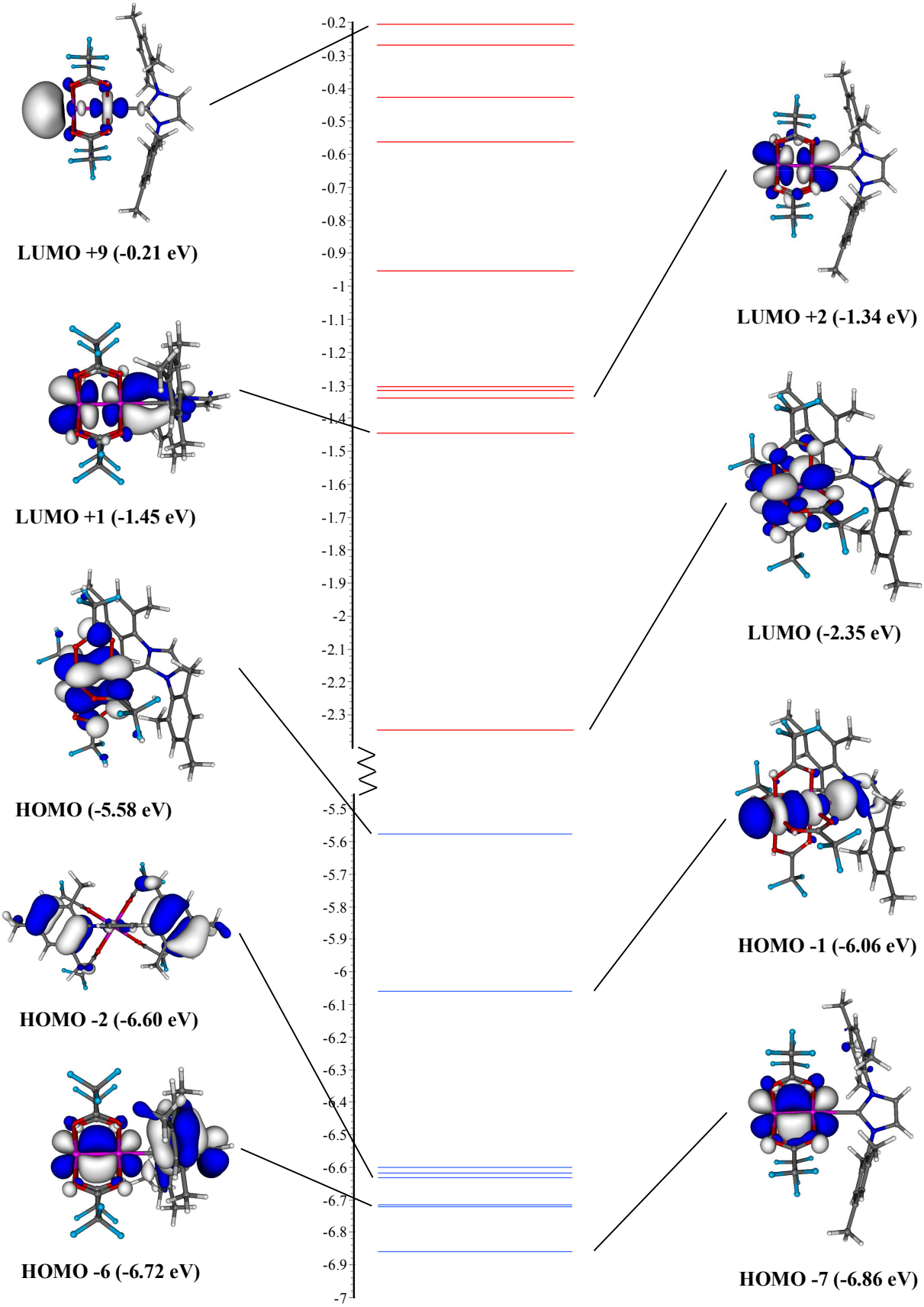

Figure 5.17: Molecular Orbital Diagram of **MoFAc·L1** and selected orbital plots.

In order to form a type **II** diaxial adduct from **MoFAc·L1** a second carbene molecule would be required to donate into the available $Mo_2\sigma^*$ orbital (LUMO+9). However, our calculations show that the energy of this orbital (-0.21 eV) is significantly higher than the $Mo_2\sigma^*$ in the parent complex **MoFAc** (-1.72 eV), which was calculated under the same conditions. This provides evidence that upon formation of the monoaxial adduct coordination of a second carbene ligand is significantly less favourable. It is therefore feasible to consider that an interaction between the relatively high lying filled π-orbitals of the mesityl substituents (HOMO-2 to HOMO-4) and the relatively low energy $Mo_2\pi^*$ orbital is favoured, providing the orbital overlap is sufficient to stabilise the interaction.

The data obtained from the electronic structure calculations also shows that coordination of the carbene in **MoFAc·L1** results in a slight polarisation in the Mo-Mo bond, observed through a difference in the calculated Mulliken atomic charges of the two metal centres. The carbene coordinated Mo atom exhibits a more positive charge than the free Mo centre, which is consistent with the longer Mo-O bonds observed in the solid state structure on the carbene-coordinated face. Although these calculations are performed in the gas-phase and do not take into account the Mo-mesityl interaction, it is fair to assume that the greater distance and poorer orbital overlap involved with the Mo-arene interaction would result in less electron donation to the molybdenum atom than the σ-interaction at the other end of the molecule and is therefore unlikely to counter the Mo-Mo bond polarisation.

5.2.3 – NMR Analyses of Axial {Mo_2} Carbene adducts

Following observation of the interesting coordinative behaviour of the aryl-substituted N-heterocyclic carbenes towards {Mo_2} carboxylate dimers in the solid-state, we were interested to see how these species behaved in solution. Unfortunately **MoAc·L1** was essentially insoluble in most common organic solvents and as such further analysis of this species was not possible. Although the product initially dissolves in d_5-pyridine, a yellow precipitate rapidly forms and subsequent NMR analysis revealed a *sub*-1:1 {Mo_2} to carbene, ratio despite elemental analysis showing that the sample is pure. We believe that the pyridine, a competitive Lewis base is able to displace some of the carbene resulting in the formation and

subsequent precipitation of a quantity of the diaxial pyridine adduct of **MoAc**, which we have observed previously in related studies.

Although **MoFAc·L1** was essentially insoluble in C_6D_6 and d_8-toluene the product was sufficiently soluble in d_8-THF to allow analysis by NMR spectroscopy. The ^{1}H spectrum exhibited a single sharp resonance corresponding to each of the carbene proton environments consistent with a single carbene environment on the NMR time-scale. The resonance corresponding to the carbene backbone was observed at δ = 7.49 ppm whilst the analogous resonance for the free carbene is observed at 7.01 ppm under the same conditions.[276] This significant down-field shift suggests that a degree of coordination is maintained in solution. The ^{19}F NMR spectrum exhibited a single sharp resonance at -73.5 ppm which exhibits negligible shift from the analogous resonance observed for **MoFAc**. Due to the absence of protons in **MoFAc** we cannot use this data to confirm the 1:1 ratio but the absence of any precipitate correlated with both crystallographic and elemental analyses suggests the presence of the same species in solution. It must be considered that this analysis was performed in a coordinating solvent and these solvent interactions may affect the solution state properties of the product.

Due to the greater solubility of the remaining products, NMR analyses of **MoPiv·L1** and **MoFAc·L2** were both performed using C_6D_6 solutions. Consistent with the observations made for **MoFAc·L1**, the ^{1}H NMR spectrum of **MoPiv·L1** exhibited a single sharp resonance for each of the carbene proton environments and a single resonance corresponding to the pivalate protons. Integration of the signals confirmed the 1:1 ratio. The backbone proton of the carbene was observed at 6.13 ppm which, unlike the **MoFAc** analougue analysed in d_8-THF, was shifted up-field from the analogous resonance observed for the free **L1** (6.49 ppm in C_6D_6). This perturbation is again suggestive of a coordinative interaction persisting in solution but also highlights that that the properties of these systems in solution are likely to be solvent dependent. The ^{1}H NMR spectrum of **MoFAc·L2** also exhibited a single resonance for each proton environment on the carbene with the exception of the isopropyl-CH_3 resonances, which were represented by two doublets. Considering the solid state structure for this species (**Figure 5.16**) the two doublets are likely to reflect magnetic environments of CH_3 groups pointing towards and away from the {Mo_2} core. The

resonance corresponding to the backbone proton appears at 6.16 ppm and, consistent with the observations made for **MoPiv·L1**, is shifted up-field relative to the free carbene (6.57 ppm).[277] The ^{19}F NMR spectrum showed a single resonance at -71.0 ppm showing a single fluorine containing species was present in solution on the NMR time-scale. As with **MoFAc·L1**, the carbene:{Mo_2} ratio cannot be confirmed from the NMR analyses but is supported by crystallographic and elemental analyses.

$^{13}C\{^1H\}$ NMR analyses were also performed on all of the discussed complexes and the data was consistent with the structures that have been assigned. It is worth mentioning that despite the long acquisition times used to collect these data, we were unable to observe a resonance corresponding to the carbenic carbon in any of the systems, which may be a product of ligand exchange within these systems.

5.2.4 – Alkyl-Substituted Carbene Adducts of {Mo_2} Carboxylate Dimers

Following the observation that the relatively bulky, aryl-substituted carbenes (**L1** and **L2**) react with {Mo_2} carboxylate dimers to form axial adducts, the second section of this work investigates the differing chemistry of alkyl-substituted carbenes **L3** and **L4** (**Scheme 5.3**). The reactions were performed using an analogous method to those described for the reactions with **L1** and **L2**, implementing a 2:1 carbene to {Mo_2} stoichiometry and using toluene as the reaction solvent.

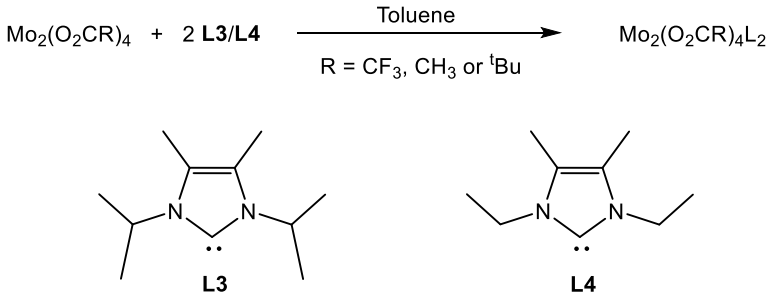

Scheme 5.3: The synthesis of alkyl-substituted carbene adducts of {Mo_2} carboxylate dimers.

The reaction between **MoFAc** and **L3** in toluene instantly resulted in the formation of a highly air-sensitive dark red solution. This colour change contrasts with the observations made in the analogous reactions performed with **L1** and **L2**, indicating

a difference in the reactivity of the alkyl-substituted carbene. The same observation was also made within the analogous reaction with **MoAc**. Crystals of **MoFAc·L3** (red) and **MoAc·L3** (purple) were grown by cooling the concentrated reaction mixtures to -28 ^{o}C.

Very similar observations were made within both reactions with **L4**, however, the products containing the ethyl-substituted carbene appeared to be significantly less soluble than the **L3**-analogues. The reaction between **MoFAc** and **L4** instantly formed a dark red solution but after a short period of stirring a pink precipitate formed which could not be re-dissolved. The reaction was repeated, stirring only briefly to dissolve the reagents and, when left to stand overnight, a crop of red crystals of **MoFAc·L4** was obtained. Unfortunately the analogous reaction with **MoAc** also resulted in the instant formation of a pink precipitate and this was insoluble in all common organic solvents, preventing separation from unreacted **MoAc** and precluding characterisation of this species. The observed colour change is, however, likely to reflect the formation of a similar class of complex to those obtained from the previous series of reactions.

The three crystalline products were characterised in the solid state using single crystal X-ray diffraction and the molecular structures of each species are displayed in **Figure 5.18**. **MoFAc·L3** crystallise in the monoclinic spacegroup *P2$_1$/n* with half a molecule within the asymmetric unit. Both **MoAc·L3** and **MoFAc·L4** crystallise in the triclinic spacegroup *P-1*. The asymmetric units of each system contain one and two symmetrically independent half-molecules respectively. The crystal lattice of the former also contains two molecules of toluene both with 100% occupancy. The structure of **MoFAc·L4** exhibited rotational disorder of the {CF_3} moieties on the μ-carboxylates of both of the independent half-molecules. Each of these groups was modelled over two positions with the major components of each half-molecule modelled at 63% and 57%. In all of the above structures the second half molecules are generated by inversion symmetry through a vector at the centre at the midpoint of the Mo-Mo bonds

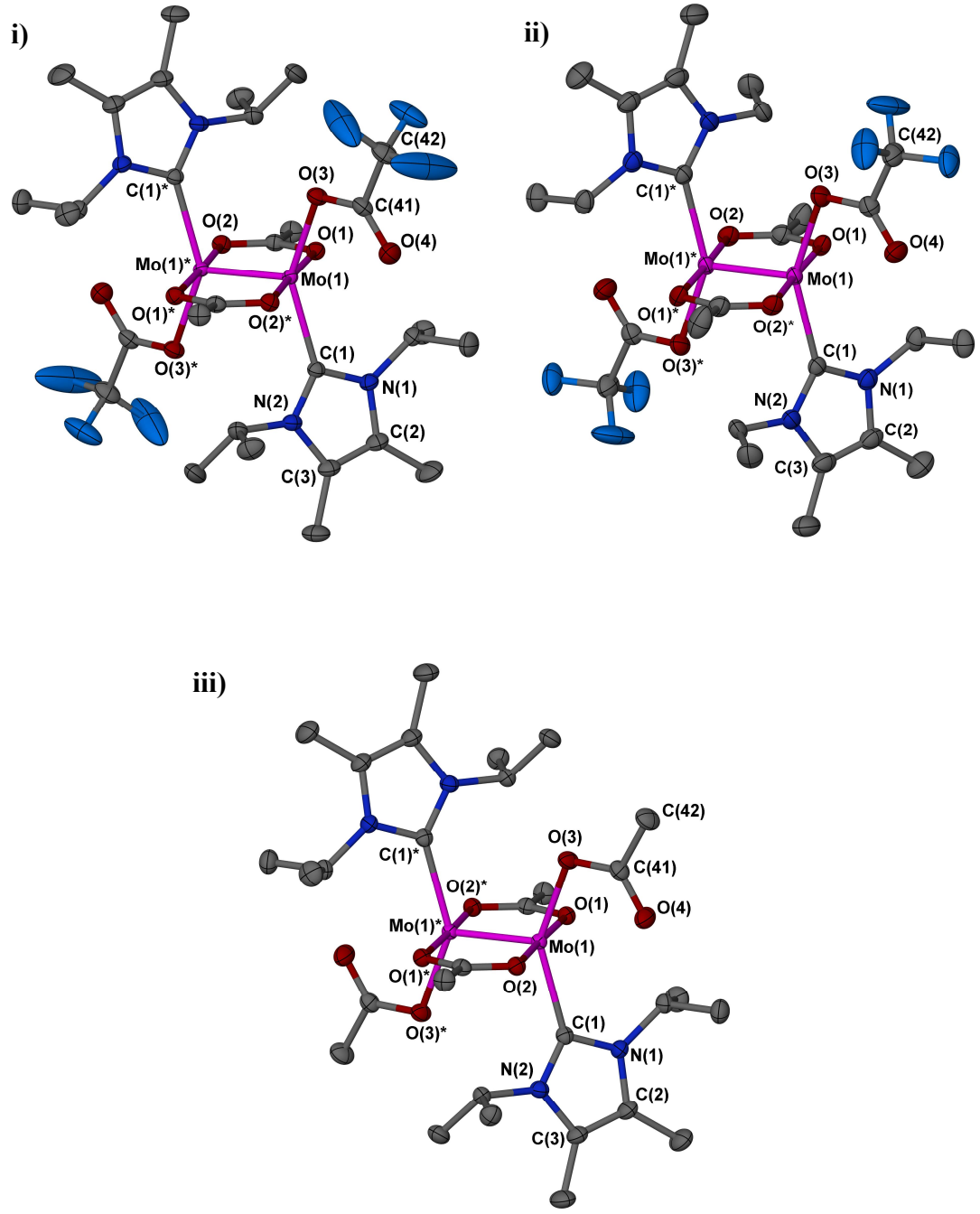

Figure 5.18: Molecular structures of **MoFAc·L3** (**i**), **MoFAc·L4** (**ii**) and **MoAc·L3** (**iii**) with ellipsoids shown at 50 % probability. All hydrogen atoms and fluorine atoms on the μ-$[O_2CCF_3]^-$ ligands have been removed for clarity.

The molecular structures are isostructural containing two coordinating carbene ligands which occupy equatorial Mo coordination sites to provide type **III** adduct systems by the classifications define in **Figure 5.1**. These contrast with the type **I** and type **II** axial adduct systems obtained from the reactions involving **L1** and **L2**, highlighting the divide in the chemistry between the alkyl- and aryl-substituted

carbenes towards {Mo_2} carboxylate systems. In order to assume the equatorial coordination sites, the carbenes displace two of the μ-carboxylate interactions within each structure resulting in the presence of both bridging and monodentate carboxylate environments. The un-bound O atoms of the monodentate carboxylate ligands project away from the {Mo_2} cores in each system facilitating apparent long-range intra-molecular Mo···O interactions. The carbene ligands also project away from the {Mo_2} resulting in pseudo trigonal-bipyramidal geometries around the Mo atoms in each system. These systems are isostructural to the type **III** that have been reported from the reactions of **MoFAc** with certain phosphine ligands, however, to the best of our knowledge **MoAc·L3** represents the first example of a type **III** adduct featuring acetate ligands. Selected bond lengths and angles for each compound are shown in **Table 5.4**. Appropriate parameters reported for phosphine analogues of our own systems are presented in **Table 5.5** to allow comparison.

Table: 5.4: Selected bond lengths (Å) and angles (°) for **MoFAc·L3**, **MoFAc·L4** and **MoAc·L3**.

	MoFAc·L3	**MoFAc·L4**	**MoAc·L3**
Mo-Mo	2.1205(3)	2.1180(6), 2.1134(7)[c]	2.1154(3)
Mo-C	2.245(2)	2.243(4), 2.234(4)[c]	2.254(2)
Mo-O[a]	2.138(1), 2.111(1)	2.125(3), 2.118(3), 2.109(3)[c], 2.147(3)[c]	2.142(1), 2.110(1)
Mo-O[b]	2.158(1)	2.163(3), 2.152(3)[c]	2.154(1)
Mo···O (axial)	2.907(2)	2.830(3), 2.925(4)[c]	2.772(2)
C(1)-Mo(1)-O(3)	144.77(6)	148.6(1), 149.4(1)[c]	144.47(6)

[a] For bridging carboxylate ligands, [b] for monodentate carboxylate ligands, [c] data for the second symmetrically independent molecule of **MoFAc·L4**.

The Mo-Mo bond lengths observed within each of the structures are similar with respect to each other but are each longer than the analogous bonds in the parent complexes (**MoFAc** (2.1036(4)[246] Å) and **MoAc** (2.0934(8)[202]). This is likely to be a

result of the loss of two of the constraining bridging carboxylate ligands in the adduct species. The Mo-carbene bond lengths are also very similar throughout the series and are significantly shorter than the axial Mo-Carbene bond lengths observed within the type **I** carbene adducts (*vide supra*), lying within the range of Mo-carbene bond lengths reported in the literature. This highlights the greater strength of the coordinative interactions at the equatorial coordination sites relative to the axial positions. The monodentate carboxylate M-O bond lengths are significantly longer than those exhibited by the bridging carboxylate ligands. This is likely to reflect the greater *trans*-influence of the carbenes relative to the respective μ-carboxylate ligands. However, each set of M-O bond lengths is very similar within the structures of both the **L3** and **L4** adducts suggesting little difference in the *trans*-influence of the two carbenes. The slightly greater O-Mo-C bond angles observed **MoFAc·L4** does, however, reflecting the subtly different steric demands of the two carbenes. Finally, the Mo···O separations at the axial positions vary significantly throughout the series and are also different within the two symmetrically independent molecules of **MoFAc·L4**, suggesting that the parameter is sensitive to the surrounding packing environment. It is counterintuitive that the **MoAc·L4** exhibits the shortest Mo···O separation despite the less Lewis acidic metal centre in this species.

Table: 5.5: Selected bond lengths (Å) and angles (°) within previously reported phosphine adducts of {Mo_2} carboxylate dimers. {Mo} represents the fragment $Mo(\mu\text{-}O_2CCF_3)_2(O_2CCF_3)_2$.

	{Mo}$(PPhEt_2)_2$[250]	**{Mo}$(PPh_2Me)_2$**[250]	**{Mo}$(PBu_3)_2$**[254]
Mo-Mo	2.100 (1)	2.107 (2)	2.105 (1)
Mo-O[a]	2.109 (2), 2.108 (2)	2.102 (6), 2.086 (6)	2.105 (5)[d]
Mo-O[b]	2.142 (3)	2.137 (6)	2.146 (4)
Mo···O[c]	2.871 (8)	2.803 (7)	2.873 (7)
P-Mo-O	148.09(8)	153.8(2)	152.73

[a] From bridging carboxylate, [b] from monodentate carboxylate, [c] from axial interaction, [d] data provided as an average

Unlike our own type **II** adducts, the phosphine analogues reported within the literature, exhibit no elongation of the Mo-Mo bond lengths relative to **MoFAc**. There is little difference in either the bridging or monodentate carboxylate Mo-O bond lengths between the phosphine and carbene containing structures. The latter suggests that there is little difference between the *trans*-influence applied by either type of Lewis base. The axial Mo···O distances within the phosphine adducts lie within the range observed within this study. The P-Mo-O bond angles, observed in the phosphine adducts, are significantly larger than the related C-Mo-O angles within **MoFAc·L3** or **MoAc·L3**. This may reflect a greater degree of steric repulsion between the carboxylate and carbene ligands across the Mo-Mo bond relative to the analogous situation in the phosphine adducts. A greater steric interaction would cause the two ligands to repel each other to a greater degree and thus result in a smaller L-Mo-O angle, where L = Lewis base (**Figure 5.19**). By this analogy, **L3** appears to be more sterically demanding within such systems than the phosphine ligands. In contrast, the C-Mo-O angles within **MoFAc·L4** lies within the range exhibited by the phosphine systems relating to the lower steric demands of this carbene.

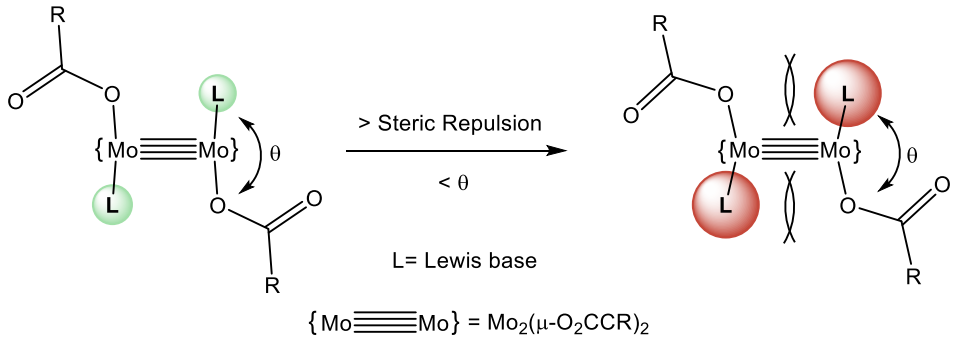

Figure 5.19: An illustration of how an increase in the size of a Lewis base can result in a decrease of the *trans*-L-Mo-O angle.

To aid our interpretation of our structural data, we have also implemented Raman spectroscopic analyses of our three carbene adducts to correlate the Mo-Mo bond length with the stretching frequency. The analyses were carries out on crystalline samples under an inert atmosphere and the measured data is reported in **Table 5.6**.

Table 5.6: Table comparing υ(Mo-Mo) and the Mo-Mo bond lengths in the type **III** {Mo_2} carbene adducts and their parent complexes.

Complex	Mo-Mo bond length (Å)	υ(Mo-Mo) (cm^{-1})
MoFAc	2.1036(4)[246]	397[247]
MoAc	2.0934(8)[202]	403
MoFAc·L3	2.1205(3)	371
MoFAc·L4	2.1180(6), 2.1134(7)	373
MoAc·L3	2.1154(3)	372

Both carbene adducts exhibit significantly lower stretching frequencies than their parent compounds, which is consistent with the longer bond lengths observed within the molecular structure of the adduct systems. We only observed a single stretching frequency for **MoFAc·L4** despite the presence of two independent molecules in the lattice. There is little difference between the υ(Mo-Mo) of the three carbene adducts despite the difference in bond lengths, suggesting that the magnitude of υ(Mo-Mo) is strongly influenced by coordinative environment than a direct reflection of the Mo-Mo bond length. Unfortunately there has been no Raman data reported in the literature for the previously reported type **III** phosphine adducts, precluding a comparative analysis.

5.2.5 – Imidazolium Salt Adduct of an {Mo_2} Carboxylate Dimer

Up until now we have focussed on the reactivity of **MoFAc** and **MoAc** towards alkyl substituted carbene ligands, showing that both {Mo_2} carboxylate dimers behave in a very similar fashion, forming type **III** adduct systems. However, the chemistry differed when the study was extended to the bulkier precursor, **MoPiv**. Following the same method described for the reactions with **MoFAc** and **MoAc** (*vide supra*), **MoPiv** was combined with two equivalents of either **L3** or **L4** and the mixtures were dissolved in toluene, both providing yellow orange solutions. This contrasts with the dark red solutions observed for the previous reactions performed with these carbene ligands suggesting that a different type of interaction occurs in solution.

Unfortunately, we were unable to isolate any product from the reaction performed with **L4**, however, yellow rod-like crystals of **MoPiv·PivL3** were obtained from the reaction with **L3** by cooling a concentrated solution to - 28 °C

MoPiv·PivL3 crystallises in the monoclinic space group *Cc* with one molecule in the asymmetric unit. One of the ^{t}Bu groups was rotationally disordered and was modelled over two positions with the major component at 70 % occupancy. The molecular structure of **MoPiv·PivL3** is presented in **Figure 2.20**.

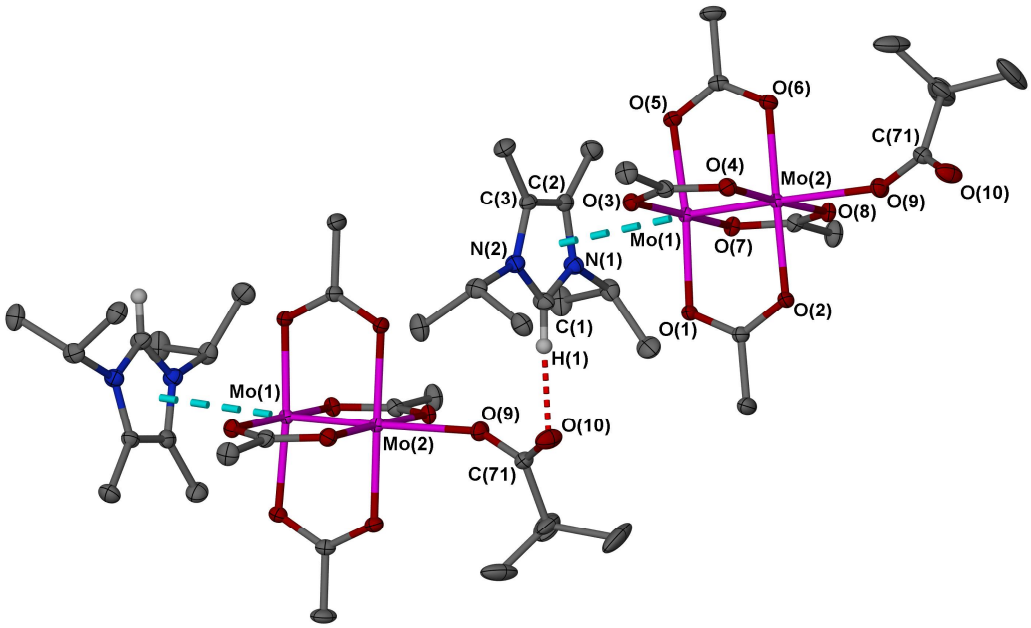

Figure 5.20: Two asymmetric units from the crystal structure of **MoPiv·PivL3** with ellipsoids shown at 30 % probability and all but the imidazolium hydrogen atoms are removed for clarity.

The structure of **MoPiv·PivL3** is composed of a **MoPiv** unit with an axially coordinated pivalate anion on one of the Mo centres. The unsymmetrical coordination about the Mo-Mo bond sees one Mo atom with a pseudo octahedral coordination geometry whilst the second exhibits a pseudo square-based pyramidal geometry. An imidazolium cation formed by protonation of **L3** is present within the lattice as a counterion and interacts with the axial pivalate ligand *via* a hydrogen bonding interaction. The donor···acceptor distance for this interaction is 2.990(4) which can be regarded a medium strength interaction.[278] The hydrogen atom

involved in this interaction was located by assessing the residual electron density within the structure after all other assignments had been made and was allowed to freely refine. Interestingly, an analysis of the crystal packing showed that the imidazolium ring then interacts in a face on fashion to a second molecule of **MoPiv·PivL3**, providing a polymeric array throughout the crystal lattice (Interaction shown in **Figure 5.20**). This Mo-Imidazolium interaction is very similar to the Mo-mesityl π-interactions observed in the type **I** carbene adducts (**Figure 5.14**) and are therefore likely to reflect e^--donation from the imidazolium π-orbitals into the Mo_2π* orbitals.[112] This represents the first example of such an interaction involving a heterocyclic donor.

Selected bond lengths and angles for **MoPiv·PivL3** are presented in **Table 5.7**.

Table 5.7: Selected bond lengths (Å) and angles (°) from **MoPiv·PivL3**.

Mo(1)-Mo(2)	2.094(2)	**Mo(2)-O(6)**	2.131(2)
Mo(1)-O(1)	2.094(2)	**Mo(2)-O(8)**	2.112(3)
Mo(1)-O(3)	2.114(2)	**Mo(2)-O(9)**	2.324(2)
Mo(1)-O(5)	2.103(2)	**C(1)-O(10)**	2.990(4)
Mo(1)-O(7)	2.115(2)	**Mo(1)···L3**[a]	3.306(2)
Mo(2)-O(2)	2.133(2)	**{MoO_4}∠L1** [b]	11.07(13)
Mo(2)-O(4)	2.120(2)		

[a] Defined as the shortest contact between Mo(1) and a plane containing the imidazolium ring.

[b] The angle made between the imidazolium ring and the close proximity MoO_4 face of the {Mo_2} carboxylate dimer.

The axial Mo-O bond length is significantly longer than those of the equatorial Mo-O bonds, showing that this interaction in a lot weaker, as would be expected of axial coordination. The Mo-Mo bond length is no different, within error, to that of parent complex **MoPiv** (2.096(1) Å)[264]. This suggests that the interactions at either side of the Mo-Mo bond are fairly weak as population of {Mo_2} antibonding orbitals would result in a weakening of the Mo-Mo bond. It can also be observed that Mo(2)-O(2)

and Mo(2)-O(6) bonds are significantly longer than the other equatorial Mo-O bonds within the molecule. These bonds are both on the {MoO_4} face that involves the axial pivalate interaction, which is consistent with our observations in our type **I** carbene adducts. We previously attributed this observation to the polarisation of the Mo-Mo bond due to the unsymmetrical coordination environment which is likely to be the same within **MoPiv·PivL3**. However, we are unsure as to why the effect is only localised on two of the four Mo-O bonds in this instance. The four Mo-O bonds on the pivalate-coordinated {MoO_4} face are all the same within error.

The distance between Mo(1) and the imidazolium ring is slightly shorter than the Mo-mesityl separation that was observed in the related species (**MoPiv·L1**). The angle between planes defined through the imidazolium ring and the appropriate {MoO_4} face shows slight deviation from coplanarity, moving the ^{i}Pr groups away from the sterically demanding pivalate ligands. The angle only differs slightly from the related angle observed in **MoPiv·L1** (10.70(8)^{o}). **Figure 5.21** displays a wireframe picture of the **MoPiv·PivL3** viewed down the Mo-Mo bond, showing that the imidazolium ring is only slightly off-centred from the axial position of the Mo-Mo bond. The two fragments are therefore well orientated for an intermolecular π-interaction although poor orbital overlap is likely to render this interaction extremely weak.

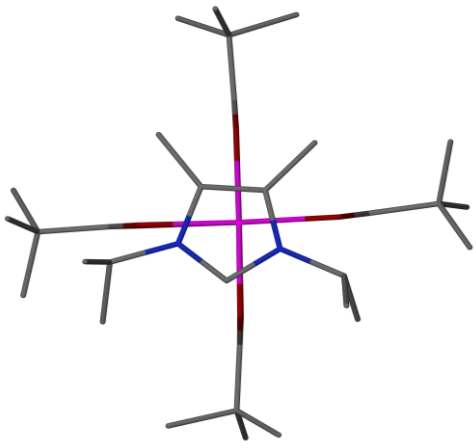

Figure 5.21: Wireframe structure of **MoPiv·L3** viewed along the Mo-Mo bond showing the position of the imidazolium ring with respect to the {Mo_2} carboxylate dimer.

To the best of our knowledge the only structurally characterised example of a molybdenum quadruple bond with an axially coordinated carboxylate ligand is $[Mo_2(O_2C^tBu)_5][N^nBu_4]$ (**Figure 5.22**),[244] which was synthesised by Chisholm *et al. via* the reaction of **MoPiv** with $[O_2C^tBu][N^nBu_4]$. Structural analysis of this species showed that the axial Mo-O bond length is comparable to our own (2.298(5) Å).[244] Unlike **MoPiv·PivL3**, there are no axial interactions at the second Mo centre in the literature species.

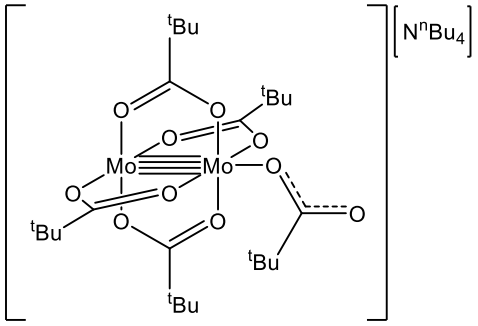

Figure 5.22: The structure of $[Mo_2(O_2C^tBu)_5][N^nBu_4]$.[244]

The ^{1}H NMR spectrum of **MoPiv·PivL3** was consistent with the determined solid-state structure (**Figure 5.20**), exhibiting a singlet at 11.7 ppm indicative of the presence of an imidizolium species in solution. The relative resonance integrals confirmed the 1:1 **MoPiv** to **$[O_2C^tBu][L3H]$** ratio. The two pivalate environments were represented by two sharp singlets showing that the two ligands environments are independent within the NMR time-scale. This contrasts with the observations made for $[Mo_2(O_2CN^tBu)_5][N^nBu_4]$ in which a broad resonance, corresponding to all five pivalate ligands was observed.[244] Variable temperature NMR studies conducted on $[Mo_2(O_2C^tBu)_5][N^nBu_4]$ showed that exchange between the axial and bridging pivalate ligands was occurring and the pivalate resonances coalesced only at -80 ^{o}C. In addition to this it was shown that when an extra equivalent of $[O_2C^tBu][N^nBu_4]$ was added to the solution, the room temperature ^{1}H NNMR spectrum exhibited both a sharp singlet, representing a single pivalate ligand, and a broad signal, representing five pivalate ligands. The additional ligand was therefore not incorporated into the fluxional system suggesting that a *penta*-pivalate species was favoured. The absence of fluxional behaviour in solutions of **MoPiv·PivL3**, provides evidence that the imidazolium···pivalate hydrogen bonding interaction persists to some degree in

solution, preventing rapid exchange of the pivalate ligands within the NMR time-scale.

It was later found that the formation of **MoPiv·PivL3** resulted from a significant impurity of pivalic acid within the sample of **MoPiv**, resulting in protonation of **L3**. This helps to explain the very low yield of the reaction (11%). Following further purification of the precursor, the reaction with **L3** was repeated. Although there was no evidence of the formation of the previously observed product, **MoPiv·PivL3**, no other products could be isolated from the reaction mixture. In order to gain a better understanding of the nature of the carbene-{Mo_2} interaction in solution, the reaction was repeated on an NMR scale using a 2:1 carbene to **MoPiv** stoichiometry. The ^{1}H spectrum of the reaction mixture recorded in C_6D_6 exhibited one sharp resonance corresponding to the pivalate protons, revealing a single ligand environment within the NMR time-scale. In contrast, the resonances corresponding to the ^{i}Pr-C*H*$_3$ and C*H* environments of the carbene were significantly broadened, reflecting a degree of fluxionality. From these observations it likely that **L3** interacts with **MoPiv** *via* weak axial interactions in solution (**Figure 5.23**). The fluxionality inferred from the ^{1}H NMR spectrum would therefore reflect association and dissociation of the carbene ligands within the NMR time-scale. The difference in the reactivity observed between **MoPiv** and **L3,** relative to **MoFAc** and **MoAc** suggests that, for **MoPiv**, displacement of the bridging carboxylate interactions is not sufficiently compensated by the equatorial coordination of the carbene to facilitate the formation of a type **III** adduct. This is likely to relate to the greater steric demands of the bulky pivalate ligands.

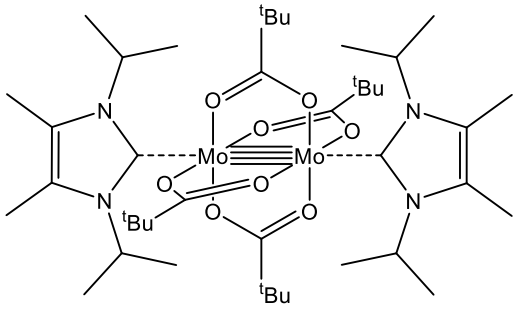

Figure 5.23: The proposed solution state interaction between **MoPiv** and **L2**.

5.2.6 – NMR Analyses of Equatorial {Mo_2} Carbene adducts

To investigate the coordinative behaviour of the type **III** carbene adducts in solution, each has been analysed in a series of NMR experiments.

The room temperature ^{1}H NMR spectra of **MoAc·L3**, **MoFAc·L3** and **MoFAc·L4,** recorded in d_8-toluene, each exhibit a series of broad resonances, representing each of the carbene proton environments and, for **MoAc·L3**, a single broad resonance corresponding to the acetate protons. These observations are consistent with a system in dynamic flux within the time-scale of the experiment. The two acetate environments observed in the solid-state structure are therefore resolved to an average resonance in solution. The room temperature ^{19}F NMR spectra of **MoFAc·L3** and **MoFAc·L4** exhibit two (δ = -72.0 ppm and -74.1 ppm) and three (δ = -71.1 ppm, -72.1 ppm and -74.6 ppm (*ca*. 2:1:3)) sharp resonances respectively. In the former, the two resonances can be assigned to the bridging[279] and monodentate[280] carboxylate ligands respectively, however, the presence of an additional resonance in **MoFAc·L4** may suggest the presence of a second isomeric conformation in solution. Similar observations have been made for related species reported in the literature.[251]

Warming a d_8-toluene solution of **MoAc·L3** to 85 ^{o}C results in significant sharpening of each of the broad resonances observed in the room temperature ^{1}H NMR spectrum, providing a single well resolved resonance corresponding to the acetate protons. The only resonance that does not fully resolve at this temperature is that corresponding to the ^{i}Pr-methine protons, which remains broad. This data is represented by the red trace in **Figure 5.24** alongside the room temperature spectrum (black).

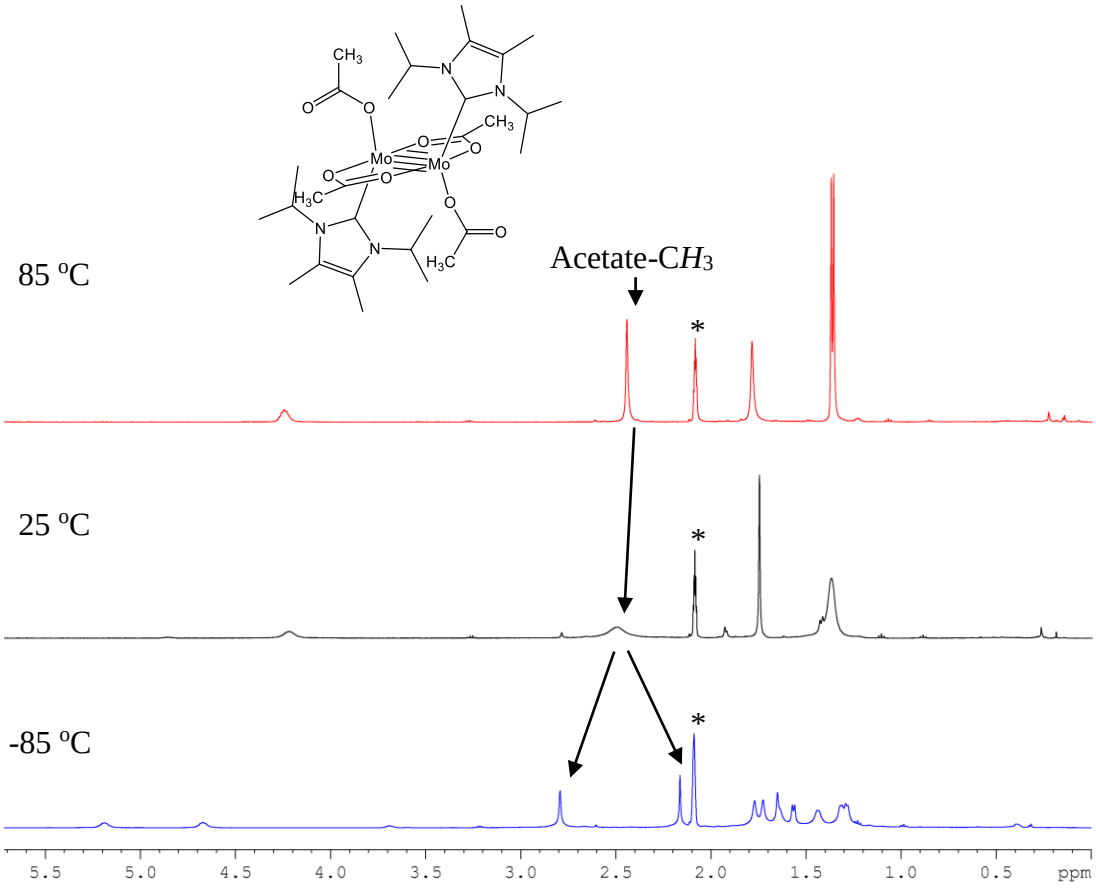

Figure 5.24: A Stack of three ^{1}H NMR spectra of **MoAc·L3** recorded at 85 °C (red), 25 °C (black) and -85 °C (blue) in d_8-toluene. Resonances corresponding to protonated solvent residue are marked with am asterisk.

Upon cooling the solution of **MoAc·L3** the broad resonance corresponding to the acetate protons began to flatten to the base line and at -85 °C it is replaced by two singlet resonances (blue trace in **Figure 5.24**). These can be attributed to bridging and monodentate acetate environments providing evidence that at low temperature the solution-state structure is similar to that observed in the solid-state. Cooling the sample also results in the splitting of each of the carbene proton resonances yielding four broad doublet resonances (^{i}Pr-CH_3) two broad singlets (backbone-CH_3) and two broad septets (^{i}Pr-CH). Additional resonances observed at δ = 3.73 ppm and 1.69 ppm are indicative of an additional carbene environment in solution and the integrals of these resonances do not appear related to those discussed above. It is possible that a degree of carbene dissociation occurs in solution and as such the unassigned signals may represent a small amount of free carbene. This suggestion is supported

by the presence of a small amount of yellow residue at the base of the NMR tube following the analysis which has been attributed to precipitated **MoAc**.

Variable temperature ^{1}H and ^{19}F NMR studies were also performed on solution of **MoFAc·L3** and **MoFAc·L4**. Consistent with the observations made for **MoAc·L3**, the ^{1}H NMR spectra recorded for each complex at 85 ^{o}C exhibited a series of well resolved resonances corresponding to each of the carbene proton environments. The increase in temperature also resulted in significant broadening of the initially sharp ^{19}F NMR resonances within both complexes. Interestingly, for **MoFAc·L3**, the two sharp resonances observed at room temperature do not broaden at the same rate when the sample is heated, suggesting that the dynamics and interchange between isomers is more complicated than can be described by a simple bridging→monodentate exchange model. Despite the broadening of the singals in **MoFAc·L3**, no coalescence of the resonances was observed at this temperature. Low temperature investigations were also performed on both of the fluorinated complexes but due to the low solubility of these species in toluene these analyses were carried out in d_8-THF. For both **MoFAc·L3** and **MoFAc·L4**, cooling the samples to -30 ^{o}C resulted in significant broadening of the ^{1}H NMR resonances that were observed at room temperature. Further cooling provided a complicated series of resolved resonances for both **MoFAc·L3** and **MoFAc·L3**, suggesting a number of carbene environments and a number of different isomeric forms trapped in solution. Unfortunately the complexity of the spectra has precluded the assignment of potential products.

Low temperature ^{19}F NMR studies of the two complexes were also largely uninformative. Upon cooling to -30 ^{o}C no broadening of the room temperature resonances was observed. Instead, at -85 ^{o}C, a large number of additional sharp resonances were observed for both **MoFAc·L3** and **MoFAc·L4** within the spectral window analysed, representing a large number of fluorine environments. These observations may once again relate to the trapping of a variety of isomers in solution but could also potentially result from intra-molecular Mo···F interactions occurring at low temperature (**Figure 5.25**). It is important to consider that the use of a coordinating solvent (d_8-THF) for the low temperature studies of **MoFAc·L3** and

MoFAc·L4 may in part be responsible for the difference in solution state behaviour relative to **MoAc·L3**.

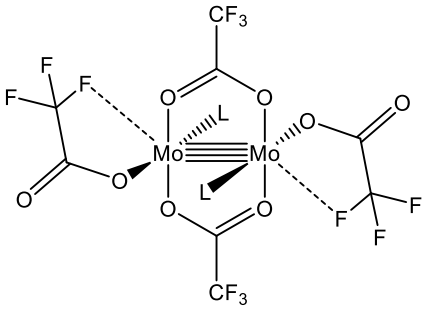

Figure 5.25: Possible Mo-F interactions present in low temperature solutions where L represents an N-heterocyclic carbene.

5.2.7 – Electronic Absorption Analyses of Equatorial {Mo_2} Carbene Adducts

To investigate how the interesting coordination modes of the alkyl-substituted N-heterocyclic carbenes affect the solution-state optical properties of their respective organometallic complexes, each of the type **III** {Mo_2} carbene adducts were analysed using electronic absorption spectroscopy. On account of their relatively low solubility, the analyses of **MoFAc·L3** and **MoFAc·L4** were performed using THF solutions whereas the solubility of **MoAc·L3** permitted the use of toluene, providing a greater spectral window. The room temperature electronic absorption spectra of each adduct is presented in **Figure 5.26**.

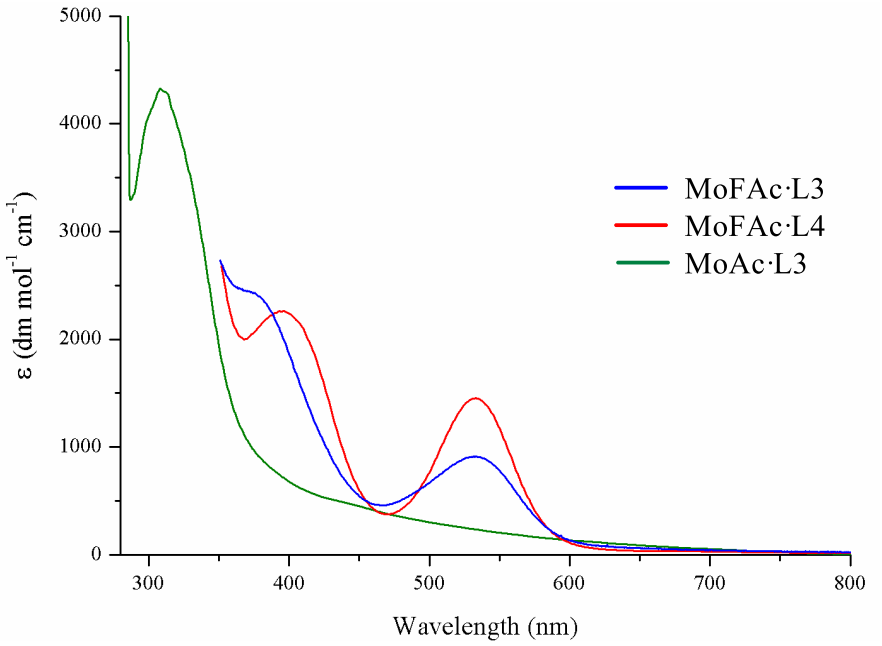

Figure 5.26: The electronic absorption spectra of **MoAc·L3** in toluene and **MoFAc·L3** and **MoFAc·L4** in THF collected at room temperature.

The spectra show that both **MoFAc·L3** and **MoFAc·L4** exhibit two clear absorption bands. The higher energy of these bands are attributed to $Mo_2\delta \rightarrow (O_2C)\pi^*$ electronic transitions which are slightly lower in energy in **MoFAc·L3**. The second absorption bands, appearing at 533 nm in both systems, correspond to the $Mo_2\delta \rightarrow Mo_2\delta^*$ transitions. For both **MoFAc·L3** and **MoFAc·L4**, the energy of this transition is red-shifted relative to the analogous absorption band observed for **MoFAc** (435 nm),[281] but is very similar to that reported for the related type-**III** PBu_3 adduct (519 nm).[254] The origin of the red shift is explained in **Figure 5.7** and **5.8** and the observation of these properties provides evidence that a type **III** adduct, or similar equatorial isomers, exist in solution to some degree at room temperature.[254]

In contrast to the adducts of **MoFAc**, **MoAc·L3** exhibits only one well resolved absorption band, appearing at 314 nm, which corresponds to the $Mo_2\delta \rightarrow (O_2C)\pi^*$ electronic transition. A low intensity shoulder is also observed at *ca*. 430 nm, attributed to the $Mo_2\delta \rightarrow Mo_2\delta^*$ electronic transition. The latter is significantly blue-shifted relative to the analogous absorption bands exhibited by **MoFAc·L3** and **MoFAc·L4** and is more characteristic of a system in which each of the carboxylate ligands is coordinating in a bridging mode. This suggests that, at room temperature, **MoAc·L3** behaves less like a type **III** adduct but more like a diaxial, type **II** adduct.

MoAc is not soluble in the absence of the carbene so some form of adduct must persist in solution.

Within the low temperature ^{1}H NMR analysis of **MoAc·L3** (*vide supra*) it was proposed that a species with both bridging and monodentate acetate ligands was present in solution at -85 ^{o}C. Although we do not have the facilities to perform low temperature electronic absorption studies, upon cooling a toluene solution of **MoAc·L3** in liquid N_2 the yellow solution turns dark orange (**Figure 5.27**). The thermochromism implies a structural change and correlated with our NMR data it suggests that, at low temperature, **MoAc·L3** exhibits the behaviour of an equatorial carbene adduct. We cannot say with certainty that this is a type **III** system in solution as other equatorial isomers are possible.

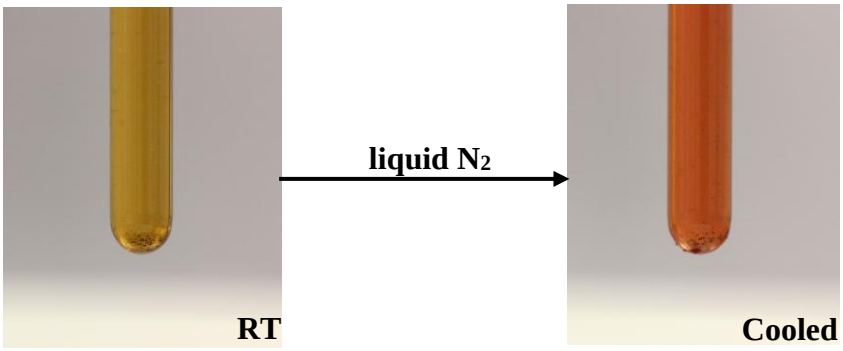

Figure 5.27: Pictures of a sample of **MoAc·L3** in toluene; at room temperature (left) and after cooling with liquid N_2 (right).

Interestingly, the electronic absorption data reported for the PBu_3 adduct of **MoFAc** was recorded at -40 ^{o}C.[254] Whilst a reason for these conditions was not provided, it is likely that the low temperature was required to provide a red-shift in the $Mo_2\delta \rightarrow Mo_2\delta^*$ absorption band on account of fluxionality in solution. This contrasts with **MoFAc·L3** and **MoFAc·L4**, which exhibit well defined absorption bands at comparable energy at room temperature. Even when solutions of the carbene adducts are heated to reflux there is no obvious colour change that could be correlated to a structural change. This may provide evidence that the N-heterocyclic carbenes employed within this study favour equatorial coordination to a greater extent than PBu_3.

5.2.8 – Further Chemistry of Equatorial {Mo_2} Carbene Adducts

With a particular interest in the design and synthesis of extended organometallic complexes featuring quadruply bonded metal units, we are working towards the incorporation of these carbene stabilised {Mo_2} fragments into such systems. Ideally we would like to do so using conjugated acetylide ligands to form oligomeric and polymeric systems as shown in **Figure 5.28**.

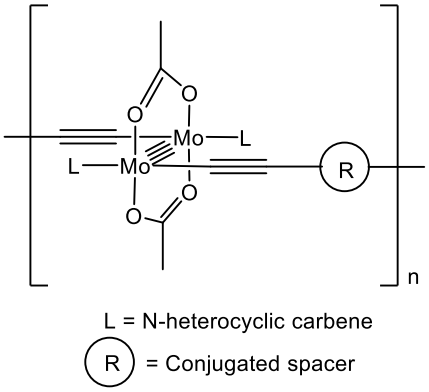

Figure 5.28: Targeted acetylide bridged {Mo_2} polymer.

A study of the literature showed that acetylide ligands have previously been coordinated to quadruply bonded Mo_2 cores, but all existing complexes are of the form $Mo_2(CCR)_4(PMe_3)_4$ with an acetylide ligand pointing in all directions.[282-284] These complexes are not set up well for the controlled formation of polymers and oligomers, so ideally we require a precursor that will direct *trans*-substitution of the acetylide ligands. The studies did, however, show significant interaction between the π-network of the acetylide ligands and the Mo *d*-orbitals, which is important when considering the potential for electronic communication between metal fragments.

The previously reported acetylide complexes were synthesised via a salt metathesis reaction between $Mo_2Cl_4(PR_3)_4$ and four equivalents of the chosen lithium acetylide. We ideally require a precursor that contains only two chlorides, arranged in a *trans*-conformation. Compounds such as this have previously been reported using phosphines to stabilise the {Mo_2} core. It was shown that treatment of **MoAc** with two equivalents of both a phosphine ligand and trimethylsilyl chloride (TMSCl)

result in the removal of two acetate ligands (*trans* to each other) replacing them with chlorides.[285-286] The free coordination sites created by the removal of the bridging acetates are then stabilised by the phosphine ligands (**Scheme 5.4**). The majority of systems made in this way have, through structural characterisation, been shown to adopt the *trans*-conformation in the solid state, as depicted in the reaction scheme. However, there is evidence that the *cis*-isomer can also be formed under certain conditions.[286]

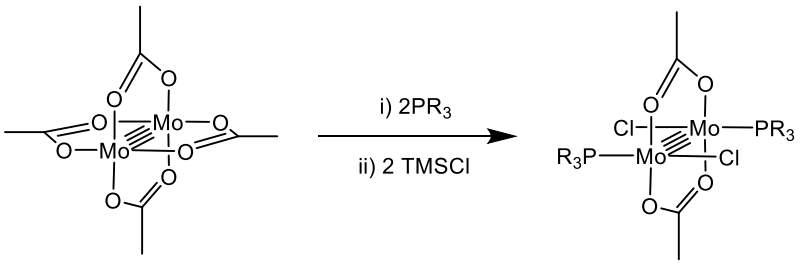

Scheme 5.4: Synthesis of dichloride substituted {Mo_2} carboxylate complexes.

These systems would potentially make good precursors for the synthesis of extended systems through standard salt metathesis chemistry with lithium acetylides and we were interested to see if the same complexes were accessible using N-heterocyclic carbenes in place of the phosphines. We therefore used an analogous method to that depicted in **Scheme 5.4**, first synthesising **MoAc·L3** *in situ*, and to the dark red solution we added two equivalents of TMSCl which immediately turned the solution dark purple. A crop of red crystals of **MoAcCl·L3**·were obtained by cooling a concentrated solution of the reaction mixture to -28 ^{o}C and these were suitable for analysis by single crystal X-ray diffraction. **MoAcCl·L3** crystallises in the triclinic spacegroup *P-1* with half a molecule within the asymmetric unit. The second half molecule is generated by an inversion centre at the mid-point of the Mo-Mo bond. The asymmetric unit also contains three toluene occupied sites, two of which are disordered over inversion centres at 100 % occupancy whilst the final molecule is rotationally disordered over two positions with the greater component modelled at 66 % occupancy. The molecular structure of **MoAcCl·L3**·is presented in **Figure 5.29** and selected bond lengths and angles observed within the structure are

displayed in **Table 5.8.** The related parameters from the previously reported phosphine analogues are also shown within the table to allow comparison.[285-287]

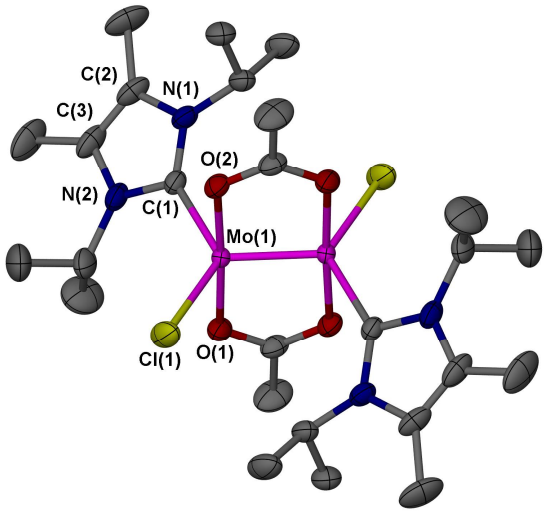

Figure 5.29: Molecular structure of **MoAcCl·L3** shown with 50 % ellipsoids and protons removed for clarity.

Table 5.8: Selected bond lengths (Å) and angles (°) from **MoAcCl·L3** and related systems of the form {Mo_2}(PR^1_3)$_2$ where {Mo_2} represents {$Mo_2(O_2CR)_2Cl_2(PR^1_3)_2$} and R = Me (I), ^{n}Bu (II) or ^{t}Bu (III).

	Mo-Mo	Mo-Cl	Mo-C	Mo-O	L-Mo-Cl
MoAcCl·L3	2.1099(3)	2.4351(7)	2.233(2)	2.115(2), 2.122(2)	128.42(7)
{Mo_2}(PBu_3)$_2$ (I)	2.099(1)	2.427(2)	N/A	2.109(5), 2.100(6)	139.8(1)
{Mo_2}(PPh_3)$_2$ (I)	2.091(1)	2.405(2)	N/A	2.009(5), 2.107(5)	139.36(9)
{Mo_2}(PPh_3)$_2$ (II)	2.102(1)	2.410(2)	N/A	2.117(3)[a]	139.3(1)
{Mo_2}(PEt_3)$_2$ (III)	2.0984(4)	2.405(2)	N/A	2.105(5), 2.105(5)	142.2(2)

[a] Reported as an average, [b] L = P or C.

The structure of **MoAcCl·L3** confirms that two of the acetate ligands from the precursor had been replaced by chlorides, with the product crystallising in a *trans*-conformation. Both the chloride and the carbene ligands project away from the {Mo_2} core resulting in *pseudo* trigonal bipyramidal geometries at both metal centres.

The Mo-Mo bond length of **MoAcCl·L3** lies in between those of **MoAc** and **MoAc·L3**, showing a slight decrease upon exchanging a monodentate acetate ligand for a chloride. It is also slightly longer than the values reported for the phosphine analogues. The C-Mo-Cl angle is over 10 ^{o} smaller than the P-Mo-C angle in each of the phosphine analogues, reflecting the difference in steric demands of the two types of ligand system. The same trend was also observed when comparing the carbene type **III** adducts with their phosphine analogues. The C-Mo-Cl angle is also *ca.* 16 ^{o} smaller than the C-Mo-O angle in **MoAc·L3**.

The Mo-Cl bond length of the carbene system is longer than the respective values of all of the phosphine complexes except for the PBu_3 complex, for which it is just within experimental error. This suggests a slightly greater *trans*-influence is being applied by the carbene than most of the phosphine ligands and is likely to relate to the stronger σ-donor ability of the carbene. Studies have shown that PBu_3 is the strongest σ-donor of the three phosphines involved in the table which may account for the longer Mo-Cl bond length in this system.[262,288]

The ^{1}H NMR spectrum of **MoAcCl·L3**, recorded in d_8-THF, suggests that multiple isomers were present in solution. Several resonances are present between 2.3 and 2.8 ppm which are attributed to various acetate CH_3 proton environments. The resonances associated with the carbene ^{i}Pr-C*H*$_3$ and -C*H* moieties appear as a sharp doublet and septet respectively as well as a number of lower intensity broad signals. Elemental analysis has confirmed that the atomic composition of the bulk product is consistent to that observed in the determined molecular structure and as such the additional resonances observed are unlikely to represent impurities. The ^{1}H NMR analysis was repeated using C_6D_6 as solvent resulting in a simpler spectrum. This exhibited a septet (^{i}Pr-C*H*), two singlets (2 x C*H*$_3$) and a doublet (^{i}Pr-C*H*$_3$), which can be attributed to a single isomer of **MoAcCl·L3**. However, there remained a number of low intensity signals in the acetate region of the spectrum suggesting a

small amount of isomeric material. The solubility of **MoAcCl·L3** is poor in both solvents and not all of the product could be dissolved in either experiment. We are therefore unable to say whether THF induces isomerisation within the sample or if it is merely a case that the isomeric forms are more soluble in THF. The poor solubility of **MoAcCl·L3** has also precluded analysis by $^{13}C\{^{1}H\}$ NMR spectroscopy.

5.3 – Conclusion

In summary, we have reported the first examples of N-heterocyclic adducts of quadruply bonded {Mo_2} systems, showing that the chemistry observed is highly dependent on the identity of the carbene that is used. The mesityl-substituted carbene (**L1**) provided a series of monoaxial adducts, examples of which are scarce within the literature and have not been observed in related studies using phosphine ligands. Within the solid-state the monoaxial carbene adducts each exhibit an equally unusual Mo···{Mesityl} π-type interaction at the vacant terminus of the Mo-Mo bond, which can be rationalised as mesityl-π→Mo_2π* interactions.[112] These interactions result in the formation of 1D 'coordination polymers' within the crystal lattice. The mono-adducts were observed even when two equivalents of carbene were used in the reaction and DFT studies have suggested that the Mo-Aryl interaction can potentially provide a lower energy alternative to σ-donation of a second carbene into the relatively high energy Mo_2σ* orbital of the monoaxial adduct. Evidence for this was provided by increasing the steric demand of the carbene aryl substituent, changing from mesityl to dipp groups. This provided a significant steric barrier towards the formation of Mo-Aryl interactions and resulted in the formation of a diaxial adduct. Interestingly, the ability to facilitate both Mo-σ and Mo_2-π interactions within the same complex was also demonstrated within the solid-state structure of **Mo_2Piv·L3Piv** in which the imidazolium ring is involved in a side-on π interaction with the Mo centre.

Similar to analogous studies using phosphine ligands, the use of less sterically demanding alkyl substituted N-heterocyclic carbenes, resulted in the formation of equatorial adduct species within the solid-state, containing two, bridging, and two monodentate carboxylate ligands. Within the series of products isolated, **MoAc·L3**

represents the first example of an equatorial adduct containing a **MoAc** core. Equatorial adducts could not be accessed using **MoPiv** which we relate to both the greater steric demand of the pivalate groups and the relatively low Lewis acidity of the {Mo_2} core. The distinction between the equatorial adducts of **MoFAc** and **MoAc** can be observed within the electronic absorption spectra of the species. The former exhibited low energy $Mo_2\delta \rightarrow Mo_2\delta^*$ transitions, indicative of an equatorial adduct in solution.[254] Such absorption bands were not observed for **MoAc·L3** providing evidence for less type **III** character in solution at room temperature, consistent with the less Lewis acidic metal centre. However, VT-NMR spectroscopic analysis suggests that equatorial conformations of **MoAc·L3** do exist at low temperature, which is accompanied by a distinct colour change of the solution.

Finally, initial steps have been investigated towards the functionalisation of {Mo_2} carbene adducts, showing that chloride substituted systems can be obtained *via* reaction with TMSCl. Such species represent potential starting materials for salt metathesis reactions that may allow the inclusion of carbene stabilised {Mo_2} units into more complicated extended systems.

Chapter 6

Time-Resolved Spectroscopic Analysis

Chapter 6 – Time-Resolved Infrared Spectroscopic Studies

6.1 – Introduction

6.1.1 – Time-Resolved Experiments

As was introduced in **Chapter 1**, there is growing interest in the study of organometallic polymers and oligomers on account of their potential application in a number of electronic devices such as LEDs,[289-290] sensors[160] and optical limiting devices.[49-50,291] To aid the design and synthesis of more efficient materials to perform these roles it is important to not only understand the ground state properties of these systems but to also probe the intricate excited-state manifolds. Such studies allow the identification and dynamic study of key charge transfer processes and the analysis of electronic delocalisation within discrete singlet and triplet excited-states.

The excited-state dynamics of an organometallic complex can be investigated using 'pump-probe' time-resolved experiments. A typical experiment first involves the electronic excitation of a solid- or solution-state sample using a pulsed laser source. An analytical probe beam is then used to analyse the sample at chosen time points along the decay profile of the sample. A simplified representation of this process is shown in **Figure 6.1**.[292]

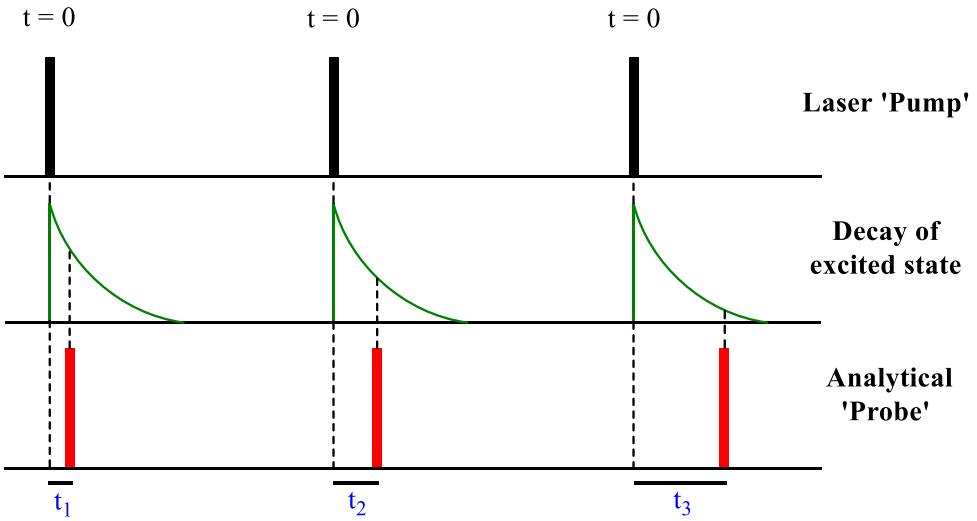

Figure 6.1: Illustration of a time-resolved pump-probe experiment sampling three time delays ($t_1 > t_2 > t_3$).

Three consecutive 'pump' pulses are shown (black), which are each accompanied by identical decay profiles (green). The analytical 'probe' pulses (red) arrive at three different time delays (t_1, t_2 and t_3) following the initial formation of the excited-state (t=0), allowing analysis at different stages of the decay process. Using this theory a number of time resolved experiments have been developed in which the excited-state is monitored using different probe techniques, including electronic absorption/emission spectroscopy[109,293-294] and, more recently, by X-ray diffraction.[292,295-296]

6.1.2 – Time-Resolved Infrared Spectroscopy

Time-resolved Infrared (TR-IR) spectroscopy is a particularly powerful technique that allows discrete molecular vibrations to be monitored following photoexcitation of a molecular ground state.[297-300] For this reason it has predominantly been utilised on samples that exhibit characteristic bond vibrations, particularly {C≡O}, {C≡C} and {C=O} containing complexes. TR-IR provides a significant advantage over other techniques because structural changes can be observed and assigned within solution-state processes. However, for full interpretation of results a combination of time-resolved studies are often required.

The diagram shown in **Figure 6.2** shows how the 'pump-probe' method can be applied to infrared spectroscopy.[18]

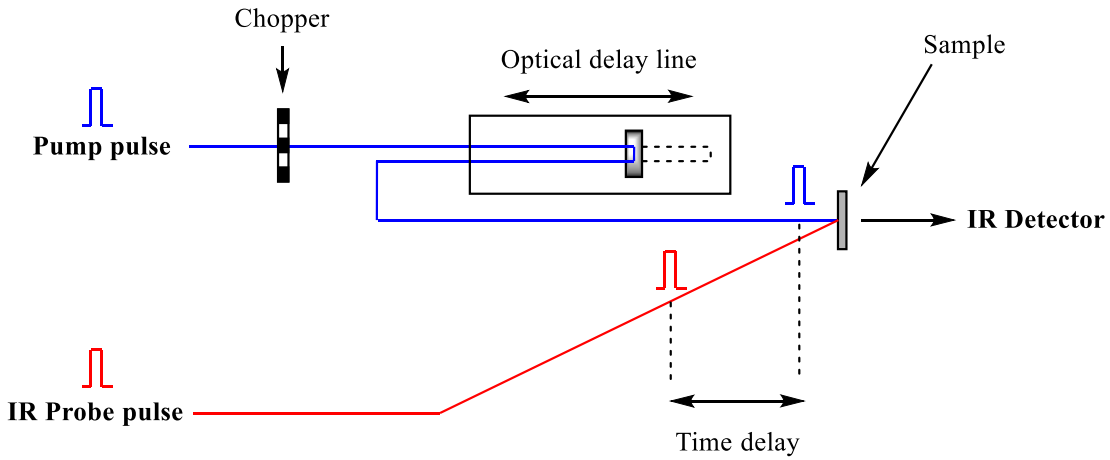

Figure 6.2: Simplified schematic of a TR-IR setup.[18]

The pump (blue) and IR-probe (red) lasers pulses are both generated from the same Ti:Sapphire laser source, which is split and then tuned to give a UV/Vis pump wavelength and an IR probe wavelength. In order to control the time delay between pump pulse and the arrival of the IR probe pulse, the former is passed through an optical delay line which alters the path length between the laser source and the sample. This allows the measurement of the IR spectrum following a series of programmed time delays following initial excitation of the sample. Importantly the pump beam also passes though a chopper, which is synchronised to remove alternate laser pulses. The IR probe continues to measure in the absence of the excitation beam and thus collects ground state spectra during alternate pulses. The ground state spectra are subtracted from each of the excited-state spectra to produce a difference spectrum for each time delay. This is illustrated in **Figure 6.3**. A more detailed explanation of the setup is described in the experimental section of this work and is well documented in the literature.[301-302]

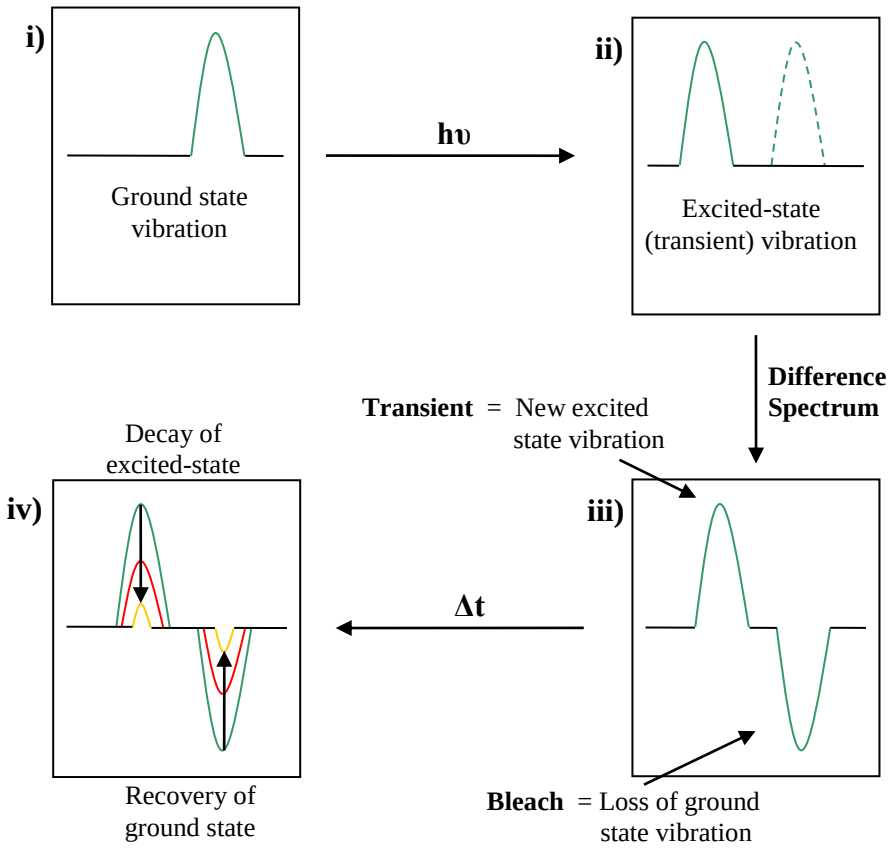

Figure 6.3: A demonstration of the formation of transient and bleach signals in a TR-IR difference spectrum.

The diagram shows that upon photo-excitation of a sample, a ground state vibration (**i**) is replaced by a second vibration corresponding to the population of an electronically excited-state (**ii**).The ground state spectrum is then subtracted from the excited-state spectrum to provide a difference spectrum (**iii**) in which the loss of the ground state is reflected by negative intensity signals (a bleach), whilst the transient vibrations are observed at positive intensity. Over a given time-frame the excited-state decays and as such the intensity of the transient vibration is reduced whilst the intensity of the bleach also decrease to reflect the recovery of the ground state (**iv**).

Because of the structural information that can be gleaned from TR-IR spectroscopic analysis it is a technique that has been used for a variety of studies. These include; the observation of transient organic reaction intermediates,[303-304] probing proton transfer processes[140,305] and a variety of studies that utilise transition metal carbonyl stretches to investigate photo-induced reactivity.[297-299,306]

To date there are only a limited number of examples where TR-IR spectroscopy has been used to study Pt-acetylide complexes. Contributions from Weinstein *et al* have investigated a range of complexes of the form shown in **Figure 6.4-i**, which contain spectroscopic probes on both the acetylide and diimine ligand systems (υ(C≡C) and υ(C=O), respectively).[300,307-311] The carbonyl groups on the diimine provide an efficient method by which to monitor charge transfer excited-states, as population of the {C=O} π*-orbitals results in a red shift of the observed υ(C=O) due to reduction in the multiple bond character. Monitoring of the υ(C≡C) stretches in such complexes showed that the identity of the acetylide ligand can have significant effects on the degree of charge transfer between the two ligand systems. For example, when R = *p*-tolyl a blue-shift of υ(C≡C) was observed in the excited-state, which was attributed to the $MLCT_{(dimine)}$ removing electron density from the Pt centre, resulting in a lesser degree of Pt→C≡C back-bonding.[309] However, when R = naphthyl, a red-shift of the analogous υ(C≡C) was observed in the excited-state. This was attributed to a loss in {C≡C} bonding electron density upon the formation of a MLCT excited-state, showing that there is significant {C≡C-naphthyl} π-contribution within the HOMO of this species.[311]

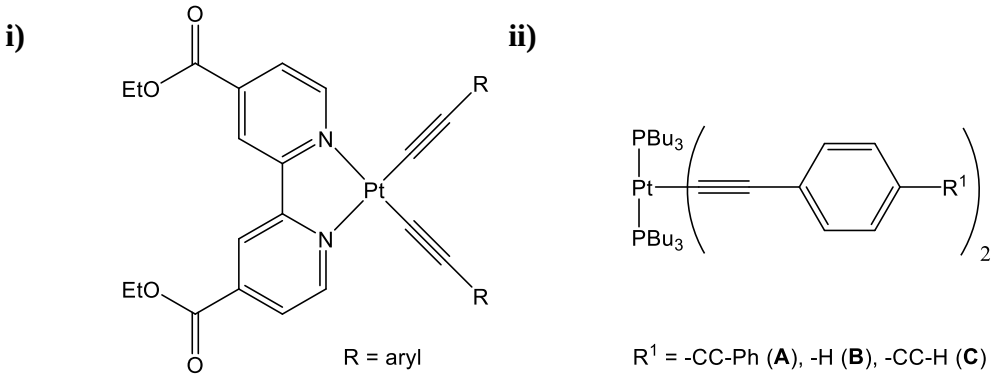

Figure 6.4: Examples of diimine-Pt-acetylide (**i**) and phosphine- Pt acetylide (**ii**) complexes that have been studied by TR-IR spectroscopy.

Two independent TR-IR studies have also been performed on the series of *trans-bis*-acetylide complexes, shown in **Figure 6.4-ii**.[172,312] The dynamics differ from the diimine systems because the lowest lying excited-state is predominantly ππ* in character. The studies performed on **A,** by Cooper *et al*., revealed the formation of cumulated {Pt=C=C=Ar} bonds in the triplet excited-state, which support previous assignments made from phosphorescence data.[141] The independent TR-IR studies, performed by Brozik *et al*., on complexes **B** and **C** provided evidence that the triplet excited-states within these species are localised on a single acetylide ligand system, reducing the symmetry of the excited-state molecule from D_{2h} to C_{2v}.[172] This was determined through the observation of two transient {C≡C} bond vibrations for each complex, one observed at higher energy than the ground state {C≡C} vibration and one at significantly lower energy. Similar charge localised triplet states have been reported for a number complexes in the literature and are thought to occur due to the high symmetry structures of the complexes and the low lying MLCT excited-states.[206,275,313-315]

More recently, TR-IR studies have also been extended to quadruply bonded $\{Mo_2\}$- and $\{W_2\}$-carboxylate and -amidinate systems.[108,206,275,316-319] By monitoring the υ(OCO), MLCT states could be assigned by a red shift of the vibration, due to population of ligand π*-orbitals. These could be differentiated from δδ* excited-states which impose a blue shift of the analogous vibrations, attributed to the removal of electron density from the Mo_2δ orbital which reduces the M→ligand back-bonding. Initial studies have shown that the identity of the carboxylate ligand

has a significant impact both on the excited-states populated and their respective lifetimes (**Figure 6.5**). For example, $Mo_2(O_2C^tBu)_4$ exhibits complicated decay dynamics involving both ^{1}MLCT and $^1\delta\delta^*$ excited-states, which both exhibit intersystem crossing (ISC) to a $^3\delta\delta^*$ state, which is observed for all $\{Mo_2\}$-containing complexes that have been studied to date. The lower lying π^*-orbitals of $Mo_2(O_2CPh)_4$ make the dynamics simpler, only involving the population of the ^{1}MLCT excited-state prior to ISC. The Singlet lifetimes (up to 50 ps[317]) of these species have been shown to be significantly longer than those observed for Pt-acetylide complexes and are especially long for complexes containing alkyl-substituted carboxylate ligands. The dynamics are further altered by replacing $\{Mo_2\}$ by $\{W_2\}$, which, when combined with electron-withdrawing ligand systems, can allow population of the less common ^{3}MLCT states. These states are much rarer for $\{Mo_2\}$ containing systems, due to the lower energy of the $Mo_2\delta$ orbitals, and have only been observed for certain systems containing polycyclic carboxylate ligands.[316,320] $\{W_2\}$-containing systems also exhibit significantly shorter singlet lifetimes than related $\{Mo_2\}$ complexes, on account of increased spin-orbit coupling.

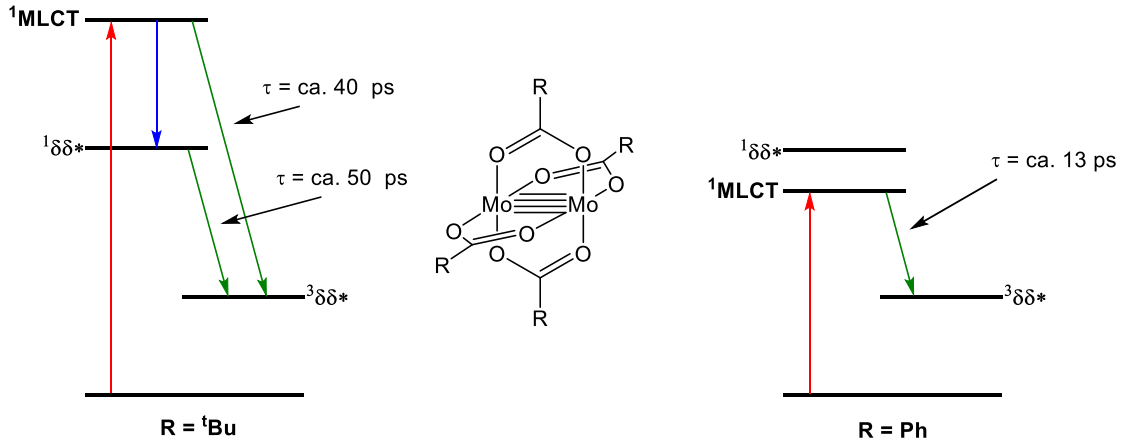

Figure 6.5: Excited-state dynamics determined for two $\{Mo_2\}$-tetracarboxylate complexes.[317]

To investigate the degree of charge delocalisation with the excited-state of $\{Mo_2\}$ complexes Chisholm *et al*. designed a series of complexes that incorporate {C≡C} or {C≡N} spectroscopic probes into the ligand system. Examples of such complexes are shown in **Figure 6.6-i** and **-ii**.[206] The conversion of the ^{1}MLCT to $^3\delta\delta^*$ states

within these complexes was observable by the disappearance of ligand-based transient vibrations following the ISC, because the excited-state is no longer localised on the ligand π*-orbitals.

i)

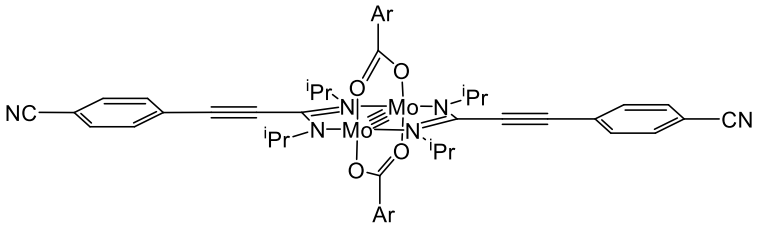

Class III

ii)

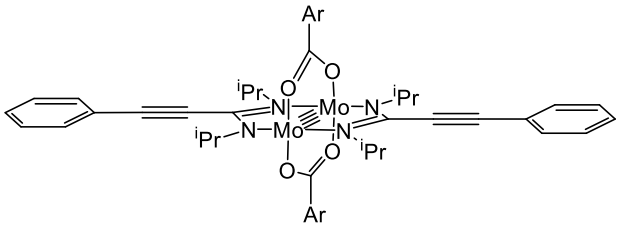

Class II

Figure 6.6: Examples of *trans*-disubsituted {Mo_2} complexes that have been studied by TR-IR spectroscopy.[206]

The photo-excited ^{1}MLCT forms of complexes, such as those shown in **Figure 6.6**, can be considered mixed valence species, in which an electron hole resides on the {Mo_2} core and the promoted electron is delocalised within the highly conjugated ligand π-orbitals.[206,275,318] Using TR-IR spectroscopy, combined with theoretical calculations, it has been possible to characterise the degree of electronic delocalisation across the two *trans*-ligands in terms of the Robin-Day classification. These studies have shown that subtle differences within the ligand system can result in a fully delocalised ^{1}MLCT (Class III – **Figure 6.6-i**) becoming only a partially delocalised excited-state (Class II – **Figure 6.6-ii**). Similar observations were also made for the related {W_2}-analogues, both in the ^{1}MLCT and ^{3}MLCT states.[206]

Building on the promise shown by the studies performed on related systems, we report here preliminary results obtained from the TR-IR analyses of selected Pt-ethynyl-ester complexes (discussed in **Chapter 2**). Studies have also been extended to the mixed-metal complex **PtMo1** in an attempt to deduce the degree of electronic delocalisation throughout the molecule in the photo-excited-state.

6.2 – Results and Discussion

6.2.1 – TR-IR Spectroscopic Analyses of Pt-Ethynyl-Ester Complexes

Our initial TR-IR experiments focussed on the Pt-ethynyl-ester complexes **Pt2a** and **Pt5a** (**Figure 6.7**) to investigate the differences in excited-state dynamics that were induced by changing the identity of the conjugated spacer. This study represents the first example where TR-IR spectroscopy has been used to study Pt-*mono*-acetylide species.

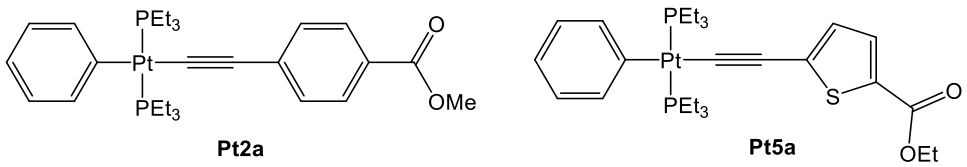

Figure 6.7: Two Pt-ethynyl-ester complexes under study in this work.

The ethynyl-ester ligand systems are particularly applicable for IR-analysis as they contain both well-defined acetylide and organic carbonyl bond stretches. The corresponding {C≡C} and {C=O} moieties are located on opposite sides of the ligand system and, as such, the excited-state dynamics observed within each spectral region may aid discussion into the degree of electronic delocalisation throughout the ligand within the photo-excited states. In agreement with reports in the literature, calculations performed on the Pt-ethynyl-ester complexes show that the lowest lying excited-state is predominantly $^1\pi\pi^*$ in character, combined with a contribution from the Pt($d\pi$) orbitals. The HOMO and LUMO calculated for **Pt2a** are displayed in **Figure 6.8**. The HOMO→LUMO electronic transition was therefore directly pumped for both **Pt2a** and **Pt2b** using an excitation wavelength of 350 nm. For both complexes the experiments were performed on the ps time-scale using DCM as solvent.

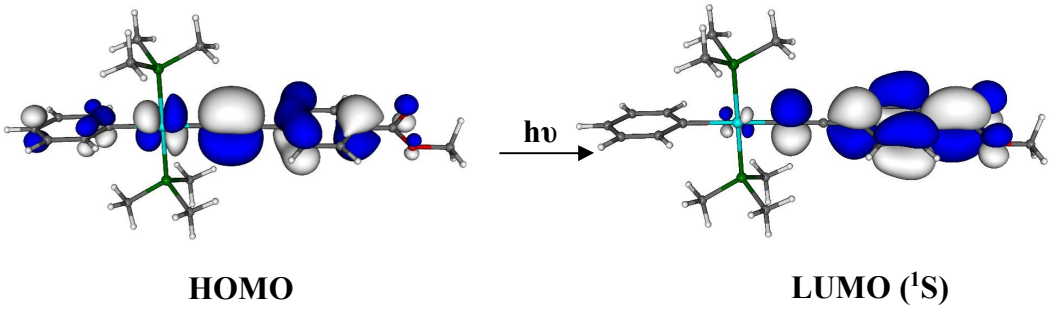

Figure 6.8: The HOMO and LUMO calculated for **Pt2a**.

The TR-IR spectrum for **Pt2a** is shown in **Figure 6.9** showing the 1350-1800 cm^{-1} (fingerprint) region of the spectrum.

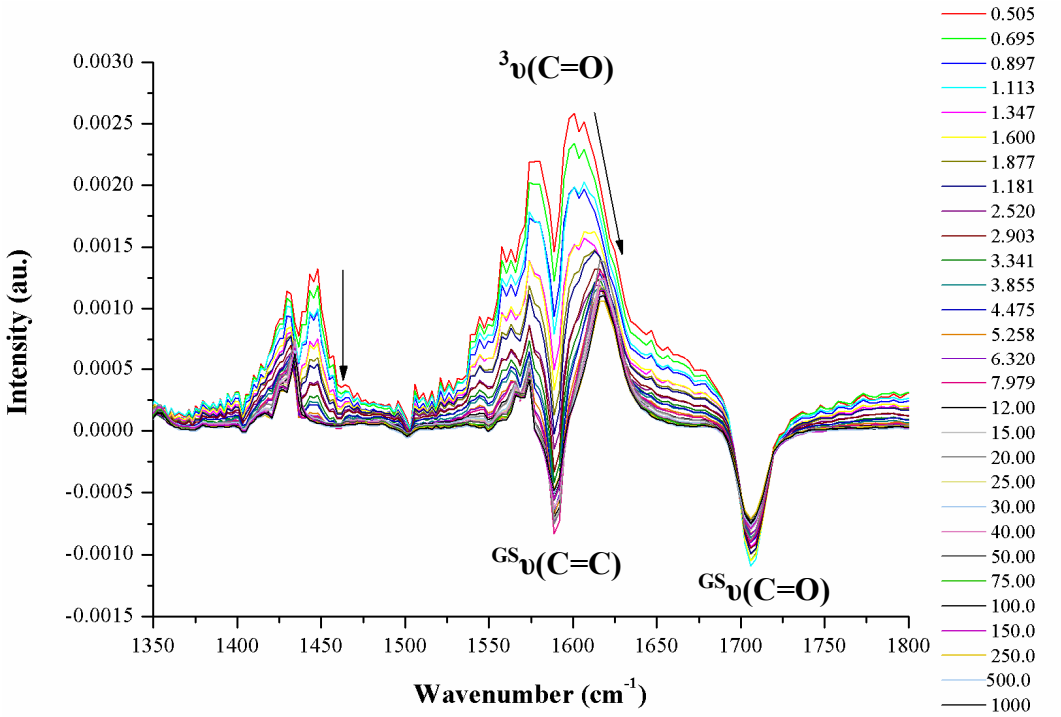

Figure 6.9: Fingerprint region of the TR-IR spectrum of **Pt2a**. Time delays reported in ps. $\lambda_{excitation}$ = 350 nm.

In the ground state, **Pt2a** exhibits a {C=O} stretch at 1706 cm^{-1} which is immediately bleached following excitation with the 350 nm laser pulse. The loss of the ground state vibration is accompanied by the simultaneous formation of a transient at *ca.* 1598 cm^{-1} (modelled with a Gaussian fit), which we have attributed to an excited-state {C=O} bond vibration. The transient signal is initially very broad and overlaps with a second bleach at 1589 cm^{-1}, which from similar assignment in the literature

can be attributed to a ground state phenylene {C=C} bond stretch.[312] This overlap results in the 'double-hump' appearance of the overlying transient vibration. Following the first 10 ps the broad transient appears to sharpen and shift to 1616 cm^{-1}. This could indicate the initial formation of a vibrationally 'hot' excited-state,[317,321] which relaxes to a long-lived state (τ >2 ns). A second transient vibration, 1400-1462 cm^{-1}, is also formed instantly upon excitation but is more complicated as it is present in a more congested region of the IR spectrum and is thus likely to represent the product of several overlapping transient and bleach signals. For this reason we are unable to assign the molecular vibration responsible. Part of this low intensity transient band decays over the same time-scale as the dynamics observed for the carbonyl transient. Using a global *mono*-exponential decay fit for the transients at both 1598 and 1445 cm^{-1}, the approximate lifetime of the initially formed excited-state is shown to be 1.8± 0.1 ps. Following this early-time process no other dynamics were observed within the timeframe of the experiment (up to 2 ns), which is consistent with the formation of a long-lived triplet excited-state.

To provide further information, the excited-state of **Pt2a** was also probed in the acetylide region of the IR spectrum over the same time-scale and the resulting TR-IR spectrum is shown in **Figure 6.10**. In the ground state **Pt2a** exhibits a {C≡C} bond vibration at 2095 cm^{-1} which immediately bleaches upon excitation at 350 nm, resulting in the formation of a very broad transient centred at *ca*. 1950 cm^{-1}. The initial transient decays over approximately 10 ps leaving a very weak transient at 1955 cm^{-1}. Although the weak and broad nature of the transient makes discussion of kinetics difficult, an approximate lifetime of 2.0 ps was calculated, by utilising peak integrations between 1800 and 2050 cm^{-1}, and is consistent with the dynamics observed in the fingerprint region. The broad appearance of the initial transient band may once again be related to the formation of a vibrationally hot excited-state.

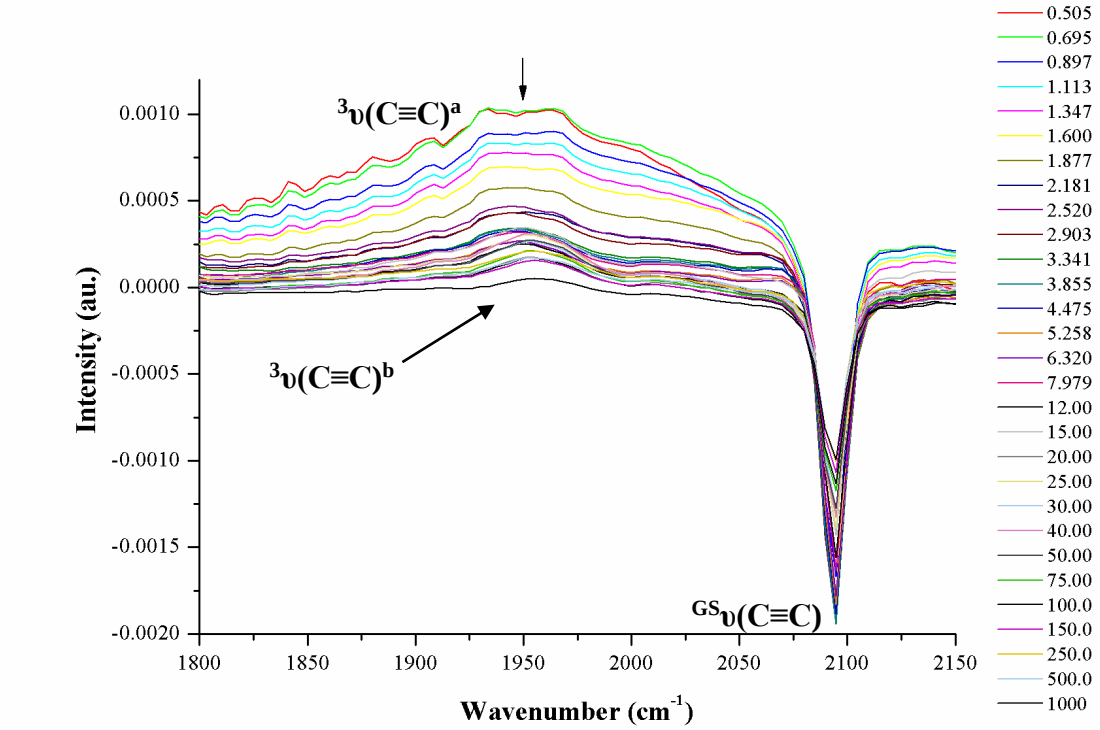

Figure 6.10: Acetylide region of the TR-IR spectrum of **Pt2a**. Time delays reported in ps. $\lambda_{excitation}$ = 350 nm.

The data for **Pt2a** shows that υ(C≡C) and υ(C=O) in the photo-excited-state are red shifted relative to the corresponding ground state vibrations. In both cases this can be attributed to the population of ligand-π* orbitals, lowering the effective bond orders of the two fragments. This observation is consistent with the formation of a $^3\pi\pi^*$, in agreement with previous studies into the excited-states of phosphine supported Pt-acetylide complexes.[60,62]

The analysis was repeated for the thienyl containing complex, **Pt5a**, and the TR-IR spectrum of **Pt5a**, recorded in the fingerprint region, is displayed in **Figure 6.11**.

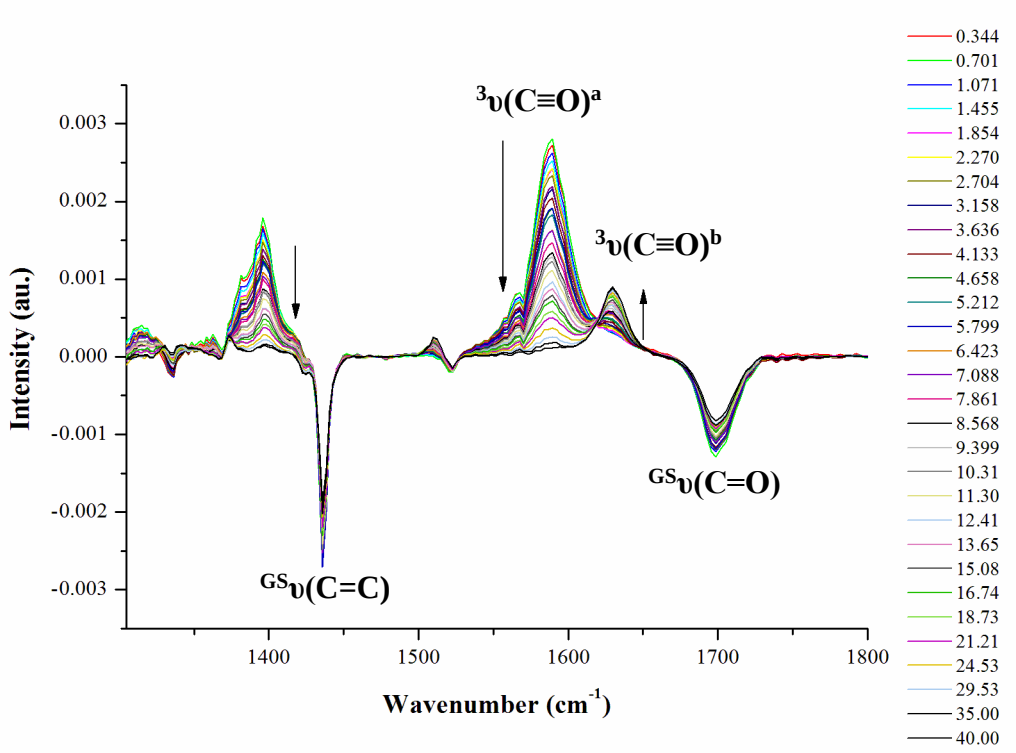

Figure 6.11: Fingerprint region of the TR-IR spectrum of **Pt5a**. Time delays reported in ps. $\lambda_{excitation}$ = 350 nm.

Photo-excitation of **Pt5a** resulted in the instant formation of bleaches at 1700 cm^{-1} and 1436 cm^{-1}, corresponding to the ground state {C=O} and thienyl-{C=C}[322] bond vibrations respectively. The formation of the two bleach signals is accompanied by the simultaneous appearance of transient vibrations at 1590 cm^{-1} and 1396 cm^{-1}. The former can be attributed to a transient {C=O} bond vibration but without further analysis it is difficult to assign the second. However, both transients decay to the baseline with a calculated approximate lifetime of 11.4±0.2 ps. The decay of the two transients is accompanied by the growth of a second transient vibration at 1630 cm^{-1}, representing a new excited-state {C=O} bond vibration. The secondary transient grows in at the same rate as the initial transients decay, reflecting the population of a second excited-state, which lives for the duration of the experimental time scale (> 2 ns). On reflection it is possible that the observations made in the analogous spectrum of **Pt2a** could be described by the growth and decay of discrete transient vibrations but the overlapping bleach makes it difficult to determine this using TR-IR spectroscopy alone. To continue the study, data was also collected over the acetylide region of the IR spectrum. This is presented in **Figure 6.12**.

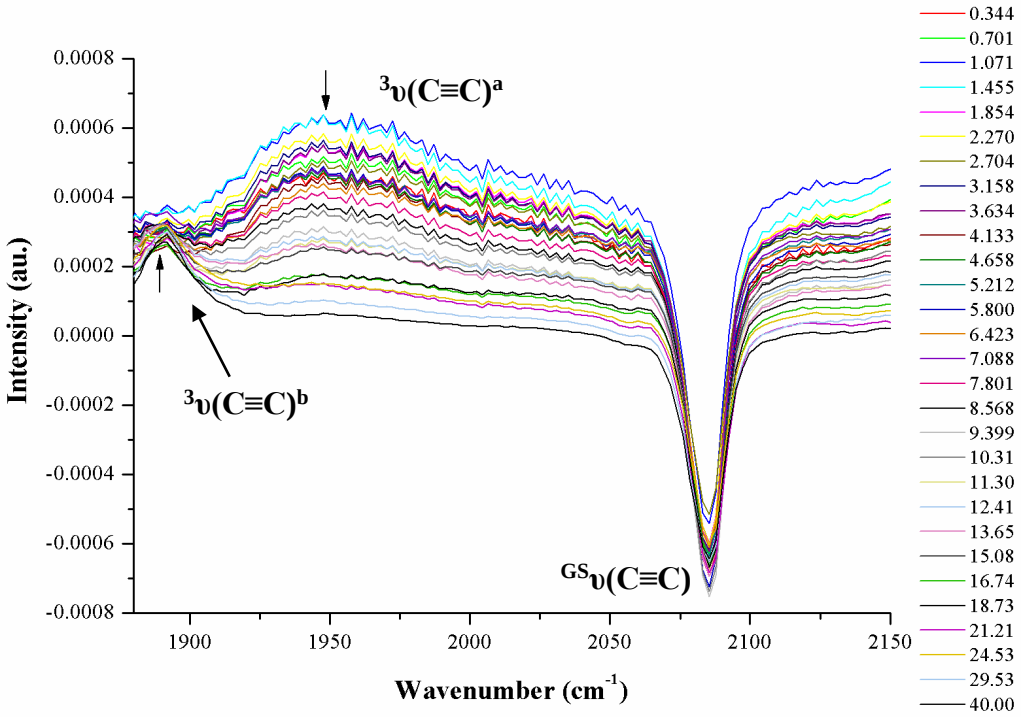

Figure 6.12: Acetylide region of the TR-IR spectrum of **Pt5a**. Time delays reported in ps. $\lambda_{excitation}$ = 350 nm.

The early-time dynamics of **Pt5a,** observed in the acetylide region of the spectrum, are very similar to those observed for **Pt2a**. The ground state {C≡C} bond vibration, at 2085 cm^{-1} is bleached upon excitation, immediately forming a relatively weak and broad transient vibration centred at *ca.* 1948 cm^{-1}. However, this transient species decays to the baseline and a second transient vibration grows in at 1890 cm^{-1}, which contrasts with the observations made for **Pt2a**. Although an accurate kinetic analysis of this process is precluded by the broadness of the initial transient band, an approximate lifetime of 11 ps was obtained by modelling the signal integrals between 1920 and 2066 cm^{-1}. This value is consistent with the dynamics observed in the fingerprint region, providing evidence that the dynamics are related.

As with **Pt2a**, the transients corresponding to both the {C=O} and {C≡C} moieties appear at lower energy than the ground-state vibration, consistent with the population of the ligand π*-orbitals in the excited-state. Following the decay of the initially formed excited-state the secondary {C=O} transient species is shifted to higher energy relative to the first ($\Delta\upsilon$ = +40 cm^{-1}). This suggests that the secondary excited-state is less localised on the {C=O} π*-orbitals. The large shift between the

ground state {C≡C} vibration and the transient at 1890 cm^{-1} ($\Delta\upsilon$ = -195 cm^{-1}) suggest that the bond order of the (C≡C) is further reduced following the population of the second excited-state that is observed. This observation is consistent with a greater degree of electron density localised on the π*-orbitals of the {C≡C} and similar observations made in the literature have led to the assignment of cumulated {Pt=C=C=C} bond vibrations.[312] Considering the respective red and blue shifts of the {C≡C} and {C=O} vibrations upon going from the initial to the secondary excited-state, it would suggest that the electron density is redistributed towards the Pt end of the ligand system during this process.

More recently, we have tried to extend analogous TR-IR studies to the related Pt *bis*-ethynyl ester complexes starting with the phenylene containing species **Pt2b** (**Figure 6.13**).

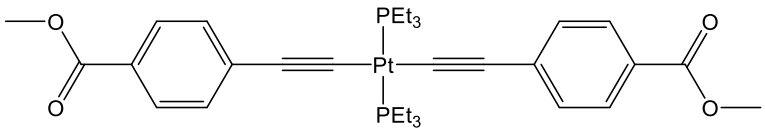

Figure 6.13: Structure of Pt *bis*-acetylide complex **Pt2b**.

As with the previously studied *mono*-substituted Pt complexes, solutions of **Pt2b** were irradiated with a 350 nm laser pulse which corresponds to direct pumping of the ligand π→π* electronic transition. Following excitation, the organic carbonyl region of the TR-IR spectrum (available in the appendices) exhibited no obvious dynamics. Bleaches corresponding to the ground state {C=O} and {C=C} vibrations were observed instantly at 1709 cm^{-1} and 1589 cm^{-1} accompanied by a poorly defined transient at 1628 cm^{-1}, similar to that observed for **Pt2a**. Only slight decay of these signals was observed on the time-scale of the experiment (2 ns). In contrast, the acetylide region of the spectrum of **Pt2b** was significantly different to that of the *mono*-substituted system (**Figure 5.14**).

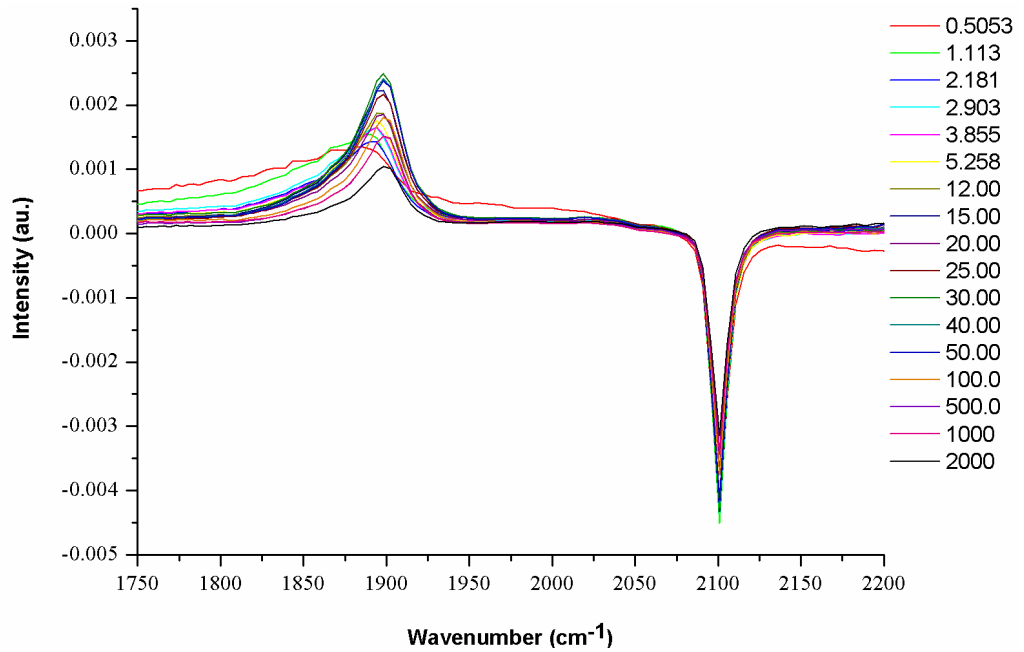

Figure 6.14: Acetylide region of the TR-IR spectrum of **Pt2b**. Time delays reported in ps. $\lambda_{excitation}$ = 350 nm.

Immediately following the excitation laser pulse, the ground state {C≡C} vibration was bleached at 2101 cm^{-1} and a broad transient was observed at 1886 cm^{-1}. This rapidly sharpened to provide a more intense transient at 1894 cm^{-1}, possibly indicating the cooling of a vibrationally hot excited-state. The energy of the transient vibration is significantly lower than the broad transient observed for **Pt2a** over the same time-scale (*ca*. 1950 cm^{-1}) and is likely to represent a cumulenic {C=C} vibration. This is consistent with the observations made by Cooper *et al*. when studying a similar phenylene containing complex.[312] The difference in behaviour between **Pt2a** and **Pt2b** is likely to be due to the greater extent of π-conjugation in the disubstituted system. Only a small degree of ground state recovery is observed within the time limits of the experiment in both the acetylide and organic carbonyl regions of the spectrum indicating the population of a long-lived triplet excited-state, consistent with the observations made for **Pt2a** and **Pt5a**.

When performing a routine repeat of the TR-IR analysis of **Pt2b**, it was noticed that the ratio between the intensities of the transient and bleach vibrations differed from those observed in the original experiment. It was proposed that the differences observed were due to perturbation in the power of the laser pulses between the two experiments. To investigate this theory, the experiment was repeated four times

using known laser powers (between 100 nJ and 800 nJ) for each analysis. A single time-delay was then selected from each of the spectra allowing a comparison of the transient intensities. **Figure 6.15-i** shows the spectra recorded from each experiment at 4.5 ps following the excitation pulse.

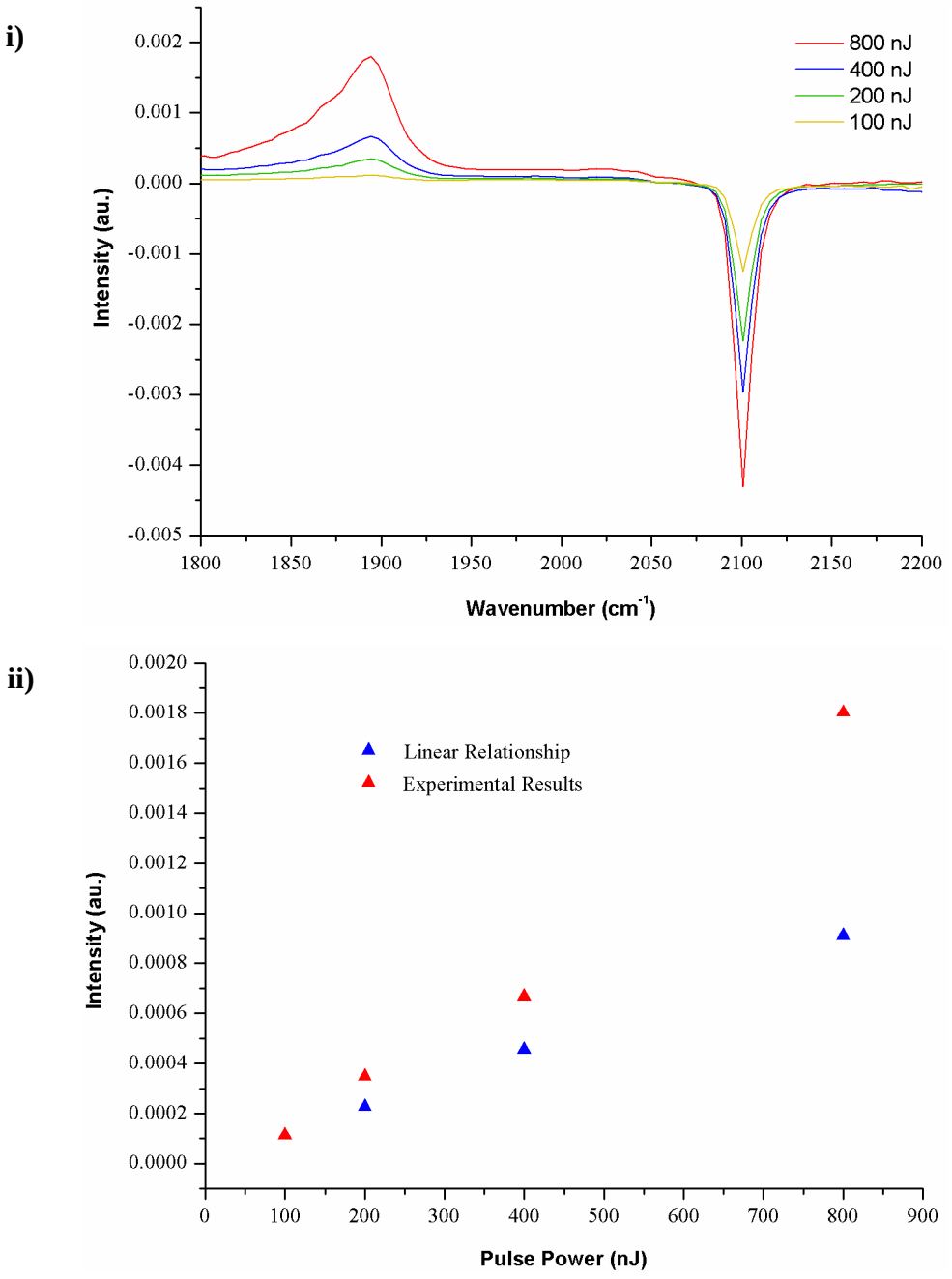

Figure 6.15: i) A comparison of the acetylide regions of the TR-IR spectra of **Pt2b** at t = 4.5 ps recorded with four pump powers. **ii)** A plot of observed intensity *versus* laser pump power for the transient at 1894 cm^{-1} at t = 4.5 ps (red) compared to a theoretical linear relationship (blue). $\lambda_{excitation}$ = 350 nm.

If the relationship between laser power and peak intensity were linear, then the intensity of the {C≡C} transient vibration would be expected to increase by a factor of two as the pump power doubled. This is represented by the blue trace in **Figure 6.15-ii**. The red trace represents the experimentally observed transient intensities showing a clear deviation from the linear model, especially at 800 nJ, and thus indicating non-linear optical properties potentially due to a multiple photon absorption process. Analysis of the difference IR spectra of **Pt2b**, recorded at 100 ps prior to the incidence of the pump pulse, revealed no residual excited-state remained from the previous excitation pulse. The postulated multiple pumping process must therefore occur within a single excitation pulse rather than the secondary excitation of an already excited species. These observations are particularly interesting because molecules that exhibit non-linear optical properties have recently been attracting a lot of interest due to their potential application in a variety of devices such as optical limiting devices, optical storage systems and non-linear photonics.[323]

Following these observations, the power dependency of the TR-IR spectra of **Pt2a** and **Pt5a** were also analysed and both systems were shown to behave linearly with respect to power. It is therefore likely to be the greater extent of conjugation within **Pt2b** that alters the nature of the observed optical properties. This is consistent with reports in the literature of Pt acetylide complexes that exhibit non-linear optical properties, which have focussed on highly conjugated frameworks.[50,291,323-325]

These preliminary results demonstrate that non-linear optical behaviour can be promoted in simple Pt-acetylide species but further study is required to characterise the process and to analyse how these properties could be potentially tuned by incorporating different conjugated spacers into the ligand systems.

6.2.3 – TR-IR Spectroscopic Analyses of {Mo_2}-Containing Complexes

Whilst a number of {Mo_2}-containing complexes have previously been analysed using TR-IR spectroscopy,[108,206,275,316-319] there have been no related studies performed on heterometallic systems. However, such studies could potentially help to elucidate MLCT processes between the different metallic units and, as such, we report the preliminary spectroscopic analyses of the novel heterometallic complex **PtMo1**. In order to aid the analysis of the excited-state dynamics of this species, the parent complex, **Mo1**, has also been analysed in this study. The structures of the two molecules are shown in **Figure 6.16**.

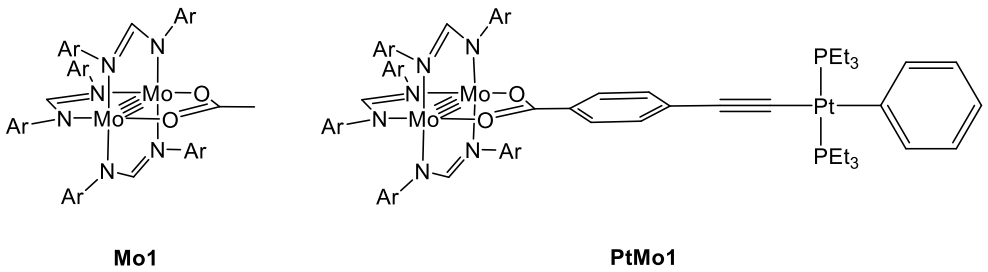

Figure 6.16: The structures of **Mo1** and **PtMo1**.

Previous studies within our group have shown that {Mo_2} tetra-formamidinate complexes exhibit strong transient {NCN} vibrations within the same region of the IR spectrum as the {OCO} vibrations reported by Chisholm *et al.* (1500-1550 cm^{-1}).[317,326] These bond vibrations, therefore, present spectroscopic probes that can be monitored within both complexes. In addition, **PtMo1** also contains a {C≡C} moiety within the bridging ligand, which allows both the {Mo_2} and the ligand environments to be monitored in the excited-state molecule.

Initial studies were attempted using DCM as a solvent, however, **PtMo1** was found to decompose rapidly in this medium and, as such, both experiments were carried out in dry degassed toluene. For **Mo1** an excitation wavelength of 350 nm was utilised and the data collected within the fingerprint region of the spectrum is shown in **Figure 6.17**.

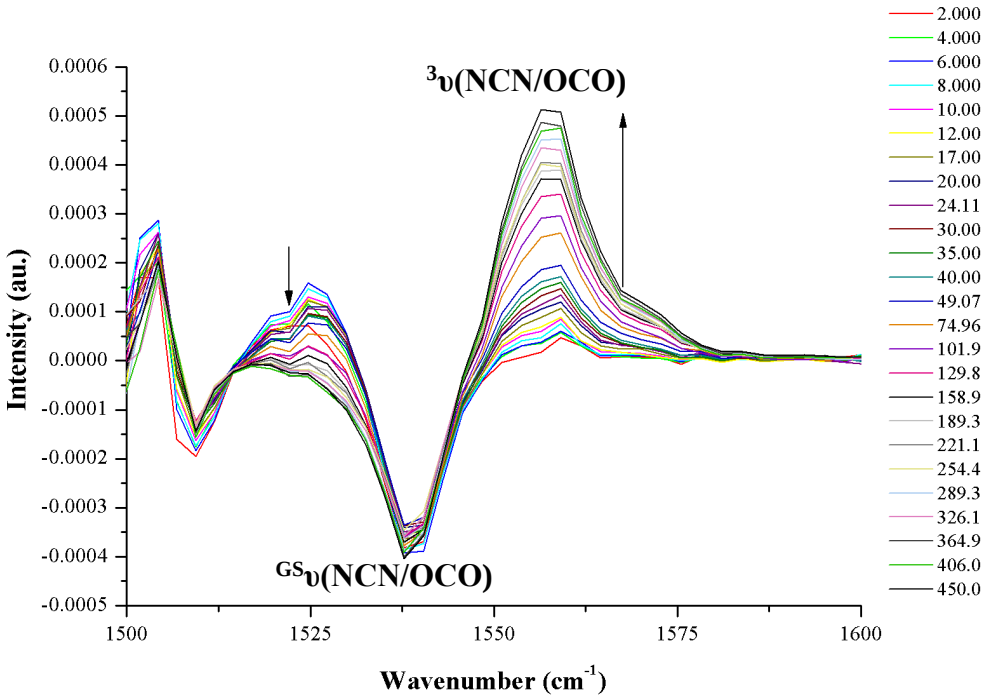

Figure 6.17: TR-IR spectrum of **Mo1** recorded in the fingerprint region. Time delays reported in ps. $\lambda_{excitation}$ = 350 nm

In the ground state, a toluene solution of **Mo1** exhibits vibration bands at 1509 cm^{-1} and 1535 cm^{-1}, which can be attributed to the {OCO} and {NCN} bond vibrations respectively.[327] Following excitation, the ground state vibration is immediately bleached and, within the first 6 ps, a low intensity transient feature grows in at approximately 1527 cm^{-1}. Unfortunately, additional time points are required within this short time frame to analyse the kinetics of this process. After 6 ps the feature at 1527 cm^{-1} begins to decay and, as it does so, a second transient band grows at 1559 cm^{-1}. By modelling the respective decay and growth of these bands, an approximate lifetime of 125.1 ± 6.3 ps was calculated for the concerted process. After the growth of the second transient, no further dynamics were observed within the time-frame of the experiment. From preliminary studies measuring microsecond time delays, the excited-state was shown to live in excess of 50 μs, which is characteristic of the long-lived triplet states that have previously been reported for {Mo_2} carboxylate and amidinate complexes.[108,110,275,317-319]

The fact that we can observe the transient vibration at 1527 cm^{-1} growing in over the first 6 ps provides evidence that two singlet excited states are involved in the decay pathway of **Mo1**, the first of which is extremely short lived. Very similar excited

state dynamics were observed by Chisholm *et al*. for the TR-IR spectral analysis of $(DAniF)_3Mo_2O_2C^tBu$ and were attributed to the initial population of a ^{1}MLCT state, which rapidly converts to a $^1\delta\delta^*$ state.[328] Similar dynamics had also been previously reported for $Mo_2(O_2C^tBu)_4$.[317] To confirm the singlet state dynamics of **Mo1**, further study is required.

The transient band of **Mo1** at 1559 cm^{-1} can be attributed to {NCN} vibrations within the excited-state, and these are blue-shifted in energy relative to the corresponding ground state vibrations. This can be rationalised by the formation of a $^3\delta\delta^*$ state, in which electron promotion from the $Mo_2\delta$ orbital reduces the degree of back-bonding to the formamidinate and acetate ligands, strengthening their respective π-bonds. Metal localised triplet states have been shown to be common to most quadruply bonded $\{Mo_2\}$ complexes, which supports this assignment. The lifetime calculated for the population of the assigned $^3\delta\delta^*$ state of **Mo1** is extremely long compared to the ^{1}MLCT and $^1\delta\delta^*$ excited state lifetimes that have been reported in the literature, for which the longest are 50 ps for $Mo_2(O_2C^tBu)_4$[317] and 70 ps for $(DAniF)_3Mo_2O_2C^tBu$.[327]

When the study was extended to the mixed-metal complex **PtMo1**, the excitation wavelength was changed to 440 nm to coincide with the tail of the MLCT absorption band (discussed in **Chapter 3**). The TR-IR spectrum of **PtMo1**, recorded over the fingerprint region of the IR spectrum, is shown in **Figure 6.18**.

In the ground state, **PtMo1** exhibits a {NCN} vibration at 1535 cm^{-1} and a {OCO} vibration at 1506 cm^{-1}. Upon irradiaition both ground state vibrations are immeadiately bleached and a transient feature is observed at *ca.* 1519 cm^{-1}. The growth of this transient is not observed within the experiment, even at sub 1 ps time delays. This may suggest that only a single singlet excited state is involved in the decay dynamics of **PtMo1**. The transient at 1519 cm^{-1} decays over approximately 10 ps and the decay is accompanied by the concomitant growth of two transient peaks at 1551 cm^{-1} and 1567 cm^{-1}. Kinetic analysis of the respective band's decay and growth provided an approximate lifetime of 9 ps for the process. It is noteworthy that an additional bleach was observed at 1600 cm^{-1} (not observed for **Mo1**), over which a transient vibration band grows in over approximately the same time scale as the

growth of the transients at 1551 cm^{-1} and 1567 cm^{-1}. Unfortunately we are unable to assign the responsible molecular vibration.

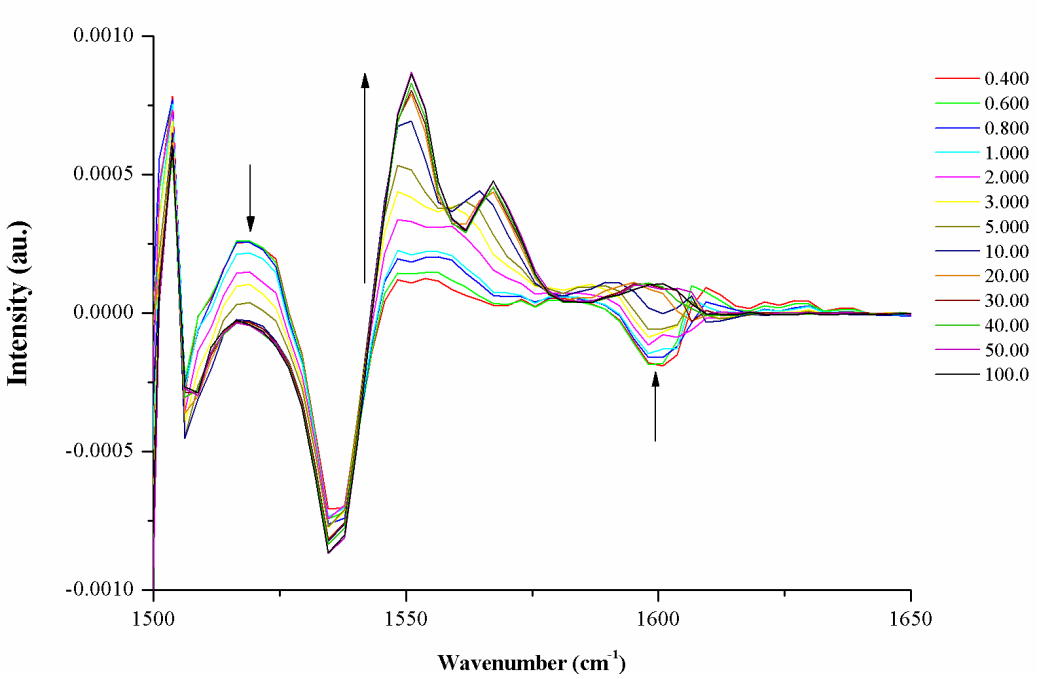

Figure 6.18: TR-IR spectrum of **PtMo1** recorded in the fingerprint region. Time delays reported in ps. $\lambda_{excitation}$ = 440 nm.

The blue shift of the transient vibrations at 1551 cm^{-1} and 1567 cm^{-1}, relative to that of the ground state (1535 cm^{-1}), again suggests the ultimate population of a $^{3}\delta\delta^{*}$ excited-state. However, the lifetime corresponding to the decay of the parent state is more than ten times smaller than that observed for **Mo1** and is more in keeping with the ^{1}MLCT excited states previously reported for photo-excited $\{Mo_2\}$ carboxylate species.[108,206,275,316-319]

In an attempt to investigate the degree of charge delocalisation within the photo-excited states of **PtMo1**, the solution of the heterometallic complex was also probed in the acetylide region of the IR spectrum. The resulting TR-IR spectrum is displayed in **Figure 6.19**.

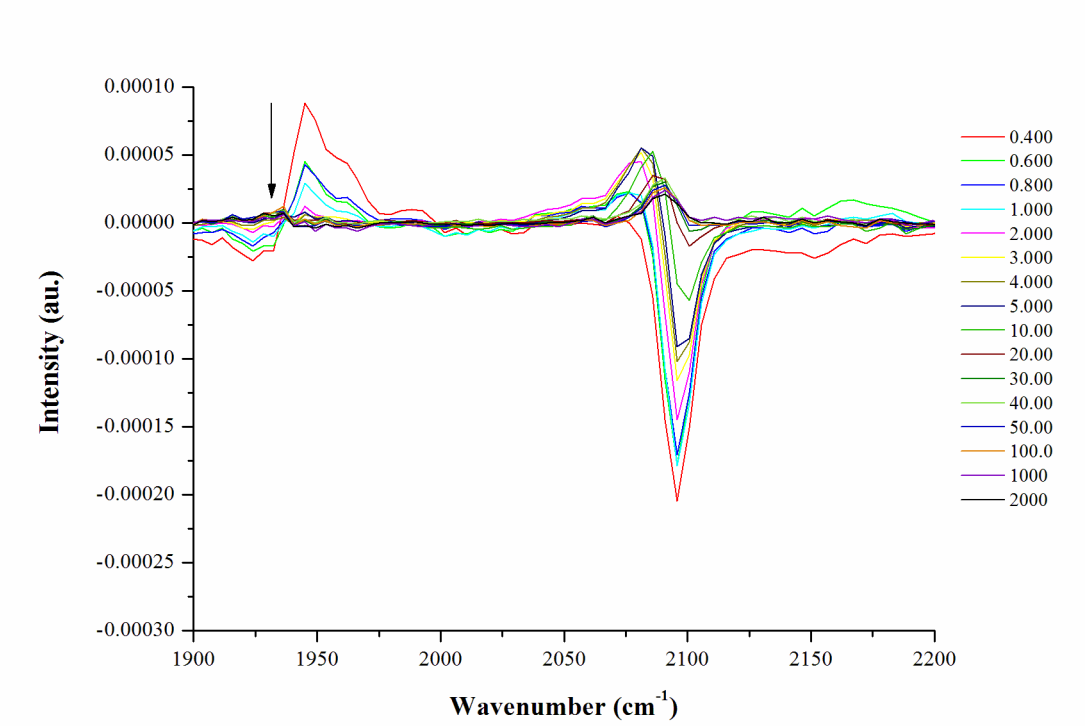

Figure 6.19: TR-IR spectrum of **PtMo1** recorded in the acetylide region. $\lambda_{excitation}$ = 440 nm.

Within the acetylide region of the TR-IR spectrum of **PtMo1**, the ground state {C≡C} vibration (2096 cm^{-1}) is bleached upon excitation and a transient vibration is observed immeadiately at 1944 cm^{-1}. This transient is shifted by ~152 cm^{-1} to lower energy of the ground state vibration, reflecting a significant loss of triple bond character within the excited state. Similar observations have been made by Chisholm *et al*. for a number of ethynyl-containing species and have been shown to provide evidence for the population of ^{1}MLCT excited states. This results in a significant amount of electron density residing in the π*-orbitals of the conjugated ligand systems, explaining the observed weakening of the C≡C bond. The low energy transient vibration decays over 5-10 ps and, as it does so, the bleach at 2096 cm^{-1} begins to recover towards the baseline. After approximately 20 ps the bleach is no longer observed, leaving only a weak transient at 2090 cm^{-1}. This transient does not decay over the 2 ns time frame of the experiment and therefore reflects the population of a triplet excited state. The fact that the bleached {C≡C} ground state vibration is no longer observed shows that the associated transient vibration occurs at almost identical energy. Therefore, very little electron density remains localised in the ligand π*-orbitals within the triplet excited state. These observations, combined

with those made in the fingerprint region of the TR-IR spectrum, provide further evidence for the assignment of a $^3\delta\delta^*$ excited state.

The observation of a {C≡C} transient vibration within the $^3\delta\delta^*$ excited state of **PtMo1** is unusual when compared to the similar studies performed by Chisholm *et al*. on ethynyl-functionalised {Mo_2} complexes. Within these, it was shown that population of the $^3\delta\delta^*$ state resulted in complete loss of both the acetylide bleach and transient vibrations.[106,206,317] However, our observation is consistent with the depopulation of the HOMO of **PtMo1** (predomiantly $Mo_2\delta$ in character), which DFT studies have shown to contain a significant contribution from the ligand π-orbitals, including a bonding contribution from the {C≡C} moiety (**Figure 6.20**). Loss of electron density from the ground state would therefore lower the {C≡C} bond order, resulting in a lower energy stretching frequency. It is therefore unclear why similar observations have not been made in the related studies in the literature, although the presence of the Pt centre may play a role.

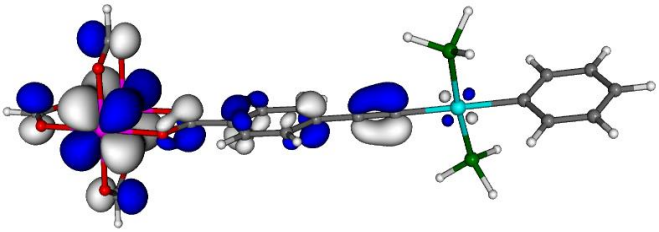

HOMO

Figure 6.20: Calculated HOMO for **PtMo1** showing a degree of electronic delocalisation over {C≡C} bonding orbitals.

Unfortunately, the low intensity of the signals that were observed for **PtMo1** within the acetylide region of the spectrum has prevented an accurate kinetic analysis of the dynamics that were observed and, as such, better resolved data is required to correlate the dynamics with those observed within the fingerprint region of the spectrum.

6.3 – Conclusion

In summary, we have performed a series of preliminary TR-IR spectroscopic studies in order to test the scope of the technique towards the elucidation of charge transfer processes within the photo-excited-state of our homo and heterometallic acetylide complexes.

Studies conducted on the Pt-ethynyl-ester complexes, **Pt2a** and **Pt5a** revealed that the early-time dynamics observed within the photo-excited-states of these species are strongly influenced by the identity of the conjugated spacer unit. **Pt2a** appears to initially populate a vibrationally hot excited-state which cools, with a lifetime of *ca* 2 ps, to a long-lived $^{3}\pi\pi^{*}$ state. The thienyl-containing complex, **Pt5a**, appears to initially form a similar $^{3}\pi\pi^{*}$ state, however, this decays (τ = *ca*. 11 ps) to a second excited-state, which appears to be significantly more localised on the {Pt-C≡C} π^{*}-orbitals of the complex, resulting in a cumulenic type structure. There is evidence of the {C=O} bond regaining a degree of double bond character during this transition, which provides evidence for an intraligand charge transfer process occurring in the excited-state.

Similar studies performed on complex **Pt2b** showed that the more conjugated system behaves non-linearly with respect to laser flux. At high laser power, strong transient vibrations were observed in the acetylide region of the spectrum, suggesting the formation of cumulated {Pt=C=C=C} bonds. However, at lower laser power very little transient vibration is observed at all. Further study is required to characterise the non-linear properties of this system and to investigate how these properties are affected by differing the ligand system.

Studies performed on both **Mo1** and **PtMo1** reveal strong transient {NCN} vibrations, appearing at higher energy relative to the corresponding ground state bond vibrations. This is consistent with the formation of $^{3}\delta\delta^{*}$ excited-states in each case, which have both been shown to be extremely long lived (>50 μs). However, the ISC process to populate the $^{3}\delta\delta^{*}$ state is significantly faster in the heterometallic complex (τ = *ca*. 9 ps) than in **Mo1** (τ = *ca*. 125 ps). This is probably due to a lower lying excited single state in **PtMo1**, coupled with the additional spin-orbit coupling

provided by the Pt centre. Whilst the excited state dynamics of **Mo1** are likely to feature both ^{1}MLCT and ^{1}δδ* singlet excited states, **PtMo1** only reveals evidence of the former, which was targeted by the 440 nm excitation wavelength. This assignment was supported by the observation of a short-lived {C≡C} transient vibration, which appeared at *ca.* 152 cm^{-1} lower in energy than the related groundstate vibration.

These studies have highlighted the potential for gaining valuable information on the short lifetime dynamic properties of the homo- and heterometallic acetylide systems. This work will compliment longer time-scale dynamic studies of these materials in solution and in the solid-state and provide a full understanding of the electronic properties as they evolve across the time-scales.

Chapter 7

Conclusions

Chapter 7 – Conclusions

The conclusions of this thesis have been separated into three subsections to aid the discussion of the appropriate concepts.

7.1.1 – Homo- and Heterometallic Polyyne Complexes

The ultimate aim of this thesis has been to develop novel heterometallic complexes that combine both Pt-acetylide and {Mo_2}-carboxylate subunits into a series of conjugated frameworks. To achieve this goal, three different heterometallic scaffolds were targeted and were reterosynthetically analysed to identify suitable precursors.

Chapter **2** has outlined the design and syntheses of a series of mono- and disubstituted Pt-ethynyl-ester complexes that represent potential synthons for 'terminating' and 'bridging' Pt units within the targeted mixed metal systems. The variety of conjugated spacer units that have been incorporated into the ligand systems allow the absorption and emission bands of these materials to be efficiently tuned over a wide range of wavelengths. Theoretical studies have provided a greater insight into the electronic structures of these species, helping to assess the degree of electronic delocalisation throughout the π-conjugated networks of these species.

The work presented in **Chapter 3** has developed the chemistry required to combine the Pt-ethynyl-ester complexes with selected {Mo_2} building blocks, resulting in the preparation of the first examples of mixed Pt-{Mo_2} acetylide complexes. Three different frameworks were isolated featuring different arrangements of the heterometallic subunits (**PtMo1**, **MoPtMo**, and **PtMoPt**). The molecular structures of each of the novel systems were unambiguously determined, revealing effective π-orbital alignment throughout the {Mo_2} and bridging ligand moieties.

Theoretical studies have shown that the filled Pt($d\pi$) orbitals mix with both the π- and π*-orbitals of the bridging ligand, which has a destabilising effect. Experimental evidence of this is observed in the electronic absorption spectrum of **PtMoPt** for which the MLCT band ($Mo_2\delta \rightarrow$bridge-π*) is significantly blue-shifted relative to the

Pt-free complex **Mo2**. Electrochemical analyses showed that the Pt-containing ligand system of **MoPtMo** did not facilitate electronic coupling between the {Mo_2} termini, which is likely due to a combination of the large intermetallic separation and the relatively high energy of the bridge π*-orbitals. However, the Pt centres were shown to have a significant effect on the energy of the {$Mo_2\delta$} orbitals and thus the overall stability of the systems. The half-wave potential of **PtMoPt** was observed at significantly lower energy than that of **Mo2**, making the heterometallic system a lot easier to oxidise.

To investigate ultra-fast charge transfer processes within the excited states of both homo- and heterometallic acetylide complexes, a series of preliminary TR-IR spectroscopic analyses have been performed (**Chapter 6**). Interestingly **Pt2a** and **Pt2b** behave very differently in the excited state, with the latter exhibiting an interesting charge redistribution process that localises electron density on the {Pt-C≡C} π*-orbitals, resulting in the formation of cumulated bonds. The differences show that subtle variations in the donor-acceptor properties within these complexes are important in tuning these excited state dynamics. Our initial investigations on the heterometallic complex, **PtMo1**, provide evidence for the initial population of a ^{1}MLCT excited state followed by conversion to a long-lived δδ* triplet state, for which the intersystem crossing is significantly faster than that observed for the parent complex **Mo1**. This is likely to be due to increased spin-orbit coupling from the Pt centre and a lower-lying LUMO orbital in the heterometallic complex.

7.1.2 – The Development of Novel Conjugated Bridging Ligands

This study has focussed on the design and synthesis of novel *bis*-amidinate bridging ligand systems that incorporate ethynyl functionality into the backbone, to promote π-conjugation throughout the molecules. Four different conjugated spacer units have been incorporated into these ligand frameworks, allowing the electron-withdrawing ability of the ligand systems to be tuned. When coordinated to redox-active Ru centres (**Ru3a-6a)**, electrochemical analyses provide no evidence that the *bis*-amidinate ligands facilitate electronic coupling between metal termini, however, the opto-electronic properties of the complexes are highly tuneable. The energy of the Ru *d*-orbitals is sensitive to the degree of stabilising backbonding interactions, which

can be promoted by using an electron withdrawing ligand (**BA3a**) or hindered using an electron rich ligand such as **BA2a**. The absorption maxima of these complexes can be tuned over *ca*. 140 nm using the current ligand set, with the highly conjugated anthracene-bridged complex providing the lowest energy absorption band.

The application of the *bis*-amidines as bridging ligands within {Mo_2} dimers has so far been unsuccessful. This has been due to uncontrolled ligand substitution with {Mo_2}-tetracarboxylate precursors and steric incompatibility with formamidinate-substituted {Mo_2} precursors. Work is currently ongoing within the group to develop the chemistry necessary to coordinate these ligand systems to {Mo_2} centres in a controlled manner.

7.1.3 – N-Heterocyclic Carbenes Adducts of {Mo_2} Carboxylate Dimers

Within this work we have synthesised the first examples of N-heterocyclic carbene adducts of quadruply-bonded {Mo_2} complexes and, through structural analyses, shown that the coordination chemistry observed is highly dependant on the properties of the carbene that is used. A series of equatorial adducts were prepared using relatively small alkyl-substituted carbenes and these exhibited interesting optical properties on account of perturbations in the $Mo_2\delta$-$Mo_2\delta^*$ energy gap. Equatorial adducts of **MoFAc** exhibit low energy absorption bands associated with this electronic transition whilst the behaviour of **MoAcL3** appears to be significantly more fluxional in solution, providing thermochromic properties. These have been correlated with VT-NMR studies.

The mesityl substituted carbene (**L1**) provided rare monoaxial adduct species for all {Mo_2} precursors that were investigated. These systems invoke further interest due to the presence of Mo-mesityl π-interactions (Mesityl-π→$Mo_2\pi^*$) at the vacant terminus of the Mo-Mo bond within the solid-state. Theoretical studies provide evidence that the coordination of a second σ-bonded carbene ligand is disfavoured by the relatively high energy of the $Mo_2\sigma^*$ orbitals within these complexes and, as such, the π-interactions provide a lower energy alternative. By increasing the steric demand of the carbene's aryl-substituent the π-interactions can be prevented, resulting in the formation of the more common diaxial adduct species (**MoFAc·L2**).

Chapter 8

Experimental

Chapter 8 – Experimental

8.1 – General Procedures

All air-sensitive reactions were carried out using standard Schlenk line and glove-box techniques under an inert atmosphere of either nitrogen or argon. DCM, hexanes and toluene utilised for air-sensitive reactions were dried over alumina columns using an Innovative Technology solvent purification system. THF was distilled from potassium benzophenone ketyl, EtOH was distilled from $Mg(OEt)_2$ and 1,2-dichlorobenzene was distilled from CaH_2. All solvents were degassed *via* repeated freeze-thaw cycles *in vacuo* and stored over 3 Å molecular sieves. All glassware was either dried in an oven at 130 ^oC or flame dried under vacuum prior to use.

NMR experiments were carried out using a Bruker AVANCE-500, AVANCE-400, AVANCE-300 or AVANCE-250 spectrometers at 298 K unless stated otherwise. ^1H and $^{13}C\{^1H\}$ NMR spectra were internally referenced to residual solvent peaks, $^{19}F\{^1H\}$ NMR spectra relative to $CFCl_3$, $^{31}P\{^1H\}$ NMR spectra relative to H_3PO_4 and ^{195}Pt NMR spectra were reported relative to Na_2PtCl_6. Assignments reported are supported by homo- and hetero-nuclear two-dimensional NMR experiments. NMR experiments performed on air-sensitive species were conducted in Young's tap NMR tubes made up and sealed in a glove-box. All deuterated solvents were purchased from Cambridge Laboratories and prior to use; C_6D_6, d_8-toluene and d_8-THF were all dried *via* distillation from molten potassium.

Electronic absorption data were recorded using a 'Cary 50 UV-Visible Spectrophotometer". Samples were prepared in high quality volumetric flasks using HPLC-grade solvents and analyses were performed in quartz cells with a path length of 1 cm. Emission data were recorded on a "Perkin Elmer LS55 Luminescence" Spectrometer using a quartz sample cell with a path length of 1 cm.

Electrochemical studies were carried out using an "Ivium Technologies Compactstat" potentiostat. Samples were analysed within a purpose-made low volume electrochemical cell with a ground glass tap to provide Schlenk line compatibility. All samples were analysed as 1 mmol solution under N_2 using dried

and degassed solvent, NBu_4PF_6 electrolyte (0.1 M) and a platinum reference electrode, gold counter electrode and glassy carbon working electrode.

Experimental IR data were recorded on a Perkin Elmer Spectrum One FT-IR spectrometer using solid samples within the range 400-4000 cm^{-1} and spectra were averaged over 16 scans.

Raman spectra were recorded on a Renishaw inVia Raman Microscope using a solid-state laser with an excitation wavelength of either 532 nm or 785 nm, and a power of 2.5 mW. Samples were sealed between two microscope slides under Ar and a 20x objective was utilised to focus on individual crystals.

Elemental Analyses were carried out by Stephen Boyer at the School of Human Sciences, London Metropolitan University, or by Elemental Microanalysis Ltd. Air-sensitive samples were flame sealed in glass ampoules prior to analysis.

Crystallographic data were collected at 150 K or 100 K on a Nonius KappaCCD diffractometer or an Oxford Diffraction Gemini Ultra Diffractometer, [$\lambda(Cu_{k\alpha})$ = 1.54184 Å] or [$\lambda(Mo_{k\alpha})$ = 0.71073 Å], solved by direct methods and refined against all F^2 using SHELXL–97.[329] Where possible non-hydrogen atoms are modelled as anisotropic and hydrogen atoms were constrained using a riding model with the exception of the amidine N*H* protons of **BA1a** and **BA1b** and the imidazolium C*H* of **MoPiv·L3** which were located and freely refined. Absorption corrections, were appropriate, were performed using either analytical or semi-empirical methods.

All computational studies reported within this work utilised the B3LYP[330-331] hybrid density functional under the Gaussian 03 package.[332] Geometry optimisation calculations were performed on all complexes prior to further analysis and were supported by frequency calculations that exhibited no imaginary molecular vibrations. All studies utilised a quasi-relativistic pseudopotential and associated basis set (SDD) for molybdenum and platinum,[333] whilst the 6-31G(d) [334-335] basis set was used for all other atoms. All computations were performed on the University of Bath's High Performance Computing Facility. Electron density plots were made

using the 'Molekel'[336] software package and both molecular orbital diagrams and orbital compositions were achieved using the 'Chemissian' software package.[337]

The time resolved infrared (TRIR) studies were performed at the 'Central Laser Facility' (CLF), within the 'Rutherford Appleton Laboratories', under the supervision of Professor Mike Towrie. The experimental setup for the picosecond resolution studies is described in detail within the literature.[338] Both pump and probe laser pulses are generated from the same 1 KHz, 800nm, 150 ps Ti:Sapphire laser for which the output is frequency doubled, using a beta barium borate crystal. The laser is then split to pump two optical parametric amplifiers (OPAs) allowing the tunability of both the UV-pump and IR-Probe. The latter is split a second time to provide a reference by which fluctuations in signal intensity may be normalized. The time delays were created by altering the path length of the pump laser pulse, using mirrors on a translating stage. The infrared spectra were recorded on HgCdTe linear array detectors, each measuring 128 pixels. Sample solutions were diluted so as to provide an approximate absorbance of 0.3 at the excitation wavelength. Solutions were flowed through a Harrick type flow cell using a peristaltic pump system and a N_2 bubbler was included in the setup to allow analysis in the absence of air. CaF_2 windows were used for all analyses with a 100 μm Teflon spacer. All solvents used were dried and degassed as detailed above.

Unless stated otherwise, all chemicals used within this study were purchased from commercial sources and used without further purification.

8.2 – Experimental Data for Chapter 2

Within this section each of the Sonogashira coupling reactions and the syntheses of the Pt-acetylide complexes were performed under an Ar atmosphere using standard Schlenk-line techniques. However, the purification of each product did not require air-sensitive consideration. The compunds: *Trans*-$Ph(PEt_3)PtCl$,[339-340] *trans*-$(PEt_3)_2PtCl_2$[341] and **2**[144], were prepared using preparations reported in the literature and **1** was purchased and used as received. Within the $^{13}C\{^1H\}$ NMR data presented for the Pt complexes, 't*' represents a virtual coupling constant.

Synthesis of **Methy-4-bromo-2,5-dimethoxybenzoate** (precursor for **3**):

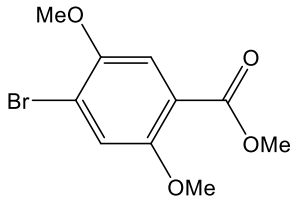

4-bromo-2,5-dimethoxybenzoic acid[154] (500 mg, 1.92 mmol) was dissolved in MeOH (50 mL) and H_2SO_4 (0.5 mL) was added. The solution was stirred at reflux for 12 h after which all volatiles were removed *in vacuo*. The residue was extracted into DCM and washed with H_2O (3 x 20 mL). The organic fraction was dried over $MgSO_4$, filtered and solvent removed *in vacuo* to give methyl-4-bromo-2,5-dimethoxybenzoate which was used for the next step without further purification. (Yield 93 %). **^{1}H NMR ($CDCl_3$, 298 K, 400.13 MHz):** δ 7.38 (s, 1H, phenylene-C*H*), 7.21 (s, 1H, phenylene-C*H*), 3.90 (s, 3H, OCH_3), 3.89 (s, 3H, OCH_3), 3.87 (s, 3H, OCH_3).

Synthesis of **3:**

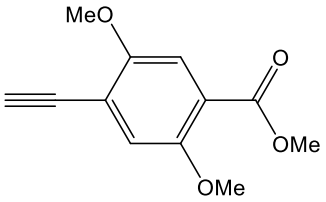

Methyl-4-bromo-2,5-dimethoxybenzoate (300 mg, 1.09 mmol), $(PPh_3)_2PdCl_2$ (38 mg, 5 mol%) and CuI (*ca.* 5 mg) were dissolved in degassed $^iPr_2NH$ (40 mL). Trimethylsilyl-acetylene (TMSA) (0.18 mL, 1.31 mmol) was added to the solution which heated at 50 ^oC for 24 h. Volatiles were removed *in vacuo* and the crude product was extracted into hexane and purified by alumina flash chromatography (hexane eluent) giving methyl-4-trimethylsilyl-2,5-dimethoxybenxoate. The product and K_2CO_3 (excess) were dissolved in a MeOH (10 mL) and THF (10 mL) mixture and stirred for 5 h after which all volatiles were removed *in vacuo*. The resulting oil was extracted into DCM (20 mL), washed with H_2O (3 x 20 mL) and the organic fraction was dried over $MgSO_4$. After filtering, all volatiles were removed *in* vacuo providing pure **3** as a colourless powder. Yield = 156 mg (68 %). **^{1}H NMR ($CDCl_3$, 298 K, 400.13 MHz):** δ 7.33 (s, 1H, phenylene-C*H*), 7.08 (s, 1H, phenylene-C*H*), 3.90 (s, 3H, ester-OCH_3), 3.89 (s, 3H, phenylene-OCH_3), 3.86 (s, 3H, phenylene-OCH_3), 3.42 (s, 1H, C≡C-*H*). **^{13}C{^{1}H} ($CDCl_3$, 298 K, 100.61 MHz):** δ 166.1

(O*C*O), 154.2 (phenylene-*C*-OMe), 152.9 (phenylene-*C*-OMe), 121.0 (phenylene-quaternary-*C*), 118.1 (phenylene-*C*H), 116.0 (phenylene-quaternary-*C*), 113.7 (phenylene-*C*H), 83.5 (ethynyl-*C*), 79.3 (ethynyl-*C*), 56.8 (phenylene-O*C*H_3), 55.5 (phenylene-O*C*H_3), 52.4 (ester-O*C*H_3). **Infrared:** 2100 cm^{-1} (C≡C), 1695 cm^{-1} (C=O). **Mp:** 94-96 ºC. **Elemental analysis:** Calculated for $C_{12}H_{12}O_4$: C 65.45, H 5.49. Observed: C 65.41, H 5.50.

Synthesis of **4-bromo-2,5-di-(trifluoromethyl)benzoic acid** (precursor for **4**):

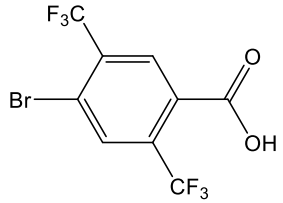

Di-bromo-2,5-di(trifluoromethyl)benzene[152] (1 g, 3.0 mmol) was converted to 4-bromo-2,5-di-(trifluoromethyl)benzoic acid following an analogous preparation to that reported for the methoxy-substituted analogue.[154] Yield = 652 mg (72 %). **^{1}H NMR (CDCl$_3$, 298 K, 400.13 MHz):** δ 8.33 (s, 1H, phenylene-C*H*) 8.18 (s, 1H, phenylene-C*H*), 6.06 (broad, 1H, COO*H*)**. ^{19}F NMR (CDCl$_3$, 298 K, 376.50 MHz):** δ 60.0 (CF_3), 63.5 (CF_3).

Synthesis of **4:**

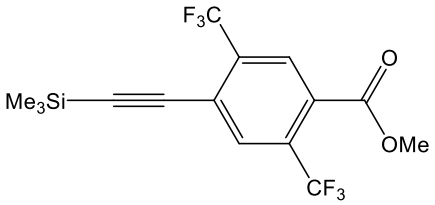

4-bromo-2,5-di(trimethylsilyl)benzoic acid (500 mg) was converted to **4** using an identical method to that reported for **3**, differing only in the absence of the final desilylation step. Yield = 361 mg (66 %). **^{1}H NMR (CDCl$_3$, 298 K, 400.13 MHz):** δ 8.10 (s, 1H, phenylene-C*H*), 7.96 (s, 1H, phenylene-C*H*), 3.97 (s, 3H, ester-CH_3), 0.29 (s, 9H, SiCH_3). **^{19}F NMR (CDCl$_3$, 298 K, 376.50 MHz):** δ 60.3 (CF_3), 63.2 (CF_3). **^{13}C{^{1}H} (CDCl$_3$, 298 K, 100.62 MHz):** δ 165.2 (O*C*O), 135.0 (q, $^2J_{C\text{-}F}$ = 32.2 Hz, *C*CF_3), 132.6 (q, $^3J_{C\text{-}F}$ = 1.8 Hz, phenylene-*C*H), 131.9 (q, $^2J_{C\text{-}F}$ = 32.2 Hz, *C*CF_3), 130.1 (q, $^3J_{C\text{-}F}$ = 1.5 Hz, phenylene-quaternary-*C*), 128.4 (q, $^3J_{C\text{-}F}$ = 5.1 Hz, phenylene-*C*H), 125.1 (q, $^3J_{C\text{-}F}$ = 1.8 Hz, phenylene-quaternary-*C*), 122.2 (q, $^1J_{C\text{-}F}$ =

274.4 Hz, 2(*C*F_3)), 106.9 (ethynyl-C), 98.2 (ethynyl-C) 53.2 (ester-*C*H_3), 0.75 (Si*C*H_3). **Infrared:** 2149 cm^{-1} (C≡C), 1697 cm^{-1} (C=O).**Mp:** 38-41 ^oC **Elemental analysis:** Calculated for $C_{15}H_{14}F_6O_2Si_1$: C 48.91, H 3.83. Observed: C 49.02, H 3.72.

Synthesis of **2-Ethyl-5-bromothiophene carboxylate** (precursor for **5**):

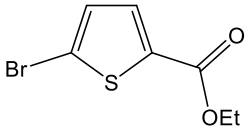

2-Ethyl-5-bromothiophene carboxylate was synthesised from 2-bromo-5-thiophene carboxylic acid (500 mg, 2.4 mmol) following the method described in the literature for the preparation of the propyl-ester analogue.[145] Yield = 540 mg (95 %). **^{1}H NMR ($CDCl_3$, 298 K, 300.22 MHz):** δ 7.55 (d, $^3J_{H-H}$ = 3.8 Hz, 1H, thienyl-C*H*), 7.08 (d, $^3J_{H-H}$ = 3.8 Hz, 1H, thienyl-C*H*), 4.34 (q, $^3J_{H-H}$ = 7.2 Hz, 2H, ethyl-CH_2), 1.37 (t, $^3J_{H-H}$ = 7.2 Hz, 3H, ethyl-CH_3).

Synthesis of **5**:

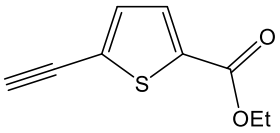

2-Ethyl-5-bromothiophene carboxylate (500 mg, 2.1 mmol) was converted to **5** using an identical method to that outlined in the literature.[145] Yield = 299 mg (78 %). **^{1}H NMR ($CDCl_3$, 298 K, 300.22 MHz):** δ 7.64 (d, $^3J_{H-H}$ = 3.8 Hz, 1H, thienyl-C*H*), 7.21 (d, $^3J_{H-H}$ = 3.8 Hz, 1H, thienyl-C*H*), 4.34 (q, $^3J_{H-H}$ = 7.2 Hz, 2 H, ethyl-CH_2), 3.45 (s, 1H, ethynyl-C*H*), 1.36 (t, $^3J_{H-H}$ = 7.2 Hz, 3H, ethyl-CH_3). **^{13}C{^{1}H} NMR ($CDCl_3$, 298 K, 75.49 MHz):** δ 161.4 (O*C*O), 134.8 (thienyl-quaternary-*C*), 133.2 (thienyl-*C*H), 132.8 (thienyl-*C*H), 128.2 (thienyl-quaternary-*C*), 83.6 (ethynyl-*C*H), 76.2 (ethynyl-*C*), 61.6 (ethyl-*C*H_2), 14.3 (ethyl-*C*H_3). **Infrared:** 2102 cm^{-1} (C≡C), 1703 cm^{-1} (C=O). **Mp:** 45-46 ^oC. **Elemental analysis:** Calculated for $C_9H_8O_2S_1$: C 59.98, 4.47. Observed: C 9.90, H 4.43.

Synthesis of **6**:

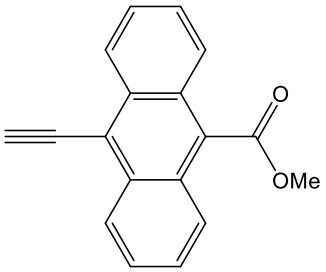

6 was synthesised from Methyl-9-bromo-10-anthracene carboxylate[156] (500 mg, 1.7 mmol) using an analogous Sonogashira reaction to that reported for **3** and purified in the same manner. Product was stored at -28 °C in the absence of light to prevent decomposition. **Yield:** 301 mg (73 %). **^{1}H NMR ($CDCl_3$, 298 K, 500.13 MHz):** δ 8.66-8.63 (m, 2H, anthracene-C*H*), 8.03-7.99 (m, 2H, anthracene-C*H*), 7.65-7.56 (m, 4H, anthracene-C*H*), 4.20 (s, 3H, ester-CH_3), 4.07 (s, 1H, ethynyl-C*H*). **^{13}C{^{1}H} ($CDCl_3$, 298 K, 125.76 MHz):** δ 169.7 (O*C*O), 132.5 (anthracene-*C*H), 130.0 (anthracene-quaternary-*C*), 129.4 (anthracene-*C*H), 128.2 (anthracene-quaternary-*C*), 127.7 (anthracene-*C*H), 127.3 (anthracene-quaternary-*C*), 125.4 (anthracene-*C*H), 119.0 (anthracene-quaternary-*C*), 89.7 (ethynyl-*C*H), 79.8 (ethynyl-*C*), 52.8 (ester-*C*H_3). **Infrared:** 2100 cm^{-1} (C≡C), 1703 cm^{-1} (C=O). **Mp**: 95-100 °C (dec.) **Elemental analysis:** Calculated for $C_{18}H_{12}O_2$: C 83.06, H 4.65. Observed: C 82.95, H 4.70.

Synthesis of **Pt1a**:

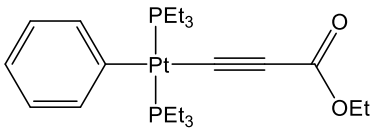

Ethyl-propiolate (0.045 mL, 0.441 mmol) and *trans*-Ph(PEt_3)$_2$PtCl (200 mg, 0.368 mmol) were dissolved in DCM (5 mL) and NEt_3 (5 mL). CuI (*ca*. 1 mg) was added and the solution was stirred in the absence of light for 12 h. All volatiles were removed *in vacuo* and the product was purified using column chromatography (1:2 DCM/Hexane). **1** was crystallised by cooling a concentrated hexane solution to -28 °C, yielding small colourless block-like crystals. **Yield:** 129 mg (58 %). **^{1}H NMR ($CDCl_3$, 298 K, 400.13 MHz):** δ 7.25 (d, $^{3}J_{H\text{-}H}$ = 7.3 Hz, 2H, *o*-phenyl-C*H*), 6.97 (t, $^{3}J_{H\text{-}H}$ = 7.3 Hz, 2H *m*-phenyl-C*H*), 8.81 (t, $^{3}J_{H\text{-}H}$ = 7.3 Hz, 1H, *p*-phenyl-C*H*), 4.14 (q, $^{3}J_{H\text{-}H}$ = 7.2 Hz, 2H, OCH_2), 1.79-1.62 (m, 12H, PEt_3-CH_2), 1.28 (t, $^{3}J_{H\text{-}H}$ = 7.2 Hz, 3H, ethyl-CH_3), 1.11-1.03 (m, 18H, PEt_3-CH_3). **^{31}P{^{1}H} NMR ($CDCl_3$, 298 K,**

161.98 MHz): δ 10.4 ($^{1}J_{P\text{-}Pt}$ = 2599 Hz). **^{195}Pt NMR (CDCl$_3$, 298 K, 85.62 MHz):** δ -4571 (t, $^{1}J_{Pt\text{-}P}$ = 2599 Hz). **^{13}C{^{1}H} NMR (CDCl$_3$, 298 K, 100.62 MHz):** δ 155.0 (O*C*O) 155.0 (t, $^{2}J_{C\text{-}P}$ = 10.4 Hz, *i*-phenyl-*C*), 138.7 (t, $^{3}J_{C\text{-}P}$ = 2.2 Hz, *o*-phenyl-*C*), 127.5 *m*-phenyl-*C*), 122.4 (t, $^{2}J_{C\text{-}P}$ = 13.9 Hz, ethynyl-*C*), 121.7 (*p*-phenyl-*C*), 102.7 (ethynyl-*C*), 60.4 (O*C*H$_2$), 15.0 (t*, ($^{1}J_{C\text{-}P}$ + $^{3}J_{C\text{-}P}$ = 34.4 Hz, PEt$_3$-*C*H$_2$), 14.4 (OCH$_2$*C*H$_3$), 8.0 (PEt$_3$-*C*H$_3$). **Mp:** 80 ^{o}C. **Infrared:** 2078 (C≡C), 1672 (C=O). **Elemental analysis:** Calculated for $C_{23}H_{40}O_2P_2Pt_1$: C 45.62, H 6.66. Observed C 45.67, H 6.76.

Synthesis of **Pt1b**:

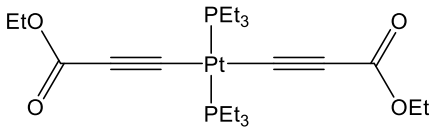

Ethyl-propiolate (0.067 mL, 0.478 mmol) and *trans*-(PEt$_3$)$_2$PtCl$_2$ (100 mg, 0.199 mmol) were dissolved in DCM (5 mL) and NEt$_3$ (5mL) and CuI (*ca.* 1 mg) was added. The solution was stirred for 12 hr after which all volatiles were removed *in vacuo*. The product was purified by silica column chromatography (1:2 DCM/Hexane) and large colourless block-like crystals were obtained by cooling a concentrated hexane solution to -28 ^{o}C. **Yield:** 80 mg (64 %). **^{1}H NMR (CDCl$_3$, 298 K, 400.13 MHz):** δ 4.12 (q, $^{3}J_{H\text{-}H}$ = 7.2 Hz, 4H, OC*H*$_2$), 2.16-2.01 (m, 12H, PEt$_3$-C*H*$_2$), 1.25 (t, $^{3}J_{H\text{-}H}$ = 7.2, 6H, OCH$_2$C*H*$_3$), 1.18-1.10 (m, 18H, PEt$_3$-C*H*$_3$). **^{31}P{^{1}H} NMR (CDCl$_3$, 298 K, 161.98 MHz):** δ 11.9 ($^{1}J_{P\text{-}Pt}$ = 2278 Hz). **^{195}Pt NMR (CDCl$_3$, 298 K, 85.62 MHz):** δ – 4757 (t, $^{1}J_{Pt\text{-}P}$ = 2284 Hz). **^{13}C{^{1}H} NMR (C$_6$D$_6$, 298 K, 100.62 MHz):** δ 154.7 (O*C*O), 112.9 (t, $^{2}J_{C\text{-}P}$ = 15.1 Hz, ethynyl-C), 102.5 (ethynyl-C), 60.5 (O*C*H$_2$), 16.2 (t*, ($^{1}J_{C\text{-}P}$ + $^{3}J_{C\text{-}P}$ = 35.1 Hz, PEt$_3$-*C*H$_2$), 14.3 (OCH$_2$*C*H$_3$), 8.18 (PEt$_3$-*C*H$_3$). **Mp:** 154 ^{o}C. **Infrared:** 2096 (C≡C), 1673 (C=O). **Elemental analysis:** Calculated for $C_{22}H_{40}O_4P_2Pt_1$: C 42.24, H 6.44. Observed: C 42.25, H 6.35.

Synthesis of **Pt2a**:

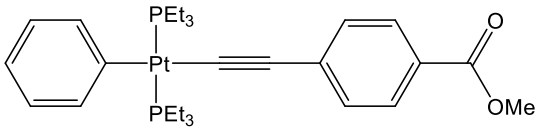

Pt2a was prepared using the same method as reported for **Pt1a** using **2** (53 mg, 3.31 mmol), *trans*-Ph(PEt_3)$_2$PtCl (150 mg, 2.76 mmol) and $^{i}Pr_2NH$ in place of NEt_3. The product was purified by column chromatography (1:1 DCM/Hexane). The oily residue of **Pt2a** was dissolved in minimal hexanes and the solution was cooled to -28 ^{o}C yielding large green-tinted crystals. **Yield:** 156 mg (85%). **^{1}H NMR (C_6D_6, 298 K, 300.22 MHz):** δ 8.21 (d, $^{3}J_{H-H}$ = 8.3 Hz, 2H, phenylene-C*H*), 7.66-751 (m, 4H, phenylene-C*H* & *o*-phenyl-C*H*), 7.23 (t, $^{3}J_{H-H}$ = 7.3 Hz, 2H, *m*-phenyl-C*H*), 7.03 (t, $^{3}J_{H-H}$ = 7.2 Hz, 1H, *p*-phenyl -C*H*), 3.48 (s, 3H, OCH_3), 1.73-1.50 (m, 12H, PEt_3-CH_2), 0.98-0.88 (m, 18H, PEt_3-CH_3). **^{31}P{^{1}H} NMR (C_6D_6, 298 K, 121.53 MHz):** δ 11.1 ($^{1}J_{P-Pt}$ = 2640 Hz). **^{195}Pt NMR ($CDCl_3$, 298 K, 85.63 MHz):** δ -4551 (t, $^{1}J_{Pt-P}$ = 2638 Hz). **^{13}C{^{1}H} NMR (C_6D_6, 298 K, 100.62 MHz):** δ 166.8 (O*C*O), 156.3 (t, $^{2}J_{C-P}$ = 10.0 Hz, *i*-phenyl *C*), 139.6 (*o*-phenyl-*C*), 135.2 (phenylene-quaternary-C), 131.1 (phenylene-*C*H), 130.0 (phenylene-*C*H), 128.2 (*m*-phenyl-*C*), 126.8 (phenylene-quaternary-*C*), 122.3 (*p*-phenyl-*C*), 120.7 (t, $^{2}J_{C-P}$ = 14.6 Hz, ethynyl-*C*), 110.9 (ethynyl-*C*), 51.4 (O*C*H_3), 15.6 (t*, ($^{1}J_{C-P}$ + $^{3}J_{C-P}$) = 35.1 Hz, PEt_3-*C*H_2), 8.1 (PEt_3-*C*H_3). **Mp:** 89 ^{o}C. **Infrared:** 2092 cm^{-1} (C≡C), 1710 cm^{-1} (C=O). **Elemental analysis:** Calculated for $C_{28}H_{42}O_2P_2Pt_1$: C 50.37, H 6.34. Observed: C 50.51, H 6.47.

Synthesis of **Pt2b**:

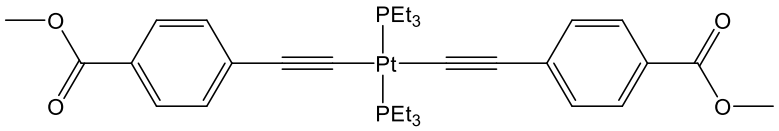

trans-(PEt_3)$_2$$PtCl_2$ (100 mg, 0.199 mmol), and **2** (77 mg, 0.478 mmol) were dissolved in DCM (5 mL) and $^{i}Pr_2NH$ (5mL) and CuI (*ca.* 1 mg) was added. The solution was stirred for 12 h after which all volatiles were removed *in vacuo*. The product was purified by silica column chromatography (1:1 DCM/Hexane followed by DCM with 1% MeOH). The yellow residue obtained was extracted into boiling hexane, filtered and allowed to cool to root temperature yielding yellow needle-like crystals of **Pt2b**. **Yield:** 121 mg (81 %). **^{1}H NMR ($CDCl_3$, 298 K, 300.22 MHz):** δ 7.88 (d, $^{3}J_{H-H}$ = 8.2 Hz, 4H, phenylene-C*H*), 7.29 (d, $^{3}J_{H-H}$ = 8.2 Hz, 4H, phenylene-

C*H*), 3.89 (s, 6H, OCH_3), 2.26-2.09 (m, 12H, PEt_3-CH_2), 1.27-1.19 (m, 18H, PEt_3-CH_3). **^{31}P{^{1}H} NMR ($CDCl_3$, 298 K, 121.53 Hz):** δ 11.3 ($^1J_{P\text{-}Pt}$ = 2369 Hz). **^{195}Pt NMR ($CDCl_3$, 298 K, 86.01 MHz):** δ -4724 (t, $^1J_{Pt\text{-}P}$ = 2369 Hz). **^{13}C{^{1}H} NMR ($CDCl_3$, 298 K, 100.62 MHz):** δ 167.3 (O*C*O), 133.8 (phenylene-quaternary-*C*), 130.8 (phenylene-*C*H), 129.5 (phenylene-*C*H), 126.4 (phenylene-quaternary-*C*), 113.7 (t, $^2J_{C\text{-}P}$ = 29.0 Hz, ethynyl-*C*), 110.0 (ethynyl-*C*), 52.1 (O*C*H_3), 16.5 (t*, ($^1J_{C\text{-}P}$ + $^3J_{C\text{-}P}$) = 35.1 Hz, PEt_3-*C*H_2). 8.5 (PEt_3-*C*H_3). **Mp:** 152 °C. **Infrared:** 2102 cm^{-1} (C≡C), 1707 cm^{-1} (C=O). **Elemental analysis:** Calculated for $C_{32}H_{44}O_4P_2Pt_1$: C 51.26, H 5.92. Observed: C 51.38, H 5.86.

Synthesis of **Pt3a**:

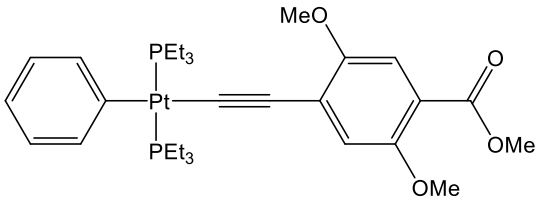

Synthesised using the same method to that reported for **Pt2a** using; *trans*-$Ph(PEt_3)_2PtCl$ (100 mg, 0.184 mmol) and **3** (49 mg, 0.221 mmol). The product was purified by silica column chromatography (1:1 DCM/hexane) and large yellow block-like crystals of **Pt3a** were obtained by cooling a concentrated pentane solution to -28 °C. **Yield:** 142 mg (89 %). **^{1}H NMR ($CDCl_3$, 298 K, 400.13 MHz):** δ 7.32 (d, $^3J_{H\text{-}H}$ = 7.3 Hz, 2H, *o*-phenyl-C*H*), 7.28 (s, 1H, phenylene-C*H*), 6.97 (t, $^3J_{H\text{-}H}$ = 7.3 Hz, 2H, *m*-phenyl-C*H*), 6.90 (s, 1H, phenylene-C*H*), 6.80 (t, $^3J_{H\text{-}H}$ = 7.3 Hz, 1H, *p*-phenyl-C*H*), 3.87 (s, 3H, ester-OCH_3), 3.85 (s, 3H, phenylene-OCH_3), 3.81 (s, 3H, phenylene-OCH_3), 1.89-1.73 (m, 12H, PEt_3-CH_2), 1.14-1.06 (m, 18H, PEt_3-CH_3). **^{31}P{^{1}H} NMR ($CDCl_3$, 298 K, 161.98 MHz):** δ 10.2 ($^1J_{P\text{-}Pt}$ = 2638 Hz). **^{195}Pt NMR ($CDCl_3$, 298 K, 85.63 MHz):** δ -4540 (t, $^1J_{Pt\text{-}P}$ = 2638 Hz). **^{13}C{^{1}H} NMR ($CDCl_3$, 298 K, 100.62 MHz):** δ 166.5 (O*C*O), 156.2 (t, $^2J_{C\text{-}P}$ = 10.2 Hz, *i*-phenyl-*C*), 153.9 (phenylene-*C*OMe), 153.8 (phenylene-*C*OMe), 139.2 (*o*-phenyl-C), 127.4 (*m*-phenyl-*C*), 124.7 (t, $^2J_{C\text{-}P}$ = 14.6 Hz, ethynyl-*C*), 124.6 (phenylene-quaternary-*C*), 121.4 (*p*-phenyl-*C*), 117.2 (phenylene-*C*H), 115.6 (phenylene-quaternary-*C*), 113.8 (phenylene-*C*H), 105.8 (ethynyl-C), 56.9 (phenylene-O*C*H_3), 56.2 (phenylene-O*C*H_3), 52.0 (ester-*C*H_3), 15.1 (t*, ($^1J_{C\text{-}P}$ + $^3J_{C\text{-}P}$) = 34.4 Hz, PEt_3-*C*H_2), 8.2 (PEt_3-*C*H_3). **Mp:** 84 °C. **Infrared:** 2091 cm^{-1} (C≡C), 1715 cm^{-1} (C=O). **Elemental analysis:** Calculated for $C_{30}H_{46}O_4P_2Pt_1$: C 49.51, H 6.37. Observed: C 49.61, H 6.49.

Synthesis of **Pt3a**:

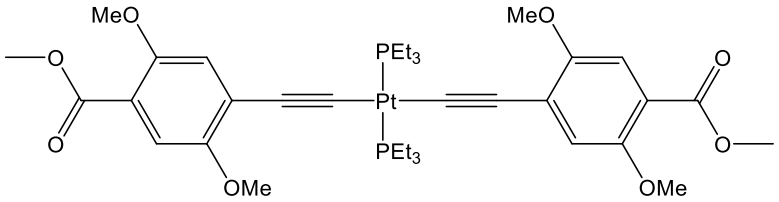

Synthesised using the same method to that reported for **Pt2b** using; *trans*-$(PEt_3)_2PtCl_2$ (100 mg, 0.200 mmol) and **3** (0.088 g, 0.478 mmol). The product was purified by silica column chromatography (DCM) and crystallised from a cooled toluene solution to provide **Pt3b** as yellow block-like crystals. **Yield:** 154 mg (89 %). **^{1}H NMR ($CDCl_3$, 298 K, 400.13 MHz):** δ 7.27 (s, 2H, phenylene-C*H*), 6.87 (s, 2H, phenylene-C*H*), 3.87 (s, 3H, ester-OCH_3), 3.84 (s, 3H, phenylene-OCH_3), 3.81 (2, 3H, phenylene-OCH_3), 2.33-2.15 (m, 12H, PEt_3-CH_2), 1.26-1.18 (m, 18H, PEt_3-CH_3). **^{31}P{^{1}H} NMR ($CDCl_3$, 298 K, 161.98 MHz):** δ 11.5 ($^1J_{P\text{-}Pt}$ = 2351). **^{195}Pt NMR ($CDCl_3$, 298 K, 85.61 MHz):** -4707 (t, $^1J_{Pt\text{-}P}$ = 2351). **^{13}C{^{1}H} NMR ($CDCl_3$, 298 K, 100.62 MHz):** 166.5 (OCO), 153.7 (2 x phenylene-*C*OCH$_3$), 123.7 (phenylene quaternary-C), 117.8 (t, $^2J_{C\text{-}P}$ = 14.6 Hz, ethynyl-*C*), 117.2 (phenylene-*C*H), 116.2 (phenylene-quaternary-*C*), 113.5 (phenylene-*C*H), 105.3 (ethynyl-*C*), 56.8 (phenylene-O*C*H$_3$), 56.1 (phenylene-O*C*H$_3$), 51.9 (ester-O*C*H$_3$), 16.2 (t*, ($^1J_{C\text{-}P}$ + $^3J_{C\text{-}P}$) = 35.1 Hz, PEt_3-*C*H$_2$), 8.4 (PEt_3-*C*H$_3$). **Mp:** 155 ^{o}C. **Infrared:** 2090 cm^{-1} (C≡C), 1688 cm^{-1} (C=O). **Elemental analysis:** Calculated for $C_{36}H_{52}O_8P_2Pt_1$: C 49.71, H 6.03. Observed: C 49.83, H 5.89.

Synthesis of **Pt4a**:

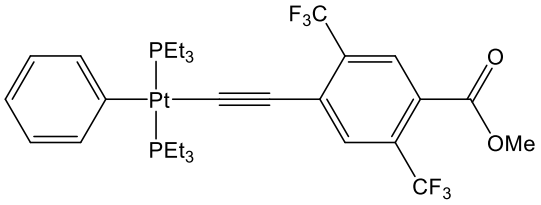

trans-Ph$(PEt_3)_2PtCl$ (100 mg, 0.184 mmol) and **4** (81 mg, 0.221 mmol) were dissolved in DCM (5 mL) and ^{i}Pr$_2$NH (5 mL). NaOMe (0.437 M, 0.63 mL, 0.276 mmol) and CuI (*ca.* 1 mg) were then added and the solution stirred for 12 h after which all volatiles were removed *in vacuo*. The product was purified by silica column chromatography (1:1 DCM/hexane). Yellow block-like crystals of **Pt4a** were obtained by cooling a concentrated pentane solution to -28^{o}C. **Yield:** 135 mg (91%).

^{1}H NMR ($CDCl_3$, 298 K, 400.13 MHz): δ 8.06 (s, 1H, phenylene-C*H*), 7.77 (s, 1H, phenylene-CH), 7.31 (d, $^{3}J_{H-H}$ = 7.3 Hz, 2H, *o*-phenyl-C*H*), 6.98 (t, $^{3}J_{H-H}$ = 7.3 Hz, 2H, *m*-phenyl-C*H*), 6.82 (t, $^{3}J_{H-H}$ = 7.3 Hz, 1H, *p*-phenyl-C*H*), 3.93 (s, 3H, OCH_3), 1.79-1.63 (m, 12H, PEt_3-CH_2), 1.12-1.05 (m, 18H, PEt_3-CH_3). **^{31}P{^{1}H} NMR ($CDCl_3$, 298 K, 161.98 MHz):** δ 10.8 ($^{1}J_{P-Pt}$ = 2622 Hz). **^{19}F NMR ($CDCl_3$, 298 K, 376.48 MHz):** δ -60.2 (CF_3), -63.5 (CF_3). **^{195}Pt NMR ($CDCl_3$, 298 K, 85.63 MHz):** δ -4543 (t, $^{1}J_{Pt-P}$ = 2622 Hz). **^{13}C{^{1}H} NMR ($CDCl_3$, 298 K, 125.76 MHz):** δ 165.8 (O*C*O), 154.9 (t, $^{2}J_{C-P}$ = 10.4 Hz, *i*-phenyl-C), 138.9 (*m*-phenyl-*C*), 135.7 (t, $^{2}J_{C-P}$ =14.5 Hz, ethynyl-*C*), 132.3 (q, $^{3}J_{C-F}$ = 5.4 Hz, phenylene-*C*H), 131.8 (q, $^{2}J_{F-C}$ = 30.0 Hz, *C*CF_3), 131.4 (q, $^{2}J_{C-F}$ = 32.7, *C*CF_3), 131.3 (phenylene-quaternary-*C*), 128.8 (q, $^{3}J_{C-F}$ = 5.4 Hz, phenylene-*C*H), 127.5 (*o*-phenyl-*C*), 124.6 (phenylene-quaternary-*C*), 122.8 (q, $^{1}J_{C-F}$ = 274.3 Hz, *C*F_3), 123.2 (q, $^{1}J_{C-F}$ = 273.4 Hz, *C*F_3), 121.6 (*p*-phenyl-*C*), 106.7 (ethynyl-*C*), 52.8 (O*C*H_3), 15.0 (t*, ($^{1}J_{C-P}$ + $^{3}J_{C-P}$) = 34.5 Hz, PEt_3-*C*H_2), 7.9 (PEt_3-CH_3). **Mp**: 64-65 °C. **Infrared:** 2084 cm^{1} (C≡C), 1724 cm^{-1} (C=O). **Elemental analysis:** Calculated for $C_{30}H_{40}F_6O_2P_2Pt_1$: C 44.84, H 5.02. Observed: C 44.96, H 4.91.

Synthesis of **Pt4b**:

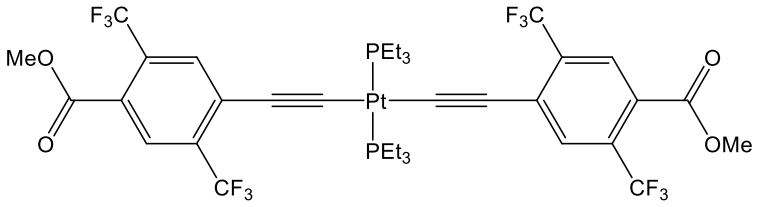

trans-$(PEt_3)_2PtCl_2$ (100 mg, 0.200 mmol) and **4** (176 mg, 0.478 mmol) were dissolved in DCM (5 mL) and $^{i}Pr_2NH$ (5 mL). NaOMe (0.437 M, 1.09 mL, 0.498 mmol) and CuI (*ca.* 1 mg) were then added and the solution stirred for 12 h after which all volatiles were removed *in vacuo*. The product was purified by silica column chromatography (1:1 DCM/hexane) and yellow block-like crystals of **Pt4b** were grown by cooling a concentrated hexane solution to -28 °C. **Yield:** 155 mg (76 %). **^{1}H NMR ($CDCl_3$, 298 K, 400.13 MHz):** δ 8.06 (s, 2H, phenylene-C*H*), 7.75 (s, 2H, phenylene-C*H*), 3.93 (s, 6H, OCH_3), 2.21-2.01 (m, 12H, PEt_3-CH_2), 1.23-1.15 (m, 18H, PEt_3-CH_3). **^{31}P{^{1}H} NMR ($CDCl_3$, 298 K, 121.53 MHz):** δ 13.4 ($^{1}J_{P-Pt}$ = 2308 Hz). **^{19}F NMR ($CDCl_3$, 298 K, 376.47 MHz):** δ -60.3 (CF_3), -63.4 (CF_3). **^{195}Pt NMR ($CDCl_3$, 298 K, 85.61 MHz):** δ -4709 (t, $^{1}J_{Pt-P}$ = 2313 Hz). **^{13}C{^{1}H}**

NMR ($CDCl_3$, 298 K, 125.77 MHz): δ 165.8 (O*C*O), 132.2 (q, $^3J_{C-F}$ = 5.4 Hz, phenylene-*C*H), 132.2 (q, $^2J_{C-F}$ = 30.6 Hz, *C*CF_3), 131.6 (q, $^2J_{C-F}$ = 32.7 Hz, *C*CF_3), 130.5 (phenylene-quaternary-*C*), 126.5 (t, $^2J_{C-P}$ = 13.5 Hz, ethynyl-*C*), 125.6 (phenylene-quaternary-*C*), 123.1 (q, $^1J_{C-F}$ = 273.4, *C*F_3), 122.8 (q, $^1J_{C-F}$ = 274.3, *C*F_3), 106.2 (ethynyl-*C*), 52.9 (O*C*H_3), 16.4 (t*, ($^1J_{C-P}$ + $^3J_{C-P}$) = 35.5 Hz, PEt_3-*C*H_2), 8.2 (PEt_3-*C*H_3). 163-164 ºC. **Infrared:** 2095 cm^{-1} (C≡C), 1734 cm^{-1} (C=O). **Elemental analysis:** Calculated for $C_{36}H_{40}F_{12}O_4P_2Pt_1$: C 42.32, H 3.95. Observed C 42.29, H 4.05.

Synthesis of **Pt5a**:

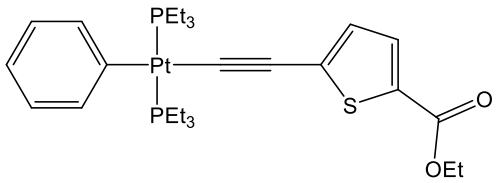

Synthesised using the same method to that reported for **Pt2a** using; *trans*-$Ph(PEt_3)_2PtCl$ (100 mg, 0.184 mmol) and **5** (40 mg 0.221 mmol). The product was purified using silica column chromatography (1:1 DCM/Hexane) and pale orange block-like crystals of **Pt5a** were obtained by cooling a concentrated hexane solution to -28 ºC. **Yield:** 113 mg (90 %). **^{1}H NMR ($CDCl_3$, 298 K, 400.13 MHz):** δ 7.58 (d, $^3J_{H-H}$ = 3.8 Hz, 1H, thienyl-C*H*), 7.31 (d, $^3J_{H-H}$ = 7.0 Hz, 2H, *o*-phenyl-C*H*), 6.97 (t, $^3J_{H-H}$ = 7.5 Hz, 2H, *m*-phenyl-C*H*), 6.78 (d, $^3J_{H-H}$ = 3.8 Hz, 1H, thienyl-C*H*), 4.31 (q, $^3J_{H-H}$ = 7.2 Hz, 2H, OCH_2), 1.81-1.66 (m, 12H, PEt_3-CH_2), 1.35 (t, $^3J_{H-H}$ = 7.2 Hz, 3H, OCH_2CH_3), 1.14-1.06 (m, 18H, PEt_3-CH_3). **^{31}P{^{1}H} NMR ($CDCl_3$, 298 K, 161.98 MHz):** δ 10.3 ($^1J_{P-Pt}$ = 2630 Hz). **^{195}Pt NMR ($CDCl_3$, 298 K, 85.62 MHz):** δ -4548 (t, $^1J_{Pt-P}$ = 2630 Hz). **^{13}C{^{1}H} NMR ($CDCl_3$, 298 K, 100.62 MHz):** δ 162.3 (O*C*O), 155.5 (t, $^3J_{C-P}$ = 10.5 Hz, *i*-phenyl-*C*), 139.0 (t, $^3J_{C-P}$ = 2.2 Hz, *o*-phenyl-*C*), 137.5 (thienyl-quaternary-C), 133.6 (thienyl-*C*H), 128.6 (thienyl-quaternary-*C*), 127.5 (*m*-phenyl-*C*), 126.7 (t, $^2J_{C-P}$ = 14.3 Hz, ethynyl-*C*), 121.6 (*p*-phenyl-*C*), 102.5 (ethynyl-*C*), 60.8 (O*C*H_2), 15.2 (t*, ($^1J_{C-P}$ + $^3J_{C-P}$) = 34.4 Hz, PEt_3-*C*H_2), 14.5 (OCH_2CH_3) 8.1 (PEt_3-*C*H_3). **Mp:** 76 ºC **Infrared:** 2088 cm^{-1} (C≡C), 1698 cm^{-1} (C=O). **Elemental analysis:** Calculated for $C_{27}H_{42}O_2P_2Pt_1S_1$: C 47.15, H 6.16. Observed: C 47.08, H 6.11.

Synthesis of **Pt5b**:

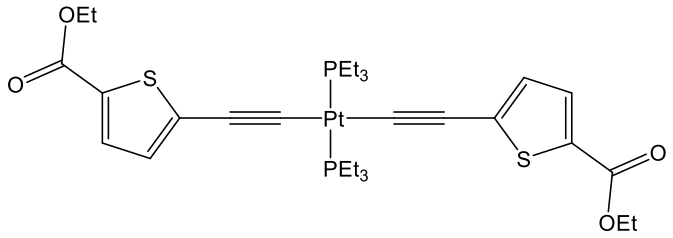

Synthesised using the same method to that reported for **Pt2b** using; *trans*-$(PEt_3)_2PtCl_2$ (100 mg, 0.199 mmol) and **5** (86 mg, 0.478 mmol). The product was purified using silica column chromatography (1:1 DCM/hexane) and dark orange block-like crystals of **Pt5b** were obtained by cooling a concentrated hexane solution to -28 ºC. **Yield:** 125 mg (83 %). **^{1}H NMR ($CDCl_3$, 298 K, 400.13 MHz):** δ 7.58 (d, $^3J_{H\text{-}H}$ = 3.9 Hz, 2H, thienyl-C*H*), 6.79 (d, $^3J_{H\text{-}H}$ = 3.9 Hz, 2H, thienyl-C*H*), 4.31 (q, $^3J_{H\text{-}H}$ = 7.1 Hz, 4H, OCH_2), 2.22-2.04 (m, 12H, PEt_3-CH_2), 1.35 (t, $^3J_{H\text{-}H}$ = 7.1 Hz, 6H, OCH_2CH_3), 1.26-1.18 (m, 18H, PEt_3-CH_3). **^{31}P{^{1}H} NMR ($CDCl_3$, 298 K, 161.98 MHz):** δ 11.8 ($^1J_{P\text{-}Pt}$ = 2326 Hz). **^{195}Pt NMR ($CDCl_3$, 298 K, 85.61 MHz):** δ -4716 (t, $^1J_{H\text{-}H}$ = 2326 Hz). **^{13}C{^{1}H} NMR ($CDCl_3$, 298 K, 100.62 MHz):** δ 162.1 (O*C*O), 136.4 (thienyl-quaternary-*C*), 133.5 (thienyl-*C*H), 129.6 (thienyl-quaternary-*C*), 128.1 (thienyl-*C*H), 118.9 (t, $^3J_{C\text{-}P}$ = 15.4 Hz, ethynyl-*C*), 102.3 (ethynyl-*C*), 60.9 (O*C*H_2), 16.5 (t*, ($^1J_{C\text{-}P}$ + $^3J_{C\text{-}P}$) = 35.5 Hz, PEt_3-CH_2), 14.5 (OCH_2CH_3), 8.4 (PEt_3-*C*H_3). **Mp:** 121ºC. **Infrared:** 2090 cm^{-1} (C≡C), 1694 cm^{-1} (C=O). **Elemental analysis:** Calculated for $C_{30}H_{44}O_4P_2Pt_1S_2$: C 45.62, H 5.62. Observed: C 45.75, H 5.75.

Synthesis of **Pt6a**:

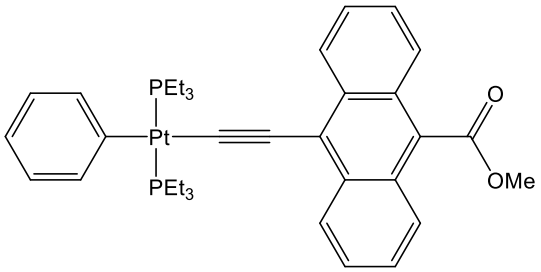

Synthesised using the same method to that reported for **Pt2a** using; *trans*-$Ph(PEt_3)_2PtCl$ (100 mg, 0.184 mmol) and **6** (57 mg, 0.221 mmol). The product was purified by silica column chromatography (2:1 DCM/hexane) and yellow block-like crystals of **Pt6a** were obtained by cooling a concentrated hexane solution to -28 ºC. **Yield:** 115 mg (81 %). **^{1}H NMR ($CDCl_3$, 298 K, 400.13 MHz):** δ 8.89 (d, $^3J_{H\text{-}H}$ =

8.4 Hz, 2H, anthracene-C*H*), 7.99 (d, $^{3}J_{H-H}$ = 8.4 Hz, 2H, anthracene-C*H*), 7.54-7.46 (m, 4H, anthracene-C*H*), 7.41 (d, $^{3}J_{H-H}$ = 7.2, 2H, *o*-phenyl-C*H*), 7.02 (t, $^{3}J_{H-H}$ = 7.2 Hz, 2H, *m*-phenyl-C*H*), 6.85 (t, $^{3}J_{H-H}$ = 7.2 Hz, 1H, *p*-phenyl-C*H*), 4.15 (s, 3H, OCH_3), 1.84-1.68 (m, 12H, PEt_3-CH_2), 1.19-1.11 (m, 18H, PEt_3-CH_3). **$^{31}P\{^{1}H\}$ NMR ($CDCl_3$, 298 K, 161.98 MHz):** δ 10.9 ($^{1}J_{P-Pt}$ = 2634 Hz). **^{195}Pt NMR ($CDCl_3$, 298 K, 85.64 MHz):** δ -4547 (t, $^{1}J_{Pt-P}$ = 2634 Hz). **^{13}C NMR ($CDCl_3$, 298 K, 100.62 MHz):** δ 170.7 (O*C*O), 155.9 (t, $^{2}J_{CP}$ = 10.4 Hz, *i*-phenyl *C*), 139.3 (*o*-phenyl-*C*), 134.3 ($^{2}J_{C-P}$ = 14.6 Hz, ethynyl-*C*), 131.1 (anthracene-quaternary-C), 128.9 (anthracene-C*H*), 128.8 (anthracene-quaternary-C), 128.3 (anthracene-quaternary-C), 127.5 (*m*-phenyl-*C*), 126.7 (anthracene-C*H*), 125.1 (anthracene-C*H*), 124.6 (anthracene-C*H*), 123.0 (anthracene-quaternary-C), 121.5 (*p*-phenyl-*C*), 107.5 (ethynyl-*C*), 52.4 (O*C*H_3), 15.4 (t*, ($^{1}J_{CP}$ + $^{3}J_{CP}$) = 34.4 Hz, PEt_3-CH_2), 8.1 (PEt_3-CH_3). **Mp**: 110 ºC (dec.). **Infrared:** 2071 cm^{-1} (C≡C), 1721 cm^{-1} (C=O). **Elemental analysis:** Calculated for $C_{36}H_{46}O_2P_2Pt_1$: C 56.32, H 6.04. Observed: C 56.50, H 5.96.

Synthesis of **Pt6b**:

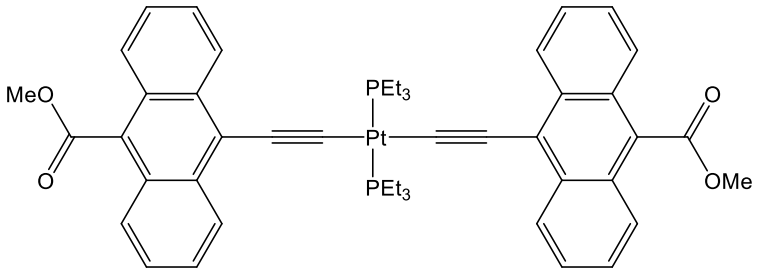

Synthesised using the same method to that reported for **Pt2b** using; *trans*-$(PEt_3)_2PtCl_2$ (100 mg, 0.200 mmol) and **6** (124 mg, 0.478 mmol). The product was purified by silica column chromatography (2:1 DCM/hexane) and yellow needle-like crystals were obtained by layering a concentrated DCM solution of **Pt6b** with hexanes. **Yield:** 125 mg (82 %). **^{1}H NMR ($CDCl_3$, 298 K, 400.13 MHz):** δ 8.85 (m, 2H, anthracene-CH), 8.01 (m, 2H, anthracene-C*H*), 7.51 (m, 4H, anthracene-CH), 4.17 (s, 6H, OCH_3), 2.19 (m, 12H, PEt_3-CH_2), 1.27 (m, 18H, PEt_3-CH_3). **$^{31}P\{^{1}H\}$ NMR ($CDCl_3$, 298 K, 161.98 MHz):** δ 12.5 ($^{2}J_{P-Pt}$ = 2367 Hz). **^{195}Pt NMR ($CDCl_3$, 298 K, 85.64 MHz):** δ -4706 (t, $^{1}J_{Pt-P}$ = 2367 Hz). **$^{13}C\{^{1}H\}$ NMR ($CDCl_3$, 298 K, 100.62 MHz):** δ 170.6 (O*C*O), 131.2 (anthracene-quaternary-C), 128.7 (anthracene-quaternary-C), 128.6 (anthracene-*C*H), 127.43 (anthracene-quaternary-*C*), 126.8 (anthracene-*C*H), 126.6 (t, $^{2}J_{C-P}$ = 15.1 Hz, ethynyl-*C*), 125.2 (anthracene-*C*H), 124.9

(anthracene-*C*H), 123.8 (anthracene-quaternary-C), 107.2 (ethynyl-*C*), 52.5 (O*C*H_3), 16.7 (t*, ($^1J_{C-P}$ + $^3J_{C-P}$) = 35.1 Hz, PEt_3-*C*H_2) 8.5 (PEt_3-*C*H_3). **Mp:** 220 ^oC (dec). **Infrared:** 2072 cm^{-1} (C≡C), 1709 cm^{-1} (C=O). **Elemental analysis:** Calculated for $C_{48}H_{52}O_4P_2Pt_1$: C 60.69, H 5.52. Observed: C 60.58, H 5.62.

8.3 – Experimental Data for Chapter 3

Within this section each of the syntheses involving {Mo_2} complexes were performed entirely under an Ar atmosphere using standard Schlenk-line and glove box techniques. All products isolated from these reactions are air-sensitive and required storage under an Ar atmosphere. The syntheses of both **Pt2c** and **Pt2d** did not require air-sensitive considerations. **MoAc**,[342] Mo_2TiPB_4,[189], 4-ethynyl-benzoic acid,[199] DPTA[343], and LiDPTA[344] were prepared using methods published in the literature. **Mo2** and 2,5-ethynyl-thiophene-carboxylic acid were prepared by the method recently reported by Chisholm *et al*. And as such are not reported here.[108]

Synthesis of **Pt2c**:

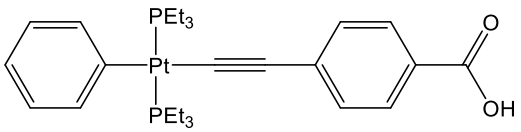

Pt2a (250 mg, 0.374 mmol) and KO^{t}Bu (63 mg, 0.561 mmol) were dissolved in THF (5 mL) and H_2O (5 mL) and the solution was stirred at 50 ^oC for 12 h. The solution was then acidified using HCl (1 M) and all volatiles were removed *in vacuo*, leaving a white precipitate suspended in the remaining aqueous medium. The precipitate was isolated on a glass frit and washed with H_2O (3 x 5 mL). After drying the residue *in vacuo* the crude product was purified by washing with cold hexane (3 x 5 mL) giving **Pt2c** as a colourless powder. **Yield:** 208 mg (85 %). **^{1}H NMR (C_6D_6, 298 K, 300.22 MHz):** δ 12.73 (broad, 1H, COO*H*), 8.17 (d, $^3J_{H-H}$ = 7.9 Hz, 2H, phenylene-C*H*), 7.58 (d, $^3J_{H-H}$ = 6.8 Hz, 2H, *o*-phenyl-C*H*), 7.49 (d, $^3J_{H-H}$ = 7.9 Hz, 2H, phenylene-C*H*), 7.23 (t, $^3J_{H-H}$ = 6.8 Hz, 2H, m-phenyl-C*H*), 7.04 (t, $^3J_{H-H}$ = 6.8 Hz, 1H, *p*-phenyl-C*H*), 1.76-1.46 (m, 12H, PEt_3-CH_2), 0.98-0.89 (m, 18H, PEt_3-CH_3). **^{31}P{^{1}H} NMR (C_6D_6, 298 K, 121.53 MHz):** δ 11.1 ($^1J_{P-Pt}$ = 2633 Hz). **^{195} Pt NMR (C_6D_6, 298 K, 86.01 MHz):** δ -4550 (t, $^1J_{Pt-P}$ = 2633 Hz). **^{13}C{^{1}H} NMR (C_6D_6, 298 K, 100.62 MHz):** δ 172.6 (O*C*O), 156.4 (t, $^2J_{C-P}$ = 10.4 Hz, *i*-phenyl-*C*), 139.6 (*o*-

phenyl-*C*), 135.9 (phenylene-quaternary-*C*), 131.3 (phenylene-*C*H), 130.6 (phenylene-*C*H), 128.0 (*m*-phenyl-*C*), 125.4 (phenylene-quaternary-*C*), 122.2 (t, $^{2}J_{C-P}$ = 14.5 Hz**,** ethynyl-*C*), 122.0 (*p*-phenyl-*C*), 111.2 (ethynyl-C), 15.7 (t, $^{2}J_{C-P}$ = 17.3 Hz, PEt_3-*C*H_2), 8.6 (PEt_3-*C*H_3). **Infrared:** 2091 cm^{-1} (C≡C), 1678 cm^{-1} (C=O). **Elemental analysis:** Calculated for $C_{27}H_{40}O_2P_2Pt$: C 49.61, H 6.17. Observed: C 49.75, H 6.27.

Synthesis of **Pt2d**:

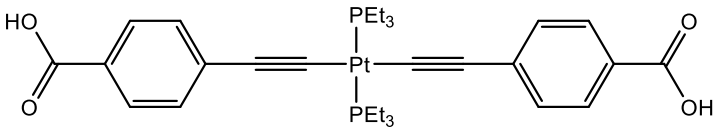

Pt2d was synthesised using an analogous method as was described for **Pt2c** using; **Pt2b** (250 mg, 0.333 mmol) and KO^{t}Bu (94 mg, 0.834 mmol). The work up was identical to that of **Pt2c** although the product was washed with DCM (3 x 5 mL) to provide **Pt2d** as a colourless powder. **Yield:** 180 mg (75 %). **^{1}H NMR (*d*$_6$-DMSO, 298 K, 500.13 MHz):** δ 7.80 (d, $^{3}J_{H-H}$ = 8.2 Hz, 4H, phenylene-C*H*), 7.24 (d, $^{3}J_{H-H}$ = 8.2 Hz, 4H, phenylene-C*H*), 2.18-2.01 (m, 12H, PEt_3-CH_2), 1.17-1.11 (m, 18H, PEt_3-CH_3). **^{31}P{^{1}H} NMR (*d*$_6$-DMSO, 298 K, 202.46 MHz):** δ 12.1 ($^{1}J_{P-Pt}$ = 2330 Hz). **^{195}Pt NMR (d$_6$-DMSO, 298 K, 107.51 MHz):** δ -4724 (t, $^{1}J_{Pt-P}$ = 2330 Hz). **^{13}C{^{1}H} NMR (d$_6$-DMSO, 298 K, 100.62 MHz):** δ 167.3 (O*C*O), 133.1 (phenylene-quaternary-*C*), 130.5 (phenylene-*C*H), 129.6 (phenylene-*C*H), 127.1 (phenylene-quaternary-C), 114.0 (t, $^{2}J_{C-P}$ = 14.5 Hz, ethynyl-*C*), 109.3 (ethynyl-*C*), 16.2 (t, $^{2}J_{C-P}$ = 17.7 Hz, PEt_3-*C*H_2), 8.3 (PEt_3-*C*H_3). **Infrared:** 2099 cm^{-1} (C≡C), 1671 cm^{-1} (C=O). **Elemental analysis:** Calculated for $C_{30}H_{40}O_4P_2Pt$: C 49.93, H 5.59. Observed: C 50.04, H 5.59.

Synthesis of **Mo1**:

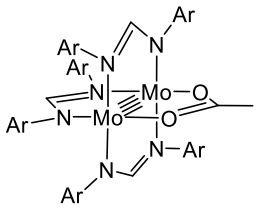

Ar = *p*-tolyl

MoAc (500 mg, 1.17 mmol) and Li-DPTA (834 mg, 3.62 mmol) were dissolved in THF (50 mL) at -78 °C. The temperature was maintained at -78 °C for 30 minutes after which the reaction was returned to room temperature and stirred for a further three hours providing a brown solution. All volatiles were removed *in vacuo* giving a yellow brown residue, which was extracted into toluene (50 mL) and filtered through celite. The resulting solution was concentrated and cooled to -28 °C, providing **Mo1** as a yellow microcrystalline powder. Yield 785 mg (73 %). Crystals of **Mo1** were obtained by layering a concentrated DCM solution with pentane. **^{1}H NMR (C_6D_6, 298 K, 400.13 MHz):** δ 8.71 (s, 2H, NC(*H*)N^{a}), 8.61 (s, 1H, NC(*H*)N^{b}), 6.80 (d, $^{3}J_{H-H}$ = 7.8 Hz, 8H, phenylene-C*H*^{a}), 6.70 (d, $^{3}J_{H-H}$ = 7.6 Hz, 8H, phenylene-C*H*^{a}), 6.67 (d, $^{3}J_{H-H}$ = 7.8 Hz, 4H, phenylene-C*H*^{b}), 6.42 (d, $^{3}J_{H-H}$ = 7.6 Hz, 4H, phenylene-C*H*^{b}), 2.51 (s, 3H, acetate-C*H*$_3$), 2.03 (s, 12H, DPTA-C*H*$_3^{a}$), 1.94 (s, 6H, DPTA-C*H*$_3^{b}$). **^{13}C{^{1}H} NMR (C_6D_6, 298 K, 100.61 MHz):** δ 180.4 (O*C*O), 157.7 (N*C*N^{a}), 156.3 (NCN^{b}), 148.4 (phenylene-quaternary-*C*^{a}), 148.2 (phenylene-quaternary-*C*^{b}), 133.1 (phenylene-quaternary-*C*^{b}), 133.0 (phenylene-quaternary-*C*^{a}), 130.6 (phenylene-*C*H^{a}), 130.3 (phenylene-*C*H^{b}), 123.0 (phenylene-*C*H^{b}), 122.4 (phenylene-*C*H^{a}), 24.2 (acetate-*C*H$_3$), 21.05 (DPTA-*C*H$_3^{a}$), 20.9 (DPTA-*C*H$_3^{b}$). **Elemental analysis:** Calculated for $C_{47}H_{48}Mo_2N_6O_2$: C 61.30, H 5.25, N 9.13. Observed C 61.27, H 5.14, N 9.02.

^{a} Refers to the DPTA ligand *cis* to the acetate ligand, ^{b} refers to the DPTA ligand *trans* to the acetate ligand.

Synthesis of **Mo2**:

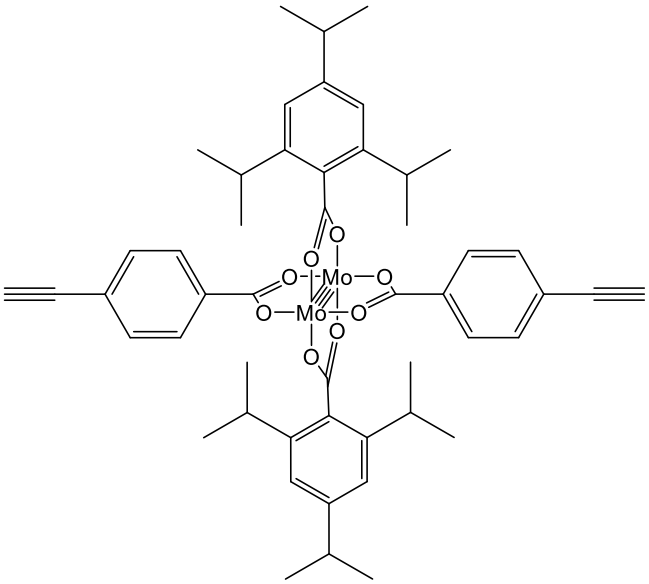

$Mo_2(TiPB)_4$ (800 mg, 0.677 mmol) and 4-ethynyl-benzoic acid (200 mg, 1.359 mmol) were combined in a Schlenk tube and ethanol (10 mL) was added providing a bright orange suspension. After stirring the mixture for three days the orange precipitate of **Mo2** was isolated on a glass frit and purified by washing with ethanol (2 x 5 mL) and hexane (2 x 5 mL). **Yield:** 0.468 g (70 %). Crystals of **Mo2** were obtained by slow evaporation of a THF solution. **^{1}H NMR (d_8-THF, 298 K, 400.13 MHz):** δ 8.34 (d, $^3J_{H-H}$ = 8.1, 4H, phenylene-C*H*), 7.68 (d, $^3J_{H-H}$ = 8.1, 4H, phenylene-C*H*), 7.00 (s, 4H, TiPB-C*H*)), 3.79 (s, 2H, ethynyl-C*H*), 3.01 (sept, $^3J_{H-H}$ = 6.9 Hz, 4H, ^{i}Pr-C*H*), 2.87 (sept, $^3J_{H-H}$ = 6.8 Hz, 2H, ^{i}Pr-C*H*), 1.23 (d, $^3J_{H-H}$ = 6.8 Hz, 12H, ^{i}Pr-CH_3), 1.03 (d, $^3J_{H-H}$ = 6.9 Hz, 24H, ^{i}Pr-CH_3). **^{13}C{H} NMR (d_8-THF, 298 K, 100.61 MHz):** δ 182.5 (TiPB-O*C*O), 176.9 (ethynyl-carboxylate-O*C*O), 150.0 (TiPB-quaternary-*C*), 145.9 (TiPB-quaternary-*C*), 135.7 (TiPB-quaternary-*C*), 133.0 (ethynyl-carboxylate-*C*H), 132.5 (ethynyl-carboxylate-phenylene-quaternary-*C*), 130.9 (ethynyl-carboxylate-*C*H), 126.8 (ethynyl-carboxylate-phenylene-quaternary-*C*), 121.3 (TiPB-*C*H), 84.1 (ethynyl-*C*), 81.6 (ethynyl-*C*), 35.7 (*p*-^{i}Pr-*C*H), 32.5 (*o*-^{i}Pr-*C*H), 24.6 (*p*-^{i}Pr-*C*H_3), 24.4 (*o*-^{i}Pr-*C*H). **Infrared:** 3303 cm^{-1} (C≡C). **Elemental analysis:** Calculated for $C_{50}H_{56}Mo_2O_8$: C 61.47, H 5.78. Observed: C 61.37, H 5.85.

Synthesis of **PtMo1**:

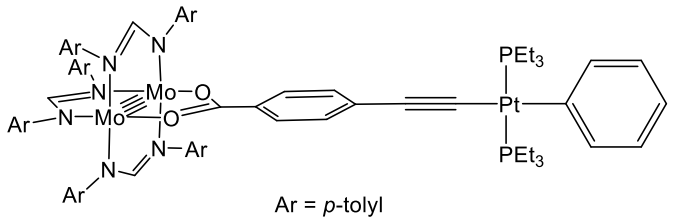

Pt2a (100 mg, 0.150 mmol) and KO^{t}Bu (25 mg, 0.225 mmol) were dissolved in THF (10 mL) and the solution was stirred for 12 h at 50 ^{o}C. The progress of the reaction was followed by silica-phase TLC analysis using DCM eluent. In a separate vessel, **Mo1** (137 mg, 0.15 mmol) was dissolved in THF (15 mL) providing a bright yellow solution and this was added to the {Pt} solution *via* cannula transfer, immediately turning the solution bright orange. The solution was stirred at room temperature for three hours after which all volatiles were removed *in vacuo*. The resultant residue was washed with hexanes (3 x 5 mL) and EtOH (3 x 5 mL) then extracted into toluene and filtered through celite. All volatiles were removed *in vacuo* and the resulting residue was suspended in hexane (5 mL). The hexane was heated to reflux at which point toluene was added drop-wise until all solid material had dissolved. The solution was allowed to cool to room temperature and was then further cooled to -28 ^{o}C, producing a crop of orange crystals of **PtMo1**. **Yield:** 120 mg (53 %). **^{1}H NMR (C$_6$D$_6$, 298 K, 400.13 MHz):** δ 8.68 (s, 1H, NC(*H*)N^a), 8.61 (d, $^3J_{H\text{-}H}$ = 8.3 Hz, 2H, ethynyl-carboxylate-phenylene-C*H*), 8.52 (s, 2H, NC(*H*)N^b), 7.67-7.52 (m, 4 H, ethynyl-carboxylate-phenylene-C*H* and *o*-phenyl-C*H*), 7.23 (t, $^3J_{H\text{-}H}$ = 7.4 Hz, 2H, *m*-phenyl-C*H*), 7.03 (t, $^3J_{H\text{-}H}$ = 7.4 Hz, 1H, *p*-phenyl-C*H*), 6.79 (d, $^3J_{H\text{-}H}$ = 8.3 Hz, 8H, DPTA-phenylene-*C*H^b), 6.74-6.67 (m, 12H, DPTA-phenylene-CH^{a+b}), 6.48 (d, $^3J_{H\text{-}H}$ = 8.1 Hz, 4H, DPTA-phenylene-C*H*^{a}), 2.03 (s, 12H, DPTA-CH_3^b), 1.97 (s, 6H, DPTA-CH_3^a), 1.68-1.53 (m, 12H, PEt$_3$-CH_2), 0.96-0.88 (m, 18H, PEt$_3$-CH_3). **^{31}P{^{1}H} NMR (C$_6$D$_6$, 298 K, 162.0 MHz):** δ 10.3 ($^1J_{P\text{-}Pt}$ = 2640 Hz). **^{195}Pt NMR (C$_6$D$_6$, 298 K, 107.51 MHz):** δ -4559 (t, $^1J_{Pt\text{-}P}$ = 2640). **^{13}C{^{1}H} NMR (C$_6$D$_6$, 298 K, 100.61 MHz):** δ 175.3 (O*C*O), 157.43 (N*C*N^b), 157.0 (t, $^2J_{C\text{-}P}$ =10.2 Hz, *i*-phenyl-*C*) 156.4 (N*C*N^a), 148.6 (-quaternary-*C*^{b}), 148.3 (-quaternary-*C*^{a}), 140.0 (*o*-phenyl-*C*), 133.8 (ethynyl-carboxylate-phenylene-quaternary-*C*), 133.1 (-quaternary-*C*^{a}), 133.0 (-quaternary-*C*^{a}), 131.3 (ethynyl-carboxylate-phenylene-*C*H), 131.2 (ethynyl-carboxylate-phenylene-*C*H), 130.6 (-*C*H^b), 130.4 (-*C*H^a), 130.2 (phenylene-quaternary-*C*), 128.9 (*m*-phenyl-*C*) 123.0 (-*C*H^a), 122.7 (-*C*H^b), 122.6 (*p*-phenyl-*C*H),

119.0 (t, $^{2}J_{C-P}$ = 14.6 Hz, Pt-*C*≡C), 111.5 (Pt-C≡*C*), 21.1 (-*C*H$_3$[b]), 21.0 (-*C*H$_3$[a]), 16.0 (t, $^{2}J_{C-P}$ = 17.2 Hz, PEt$_3$-*C*H$_2$), 8.5 (PEt$_3$-*C*H$_3$). **Infrared:** 2091 cm^{-1} (C≡C). **Elemental analysis:** Calculated for $C_{72}H_{84}Mo_2N_6O_2P_2Pt_1$: C 57.10, H 5.59, N 5.55. Observed: C 56.98, H 5.62, N 5.61.

[a] Corresponds to DPTA ligand *trans* to the ethynyl-carboxylate ligand, [b] corresponds to the DPTA ligands *trans* to each other.

Synthesis of **MoPtMo**:

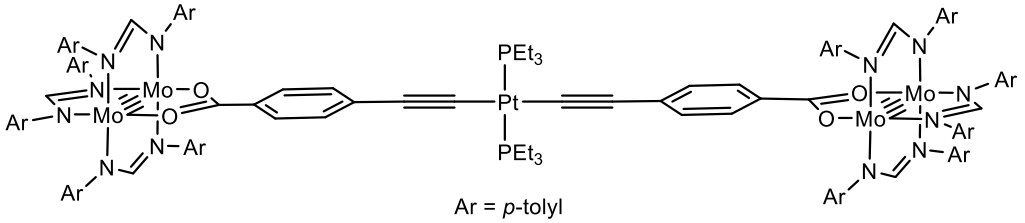

Mo1 (100 mg, 0.109 mmol) was dissolved in THF (10 mL) and NaOMe (0.25 mL, 0.109 mmol, 0.437 M) was added drop-wise giving an orange solution. The solution was stirred for three hours, resulting in the formation of a precipitate of Li-acetate which was removed by filtration through celite. **Pt2d** (40 mg, 0.0543 mmol) in THF (10 mL) was then added to the solution *via* cannula transfer resulting in a darkening of the reaction mixture. After stirring for a further three hours all volatiles were removed *in vacuo* and the residue was washed with hexanes (3 x 5 mL) and EtOH (3 x 5 mL). The crude product was extracted into toluene and filtered through celite. The toluene was removed *in vacuo* and THF (1 mL) was added. After stirring the resulting slurry for 30 minutes the mixture was cooled to -28 ^{o}C for 12 h, yielding an orange precipitate of **MoPtMo** which was isolated by decantation of the solution. Crystals suitable for single crystal X-ray crystallography were grown using the same method described for **PtMo1**. **Yield:** 53 mg (40 %). **^{1}H NMR (C_6D_6, 298 K, 400.22 MHz):** δ 8.68 (s, 2H, NC(H)N[a]), 8.60 (d, $^{3}J_{H-H}$ = 8.3 Hz, 4H, phenylene-C*H*), 8.53 (s, 4H, NC(H)N), 7.57 (d, $^{3}J_{H-H}$ = 8.3 Hz, phenylene-C*H*), 6.80 (d, $^{3}J_{H-H}$ = 8.1 Hz, 16H, *p*-tolyl-C*H*), 6.73-6.69 (m, 24H, p-tolyl-C*H*), 6.48 (d, $^{3}J_{H-H}$ = 8.3 Hz, 8H, *p*-tolyl-C*H*), 2.03 (s, 24H, *p*-tolyl-C*H*$_3$), 1.97 (s, 122100 cm^{-1}(C≡C). **Elemental analysis:** Calculated for $C_{120}H_{128}Mo_4N_{12}O_4P_2Pt_1$: C 58.99, H 5.28, N 6.88. Observed: C 57.01, H 6.21, N 6.88. (A small impurity of **Mo1** prevented the collection of satisfactory data)

[a] Corresponds to DPTA ligands *trans* to each other, [b] corresponds to DPTA ligand *trans* to the ethynyl-carboxylate ligand.

Synthesis of **PtMoPt**:

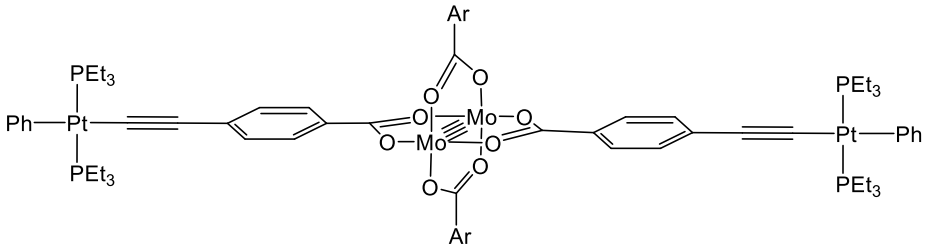

Method 1:

PtMoPt was synthesised and purified using the same method as described for **Mo2** using **Pt2c** (110 mg, 0.168 mmol) and $Mo_2(TiPB)_4$ (90 mg, 0.0765 mmol). Yield 53 mg (35 %).

Method 2:

Mo2 (100 mg, 0.102 mmol), *trans*-$Ph(PEt_3)_2PtCl$ (67 mg, 0.123 mmol) and CuI (*ca.* 2 mg) dissolved in THF (8 mL) and NEt_3 (8 mL). The solution was stirred in the absence of light for 12 h after which all volatiles were removed *in vacuo*. The residue was washed with hexanes (3 x 5 mL) and EtOH (3 x 5 mL) and was then extracted into toluene. The solution was filtered and the all volatiles were removed *in vacuo*. The crude product was then dissolved in minimal THF and layered with hexanes, yielding **PtMoPt** as a crop of orange crystals. Yield 120 mg (59 %). **^{1}H NMR (*d*$_8$-THF, 298 K, 500.13):** δ 8.19 (d, $^{3}J_{H\text{-}H}$ = 7.8 Hz, 4H, phenylene-C*H*), 7.39 (d, $^{3}J_{H\text{-}H}$ = 7.8 Hz, 4H, phenylene-*C*H), 7.35 (d, $^{3}J_{H\text{-}H}$ = 7.3 Hz, 4H, *o*-phenyl-C*H*), 6.99 (s, 4H, TiPB-C*H*), 6.92 (t, $^{3}J_{HH}$ = 7.3 Hz, 4H, *m*-phenyl-C*H*), 6.73 (t, $^{3}J_{H\text{-}H}$ = 7.3 Hz, 2H, *p*-phenyl-C*H*), 3.05 (sept, $^{3}J_{H\text{-}H}$ = 6.8 Hz, 4H, ^{i}Pr-C*H*), 2.87 (sept, $^{3}J_{H\text{-}H}$ = 6.8 Hz, 2H, ^{i}Pr-C*H*), 1.93-1.77 (m, 24H, PEt_3-CH_2), 1.23 (d, $^{3}J_{H\text{-}H}$ = 6.8 Hz, 12H, ^{i}Pr-CH_3), 1.19-1.11 (m, 36H, PEt_3-CH_3), 1.05 (d, $^{3}J_{H\text{-}H}$ = 6.8 Hz, 12H, ^{i}Pr-CH_3). **^{31}P{^{1}H} NMR (*d*$_8$-THF, 298 K, 161.98 MHz):** δ 10.4 ($^{1}J_{P\text{-}Pt}$ = 2638 Hz). **^{195}Pt NMR (*d*$_8$-**

THF, 298 K, 107.51 MHz): δ -4563.6 (t, $^{1}J_{Pt-P}$ = 2638 Hz). **$^{13}C\{^{1}H\}$ NMR (*d*$_8$-THF, 298 K, 125.76 MHz):** δ 182.0 (TiPB-O*C*O), 178.3 (Bridge-O*C*O), 157.0 (*i*-phenyl-*C*), 149.8 (TiPB-quaternary-*C*), 146.0 (TiPB-quaternary-*C*), 140.2 (*o*-phenyl-*C*), 135.9 (TiPB-quaternary-*C*), 134.4 (phenylene-quaternary-*C*), 131.3 (phenylene-*C*H), 130.7 (phenylene-*C*H), 128.9 (phenylene-quaternary-C), 128.4 (*m*-phenyl-*C*), 122.5 (*p*-phenyl-*C*), 121.5 (t, $^{2}J_{C-P}$ = 14.2 Hz, ethynyl-*C*), 121.2 (TiPB-*C*H), 111.3 (ethynyl-*C*), 35.7 (^{i}Pr-*C*H), 32.5 (^{i}Pr-*C*H), 24.6 (^{i}Pr-*C*H$_3$), 24.4 (^{i}Pr-*C*H$_3$), 16.3 (t, $^{2}J_{C-P}$ = 17.3 Hz, PEt$_3$-*C*H$_2$), 8.5 (PEt$_3$-*C*H$_3$). **Infrared:** 2091 cm^{-1} (C≡C). **Elemental analysis:** Calculated for $C_{86}H_{124}Mo_2O_8P_4Pt_2$: C 51.86, H 6.27. Observed: C 51.71, H 6.25.

8.4 – Experimental Data for Chapter 4

Within this section all syntheses were performed under an atmosphere of Ar using standard Schlenk line techniques. However, all products were stable to air and did not require any specialised storage. The compounds: 9-ethynyl-anthracene,[345] 1,4-diethynyl-benzene,[346] 1,4-diethynyl-2,5-*bis*-(CF$_3$)benzene,[347] 1,4-diethynyl-2,5-*bis*-(OMe)benzene,[54] 9,10-diethynyl-anthracene[348] and [(*p*-cymene)RuCl$_2$]$_2$,[349] were all prepared by methods published within the literature.

Synthesis of **A1a**:

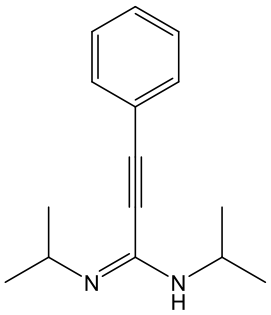

The Lithium salt of **A1a** was synthesised as described by Chisholm *et al*.[184] using phenyl-acetylene (0.3 mL, 2.73 mmol), BuLi (1.09 mL, 2.73 mmol, 2.5 M) and N,N-diisopropylcarbodiimide (0.42 mL, 2.73 mmol). The ligand was protonated *via* the addition of a slight excess of H_2O (*ca.* 0.1 mL) and all volatiles were removed *in vacuo*. The product was extracted into DCM (20 mL) and washed with H_2O (3 x 20 mL). The combined organic fractions were dried over $MgSO_4$ and the solvent removed *in vacuo*. The product was purified by crystallisation from hot hexanes. **Yield:** 450 mg (72 %). **^{1}H NMR($CDCl_3$, 298 K, 300.22 MHz):** δ 7.54-7.48 (m, 2H, *o*-phenyl-C*H*), 7.41-7.33 (m, 3H, *m*- and *p*-phenyl-C*H*), 3.97 (sept, $^3J_{H-H}$ = 6.3 Hz, ^{i}Pr-C*H*), 1.18 (d, $^3J_{H-H}$ = 6.3 Hz, ^{i}Pr-CH_3). **Infrared:** 2226 cm^{-1} (C≡C).

Full characterisation data is reported in the literature by Wang *et al*. whom synthesised **A1a** using an alternative preparation.[214]

Synthesis of **A1b**:

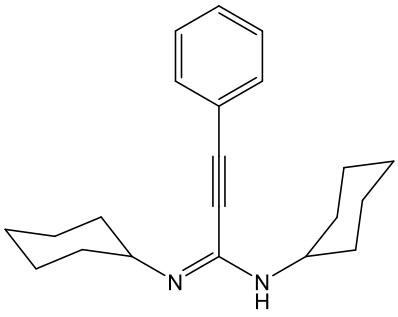

Synthesised using the same method as **A1a** using phenyl-acetylene (0.3 mL, 2.73 mmol), BuLi (1.09 mL, 2.73 mmol, 2.5 M), N,N-dicyclohexylcarbodiimide (563 mg, 2.73 mmol). **Yield:** 733 mg (87 %). **^{1}H NMR ($CDCl_3$, 298 K, 300.22 MHz):** δ 7.5-7.47 (m, 2H, *o*-phenyl C*H*), 7.42-7.33 (m, 3H, *m*- and *p*-phenyl C*H*), 3.67-3.55 (m, 2H, cy-C*H*), 1.91-1.11 (m, 20H, cy-CH_2). **Infrared:** 2207 cm^{-1} (C≡C).

Full characterisation data is reported in the literature by Wang *et al*. whom synthesised **A1b** using an alternative preparation.[214]

Synthesis of **A4a**:

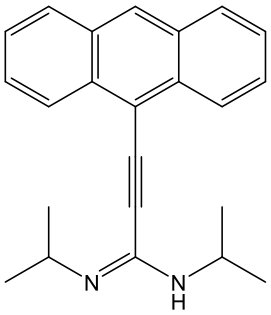

Synthesised using the same method as **A1a** using 9-ethynyl-anthracene (100 mg, 0.494 mmol), BuLi (0.20 mL, 0.494 mmol, 2.5 M) and N,N-diisopropylcarbodiimide (0.08 mL, 0.516 mmol). Purification was achieved by filtering a hot hexane solution of the crude product and removing the solvent *in vacuo*. The resultant residue was washing with a small amount of cold hexane yielding an orange powder. **Yield:** 119 mg (73 %). **^{1}H NMR ($CDCl_3$, 298 K, 300.22 MHz):** δ 8.51 (d, $^{3}J_{H-H}$ = 15.5 Hz, 2H, anthracene-C*H*), 8.49 (s, 1H, *p*-anthracene-C*H*), 8.05 (d, $^{3}J_{H-H}$ = 15.5 Hz, 2H, anthracene-C*H*), 7.66-7.50 (m, 4H, anthracene-C*H*), 4.21 (sept, $^{3}J_{H-H}$ = 6.4 Hz, 2H, ^{i}Pr-C*H*), 1.29 (d, $^{3}J_{H-H}$ = 6.4 Hz, 12H, ^{i}Pr-CH_3). **^{13}C{^{1}H} NMR ($CDCl_3$, 298 K, 75.49 Hz):** δ 141.8 (N*C*N), 133.1 (anthracene-quaternary-*C*), 131.0 (anthracene-quaternary-*C*), 129.2 (*p*-anthracene-*C*) 128.9 (anthracene-*C*H), 127.2 (anthracene-*C*H), 126.2 (anthracene-*C*H), 125.8 (anthracene-*C*H), 115.1 (*i*-anthracene-*C*), 90.0 (ethynyl-*C*), 88.9 (ethynyl-*C*), 48.1 (broad, ^{i}Pr-*C*H), 24.1 (^{i}Pr-*C*H_3). **Infrared:** 2181cm^{-1}, 2203 cm^{-1} (C≡C). **Mp:** 81-83 ^{o}C. **Elemental analysis:** Calculated for $C_{23}H_{24}N_2$: C 84.11, H 7.37, N 8.53. Observed: C 84.22, H 7.31, N 8.67.

Synthesis of **A2b**:

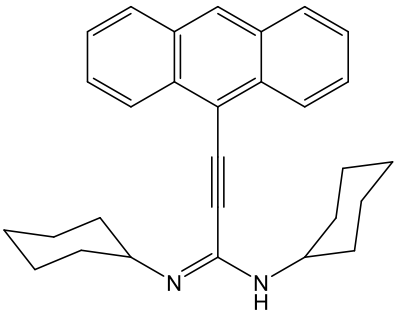

Synthesised using the same method as **A1a** using 9-ethynyl-anthracene (100 mg, 0.494 mmol), BuLi (0.20 mL, 0.494 mmol, 2.5 M) and N,N-dicyclohexylcarbodiimide (102 mg, 0.494 mmol). Product was purified in the same manner described for **A2a** and was isolated as an orange powder. **Yield:** 162 mg (80 %). **^{1}H NMR (CDCl$_3$, 298 K, 300.22 MHz):** δ 8.55 (d, $^{3}J_{H-H}$ = 8.2 Hz, 2H, anthracene-C*H*), 8.51 (s, 2H, *p*-anthracene-C*H*), 8.05 (d, $^{3}J_{HH}$ = 8.2 Hz, 2H, anthracene-C*H*), 7.66-7.50 (m, 4H, anthracene-C*H*), 3.99-3.85 (m, 2H, cy-C*H*), 2.12-1.14 (m, 20H, cy-CH_2). **^{13}C{^{1}H} NMR (CDCl$_3$, 298 K, 75.49 MHz):** δ 142.5 (N*C*N), 133.2 (anthracene-quaternary-*C*), 131.1 (anthracene-quaternary-*C*), 129.3 (*p*-anthracene-*C*H), 129.0 (anthracene-*C*H), 127.3 (anthracene-*C*H), 126.3 (anthracene-*C*H), 125.9 (anthracene-*C*H), 115.3 (*i*-anthracene-*C*), 90.0 (ethynyl-*C*), 89,7 (ethynyl-C) 56.1 (broad, cy-*C*H), 34.7 (cy-*C*H$_2$), 25.8 (cy-*C*H$_2$), 25.3 (cy-*C*H$_2$). **Infrared:** 2195 cm^{-1}, 2118 cm^{-1} (C≡C). **Mp:** 122-125 ºC. **Elemental analysis:** Calculated for $C_{29}H_{32}N_2$: C 85.25, H 7.89, N 6.86. Observed: C 85.35, H 7.80, N 6.74.

Synthesis of **BA1a**:

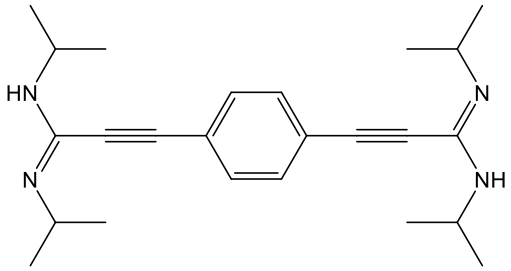

A solution of 1,4-diethynyl-benzene (0.200 g, 1.59 mmol) in THF (15 mL) was cooled to -78 ºC and to it BuLi (1.26 mL 3.17 mmol, 2.5 M) was added dropwise giving a beige slurry. After returning to room temperature the solution was stirred for 30 minutes and the solution was cooled to 0 ºC and N,N'-diisopropyl-carbodiimide

(0.49 mL, 3.17 mmol) was added drop-wise turning the slurry white. The slurry was stirred for eight h after which water (*ca.* 0.5 mL) was added giving a yellow solution. Volatiles were removed *in vacuo*. and the resulting residue was extracted into CH_2Cl_2 (30 mL) and washed with water (3 x 20 mL). The organic fraction was dried with $MgSO_4$, filtered and all volatiles were removed *in vacuo*. The residue was washed with cold hexane (3 x 10 mL) yielding a yellow powder. Crystals suitable for single crystal X-ray diffraction were obtained by DCM/pentane vapour diffusion. **Yield:** 456 mg (76 %). **^{1}H NMR ($CDCl_3$, 298 K, 250.13 MHz):** δ 7.48 (s, 4H, phenylene-C*H*), 3.94 (sept, $^3J_{H\text{-}H}$ = 6.4 Hz, 4H, ^{i}Pr-C*H*), 1.17 (d, $^3J_{H\text{-}H}$ = 6.4 Hz, 24H, ^{i}Pr-CH_3). **^{13}C{^{1}H} NMR ($CDCl_3$, 298 K, 75.49 MHz):** δ 140.1 (N*C*N), 132.6 (phenylene-*C*H), 123.2 (phenylene-quaternary-*C*), 89.8 (ethynyl-*C*), 83.2 (ethynyl-*C*), 48.7 (broad, ^{i}Pr-*C*H), 24.4 (^{i}Pr-CH_3). **Infrared:** 2223 cm^{-1} (C≡C). **Mp:** 169 ^{o}C. **Elemental analysis:** Calculated for $C_{24}H_{34}N_4$: C 76.15, H 9.05, N 14.80, Observed: C 76.23, H 9.19, N 14,74.

Synthesis of **Ba1b**:

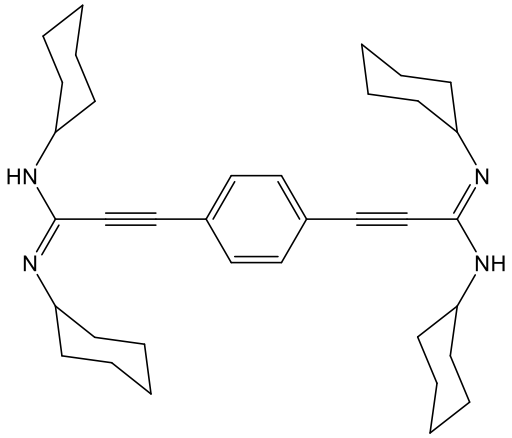

Synthesised using the same method as **BA1a** using; 1,4-diethynyl-benzene (200 mg, 1.59 mmol), BuLi (1.26 mL, 3.17 mmol, 2.5 M), N,N-dicyclohexyl-carbodiimide (0.654 mg, 3.17 mmol). Product was isolated as a yellow powder. Crystals suitable for single crystal X-ray diffraction were grown by DCM/Pentane vapour diffusion. **Yield:** 682 mg (80 %). **^{1}H NMR ($CDCl_3$, 298 K, 300.22 MHz):** δ 7.47 (s, 4H, phenylene-C*H*), 3.65-3.52 (m, 4H, cy-C*H*), 1.90-1.23 (m, 40H, cy-CH_2). **^{13}C{^{1}H} NMR** (**$CDCl_3$, 298 K, 75.49 MHz):** δ 140.1 (N*C*N), 132.7 (phenylene-*C*H), 123.2 (phenylene-quaternary-*C*), 89.8 (ethynyl-*C*), 83.5 (ethynyl-*C*), 34.8 (broad, cy-C*H*), 26.7 (cy-*C*H_2), 25.7 (2 x cy-CH_2) **Infrared:** 2120 cm^{-1}, 2219 cm^{-1} (C≡C). **Mp:** 196

^{o}C (dec.). **Elemental analysis:** Calculated for $C_{36}H_{50}N_4$: C 80.25, H 9.35, N 10.4. Observed: C 80.34, H 9.49, N 10.32.

Synthesis of **BA2a**:

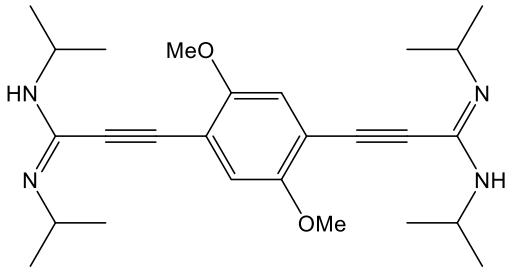

Synthesised using the same method as **BA1a** using; 1,4-diethynyl-2,5-dimethoxybenzene (300 mg, 1.61 mmol), BuLi (1.29 mL, 3.22 mmol, 2.5 M), N,N-diisopropyl-carbodiimide (0.50 mL, 3.22 mmol). Product was isolated as a white powder. **Yield:** 526 mg (74 %). **^{1}H NMR ($CDCl_3$, 298 K, 400.13 MHz):** δ 6.92 (s, 2H, phenylene-C*H*), 3.98 (sept, $^{3}J_{H\text{-}H}$ = 6.4 Hz, 4H, ^{i}Pr-C*H*), 3.85 (s, 6H, OCH_3), 1.17 (d, $^{3}J_{H\text{-}H}$ = 6.4 Hz, 24H, ^{i}Pr-CH_3). **^{13}C{^{1}H} NMR ($CDCl_3$, 298 K, 75.49 MHz):** δ 154.5 (*C*OCH_3), 141.3 (N*C*N), 115.6 (phenylene-*C*H), 112.9 (phenylene-quaternary-*C*), 87.7 (ethynyl-*C*), 85,1 (ethynyl-*C*), 56.5 (O*C*H_3), 47.9 (broad, ^{i}Pr-*C*H), 24.0 (^{i}Pr-*C*H_3). **Infrared:** 2217 cm^{-1} (C≡C). **Mp:** 171 ^{o}C. **Elemental analysis:** Calculated for $C_{26}H_{38}N_4O_2$: C 71.20, H 8.73, N 12.77. Observed: C 71.04, H 8.87, N 12.66.

Synthesis of **BA3a**:

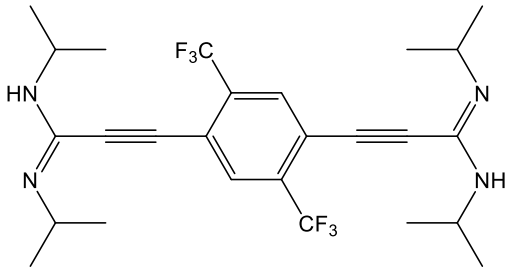

Synthesised using the same method as **BA1a** using 1,4-diethynyl-2,5-ditrifluoromethylbenzene (400 mg, 1.52 mmol), BuLi (1.22 mL, 3.05 mmol, 2.5 M), N,N-diisopropyl-carbodiimide (0.473 mL, 3.05 mmol). Product was isolated as an orange powder. **Yield:** 418 mg (53 %). **^{1}H NMR ($CDCl_3$, 298 K, 400.13 MHz)**: δ 7.93 (s, 2H, phenylene-C*H*), 3.94 (sept, $^{3}J_{H\text{-}H}$ = 6.3 Hz, 4H, ^{i}Pr-C*H*), 1.18 (d, $^{3}J_{H\text{-}H}$ = 6.3 Hz, 24H, ^{i}Pr-CH_3). **^{19}F NMR** (**$CDCl_3$, 298 K, 276.5 MHz**): δ -63.0. **^{13}C{^{1}H}**

NMR ($CDCl_3$, 298 K, 127.6 MHz): 139.7 (N*C*N)**,** 134.7 (q, $^2J_{C-F}$ = 31.8 Hz, *C*CF_3), 132.1 (q, $^3J_{C-F}$ = 5.5 Hz, phenylene-*C*H), 122.0 (q, $^1J_{C-F}$ = 274.3 Hz, *C*F_3), 120.8 (phenylene-quaternary-*C*), 88.1 (ethynyl-*C*), 84.9 (ethynyl-*C*), 47.6 (broad ^{i}Pr-*C*H), 23.9 (^{i}Pr-*C*H_3). **Infrared:** υ(C≡C) not observed. **Mp:** 148-149 ^{o}C. **Elemental analysis:** Calculated for $C_{26}H_{32}F_6N_4$: C 60.69, H 6.27, N 10.89. Observed: C 60.53, H 6.33, N 10.99.

Synthesis of **BA4a**:

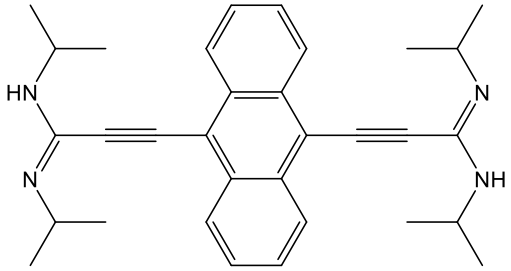

Synthesised using the same method as **BA1a** using 9,10-diethynyl-anthracene (100 mg, 0.442 mmol), BuLi (0.35 mL, 0.884 mmol, 2.5 M), N,N-diisopropyl-carbodiimide (0.14 mL, 0.884 mmol). Product was isolated as an orange powder. Yield 177 mg (83 %). **^{1}H NMR ($CDCl_3$, 298 K, 300.22 MHz):** δ 8.64-8.50 (m, 4H, anthracene-C*H*), 7.76-7.63 (m, 4H, anthracene-C*H*), 4.19 (sept, $^3J_{H-H}$ = 6.4 Hz, ^{i}Pr-C*H*), 1.29 (d, $^3J_{H-H}$ = 6.4 Hz, ^{i}Pr-CH_3). **^{13}C {^{1}H} NMR ($CDCl_3$, 298 K, 75.49 MHz):** δ 141.2 (N*C*N), 132.3 (anthracene-quaternary-*C*), 127.5 (anthracene-*C*H), 126.9 (anthracene-*C*H), 117.8 (anthracene-quaternary-*C*), 92.0 (ethynyl-*C*), 88.1 (ethynyl-*C*), 48.7 (broad, ^{i}Pr-*C*H), 24.1 (^{i}Pr-*C*H_3). **Infrared:** 2188 cm^{-1} (*C*≡C). **Mp:** 128 ^{o}C (dec.). **Elemental analysis:** Calculated for $C_{32}H_{38}N_4$: C 80.29, H 8.00, N 11.70. Observed: C 80.18, H 8.12, N 11.81.

Synthesis of **BA4b**:

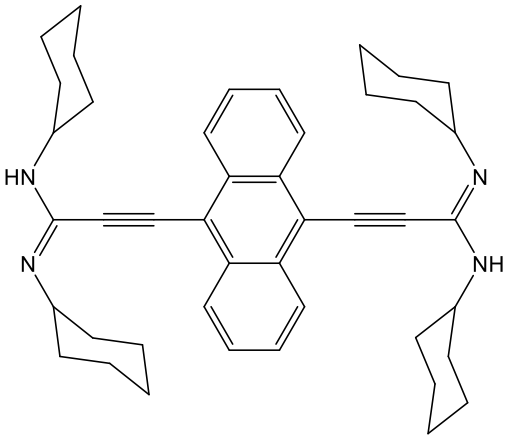

Synthesised using the same method as **BA1a** using 9,10-diethynyl-anthracene (100 mg, 0.442 mmol), BuLi (0.35 mL, 0.884 mmol, 2.5 M), N,N-dicyclohexyl-carbodiimide (0.182 mg, 0.884 mmol). Product was isolated as an orange powder. Yield 247 mg (88 %). **^{1}H NMR ($CDCl_3$, 298 K, 400.13 MHz):** 8.65-8.56 (m, 4H, anthracene-C*H*), 7.75-7.64 (m, 4H, anthracene-C*H*), 3.96-3.84 (m, 4H, cy-C*H*), 2.09- 1.17 (m, 40H, Cy-CH_2). **^{13}C{^{1}H} NMR ($CDCl_3$, 298 K, 100.62 MHz):** 142.0 (N*C*N), 132.6 (anthracene-quaternary-*C*), 127.6 (anthracene-*C*H), 127.1 (anthracene-*C*H), 118.2 (anthracene-quaternary-*C*), 92.1 (ethynyl-*C*), 89.1 (ethynyl-*C*), 56.1 (cy-*C*H), 34.7 (cy-*C*H_2), 25.8 (cy-*C*H_2), 25.3 (cy-*C*H_2). **Infrared:** 2194 cm^{-1} (C≡C). **Mp:** 161 ^{o}C (dec.). **Elemental Analysis:** Calculated for $C_{44}H_{54}N_4$: C 82.71, H 8.52, N 8.77. Observed: C 76.56, H 8.66, N 8.68. (Satisfactory data could not be collected for this system despite the repeat analyses of crystalline samples).

Synthesis of **Ru1a**:

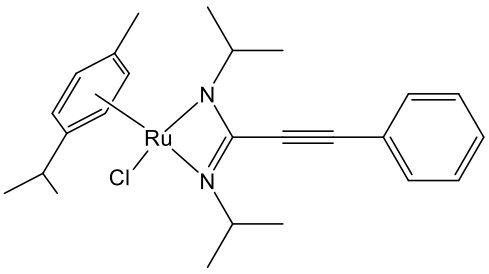

To a solution of **A1a** (0.075 g, 0.327 mmol) in THF (10 mL) was added NaOMe (0.437 M, 0.74 mL, 0.327 mmol) to give a cloudy yellow solution. After stirring for two hours the solution was combined with a solution of [(p-cymene)$RuCl_2$]$_2$ (0.100 g, 0.327 mmol) also in THF (5 mL) giving a red/orange solution. This was stirred for 8 h after which all volatiles were removed *in vacuo* giving a brown orange oily residue.

The residue was extracted into hexane (10 mL) and the solution was filtered through celite. The solution was concentrated *in vacuo* and bright orange crystals suitable for X-ray diffraction were formed upon cooling to – 28 °C and were isolated by filtration. Yield 0.130 g (80 %)**. ^{1}H NMR (C_6D_6, 298 K, 250.13 MHz)**: δ 7.26–7.20 (m, 2H, *o*-phenyl-C*H*), 6.93–6.80 (m, 3H, *m*- and *p*-phenyl-C*H*), 4.97 (d, $^{3}J_{H-H}$ = 5.9 Hz, 2H, *p*-cymene-C*H*), 4.71, (d, $^{3}J_{H-H}$ = 5.9 Hz, 2H, *p*-cymene-C*H*), 4.03 (sept, $^{3}J_{H-H}$ = 6.4 Hz, 2H, amidinate-^{i}Pr-C*H*), 2.64 (sept, $^{3}J_{H-H}$ = 6.9 Hz, 1H, *p*-cymene-^{i}Pr-C*H*), 2.05 (s, 3H, *p*-cymene-CH_3), 1.48 (d, $^{3}J_{H-H}$ = 6.4 Hz, 6H, amidinate-^{i}Pr-CH_3), 1.39 (d, $^{3}J_{H-H}$ = 6.4 Hz, amidinate-^{i}Pr-CH_3), 1.08 (d, $^{3}J_{H-H}$ 6.9 Hz, 6H, *p*-cymene-^{i}Pr-CH_3). **^{13}C NMR (C_6D_6, 298 K, 74.49 MHz):** δ 157.0 (N*C*N), 132.6 (*o*-ph-*C*), 129.5 (*p*-ph-*C*), 128.9 (*m*-ph-*C*), 122.3 (*i*-ph-*C*), 99.9 (*p*-cymene quaternary), 98.5 (*p*-cymene-quaternary-*C*), 91.8 (ethynyl-*C*), 80.0 (ethynyl-*C*), 79.4 (*p*-cymene-*C*H), 78.8 (*p*-cymene-*C*H) , 50.4 (amidinate-^{i}Pr-*C*H), 32.4 (*p*-cymene-^{i}Pr-*C*H), 26.0 (amidinate-^{i}Pr-*C*H_3), 25.9 (amidinate-^{i}Pr-*C*H_3), 22.7 (*p*-cymene-^{i}Pr-*C*H_3), 19.31 (*p*-cymene methyl *C*H_3). **Infrared:** 2212 cm^{-1} (C≡C). **Elemental analysis:** Calculated for $C_{25}H_{33}Cl_1N_2Ru_1$: C 60.29, H 6.68, N 5.62. Observed: C 60.15, H 6.78, N 5.73.

Synthesis of **Ru1b**:

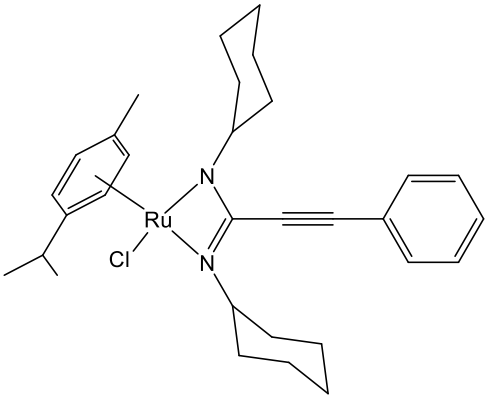

Synthesised using the same method reported for **Ru1a** using; **A1b** (0.101 g, 0.327 mmol), NaOMe (0.437 M, 0.74 mL, 0.327 mmol) and [(p-cymene)$RuCl_2$]$_2$ (0.100 g, 0.327 mmol). Product was purified by layering a concentrated DCM solution with hexanes yielding large orange block crystals. Yield 0.155 g, 82 %. **^{1}H NMR (C_6D_6, 298 K, 400.13 MHz):** δ 7.33 – 7.30 (m, 2H, *o*-ph-C*H*), 6.90 – 6.88 (m, 3H, *m*- and *p*-ph-C*H*), 5.05 (d, $^{3}J_{H-H}$ = 5.7 Hz, 2H, *p*-cymene-C*H*), 4.75 (d, $^{3}J_{H-H}$ = 5.7 Hz, 2H, *p*-cymene-C*H*), 3.62 (m, 2H, Cy-C*H*), 2.69 (sept, $^{3}J_{H-H}$ = 6.9 Hz, 2H, ^{i}Pr-C*H*), 2.57-2.54 (m, 2H, Cy-CH_2), 2.31-2.28 (m, 2H, Cy-CH_2), 2.09 (s, 3H, *p*-cymene-CH_3), 1.87-1.21 (m, 16H Cy-CH_2), 1.13 (d, $^{3}J_{HH}$ 6.9, ^{i}Pr-CH_3). **^{13}C NMR (C_6D_6, 298 K,**

100.62 MHz): δ 157.3 (N*C*N), 132.3 (*o*-ph-*C*), 129.2 (*p*-ph-*C*), 128.6 (*m*-ph-*C*), 122.1 (*i*-ph-*C*), 99.1 (*p*-cymene-quaternary-*C*), 98.8 (*p*-cymene-quaternary-*C*), 91.4 (ethynyl-*C*), 80.0 (ethynyl-*C*), 79.8 (*p*-cymene-*C*H), 78.4 (*p*-cymene-*C*H), 58.9 (cy-*C*H), 37.1 (cy-*C*H_2), 36.4 (cy-*C*H_2), 32.5 (*p*-cymene-^{i}Pr-*C*H), 26.7 (cy-*C*H_2), 26.4 (cy-*C*H_2), 26.3 (cy-*C*H_2), 22.8 (*p*-cymene-^{i}Pr-*C*H_3), 19.4 (*p*-cymene-*C*H_3). **Infrared:** 2207 cm^{-1} (C≡C). **Elemental analysis:** Calculated for $C_{31}H_{41}Cl_1N_2Ru_1$: C 64.40, H 7.15, N 4.84. Observed: C 64.35, H 7.17, N 4.77.

Synthesis of **Ru2a**:

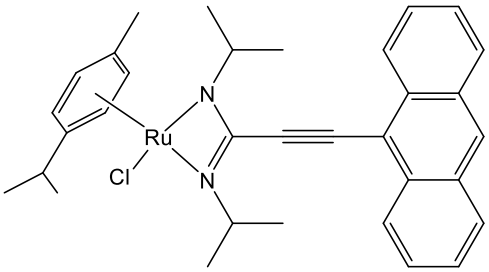

Synthesised using the same method reported for **Ru1a** using; **A2a** (0.108 g, 0.329 mmol), NaOMe (0.437 M, 0.75 mL, 0.327 mmol) and $[(p\text{-cymene})RuCl_2]_2$ (0.100 g, 0.327 mmol). The product was purified by crystallisation from hot toluene yielding large orange block crystals. **Yield:** 108 mg (72 %). **^{1}H NMR (C_6D_6, 298 K, 300.22 MHz):** δ 8.71 (d, $^{3}J_{H\text{-}H}$ = 8.6 Hz, 2H, anthracene-C*H*), 8.02 (s, 1H, *p*-anthracene-C*H*), 7.67 (d, $^{3}J_{H\text{-}H}$ = 8.6 Hz, 2H, anthracene-C*H*), 7.28 (m, 2H, anthracene-C*H*), 7.00 (m, 2H, anthracene-C*H*) 5.03 (d, $^{3}J_{H\text{-}H}$ = 5.9 Hz, 2H, *p*-cymene-C*H*), 4.77 (d, $^{3}J_{H\text{-}H}$ = 5.9 Hz, 2H, *p*-cymene-C*H*), 4.31 (sept, $^{3}J_{H\text{-}H}$ = 6.4 Hz, 2H, amidinate-^{i}Pr-C*H*), 2.71 (sept, $^{3}J_{H\text{-}H}$ = 6.9 Hz, 1H, *p*-cymene-^{i}Pr-C*H*), 1.59 (d, $^{3}J_{H\text{-}H}$ = 6.4 Hz, 6H, amidinate-^{i}Pr-C*H*$_3$), 1.52 (d, $^{3}J_{H\text{-}H}$ = 6.4 Hz, 6H, amidinate-^{i}Pr-C*H*$_3$), 1.31 (d, $^{3}J_{H\text{-}H}$ = 6.9 Hz, 6H, *p*-cymene-^{i}Pr-C*H*$_3$). **^{13}C{^{1}H} (C_6D_6, 298 K, 75.50 MHz):** δ 157.4 (N*C*N), 133.7 (anthracene-quaternary-*C*), 131.4 (anthracene-quaternary-*C*), 129.5 (anthracene-*C*H), 129.3 (anthracene-*C*H), 129.0 (anthracene-*C*H), 127.5 (anthracene-*C*H), 126.7 (anthracene-*C*H), 125.9 (anthracene-*C*H), 115.9 (*i*-Anthracene-*C*), 99.8 (*p*-cymene-quaternary-*C*), 98.1 (*p*-cymene-quaternary-*C*), 90.5 (ethynyl-*C*), 88.6 (ethynyl-*C*), 79.4 (*p*-cymene-*C*H), 78.9 (*p*-cymene-*C*H), 50.7 (amidinate-^{i}Pr-*C*H), 32.4 (*p*-cymene-^{i}Pr-*C*H), 26.2 (amidinate-^{i}Pr-*C*H_3), 26.0 (amidinate-^{i}Pr-*C*H_3), 22.8 (*p*-cymene-^{i}Pr-*C*H_3), 19.4 (*p*-cymene-*C*H_3). **Infrared:** 2182 cm^{-1} (C≡C). **Elemental**

analysis: Calculated for $C_{33}H_{37}Cl_1N_2Ru_1$: C 66.26, H 6.23, N 4.68. Observed: C 63.14, H 6.34, N 4.55.

Synthesis of **Ru2b**:

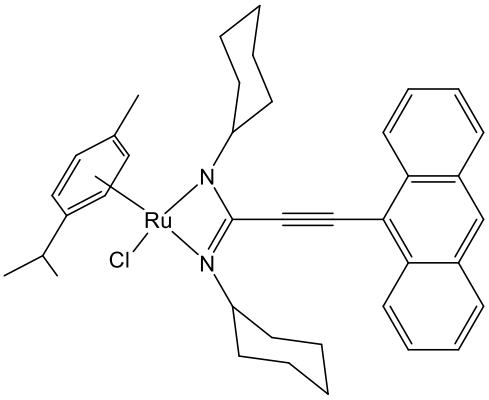

Synthesised using the same method reported for **Ru1a** using; **A2b** (133 mg, 0.327 mmol), NaOMe (0.75 mL, 0.327 mmol, 0.437 M) and $[(p\text{-cymene})RuCl_2]_2$ (0.100 g, 0.327 mmol). Product was purified by layering a concentrated DCM solution with hexanes yielding bright orange block crystals. **Yield:** 166 mg (75 %). **^{1}H NMR ($CDCl_3$, 298 K, 300.22 MHz):** δ 8.70 (d, $^3J_{H\text{-}H}$ = 8.5 Hz, 2H, anthracene-C*H*), 8.07 (s, 1H, *p*-anthracene-C*H*), 7.72 (d, $^3J_{H\text{-}H}$ = 8.5 Hz, 2H, anthracene-C*H*), 7.38-7.33 (m, 2H, anthracene-C*H*), 7.24-7.18 (m, 2H, anthracene-C*H*), 5.09 (d, $^3J_{H\text{-}H}$ =5.9 Hz, 2H, *p*-cymene-C*H*), 4.80 (d, $^3J_{H\text{-}H}$ = 5.9 Hz, 2H, *p*-cymene-C*H*), 3.98-3.86 (m, 2H, cy-C*H*), 2.74 (sept, $^3J_{H\text{-}H}$ = 6.9 Hz, 1H, *p*-cymene-^{i}Pr-C*H*), 2.79-2.64 (m, 2H, cy CH_2), 2.50-2.36 (m, 2H, cy-CH_2), 2.13 (s, 6H, *p*-cymene-CH_3), 2.01-1.26 (m, 16H, cy-CH_2), 1.17 (d, $^3J_{H\text{-}H}$ = 6.9 Hz, 6H, *p*-cymene-^{i}Pr-CH_3). **^{13}C{^{1}H} (C_6D_6, 298 K, 100.62 MHz):** δ 157.6 (N*C*N), 133.7 (anthracene-quaternary-*C*), 131.5 (anthracene-quaternary-*C*), 129.5 (*p*-anthracene-*C*H), 129.1 (anthracene-*C*H), 127.3 (anthracene-*C*H), 126.9 (anthracence-*C*H), 125.9 (anthracene-*C*H), 116.3 (*i*-anthracene-*C*), 99.3 (*p*-cymene-quaternary-*C*), 99.0 (*p*-cymene-quaternary-*C*), 90.9 (ethynyl-*C*), 88.4 (ethynyl-*C*), 79.9 (*p*-cymene-*C*H), 78.4 (*p*-cymene-*C*H), 59.2 (cy-*C*H), 37.3 (cy-*C*H_2), 36.5 (cy-*C*H_2), 32.5 (*p*-cymene-^{i}Pr-*C*H), 26.8 (cy-*C*H_2), 26.5 (cy-*C*H_2), 26.5 (cy-*C*H_2), 22.9 (cy-*C*H_2), 19.5 (*p*-cymene-^{i}Pr-*C*H_3). **Infrared:** υ2189 cm^{-1} (C≡C). **Elemental analysis:** Calculated for $C_{39}H_{45}Cl_1N_2Ru_1 \cdot CH_2Cl_2$: C 63.27, H 6.48, N 3.60. Observed: C 63.39, H 6.38, N 3.75.

Synthesis of **Ru3a**:

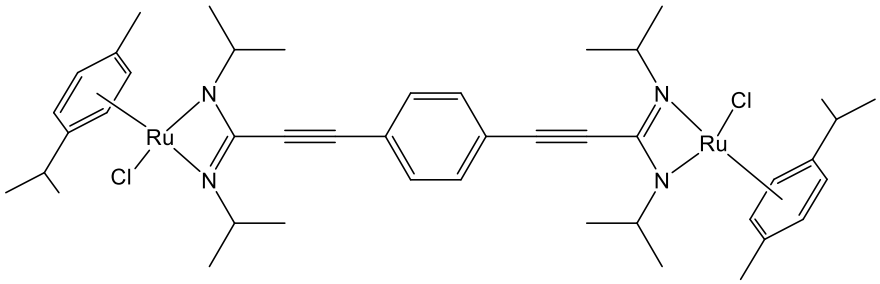

To a solution of **BA1a** (0.062 g, 0.163 mmol) in THF (10 mL) was added NaOMe (0.74 mL, 0.327 mmol, 0.437 M) to give a cloudy yellow solution. After stirring for two hours the solution was combined with a solution of $[(p\text{-cymene})RuCl_2]_2$ (0.100 g, 0.285 mmol) also in THF (5 mL) giving a red/orange solution. This was stirred for 8 h after which all volatiles were removed *in vacuo*. The bright orange residue extracted into toluene (10 mL). The solution was filtered through celite and the toluene was removed *in vacuo*. The residue was dissolved in THF (5 mL) and hexane (10 mL) was layered upon the solution. After 24 h at room temperature large red/orange block crystals suitable for X-ray diffraction were formed and isolated by filtration. Yield 0.082g (55 %). **^{1}H NMR (C_6D_6, 298 K, 300.22 MHz):** δ 6.99 (s, 4H, phenylene-C*H*), 4.97 (d, $^3J_{H\text{-}H}$ = 6.3 Hz, 4H, *p*-cymene-C*H*), 4.71 (d, $^3J_{H\text{-}H}$ = 6.3 Hz, 4H, *p*-cymene-C*H*), 3.97 (sept, $^3J_{H\text{-}H}$ = 6.4 Hz, 4H, amidinate-^{i}Pr-C*H*), 2.62 (sept, $^3J_{H\text{-}H}$ = 6.9 Hz, 2H, *p*-cymene-^{i}Pr-CH), 2.04 (s, 6H, *p*-cymene-CH_3), 1.47 (d, $^3J_{H\text{-}H}$ = 6.4 Hz, 12H, amidinate-^{i}Pr-CH_3), 1.37 (d, $^3J_{H\text{-}H}$ = 6.4 Hz, 12H, amidinate-^{i}Pr-CH_3), 1.07 (d, 12H, $^3J_{H\text{-}H}$ = 6.9 Hz, *p*-cymene-^{i}Pr-CH_3). **^{13}C{H^1} NMR (C_6D_6, 298 K, 74.49 MHz):** 156.5 (N*C*N), 132.2 (phenylene-*C*H), 122.6 (phenylene-quaternary-*C*), 99.7 (*p*-cymene-quaternary-*C*), 98.3 (*p*-cymene-quaternary-*C*), 90.7 (ethynyl-*C*), 81.5 (ethynyl-*C*), 79.4 (*p*-cymene-*C*H), 78.8 (*p*-cymene-*C*H), 50.4 (amidinate-^{i}Pr-*C*H), 32.4 (*p*-cymene-^{i}Pr-*C*H), 25.9 (amidinate-^{i}Pr-*C*H_3), 25.8 (amidinate-^{i}Pr-*C*H_3), 22.7 (*p*-cymene-^{i}Pr-*C*H_3), 19.3 (*p*-cymene-*C*H_3). **Infrared:** 2214 cm^{-1} (C≡C). **Elemental analysis:** Calculated for $C_{44}H_{60}Cl_2N_4Ru_2$: C 57.57, H 6.59, N 6.10. Observed: C 57.61, H 6.70, N 6.05.

Synthesis of **Ru3b**:

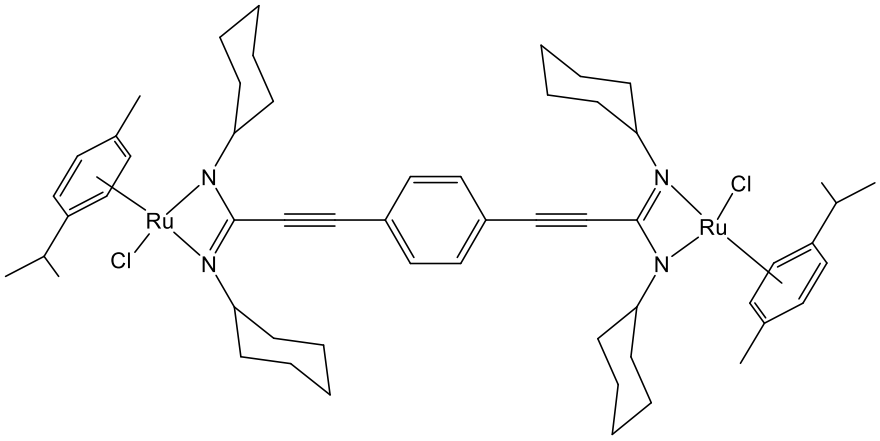

Synthesised using the same method reported for **Ru3a** using; **BA1b** (0.088 g, 0.163 mmol), NaOMe (0.74 mL, 0.327 mmol, 0.437 M) and $[(p\text{-cymene})RuCl_2]_2$ (0.100 g, 0.327 mmol). Diffraction quality crystals were obtained *via* DCM/Pentane vapour diffusion. Yield 132 mg (75 %). **^{1}H NMR ($CDCl_3$, 298 K, 300.22 MHz):** δ 7.21 (s, 4H, phenylene-C*H*), 5.44 (d, $^3J_{H\text{-}H}$ = 5.9 Hz, 4H, *p*-cymene-C*H*), 5.11 (d, $^3J_{HH}$ = 5.9 Hz, 4H, p-cymene-C*H*), 3.25-3.13 (m, 4H, cy-C*H*), 2.74 (sept, $^3J_{H\text{-}H}$ = 6.8 Hz, 2H, *p*-cymene-^{i}Pr-C*H*), 2.18 (s, 6H, p-cymene CH_3), 2.11-1.08 (m, 40H, Cy CH_2), 1.25 (d, $^3J_{H\text{-}H}$ = 6.8 Hz, 12H, iPr CH_3, p-cymene CH_3). **^{13}C{^{1}H} NMR ($CDCl_3$, 298 K 74.49 MHz):** 154.9 (N*C*N), 130.9 (phenylene *C*H), 121.4 (phenylene-quaternary-C), 98.4 (*p*-cymene-quaternary-*C*), 97.3 (*p*-cymene-quaternary-*C*), 88.3 (ethynyl-*C*), 79.8 (ethynyl-*C*), 79.1 (*p*-cymene-*C*H), 77.4 (*p*-cymene *C*H), 57.5 (cy-*C*H) 35.4 (cy-*C*H_2), 34.8 (cy-*C*H_2), 31.1 (p-cymene-^{i}Pr-*C*H), 25.1 (cy-*C*H_2), 24.9 (cy-*C*H_2), 24.8 (cy-*C*H_2), 21.7 (p-cymene-^{i}Pr-*C*H_3), δ 18.3 (p-cymene-*C*H_3). **Infrared:** 2220 cm^{-1} (C≡C). **Elemental Analysis:** Calculated for $C_{56}H_{76}Cl_2N_4Ru_2$: C 62.38, H 7.10, N 5.20. Observed: C 59.59, H 8.20, N 4.97. (Multiple crystalline samples were submitted for analysis but satisfactory results could not be obtained)

Synthesis of **Ru4a**:

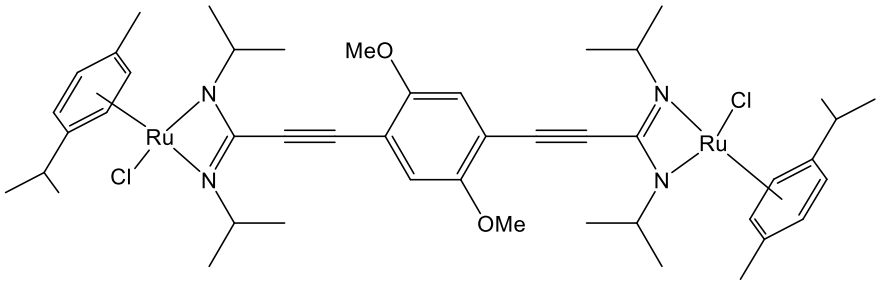

Synthesises using the same method reported for Ru3a using; **BA2a** (72mg, 0.163 mmol), NaOMe (0.75 mL, 0.437M in THF) and $[(p\text{-cymene})RuCl_2]_2$ (100 mg, 0.327 mmol). Product was purified by crystallisation from toluene to yield small red plate crystals. Yield 92 mg (53 %). **^{1}H NMR (C_6D_6, 298K, 400.13 MHz):** δ 6.69 (s, 2H, phenylene-C*H*), 5.00 (d, $^3J_{H\text{-}H}$ = 5.8 Hz, 4H, *p*-cymene-C*H*), 4.73 (d, $^3J_{H\text{-}H}$ = 5.8 Hz, 4H, *p*-cymene-C*H*), 4.13 (sept, $^3J_{H\text{-}H}$ = 6.4, 4H, amidinate-^{i}Pr-C*H*), 3.06 (s, 6H, OCH_3), 2.66 (sept, $^3J_{H\text{-}H}$ = 7.0 Hz, 2H, *p*-cymene-^{i}Pr-C*H*), 2.05 (s, 6H, *p*-cymene-CH_3), 1.50 (d, $^3J_{H\text{-}H}$ = 6.4 Hz, 12H, amidinate-^{i}Pr-CH_3), 1.44 (d, $^3J_{H\text{-}H}$ = 6.4 Hz, 12H, amidinate-^{i}Pr-CH_3), 1.09 (d, $^3J_{H\text{-}H}$ = 7.0 Hz, *p*-cymene-^{i}Pr-CH_3). **^{13}C{^{1}H} NMR (C_6D_6, 298 K, 400.13 MHz):** δ 157.1 (NCN), 155.5 (*C*-OMe), 116.1 (phenylene-*C*H), 113. 9 (phenylene quaternary-*C*), 100.0 (*p*-cymene-quaternary-*C*), 98.5 (*p*-cymene-quaternary-*C*), 92.6 (ethynyl-*C*), 88.3 (ethynyl-*C*), 79.7 (*p*-cymene-*C*H), 79.1 (*p*-cymene-*C*H), 56.0 (O*C*H_3), 50.8 (amidinate-^{i}Pr-*C*H), 32.7 (*p*-cymene-^{i}Pr-*C*H), 26.3 (amidinate-^{i}Pr-*C*H_3), 26.2 (amidinate-^{i}Pr-*C*H_3), 23.1 (*p*-cymene-^{i}Pr-CH_3), 19.7 (*p*-cymene-*C*H_3). **Infrared:** 2204 cm^{-1} (C≡C). **Elemental analysis:** Calculated for $C_{46}H_{64}Cl_2N_4O_2Ru_2 \cdot C_7H_8$: C 59.48, H 6.78, N 5.24. Observed: C 59.58, H 6.75, N 5.11.

Synthesis of **Ru5a**:

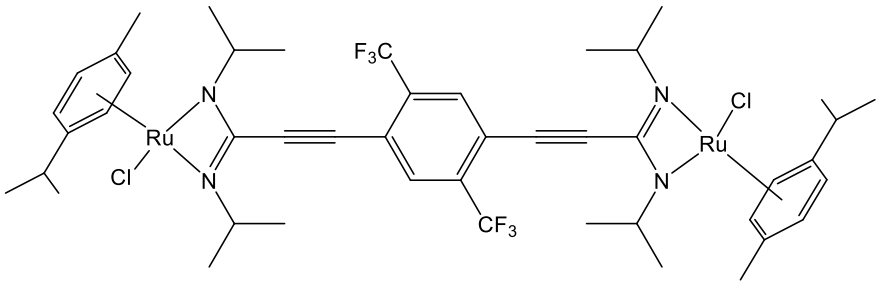

Synthesised using the same method reported for **Ru3a** using; **BA3a** (84mg, 0.163 mmol), NaOMe (0.75 mL, 0.327 mmol, 0.437 M) and $[(p\text{-cymene})RuCl_2]_2$ (100 mg, 0.327 mmol). Product was purified by crystallisation from hot toluene yielding large

red block crystals. **Yield:** 75 mg (44 %). **^{1}H NMR (C_6D_6, 298 K, 400.13 MHz):** δ 7.36 (s, 2H, phenylene-C*H*), 4.96 (d, $^{3}J_{H-H}$ = 5.4 Hz, 4H, *p*-cymene-C*H*), 4.70 (d, $^{3}J_{H-H}$ = 5.4 Hz, 4H, *p*-cymene-C*H*), 4.00 (sept, $^{3}J_{H-H}$ = 6.4 Hz, amidinate-^{i}Pr-C*H*, 4H), 2.62 (sept, $^{3}J_{H-H}$ = 6.8 Hz, *p*-cymene-^{i}Pr-C*H*, 2H), 2.02 (s, 6H, *p*-cymene-CH_3), 1.48 (d, $^{3}J_{H-H}$ = 6.4 Hz, 12H, amidinate-^{i}Pr-CH_3), 1.06 (d, $^{3}J_{H-H}$ = 6.8 Hz, 12H, *p*-cymene-^{i}Pr-CH_3). **^{19}F NMR (C_6D_6, 298 K, 376.47 Hz):** δ -62.98 (s, CF_3). **^{13}C NMR (C_6D_6, 298 K, 125.77 MHz):** 154.9 (N−*C*=N), 134.0 (q, $^{2}J_{C-F}$ = 31.7 Hz, *C*CF_3), 131.8 (q, $^{3}J_{C-F}$ = 5.2 Hz, bridge aromatic *C*H), 122.4 (q, $^{1}J_{C-F}$ = 274.5 Hz, *C*F_3), 100.2 (*p*-cymene-quaternary-*C*), 98.5 (*p*-cymene-quaternary-*C*), 87.5 (ethynyl-*C*), 85.0 (ethynyl-C), 79.5 (*p*-cymene-*C*H), 78.8 (*p*-cymene-*C*H), 50.5 (amidinate-^{i}Pr-*C*H), 32.4 (*p*-cymene-^{i}Pr-*C*H)), 26.0 (amidinate-^{i}Pr-*C*H_3), 25.8 (amidinate-^{i}Pr-*C*H_3), 22.7 (*p*-cymene-^{i}Pr-*C*H_3), 19.3 (s, *p*-cymene-*C*H_3). **Infrared:** 2218 cm^{-1} (C≡C). **Elemental Analysis:** Calculated for $C_{46}H_{58}Cl_2F_6N_4Ru_2\cdot(C_7H_8)$: C 55.54, H 5.80, N 4.89. Observed: C 55.60, H 5.86, N 5.03.

Synthesis of **Ru6a**:

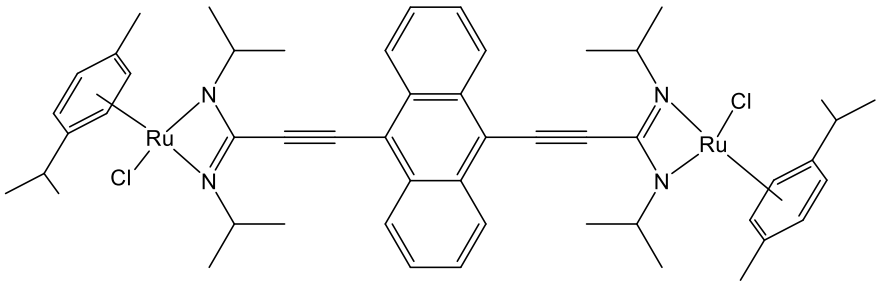

Synthesised using the same method reported for **Ru3a** using; **BA4a** (78.0 mg, 0.163 mmol), NaOMe (0.75 mL, 0.327 mol, 0.437 M) and [(p-cymene)$RuCl_2$]$_2$ (0.100 g, 0.327 mmol). Product was purified by layering a concentrated DCM solution with hexanes, yielding large red rod shaped crystals. **Yield:** 0.097 g (58 %). **^{1}H NMR (C_6D_6, 298 K, 300.22 MHz):** δ 8.70-8.51 (m, 4H, anthracene-C*H*), 7.32-7.21 (m, 4H, anthracene-C*H*), 5.04 (d, $^{3}J_{H-H}$ = 5.8 Hz, 4H, *p*-cymene C*H*), 4.78 (d, $^{3}J_{H-H}$ = 5.8 Hz, 4H, *p*-cymene C*H*), 4.27 (sept, $^{3}J_{H-H}$ = 6.4 Hz, 4H, amidinate-^{i}Pr-C*H*), 2.71 (sept, $^{3}J_{H-H}$ = 6.9 Hz, 2H, *p*-cymene-^{i}Pr-C*H*), 2.08 (s, 6H, *p*-cymene-CH_3), 1.58 (d, $^{3}J_{H-H}$ = 6.4 Hz, 12H, amidinate-^{i}Pr-CH_3), 1.51 (d, $^{3}J_{HH}$ = 6.4 Hz, 12H, amidinate-^{i}Pr-CH_3), 1.13 (d, $^{3}J_{HH}$ = 6.9 Hz, 12H, *p*-cymene-^{i}Pr-CH_3). **^{13}C{H^{1}} NMR (C_6D_6, 298 K, 100.62 MHz):** δ 156.9 (N*C*N), 132.9 (anthracene-quaternary-*C*), 127.8 (anthracene-*C*H), 127.1 (anthracene-*C*H), 118.3 (anthracene-quaternary-*C*), 99.9 (*p*-cymene-

quaternary-*C*), 98.2 (*p*-cymene-quaternary-*C*), 92.1 (ethynyl-*C*), 88.4 (ethynyl-*C*), 79.5 (*p*-cymene-*C*H), 78.9 (*p*-cymene-*C*H), 50.7 (amidinate-^{i}Pr-*C*H), 32.4 (*p*-cymene-^{i}Pr-*C*H), 26.2 (amidinate-^{i}Pr-*C*H_3), 26.0 (amidinate-^{i}Pr-*C*H_3), 22.8 (*p*-cymene-^{i}Pr-*C*H_3), 19.4 (*p*-cymene-*C*H_3). **Infrared:** 2182 cm^{-1} (C≡C). **Elemental analysis:** Calculated for $C_{52}H_{64}Cl_2N_4Ru_2$: C 61.34, H 6.34, N 5.50. Observed: C 61.25, H 6.28, N 5.41.

Synthesis of **Ru6b**:

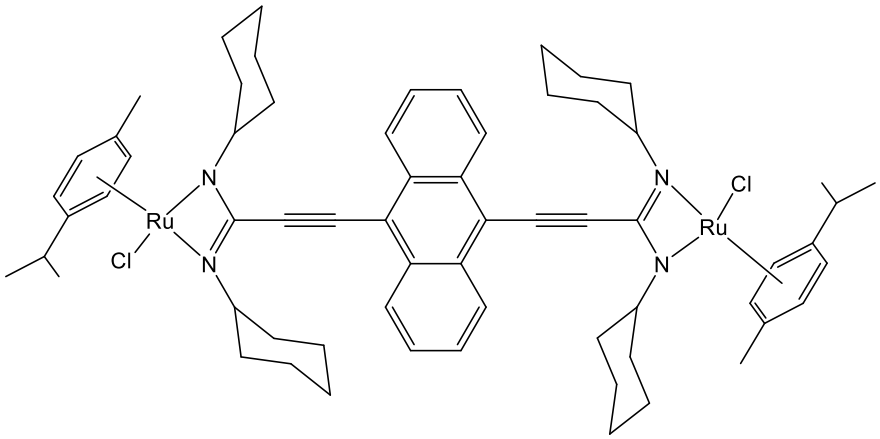

Synthesised using the same method reported for **Ru3a** using; **BA4b** (0.100 g, 0.157 mmol), NaOMe (0.72 mL, 0.313 mmol, 0.437 M) and [(p-cymene)$RuCl_2$]$_2$ (0.096 g, 0.313 mmol). The product was purified by layering a concentrated DCM solution with pentane, yielding dark red iridescent needle crystals. **Yield:** 120 mg (65 %). **^{1}H NMR ($CDCl_3$, 298 K, 400.13 MHz):** δ 8.52-8.46 (m, 4H, anthracene-C*H*), 7.59-7.49 (m, 4H, anthracene-C*H*), 5.56 (d, $^{3}J_{H-H}$ = 5.8 Hz, 4H, *p*-cymene-C*H*), 5.22 (d, $^{3}J_{H-H}$ = 5.8 Hz, 4H, p-cymene-C*H*), 3.68-3.59 (m, 4H, cy-C*H*), 2.85 (sept, $^{3}J_{H-H}$ = 6.9 Hz, 2H, p-cymene-^{i}Pr-C*H*)), 2.28 (s, 6H, *p*-cymene-CH_3), 2.27-2.15 (m, 8H, cy-CH_2), 1.98-1.20 (m, 32H, cy-CH_2) 1.29 (d, $^{3}J_{H-H}$ = 6.9 Hz, 12H, *p*-cymene-^{i}Pr-CH_3). **^{13}C{H^{1}} NMR ($CDCl_3$, 298 K, 100.62 MHz):** δ 156.2 (N*C*N), 132.4 (anthracene-quaternary-*C*), 127.1 (anthracene-*C*H), 127.0 (anthracene-*C*H), 118.1 (anthracene-quaternary-*C*), 99.7 (*p*-cymene-quaternary-*C*), 98.5 (*p*-cymene-quaternary-*C*), 91.5 (ethynyl-*C*), 87.7 (ethynyl-*C*), 80.2 (*p*-cymene-*C*H), 78.4 (*p*-cymene-*C*H), 58.8 (cy-*C*H), 36.7 (cy-*C*H_2), 36.0 (cy-*C*H_2), 32.2 (*p*-cymene-^{i}Pr-*C*H), 26.1 (cy-*C*H_2), 26.0 (cy-*C*H_2), 22.8 (cy-*C*H_2), (*p*-cymene-^{i}Pr-*C*H_3), 19.4 (*p*-cymene-*C*H_3). **Infrared:** 2196 cm^{-1} (C≡C). **Elemental analysis:** Calculated for $C_{64}H_{80}Cl_2N_4Ru_2$: C 65.23, H 6.84, N 4.75. Observed: C 65.18, H 6.94, N 4.63.

8.5 – Experimental Data for Chapter 5

All syntheses reported within this section were performed under an atmosphere of Ar using standard Schlenk line techniques. All products are highly air-sensitive and were stored in a glovebox under an Are atmosphere. The compounds: **MoFAc**,[342] **MoAc**[342] **MoPiv**,[342] **L1**,[350] **L2**,[277] **L3**[351] and **L4**,[351] were obtained using preparative methods described within the literature. TMS-Cl was purchased from Sigma Aldrich and used as received.

Synthesis of **MoFAc·L1**:

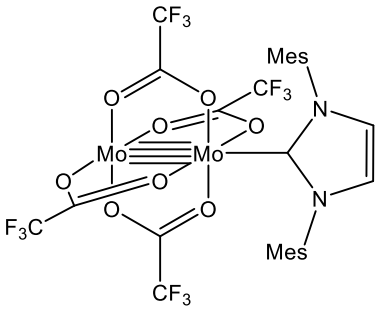

MoFAc·THF$_2$ (100 mg, 0.127 mmol) and **L1** (39 mg, 0.127 mmol) were suspended in toluene (10 mL) giving a yellow powdery precipitate. The mixture was stirred for 30 minutes after which the solution was heated to reflux, which dissolved all material. Upon cooling yellow block crystals formed which were suitable for X-ray diffraction. These were isolated by cannula filtration. **Yield:** 109 mg (64 %). **^{1}H NMR (*d*$_8$-THF, 298 K, 400.13 MHz):** δ 7.49 (s, 2H, carbene-backbone-C*H*) 7.07 (s, 4H, Mes-C*H*), 2.40 (s, 6H, Mes-*o*-C*H*$_3$), 2.00 (s, 12H, Mes-*p*-CH$_3$). **^{19}F NMR (*d*$_8$-THF, 298 K, 376.50 MHz):** δ -73.5 (C*F*$_3$). **^{13}C{^{1}H} NMR (*d*$_8$-THF, 298 K, 100.61 MHz):** δ 164.9 (q, $^2J_{C\text{-}F}$ = 40 Hz, O*C*O), 140.37 (Mes-*p*-*C*), 137.3 (Mes-*i*-*C*), 136.2 (Mes-*o*-*C*), 130.2 (Mes-*C*H), 127.5 (carbene-backbone-*C*), 114.8 (q, $^1J_{C\text{-}F}$ = 284.7 Hz, *C*F$_3$), 21.1 (Mes-*p*-*C*H$_3$), 17.9 (Mes-*o*-*C*H$_3$). **Elemental analysis:** Calculated for $C_{29}H_{24}F_{12}Mo_2N_2O_8$: C 36.73, H 2.55, N 2.95. Observed: C 36.70, H 2.59, N 3.02.

Synthesis of **MoAc·L1**:

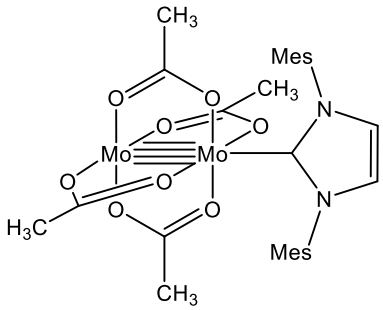

MoAc·L1 was synthesised and crystallised using the same method reported for **MoFAc·L1** using; **MoAc** (100 mg, 0.234 mmol) and **L1** (71 mg, 0.234 mmol). Product was isolated as large yellow block crystals. **Yield:** 109 mg (64 %). **Elemental analysis:** Calculated for $C_{29}H_{36}Mo_2N_2O_8$: C 47.55, H 4.95, N 3.82. Observed: C 47.32, H 4.95, N 3.77.

Low solubility precluded the solution state characterisation of this product.

Synthesis of **MoPiv·L1**:

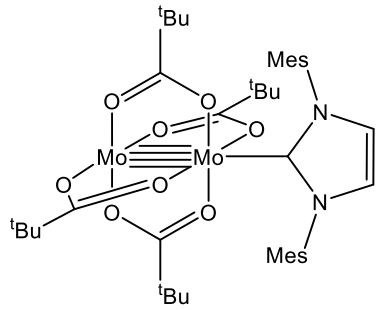

MoPiv (100 mg, 0.168 mmol) and **L1** (51 mg, 0.168 mmol) were dissolved in toluene (10 mL) and the solution was stirred for 15 minutes after which it was filtered through celite. The solution was concentrated *in vacuo* and cooled to -28 °C yielding large yellow needle-like crystals. These were isolated by cannula filtration. **Yield:** 128 mg (85 %). **^{1}H NMR (C_6D_6, 298 K, 400.13 MHz):** δ 6.85 (s, 4H, Mes-C*H*), 6.13 (s, 2H, carbene-backbone-C*H*), 2.21 (s, 6H, Mes-*o*-CH_3), 2.14 (s, 12H, Mes-*p*-CH_3), 1.41 (s, 36H, ^{t}Bu-CH_3). **^{13}C{^{1}H} NMR (C_6D_6, 298 K, 100.61 MHz):** δ 189.5 (O*C*O), 138.4 (Mes-*i*-*C*), 137.4 (Mes-*p*-*C*), 135.5 (Mes-*o*-*C*), 129.3 (Mes-*C*H), 122.3 (carbene-backbone-*C*), 40.6 (^{t}Bu-*C*CH$_3$), 28.8 (^{t}Bu-*C*H$_3$), 21.1 (Mes-*p*-*C*H$_3$), 18.3 (Mes-*o*-*C*H$_3$). **Elemental analysis:** Calculated for $C_{41}H_{60}Mo_2N_2O_8$: C 54.66, H 6.71, N 3.11. Observed: C 54.68, H 6.83, N 2.97.

Synthesis of **MoFAc·L2**:

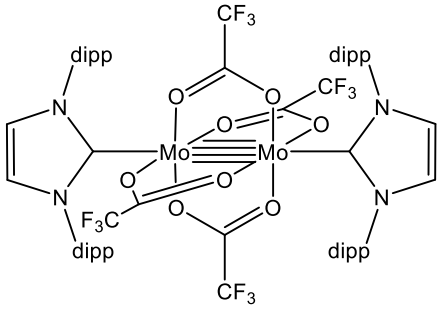

MoFAc·THF_2 (100 mg, 0.127 mmol) and **L2** (99 mg, 0.25 mmol) were dissolved in toluene (5 mL) and the solution was stirred for 15 minutes after which it was filtered through celite. The solution was then concentrated *in vacuo* and cooled to -28 ^{o}C producing large yellow block crystals, which were isolated *via* cannula filtration. **Yield:** 150 mg (83 %). For X-ray diffraction studies the product was recrystallised from xylene at -28 ^{o}C. **^{1}H NMR (C_6D_6, 298 K, 400.13 MHz):** δ 7.35 (t, $^{3}J_{H-H}$ = 7.8 Hz, 2H, dipp-*m*-C*H*), 7.14 (dipp-*p*-C*H*), 6.16 (s, 2H, carbene-backbone-C*H*), 2.53 (sept, $^{3}J_{H-H}$ = 6.8 Hz, 4H, ^{i}Pr-C*H*), 1.28 (d, $^{3}J_{H-H}$ = 6.8 Hz, 12H, ^{i}Pr-CH_3), 0.94 (d, $^{3}J_{H-H}$ = 6.8 Hz, 12H, ^{i}Pr-CH_3). **^{19}F NMR (C_6D_6, 298 K, 376.50 MHz):** - 71.0 (CF_3). **^{13}C{^{1}H} NMR (C_6D_6, 298 K, 100.61 MHz):** 164.7 (q, $^{2}J_{C-F}$ = 40.3 Hz, O*C*O), 145.3 (dipp-*o*-*C*), 137.1 (dipp-*i*-*C*), 129.8 (dipp-*p*-*C*H), 124.5 (carbene-backbone-*C*), 123.8 (dipp-*m*-*C*H), 113.7 (q, $^{1}J_{C-F}$ = 283.2 Hz, *C*F_3), 28.1 (^{i}Pr-*C*H), 24.9 (^{i}Pr-*C*H_3), 23.1 (^{i}Pr-*C*H_3). **Elemental analysis:** Calculated for $C_{62}H_{72}F_{12}Mo_2N_4O_8$: C 54.76, H 5.33, N 3.70. Observed: C 54.85, H 5.44, N 3.83.

Synthesis of **MoFAc·L3**:

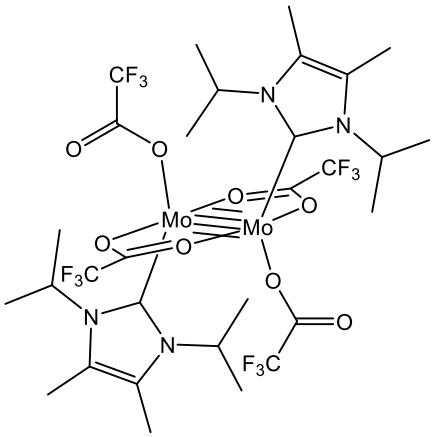

MoFAc·THF_2 (100 mg, 0.127 mmol) and **L3** (39 mg, 0.254 mmol) were dissolved in toluene (10 mL) and the dark red solution was stirred until all solid material had

dissolved. The solution was then left to stand at room temperature yielding red block crystal, which were isolated *via* cannula filtration. Yield 102 mg (80 %). **^{1}H NMR (d_8-tol, 353 K, 400.13 MHz):** δ 4.48 (broad signal, 2H, ^{i}Pr-C*H*), 1.81 (s, 6H, carbene-backbone-CH_3), 0.97 (d, $^{3}J_{H\text{-}H}$ = 7.1 Hz, 12H, ^{i}Pr-CH_3). **^{19}F NMR (d_8-tol, 298 K, 376.50 MHz):** δ -72.0 (μ-CF_3), -74.1 (CF_3). **Elemental analysis:** Calculated for $C_{30}H_{40}F_{12}Mo_2N_4O_8$: C 35.87, H 4.01, N 5.58. Observed: C 35.74, H 3.95, N 5.46.

Synthesis of **MoAc·L3**:

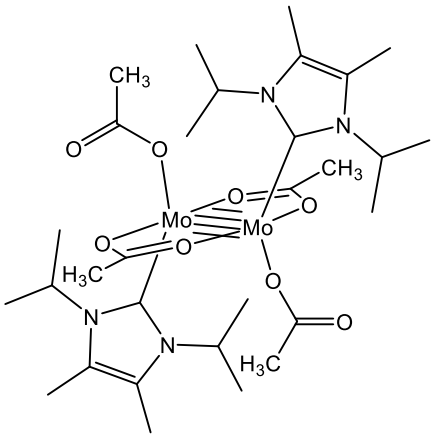

MoAc (100 mg, 0.234 mmol) and **L3** (84 mg, 0.467 mmol) were dissolved in toluene (10 mL) and the dark purple solution was stirred for 30 minutes after which it was filtered through celite. The solution was concentrated *in vacuo* and cooled to -28 ^{o}C yielding purple block crystals, which were isolated *via* cannula filtration. Yield 132 mg (72 %). **^{1}H NMR (d_8-tol, 353 K, 400.13 MHz):** δ 4.23 (broad signal, 4H, ^{i}Pr-C*H*), 2.43 (s, 12H, acetate-CH_3), 1.78 (s, 12H, carbene-backbone-CH_3), 1.36 (d, $^{3}J_{H\text{-}H}$ = 6.8 Hz, 24H, ^{i}Pr-CH_3). **Elemental analysis:** Calculated for $C_{30}H_{52}Mo_2N_4O_8$: C 45.69, H 6.65, N 7.10. Observed: C 45.59, H 6.74, N 7.13.

Synthesis of **MoFAc·L4**:

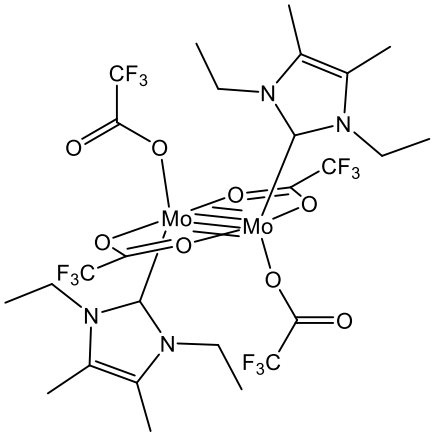

MoFAc·L4 was synthesised and crystallised using the same method reported for **MoAc·L3** using; **MoFAc·THF$_2$** (100 mg, 0.127 mmol) and **L4** (39 mg, 0.254 mmol). **Yield:** 87 mg (73 %). **^{1}H NMR (*d*$_8$-tol, 353 K, 400.13 MHz):** δ 3.87 (broad signal, 4H, Et-C*H*$_2$), 1.63 (s, 6H, carbene-backbone-C*H*$_3$) 0.97 (t, $^3J_{H\text{-}H}$ = 7.2 Hz, 6H, Et-C*H*$_3$). **^{19}F NMR (d^8-tol, 298 K, 376.50 MHz):** δ -71.1, -72.1, -74.6. **Elemental analysis:** Calculated for $C_{26}H_{32}F_{12}Mo_2N_4O_8$: C 32.92, H 3.40 N 5.91. Observed: C 33.05, H 3.42, N 5.93.

Synthesis of **MoPiv·PivL3**:

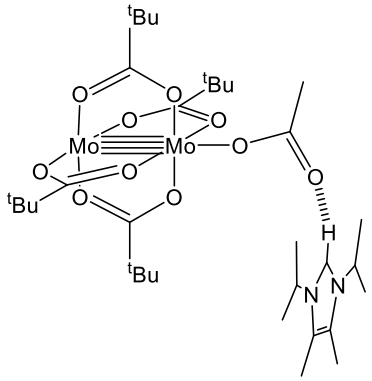

MoPiv·L3Piv was isolated from the reaction between **MoPiv**[a] (150 mg, 0.252 mmol), and **L3** (91 mg, 0.503 mmol) in toluene. The yellow solution of the reaction mixture was concentrated *in vacuo* and a small crop of yellow rod-like crystals of **MoPiv·PivL3** were obtained by cooling the solution to -28 °C. These were isolated by cannula filtration. **Yield:** 10 mg (11 %). ^{1}H NMR (*d*$_8$-toluene, 298 K, 300.22 MHz): δ 11.66 (s, 1H, imidazolium-C*H*), 3.66 (sept, 2H, $^3J_{H\text{-}H}$ = 6.8, iPr-C*H*), 1.52 (s,

9H, monodentate-pivalate-C*H*$_3$), 1.48 (s, 36H, μ-pivalate-C*H*$_3$), 1.40 (d, $^3J_{H-H}$ = 6.8, 12H, iPr-C*H*$_3$), 1.36 (s, 6H, imidazolium backbone-C*H*$_3$).

[a]The sample of **MoPiv** was shown to contain an impurity of pivalic acid, explaining the formation of this unusual product.

Synthesis of **MoAcCl·L3**:

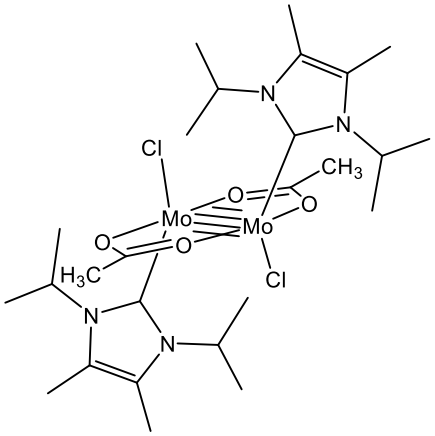

MoAc (150 mg, 0.350 mmol) and **L3** (126 mg, 0.701 mmol) were dissolved in THF (15 mL) giving a dark red solution. The solution was filtered through celite and TMS-Cl (0.10 mL, 0.800 mmol) was added drop-wise turning the solution dark purple. The solution was filtered through celite and concentrated *in vacuo* and a crop of red crystals were obtained by cooling the solution to -28 ^oC. These were isolated by cannula filtration. **Yield:** 135 mg, 52 %. **^{1}H NMR (C_6D_6, 298 K, 400.13 MHz):** δ 4.93 (sept, $^3J_{H-H}$ = 6.9 Hz, 4H, ^{i}Pr-C*H*), 2.64 (s, 6H, acetate-C*H*$_3$), 1.69 (s, 12H, carbene-backbone-C*H*$_3$), 1.35 (d, $^3J_{H-H}$ = 6.9 Hz, 24H, ^{i}Pr-C*H*$_3$). **Elemental analysis:** Calculated for $C_{26}H_{46}Cl_2Mo_2N_4O_2$: C 42.11, H 6.25, N 7.56. Observed: C 41.97, H 6.31, N 7.38.

Chapter 9 – References

(1) Moore, G. E., *Electronics*, **1965**, *38*, 114.
(2) Chiang, C. K.; Fincher, C. R.; Park, Y. W.; Heeger, A. J.; Shirakawa, H.; Louis, E. J.; Gau, S. C.; Macdiarmid, A. G., *Phys. Rev. Lett.*, **1977**, *39*, 1098.
(3) Shirakawa, H.; Louis, E. J.; Macdiarmid, A. G.; Chiang, C. K.; Heeger, A. J., *J. Chem. Soc. Chem. Comm.*, **1977**, 578.
(4) Fan, L. J.; Zhang, Y.; Murphy, C. B.; Angell, S. E.; Parker, M. F. L.; Flynn, B. R.; Jones, W. E., *Coord. Chem. Rev.*, **2009**, *253*, 410.
(5) Irie, M., *Chem. Rev.*, **2000**, *100*, 1685.
(6) Burroughes, J. H.; Bradley, D. D. C.; Brown, A. R.; Marks, R. N.; Mackay, K.; Friend, R. H.; Burns, P. L.; Holmes, A. B., *Nature*, **1990**, *347*, 539.
(7) Sreeja, S.; Sreedhanya, S.; Smijesh, N.; Philip, R.; Muneera, C. I., *J. Mater. Chem. C.*, **2013**, *1*, 3851.
(8) Roncali, J., *Chem. Rev.*, **1997**, *97*, 173.
(9) Roncali, J., *Chem. Rev.*, **1992**, *92*, 711.
(10) Bernius, M. T.; Inbasekaran, M.; O'Brien, J.; Wu, W. S., *Adv. Mater.*, **2000**, *12*, 1737.
(11) Fukuda, M.; Sawada, K.; Morita, S.; Yoshino, K., *Synth. Met.*, **1991**, *41*, 855.
(12) Burroughes, J. H.; Jones, C. A.; Friend, R. H., *Nature*, **1988**, *335*, 137.
(13) Rumer, J. W.; Levick, M.; Dai, S. Y.; Rossbauer, S.; Huang, Z. G.; Biniek, L.; Anthopoulos, T. D.; Durrant, J. R.; Procter, D. J.; McCulloch, I., *Chem. Commun.*, **2013**, *49*, 4465.
(14) Baeg, K.-J.; Binda, M.; Natali, D.; Caironi, M.; Noh, Y.-Y., *Adv. Mater.*, **2013**, *25*, 4267.
(15) Gunes, S.; Neugebauer, H.; Sariciftci, N. S., *Chem. Rev.*, **2007**, *107*, 1324.
(16) AlSalhi, M. S.; Alam, J.; Dass, L. A.; Raja, M., *Int. J. Mol. Sci.*, **2011**, *12*, 2036.
(17) Wong, W. Y.; Ho, C. L., *Coord. Chem. Rev.*, **2006**, *250*, 2627.
(18) Korshak, V. V.; Sosin, S. L.; Alexeeva, V. P., *Dokl. Akad. Nauk. Sssr.*, **1960**, *132*, 360.
(19) Nguyen, P.; Gomez-Elipe, P.; Manners, I., *Chem. Rev.*, **1999**, *99*, 1515.
(20) Younus, M.; Long, N. J.; Raithby, P. R.; Lewis, J., *J. Organomet. Chem.*, **1998**, *570*, 55.
(21) Davies, S. J.; Johnson, B. F. G.; Lewis, J.; Raithby, P. R., *J. Organomet. Chem.*, **1991**, *414*, C51.
(22) Johnson, B. F. G.; Kakkar, A. K.; Khan, M. S.; Lewis, J., *J. Organomet. Chem.*, **1991**, *409*, C12.
(23) Matsuura, Y.; Tanaka, Y.; Akita, M., *J. Organomet. Chem.*, **2009**, *694*, 1840.
(24) Lavastre, O.; Plass, J.; Bachmann, P.; Guesmi, S.; Moinet, C.; Dixneuf, P. H., *Organometallics*, **1997**, *16*, 184.
(25) Zhu, Y. B.; Millet, D. B.; Wolf, M. O.; Rettig, S. J., *Organometallics*, **1999**, *18*, 1930.
(26) Bruce, M. I., *Chem. Rev.*, **1998**, *98*, 2797.
(27) Lewis, J.; Long, N. J.; Raithby, P. R.; Shields, G. P.; Wong, W. Y.; Younus, M., *J. Chem. Soc., Dalton Trans.*, **1997**, 4283.
(28) Lewis, J.; Raithby, P. R.; Wong, W. Y., *J. Organomet. Chem.*, **1998**, *556*, 219.
(29) Irwin, M. J.; Vittal, J. J.; Puddephatt, R. J., *Organometallics*, **1997**, *16*, 3541.
(30) Harriman, A.; Sauvage, J. P., *Chem. Soc. Rev.*, **1996**, *25*, 41.

(31) Grosshenny, V.; Harriman, A.; Ziessel, R., *Angew. Chem. Int. Ed.*, **1995**, *34*, 1100.
(32) Klein, A.; Lavastre, O.; Fiedler, J., *Organometallics*, **2006**, *25*, 635.
(33) Hou, S. J.; Chan, W. K., *Macromol. Rapid Commun.*, **1999**, *20*, 440.
(34) Altmann, M.; Bunz, U. H. F., *Macromol. Rapid Commun.*, **1994**, *15*, 785.
(35) Altmann, M.; Enkelmann, V.; Beer, F.; Bunz, U. H. F., *Organometallics*, **1996**, *15*, 394.
(36) Fink, H.; Long, N. J.; Martin, A. J.; Opromolla, G.; White, A. J. P.; Williams, D. J.; Zanello, P., *Organometallics*, **1997**, *16*, 2646.
(37) Long, N. J.; Martin, A. J.; de Biani, F. F.; Zanello, P., *J. Chem. Soc., Dalton Trans.*, **1998**, 2017.
(38) Long, N. J.; Martin, A. J.; White, A. J. P.; Williams, D. J.; Fontani, M.; Laschi, F.; Zanello, P., *J. Chem. Soc., Dalton Trans.*, **2000**, 3387.
(39) Yam, V. W. W.; Tao, C. H.; Zhang, L. J.; Wong, K. M. C.; Cheung, K. K., *Organometallics*, **2001**, *20*, 453.
(40) Long, N. J.; Williams, C. K., *Angew. Chem. Int. Ed.*, **2003**, *42*, 2586.
(41) Wong, K. M.-C.; Yam*, V. W.-W. In *Molecular Design and Applications of Photofunctional Polymers and Materials*; Wong, K. M.-C., Abd-El-Aziz, A. S., Eds.; The Royal Society of Chemistry: Cambridge, 2012, 245.
(42) Sakamoto, R.; Nishihara*, H. In *Molecular Design and Applications of Photofunctional Polymers and Materials*; Wong, K. M.-C., Abd-El-Aziz, A. S., Eds.; The Royal Society of Chemistry: Cambridge, 2012, 199.
(43) Jura, M.; Raithby*, P. R.; Wilson, P. J. In *Molecular Design and Applications of Photofunctional Polymers and Materials*; Wong, K. M.-C., Abd-El-Aziz, A. S., Eds.; The Royal Society of Chemistry: Cambridge, 2012, 56.
(44) Inkpen, M. S.; Long*, N. J. In *Molecular Design and Applications of Photofunctional Polymers and Materials*; Wong, K. M.-C., Abd-El-Aziz, A. S., Eds.; The Royal Society of Chemistry: 2012, 85.
(45) Ho, C.-L.; Wong*, W.-Y. In *Molecular Design and Applications of Photofunctional Polymers and Materials*; Wong, K. M.-C., Abd-El-Aziz, A. S., Eds.; The Royal Society of Chemistry: Cambridge, 2012, 1.
(46) Cheung, W. K.; Mak*, C. S. K. In *Molecular Design and Applications of Photofunctional Polymers and Materials*; Wong, K. M.-C., Abd-El-Aziz, A. S., Eds.; The Royal Society of Chemistry: Cambridge, 2012, 287.
(47) Brady, S. E.; Tyler*, D. R. In *Molecular Design and Applications of Photofunctional Polymers and Materials*; Wong, K. M.-C., Abd-El-Aziz, A. S., Eds.; The Royal Society of Chemistry: Cambridge, 2012, 31.
(48) Wong, W. Y., *Dalton Trans.*, **2007**, 4495.
(49) Staromlynska, J.; McKay, T. J.; Wilson, P., *J. Appl. Phys.*, **2000**, *88*, 1726.
(50) McKay, T. J.; Staromlynska, J.; Wilson, P.; Davy, J., *J. Appl. Phys.*, **1999**, *85*, 1337.
(51) Cetinkay.B; Lappert, M. F.; Mcmeekin.J; Palmer, D. E., *J. Chem. Soc., Dalton Trans.*, **1973**, 1202.
(52) Sonogashira, K.; Takahashi, S.; Hagihara, N., *Macromolecules*, **1977**, *10*, 879.
(53) Takahashi, S.; Kariya, M.; Yatake, T.; Sonogashira, K.; Hagihara, N., *Macromolecules*, **1978**, *11*, 1063.
(54) Khan, M. S.; Al-Mandhary, M. R. A.; Al-Suti, M. K.; Corcoran, T. C.; Al-Mahrooqi, Y.; Attfield, J. P.; Feeder, N.; David, W. I. F.; Shankland, K.;

Friend, R. H.; Kohler, A.; Marseglia, E. A.; Tedesco, E.; Tang, C. C.; Raithby, P. R.; Collings, J. C.; Roscoe, K. P.; Batsanov, A. S.; Stimson, L. M.; Marder, T. B., *New J. Chem.*, **2003**, *27*, 140.

(55) Brayshaw, S. K.; Schiffers, S.; Stevenson, A. J.; Teat, S. J.; Warren, M. R.; Bennett, R. D.; Sazanovich, I. V.; Buckley, A. R.; Weinstein, J. A.; Raithby, P. R., *Chem-Eur J*, **2011**, *17*, 4385.

(56) Devi, L. S.; Al-Suti, M. K.; Zhang, N.; Teat, S. J.; Male, L.; Sparkes, H. A.; Raithby, P. R.; Khan, M. S.; Kohler, A., *Macromolecules*, **2009**, *42*, 1131.

(57) Khan, M. S.; Al-Mandhary, M. R. A.; Al-Suti, M. K.; Al-Battashi, F. R.; Al-Saadi, S.; Ahrens, B.; Bjernemose, J. K.; Mahon, M. F.; Raithby, P. R.; Younus, M.; Chawdhury, N.; Kohler, A.; Marseglia, E. A.; Tedesco, E.; Feeder, N.; Teat, S. J., *Dalton Trans.*, **2004**, 2377.

(58) Jiang, B.; Chen, L. J.; Xu, L.; Liu, S. Y.; Yang, H. B., *Chem. Commun.*, **2013**, *49*, 6977.

(59) Khan, M. S.; Al-Suti, M. K.; Al-Mandhary, M. R. A.; Ahrens, B.; Bjernemose, J. K.; Mahon, M. F.; Male, L.; Raithby, P. R.; Friend, R. H.; Kohler, A.; Wilson, J. S., *Dalton Trans.*, **2003**, 65.

(60) Wilson, J. S.; Kohler, A.; Friend, R. H.; Al-Suti, M. K.; Al-Mandhary, M. R. A.; Khan, M. S.; Raithby, P. R., *J. Chem. Phys.*, **2000**, *113*, 7627.

(61) Markwell, R. D.; Butler, I. S.; Kakkar, A. K.; Khan, M. S.; AlZakwani, Z. H.; Lewis, J., *Organometallics*, **1996**, *15*, 2331.

(62) Chawdhury, N.; Kohler, A.; Friend, R. H.; Wong, W. Y.; Lewis, J.; Younus, M.; Raithby, P. R.; Corcoran, T. C.; Al-Mandhary, M. R. A.; Khan, M. S., *J. Chem. Phys.*, **1999**, *110*, 4963.

(63) James, E. C.; Jura, M.; Kociok-Kohn, G.; Raithby, P. R.; Sharp, E. L.; Wilson, P. J., *Inorg. Chem.*, **2007**, *46*, 7232.

(64) Poon, S. Y.; Wong, W. Y.; Cheah, K. W.; Shi, J. X., *Chem-Eur J*, **2006**, *12*, 2550.

(65) Wong, W. Y.; Poon, S. Y., *J. Inorg. Organomet. Polym.*, **2008**, *18*, 155.

(66) W.-Y. Wong; C.-Y. Wong; G.-L. Lu; K, -. W. C.; J.-X. Shi; Z. Lin, *Dalton Trans.*, **2002**, 4587.

(67) Rogers, J. E.; Cooper, T. M.; Fleitz, P. A.; Glass, D. J.; McLean, D. G., *J. Phys. Chem. A*, **2002**, *106*, 10108.

(68) Packheiser, R.; Ecorchard, P.; Ruffer, T.; Lang, H., *Organometallics*, **2008**, *27*, 3534.

(69) Soliman, A. M.; Fortin, D.; Harvey, P. D.; Zysman-Colman, E., *Chem. Commun.*, **2012**, *48*, 1120.

(70) Shiotsuka, M.; Nishiko, N.; Keyaki, K.; Nozaki, K., *Dalton Trans.*, **2010**, *39*, 1831.

(71) Wong, W. Y.; Wong, W. K.; Raithby, P. R., *J. Chem. Soc., Dalton Trans.*, **1998**, 2761.

(72) Long, N. J.; Martin, A. J.; Vilar, R.; White, A. J. P.; Williams, D. J.; Younus, M., *Organometallics*, **1999**, *18*, 4261.

(73) Creutz, C.; Taube, H., *J. Am. Chem. Soc.*, **1969**, *91*, 3988.

(74) Weiss, E. A.; Tauber, M. J.; Kelley, R. F.; Ahrens, M. J.; Ratner, M. A.; Wasielewski, M. R., *J. Am. Chem. Soc.*, **2005**, *127*, 11842.

(75) Low, P. J., *Dalton Trans.*, **2005**, 2821.

(76) Chisholm, M. H.; Patmore, N. J., *Chem Rec*, **2005**, *5*, 308.

(77) Cotton, F. A.; Donahue, J. P.; Murillo, C. A.; Perez, L. M., *J. Am. Chem. Soc.*, **2003**, *125*, 5486.

(78) M. B. Robin; P. Day, *Adv. Inorg. Chem. Radiochem.*, **1967**, *10*, 247.
(79) Brunschwig, B. S.; Creutz, C.; Sutin, N., *Chem. Soc. Rev.*, **2002**, *31*, 168.
(80) Chisholm, M. H.; Patmore, N. J., *Acc. Chem. Res.*, **2007**, *40*, 19.
(81) C. G. Zoski *Handbook of Electrochemistry*; Elsevier: Amsterdam, 2007.
(82) P. Zanello *Inorganic Electrochemistry; Theory, Practise and Application,*; Royal Society of Chemistry,: Cambridge, 2003.
(83) D'Alessandro, D. M.; Keene, F. R., *Dalton Trans.*, **2004**, 3950.
(84) N. S. Hush, *Prog. Inorg. Chem.*, **1967**, *8*, 391.
(85) Colbert, M. C. B.; Lewis, J.; Long, N. J.; Raithby, P. R.; Younus, M.; White, A. J. P.; Williams, D. J.; Payne, N. N.; Yellowlees, L.; Beljonne, D.; Chawdhury, N.; Friend, R. H., *Organometallics*, **1998**, *17*, 3034.
(86) Cowan, D. O.; Levanda, C.; Park, J.; Kaufman, F., *Acc. Chem. Res.*, **1973**, *6*, 1.
(87) Hupp, J. T.; Dong, Y. H.; Blackbourn, R. L.; Lu, H., *J. Phys. Chem.*, **1993**, *97*, 3278.
(88) Lear, B. J.; University of California, S. D. C. *The Effects of Electronic Delocalization in Highly Coupled Mixed Valence Systems*; University of California, San Diego, 2007; 14-16.
(89) Braun-Sand, S. B.; Wiest, O., *J. Phys. Chem. A*, **2003**, *107*, 285.
(90) Demadis, K. D.; Hartshorn, C. M.; Meyer, T. J., *Chem. Rev.*, **2001**, *101*, 2655.
(91) Lear, B. J.; Chisholm, M. H., *Inorg. Chem.*, **2009**, *48*, 10954.
(92) Cotton, F. A.; Curtis, N. F.; Johnson, B. F. G.; Mague, J. T.; Wood, J. S.; Harris, C. B.; Robinson, W. R.; Lippard, S. J., *Science*, **1964**, *145*, 1305.
(93) F. A. Cotton; C. A. Murillo; R. A. Walton *Multiple Bonds between Metal Atoms*; 3 ed.; Springer: New York, 2005.
(94) Cotton, F. A. *Advanced Inorganic Chemistry*; Wiley: Chichester, 1999.
(95) Chisholm, M. H.; Macintosh, A. M., *Chem. Rev.*, **2005**, *105*, 2949.
(96) Cotton, F. A.; Donahue, J. P.; Lin, C.; Murillo, C. A., *Inorg. Chem.*, **2001**, *40*, 1234.
(97) Cotton, F. A.; Jin, J. Y.; Li, Z.; Murillo, C. A.; Reibenspies, J. H., *Chem. Commun.*, **2008**, 211.
(98) Cayton, R. H.; Chisholm, M. H.; Huffman, J. C.; Lobkovsky, E. B., *J. Am. Chem. Soc.*, **1991**, *113*, 8709.
(99) Chisholm, M. H., *Acc. Chem. Res.*, **2000**, *33*, 53.
(100) Cotton, F. A.; Daniels, L. M.; Jordan, G. T.; Lin, C.; Murillo, C. A., *J. Am. Chem. Soc.*, **1998**, *120*, 3398.
(101) Cotton, F. A.; Li, Z.; Murillo, C. A.; Wang, X. P.; Yu, R. M.; Zhao, Q. L., *Inorg. Chem.*, **2007**, *46*, 3245.
(102) Cotton, F. A.; Daniels, L. M.; Jordan, G. T.; Lin, C.; Murillo, C. A., *Inorg Chem Commun*, **1998**, *1*, 109.
(103) Fang, W. J.; He, Q.; Tan, Z. F.; Liu, C. Y.; Lu, X.; Murillo, C. A., *Chem-Eur J*, **2011**, *17*, 10288.
(104) Tan, Z. F.; Liu, C. Y.; Li, Z. Y.; Meng, M.; Weng, N. S., *Inorg. Chem.*, **2012**, *51*, 2212.
(105) Cotton, F. A.; Daniels, L. M.; Guimet, I.; Henning, R. W.; Jordan, G. T.; Lin, C.; Murillo, C. A.; Schultz, A. J., *J. Am. Chem. Soc.*, **1998**, *120*, 12531.
(106) Wilkinson, L. A.; McNeill, L.; Meijer, A. J. H. M.; Patmore, N. J., *J. Am. Chem. Soc.*, **2013**, *135*, 1723.
(107) Chisholm, M. H.; Epstein, A. J.; Gallucci, J. C.; Feil, F.; Pirkle, W., *Angew. Chem. Int. Ed.*, **2005**, *44*, 6537.

(108) Brown-Xu, S. E.; Chisholm, M. H.; Durr, C. B.; Spilker, T. F., *J. Am. Chem. Soc.*, **2013**, *135*, 8254.
(109) Burdzinski, G. T.; Chisholm, M. H.; Chou, P. T.; Chou, Y. H.; Feil, F.; Gallucci, J. C.; Ghosh, Y.; Gustafson, T. L.; Ho, M. L.; Liu, Y.; Ramnauth, R.; Turro, C., *Proc. Natl. Acad. Sci. USA.*, **2008**, *105*, 15247.
(110) Brown-Xu, S. E.; Chisholm, M. H.; Gallucci, J. C.; Ghosh, Y.; Gustafson, T. L.; Reed, C. R., *Dalton Trans.*, **2012**, *41*, 2257.
(111) Chisholm, M. H.; Dann, A. S.; Dielmann, F.; Gallucci, J. C.; Patmore, N. J.; Ramnauth, R.; Scheer, M., *Inorg. Chem.*, **2008**, *47*, 9248.
(112) Calvo-Perez, V.; Vega, A.; Spodine, E., *Organometallics*, **2006**, *25*, 1953.
(113) Calvo-Perez, V.; Vega, A.; Cortes, P.; Spodine, E., *Inorg. Chim. Acta.*, **2002**, *333*, 15.
(114) Cotton, F. A.; Lin, C.; Murillo, C. A., *Inorg. Chem.*, **2001**, *40*, 575.
(115) Ke, Y. X.; Collins, D. J.; Zhou, H. C., *Inorg. Chem.*, **2005**, *44*, 4154.
(116) Cotton, F. A.; Liu, C. Y.; Murillo, C. A.; Wang, X. P., *Inorg. Chem.*, **2006**, *45*, 2619.
(117) Cotton, F. A.; Jin, J. Y.; Li, Z.; Liu, C. Y.; Murillo, C. A., *Dalton Trans.*, **2007**, 2328.
(118) Cotton, F. A.; Liu, C. Y.; Murillo, C. A., *Inorg. Chem.*, **2004**, *43*, 2267.
(119) Cotton, F. A.; Lin, C.; Murillo, C. A., *Inorg. Chem.*, **2001**, *40*, 478.
(120) Cotton, F. A.; Lin, C.; Murillo, C. A., *Inorg. Chem.*, **2001**, *40*, 472.
(121) Barybin, M. V.; Chisholm, M. H.; Dalal, N. S.; Holovics, T. H.; Patmore, N. J.; Robinson, R. E.; Zipse, D. J., *J. Am. Chem. Soc.*, **2005**, *127*, 15182.
(122) Byrnes, M. J.; Chisholm, M. H.; Clark, R. J. H.; Gallucci, J. C.; Hadad, C. M.; Patmore, N. J., *Inorg. Chem.*, **2004**, *43*, 6334.
(123) Lin, C.; Protasiewicz, J. D.; Smith, E. T.; Ren, T., *Inorg. Chem.*, **1996**, *35*, 6422.
(124) Chisholm, M. H.; Patmore, N. J., *Dalton Trans.*, **2006**, 3164.
(125) Han, M. J.; Liu, C. Y.; Tian, P. F., *Inorg. Chem.*, **2009**, *48*, 6347.
(126) Cotton, F. A.; Liu, C. Y.; Murillo, C. A.; Villagran, D.; Wang, X. P., *J. Am. Chem. Soc.*, **2003**, *125*, 13564.
(127) Cotton, F. A.; Daniels, L. M.; Donahue, J. P.; Liu, C. Y.; Murillo, C. A., *Inorg. Chem.*, **2002**, *41*, 1354.
(128) Bursten, B. E.; Chisholm, M. H.; Clark, R. J. H.; Firth, S.; Hadad, C. M.; MacIntosh, A. M.; Wilson, P. J.; Woodward, P. M.; Zaleski, J. M., *J. Am. Chem. Soc.*, **2002**, *124*, 3050.
(129) Chisholm, M. H.; Clark, R. J. H.; Gallucci, J.; Hadad, C. M.; Patmore, N. J., *J. Am. Chem. Soc.*, **2004**, *126*, 8303.
(130) Chisholm, M. H.; Feil, F.; Hadad, C. M.; Patmore, N. J., *J. Am. Chem. Soc.*, **2005**, *127*, 18150.
(131) Bursten, B. E.; Chisholm, M. H.; Hadad, C. M.; Li, J.; Wilson, P. J., *Chem. Commun.*, **2001**, 2382.
(132) Byrnes, M. J.; Chisholm, M. H.; Dye, D. F.; Hadad, C. M.; Pate, B. D.; Wilson, P. J.; Zaleski, J. M., *Dalton Trans.*, **2004**, 523.
(133) Cen, W.; Lindenfeld, P.; Fehlner, T. P., *J. Am. Chem. Soc.*, **1992**, *114*, 5451.
(134) Brown-Xu, S. E.; Chisholm, M. H.; Durr, C. B.; Gustafson, T. L.; Naseri, V.; Spilker, T. F., *J. Am. Chem. Soc.*, **2012**, *134*, 20820.
(135) Mashima, K.; Nakano, H.; Nakamura, A., *J. Am. Chem. Soc.*, **1996**, *118*, 9083.

(136) Mashima, K.; Nakano, H.; Nakamura, A., *J. Am. Chem. Soc.*, **1993**, *115*, 11632.
(137) Mashima, K.; Nakano, H.; Mori, T.; Takaya, H.; Nakamura, A., *Chem. Lett.*, **1992**, 185.
(138) Chisholm, M. H.; Hadad, C. M.; Heinze, K.; Hempel, K.; Singh, N.; Vyas, S., *J. Cluster Sci.*, **2008**, *19*, 209.
(139) Alberding, B. G.; Chisholm, M. H.; Gustafson, T. L.; Reed, C. R.; Singh, N.; Turro, C., *J. Cluster Sci.*, **2009**, *20*, 307.
(140) Towrie, M.; Parker, A. W.; Ronayne, K. L.; Bowes, K. F.; Cole, J. M.; Raithby, P. R.; Warren, J. E., *Appl. Spectrosc.*, **2009**, *63*, 57.
(141) Beljonne, D.; Wittmann, H. F.; Kohler, A.; Graham, S.; Younus, M.; Lewis, J.; Raithby, P. R.; Khan, M. S.; Friend, R. H.; Bredas, J. L., *J. Chem. Phys.*, **1996**, *105*, 3868.
(142) Zhou, G. J.; He, Y.; Yao, B.; Dang, J. S.; Wong, W. Y.; Xie, Z. Y.; Zhao, X. A.; Wang, L. X., *Chem-Asian J*, **2010**, *5*, 2405.
(143) Ho, C. L.; Wong, W. Y., *Coord. Chem. Rev.*, **2013**, *257*, 1614.
(144) Vivas, M. G.; Silva, D. L.; De Boni, L.; Bretonniere, Y.; Andraud, C.; Laibe-Darbour, F.; Mulatier, J. C.; Zalesny, R.; Bartkowiak, W.; Canuto, S.; Mendonca, C. R., *J. Phys. Chem. B*, **2012**, *116*, 14677.
(145) Yaegashi, M.; Shishido, A.; Shiono, T.; Ikeda, T., *Chem. Mater.*, **2005**, *17*, 4304.
(146) Romanazzi, G.; Dell'Aquila, A.; Suranna, G. P.; Marinelli, F.; Cotrone, S.; Altamura, D.; Giannini, C.; Torsi, L.; Mastrorilli, P., *J. Mater. Chem.*, **2011**, *21*, 15186.
(147) Long, E. M.; Brown, N. J.; Man, W. Y.; Fox, M. A.; Yufit, D. S.; Howard, J. A. K.; Low, P. J., *Inorg. Chim. Acta.*, **2012**, *380*, 358.
(148) Fox, M. A.; Harris, J. E.; Heider, S.; Perez-Gregorio, V.; Zakrzewska, M. E.; Farmer, J. D.; Yufit, D. S.; Howard, J. A. K.; Low, P. J., *J. Organomet. Chem.*, **2009**, *694*, 2350.
(149) Osakada, K.; Hamada, M.; Yamamoto, T., *Organometallics*, **2000**, *19*, 458.
(150) Werner, H.; Otto, H.; Ngokhac, T.; Burschka, C., *J. Organomet. Chem.*, **1984**, *262*, 123.
(151) Zhao, Y.; Zhang, P.; Li, B.; Meng, X. G.; Zhang, T. L., *Inorg. Chem.*, **2011**, *50*, 9097.
(152) Duan, J. X.; Zhang, L. H.; Dolbier, W. R., *Synlett*, **1999**, 1245.
(153) Miyakoshi, R.; Shimono, K.; Yokoyama, A.; Yokozawa, T., *J. Am. Chem. Soc.*, **2006**, *128*, 16012.
(154) Gothard, C. M.; Nowick, J. S., *J. Org. Chem.*, **2010**, *75*, 1822.
(155) Barbarella, G.; Zambianchi, M.; Ventola, A.; Fabiano, E.; Della Sala, F.; Gigli, G.; Anni, M.; Bolognesi, A.; Polito, L.; Naldi, M.; Capobianco, M., *Bioconjugate Chem.*, **2006**, *17*, 58.
(156) Shi, Z. W.; Liang, W.; Luo, J. D.; Huang, S.; Polishak, B. M.; Li, X. S.; Younkin, T. R.; Block, B. A.; Jen, A. K. Y., *Chem. Mater.*, **2010**, *22*, 5601.
(157) Sonogashira, K., *J. Organomet. Chem.*, **2002**, *653*, 46.
(158) Cooper, T. M.; Krein, D. M.; Burke, A. R.; McLean, D. G.; Haley, J. E.; Slagle, J.; Monahan, J.; Fratini, A., *J. Phys. Chem. A*, **2012**, *116*, 139.
(159) La Groia, A.; Ricci, A.; Bassetti, M.; Masi, D.; Bianchini, C.; Lo Sterzo, C., *J. Organomet. Chem.*, **2003**, *683*, 406.
(160) Caliendo, C.; Fratoddi, I.; Russo, M. V.; Lo Sterzo, C., *J. Appl. Phys.*, **2003**, *93*, 10071.

(161) Jagadeesh, S. G.; Reddy, L. M.; Nasjletti, A.; Falck, J. R., *Tetrahedron Lett.*, **2004**, *45*, 7111.
(162) Reetz, M. T.; Sommer, K., *Eur. J. Org. Chem.*, **2003**, 3485.
(163) Heasley, V. L.; Elliott, S. L.; Erdman, P. E.; Figueroa, D. E.; Krosley, K. W.; Louie, T. J.; Moore, H. B.; Mudge, B. P.; Nogales, D. F.; Nordeen, J.; Oakes, M. L.; Rosbrugh, J. W.; Sauerbrey, A. M.; Shibuya, T. Y.; Stanley, M. S.; Stewart, C. C.; Shellhamer, D. F.; Heasley, G. E., *J. Chem. Soc., Perkin Trans. 2*, **1991**, 393.
(164) Carpenter, J. P.; Lukehart, C. M., *Inorg. Chim. Acta.*, **1991**, *190*, 7.
(165) Zhu, L.; Agarwal, A.; Lai, J.; Al-Kaysi, R. O.; Tham, F. S.; Ghaddar, T.; Mueller, L.; Bardeen, C. J., *J. Mater. Chem.*, **2011**, *21*, 6258.
(166) More, R.; Scholz, M.; Busse, G.; Busse, L.; Paulmann, C.; Tolkiehn, M.; Techert, S., *Phys. Chem. Chem. Phys.*, **2012**, *14*, 10187.
(167) Charlier, J. C.; Michenaud, J. P.; Gonze, X., *Phys. Rev. B*, **1992**, *46*, 4531.
(168) Charlier, J. C.; Gonze, X.; Michenaud, J. P., *Carbon*, **1994**, *32*, 289.
(169) Charlier, J. C.; Gonze, X.; Michenaud, J. P., *Phys. Rev. B*, **1991**, *43*, 4579.
(170) Zhou, G. J.; Wong, W. Y.; Poon, S. Y.; Ye, C.; Lin, Z. Y., *Adv. Funct. Mater.*, **2009**, *19*, 531.
(171) Glimsdal, E.; Dragland, I.; Carlsson, M.; Eliasson, B.; Melo, T. B.; Lindgren, M., *J. Phys. Chem. A*, **2009**, *113*, 3311.
(172) Emmert, L. A.; Choi, W.; Marshall, J. A.; Yang, J.; Meyer, L. A.; Brozik, J. A., *J. Phys. Chem. A*, **2003**, *107*, 11340.
(173) Choi, C. L.; Cheng, Y. F.; Yip, C.; Phillips, D. L.; Yam, V. W. W., *Organometallics*, **2000**, *19*, 3192.
(174) Becke, A. D., *J. Chem. Phys.*, **1993**, *98*, 5648.
(175) Becke, A. D., *Phys. Rev. A*, **1988**, *38*, 3098.
(176) Wiberg, K. B., *J. Comput. Chem.*, **1986**, *7*, 379.
(177) Nguyen, K. A.; Day, P. N.; Pachter, R., *J. Phys. Chem. A*, **2009**, *113*, 13943.
(178) Glimsdal, E.; Carlsson, M.; Kindahl, T.; Lindgren, M.; Lopes, C.; Eliasson, B., *J. Phys. Chem. A*, **2010**, *114*, 3431.
(179) Green, K. A.; Cifuentes, M. P.; Corkery, T. C.; Samoc, M.; Humphrey, M. G., *Angew. Chem. Int. Ed.*, **2009**, *48*, 7867.
(180) Schmidbaur, H.; Schier, A., *Chem. Soc. Rev.*, **2012**, *41*, 370.
(181) Gao, L.; Partyka, D. V.; Updegraff, J. B.; Deligonul, N.; Gray, T. G., *Eur. J. Inorg. Chem.*, **2009**, *2009*, 2711.
(182) Zhou, Y. P.; Zhang, M.; Li, Y. H.; Guan, Q. R.; Wang, F.; Lin, Z. J.; Lam, C. K.; Feng, X. L.; Chao, H. Y., *Inorg. Chem.*, **2012**, *51*, 5099.
(183) Payne, N. C.; Ramachandran, R.; Puddephatt, R. J., *Can. J. Chem.*, **1995**, *73*, 6.
(184) Brown, D. J.; Chisholm, M. H.; Gallucci, J. C., *Dalton Trans.*, **2008**, 1615.
(185) Casas, J. M.; Cayton, R. H.; Chisholm, M. H., *Inorg. Chem.*, **1991**, *30*, 358.
(186) Chisholm, M. H., *Dalton Trans.*, **2003**, 3821.
(187) Cotton, F. A.; Jordan, G. T.; Murillo, C. A.; Su, J. R., *Polyhedron*, **1997**, *16*, 1831.
(188) Han, L. J.; Fan, L. Y.; Meng, M.; Wang, X. F.; Liu, C. Y., *Dalton Trans.*, **2011**, *40*, 12832.
(189) Cotton, F. A.; Daniels, L. M.; Hillard, E. A.; Murillo, C. A., *Inorg. Chem.*, **2002**, *41*, 1639.

(190) Alberding, B. G.; Chisholm, M. H.; Chou, Y.-H.; Gallucci, J. C.; Ghosh, Y.; Gustafson, T. L.; Patmore, N. J.; Reed, C. R.; Turro, C., *Inorg. Chem.*, **2009**, *48*, 4394.
(191) Bunting, P.; Chisholm, M. H.; Gallucci, J. C.; Lear, B. J., *J. Am. Chem. Soc.*, **2011**, *133*, 5873.
(192) Cotton, F. A.; Li, Z.; Liu, C. Y.; Murillo, C. A., *Inorg. Chem.*, **2007**, *46*, 7840.
(193) Cotton, F. A.; Liu, C. Y.; Murillo, C. A.; Zhao, Q. L., *Inorg. Chem.*, **2007**, *46*, 2604.
(194) Cotton, F. A.; Li, Z.; Liu, C. Y.; Murillo, C. A., *Inorg. Chem.*, **2006**, *45*, 9765.
(195) Yamaguchi, Y.; Ozaki, S.; Hinago, H.; Kobayashi, K.; Ito, T., *Inorg. Chim. Acta.*, **2005**, *358*, 2363.
(196) Cotton, F. A.; Feng, X. J.; Matusz, M., *Inorg. Chem.*, **1989**, *28*, 594.
(197) Dyker, G.; Kadzimirsz, D.; Thone, A., *Eur. J. Org. Chem.*, **2003**, 3162.
(198) Kang, S. H.; Ma, H.; Kang, M. S.; Kim, K. S.; Jen, A. K. Y.; Zareie, M. H.; Sarikaya, M., *Angew. Chem. Int. Ed.*, **2004**, *43*, 1512.
(199) Landgreb.Ja; Rynbrand.Rh, *J. Org. Chem.*, **1966**, *31*, 2585.
(200) Suzuki, T.; Ota, Y.; Kasuya, Y.; Mutsuga, M.; Kawamura, Y.; Tsumoto, H.; Nakagawa, H.; Finn, M. G.; Miyata, N., *Angew. Chem. Int. Ed.*, **2010**, *49*, 6817.
(201) Wu, Y. Y.; Kao, Y. C.; Chen, J. D.; Hung, C. H., *Inorg. Chim. Acta.*, **2004**, *357*, 1002.
(202) Cotton, F. A.; Mester, Z. C.; Webb, T. R., *Acta Crystallogr. B*, **1974**, *B 30*, 2768.
(203) Ogawa, H.; Onitsuka, K.; Joh, T.; Takahashi, S.; Yamamoto, Y.; Yamazaki, H., *Organometallics*, **1988**, *7*, 2257.
(204) Norman, J. G.; Kolari, H. J.; Gray, H. B.; Trogler, W. C., *Inorg. Chem.*, **1977**, *16*, 987.
(205) Cotton, F. A.; Li, Z.; Liu, C. Y.; Murillo, C. A.; Villagran, D., *Inorg. Chem.*, **2006**, *45*, 767.
(206) Alberding, B. G.; Chisholm, M. H.; Gallucci, J. C.; Ghosh, Y.; Gustafson, T. L., *Proc. Natl. Acad. Sci. USA.*, **2011**, *108*, 8152.
(207) Grundy, J.; Coles, M. P.; Hitchcock, P. B., *J. Organomet. Chem.*, **2002**, *662*, 178.
(208) Grundy, J.; Coles, M. P.; Hitchcock, P. B., *New J. Chem.*, **2004**, *28*, 1195.
(209) Clare, B.; Sarker, N.; Shoemaker, R.; Hagadorn, J. R., *Inorg. Chem.*, **2004**, *43*, 1159.
(210) Baker, R. J.; Jones, C., *J. Organomet. Chem.*, **2006**, *691*, 65.
(211) Jenkins, H. A.; Abeysekera, D.; Dickie, D. A.; Clyburne, J. A. C., *J. Chem. Soc., Dalton Trans.*, **2002**, 3919.
(212) Coles, M. P., *Dalton Trans.*, **2006**, 985.
(213) Seidel, W. W.; Dachtler, W.; Pape, T., *Z. Anorg. Allg. Chem.*, **2012**, *638*, 116.
(214) Zhou, S. L.; Wang, S. W.; Yang, G. H.; Li, Q. H.; Zhang, L. J.; Yao, Z. J.; Zhou, Z. K.; Song, H. B., *Organometallics*, **2007**, *26*, 3755.
(215) Boere, R. T.; Klassen, V.; Wolmershauser, G., *J. Chem. Soc., Dalton Trans.*, **1998**, 4147.
(216) Schmidt, J. A. R.; Arnold, J., *Chem. Commun.*, **1999**, 2149.
(217) Schmidt, J. A. R.; Arnold, J., *J. Chem. Soc., Dalton Trans.*, **2002**, 2890.
(218) Hayashida, T.; Miyazaki, K.; Yamaguchi, Y.; Nagashima, H., *J. Organomet. Chem.*, **2001**, *634*, 167.

(219) Terasawa, J. I.; Kondo, H.; Matsumoto, T.; Kirchner, K.; Motoyama, Y.; Nagashima, H., *Organometallics*, **2005**, *24*, 2713.
(220) Kondo, H.; Matsubara, K.; Nagashima, H., *J. Am. Chem. Soc.*, **2002**, *124*, 534.
(221) Banerjee, P.; Das, S.; Fanwick, P. E.; Goswami, S., *J. Organomet. Chem.*, **2006**, *691*, 2915.
(222) Hayashida, T.; Nagashima, H., *Organometallics*, **2002**, *21*, 3884.
(223) Hayashida, T.; Kondo, H.; Terasawa, J.; Kirchner, K.; Sunada, Y.; Nagashima, H., *J. Organomet. Chem.*, **2007**, *692*, 382.
(224) Nagashima, H.; Gondo, M.; Masuda, S.; Kondo, H.; Yamaguchi, Y.; Matsubara, K., *Chem. Commun.*, **2003**, 442.
(225) Hayashida, T.; Yamaguchi, Y.; Kirchner, K.; Nagashima, H., *Chem. Lett.*, **2001**, 954.
(226) Kondo, H.; Sue, T.; Kageyama, A.; Yamaguchi, Y.; Sunada, Y.; Nagashima, H., *J. Organomet. Chem.*, **2009**, *694*, 795.
(227) Robinson, S. D.; Sahajpal, A.; Steed, J., *Inorg. Chim. Acta.*, **2000**, *303*, 265.
(228) Holman, K. T.; Robinson, S. D.; Sahajpal, A.; Steed, J. W., *J. Chem. Soc., Dalton Trans.*, **1999**, 15.
(229) Zhang, J. B.; Gunnoe, T. B.; Peterson, J. L., *Inorg. Chem.*, **2005**, *44*, 2895.
(230) Bailey, P. J.; Mitchell, L. A.; Parsons, S., *J. Chem. Soc., Dalton Trans.*, **1996**, 2839.
(231) Dinger, M. B.; Henderson, W.; Nicholson, B. K., *J. Organomet. Chem.*, **1998**, *556*, 75.
(232) Singh, T.; Kishan, R.; Nethaji, M.; Thirupathi, N., *Inorg. Chem.*, **2012**, *51*, 157.
(233) Winter, S.; Weber, E.; Eriksson, L.; Csoregh, I., *New J. Chem.*, **2006**, *30*, 1808.
(234) Surin, M.; Samori, P.; Jouaiti, A.; Kyritsakas, N.; Hosseini, M. W., *Angew. Chem. Int. Ed.*, **2007**, *46*, 245.
(235) Nguyen, P.; Todd, S.; Vandenbiggelaar, D.; Taylor, N. J.; Marder, T. B.; Wittmann, F.; Friend, R. H., *Synlett*, **1994**, 299.
(236) Fasina, T. M.; Collings, J. C.; Lydon, D. P.; Albesa-Jove, D.; Batsanov, A. S.; Howard, J. A. K.; Nguyen, P.; Bruce, M.; Scott, A. J.; Clegg, W.; Watt, S. W.; Viney, C.; Marder, T. B., *J. Mater. Chem.*, **2004**, *14*, 2395.
(237) Dang, H.; Levitus, M.; Garcia-Garibay, M. A., *J. Am. Chem. Soc.*, **2002**, *124*, 136.
(238) Hoshino, Y.; Suzuki, T.; Umeda, H., *Inorg. Chim. Acta.*, **1996**, *245*, 87.
(239) Handa, M.; Yamada, K.; Nakao, T.; Kasuga, K.; Mikuriya, M.; Kotera, T., *Chem. Lett.*, **1993**, 1969.
(240) Santure, D. J.; Huffman, J. C.; Sattelberger, A. P., *Inorg. Chem.*, **1984**, *23*, 938.
(241) Majumdar, M.; Rahaman, S. M. W.; Sinha, A.; Bera, J. K., *Inorg. Chim. Acta.*, **2010**, *363*, 3078.
(242) Cotton, F. A.; Falvello, L. R.; Han, S.; Wang, W., *Inorg. Chem.*, **1983**, *22*, 4106.
(243) Cayton, R. H.; Chisholm, M. H.; Huffman, J. C.; Lobkovsky, E. B., *Angew. Chem. Int. Ed.*, **1991**, *30*, 862.
(244) Cayton, R. H.; Chacon, S. T.; Chisholm, M. H.; Folting, K., *Polyhedron*, **1993**, *12*, 415.

(245) Baral, S.; Cotton, F. A.; Ilsley, W. H.; Kaim, W., *Inorg. Chem.*, **1982**, *21*, 1644.
(246) Li, B.; Zhang, H.; Huynh, L.; Shatruk, M.; Dikarev, E. V., *Inorg. Chem.*, **2007**, *46*, 9155.
(247) Kerby, M. C.; Eichhorn, B. W.; Creighton, J. A.; Vollhardt, K. P. C., *Inorg. Chem.*, **1990**, *29*, 1319.
(248) Campana, C.; Dunbar, K. R.; Ouyang, X., *Chem. Commun.*, **1996**, 2427.
(249) Kuang, S. M.; Fanwick, P. E.; Walton, R. A., *Inorg Chem Commun*, **2002**, *5*, 134.
(250) Cotton, F. A.; Lay, D. G., *Inorg. Chem.*, **1981**, *20*, 935.
(251) Girolami, G. S.; Mainz, V. V.; Andersen, R. A., *Inorg. Chem.*, **1980**, *19*, 805.
(252) Mountford, P.; Williams, J. A. G., *J. Chem. Soc., Dalton Trans.*, **1993**, 877.
(253) Girolami, G. S.; Andersen, R. A., *Inorg. Chem.*, **1982**, *21*, 1318.
(254) Santure, D. J.; Sattelberger, A. P., *Inorg. Chem.*, **1985**, *24*, 3477.
(255) Santure, D. J.; Mclaughlin, K. W.; Huffman, J. C.; Sattelberger, A. P., *Inorg. Chem.*, **1983**, *22*, 1877.
(256) Arduengo, A. J.; Harlow, R. L.; Kline, M., *J. Am. Chem. Soc.*, **1991**, *113*, 361.
(257) Herrmann, W. A.; Kocher, C., *Angew. Chem. Int. Ed.*, **1997**, *36*, 2162.
(258) Gusev, D. G., *Organometallics*, **2009**, *28*, 6458.
(259) Dorta, R.; Stevens, E. D.; Scott, N. M.; Costabile, C.; Cavallo, L.; Hoff, C. D.; Nolan, S. P., *J. Am. Chem. Soc.*, **2005**, *127*, 2485.
(260) Clavier, H.; Nolan, S. P., *Chem. Commun.*, **2010**, *46*, 841.
(261) Huang, J. K.; Schanz, H. J.; Stevens, E. D.; Nolan, S. P., *Organometallics*, **1999**, *18*, 2370.
(262) Tolman, C. A., *Chem. Rev.*, **1977**, *77*, 313.
(263) Clayden, J.; Greeves, N.; Warren, S. *Organic Chemistry*; OUP Oxford, 2012.
(264) Cotton, F. A.; Extine, M.; Gage, L. D., *Inorg. Chem.*, **1978**, *17*, 172.
(265) Macrae, C. F.; Bruno, I. J.; Chisholm, J. A.; Edgington, P. R.; McCabe, P.; Pidcock, E.; Rodriguez-Monge, L.; Taylor, R.; van de Streek, J.; Wood, P. A., *J. Appl. Crystallogr.*, **2008**, *41*, 466.
(266) Wu, F.; Dioumaev, V. K.; Szalda, D. J.; Hanson, J.; Bullock, R. M., *Organometallics*, **2007**, *26*, 5079.
(267) Ofele, K.; Herrmann, W. A.; Mihalios, D.; Elison, M.; Herdtweck, E.; Priermeier, T.; Kiprof, P., *J. Organomet. Chem.*, **1995**, *498*, 1.
(268) Buhro, W. E.; Chisholm, M. H.; Martin, J. D.; Huffman, J. C.; Folting, K.; Streib, W. E., *J. Am. Chem. Soc.*, **1989**, *111*, 8149.
(269) Trindade, A. F.; Gois, P. M. P.; Veiros, L. F.; Andre, V.; Duarte, M. T.; Afonso, C. A. M.; Caddick, S.; Cloke, F. G. N., *J. Org. Chem.*, **2008**, *73*, 4076.
(270) Na, S. J.; Lee, B. Y.; Bui, N. N.; Mho, S. I.; Jang, H. Y., *J. Organomet. Chem.*, **2007**, *692*, 5523.
(271) Kwak, J.; Kim, M.; Chang, S., *J. Am. Chem. Soc.*, **2011**, *133*, 3780.
(272) Snyder, J. P.; Padwa, A.; Stengel, T.; Arduengo, A. J.; Jockisch, A.; Kim, H. J., *J. Am. Chem. Soc.*, **2001**, *123*, 11318.
(273) Cotton, F. A.; Norman, J. G., *J. Am. Chem. Soc.*, **1972**, *94*, 5697.
(274) Trogler, W. C.; Gray, H. B., *Abstr. Pap. Am. Chem. Soc.*, **1977**, *174*, 26.
(275) Alberding, B. G.; Brown-Xu, S. E.; Chisholm, M. H.; Gallucci, J. C.; Gustafson, T. L.; Naseri, V.; Reed, C. R.; Turro, C., *Dalton Trans.*, **2012**, *41*, 12270.

(276) Gorodetsky, B.; Ramnial, T.; Branda, N. R.; Clyburne, J. A. C., *Chem. Commun.*, **2004**, 1972.
(277) Jafarpour, L.; Stevens, E. D.; Nolan, S. P., *J. Organomet. Chem.*, **2000**, *606*, 49.
(278) Jeffrey, G. A. *An Introduction to Hydrogen Bonding*; Oxford University Press, 1997.
(279) Teramoto, K.; Sasaki, Y.; Migita, K.; Iwaizumi, M.; Saito, K., *Bull. Chem. Soc. Jpn.*, **1979**, *52*, 446.
(280) Dobson, A.; Robinson, S. D., *Inorg. Chem.*, **1977**, *16*, 1321.
(281) Santure, D. J.; Huffman, J. C.; Sattelberger, A. P., *Inorg. Chem.*, **1985**, *24*, 371.
(282) Stoner, T. C.; Geib, S. J.; Hopkins, M. D., *Angew. Chem. Int. Ed.*, **1993**, *32*, 409.
(283) Stoner, T. C.; Dallinger, R. F.; Hopkins, M. D., *J. Am. Chem. Soc.*, **1990**, *112*, 5651.
(284) John, K. D.; Stoner, T. C.; Hopkins, M. D., *Organometallics*, **1997**, *16*, 4948.
(285) Green, M. L. H.; Parkin, G.; Bashkin, J.; Fail, J.; Prout, K., *J. Chem. Soc., Dalton Trans.*, **1982**, 2519.
(286) Arenivar, J. D.; Mainz, V. V.; Ruben, H.; Andersen, R. A.; Zalkin, A., *Inorg. Chem.*, **1982**, *21*, 2649.
(287) Suen, M. C.; Chen, J. D.; Keng, T. C.; Wang, J. C., *J. Chin. Chem. Soc.*, **2003**, *50*, 233.
(288) Bursten, B. E.; Darensbourg, D. J.; Kellogg, G. E.; Lichtenberger, D. L., *Inorg. Chem.*, **1984**, *23*, 4361.
(289) Baldo, M. A.; O'Brien, D. F.; You, Y.; Shoustikov, A.; Sibley, S.; Thompson, M. E.; Forrest, S. R., *Nature*, **1998**, *395*, 151.
(290) Lu, W.; Mi, B. X.; Chan, M. C. W.; Hui, Z.; Che, C. M.; Zhu, N. Y.; Lee, S. T., *J. Am. Chem. Soc.*, **2004**, *126*, 4958.
(291) Zhou, G. J.; Wong, W. Y., *Chem. Soc. Rev.*, **2011**, *40*, 2541.
(292) Coppens, P.; Vorontsov, I. I.; Graber, T.; Gembicky, M.; Kovalevsky, A. Y., *Acta Crystallogr. A*, **2005**, *61*, 162.
(293) Shikhova, E.; Danilov, E. O.; Kinayyigit, S.; Pomestchenko, I. E.; Tregubov, A. D.; Camerel, F.; Retailleau, P.; Ziessel, R.; Castellano, F. N., *Inorg. Chem.*, **2007**, *46*, 3038.
(294) Liu, R.; Chen, H. B.; Chang, J.; Li, Y. H.; Zhu, H. J.; Sun, W. F., *Dalton Trans.*, **2013**, *42*, 160.
(295) Coppens, P.; Gerlits, O.; Vorontsov, I. I.; Kovalevsky, A. Y.; Chen, Y. S.; Graber, T.; Gembicky, M.; Novozhilova, I. V., *Chem. Commun.*, **2004**, 2144.
(296) Kim, C. D.; Pillet, S.; Wu, G.; Fullagar, W. K.; Coppens, P., *Acta Crystallogr. A*, **2002**, *58*, 133.
(297) George, M. W.; Turner, J. J., *Coord. Chem. Rev.*, **1998**, *177*, 201.
(298) Calladine, J. A.; Duckett, S. B.; George, M. W.; Matthews, S. L.; Perutz, R. N.; Torres, O.; Khuong, Q. V., *J. Am. Chem. Soc.*, **2011**, *133*, 2303.
(299) Batool, M.; Martin, T. A.; Algarra, A. G.; George, M. W.; Macgregor, S. A.; Mahon, M. F.; Whittlesey, M. K., *Organometallics*, **2012**, *31*, 4971.
(300) Weinstein, J. A.; Grills, D. C.; Towrie, M.; Matousek, P.; Parker, A. W.; George, M. W., *Chem. Commun.*, **2002**, 382.
(301) Vlcek, A.; Farrell, I. R.; Liard, D. J.; Matousek, P.; Towrie, M.; Parker, A. W.; Grills, D. C.; George, M. W., *J. Chem. Soc., Dalton Trans.*, **2002**, 701.
(302) Kaucikas, M.; Barber, J.; Van Thor, J. J., *Opt. Express*, **2013**, *21*, 8357.

(303) Wang, Y. H.; Yuzawa, T.; Hamaguchi, H. O.; Toscano, J. P., *J. Am. Chem. Soc.*, **1999**, *121*, 2875.
(304) Pritchina, E. A.; Gritsan, N. P.; Maltsev, A.; Bally, T.; Autrey, T.; Liu, Y. L.; Wang, Y. H.; Toscano, J. P., *Phys. Chem. Chem. Phys.*, **2003**, *5*, 1010.
(305) Stoner-Ma, D.; Jaye, A. A.; Matousek, P.; Towrie, M.; Meech, S. R.; Tonge, P. J., *J. Am. Chem. Soc.*, **2005**, *127*, 2864.
(306) Blake, A. J.; Champness, N. R.; Easun, T. L.; Allan, D. R.; Nowell, H.; George, M. W.; Jia, J.; Sun, X. Z., *Nat. Chem.*, **2010**, *2*, 688.
(307) Chen, P. Y.; Omberg, K. M.; Kavaliunas, D. A.; Treadway, J. A.; Palmer, R. A.; Meyer, T. J., *Inorg. Chem.*, **1997**, *36*, 954.
(308) Omberg, K. M.; Smith, G. D.; Kavaliunas, D. A.; Chen, P. Y.; Treadway, J. A.; Schoonover, J. R.; Palmer, R. A.; Meyer, T. J., *Inorg. Chem.*, **1999**, *38*, 951.
(309) Whittle, C. E.; Weinstein, J. A.; George, M. W.; Schanze, K. S., *Inorg. Chem.*, **2001**, *40*, 4053.
(310) Adams, C. J.; Fey, N.; Harrison, Z. A.; Sazanovich, I. V.; Towrie, M.; Weinstein, J. A., *Inorg. Chem.*, **2008**, *47*, 8242.
(311) Glik, E. A.; Kinayyigit, S.; Ronayne, K. L.; Towrie, M.; Sazanovich, I. V.; Weinstein, J. A.; Castellano, F. N., *Inorg. Chem.*, **2008**, *47*, 6974.
(312) Cooper, T. M.; Blaudeau, J. P.; Hall, B. C.; Rogers, J. E.; McLean, D. G.; Liu, Y. L.; Toscano, J. P., *Chem. Phys. Lett.*, **2004**, *400*, 239.
(313) Yeh, A. T.; Shank, C. V.; McCusker, J. K., *Science*, **2000**, *289*, 935.
(314) Riesen, H.; Wallace, L.; Krausz, E., *Inorg. Chem.*, **1996**, *35*, 6908.
(315) Gold, J. S.; Milder, S. J.; Lewis, J. W.; Kliger, D. S., *J. Am. Chem. Soc.*, **1985**, *107*, 8285.
(316) Byrnes, M. J.; Chisholm, M. H.; Gallucci, J. A.; Liu, Y.; Ramnauth, R.; Turro, C., *J. Am. Chem. Soc.*, **2005**, *127*, 17343.
(317) Alberding, B. G.; Chisholm, M. H.; Gustafson, T. L., *Inorg. Chem.*, **2012**, *51*, 491.
(318) Alberding, B. G.; Brown-Xu, S. E.; Chisholm, M. H.; Gustafson, T. L.; Reed, C. R.; Naseri, V., *Dalton Trans.*, **2012**, *41*, 13097.
(319) Alberding, B. G.; Brown-Xu, S. E.; Chisholm, M. H.; Epstein, A. J.; Gustafson, T. L.; Lewis, S. A.; Min, Y., *Dalton Trans.*, **2013**, *42*, 5275.
(320) Burdzinski, G. T.; Ramnauth, R.; Chisholm, M. H.; Gustafson, T. L., *J. Am. Chem. Soc.*, **2006**, *128*, 6776.
(321) Hamm, P.; Ohline, S. M.; Zinth, W., *J. Chem. Phys.*, **1997**, *106*, 519.
(322) Mills, P.; Korlann, S.; Bussell, M. E.; Reynolds, M. A.; Ovchinnikov, M. V.; Angelici, R. J.; Stinner, C.; Weber, T.; Prins, R., *J. Phys. Chem. A*, **2001**, *105*, 4418.
(323) Powell, C. E.; Humphrey, M. G., *Coord. Chem. Rev.*, **2004**, *248*, 725.
(324) Chan, C. K. M.; Tao, C. H.; Li, K. F.; Wong, K. M. C.; Zhu, N. Y.; Cheah, K. W.; Yam, V. W. W., *Dalton Trans.*, **2011**, *40*, 10670.
(325) Tao, C. H.; Yang, H.; Zhu, N. Y.; Yam, V. W. W.; Xu, S. J., *Organometallics*, **2008**, *27*, 5453.
(326) Johnson, A. L.; Raithby, P. R.; Robinson, T. P.; Towrie, M., *Unpublished works*.
(327) Brown-Xu, S. E.; Chisholm, M. H.; Durr, C. B.; Lewis, S. A.; Spilker, T. F.; Young, P. J., *Inorg. Chem.*, **2013**, *53*, 637.
(328) Brown-Xu, S. E.; Chisholm, M. H.; Durr, C. B.; Lewis, S. A.; Spilker, T. F.; Young, P. J., *Inorg. Chem.*, **2014**, *53*, 637.

(329) Sheldrick, G. M., *Acta Crystallogr. A*, **2008**, *64*, 112.
(330) Lee, C.; Yang, W.; Parr, R. G., *Phys. Rev. B*, **1988**, *37*, 785.
(331) Becke, A. D., *J. Chem. Phys.*, **1993**, *98*, 5648.
(332) Frisch, M. J.; Revision D.01 ed.; M. J. Frisch *et al*. Gaussian, Inc., Wallingford CT: 2004, p Gaussian 03.
(333) Andrae, D.; Haussermann, U.; Dolg, M.; Stoll, H.; Preuss, H., *Theor. Chim. Acta*, **1990**, *77*, 123.
(334) Ditchfield, R.; Hehre, W. J.; Pople, J. A., *J. Chem. Phys.*, **1971**, *54*, 724.
(335) Hariharan, P. C.; Pople, J. A., *Theor. Chem. Acta.*, **1973**, *28*, 213.
(336) Varetto, U.; Giuffreda, M. G.; Jang, Y., *Abstr. Pap. Am. Chem. Soc.*, **2009**, *238*.
(337) Leonid, S., *Chemissian Version 1.771*, **2005-2010**.
(338) Towrie, M.; Grills, D. C.; Dyer, J.; Weinstein, J. A.; Matousek, P.; Barton, R.; Bailey, P. D.; Subramaniam, N.; Kwok, W. M.; Ma, C. S.; Phillips, D.; Parker, A. W.; George, M. W., *Appl. Spectrosc.*, **2003**, *57*, 367.
(339) Siegmann, K.; Pregosin, P. S.; Venanzi, L. M., *Organometallics*, **1989**, *8*, 2659.
(340) Parshall, G. W., *J. Am. Chem. Soc.*, **1964**, *86*, 5367.
(341) Parshall, G., W., *Inorg. Synth.*, **1970**, *12*, 27.
(342) A. B. Brignole; F. A. Cotton, *Inorg. Synth.*, **1972**, *13*, 81.
(343) Bradley, W.; Wright, I., *J. Chem. Soc.*, **1956**, 640.
(344) Cotton, F. A.; Haefner, S. C.; Matonic, J. H.; Wang, X. P.; Murillo, C. A., *Polyhedron*, **1997**, *16*, 541.
(345) Heuft, M. A.; Collins, S. K.; Yap, G. P. A.; Fallis, A. G., *Org. Lett.*, **2001**, *3*, 2883.
(346) Pelter, A.; Jones, D. E., *J. Chem. Soc., Perkin Trans. 1*, **2000**, 2289.
(347) Nagai, A.; Miyake, J.; Kokado, K.; Nagata, Y.; Chujo, Y., *J. Am. Chem. Soc.*, **2008**, *130*, 15276.
(348) Ou, Y. P.; Jiang, C. Y.; Wu, D.; Xia, J. L.; Yin, J.; Jin, S.; Yu, G. A.; Liu, S. H., *Organometallics*, **2011**, *30*, 5763.
(349) Bennett, M. A.; Huang, T. N.; Matheson, T. W.; Smith, A. K., *Inorg. Synth.*, **1982**, *21*, 74.
(350) Arduengo, A. J.; Dias, H. V. R.; Harlow, R. L.; Kline, M., *J. Am. Chem. Soc.*, **1992**, *114*, 5530.
(351) Kuhn, N.; Kratz, T., *Synthesis-Stuttgart*, **1993**, 561.